Investigation of Machinability and Dust Emissions in Edge Trimming of Laminated Carbon Fiber Composites

Jeffrey Lawrence Miller

A dissertation

submitted in partial fulfillment of the

requirements for the degree of

Doctor of Philosophy

University of Washington

2014

Reading Committee:

Ramulu Mamidala, Chair

Mark Tuttle

Daniel Sanders

Program Authorized to offer Degree:

Mechanical Engineering

University of Washington

Abstract

Investigation of Machinability and Dust Emissions in Edge Trimming of Laminated Carbon Fiber Composites

Jeffrey Lawrence Miller

Chair of the Supervisory Committee:
Professor Ramulu Mamidala
Department of Mechanical Engineering

The use of carbon fiber reinforced plastic (CFRP) systems for product structures has been steadily increasing because of superior material properties, including high strength, low weight, and corrosion resistance. CFRP parts may be molded to near net-shape geometry; however, machining operations are often necessary to provide final shape. Edge trimming by the milling process is commonly employed to provide required surface finish and dimensional accuracy and can be performed wet or dry. CFRP does not machine similar to ductile metals as the chip formation mechanism consists mostly of a series of brittle factures by shearing of the fibers and matrix where ductile metals produce a uniform chip through plastic deformation. In dry machining, CFRP produces powder like chips or dust which are electrically conductive and currently classified as a nuisance particulate. Further machining challenges of CRFP include delamination, fuzzing, fiber pullout, and short tool life due to the inhomogeneity of the material and abrasive nature of the fibers.

In this work, experimental studies were performed to determine methods best suited to analyze dust particles generated from machining of composite materials. Data was initially collected using cascade impactors where mass median aerodynamic diameter (MMAD) was found to be .12 μm - .35 μm when machining at 0^o to 135^o of fiber direction without using local exhaust ventilation. Real-time particle analysis instruments were introduced into the test protocol which demonstrated the ability to reduce sampling times from greater than 6 minutes to

as short as 30 seconds without the need of an additional 48 hours of filter conditioning. Dust profiles where found consistent between six real-time instruments evaluated for this application including four used in a unique isokinetic configuration designed specifically for dust analysis of particle producing manufacturing processes.

A major development from this research is a process to safely and completely analyze all dust produced from machining of carbon fiber laminates using isokinetic sampling of particles as they travel from the work piece to a dust collection system with short sample times. This is a significant improvement over existing methods which involve open air sampling or recovering dust from vacuum filters. Dust was analyzed using both cascade impactors and with parallel use of real-time instruments. Dust concentrations from typical edge trimming conditions were found to exceed permissible limits of 5 mg/m^3 for nuisance dust at the source, thus meriting the use of fully self-contained systems for collection and analysis. Supporting analysis tools were developed that enable comparison of dust concentrations reported by different instruments and measured gravimetrically.

A method to determine cutting force at the cutting edge and cutting coefficients used in a mechanistic model for cutting force prediction of multi-directional composite laminates was also demonstrated. In this method milling force cutting coefficients are empirically determined for all cutting orientations using a series of milled semi-circular slots that incorporate the effects of fiber orientation in unidirectional laminates. In limited testing, linearity was found with a correlation coefficient greater than .99 using tangential forces from a rotating dynamometer for determination of tangential and edge milling coefficients and an average of .77 using radial force for radial and edge coefficients.

TABLE OF CONTENTS

Page

LIST OF FIGURES

LIST OF TABLES

APPENDICES

ACKNOWLEDGEMENTS

I would first like to acknowledge the University of Washington, Department of Mechanical Engineering for providing me with the opportunity to pursue a PhD. The Department made this possible while still enabling me to work full time. My deepest gratitude is extended to Professor Ramulu. Without his encouragement and tireless support I would not be where I am today. His dedication to students is unmatched and rarely a Saturday goes by where he is not in his office ready to help. I would also like to thank my PhD Committee of Professor Mark Tuttle, Professor Joseph Garbini, Dr. Daniel Sanders, and GSR Professor Kuen Lin for their time and constructive feedback. My sincere appreciation to Professor Michael Kleinman from the University of California, Irvine, for his support in the pursuit of dust particle studies and loaning of several key instruments for the investigation. My thanks also to Professor Tim Larson and Tim Gould from the University of Washington Civil Engineering Department for providing access to their weighing lab and for guidance and support of particle analysis. I would also like to thank the present and former MSTL students whom I shared a lab with for their assistance. My gratitude also to the ME Student Machine Shop where I spent numerous hours building parts for the experiments and could always get support when needed. Finally, I would also like to thank The Boeing Company Learning Together Program for supporting my continuing education.

DEDICATION

I dedicate this work to my wife and kids without whose support I could not have pursued this endeavor.

CHAPTER 1

INTRODUCTION

The application of fiber reinforced polymer composite materials is being used in increasing quantities in advanced structures because of its superior specific strength and stiffness relative to other material systems including metals. Major structural application areas include aircraft, space, automotive, sporting goods, marine, and infrastructure. Other application areas include electronics with fiber reinforced polymer composites being used for circuit boards. In the medical industry, composites are being used for sockets, implants, and prosthetic limbs. Many industrial products utilize composites including ladders, tanks, and power transmission shafts. The power industry is utilizing fiber reinforced composites for wind generation and transformer housings. The potential use exists in many additional fields that would benefit from the performance advantages of composites including, but not limited to, the ability to produce near net shape parts, design flexibility, increased specific strength, corrosion resistance, dimensional stability, and fatigue damage tolerance. Fiber reinforced polymer composites are being utilized in increasing percentages of the total structural weight for both military and commercial aircraft where weight reduction is essential for higher speeds, increased payloads, and improved fuel economy. Starting with the use of boron fiber-reinforced epoxy skins for the F-14 stabilizers in 1969, the use of fiber reinforced composites in aircraft structure has seen steady growth. With composites first being used in selective secondary aircraft structural components, carbon fiber reinforced epoxy has become the primary material in many wing, fuselage, and empennage components as shown in Table 1.1 and typical percentage of composite usage is shown in B-2, and V-22 military aircrafts in Figure 1.1. In 1988, Airbus introduced the A320 with an all composite tail including tail cone, horizontal, and vertical stabilizers. In 1995, Boeing introduced the 777, which utilizes composites for approximately 10% of its total structural weight. The structural weight of the Airbus A380, introduced in 2007, is approximately 20% composites utilizing carbon, glass, and quartz fibers. The Boeing 787 and Airbus A350 XWB are both advertising 50% and 52%, respectively of the total structural aircraft weight being made from primarily carbon epoxy composites as illustrated in Figure 1.2.

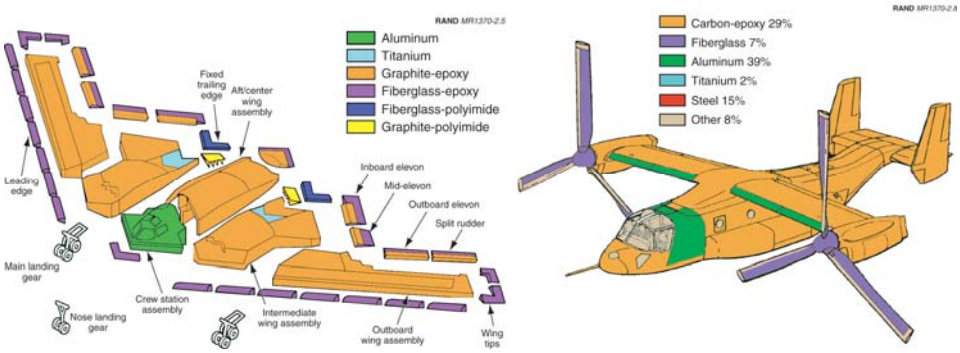

a) B-2 Bomber (1987) b) V-22 Osprey (1997)

Figure 1.1. Use of composites in US military aircraft (B-2, V-22)

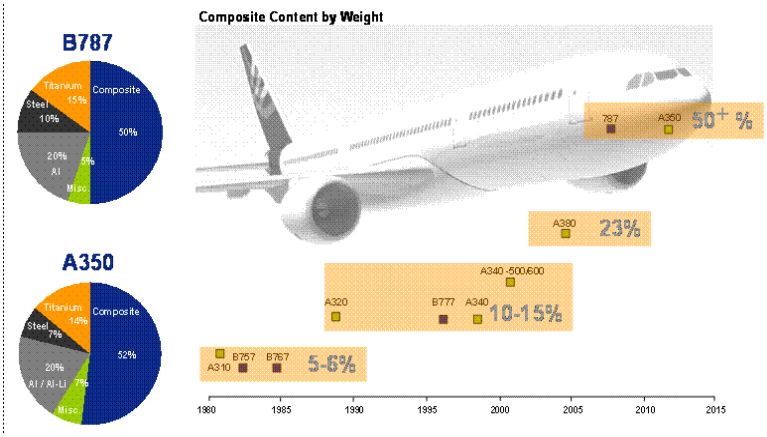

Figure 1.2. Use of composites in commercial aircraft (source: Hexcel)

The application of these, primarily carbon fiber reinforced plastic (CFRP) systems for aerospace structures, has led to the development of stronger, lighter, and more corrosion resistance products with improved fatigue life. Carbon/epoxy material may be molded to near net-shape geometry; however, because of tolerance and surface finish requirements machining is often necessary to enable assembly. Edge trimming by the milling process is one of the most common machining processes employed to provide required surface finish and dimensional accuracy. Edge trimming is performed after the laminates are fully cured using hand held routers or large numerically controlled (NC) multi-axis routers or milling machines. Milling of composites is challenging because of the anisotropic and abrasive nature of the material. Some of the challenges include delamination, fuzzing, fiber pullout, and short tool life. The chips or dust generated through machining of carbon fibers are electrically conductive and can cause shorting in electrical equipment. In addition, exposure to airborne carbon fibers, currently

classified as a nuisance particulate, may sensitize and irritate nasal and respiratory systems and may cause skin irritation in some individuals. These challenges are considerably different issues than those encountered during milling of homogenous materials such as metals and thus merit study to understand the mechanics of the edge trimming and milling processes.

This dissertation is organized into ten chapters. Chapter 1 provides an introduction to the current field and challenges. Chapter 2 presents a review of the current knowledge of experimental, numerical, and analytical approaches used for milling of composite materials. The scope and objectives of this research are presented in Chapter 3. Chapter 4 describes the experimental approach, equipment, materials, and tools utilized to accomplish the stated objectives. Chapter 5 provides the experimental methods and results for a preliminary machinability assessment of composite materials. Chapter 6 provides the experimental work performed to develop a self-contained system for dust collection and analysis. Chapter 7 provides the experimental work in support of a cutting force prediction model for composite materials. Chapter 8, 9 presents the tools and models developed for particle analysis and cutting force prediction, respectively. Chapter 10 presents the conclusions and recommendations from this experimental study of edge trimming composite materials.

CHAPTER 2

LITERATURE REVIEW

2.1 Introduction to Fiber Reinforced Composite Materials

A composite material is a macroscopic combination of two or more distinct materials, having a recognizable interface between them [1, 2]. The constituents retain their own physical and chemical identities, but the resulting material has better properties than when the individual constituents are used alone. Fiber reinforced composite (FRC) materials consist of high strength and high modulus fibers embedded in a matrix. Composites are used not only for their structural properties, but also for their electrical, thermal, tribological, and environmental capabilities, depending on the application. The two constituents of the composite material are typically a fiber or particle and a matrix. Composites will typically have a fiber or particle phase that is stiffer and stronger than the continuous matrix phase. Composites are commonly classified at two distinct levels. The first level is made with respect to the matrix constituent. Classes of composite matrix constituents include organic matrix composites (OMC), metal matrix composites (MMC), ceramic matrix composites (CMC), and polymer matrix composites (PMC).

The second level classification includes the reinforcement constituents. Different classes of reinforcements include particle reinforcements, whisker reinforcements, continuous and discontinuous fiber reinforcements, and woven reinforcements. A reinforcement is considered to be a particle if all its dimensions are approximately equal. Continuous fiber reinforcements have lengths much greater than their cross-sectional dimensions. The architecture of a woven reinforcement includes weaving, braiding, or knitting the fiber or fiber bundle tows to create interlocking fibers that have an orientation slightly or fully orthogonal to the primary structural plane. The principal purpose of the reinforcement is to provide superior levels of strength and stiffness to the composite, where fibers are the principal load carrying members. The purpose of the matrix is to bind the reinforcements together through its adhesive characteristics, to transfer load between the reinforcements, keep the fibers in the desired orientation, and to protect the reinforcements from environmental and handling damage. Longitudinal tension and compression loads are carried by the fibers, while the matrix distributes the loads between the

fibers in tension, and stabilizes and prevents the fibers from buckling in compression. The matrix is also the primary load carrier for interlaminar shear and for transverse tension.

There are several different types of matrix systems including: thermosetting resins (polyester, epoxy, bismaelimide, cyanide ester, polyamide, phenolic), thermoplastic resins (PEEK, PPS, PP, PE), ceramic matrices, and metallic matrices. Several different types of reinforcements are also available including: Glass fibers, aramid fibers (Kevlar), carbon fibers, boron fibers, graphite fibers, ultra high molecular weight polyethylene (spectra) fibers, silicon carbide fibers, ceramic fibers, and metallic fibers. *The research herein will focus primarily on carbon fiber reinforced epoxy composites.* Epoxy resins are presently used far more than other matrices in advanced composite materials for structural aerospace applications. A substantial database exists for epoxy resins because both the US Air Force and the U.S. Navy have been flying aircraft with epoxy material structural components since 1972. Carbon fibers are currently the best known and most widely used reinforcing material in advanced composite structures, and are prevalent in aerospace applications. Epoxy resin, first produced in the 1930s, describes a broad class of thermosetting polymers in which the primary cross-linking occurs through the reaction of an epoxide group. The three primary classes of epoxies used in composite applications include: phenolic glycidyl esters (DGEBA), aromatic glycidyl amines (TGMDA), and cycloaliphatics. Epoxies offer high-strength, low shrinkage, excellent adhesion to different substrates, effective electrical insulation, chemical and solvent resistance, low cost, and low toxicity. Epoxies are also easily cured without evolution of volatiles and are chemically compatible with most substrates and tend to wet surfaces easily.

The term carbon fiber is often applied interchangeably for both carbon and graphite fibers. Carbon fibers were first commercially available in the late 1950's and were developed in pursuit of ablative materials for rockets. Carbon and graphite fibers are produced from a variety of precursor materials such as rayon, polyacrylonitrile (PAN), and pitch. The majority of all carbon used today are made from PAN precursor, which is a form of acrylic fiber. Precursor is accomplished by spinning the PAN polymer into filaments using standard textile fiber manufacturing processes. The PAN fibers are then stabilized by stretching and heating to approximately 200 to 300°C in an oxygen containing atmosphere to orient and cross-link the

molecules. Carbonization of standard and intermediate modulus fiber involves pyrolyzing the fibers to temperatures ranging from 1000 to 1500°C in an inert atmosphere, typically to a 93% - 95% carbon content. An additional heat treatment step is included just after carbonization for some very high modulus fibers. A sizing or finish is then applied to minimize handling damage during spooling and enhance bonding with matrix resins. In contrast, graphite fibers are produced by heating their precursor at temperatures from 2200-2700°C resulting in a crystalline fiber structure and higher elastic modulus, with carbon content greater than 99%. Rayon is processed similar to PAN, but has half the carbon yield of PAN based fibers. Pitch can be made from petroleum, coal tar, asphalt, or PVC and is processed through a pre-treatment step to attain the desired viscosity and molecular weight for making high-performance carbon fibers. Process details for the final composition and method of spinning pitch are generally held secret by the manufacturers. Actual process parameters, such as temperatures, ramp rates, and time are different for pitch then PAN. Aerospace-type precursor is processed in 3K to 12K filament tows that can be assembled into 24K or larger tows after carbonization. Generally, aerospace carbon fibers are available in bundles of 3K, 6K, 12K, and 24K filaments, while most commercial-grade fibers are available in 48K or larger filament counts. PAN fibers used to be categorized into standard modulus, intermediate modulus, and high modulus, however; new offerings by fiber producers have somewhat blurred these categories. Typical carbon fiber (filament) diameter is between 5 to 10 μm. Fiber orientation and stacking sequence can be controlled to generate a range of mechanical properties for a composite laminate.

2.2 Milling Fundamentals

Milling is a machining process where material is removed from the work piece by a rotating multiple-tooth cutting tool. Each tooth of the milling cutting tool removes a small amount of material as it revolves around a spindle. In a typical milling operation, both the work piece and the milling cutter can be moved in more than one direction which enables surfaces of almost any orientation to be machined. Milling differs from other machining processes as there are interrupted cuts that occur because the cutting teeth periodically engage and leave the work piece. Further, the chips in milling are relatively small and there is variation in thickness within each chip. The chip thickness varies during the cut of an individual tooth because feed is

measured in direction of table motion while chip thickness is measured along the radius of the cutter.

The two primary milling methods are peripheral milling and face milling as illustrated in figure 2.1. In addition, there are variations of these two primary methods depending on the type of work piece and cutter. In peripheral milling, sometimes called slab milling, the milled surface is in a plane parallel to the cutter axis. Peripheral milling is typically performed on milling machines with the spindle positioned horizontally, but can also be accomplished on vertical spindle milling machines. The milling cutters are mounted on an arbor which is generally supported at the outer end for increased rigidity. Peripheral milling should generally not be performed if the part can be face milled. Face milling is performed on both horizontal and vertical milling machines. The milled surface is flat and generally at right angles to the cutter axis. Other milling methods including: end milling, side and straddle milling, gang milling, cam milling, thread milling, plunge milling, crankshaft milling, and die sinking can be classified as either peripheral or face milling operations.

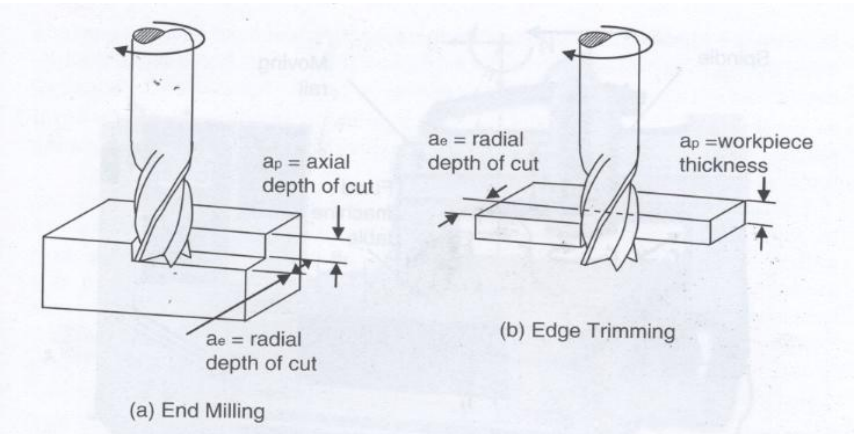

Figure 2.1.Basic types of milling operations

2.2.1 Milling Process Parameters and Cutting Conditions

Milling and metal cutting in general consist of independent (input) variables, dependent variables, and interactions between both variables. Some of the independent input variables include, work piece material, geometry of the work piece, the type of machining process selected, choice of cutting tool material, cutting parameters (axial depth of cut, radial depth of cut, spindle speed, feed rate), cutting tool geometry, work holding devices, and cutting fluids.

The work piece material is typically chosen for its intended application, however, machinability, or the relative ease with which a chip can be separated from the base material to an acceptable finish, may be part of the selection criteria [3]. While no one characteristic has been adopted as a standard for machinability, the following parameters may be considered:

- Cutting speed for a target tool life (e.g. 60 min)
- Volume of material removed for a tool life
- Tool life (min.)
- Tool forces
- Power required
- Surface finish
- Temperature

The initial geometry of the work piece may be determined by preceding processes such as casting, forging, extrusion, plate, etc., or in the case of composites materials; part layup and cure. The role of the machining process is to transform the initial work piece geometry into a final geometry, with the process selected capable of achieving the desired final form. The three most common cutting tool materials include high speed steel (HSS), carbides, and coated tools. Other cutting material types including cubic boron nitride (CBN), and diamond tools such as polycrystalline diamond (PCD) are also utilized. The objective of cutting tool selection is to achieve a maximum material removal rate while having maximum tool life to minimize machining cost, and simultaneously achieving desired part quality and surface finish. Cutting parameters including feed, speed, and depth of cut and are selected to again achieve maximum material removal rate for the type of cutter selected. Cutting tool geometry is selected to accomplish a specific machining function such as roughing or finishing. Work holding devices are essential to properly fixture the work piece in the milling machine. Failure to correctly fixture the work piece can lead to part defects and other undesired effects. Cutting fluids are selected based on the combination of work piece and cutting tool material. The cutting fluids cool the work piece, cutter, and chips; reduce friction; carry the chips away from the work piece; and help improve the surface finish. *In the case of this research, the emphasis is on dry cutting of composite laminates and the dust generated.*

Dependent variables are determined from the selection of independent or input process variables discussed in the preceding paragraph. Dependent or derived parameters include:

cutting force and power, geometry and properties of the finished work piece, surface finish, and tool wear. The selection of feed, speed, cutter geometry, and depths of cut determines the cutting force and power required to make the cut. The combination of input parameters will determine the final size and properties of the finished part as machined surface possess residual stresses from the machining operation. Surface finish is dependent on the cutting tool geometry, tool material, work piece material, and process parameters including feed, speed, depths of cut, and type of cutting fluid. Tool wear occurs as a result of the process parameters and inherent friction in the machining process which raises the cutting tool temperature and lowers its wear resistance. A dull cutting tool can result in increased cutting forces which in turn may increase deflections in the work piece and cause a chatter condition impacting surface finish. Thereby, one should be able to conclude that proper selection of the input parameters is essential to have the desired outcome on the dependent variables and ultimately on part quality and total manufacturing cost.

The cutting conditions that determine the rate of material removal include the Cutting Speed, V, the Feed Rate, f_m, and Depth of Cut, d. [4]. These cutting parameters and the type of material to be milled determine the power required to make the cut and need to be adjusted to stay within the power available on the machine tool to be used. The cutting parameters selected will also impact tool life. Tool life is the time duration that a cutting tool will cut before becoming dull, requiring replacement. Tool life is influenced most by cutting speed, V, followed by feed rate, f_m, and least by the depth of cut, d. The first step is to select the depth of cut, d. The depth of cut is determined by the amount of material that is to be machined from the work piece, the power available on the machine tool, and the rigidity of the setup. Because the depth of cut has the least impact on tool life, the largest depth of cut that is possible should be selected. The second step is to select the feed rate, where the power available must be considered. The maximum feedrate possible should be selected, however, it should not be greater than will produce an acceptable finish. The last parameter to be selected should be the cutting speed. For metals, tables are available to find cutting speeds and feed per tooth. For composites, guidelines are that feed rate (mm/rev) should be within 1/3 to 1/2 of ply thickness.

For milling and other machining operations that are conducted with a rotating spindle, Cutting Speed, V, must be converted into rotations per minute using the following formula:

$$N = \frac{12V}{\pi D} \text{ (for US Customary units)} \qquad (2.2.1)$$

V = Cutting Speed, feet/min, or m/min.

D = Cutter Diameter, in., or mm.

In milling when a power feed is to be used, the feed rate, should be calculated as it governs the production rate. Failure to calculate an appropriate feed rate may cause overloading of the milling cutter which will result in reduction of cutting tool life. The basic feed rate for milling cutters is feed per tooth, f_t. Many factors are involved in selected feed per tooth, including: cutting tool material, hardness of the work piece material, width and depth of cut to be taken, type of milling cutter and size, desired surface finish, available power of the machine tool, and the rigidity of the setup. Like for cutting speed, tables are available for metals depending on alloy and choice of cutting tool material. Again, as a general rule, the maximum feed rate should be selected that conditions permit to minimize production time, or maximize material removal rate. The material removal rate, Q, can be calculated, where Q is the product of the depth of cut, d, width of cut, w, and machine table feed rate, f_m. From the material removal rate, Q, the power at the cutting tool, P_c, and power at the motor, P_m, can be estimated. The formula for calculating table feed rate, f_m, when the feed rate in feed per tooth, f_t, spindle speed, N, and number of teeth, n_t, is known is as follows:

$$f_m = f_t . n_t . N \qquad (2.2.2)$$

$$Q = d \cdot w \cdot f_m \quad \text{(per pass)} \qquad (2.2.3)$$

$$P_c = K_p . C . Q . W \qquad (2.2.4)$$

$$P_m = P_c / \eta \qquad (2.2.5)$$

where

N = Spindle speed, RPM

f_m = Milling machine table feed rate, mm/min (in/min)

$$P = F_c \times V \qquad (2.2.6)$$

f_t = Feed Rate in mm (inch) per tooth

$n_{t=}$ number of teeth in the cutter

Q = Material Removal Rate, cubic inches/minute

P_c = Power at the cutting tool in hp, or kW

P_m = Power at the motor, hp, or KW

η = Machine tool efficiency factor (available from tables)

C = Feed factor for power constant (available from tables)

W = Tool wear factor (available from Tables)

The rate of energy consumption during machining, P, is the product of the cutting speed V and cutting force F_c, such that [5]:

$$P = F_c \text{ x } V \qquad (2.2.6)$$

The rate of energy consumption and material removal rate are proportional to the cutting speed. Specific cutting energy, $p_{s,}$ is parameter which gives an indication of the efficiency of the process in terms of the energy consumed per unit volume of material removed.

$$p_s = P/Q = F_c/A_c \qquad (2.2.7)$$

where A_c is the cross-sectional area of the uncut chip and Q is the material removal rate.

2.2.2 Climb versus Conventional Milling

There are two methods of milling, up milling (conventional milling), and down milling (climb milling) depending on the relationship between cutter rotation and work piece feed direction (figure 2.2) [6]. As the name implies, in climb milling or down milling, the cutting tool attempts to climb the work piece. In climb milling, chips are produced at maximum thickness at initial engagement of the cutter teeth to the work piece and then decrease to zero thickness at the end of engagement. In conventional or up milling, the process is reversed as chips start with zero thickness and increase in thickness as the milling teeth progress through the cut. Climb milling (down milling) has several advantages over conventional (up milling) including requiring simpler fixtures because down milling exerts a downward force on the work piece, allows the use

of higher rake angles on the cutting tools which reduces power requirements, reduces the likelihood that chips will be carried by the tooth which lessens the possibility of marring the surface, makes chip removal easier because chips pile up behind the cutter rather than in front of it, reduces cutter wear because chip thickness is greatest at the start of the cut, and surface finish is improved because rubbing action at the start of chip making is eliminated. A disadvantage of climb milling is that it must be avoided on milling machines that are not equipped with a backlash compensation mechanism. The primary advantage of conventional (up milling) is lower impact during the initial cutter/work piece engagement when the chip is zero thickness. In up milling, the direction of milling force compensates for backlash in the feed mechanism as the cutter rotation is against the feed direction. Conventional milling (up milling) is also preferred over down milling when the depth of cut on the surface to be milled varies excessively (greater than 20%) and for the milling of castings or forgings or other materials with very rough surfaces.

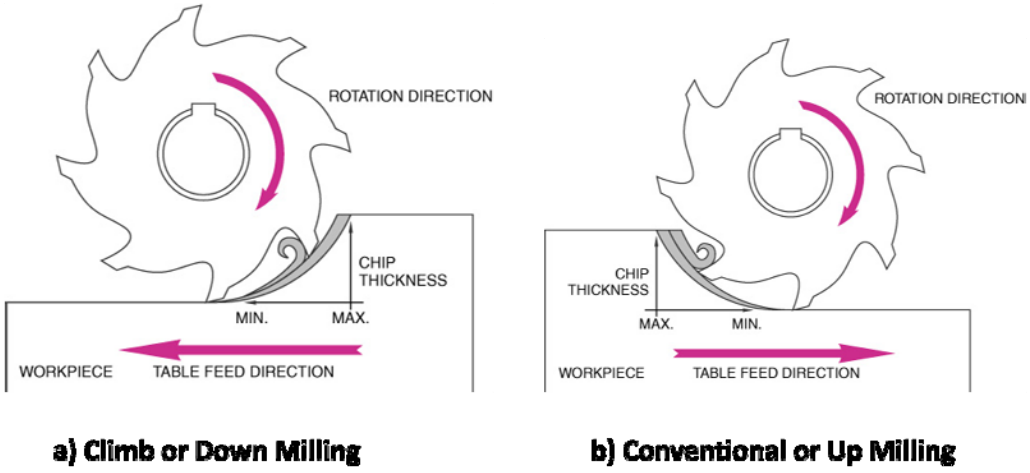

Figure 2.2. Climb vs. Conventional Milling

2.2.3 Cutting Tool Materials

There are a variety of materials and configurations of milling cutters available. The reader is encouraged to review specification ANSI/ASME B94.19 [7] which covers high speed milling cutters and end mills of one piece construction and ANSI B212.4-1995 [8] which covers indexable type inserts for both single point and multiple point cutting tools for geometric details. In addition to cutter geometry, cutting tools are made from different materials depending on the work piece material to be machined. Factors that influence the selection of a cutting tool

material include: hardness of the work piece, operations to be performed, amount of material to be removed, accuracy and finish requirements, capability of the machine tool to be used, rigidity of the tool and work piece, operating conditions including cutting forces and temperatures, and cost factors consisting of tool cost per part machined and labor cost. While desirable, it is unlikely that any single cutting tool material will meet the needs of all applications due to the wide range of conditions.

For discussion of tool materials we will consider: carbon and low-alloy tool steels, High Speed Steels (HSS), powdered metal HSS, cast cobalt-based alloys, Cemented Tungsten Carbides (WC-Co), Titanium Carbides (TiC), Coated Carbides, Ceramics, Single-Crystal Diamonds, Polycrystalline diamond (PCD), and Cubic Boron Nitride (CBN). Plain carbon and low-alloy tool steels having a lower alloy count than HSS, are rarely used anymore for metal cutting because of their low hot hardness and that they must be operated at low cutting speeds. There are still some applications for plain carbon steels including knurling, burnishing, and woodworking. Cutting tool material types are summarized in Table 2.1.

Table 2.1. Cutting tool material summary.

Tool Material	Description
High Speed Steel (HSS)	Designed to cut material at high speeds. Classified according to chemical composition: M-Molybdenum (M); Tungsten (T). Can be heat treated to high hardness. High wear resistance. Adequate impact toughness. Disadvantage is hardness falls off when temperatures exceed 1100 F.
Cemented Tungsten Carbides (WC-Co)	Include a broad family of hard metals produced by power metallurgy. Can provide about a 5-fold increase in cutting speed over tool steels and can cut harder materials with greater efficiency. High compressive strength. May be alloyed with TiC and TaC to improve performance. Four basic types: indexable inserts, regrindable carbide tools, brazed carbide tools, solid carbide tools.
Titanium Carbides (TiC)	Produced by cold pressing and vacuum sintering. High melting point, high hardness, good crater resistance, low thermal conductivity, lower coefficient of friction than WC. Capable of producing smooth surface finishes. Less expensive than WC.
Coated Carbides	Carbide inserts with wear-resistant compounds for increased performance and longer tool life. Five-fold increase in tool life over uncoated carbide tools, and capable of higher cutting speeds. As a general rule, toughness or impact resistance decreases as hardness increases. Should not be used for heavy roughing operations or interrupted cuts.
Ceramics	Two basic types: plain ceramics and composite ceramics. Plane Ceramics are highly pure greater than 99% AL_2O_3. Produced by cold pressing fine alumina powder under high pressure by sintering at high temperature. Composite ceramics contain are also Al_2O_3 based, but contain 15-30% of titanium carbide (TiC) and other alloying elements. Ceramic cutting tools may be operated at higher cutting speeds than tungsten carbide tools. A disadvantage is that ceramics are more brittle than carbides so mechanical shock must be avoided such as with interrupted cutting.
Single Crystal Diamond	Made from the cubic crystalline form of carbon that is produced in various sizes under high heat and pressure. Natural, mined single crystal stones of the industrial type are cut to produce the required geometry for the application. Single crystal diamond tools have high thermal conductivity, low coefficient of friction, low compressibility and thermal expansion. Much more expensive than other materials. Not recommended for interrupted cutting of hard materials.
Polycrystalline Diamond (PCD)	Consist of fine diamond crystals that are bonded together under high temperature and pressure. Natural and synthetic diamonds may both be sintered in this manner. Bonding to tungsten or tungsten carbide substrate produces tools that not only have high hardness and abrasion resistance, but also have greater strength and shock resistance. Hardness for PCD tools is approximately 4 times that of carbide and nearly equal to single crystal tools. PCD tools can provide much longer tool life, superior finish, reduced scrap, and lower tool cost per part than carbide cutting tools.
Cubic Boron Nitride (CBN)	Made from a superabrasive crystal that is second in hardness and abrasion resistance only to diamond. Produced by a high pressure and high temperature process similar to what is used to make synthetic diamonds. CBN cutting tools have greater heat resistance than diamond tools. High wear resistance results in increased productivity. CBN is not recommended for heavy interrupted cutting.

2.2.4 Milling Chip Formation Process for Metals

The chip formation process in milling is fundamentally the same as for all other metal cutting operations (figure 2.3). The process of metal cutting consists of a wedge shaped cutting tool that engages the work piece to remove a thin layer of material in the form of a chip [9]. Three different types of chips may be produced in metal cutting operations including discontinuous, continuous without built-up edges, and continuous with built up edges. The type

of chip depends on the work piece material, tool geometry, and process parameters. The first type of chip is a discontinuous chip which consists of individual segments that are produced by fracture of the metal ahead of the cutting edge. Discontinuous chips are most common when machining brittle materials, which are not ductile enough to undergo plastic deformation, and don't require a chip breaker. The second type of chip are continuous chips without built-up edges and are the preferred type of chip when machining ductile materials such as steels or aluminums. This type of chip is formed by continuous deformation of the metal without fracture ahead of the tool. Usually, a chip breaker is needed to control this type of chip. The third type of chip is a continuous chip with a built-up edge. The built-up edge is essentially a stagnant mass of chip material which welds to the tool face and occasionally breaks loose. Built-up edges are caused by excessive pressure and friction in the interface zone between the tool and work piece. Built-up edges can usually be controlled by increasing the surface speed, using a positive rake angle, or with coolant. Regardless of which type of chip is produced, compressive deformation will cause the chip to be thicker and shorter than the layer of the work piece material removed. The work required to deform the material typically accounts for the majority of power consumed in metal cutting. In general, the thicker the chip, the greater the force required to produce it. The direction of chip flow is determined by the angle of inclination which is the angle formed by the cutting edge and a plane perpendicular to the direction of tool travel. As the angle of inclination is increased, the chips are directed farther away from the machined surface which helps prevent binding of the cutter due to packing of the chip spaces. The magnitude of the angle of inclination determines the helix angle of the coiled chip.

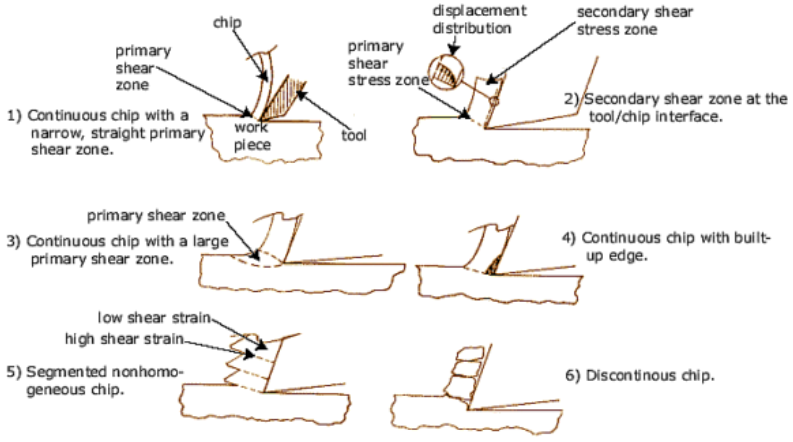

Figure 2.3. Typical chip formation in metallic machining

The chip formed has always a chip thickness of t_c that is greater than the depth of cut, and this chip thickness can be found by knowing the rake angle α, the shear angle ϕ, and the depth of cut. The ratio of the depth of cut to the chip thickness is called chip thickness ratio (r). Using the geometric relation as shown in Figure 2.4, this chip thickness ratio can be expressed in terms of the rake angle α, the shear plane angle ϕ, and the length of the shear plane l_s as shown in equations (2.2.8) - (2.2.11).

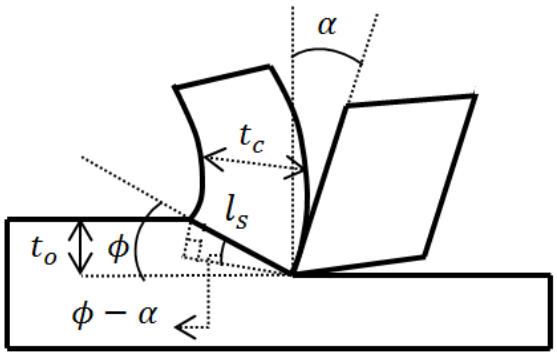

Figure 2.4 Geometric relation of chip formation

$$r = \frac{t_o}{t_c} \tag{2.2.8}$$

From the geometric relation we have

$$t_o = l_s * sin\phi \quad and \quad t_c = l_s * \cos(\phi - \alpha) \tag{2.2.9}$$

Substituting Equation (2.2) into Equation (2.1) gives

$$r = \frac{sin\phi}{\cos(\phi - \alpha)} \tag{2.2.10}$$

Solving Equation (2.3) using trigonometric relations gives the following expression for the shear plane angle ϕ.

$$\phi = \tan^{-1}\frac{r * cos\alpha}{1 - r * sin\alpha} \tag{2.2.11}$$

The prediction of the shear plane angle ϕ and its relation to the rake angle α and other cutting tool geometries play an important role in the analysis of the cutting mechanism and chip formation processes. In addition, these angles are the main geometric values in the derivation of cutting force components that can be measured directly in the cutting process.

2.2.5 Orthogonal Cutting Model

Metal cutting theory assumes a continuous plastic deformation with a high strain rate under the compressive stress exerted by a wedge-shaped cutting tool. The material removal process for metal cutting is characterized by chip formation during plastic deformation. Metal cutting can be classified into two-dimensional (orthogonal) and three dimensional (oblique) cutting processes as shown in figure 2.5, with oblique cutting the general case due to the inclination angle. The simplest type of metal cutting operation is orthogonal cutting where the cutting edge inclination of the tool is perpendicular to the direction of cutting which may be represented by the planing process using a 0^o lead angle tool with a cutting edge wider than the width of the part. As the cutting tool engages the work piece, material directly ahead of the tool is deformed. The deformed material then flows into the space above the tool as the tool advances. Metal deforms by shear in a narrow zone extending from the cutting edge to the work surface. In practice, the shear zone is normally curved, but for analysis it is usually considered to be a plane called the shear plane. The angle formed by the shear plan and the direction of tool travel is called the shear angle.

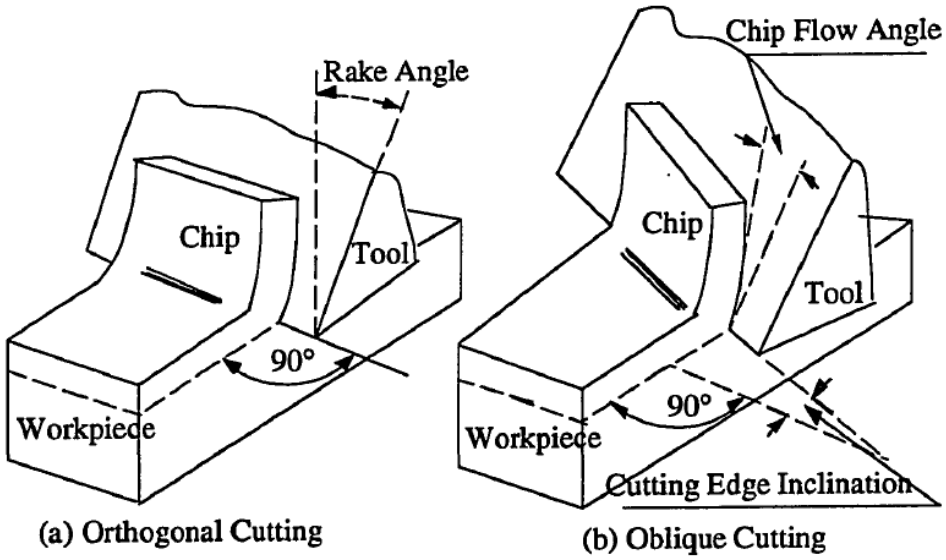

Figure 2.5. Orthogonal and Oblique Cutting [5].

The orthogonal cutting model is an ideal or simplified model used to describe the cutting process, which ignores various complex parts of the cutting geometry, but is still useful for describing the mechanics of the cutting process. This ideal model completely suppresses the

concept of inhomogeneous strain by assuming the material to behave in a completely homogenous fashion. In orthogonal cutting model, the cutting tool is assumed to have a straight edge, which is perpendicular to the direction of cut and feed direction. In this model, the tool comprises only two geometric components, the rake angle α and the relief (clearance) angle θ as shown in figure 2.6.

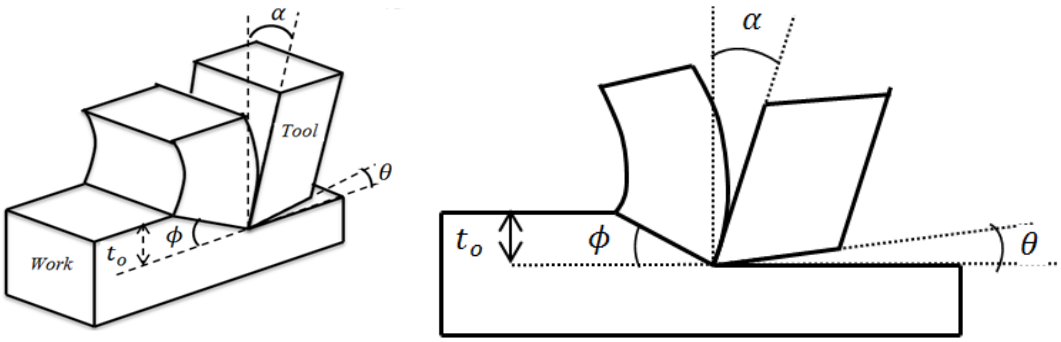

Figure 2.6. Orthogonal cutting model

In the 1940s for orthogonal cutting, M. Eugene Merchant developed a 2-dimensional model of forces at the cutting tool which is widely cited in literature [10]. In the orthogonal cutting model, various force components act on the tool and the workpiece. The force applied by the cutting tool on the chip can be classified into two force components which are perpendicular to each other as shown in Figure 2.7. These two forces are the friction force, (*F*), the force between the chip and the tool, which resists the flow of chip along the tool face, and the normal force, (*N*), the force normal to the friction force. The vector addition of these two force components gives the resultant force (*R*), which is oriented at an angle β relative to the normal force, which is also called the friction angle. The coefficient of friction μ between the chip and the tool face can be defined using these two forces and the friction angle as shown in Equation (2.2.12).

$$\mu = \frac{F}{N} = tan\beta \qquad (2.2.12)$$

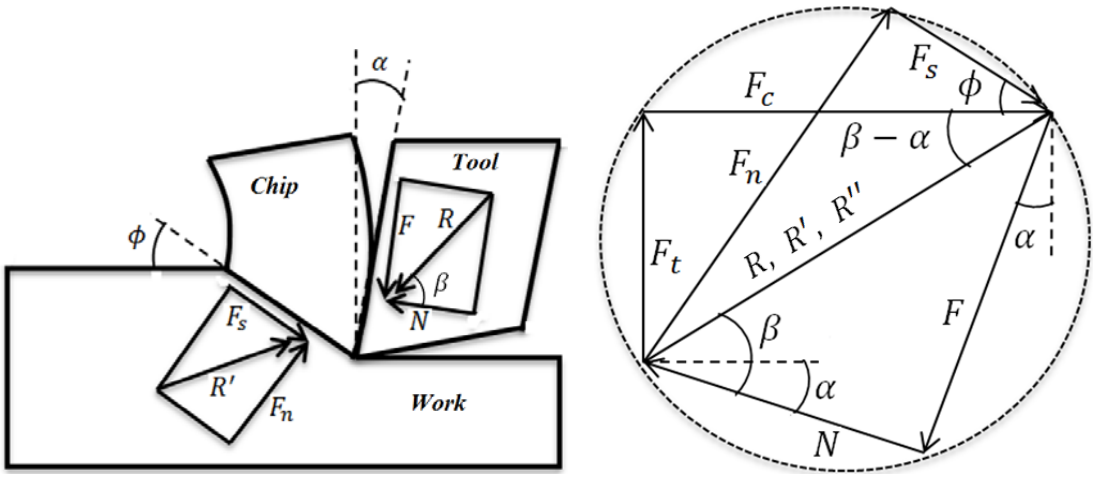

Figure 2.7. Forces acting on the tool and chip (left), geometric relation of all forces (right).

In addition to the force applied by the tool, the chip is also subjected to two force components exerted by the workpiece, the shear force (F_s), which causes shear deformation in the shear plane and the normal force (F_n), which is normal to the shear force. The vector addition of these two force components gives the resultant force *R'*, which must be equal and opposite to the resultant force, *R,* in order to make the forces acting on the chip balance. All of these force components *F*, *N*, F_s, F_n, cannot be measured directly from the cutting process; however, two additional force components, including the cutting force F_c, which is the force in the direction of cutting, and the thrust force F_t, which is the force in the direction of the depth of cut and perpendicular to the cutting force, can be directly measured. The third resultant force *R''*, can be found by vector addition of these two measured force components.

Using the two measured force components, and the geometric relation, a series of equation can be derived to express the four force components in terms of the measured components as given by from equations (2.2.13-2.2.16)

$$F = F_c sin\alpha + F_t cos\alpha \quad (2.2.13)$$

$$N = F_c cos\alpha - F_t sin\alpha \quad (2.2.14)$$

$$F_s = F_c cos\phi - F_t sin\phi \quad (2.2.15)$$

$$F_n = F_c sin\phi + F_t cos\phi \quad (2.2.16)$$

From these force components and the area of the shear plane, it is possible to calculate the shear stress. Using the geometric relation shown in Figure 2.8 and the calculated force

components, the shear stress τ and the normal stress σ can be derived as shown by Equations (2.2.17)-(2.2.18).

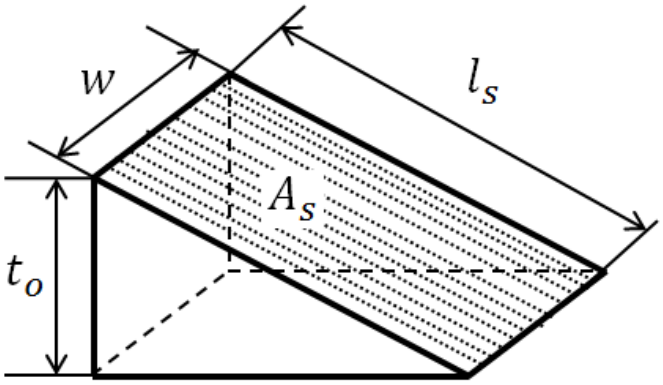

Figure 2.8. Geometric relation of the shear plane.

$$\tau = \frac{F_s}{A_s} \qquad (2.2.17)$$

$$A_s = \frac{t_o w}{sin\phi} \qquad (2.2.18)$$

By substituting Equation (2.2.15) and Equation (2.2.18) into Equation (2.2.17), the expression for the shear stress can be defined in terms of the measured quantities by Equation (2.2.19).

$$\tau = \frac{(F_c cos\phi - F_t sin\phi\ )Sin\phi}{t_o w} \qquad (2.2.19)$$

The normal stress in the shear plane can be find in the same fashion and given by equation (2.2.20).

$$\sigma = \frac{F_n}{A_s} = \frac{(F_c sin\phi + F_t cos\phi\ )sin\ \phi}{t_o w} \qquad (2.2.20)$$

Chip formation for milling differs from single point metal cutting as nearly every milling operation consists of an interrupted cut such that each insert of a milling cutter is in the cut less than half the total machining time. Further, while the insert or tooth is in the cut, the thickness of the chip being formed is constantly changing because of the effect of cutter rotation and work piece feed motion. As each insert or tooth engages the work piece, it is subjected to a mechanical shock load with magnitude dependent on work piece material, cutter position, machining parameters, and cutter geometry. The cutting forces during milling are cyclical and roughly proportional at any position in the cut to the undeformed chip thickness at that position.

Heat generated during the milling operation is also roughly proportional to the undeformed chip thickness.

During the milling operation three force components act on an individual milling insert including the tangential force F_t, the radial force F_r, and the axial force F_a as shown in figure 2.9. The tangential force, F_t, acts in a direction tangential to the revolving work piece and represents resistance to the rotation of the work piece. The tangential force is generally the highest of the three force components and accounts for 99% of the total required power for the operation. The radial force, F_r, acts along the radius of the cutter and represents part of the thrust force. The thrust force is the force which attempts to push the insert out of the cut. The radial force is approximately 50% of the tangential force, but since the radial velocity during the cut is low relative to the velocity of the rotating cutter, the radial force accounts for only 1% of the total power required. The axial force, F_a, acts in an axial direction toward the back of the spindle. If a lead angle is used then the thrust force contributes to the axial force. In general, the axial force is the smallest of the three force components and is approximately 50% as large as the tangential force. The effect of the axial force on power requirement is small because velocity in the axial direction is negligible.

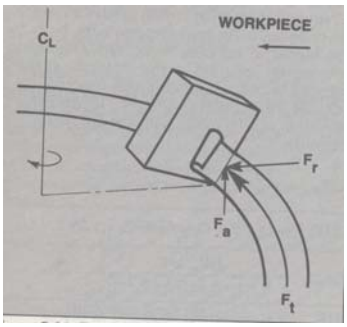

Figure 2.9. Force components in milling.

The total force, F_R, acting on the cutting tool is the resultant of the three force components, F_t, F_r, F_a, and is determined by the following formula:

$$F_R = \sqrt{(F_t^2 + F_r^2 + F_a^2)} \qquad (2.2.21)$$

Horsepower consumed at the spindle, HP_s, may be calculated using the three force components and their respective velocities where:

$$HP_s = \frac{F_t \,.\, V_t}{33{,}000} + \frac{F_r \text{ x } V_r}{33{,}000} + \frac{F_a \text{ x } V_a}{33{,}000} \qquad (2.2.22)$$

V_t = tangential velocity (cutting speed in feet/min)

V_r = radial velocity (feet/min)

V_a = axial velocity (feet/min)

Since the radial velocity, V_r, and axial velocity, V_a, are very small, the equation for horsepower at the spindle may be simplified to:

$$HP_s = \frac{F_t \,.\, V_t}{33{,}000} \qquad (2.2.23)$$

In turn, by re-arranging the above equation, the tangential force, F_t, may be estimated.

$$F_t = \frac{33{,}000.HP_s}{V_t} \qquad (2.2.24)$$

Rake angle of the insert will affect thrust force, F_{th}. When the rake angle is negative the chip will press on the face of the insert attempting to lift it out of the cut which causes a higher thrust force. However, when the rake angle is positive, the chip will press the tool face into the cut causing a lower thrust force. Lead angle, χ, determines the direction of the thrust force, so that if the lead angle is zero, the thrust force will be directed parallel to the face of the tool which will then cause the radial force, F_r, to approximately the thrust force, F_{th}. If a milling cutter with a lead angle, χ is used, thrust force will contribute to both radial and axial forces. The following equations are used to determine the effect of thrust force, F_{th} on radial, F_r, and axial, F_a, forces.

$$F_r = F_{th} \,.\, \cos(\chi)$$
$$F_a = F_{th} \,.\, \sin(\chi) \qquad (2.2.25)$$

The equations above estimate the average forces that are active on a single milling inserts or teeth based on the average material removal rate for that cutting edge. Because of the nature of the milling process, the instantaneous material removal rate (MRR) may be higher or lower than the average MRR at any instant depending on the number of inserts or teeth in the cut and

their respective undeformed chip thicknesses. To determine the maximum force on a single insert, or on the cutter body and work piece requires first finding the maximum instantaneous MRR and then calculating the tangential force and thrust force for each insert based on its individual removal rate at the point where instantaneous MRR is maximized. Instantaneous material removal rate can calculated with the following formula:

$$Q_i = t_i \,.\, V_t \,.\, d \,.\, 12 \qquad (2.2.26)$$

$$t_i = f_i \,.\, \sin\theta \qquad (2.2.27)$$

where

Q_i = instantaneous material removal rate (in^3/min)

t_i = instantaneous undeformed chip thickness (in)

V_t = cutting speed (feet/min)

d = depth of cut (in)

f_i = feed per insert (in)

θ = position of insert (degrees away from perpendicular to feed axis on insert entry side)

The maximum force that must be withstood by the work piece, fixturing, and machine tool is the sum of the components for each insert in the tangential, radial, and axial directions.

2.2.5 Surface Finish

Surface finish is a common requirement of machining operations. ANSI/ASME B46.1 "Surface Texture (Surface Roughness, Waviness, and Lay)" is an American National Standard concerned with the geometric irregularities of surfaces and defines surface texture and its constituents: roughness, waviness, and lay [11]. The terms and ratings in this standard relate to surfaces produced by cutting and for this research, we will focus on the surface finish produced by milling. The nominal surface is the intended surface boundary including the shape and extent of which is usually shown and dimensioned on a drawing. The real surface is the actual boundary of an object. Its deviation from the nominal surface stem from the processes used to produce the surface, in this case milling. A measured surface is a representation of the real surface obtained by the use of measuring instruments. The real surface differs from the nominal surface in that it contains surface texture, flaws, and errors of form. We will focus on surface

texture which consists of deviations that are typical of the real surface including roughness and waviness. Roughness consists of the finer irregularities of the surface texture that usually result from the inherent action of the production process which may include marks left by the process. Waviness is the more widely spaced components of the surface texture which may be caused by machine or work piece deflection, vibrations, and chatter. Roughness may be superimposed on a wavy surface. Roughness and waviness may be described by a surface profile. Profile is the curve of intersection of a normal sectioning plane with the surface. The most common surface finish requirement is roughness height. The numerical value given for roughness height is the average distance in micrometers or microinches of each point on the surface profile from a center line. The center line is located so that the area of roughness peaks above is equal to the area of the roughness peaks below the line. Two methods may be used to compute the average distance of surface profile points from the center line including arithmetic average, Ra, and root mean square Rq. The average roughness of the surface may be defined as (figure 2.10):

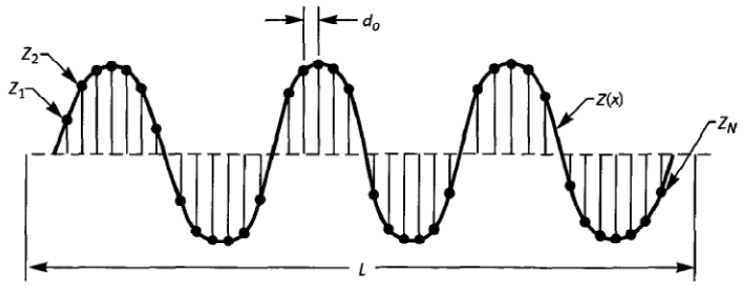

Figure 2.10. Illustration for the calculation of Ra (source ANSI B46.1-2002 [11])

$$\mathrm{Ra} = \left(\frac{1}{L}\right)\int_0^L |\mathrm{Z(x)}|\mathrm{dx} \qquad (2.2.28)$$

$$\mathrm{R_a} = \frac{(|\mathrm{Z_1}|+|\mathrm{Z_2}|+|\mathrm{Z_3}|+.....+|\mathrm{Z_N}|)}{N} \qquad (2.2.29)$$

where Z_i are individual profile values and N is the number of data points. The root mean square average of the surface is:

$$Rq = \left[\left(\frac{1}{L}\right)\int_0^L Z(x)^2 dx\right]^{1/2} \qquad (2.2.30)$$

$$R_q = \sqrt{\frac{(Z_1^2 + Z_2^2 + Z_3^2 + ... + Z_N^2)}{N}} \qquad (2.2.31).$$

An approximate conversion between average roughness and root mean square average is:

$$\frac{R_a}{R_q} = 1.11 \qquad (2.2.32).$$

Roughness and waviness are critical elements in most milled surfaces, especially for those surfaces that must be mechanically sealed. The major causes of waviness in milling are cutter runout, spindle runout, and flexing of the part or fixture during the machining operation. Waviness height is the maximum peak to valley distance of the waves and waviness width is the spacing between successive peaks or valley which is generally equal to the feed per revolution. Roughness width is the distance between successive peaks or values in the profile and usually equals the feed per insert. The level of roughness and waviness which would be achieved if the machined surface exactly matched the path and contour of the cutting tool is called the theoretical surface finish which can be mathematically calculated. Unfortunately, due to a variety of process parameters and tolerances, the actual surface finish is never as goods as the theoretical surface finish.

For face milling, the theoretical roughness and waviness are determined by: insert corner geometry, feed per insert, spindle and cutter runout, and stability of the part and fixture. Face runout of the inserts that produce the surface is critical to achieving a very fine surface finish. The theoretical average roughness, Ra, may be calculated as follows when an insert with a corner radius is used as illustrated in Figure 2.11.

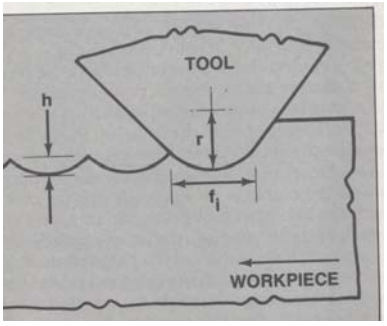

Figure 2.11. Estimating roughness height in face milling with a nose radius insert.

$$R_a = \frac{\sqrt{r - (r^2 - (f_i/2)^2)}}{2.10^6} \qquad (2.2.33)$$

where r = nose radius (in) and f_i = feed per insert (in)

In peripheral milling, the theoretical roughness and waviness are determined by: feed per insert, cutter diameter, number of inserts in the cutter body, type of milling (up or down), cutter face runout, spindle runout, and the stability of the part and fixturing. The theoretical average roughness, Ra, for peripheral milling can be estimated as follow as shown in Figure 12:

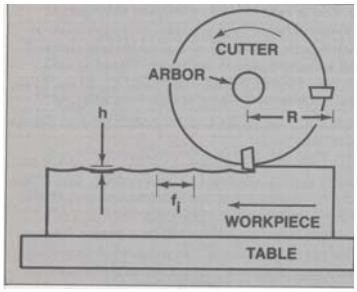

Figure 12 Estimating roughness height in peripheral milling.

$$R_a = \frac{3.18.10^5.f_i^2}{8R} \qquad (2.2.34)$$

where R = cutter radius, and f_i = feed per insert. More accurate values can be calculated for the roughness height generated by peripheral milling for climb and conventional cutting per equations 2.2.35 and 2.2.36 respectively.

$$Ra = \frac{f_i^2}{8\times\left(R+\left(\frac{f_i * N}{\pi}\right)\right)} \times 3.18 \times 10^5 \qquad (2.2.35)$$

$$Ra = \frac{f_i^2}{8\times\left(R-\left(\frac{f_i * N}{\pi}\right)\right)} \times 3.18 \times 10^5 \qquad (2.2.36)$$

From this formula, feed per inset, f_i, and cutter radius, R, are significant factors for determining roughness in peripheral milling. Major causes of waviness in peripheral milling operations include cutter runout, spindle runout, and flexing of the part or fixturing. Waviness

width in peripheral milling is generally equal to the feed per revolution and can modified by changing that value.

2.2.7 Tool Wear

Cutting tools are subjected to high surface loads. High surface temperatures are generated as the chip slides at high speed along the tool rake face while exerting high normal pressure and friction force on this face. Further, cutting forces may fluctuate due to interrupted cutting or due to hard particles in the micro-structure of the work piece. Therefore, cutting tools require strength at elevated temperatures, high toughness, high wear resistance, and high hardness. There are several tool wear modes that may occur including flank wear, cratering, built-up edge, chipping, thermal cracking, deformation, notching, and fracture. It is desirable to have the tool fail through normal flank wear as it has a highly predictable tool life and a better tool life than it would have if it failed from any other failure mechanism at the same operating conditions. Flank wear is identified by a wear land on the flank face of the insert directly adjacent to the rake face. Tool life may with respect to flank wear may be expressed by the Taylor Tool Life equation.

$$V_c T^n = C \qquad (2.2.37)$$

where V_c = cutting speed, T = tool life, n and C are constants. n and C may be found by experiment or from published data. Types of tool wear, causes, results, and preventative actions to mitigate are summarized in Table. 2.2.

Table 2.2. Tool wear summary.

Tool Wear Type	Identification/Cause	Result	Preventative Action
Flank Wear	Wear land on the flank face	Predictable tool life by Taylor equation.	Preferred form of tool wear.
Cratering	Smooth and regular depressions on the rake face of an insert caused by welding and galling between chip and rake face.	If cratering continues unchecked, erosion will continue until breakthrough at the cutting edge.	Proper selection of cutting tool coatings. Reducing the cutting speed.
Built up Edges	Deposits on the rake face of the tool caused by chip welding.	Leaves irregularly shaped depressions on the cutting edge.	Increase the cutting speed for soft materials. Decrease the cutting speed for hard materials.
Chipping	Cutting edge is broken off in small fragments so edge is ragged which is caused by non-uniform wear.	Higher cutting forces and possible catastrophic failure of the cutting tool.	Minimize deflection in the workpiece, machine tool, and fixturing to reduce shock loading. Use honed inserts or more shock resistant materials. Reduce feed/insert.
Thermal Cracking	Perpendicular cracks on the rake face that migrate toward the cutting edge caused by large and rapid changes at the cutting edge due to thermal stresses.	Can cause areas of the cutting tool to be dislodged by the cutting forces.	Use of coolant, use of shock resistant materials, reduction of cutting speed.
Edge Deformation	Looks like flank wear, but rake face is depressed and flank is mushroomed out. Occurs when cutting edge temperature rises, and this is deformed by cutting forces.	Improper cutting. High temperatures.	Use of coolant. Reduce cutting speed to reduce cutting edge temperatures. Reduce feed per insert to reduce heat and pressure.
Edge Notching	High degree of localized wear on rake and flank face caused by chemical and mechanical factors.	Accelerates abrasive wear of the cutting tool and causes oxidation of the tool which wears away quickly.	Use large lead angles, change the depth of cut line to strengthen the cutting edge to improve abrasive resistance. Reduce feed/insert.
Tool Fracture	Section of an insert breaks off when	Broken section is large enough to cause immediate failure of the cutting edge.	Avoid fracture by indexing the insert when recommended flank wear is reached. Use shock resistant tool1 grades.

2.3 Milling of Composite Materials

Section 2.2 focused on milling fundamentals developed from experience in machining homogeneous metallics. Technical issues to be discussed in this section include experimental

work that has been performed to characterize the nature of milling composite materials. Fundamental issues such as the type and nature of chip formation will be reviewed as there is significant difference between chip formation in homogeneous materials and composites. The effect of different type, geometry, and cutting tool material will be evaluated with respect to tool wear and cut quality. The influence of machining parameters such as cutting speed and feedrate will be discussed as they have been found to influence surface finish and delamination of composite materials. Force prediction models will be reviewed as methods used to calculate cutting forces in metals are not directly applicable to composite materials and an understanding of cutting force directly relates to machining quality. This section will address the limited body of published work on the milling of fiber reinforced polymer composite materials.

2.3.1 Experimental Studies

A series of experimental papers were published that characterize some of the basic challenges associated with milling or edge trimming CFRP laminates. Gordon, 2003 [12], presented a brief review of work performed to date on the cutting of FRP composite and medium density fiberboard (MDF). The authors concluded that machining of composites is significantly different than that of metals and that most of the published work to date concentrated on orthogonal cutting of FRP materials with predetermined fiber orientations. A detailed study of the body of work is necessary to understand the effects of process parameters and tool selection on the quality of machined CFRP parts. Experimental work reviewed addresses chip formation and damage, the influence of milling parameters on tool wear and surface roughness, use of diamond abrasive tools, and the effect of edge trimming on mechanical properties.

2.3.1.1 Chip formation and damage

The following published works identify the type of chip formation and effects of delamination damage relative to cutting direction and associated cutting forces. In one of the earliest published works on trim routing of glass and carbon fibers, König [13] identified that the polycrystalline diamond (PCD) cutting tools were far superior to carbide for milling of composites. König also found that the best machining quality for trimming GFRP and CFRP materials was achieved by up milling, independent of tool geometry and cutting conditions. Cutting force and surface quality in routing was found to be dependent on fiber orientation, where the highest force and worst quality was achieved under compressive load of the fiber at a

45° fiber angle. The lowest cutting force occurs when milling parallel to fiber orientation as the matrix rather than the fiber is being cut.

Wang, Ramulu, and Arola from the University of Washington [14,15] found that chip formation was critically dependent on fiber orientation. Further, principal cutting and thrust forces were also primarily influenced by fiber orientation, where operating conditions and tool geometry had far less influence. Orthogonal cutting experiments were conducted using a hydraulic shaper and PCD inserts on a 4mm thick unidirectional graphite epoxy panel. Additional tests were conducted on a multi-directional panel, with chip formation similar to the unidirectional material. Chip formation mechanisms noted in orthogonal trimming of unidirectional composites determined from this research are shown schematically in Figure 2.13.

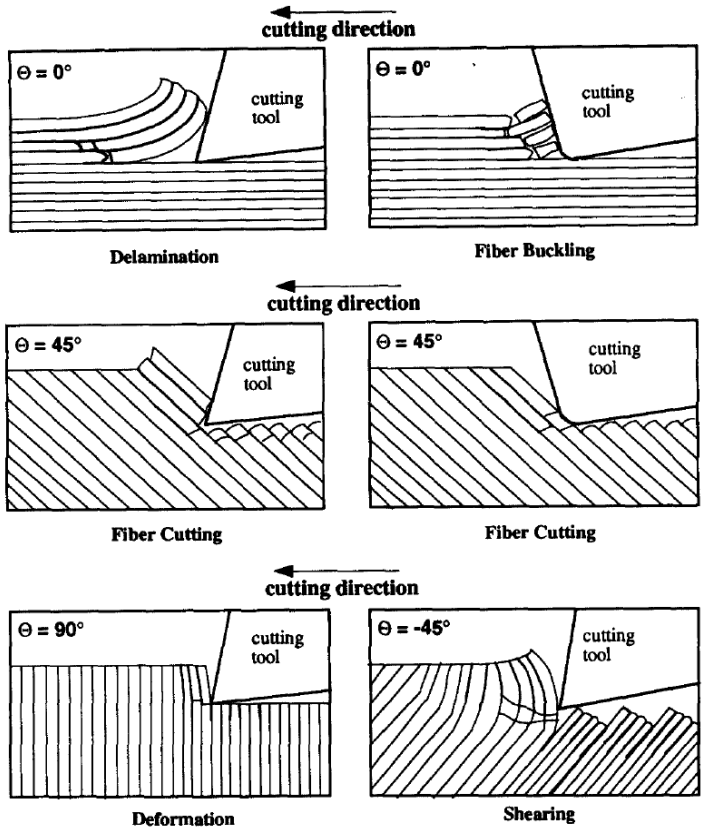

Figure 2.13. Cutting mechanisms in orthogonal machining of Gr/Ep [14].

Colligan and Ramulu [16] studied delamination and identified three distinct types of damage modes as illustrated in figure 2.14. In their experiment they used a 24 ply cured panel made from IM6 fibers and 3501-6 resin system. Four flute carbide and PCD cutters were used

on a 5-axis CNC router to perform edge trimming. Type I delaminations are characterized as areas where the surface ply fibers have broke some distance inward from the trimmed edge and are missing. Type II delaminations consist of uncut fibers that protrude from the trimmed edge and may be delaminated from the next ply a distance from the edge of the part. Type III delaminations are characterized as loose fibers that are partially attached to the machined edge causing a fuzzy appearance. Type II and III delaminations are similar as they appear to be created by fibers moving out of the way of the advancing cutting edge without completely breaking which leaves uncut fibers protruding from the edge of the laminate. A recommendation from this study is to use fibers that are parallel to the trimmed edges on all straight edges and fabric surface plies on all curved edges to minimize delamination of surface plies and increase the ease of fabrication.

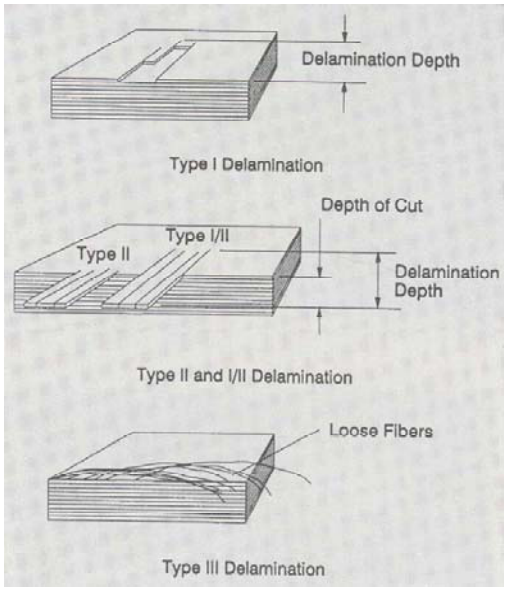

Figure 2.14. Types of surface ply delaminations (Source: Ramulu and Colligan [16])

Puw and Hocheng [17,18] evaluated machinability as a function of fiber direction and cutting conditions, with observations provided on chip characteristics. This study was performed using a plate of CFRP with 60% fiber volume fraction and a square carbide insert cutter. Three different chip types were described. Powder-like chips were produced primarily by fracture. Ribbon-like chips consisting of unbroken segments were produced by fracture with fiber breakage. Large delaminated brush-like chips were produced by interlaminar facture in shear. Formation of burrs is determined by fiber orientation and cannot be avoided accept when cutting

parallel to the fibers, which is the recommended cutting direction. The three components of cutting forces; X, Y, Z were measured for 0^o, 45^o, and 90^o fiber orientations. The cutting force component parallel to the fiber axis was found to have the lowest magnitude because as the tool cuts parallel to the fiber, the load is axial and the fiber fails by buckling due to its brittle nature and slenderness. When cutting transverse to the fiber, the load shears the fibers which requires a higher load than fiber buckling, thus the force component parallel to the fiber direction is of a lower magnitude than the transverse force component. Figure 2.15 illustrates the mechanisms when cutting parallel (a) and transverse (b) to the fibers.

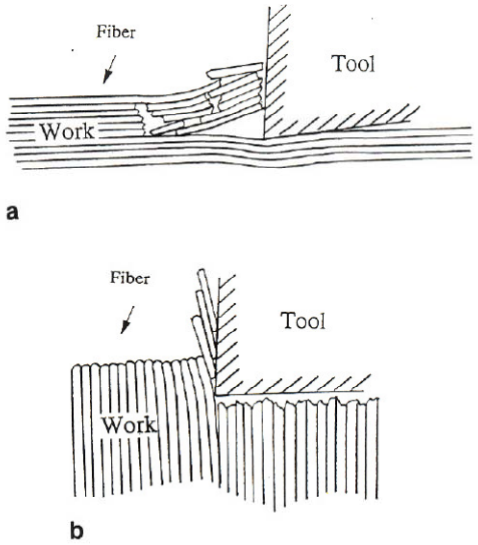

Figure 2.15. Fiber failure (a) buckling; (b) shearing.

Müller-Hummel [19] found that climb milling is better suited for machining of CFRP than conventional milling, which is common practice in metals machining. In climb milling, dust removal is facilitated whereas in conventional milling, the dust is pressed into the surface zone when the capacity of the dust chamber created by the tool is exceeded. Further, in climb milling the cutting edge can cool down in the air minimizing heat generation, where in conventional machining, the temperature of the cutting edge reaches a maximum in the area where rubbing against the work piece and chip occurs. Muller-Hummel recommends cutting tools with appropriate chipping space volume to avoid chips piling up at high feed rates which leads to an increase in friction and overheating that could lead to early cutter failure.

Hintze [20, 21] studied the occurrence and propagation of delamination of the top layers of a laminate by milling slots in unidirectional CFRP specimens having different fiber orientations with 0^o double-edge PCD end mills. Hintze showed that delamination and overhangs of the top layers is highly dependent on fiber orientation and tool sharpness. A preferred fiber cutting angle range resulting in no delamination and no fiber overhangs, even with worn tools, was found when the fiber cutting angle, θ, is between 0 and 90^o. Delamination and fiber overhangs occur when fibers are cut in the critical cutting range, where θ is between 90^o and 180^o. When milling below the critical cutting range, the length of fiber overhang was found to equal the distance from the component edge to the point at which the cutting edge cuts a fiber at a critical cutting angle for the first time. The work included an analytical model to describe the development and propagation of delamination during edge trimming where the active force leads to initial damage of the laminate such that the fibers deflect instead of being cut. The deflection versus breakage of the fibers is caused by the transverse rupture strain not being attained. Delamination can be avoided by keeping the initial damage depths below the minimum damage depths for fiber deflection. The model is applicable for CFRP laminates with unidirectional top layers.

Pecat [22], presented a study where circumferential slot milling was performed on unidirectional CFRP specimens with 50% fiber volume to find a relation between cutting conditions and surface integrity. A discmill using solid carbide inserts was used to cut slots under dry conditions in an up milling configuration. Feed per tooth and depth of cut were kept constant with fiber orientation, work piece temperature and cutting speed varied. Surface integrity was evaluated on the basis of micrographs. Smooth surfaces were found when cutting at 0^o and $+45^o$, however, cutting at -45^o and 90^o showed serious damage in the form of cracks. Frequently occurring cracks were induced at low workpiece temperatures of -40 ^{o}C to 20 ^{o}C and could be avoided at higher temperatures. However, temperatures of 120^oC showed subsurface thermal damage. The authors found that milling CFRP at 80^oC led to the best results as this is close to the glass transition temperature of the epoxy.

Meshreki [23], performed a study on high speed milling of CFRP in the range of 10,000 to 40,000 rpm with a range of 200 to 800 m/min cutting speed, using a 6.35mm diameter solid

carbide end mill. The material was a 35 ply 8-harness satin weave quasi-isotropic laminate. Slotting was performed at the full thickness of the 6.35mm material. Tool wear was measured after 32 mm of cutting distance on the flank and rake faces. Cutting forces and temperature were measured using a Kistler 9255B dynamometer and ThermoVision A20M infra-red camera, respectively. Surface delamination occurred when fiber direction in the top ply was perpendicular to the feed direction. The authors found that a decrease in feed per tooth with increasing speed generates lower forces, lower temperatures, less tool deflection, and provides a better surface finish.

Wang [24] studied cutting performance of CFRP milling using a PCD cutting tool at high speed. The 18 ply multidirectional CFRP laminate used in the study had a 55% fiber volume made from T800 fibers. A 8mm diameter two-flute PCD tool was used. Axial forces were measured with a Kistler 5070 dynamometer. A regression orthogonal experimental method of three factors and three levels was used to study the effect of cutting speed, feed rate, and cutting width on cutting force, delamination factor, and surface roughness. Delamination was found to be in an acceptable range when the cutting force was below 200N, but tended to rise when the cutting force was over 200N. Surface roughness tends to rise with increasing cutting force when cutting force is below 250N, but decreases with increasing cutting force when cutting force is over 250N.

Yashiro [25] compared cutting temperature in edge trimming using three methods as temperatures higher than the glass transition temperature of the thermosetting matrix will result in degradation of the resin which can cause delamination leading to reduced strength. The first method used tool-workpiece thermocouple. In the second method, the endmill surface during cutting was measured using a infrared thermographic camera. In the third method, the machined surface temperature was measured using a thermocouple embedded in the workpiece during layup. The workpiece was a 7.2 mm CFRP plate made from plain weave prepreg. Downmilling and dry cutting were employed during the measurements. The authors found that high-speed cutting up to 300 m/min was feasible without exceeding the glass transition temperature of the matrix.

Geis [26] presented a method to prevent delamination in the top layer of composite laminates by using a measurement and scoring process prior to milling. The authors found that the machined groove of the scoring process interrupts delamination propagation when milling. Measurement is first used to correct for variations in workpiece thickness to ensure constant width of the scored slot. The scored slot depth is less than .5 mm with feed velocity up to 16 m/min. The scored component was then machined with a PCD tool with two cutting edges producing no delamination in the top layer.

Hintze [27] studied the influence of trimmed edge position relative to the weaves when milling CFRP woven fabrics. The authors found delamination of different types and magnitudes compared to non-crimp fabrics with one factor being varying thickness of the top resin layer. The maximum length of protruding fibers was found to be always smaller than half the tool diameter and reach maximum length when the milled edge and next crossing fill yarn is largest.

Hagino [28], studied the effect of edge trimming using cutting tools with three different helix angles (0^o, 30^o, 45^o), three different fiber orientations (0^o, $\pm 45^o$, 90^o), at constant cutting conditions (70 m/min, .056 mm/tooth, 3 mm depth of cut). The authors measured surface finish, flank wear, cutting force, cutting temperature, and chip geometry. The authors found that cutting the 90 degree fiber orientation had the best surface finish and lowest cutting temperature. The authors also found that forces (Fx, Fy) were greatly affected by carbon fiber orientation with the 0^o helix angle tool having the lowest cutting force. In another paper by the same group, Inoue [29], studied machinability of quasisotropic and plain weave laminates using HSS, Nitride coated HSS, Carbide, TiAIN coated carbide, and PCD tools and measured cutting force, cutting temperature, and tool wear. The authors found that the PCD tool had the lowest cutting temperature and coating of tools with the same base materials did not improve tool life.

2.3.1.2 Influence of milling parameters on tool wear and surface roughness

A series of other types of papers utilized experimental design to evaluate the effect of cutting tool material with respect to tool life. Kohkonen [30] used six basic milling cutters to machine a unidirectional laminate made from AS4 carbon fiber using 3501-6 resin. Two of the cutters were helical carbide end mills, two cutters were PCD straight flute end mills, and two

cutters were PCD helical end mills. Among some of their results they found that the carbide wear ratio (flank wear per length of cut) was much higher than for PCD tools and further that the wear ratio was higher when cutting parallel to the fiber direction compared to machining perpendicular to the fiber direction. Surface finish roughness was found to be higher when machining perpendicular to the fibers because of whisker fibers protruding from the matrix. Cutting speed did not show any significant difference in either the tool wear ratio or in the work piece surface finish. Not surprising, the PCD end mills maintained a sharper edge when cutting the composite material than did the carbide tools.

Chao and Hwang [31] conducted experiments in milling CFRP composites to validate a Taguchi model with factors including federate, cutting speed, depth of cut, grade of carbide tool, and tool relief angle. In this work, the authors assumed the best operating condition was the combination of factors and levels that produced the minimum cutting force which was measured by a 3 channel milling dynamometer. Rahman [32] performed a machining study of a 450AC carbon/PEEK thermoplastic with a 30% fiber volume fraction to investigate the effects of machining parameters on tool wear and surface quality of the workpiece. The design of experiments used factors including cutting speed, feedrate, depth of cut, and use of coolant. The tools used in the study were uncoated cemented carbides. The authors found that depth of cut, feed rate, and cutting speed were the most significant factors affecting the amount of tool wear, where use of coolant had the least significant effect. Surface finish was found to improve until a critical cutting speed was reached and then became independent of the machining parameters above this critical cutting speed. The cutting temperature at this critical cutting speed was found to exceed the glass transition temperature of the material, at which point the polymer becomes rubbery, thus cutting marks became indistinguishable. Lower cutting force was encountered above the critical cutting speed.

Davim [33,34] performed an experimental study using analysis of variance (ANOVA) and Multiple Regression Analysis (MRA) to investigate the influence of milling parameters including; cutting velocity and feed rate on the machining force, delamination factor, surface roughness, and international dimension precision (IT) of two glass fiber reinforced plastic (GFRP) composites. IT is approximately 30xRa surface roughness in μm. The matrices used in the study were Viapal VUP 9731 and ATLAC 382-05 with 65% glass fiber volume. The cutting

tool was a cemented carbide end mill. The value of the machining force in the workpiece is the square root of the sum of the squares of the X, Y, Z orthogonal components of machining force in the workpiece measured using a dynamometer. The delamination factor is the ratio of the width of maximum damage to nominal width of cut. International dimensional precision is approximately 30 times the arithmetic average roughness. In this study the authors found that machining force in the work piece increases with feedrate and decreases with cutting velocity, where feedrate was found to have a more significant influence on machining force than cutting velocity. The delamination factor was found to increase with both feedrate and cutting velocity with feedrate having the highest physical influence on delamination factor. The surface roughness and IT increases with feed rate and decreases with cutting velocity, with feedrate having the most significant influence. MRA was used to correlate factors of cutting speed and feedrate to machining force in the workpiece, maximum peak-to-valley height, and delamination factor for both materials. For both materials, the multiple correlation coefficient, or R-value, was between .96 and .99 for cutting force, peak-to-valley height, and delamination factor.

In another study, Davim and Reis [35] evaluated the effect of cutting parameters including cutting speed and feedrate on surface roughness and damage of a CFRP material with 55% fiber volume. The cutting tools were two-flute and six-flute cemented carbide K10 end mills each 6mm in diameter. Three levels of both cutting speed and feedrate were used in a L_9 orthogonal array experiment for both types of end mills. Delamination factor was measured in addition to surface roughness. MRA was used to correlate factors of cutting speed and feedrate to surface roughness and delamination factor. The R value, for the two-flute end mill was R=.93 for surface finish and R=.89 for the delamination factor. For the six-flute end mill, R=.94 for surface finish and R=.67 for the delamination factor. From the cutting tests, the two flute end mill was found to produce less damage on the CFRP composite than the six-flute end mill and had a smaller delamination factor. Feedrate was found to have a more significant influence than cutting speed on surface roughness and delamination factor for both end mill sizes. Surface roughness was found to increase with feedrate and decrease with cutting velocity. Delamination factor increases slightly with increasing feedrate for both size end mills.

Ucar and Wang [36] performed end milling experiments on CFRP using four-flute TiN-coated carbide end mills with a 30 degree helix angle and 11.11mm tool diameter. The composite material was R6376 resin reinforced with IM6 carbon fibers with a 63% fiber volume fraction. Two components of cutting force were measured in addition to workpiece surface roughness and tool flank wear. The authors found that increasing cutting speed decreases cutting forces; however, increasing the feedrate while keeping the cutting speed constant increases chip thickness thus increasing cutting forces. Surface roughness decreases as the cutting speed increases and surface roughness increases as the feedrate increases. As cutting speed and feedrate increases, tool flank wear increases and further increases as cutting length increases, thus tool wear was highly affected by cutting speed and feedrate. The authors also observed parallelogram shaped discontinuous chips and fine powder chips consistent with other observations. This study demonstrated that TiN coated carbide tools could be used for machining CFRP.

Sheik-Ahmad and Sridhar [37] performed experiments to characterize the wear behavior of chemical vapor deposition (CVD) diamond coated carbide tools during edge trimming of CFRP using a low and high feedrate. The material used in the study was a CFRP laminate consisting of 12 plies of interwoven fiber fabric with a 50% fiber volume fraction. A four flute helical end mill was used in the study with (3) coating configurations. The first cutter configuration was an uncoated C2 grade tungsten carbide with medium grain size and 6% cobalt content. The second cutter used had a thin 10 μm diamond coating applied to the substrate by the hot filament CVD process and third cutter consisted of a thicker 20 μm diamond coating applied to the substrate. Measurements included cutting force, tool flank wear, and workpiece surface roughness. The diamond coated tools demonstrated much better performance in wear resistance than the uncoated tool at low and high feedrates. Wear of the diamond coated tools is dependent on the feedrate, where at low feedrates the tool wore by uniform abrasion of the diamond film and substrate, and at high feedrates the diamond film chipped with apparent delamination.

2.3.1.3 Diamond abrasive tools for edge trimming

Another series of publications investigated the use of diamond abrasives for edge trimming of CFRP composites in place of more conventional fluted cutters. Colligan and Ramulu [38], studied the characteristics of machined edges produced by diamond abrasive cutters in CFRP and documented the cutting forces produced by representative cutters with varying grit sizes and feedrates. For this study, a 25 ply, 8 mm thick laminate made from fabric plies consisting of 3506-1 resin and IM-6 fibers was used. Four diamond abrasive grit sizes were used in the tests, with 1 or 2 different diameter cutters per grit size. Side and thrust forces were recorded by a piezoelectric load cell. Surface finish was measured with a surface analyzer and from photographs of the machined surface using an optical microscope. The authors concluded that the machined surface finish was directly related to the grit size of the cutter being used and was not significantly related to the other process parameters such as feedrate, cutting mode, and cutter diameter. The thrust and sideload forces were found to be inversely proportional to the grit number and directly proportional to the material removal rate. For full width cuts, the sideload was 40% less than the thrust load, where for partial width cut using fine grit cutters, the sideload was greater than the thrust force and in the opposite direction of the full width case. In all the trimming tests conducted using the diamond abrasive cutters, no delaminations were found in the workpiece material.

Janardhan [39] studied the effects of edge trimming CFRP using a diamond interlocking burr tool. The material used in this study was a CFRP laminate of 10 plies of plain weave carbon fiber fabric. The cutter used was a 6.3mm diameter router bit with pyramid shape cutting points generated by an intersecting spiral ground into the tool. Three levels of cutting speed and three levels of feedrate were used in the experiment with a constant radial depth of cut. Measurements were made for tool flank wear, net spindle power, and surface roughness. Three types of delaminations were observed which were distinguished by size and geometry. Up milling provided less delamination than down milling. Surface roughness increased with increasing feedrate and fracture of the pyramid tips generally occurred at high feedrates and low spindle speeds. Feedrate was found to be more significant on the process than spindle speed.

López De LaCalle [40,41] presented a process for developing a family of router tools for high performance milling of CFRP. In this work, five levels of tests were performed to optimize the design of multi-tooth milling tools by conducting trimming experiments using multidirectional laminates of CFRP and multidirectional laminates consisting of an epoxy matrix with carbon and Kevlar fibers. The first test was performed to define the specific cutting force for CFRP and compare it to other known materials. The second test was performed to identify the appropriate carbide grade for the tool substrate. The third test was to find the best coating. The fourth test was performed to define the best pyramidal-like edge geometry. The fifth test was to find the highest productivity conditions for trimming CFRP with PCD cutting tools. After completion of the tests the authors found that multi-tooth milling tools made using a micrograin carbide with a 6% cobalt substrate coated with a 4 μm layer of TiAlN resulted in the best tool life, reaching 40-50m before bad cutting was detected. Tool wear was found to be caused by abrasion so, in general, the thicker the coating layer the longer the tool life. A 4μm coating is recommended as a thicker coat affects cutting edge sharpness. The carbon and Kevlar reinforced composite were more difficult to machine than CFRP. Up milling provided a better finish than down milling where some delamination was detected. In this study, PCD tools were not found to be economically feasible so the authors concluded the multi-tooth milling tool was the first choice for trimming CFRP.

2.3.1.4 Effect of edge trimming damage on mechanical properties

Another area of interest in edge trimming of composites is the effect of milling on mechanical properties as high temperatures generated during machining and surface damage may cause a reduction in mechanical performance. Ghidossi [42,43,44] studied the influence of cutting parameters on the damage level and mechanical response of glass epoxy unidirectional coupons by side milling on three fiber orientations. In one study, the authors used a glass/epoxy prepreg unidirectional composite with a 47% fiber volume manufactured by hand layup. Two types of cutting tools were used in the experiments including a tungsten carbide tool (CW) and polycrystalline diamond (PCD). The authors found that off-axis tensile failure stress of glass/epoxy composites are significantly influenced by machining parameters and that roughness criteria used to quantify the quality of machined surfaces are not representative of the mechanical performance. A reason for this is that mechanical surface analysis is not able to detect

subsurface damage which is considered to be a factor responsible for the reduction of ultimate stress capability. Further, the type of damage is strongly influenced by the angle between the fiber direction and cutting edge. Figure 2.16 illustrates the effect of cutting speed on ultimate stress for a fiber angle of 15 degrees using both CW and PCD tools at two different feed rates. The authors concluded that there is still considerable work to be performed to fully understand how the damage caused by machining processes propagates and leads to a reduction in mechanical performance.

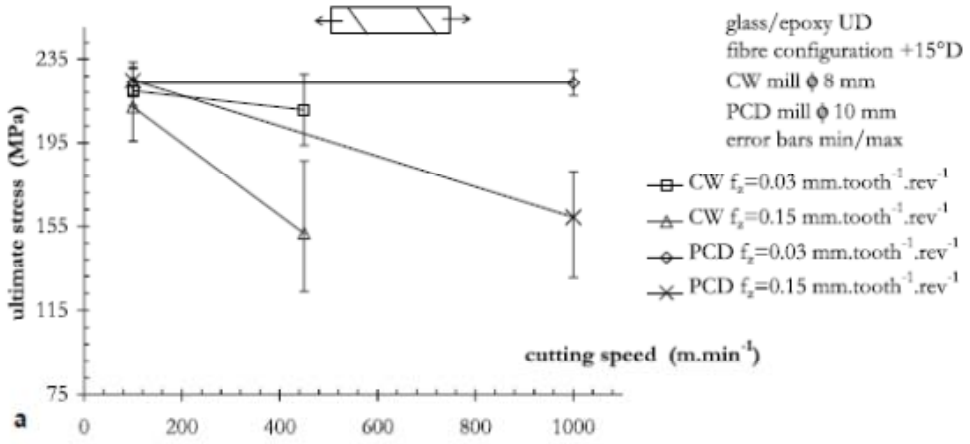

Figure 2.16. Effect of cutting speed on ultimate stress (Source: Ghidossi [44]).

Haddad [45] studied the effect of compression strength of multidirectional CFRP specimens trimmed using three types of cutting tools including a tungsten carbide burr tool, diamond coated burr tool, and a 4-flute diamond coated end mill at two different cutting speeds of 150 and 250 m/min. Compression strength was approximately 275-300 MPa for all cases with an R_a between 1 – 8 μm. For the uncoated burr tool, separate data was provided where compression strength ranged from 302 MPa to 235 MPa with the former corresponding to an approximate R_a of 4 μm and the latter to an R_a of 35 μm.

2.3.2 Force Prediction Models

A series of papers were presented that attempt to predict milling force when machining composite materials. Other papers investigated models for predicting stability while milling from cutting force measurement. Models for calculating cutting forces in metals are not directly transferable to the machining of composites because of material anisotropy. The material anisotropy attributed to fiber reinforcement within the matrix influences chip formation. Other

characteristics such as orientation of the fiber axis relative to the cutting direction further complicate cutting force analysis. No papers on finite element numerical methods for milling composite materials have been published; however, papers that address orthogonal FEM work are included for completeness.

2.3.2.1 Analytical and Empirical Approaches

Puw and Hocheng [46,47,48,49] presented a mechanistic model for predicting milling force when machining both thermoplastic and thermoset fiber reinforced plastics, and metal matrix composites. In metal cutting, the milling force is found from chip load on the cutter where instantaneous cutting force is proportional to the sectional area of the chip. In their model, Puw and Hocheng first conducted planing experiments both parallel and perpendicular to fiber direction. From these experiments, empirical expressions of the major forces in the X and Y directions were derived. The mechanistic model of proportionality was then used to predict milling forces in Carbon/ABS and SiC/Al composites. The model of proportionality states that the force component perpendicular to tool velocity is proportional to the parallel component. According to the data presented, the predicted milling force in the X and Y directions closely matched the milling force for angular positions of the cutter between 0 and 40 degrees for Carbon/ABS for two different feed/tooth rates. The plot of milling force predicted for SiC/AL was of the right shape compared to the experimental data, but off by nearly 100%, with a larger error for a larger width of cut. The model of independency was used to predict milling force in Carbon/PEEK composites. The model of independency states that the force components perpendicular and parallel to the tool velocity are not functions solely of tool geometry, but also of the anisotropic material structure. The milling force predicted for Carbon/PEEK was of the right shape, but was up to approximately 50% off the experimental data, with roughly the same accuracy for the two different feed/tooth rates presented when both cutting parallel and perpendicular to the fiber axis. The force prediction model showed significant deviation when used to predict cutting forces in Carbon Epoxy laminates compared to measured results for cutting parallel and perpendicular to the fiber axis. The authors proposed a modification to their model using multiple directional cutting energy and effective chip load to improve the model prediction accuracy for carbon epoxy. Further, since damage cannot be avoided in low plasticity thermosets, the milling force predictions required adjustment for the existence of surface

damage. The force prediction model for carbon epoxy better represented the experimental results when damage effects were incorporated into the model; however there was still significant difference between the model and experimental results as shown in figure 2.17.

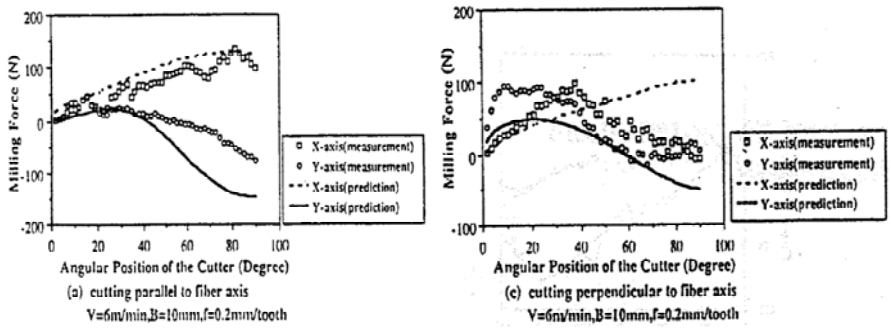

Figure 2.17. CFRP Milling force predictions (source: Puw and Hocheng [48]).

Sheik-Ahmad, et. al. [50,51,52,53,54,55] expanded upon the work by Puw and Hocheng by using a milling test instead of a linear planing test to generate specific cutting energy functions. This was done because the cutting direction in milling continuously changes its inclination with respect to fiber direction. A continuous range of chip thicknesses becomes possible because the chip thickness in milling varies with the angular position of the cutting edge. The authors concluded that by conducting milling experiments on a few laminate orientations, a specific cutting energy function for a wide range of fiber orientations and chip thicknesses could be obtained. The specific cutting energy function can then be used to predict cutting forces for any cutting geometry and fiber orientation. The force prediction model was compared to experimental results using four unidirectional laminates, each 2.5 mm thick, with fiber directions of 0, 45, 90, and 135 degrees. In addition, a multi-directional laminate, 10 mm thick consisting of all four primary fiber orientations was tested. A vertical milling machine and cutting tool with a single carbide cutting edge was used in the experiments and X and Y cutting forces were measured using a dynamometer. From data presented, the 45 degree laminate test seemed to be the closest to the X, Y cutting forces predicted by the model. The measured X, Y forces in the other three laminate directions 0^o, 90^o, and 135^o differed significantly more from the model predictions, with the 0^o and 90^o results as shown in figure 2.18. In the experimental results from the multi directional laminate, the Y force component more closely matched the prediction than the X force component, yet with still some significant error. Expansions of their work include incorporating artificial neural networks (ANN) in their model to predict specific

cutting energies of unidirectional composites as a continuous function of fiber orientation and chip thickness for helical end mills. Accuracy of the model for helical milling was approximate for unidirectional 0^o and 60^o laminates for the X, Y, and Z cutting force components, but had significantly larger prediction errors for a $60^o/0^o/120^o$ multidirectional composite laminate.

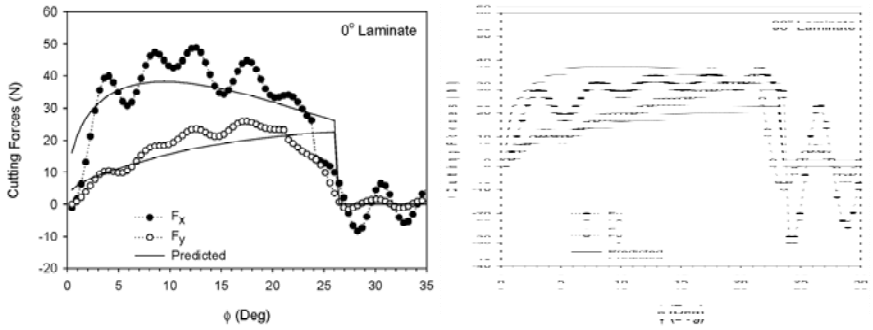

Figure 2.18. Milling force prediction (source: Sheikh-Ahmad and Yadav [50])

Karpat [56,57,58] proposed a mechanistic milling force model for multidirectional CFRP laminates based on experimental investigation A two-flute, 10mm diameter PCD and 9.575mm diameter three-flute PCD cutting tool were used in this study. Slotting experiments using 30 ply unidirectional CFRP laminates were performed with forces measured using a Kistler 9123C rotating dynamometer. The x-axis of the dynamometer was aligned with the radial direction of the milling tool. Tangential and radial cutting force coefficients were calculated at 0^o, 45^o, 90^o, 135^o positions of tool rotation. A sine function was then used to relate the cutting force coefficients to fiber cutting angle by means of a least squares optimization. The results from the model were then validated using a 72 ply multidirectional laminate with repeating 0/45/90/135 fiber directions. The predicted results presented approximated the magnitude and shape of the experimental measurements for the laminate and cutter combination. Further cutting tests were performed to study milling forces and surface quality. Delamination and maximum tangential force locations were within the same range for 0^o, 45^o, and 90^o fiber directions. Maximum location of radial forces was in the same range for all fiber directions. The $45^o/135^o$ fiber directions yielded lower machining forces than the $0^o/90^o$ fiber directions. The authors found an approximate match between the location of maximum tangential force and regions of delamination. This work was expanded to include a mechanistic model for trimming with double helix angle compression cutters [58]. In this work, cutting force coefficients are calculated based on laminate fiber direction directly using tangential and radial forces which may

be an advantage for testing using rotating dynamometers. The technique described in this paper was leveraged in the milling model discussed in Chapter 8.

Sen [59] investigated multiscale dynamics of cutting force during milling of epoxy polymer matrix reinforced by carbon fibers (EPMC) at different spindle speeds using multifractals and wavelets. The spindle speeds ranged from 2000 to 8000 rpm, with a fixed feed rate of 520/min. A 12mm diameter steel diamond coated cutting tool was used in the experiments. The largest cutting force, Fx, in the machining direction was measured. Compared to traditional Fourier Transforms, wavelet analysis provides a way of adjusting the time and frequency resolutions in an adaptive fashion. The wavelet analysis revealed that short or high frequency periodicities of 2 and 10 sampling periods are intermittent. The authors conclude that this method can be used to study the stability of the milling process and develop new methods of control.

Rusinek [60,61] studied the effect of feed rate and rotational speed on cutting force during milling of EPMC with the objective to develop a new mathematical model of the composite material cutting process. In their experiments, rotational speed was varied from 2000 to 8000 rpm and feed rate from 200 to 720 mm/min, with depth of cut at .5mm. The cutting tool was 12mm diameter diamond coated steel. Three axial components of cutting force were measured. The recorded cutting force data was analyzed using the method of delay coordinates to recognize the type of vibration from the cutting conditions. In this study, the authors used the ratio of force amplitude to mean force as a simple stability criterion. If this ratio is greater than 4, the process is considered unstable. From this study, the authors observed that when feed rate increases cutting resistance increases. Further, change of rotational speed can lead to stable and unstable cutting regions (lobes). As a result, in order to avoid chatter vibrations, rotational speed should be set in the region where cutting force is minimized. The authors found oscillations in cutting force are more regular with larger amplitude during unstable cutting while cutting is stable with less amplitude.

Zaghbani [62] presented a model for predicting average cutting forces during milling of CFRP using a third degree polynomial to describe the average feed and thrust forces that vary

non-linearly with feedrate. The non-linear correlation expresses average cutting forces as a function of the feed per tooth. The authors provided data that demonstrated the instantaneous cutting force increases with increasing feedrate, and for a given feedrate, the cutting forces increases with increasing cutting speed. For the cases presented, the model estimation errors were between 7-15%. Tool wear is not considered in the model with influence avoided through short machining periods. Forces from machining 6061-T6 aluminum were compared to forces machining a 0 degree unidirectional laminate to illustrate the effect of material non-linearities. The resultant force from trimming a unidirectional 0 degree CFRP compared to 6061-T6 was approximately 40% greater using an uncoated carbide straight 2-flute end mill under identical cutting conditions of .1016 mm/tooth feed rate and 100 m/min cutting speed.

2.3.2.2 Finite Element Modeling

Finite element modeling applied to the machining of FRP material is relatively new. One of the first, if not the first, papers on this application was published in 1997 by Arola and Ramulu [63]. In this paper, numerical simulations were conducted to demonstrate the use of finite element analysis and its ability to describe observed fracture mechanisms of orthogonal cutting of FRPs which were verified with experimental results. The authors concluded that numerical modeling has unlimited potential for future tool designs in machining of FRPs. Ramesh, et. al. [64] presented a Langrangian formulation-based elasto-plastic finite element analysis that was applied to four different materials. Mahdi and Zhang [65] further concluded that when using the Tsai-Hill criterion for chip separation and the segmental contact treatment that the FE model leads to a reasonable prediction when compared to experimental results. Arola, et. al. [66], developed a FE model for chip formation for orthogonal machining of unidirectional FRPs which utilized a dual fracture criterion comprised of primary and secondary fracture. Primary fracture consisted predominantly of fiber failure and secondary fracture occurred through matrix failure. This model was capable of predicting the principal and thrust cutting forces. The authors found that sub-surface edge trimming damage increased with increasing fiber orientation and generally increased with decreasing rake angle of the cutting tool such that the optimum rake angle to minimize sub-surface delamination should be designed for machining 75^{o} and 90^{o} fiber orientations. Finally, the authors recommend the best tool geometry to have a 15^{o} rake angle to

minimize cutting forces or a 10^{o} rake angle to minimize sub-surface damage, thus validating the conclusion that FE modeling could be used for future tool designs.

Nayak [67,68] presented a Finite Element (FE) analysis of a macro-mechanical Equivalent Homogeneous Material (EHM) model during an orthogonal machining operation and a micro-mechanical FE analysis of machining considering the workpiece as a two phase material system comprised of both fiber and matrix. For the macro-mechanical model, the authors made the following assumptions:

1. The work material is anisotropic, but locally homogeneous
2. The cutting tool is a rigid body
3. A quasi-static simulation process was utilized
4. The effect of heat generation during machining is neglected
5. Coefficient of friction between the tool flank and work material was used
6. Model dimensions are 100mm x 40mm
7. Cutting speed was limited to .5m/min

The coefficient of friction was incorporated in the FE model because the authors believe it is dependent on fiber orientation of the workpiece and cutting tool, and could substantially vary. This in turn could affect the accuracy and reliability of the model in predicting machining responses. A pin-on-disc experiment was used to determine the coefficient of friction between the machining plane and the tool flank surface during orthogonal machining. To determine the coefficient of friction, a High Speed Steel (HSS) disc is used on a rotating surface to simulate the flank of the tool and a Uni-Directional Glass Reinforced Plastic (UD-GFRP) specimen used in a specially designed holder acts as the pin. A total of 32,000 elements were used in the finite element mesh with a combination of plane stress quadrilateral (CPS4) elements with four nodes, and triangular (CPS3) elements with three nodes used to construct the model. The friction property used in the FE analysis is based on the "Basic Coulomb Friction model", and the different friction coefficients obtained from the pin-on-disc experiment were incorporated at the tool flank and workpiece interface at corresponding fiber orientations. The authors used two different failure criteria. One was for node debonding along the trim plane due to a specified critical stress, and the other due to Tsai-Hill for chip release. The stress developed at the node nearest to the tool tip was compared to a pre-defined critical stress, and node separation was allowed when the state of stress exceeded a specified threshold value. The Tsai-Hill failure envelope was used as the material failure criterion, such that failure occurred when the calculated

value was greater than or equal to 1, according to the famous Tsai-Hill equation. The cutting and thrust forces are calculated during the simulation from the reaction exerted by the workpiece on the rigid tool. The horizontal and vertical components of the reaction forces are the cutting and thrust forces, respectively. Both components of the cutting forces were calculated at the disbonding of two consecutive nodes on the trim plane, namely chip release, when the Tsai-Hill criteria was satisfied. The first block of chip is then removed, prior to the start of the next simulation. The sub-surface damage was considered to be the extent of the spread of the Tsai-Hill envelope below the trim plane.

In the micro-mechanical machining model, the authors use a two-phase FE model consisting of both fiber and surrounding matrix as distinct physical entities to simulate the machining process and to investigate the role of fiber in influencing the machining response with mode of fiber failure. For computational efficiency, the authors used a single fiber to model the problem. Six different FE mesh models were constructed for 15, 30, 45, 60, 75, and 90 degree fiber orientations. The total number of elements varied between 30,000-110,000 elements, depending on fiber orientation, such that the higher the fiber orientation, the lower the number of elements used. A combination of 2-D plane stress continuum (CPS3) and quadrilateral (CPS4) elements were used to construct the FE mesh. The typical size of the elements in the fiber and at the fiber-matrix interface was 1μm x 1μm and made courser farther away from the interface region. The assumptions used in the micro-mechanical model are as follows:

1. The work material is two physically distinct parts of fiber and matrix, each isotropic
2. The cutting tool is a rigid body
3. The diameter of the glass fiber is 10μm
4. The simulation is quasi-static and restricted to 2 dimensions
5. The coefficient of friction was neglected

The purpose of the micro-mechanical model was to effect node release when the normal and shear strength of the fiber-matrix interface was overcome due to tool movement against the fiber. This was accomplished by giving a displacement to the rigid body tool against the fiber embedded in the matrix. This in turn induced stress in the fiber and when the stress at the node nearest to the tool tip along the fiber-matrix interface reached a pre-defined value, the nodes are allowed to separate. The node separation at the fiber-matrix interface continues until fiber fracture initiates. The fiber fails when the maximum in-plane principal stress exceeds the fiber

tensile or compressive strength. The cutting and thrust force due to the reaction at the rigid body node are calculated at fiber failure.

In the paper by Lasri [69], the authors use numeric modeling of the orthogonal cutting process to show the influence of working parameters including tool geometry, cutting conditions, fiber orientation on chip formation. This is accomplished using Abaqus with a User-Defined subroutine (USFLD). The subroutine is used to introduce solution-dependent material properties. Further, the authors use the "Stiffness Degradation Concept" for machining. The authors computed strain distribution, damage evolution, and strength of the laminate and compare these to experimental data. The authors adopted a mixed failure criteria combining Hashin and Maximum Shear Stress theory to simulate the chip formation and progression of damage during machining. In order to accurately simulate damage evolution, the authors applied a combination Hashin and Maximum Shear Stress failure criteria to five modes including:

1. Matrix tensile failure
2. Matrix compression failure
3. Fiber-Matrix shear failure
4. Fiber tensile failure
5. Fiber compression failure

After the failure indice values are obtained, the mechanical properties in the damaged area are automatically reduced according to a numerical scheme of implemented stiffness degradations. The applied degradation rules correspond to a brittle failure with no energy absorption, as the assumption of brittle failure had been previously confirmed. The authors used a constant friction coefficient of 0.5 to specify friction for the contact between the tool rake face and workpiece.

2.3.3 Acoustic Emission Signal Processing for Manufacturing Applications

Acoustic Emission (AE) has seen significant growth in use for process monitoring and quality control in manufacturing processes since discovery in the early 1950's in Germany as identified by Dornfeld [70]. In machining, AE may be used to detect tool fracture, tool wear, chip formation, and chatter due to its sensitivity to process parameters. A major advantage of using AE to detect the condition of tool wear is that the frequency range of the AE is much higher than that of the machine vibrations and environmental noise. A few selected works of AE and vibration signal monitoring in composite drilling and milling are summarized in the

following paragraphs to illustrate the potential for AE monitoring of milling operations in composite materials for tool wear, surface integrity, and possibly chip formation.

Drilling and machining experiments at the University of Washington were conducted using HSS, PCD, carbide and cryogenic treated carbide drills into carbon fiber-reinforced thermoset and thermoplastic composites, namely Graphite/Epoxy, Graphite/PIXA-M composites since 1989. Ramulu and Kim characterized cutting mechanisms by cutting force signal analysis [71]. During drilling, force signals were collected from all conditions and analyzed using Fast Fourier transformations and autoregressive (AR) time series models. Power spectrums were used to examine the cutting characteristics in the drilling process. The authors found a strong correlation between AR coefficients and the cutting characteristics.

Mascaro [72] studied the characteristics of acoustic emission during drilling of CFRP composites and reported experimental results. During the drilling process of the full thickness laminate, five AE signals from different drill depths were stored and concatenated to make only one representative signal. The authors reported in all drilling configurations, the drilling process produced a characteristic acoustic signature in the frequency range of 150 – 200 kHz, and that this frequency band is independent of the tool geometry, rotation speed, and thrust force. It was also reported that, the energy of this acoustic signature is sensitive to tool wear and constitutes a good feature for AE monitoring. In addition, the higher frequencies of the AE were related to the cutting of the carbon fiber.

Arul [73] conducted an experimental investigation to determine the relationship between AE rms and cutting parameters during drilling of polymeric composites. Drilling trials were performed on 4 mm thick woven GFRP composites using a 6 mm diameter HSS drill with a cutting speed of 9.43 – 30.16 m/min and feed rate of 0.02 – 0.08 mm/rev. AE signals were measured with a Kistler wide band piezoelectric AE sensor, and the thrust force during drilling was also measured using a Kistler two-component dynamometer. Two small and large spikes in the AE signal were associated with damage modes, where the small spike was attributed to delamination, while the large spike was attributed to breakage of the glass fibers. The power of the AE signal was found to progressively increase with the number of holes drilled, and after 30 holes there is a sudden rise in power. The rise in power was attributed to a higher order of

stressing of the material which resulted in fiber cracking, matrix crazing, and other associated defects. The AE rms values increased with an increase of cutting speed from 18.85 – 23.56 m/min which provided an indication of favorable drilling conditions in this region, whereas the decrease of the AE rms value was associated with a deterioration in performance of the drill.

Chibane [74], performed vibration analysis to study defects when milling CFRP. The authors conducted 20 combinations of tests using a 80 mm diameter milling cutter equipped with a single PCD insert and varied three parameters including cutting speed, feed rate, and depth of cut. Vibrations were measured with a triaxial accelerometer mounted on the workpiece and RMS acceleration was calculated for each test. Regression factors and ANOVA was used to determine significance of the model. The authors found a correlation between recorded vibration level and defects such as delamination with RMS vibrations being influenced only by the interaction of feed rate and depth of cut. To apply this method for different configurations, experimentation is required to address the affects of different materials, cutting tools, machine type, clamping, and position of the accelerometer.

Marinescu [75], studied the use of AE sensors for monitoring both tool wear and surface integrity during milling of Inconel 718 using a 16 mm diameter end milling cuter with two coated inserts. A 4-component stationary dynamometer and AE sensor bolted on the workpiece were used to acquire force and AE signals during the milling trials. Synchronized signals were acquired using two National Instruments PCI boards with data processing using MatLab codes. A low-pass filter with a cut-off frequency of 500 Hz was used to filter cutting force signals that had poor signal-to-noise. The authors found use of the resultant force was more effective to identify correlations between increasing tool wear and amplitude of force signals due to sign changing of the individual Fx, Fy force components. However, the resultant force did not have sufficient resolution to detect the moment when each cutting edge start and ends cutting and further to monitor tool wear. To address this, short-time Fourier Transformation (STFT) of the AE signal was used to identify entrance/exit of the cutting edge. This was used to support calculation of areas under the resultant force curve combined with averaged resultant force values to predict critical levels of tool wear. The identification of a targeted frequency band (TFB) was in correlation with the gradual increase of tool wear. The authors also found that simply using average resultant force values was not sufficient for

detecting surface integrity. To addresses this, plots of AE energy counts were combined with average resultant force and cutting length to determine when milling generates damage-free or anomalous workpiece conditions which was supported by surface and metallographic investigation.

2.4 Machining Dust Studies of Composite Materials

Unlike metals, chips produced from milling of CFRPs are largely a powder-like material or dust which is currently classified a nuisance particulate. Some portion of the generated dust from composite milling has been shown to be an aerosol. An area of concern for any manufacturing process is safety for the workers and environment. The next sections provide an introduction to aerosol science and discuss the current work and results of studies on the effect of carbon fiber dust in the workplace.

2.4.1 Introduction to Aerosol Science

An aerosol is a suspension of solid or liquid particles in a gas. Particle size is the most important parameter for characterizing the behavior of aerosols. Particles less than 50 nm are called nanometer particles or nanoparticles. The European Commission adopted a recommendation in October 2011 for a common definition of nanomaterials, which consists of a natural or manufactured material containing particles where for 50% or more of the particles in the number size distribution, one or more external dimension is in the size range of 1 nm – 100 nm [76]. Where warranted by concerns for health and safety, the number size distribution threshold may be between 1 and 50%, such that fullerenes, graphene flakes, and single wall carbon nanotubes with one or more external dimensions below 1 nm should be considered as nanomaterials.

Particles greater than 10 μm have limited stability in the atmosphere. An equivalent diameter is the diameter of the sphere that has the same value of a particular physical property as that of an irregular particle. For approximate analysis, shape can usually be ignored, as it seldom produces more than a twofold change in any property. Particles with extreme shapes, such as long and thin fibers are treated as simplified non-spherical shapes in different orientations. The most commonly measured aerosol property, and the most important one for health and

environmental effects, is the mass concentration, which is the mass of particulate matter in a unit volume of aerosol (e.g. mg/m^3). Another common measure of concentration is the number concentration or the number of particles per unit volume of aerosol (e.g. $number/cm^3$).

Particle concentration is used to describe spatial distribution of a particular aerosol property and is defined as the specific property of the particle suspension per unit volume of gas [77]. Depending on the application, aerosol concentrations are described in different ways. Most common types of particle concentration are number, mass, surface area, and volume concentration. Particle number concentrations are used to characterize clean rooms. Workplace exposure standards are usually stated in terms of aerosol mass per unit volume of gas. Toxicology studies may utilize surface area concentrations. Volume fraction is used as a measure of particle concentration where the overall viscosity of the suspension is of interest. Particle number concentration is defined as the number of particles per unit volume of a gas (e.g. $particles/cm^3$). Particle mass concentration is usually determined by filtering a known volume of an aerosol and weighing the collected particles. The average mass concentration over the measurement time is obtained by dividing the measured particulate mass by the volume of gas filtered (e.g $\mu g/m^3$ or mg/m^3). An important characteristic of poly-disperse aerosols, such as those from milling operations, is the particle size distribution which represents the distribution of a specific aerosol property over the particle size range of interest. The representative size of a population of particles may be reported as the mean size (average of all sizes), median size (equal number of particles above and below the size), or mode size (highest frequency). The spread of particle size distribution is characterized by an arithmetic or geometric (logarithmic) standard deviation. Because of the way particles tend to be produced by successive breakups, aerosol particles size is generally plotted on a logarithmic size scale.

Stoke's law states that externally applied forces on an aerosol particle are opposed and rapidly balanced by the aerodynamic drag force, such that:

$$F_D = 3\pi\eta V_d \qquad (2.4.1)$$

One important application of Stoke's law is the determination of the velocity of an aerosol particle undergoing gravitational settling in still air. When a particle is released in air, it quickly reaches its terminal settling velocity, a condition of constant velocity where the drag

force of the air on the particle, F_D, is exactly equal and opposite to the force of gravity , F_G. Under this condition,

$$F_D = F_g = mg \qquad (2.4.2)$$

$$3\pi\eta V_d = \frac{(\rho_p - \rho_g)\pi d^3 g}{6} \qquad (2.4.3)$$

where

F_G = drag force of gravity

F_D = drag force of the air on the particle

d = particle diameter

ρ_p = particle density

ρ_g = density of the gas

η = viscosity

g = gravity

$$V_{TS} = \frac{(\rho_p d^2 g)}{18\eta} \text{ (stokes settling equation)} \qquad (2.4.4)$$

V_{TS} = terminal settling velocity for d > 1 μm and Re < 1.0 (Re = Reynold's number)

Terminal settling velocity increases rapidly with particle size being proportional to the square of the particle diameter. The above equation cannot be used for particles less than 1 μm unless a slip correction factor is applied. A simpler version of the equation which is valid only for spheres with standard density of 1000 kg per meter cubed at standard conditions is:

$$V_{TS} \sim 3.10^{-5}\ d^2 \text{ m/s ----------for } 1 < d < 100\ \mu m \qquad (2.4.5)$$

The terminal velocity for other kinds of external forces, such as centrifugal force, can be obtained by derivations similar to that given for gravity. In a centrifugal force field, the terminal velocity is:

$$V_{TC} = \frac{\rho_p^2\ d^2 a_c}{18\eta} = \frac{V_T^2}{R} \qquad (2.4.6)$$

a_c = centrifugal acceleration at the location of the particle

V_T = tangential velocity

R = radius of motion

The Stokes settling equation is of fundamental importance to aerosol studies, however it is only accurate (±10%) for determining the settling velocity of standard density particles having diameters of 1.5-75 μm. When a slip correction factor is applied, it is accurate for particles as small as .001 μm. An important assumption of Stoke's law is that the relative velocity of the gas right at the surface of the sphere is zero. Small particles, < 1μm, do not meet this assumption when their size approaches the mean free path of the gas. These particles settle much faster than predicted by Stoke's law because there is a slip at the surface of the particle. At standard conditions, this error becomes significant for particles less than 1 μm in diameter.

$$C_c = 1 + \frac{\lambda}{d}[2.34 + 1.05e^{-\frac{0.39d}{\lambda})}] \qquad (2.4.7)$$

where C_c = Cunningham correction factor, λ = mean free path = .066 μm for air at 101 kPa and 293K.

The slip corrected form of the terminal settling equation becomes:

$$V_{TS} = \frac{(\rho_p d^2 g C_c)}{18\eta} \qquad (2.4.8)$$

The equations discussed so far are based on spherical particles. Carbon fibers are not spherical so correction factors are required. The shape of a particle affects its drag force and settling velocity. The correction factor called the dynamic shape factor is applied to Stokes law to account for the effect of shape on particle motion. The dynamic shape factor is defined as the ratio of the actual resistance force of the nonspherical particle to the resistance force of a sphere having the same volume and velocity as the nonspherical particle. The dynamic shape factor is:

$$X = \frac{F_D}{3\pi\eta V d_e} \qquad (2.4.9)$$

d_e = equivalent volume diameter, diameter of a sphere having the same volume as that of the irregular particle

Applying the dynamic shape factor to the terminal settling velocity equation becomes:

$$V_{TS} = \frac{(\rho_p d^2 g)}{18\eta X} \qquad (2.4.10)$$

Note that the calculation of a slip correction factor for irregular particles is complicated, and that the approximate factor calculated for the equivalent volume sphere is adequate for most irregular particles. Except for certain streamlined shapes, the dynamic shape factor is greater

than 1.0 meaning that nonspherical particles settle more slowly than their equivalent volume spheres. Elongated particles such as fibers tend to line up with streamline while flowing in tubes. These particles are oriented perpendicular to the direction of settling.

A common equivalent diameter, is the aerodynamic diameter, d_a, which is defined as the diameter of a spherical particle with a density of 1000 kg/m3, the density of a water droplet, that has the same settling velocity as the particle. A related, but less common equivalent diameter is the stokes diameter, d_s, which is the diameter of a sphere that has the same density and settling velocity as the particle. A particle with an aerodynamic diameter of 1 μm is aerodynamically indistinguishable from other particles of different size, shape, and density having aerodynamic diameters of 1 μm. The aerodynamic diameter is the key particle property for characterizing filtration, respiratory deposition, and the performance of many types of air cleaners. Equivalent diameters based on a particle's mass, volume, or surface area have also been defined, which can be useful in describing particles with complex shapes, structures, or internal voids. Summarized definitions of these equivalent diameters include:

CMD - *Count Median Diameter* is defined as the particle size for which half the total number of particles are larger and half are smaller.

MMD - *Mass Median Diameter* defined as the diameter for which half the mass is contributed by particles larger than the MMD and half by particles smaller than the MMD. It is the diameter that divides the graphical representation of the distribution of mass into two segments of equal area.

MMAD - *Mass Median Aerodynamic Diameter* is defined as the mass median of the distribution of mass with respect to aerodynamic diameter.

CMAD - *Count Median Aerodynamic Diameter* is defined as the count median of the distribution of count with respect to aerodynamic diameter.

AMD - *Activity Median Diameter* is the median of the distribution of radioactivity or toxological or biological activity with respect to size.

MoED – *Mobility Equivalent Diameter* is the diameter of a sphere with the same mobility as the particle in question

VED - *Volume Equivalent Diameter* is defined as the diameter of a spherical particle of the same volume as the particle under consideration.

MED - *Mass Equivalent Diameter* of a particle is the diameter of a non-porous sphere composed of a bulk particle material that has the same mass particle in question.

EED - *Envelope Equivalent Diameter* is defined as the diameter of a sphere that is composed of a bulk particle material and includes the same internal volume of voids, and has the same mass as the particle in question.

PAED - *Projected Area Equivalent Diameter* is the diameter of a circle having the same area as that of a particle's cross-sectional area projected on a plane.

SMD - *Sauter Mean Diameter* is the diameter of a sphere with the same surface area-to-volume ratio as the particle under consideration.

2.4.2 Fibers

The term fiber has been applied to a wide variety of particles having an elongated shape, where one particle dimension is significantly greater than the other two [77]. Because of this elongation, fibers can have aerodynamic and other properties quite different from more compact particles. A variety of materials can be considered fibers from an aerosol behavior standpoint. Several materials, including glass and mineral slags, have been melted and spun into fibers. Ceramic materials have similarly been spun into fibers, as well as grown by chemical and vapor crystallization. Carbon and graphite fibers are produced commercially for high-strength products. Organic fibers, such as cotton, wood and other cellulosic materials are widely present in the environment, from both commercially produced materials and natural sources. Carbon "nanotubes" are a tubular form of carbon "buckyballs" (C_{60}), a molecular structure of pure carbon with very high strength and high conductivity. Airborne fibers can be single fibrils or various-size bundles with a range of diameters, while lengths can be less than 0.5 μm to several hundred micrometers. The magnitude of disparity between length and diameter often makes it difficult to make accurate size distribution measurements. The behavior of fibers suspended in a gas is a function of the fiber dimensions. Assuming either a cylindrical or prolate spheroidal shape, these dimensions can be defined by length and diameter. However, real fibers frequently do not meet either the ideal cylindrical or the prolate spheroid shape assumption.

Distributions of fibers are rarely monodisperse in diameter and even more rarely in length. This makes it difficult to provide adequate calibration for instruments that attempt to

measure fibers as well as to perform measurements of fiber toxicity as a function of fiber dimensions. Smaller fibers are affected primarily by diffusional forces, while the larger ones are affected by flow shear and inertial and gravitational forces. Fiber behavior differs depending on whether the major access is oriented parallel or perpendicular to the direction of motion relative to the surrounding gas. Drag of the fiber is greatest when it is oriented perpendicular to the flow of the surrounding gas. In the presence of air gradients, the fiber will experience a torque until the fiber is oriented parallel to the direction of shear force. A fiber settling in a horizontal laminar flow will tend to be oriented horizontally, parallel to shear. However, the fiber will experience a periodic instability and flip. Inertial separation is commonly used for particle separation and sizing such as with cascade impactors. In such systems where flow conditions are rapidly changing, the fiber mechanics are governed by initial orientation and flow relaxation time besides the usual parameters observed for spherical particles. Fibers are expected to be randomly oriented unless affected by shear flow or other forces, with the longer fibers more likely to be oriented by such forces. Due to electric field effects, a fiber may be aligned in an electric field by an induced dipole in the fiber. Burke [78] developed a semi-empirical method for calculating aerodynamic equivalent diameters for fibers based on experimental values obtained using a cascade impactor. The aerodynamic equivalent diameter is based on the aerodynamic resistance of the particle due to a linear motion. Burke suggests the following equation:

$$D_e = D_f \sqrt{\rho(k_1 + k_2 \ln\beta)} \qquad (2.4.11)$$

where

D_e = aerodynamic equivalent diameter

ρ= fiber density

β = aspect ratio (fiber length/fiber diameter)

D_f = fiber diameter

k_1 = constant

k_2 = constant

The constants k_1 and k_2 depend on the initial orientation of the fiber, and a least squares fit was taken from literature. For glass fibers, k_1 and k_2, are 0.7 and 0.91, respectively. The equation addresses that the impactive behavior of fibers is influenced by the aspect ratio of the fibers, whereas the behavior of the non-fibrous aerosol would not be influenced by aspect ratio.

Therefore, an increased length of fiber would increase not only deposition by interception and sedimentation, but also the deposition by impaction.

2.4.3 Inhalation Mechanisms

The hazard caused by inhaled particles depends on their chemical composition and on the site at which they deposit within the respiratory system, and with particles such as asbestos, the aspect ratio [77,79]. The respiratory system can be divided into three regions, each covering several anatomical units. The first region is the head airways region, extrathoracic, or nasopharyngeal region which includes the nose, mouth, pharnyx, and larnyx. The second region is the lung airways or tracheobronchial region, which includes the airways from the trachea to the terminal bronchioles. The third region is the pulmonary or alveolar region, where gas exchange takes place. There are five basic mechanisms by which an aerosol particle can be deposited onto a fiber and a filter. These five deposition mechanisms form the basic set of mechanisms for all types of aerosol particle deposition, including disposition in a lung.

1. Interception
2. inertial impaction
3. diffusion
4. gravitational settling
5. electrostatic attraction

The most important of these mechanisms for respiration are impaction, settling, and diffusion. The extent and location of particle deposition depend on particle size, density, shape, airway geometry, and the individual's breathing pattern. While impaction is of primary concern in the large airways, settling is most important in the smaller airways and the alveolar region, where flow velocities are low and airway dimensions are small. Alveolar deposition is usually expressed as a fraction of the inhaled particles traversing the head airways region that ultimately deposit in the alveolar region. Because of size selective particle deposition in the tracheobronchial region, particles larger than 10 μm generally do not reach the alveolar region, and particles in the 2-10 μm range reach the alveolar region in attenuated numbers.

Deposition in the alveolar region depends on particle size, breathing frequency, and tidal volume. The particle size having the greatest deposition the alveolar region during mouth

breathing is about 3 μm, with approximately 50% of these particles being captured in the alveolar region. During nose breathing, the size for maximum alveoli area deposition is reduced to about 2 μm with about 10 to 20% of these particles being retained. We need information on the amount of dust that can deposit at the site of toxic action, namely the alveolar region of the lungs. Because of the size selective characteristics of the human respiratory system, particles larger than a certain size are unable to reach the alveolar region and therefore can be considered non-hazardous with respect to alveolar injury. As an example, the mineral asbestos possesses some unique properties that causes lung injury due to the characteristic fibrous shape of asbestos particles that enables them to get past respiratory defense mechanisms and cause asbestosis (scarring of lung tissue), mesothelioma, (cancer of the lining of the lung), and lung cancer.

Asbestos includes six commercial fibrous minerals that have high tensile strength, chemical resistance, and excellent thermal and acoustic insulation characteristics that make it very useful in a variety of products, including friction materials, high-temperature insulation materials, acoustic insulation, fire-proof cloth and rope, and floor tiles. Asbestos originates as fiber bundles that break longitudinally into finer and finer fibers during milling. Because of the high strength material, fibers of long aspect ratio (length to diameter) are formed. The aerodynamic properties of the asbestos fibers are such that fibers as long as 50 μm or as big as 3 μm in diameter can reach the alveolar region and are considered respirable. The reason the asbestos fibers can do this is that the fibers align themselves with the streamlines and snake their way through the narrow airways to the alveolar region. Once lodged in an alveolus, large asbestos fibers cannot be removed by normal clearance mechanisms, and are in soluble in lung fluids, too long to be engulfed by macrophages, and only slightly able to migrate to lymph nodes. It is thought that when macrophages try to engulf long fibers, they leak enzymes that cause fibrosis, the scarring and thickening of alveolar surfaces associated with asbestosis. Asbestos fibers less than 5 μm in length are cleared by normal respiratory clearance mechanisms. Each of the asbestos-related diseases is associated with fibers in a specific size range. Fibers .15-3 μm in diameter and 2-100 μm long are associated with asbestosis, fibers less than .1 μm in diameter and 5-100 μm long with mesothelioma, and fibers .15-3 μm in diameter and 10-100 μm long with lung cancer. In the United States, the Occupational Safety and Health Administration (OSHA) has specific exposure limits for asbestos. On a similar note, the mine safety and health

administration (MSHA) regulates exposure in mines and mills. Regulation of other fibers has generally dealt with these materials as nuisance dust. This brings us to the interest in carbon fibers, currently classified as a nuisance dust.

2.4.4 Review of Carbon Fiber Dust Studies

Inhalation of carbon fiber could cause adverse health effects from several mechanisms. With the expanding use of carbon fiber materials in the 1970s, workers began to ask questions regarding concerns that carbon fibers may be a carcinogen similar to asbestos. A concern being that fibers less than .5 μm in diameter and more than 10 μm in length are more likely to produce tumors, as with asbestos, due to the size and shape of the fibers. A limited number of studies have been performed to evaluate the effects of carbon fiber dust on a variety of animals as well as measuring both concentration and morphology of the particles.

In an early study by Holt [80], RAE carbon fiber was fed into a hammer mill and chopped in an attempt to produce respirable carbon fibers. From a microscopic examination of the dust taken from the air within the dust chamber, four types of particles were found:

1. Fibers about 10 μm in diameter greater than 100 μm long (non-respirable)
2. non-fibrous particles with diameters ranging from sub micron to several microns
3. fibers 1.0 to 2.5 μm diameter and up to 15 μm long (respirable)
4. transparent fibers of unknown composition probably glass (processed in same area)

Holt claimed it was difficult to produce a cloud of dust particles in the respirable size range from carbon fiber suggesting that with typical industrial use, carbon fiber is unlikely to produce much dust that would reach the smaller air vessels of the lung. In this study about 99% of the airborne particles of respirable size were nonfibrous and most were approximately 1 μm in diameter. The few respirable fibers that were found were mainly less than 10 μm and length and between 1 to 2.5 μm in diameter. Pathogen free guinea pigs were exposed to the dust collected in this experiment and no pathological effects were found in the short term. However the author suggested that only long-term experiments would show whether or not exposure to carbon fiber dust is innocuous. In a follow-up study Holt [81], evaluated the effects of carbon fiber dust over periods up to two years in pathogen- free guinea pigs. The longer-term experiment gave similar

results as the initial shorter-term experiment, but again the respirable fraction of the dust was seen to be mainly nonfibrous.

Wagman [82] in 1982 cut samples of (12) types of carbon/epoxy composites with a hack saw blade and drilled other samples using carbide-tipped drills in a press [61]. Microscopic analysis was then performed on the dust samples that were generated and settled. The authors concluded that since most of the fibers generated have diameters (about 6-8 μm), that health effects would likely be limited to skin, eye, and upper respiratory tract irritation. However, the evidence that longitudinal cleavage of fibers can occur requires that consideration be given to possible generation from manufacturing operations of significant numbers of smaller diameter fibers which could penetrate more deeply into the lungs and therefore constitute a greater respiratory hazard.

In another study by Siebert [83], carbon and glass fibers without epoxy resin or sizing material were ground in a ball mill to compare the size and shape of carbon fibers to fibrous glass under similar conditions. Three types of carbon fiber dust can be generated:

1. fibers having the diameter of the parent fiber (6-8 μm), resulting from transverse fracture
2. carbon particles (non-fibers with aspect ratios less than 3:1)
3. fibers having diameters less than that of the parent fiber, resulting from longitudinal fracture

Fibers of reduced diameter were found for both carbon and glass fibers with the largest single size group of fibers being .5 μm in diameter and 1.5 μm long. The issue of longitudinal versus transverse fracturing of the fiber is important because the aspect ratio can be largely affected. With the parent fiber diameter being between 6-8 μm, the fibers of significance would be those that result from longitudinal splitting. In this study the carbon and glass fibers were milled to an aspect ratio of less than 10. It was assumed that if only "long and thin" fibers are significant than the fibers in this study had a low potential for adverse health effects as a result of the physical size.

Aerosols from carbon fiber laminates and virgin fiber bundles were generated by grinding inside an airtight box to prevent respiratory and dermal contact by Mazumder [84]. The experiment used a small electrically operated grinding wheel inside the box to grind the laminate along the edges. For the virgin fiber bundles, two methods were used to generate carbon fiber aerosols including chopping the fibers with an electric razor and grinding the fibers with an electric grinder. Sampling was performed for 15 min. while particles were generated. The grinding process produced fibrillation or splitting, resulting in sharp edges. For the virgin fibers, the mass median aerodynamic diameter was found to be approximately 4 μm. The mass median aerodynamic diameter of the composite aerosol was approximately 2.7 μm. The study indicated that similar results could be expected for a variety of different fibers types and laminates. Further, aerosol particles generated could have an enormously wide geometric size distribution as a result of the mechanical process. Experimental results show that mechanical chopping of carbon fibers produced sharp edge fiber like particles in a respirable size range. The sharp edges were caused by fibrillation of the parent fibers. Carbon fiber aerosols were produced in significant quantities within the range of .1-10 μm in aerodynamic diameter. The authors noted the effect of inhalation on an industrial worker depends upon the size distribution of the aerosol and the length and rate of respiration.

Owen [85] exposed rats to Celion PAN-based carbon fibers of 7 μm in diameter that were 20 to 60 μm in length for six hours per day and five days per week for 16 weeks at a concentration of 20 mg/m3 that were chopped using a hammer mill. Using a hammer mill, the authors found that about 370 carbon particles/cm3 could be produced that were less than 5 μm, and less than 1% were fibrous. The only differences shown by the animals exposed to carbon fiber, compared to control animals was a slight decrease in the gain in body weight during the first four weeks, and a measured increase in airway resistance and decrease in respiratory rate. There was no consistent effect on lung function with respect to time of exposure, and the variable changes in airway resistance are believed to be related to exposure to carbon fibers. There was no evidence of an associated inflammatory or fibrotic response during the 16 week exposure or 32 weeks after final exposure. These findings indicate that inhalation of 7 μm diameter carbon fibers from 20 to 60 μm in length and a concentration of 20 mg/m3 did not cause any effects suggestive of system toxicology or progressive pulmonary dysfunction.

In a three-part study conducted by (Boatman 1988), (Luchtel, 1989), (Martin, 1989), and summary work by (Bourcier, 1989), respirable dust collected from machining of six carbon epoxy composite materials were evaluated to determine if the dust presents a health risk [86,87,88,89]. The three-part study focused on the aerodynamic, morphological, and chemical features; cytotoxicological evaluation; and effects on rodents following intratracheal administration of dust derived from graphite epoxy fiberglass-epoxy composite materials as machined in the aerospace industry. The composite samples were subjected to routine machining operations and dust was collected at the tool face through use of an industrial vacuum cleaner. The composite dust released at the tool face ranged in width from 7 to 11 μm. Particle length varied significantly within each sample. The segregated dusts showed the presence of particles between .8 and 2 μm in all of the materials tested. Particles of this size may deposit in the upper and lower respiratory tract by impaction and sedimentation, respectively. All samples were found to have contained a small fraction of particles below .2 μm in diameter. The authors found that the proportion of particles of respirable dimensions on a mass basis was only a small percentage of the whole population of particles collected. Particle sizing was determined by light microscopy (LM) and by scanning electron microscope (SEM). A summary of the material, machining operation, particle sizes, and aspect ratios as noted by the authors is summarized in table 2.3.

Table 2.3: Results summary (Boatman [65])

Sample	**Material**	**Machine Operation**	**LM (μm) Length**	**LM (μm) Width**	**Aspect Ratio**	**SEM (μm) Length**	**SEM (μm) Width**
1	Graphite-PEEK	Shaper 10,000 rpm	38	10	4:1	71	7
2	Fiberglass/ Epoxy	Shaper 3,450 rpm	295	11	26:1	262	10
3	Graphite-PAN/Kevlar/ Epoxy	Hand router 23,000 Shaper 3,450 rpm	68	8	8:1	109	9
4	Graphite-PAN / Epoxy	Hand router 23,000 rpm	53	7	8:1	87	8
5	Graphite-Pitch / Epoxy	Shaper 3,450 rpm	27	8	4:1	63	10
6	Graphite-PAN / Epoxy	Hand router 23,000 rpm	29	7	4:1	210	8

The goal of the second part of the study was to define the pathologic changes in the lungs of rats following a single intratracheal dose of various graphite or fiberglass epoxy materials as noted from the previous table. For comparison, aluminum oxide was used as an inert material and quartz was used as a known fibrogenic agent. In this experiment, each animal received a single 5 mg intratracheal injection of a respirable fraction of composite material followed by air to disperse the material in the lungs. Four of the six samples of composite fiber-epoxy dust caused a definitive histopathologic response in the rat lung. These changes were greater than those caused by aluminum oxide but much less than those caused by quartz. This suggests the possibility that some types of composite dusts may be fibrogenic in humans.

In the third part of the study, two experiments were performed. First, first the composite control samples were incubated with normal rabbit alveolar microphages in vitro. Second, the composite and control samples were injected into specific pathogen-free rats, and one month later the lungs of the animals were studied by bronchoalveolar lavage and semiquantitative light microscopy. Since in the evaluation of the potential health risks of inhaled particles, no single test that accurately predicts the biologic effects in the lungs of the exposed humans exists, a common approach has been to test potentially harmful materials in vitro or in vivo in animal lungs, and to compare the results with those produced by substances whose toxicity for human lungs is known. The results indicated that these composite samples tend to produce responses that are generally more similar to aluminum oxide than to quartz. However, the samples were not all complete and there and at least two materials (graphite-PAN/epoxy and graphite-pitch/epoxy) may have the potential to cause biologic effects in the human lung. The results of the studies do not indicate the specific type of biologic response that may occur in human lungs following prolonged exposure to these composites nor do they allow the calculation of a safe exposure level for aerosols of these composites. The authors concluded that longer-term inhalation exposure studies with (graphite-PAN/epoxy and graphite-pitch/epoxy) would help to better define their potential effects on the lungs of exposed humans.

Results of toxicological studies of cured composite dust suggest that the material produces a relatively wide variation in response across different types of dust without evidence of the responses related to the presence of a specific type of resin or fabric. Potency of this

material to produce lung insult is greater than nuisance dust, but far below that of quartz. Bourcier noted that total dust concentrations are quite variable even within each specific type of operation, but lower dust concentrations appear to reside in drilling operations and the upper range in composite cutting, with grinding/sanding and routing/milling falling between those two boundaries. In the case of respirable dust, the highest concentrations were found within routing/milling and the lowest in grinding/sanding. The author noted that it is difficult to interpret without further investigation of the specific type of equipment used. Bourcier recommends further evaluation of the work environment to establish the relationship between total and respirable dust loadings for various composite processing operations and to continue investigations which would target those work processes which need special attention relative to dust control. A suggestion is to develop local exhaust systems which are engineered into the tool resulting in the most effective removal of dust.

Siebert [90] noted that particles with an aerodynamic equivalent diameter (AED) above 10 μm are considered "non-respirable", as they will impact in the nose, throat or tracheal-bronchial tree, but will not deposit in the pulmonary gas exchange region [69]. Assuming a minimum fiber length to width (aspect) ratio of 3:1, carbon fibers have a 12 μm or greater AED and are considered non-respirable. These would be caught in the throat and nose, with few making it to the aveoli. Only if the fibers are split lengthwise could they become thinner respirable fibers. During grinding on carbon fiber composites, most of the fibers fragment into a nonfibrous dust and of those particles retaining a fiber shape (aspect ratio greater than 3:1), only about 1% fulfill the "long and thin" criteria. Siebert concludes the fiber fragments typically occur as non-respirable fibers, non-respirable nonfibrous dust, and respirable nonfibrous dust. Therefore exposure to respirable fiber is unlikely and carbon composite dust should be *considered a nuisance dust*.

Kwan [91] used an Anderson Cascade Impactor to determine the aerodynamic size distribution for milled, drilled, and ground carbon composite particles according table 2.4 and figure 2.19. For all of the machining operations monitored, the majority of the particulates were of non-respirable sizes, where the aerodynamic diameter was > 5μm. The weight percentage of the non-respirable fraction ranged from 51% for milling of sample R3 to 88% for drilling of

sample R1. Particles that could reach the bronchial portion of the respiratory system (2-5 μm in aerodynamic diameter) ranged from 9.3% in drilling sample R1 to 28.7% in milling of sample R3. Particles capable of reaching the alveoli (< 2 μm in aerodynamic diameter) ranged from 2.5% in drilling of sample R1 to 20% in milling of sample R3.

Table 2.4. Matrix material and machining operations (Source: Kwan [90]).

Table 2.1. Conventional machining operations.

Sample Number	Matrix Material	Operation
R1	Fiberite 934 epoxy	Drilling 2000 RPM
R2	Hexel F263 epoxy	Drilling 2000 RPM
R3	Hexel F263 epoxy	Milling 2000 RPM
R4	Hexel F263 epoxy	Milling 4000 RPM
R5	Dow 332 epoxy	Grinding 4000 RPM

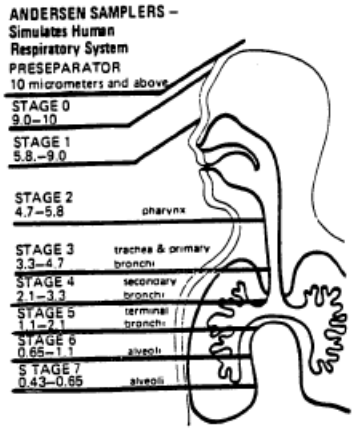

Figure 2.4. Andersen sampler and stages of impaction vs respiratory deposition. (From Andersen sampler instruction booklet.)

Figure 2.19. Stages of impaction vs. respiratory deposition (source: Kwan [70]).

Warheit [92] conducted a study to determine the biological effects in rats of acute and repeated inhalation of aerosol concentrations of respirable pitch based carbon fibers and non-respirable PAN-based carbon fibers. The pitch based fibers used in the study had nominal diameters of 1-2 μm and were considered in the respirable range because they were less than 4 μm MMAD and have the potential to cause toxic pulmonary effects. A five day exposure to respirable size pitch based carbon fibers at concentrations of 47 or 106 mg/m^3 produced dosed dependent transient inflammatory responses in the lungs of exposed rats. However, all of the carbon fiber induced inflammatory effects reversed within 10 days after exposure. The authors

concluded that under appropriately controlled occupational settings, respirable sized pitch based carbon fibers should not present a hazard for pulmonary fibrosis.

A study was performed by Burr [93] of the National Institute for Occupational Safety and Health (NIOSH) at General Electric in Evendale, OH where part of the evaluation looked at reviewing the grinding, milling, and cutting of PMR-15 used in some prototype aircraft engine parts. The authors noted that only fibers with diameters of less than 3.5 μm are considered respirable or small enough to enter the lungs. The authors recommended the use of a portable vacuum system whenever composite parts were machined dry. As an alternative, the authors suggested the use of flood coolant during machining to reduce dust levels.

Klocke [94] states that during milling of FRPs, the fraction of respirable dust is small, on the order of .1 - .5% of the total generated, or total dust that equals the weight of the milled material. The respirable fraction increases with tools that have a better cutting edge. Fine dust generated for a thermoplastic composite using a PCD, 8 mm diameter cutting tool, at cutting speed of 1000 m/min, and depth of cut of .025 mm was .25% of the machined mass. The author notes that after the milling procedure, the larger particles settle out very quickly, but the small particles (aerosols) can be detected by dispersion photometer. During milling of a carbon epoxy laminate with 60% fiber volume using a PCD milling tool and feed rate of .025 mm/rev, aerosol concentration is shown to rise from 5 mg/m^3 to approximately 13 mg/m^3 as cutting speed increases from 200 m/min to 750 m/min. The emissions were detected using a gravimetric method and a dispersion photometer.

During milling a carbon-epoxy laminate with cutting speed 1000 m/min, feed rate .025 mm/rev, cutting depth 4 mm, and measurement time of 10 min, a PCD tool was found to produce approximately 25% more fine dust than a carbide tool under the same conditions measure using a Gravicon VC 25 air sampler. The aerosol dust for the PCD tool was approximately 1.4 g/100g per milled material compared to 1.1 g/100g milled material for the carbide tool. Another test conducted during milling carbon epoxy at a cutting speed of 200 m/min, feed rate of .025 mm/rev and depth of cut 4 mm showed the PCD tool generated an aerosol dust concentration of 3 mg/m^3 whereas a carbide tool under the same conditions generated an aerosol dust

concentration of 2.8 mg/m^3 as measured by a dispersion photometer. Both measuring methods showed PCD tools produce more aerosol dust than carbide tools during milling of FRPs, which can most likely be explained by differences in the cutting edge radius of tools, as the PCD tool has a significantly smaller radius than the carbide tool. The PCD tool also produces better surface integrity in the finished surface as it produces smaller chips, thus more dust. The author shows that by using a milling cutter with larger flutes, dust concentration can by shifted towards coarser particulates, which offers the possibility of reducing fine dusts by changing tool geometry. However, the effect on surface integrity needs to be validated.

In a study performed by Darne [95], different PAN-based carbon dust was sampled during the production process of pure carbon pieces. The authors examined the cytotoxicity and carcinogenic potential of the samples in relation to their ability to generate reactive oxygen species (ROS) in a liquid system using in vitro short-term assays. In the conditions used by the authors, the carbon fiber particle samples tested showed no carcinogenic potential and have low cytotoxicity and little effect on cell proliferation compared to chryostile asbestos fibers. However, the authors also note that in vitro evaluation of carbon nano tubes gives different results compared to what was obtained with carbon dust, namely they are mostly cytotoxic and could contribute to alteration of DNA. The authors note that the fibers and particles of carbon used in their study were generated by one type of process and therefore it is also necessary to study other samples coming from other firms using the same manufacturing technique and also fibers generated by other methods.

Ramulu and Kramlich [96] conducted a study reviewing environmental and health effects of machining carbon fiber composites. Ramulu points out that chip geometry which is directly related to airborne dust geometry is critically dependent on fiber orientation within the composite material. Further, machining parameters can also influence the airborne particle concentration and size. Ramulu suggests the size distribution and concentration of amended particles from traditional machining processes may be controlled by the fiber orientation within the composite material and by machining parameters such as the tool material type, tool geometry, and cutting speed. Therefore, a reduction in the potential health hazards associated with machining

composite material may be possible through modification of the parameters and conditions under which the machining operations are performed.

Yon [97] cut 12-ply panels of B-2 aircraft graphite epoxy panels on a portal milling machine using cubic boron nitride (CBN) and polycrystalline diamond (PCD) cutting tools with an attached local exhaust ventilation (LEV) system [76]. The author noted that the CBN cutting tool overheated and the machine operator switched to a PCD bit to avoid burning of the material. A TSI P-Trak ultrafine particle counter was used to measure particle count in addition to (4) air sampling pumps and filters for particulate matter collection. The average mass collected for particulate matter was 1.319 mg and the average mass collected for respirable particulate matter was .317 mg.

Haddad [45,98,99], studied the influence of cutting conditions on dust size and surface quality during high speed trimming of multidirectional CFRP using a 6mm diameter tungsten carbide burr tool. SEM and a profilometer were used to characterize surface finish. A GRIMM 1.209 dust monitor which measures the percentages of dust sizes from .25 μm to above 30 μm was used to estimate average particle size. The material was T700/M21 with a fiber volume of 59%. Spindle speed was varied between 18570 and 74270 rpm with linear feed rate between 125 to 500 mm/min. Depth of cut was 2 mm and cutting direction was down milling. Dust monitoring showed the presence of different chip sizes for all cutting conditions, with the highest percentage of particles between .25 and 1 μm. Increasing the cutting distance was found increase the size of the damage zones due to tool wear. Increasing the cutting speed or decreasing the feed rate leads to an increase in roughness, which contradicts other studies. Chip size measurements showed that 87% – 95% of the inhaled dust could reach the pulmonary alveoli. In an expanded study utilizing three different cutting tools including a tungsten carbide burr tool, diamond coated burr tool, and a 4-flute diamond coated tool, the authors claim that 2 to 8 times more dust is generated during high speed trimming compared to standard cutting conditions. From the data, a general observation was an increase in the number of particles with increasing cutting speed. The feedrate appears to have less of an effect at a constant cutting speed on the number of particles generated. In comparing the results of the three cutting tool types, the uncoated burr tool appears to generate slightly less dust. The authors appear to be

mixing the optical diameter measured by the particle counter with the aerodynamic diameter when determining inhalation and penetration of the particles within human lungs.

Bello [100], investigated airborne exposures to particles and fibers generated during dry and wet abrasive machining of a hybrid composite consisting of carbon nanotubes (CNT) and CFRP. CNTs were placed at the center ply interface of a 24 ply laminate made from AS4/8552 carbon/epoxy. Samples were machined dry using a band-saw and wet with a rotary cutting wheel, both with 220 diamond grit. The cutting wheel used water to flush the dust particles during machining, while the band saw represented dry cutting with no vacuum deployed. The carbon-fiber composites were cut perpendicular to the fiber direction. Two real-time particle counters and a condensation particle counter were used. Respirable fibers having a length of >5 – 20 μm and an aspect ratio (length/width ratio) > 3 are of the greatest toxicological interest due to the fact that this fiber length is capable of causing lung cancers. Fibers shorter than 1 μm in length are referred to as submicron fibers, whereas those longer than 30 μm are termed supramicron fibers. Supramicron fibers may be too large to enter the respiratory tract and are of lesser concern, whereas fibers < 5 μm are expected to behave like particles in the lungs. Submicron and respirable fibers were generated from dry cutting resulting in high airborne exposures to nanoscale and fine particles. Concentrations of nanoscale and fine particles did not vary between composites with and without CNTs. The toxological profile of airborne nanoscale and fine particles and fibers generated during dry cutting of advanced CNT composites is not well known, but concerning nonetheless. Further investigations are needed to understand various exposure determinants, such as tool geometry and composite properties, and to evaluate efficiency of various controls. The authors claim that wet cutting is a superior post-processing method.

2.5 Summary

A review of the current state of the art in milling of composite materials has been presented. Fiber orientation plays a major role in milling of composite materials. Fiber orientation is not constant and varies continuously with the cutting edge position. Further, chip formation is controlled by fiber orientation and is effectively a series of uncontrolled fractures

where the chips exhibit very little plastic deformation as is observed with metals. The matrix material also influences chip formation. Thermoset and thermoplastics result in different types of chips due to property differences. For example, epoxy produces fragmented and powdery chips because of its brittle nature where PEEK thermoplastic may produce continuous and curling chips which exhibit deformation due to the elevated temperatures from machining. There is also a high degree of fluctuation in cutting forces when milling composites. The fluctuation depends largely on fiber orientation and uncut chip thickness and may be correlated to the mode of chip formation.

For a homogeneous material such as metals, cutting forces in milling follow a sinusoidal function. Milling force is derived from chip load on the cutter. When milling composites, fiber angle plays a very significant role in determining the cutting force response. In composites, the cutting forces change with engagement angle to the fibers. This complicates milling force prediction as the cutting force varies with chip thickness and change in fiber orientation. The methods reviewed for predicting milling cutting forces for composites were of limited accuracy when compared to the experimental results. Further, the models were limited to the specific cases studied and required planing or milling experiments to generate data that was then used to predict milling cutting forces. Opportunities exist to develop more accurate and generalized methods for cutting force prediction potentially using numerical models or analytical techniques.

Tool wear changes the cutting edge geometry which also affects the cutting forces. Tool wear is in turn influenced by machining process parameters including cutting speed, feed rate, and depth of cut. The hardness of the fibers results in high levels of tool wear. Cutting edge sharpness is important to ensure the fibers are cut cleanly. The tool material requires high hardness and toughness to resist the abrasiveness of the fibers and the intermittent loads from the milling process and fiber fracture. Thermal conductivity of the cutting tool is also important because heat generated during the cutting process needs to be dissipated through the cutting tool. Because of these requirements, a limited choice of cutting tool materials are available that satisfy the requirements for machining composites. From the studies presented, PCD tools had lower wear than carbide tools; however, coated carbides improved tool wear performance. In addition,

diamond abrasive tools produced a surface finish proportional to the grit size of the cutter, independent of process parameters.

Surface finish, while necessary and quantifiable to meet engineering requirements, may not sufficiently represent the mechanical performance of the component as it does not address subsurface damage caused by machining. Further, mechanical surface inspection is unable to detect subsurface damage which is strongly influenced by the angle between the fiber and tool cutting edge. Different inspection techniques and criteria may be required that address the extent of subsurface damage and the impact on mechanical performance. It may be possible to utilize numerical simulation to improve the understanding of how damage caused by the machining process leads to a reduction in mechanical performance.

Many toxicology studies on fibrous dust present different results with respect to the carcinogenic potential of airborne particles generated from carbon composite materials. Differences in the results and interpretation of findings include the dust sampling processes used, the particle size distribution, exposure mechanism, and the relevance of animal studies to human health hazards. *Further, all the studies cited do not clearly identify specific geometry and type of cutting tools utilized, or the specific machining process parameters and conditions. Nor is the composite laminate sufficiently described with respect to fiber orientation, which has been demonstrated to be a significant factor in chip formation.* These inconclusive findings do not eliminate the concern that dust from milling of composites could present a potential health hazard and leave open the potential that particle size generation may be controlled to directly impact the safety of the operation.

A limited amount of published works are available that address milling of composite materials. The anisotropy of composite materials makes cutting force analysis difficult as the existing models don't accurately predict the cutting forces compared to experimental results. Opportunities exist to further improve the predictive accuracy of the cutting force models. *Current research suggests that fiber orientation may significantly influence the geometry of emitted dust particles which may enable a reduction in potential health hazards by optimization of cutting parameters and machining conditions for composite materials to achieve non-*

hazardous particle sizes. In conjunction with cutting tool development, cutting parameters including cutting speed, feed rate, depth of cut can be optimized for composite material systems that maximize productivity while satisfying all necessary part requirements including geometry and surface integrity with dust generation controlled to maximize safety.

CHAPTER 3

RESEARCH SCOPE AND OBJECTIVES

3.1 Scope

The scope of this research includes the development of techniques, systems and processes for evaluation of edge trimming for unidirectional and multidirectional CFRP composite material. An initial evaluation of composite edge trimming processes was performed which included measurement of cutting forces, surface finish, tool wear, acoustic emission, and assessment of particles produced from the cutting process. Six different cutting tools were utilized to address a wide range of material removal options available to industry as part of this initial evaluation. Different cutting conditions were utilized to contrast the effects of controllable process parameters on the response variables. Cutting conditions include: spindle speed, cutting velocity, axial depth of cut, radial depth of cut, and cutting direction. The response variables include: axial, radial, and tangential cutting forces; acoustic emission signature; surface finish; tool wear; particle size and distribution. With basic processes established for tool wear measurement, surface finish measurement, and AE data acquisition, the focus of the research centered on particle collection and analysis, and cutting force modeling and prediction of which there are limited evaluation techniques.

The motivation for this research is due to the increasing worldwide demand for carbon fiber reinforced advanced composites, and the need for secondary processing of composite parts using milling. In the aerospace industry, trends are easily verified by following both the Boeing 787 and Airbus A350XB development, sales, and planned production increases. Other aerospace applications for CFRP include cryogenic rocket tanks, fairings, intertank structure, and satellite components. In the automotive industry, BMW announced plans to incorporate carbon fiber in the passenger compartment for the i3 electrical vehicle, with a new plant in Moses Lake, WA to produce carbon fibers. High end automobiles including Tesla and Lamborghini incorporate carbon fiber into car bodies. According to the Toray website [101], Toray claims 34% of the global PAN-based carbon fiber market by sales in March 2011. Of this 34% world-wide sales volume, aircraft is approximately 41% (¥27.7 billion), industrial 38% (¥25.5 billion), and sports

21% (¥13.8 billion). With the increasing historical trends of composites usage in high performance systems such as aircraft, and planned production rate increases, it is unlikely this demand will reduce within the next couple of decades. While the automotive industry may tend to use more resin infusion or compression molded applications for higher volumes, the aerospace industry will continue to require large amounts of milling and hole drilling for composite part processing in order to meet dimensional tolerance and assembly requirements.

The scope of work in this research advances and provides techniques, systems and processes for particle collection and analysis and cutting force prediction to further the understanding of machinability for laminated composites. Not only do composite fly-away parts require edge trimming for assembly, but the composite layup tools used to fabricate these parts require extensive milling to achieve the necessary geometry and surface integrity for part layup. There is significant cost in terms of machine time and cutting tools involved in these operations, so maximizing material removal rates at the lowest costs is of value to end users. In addition, health effects of composite dust may not be fully understood, so the ability to influence chip size to non-respirable particles, and particle sizes more effectively collected using conventional vacuum systems, may improve the health and safety for the workers performing these operations, where dry cutting is desired. To accomplish this, a safe and self-contained system is necessary to ideally capture particles at the source to determine effects of cutting conditions on size and mass distribution. The particle collection and analysis techniques developed can also be applied to other processes and equipment, and portable systems, where there is an interest of capturing and analyzing particles from the source. This research was intended to further the understanding of the challenges in milling of CFRPs to maximize productivity in a safe manner.

3.2 Research Objectives

The objective of this research is to conduct an investigation for machinability of edge trimming and milling carbon reinforced composite laminates in terms of dust emission, cutting force, and process conditions. The primary focus is to develop and demonstrate a method to safely investigate and characterize dust particle emissions from dry machining of CFRP laminates. This includes development of a technique, working system, and process for particle collection and analysis *in a safe and closed environment* that can be used to further the

understanding of cutting conditions on particle size and mass distribution, with the objective to maximize productivity and minimize worker hazards. Cutting forces experienced during edge trimming of composite laminates will be investigated. The objective is to develop a model to predict cutting forces that would be experienced during trimming of multi-dimensional laminates at any relative fiber orientation using a minimum number of calibration cuts on a unidirectional laminate. The effect of process conditions including machining parameters and fiber direction on tool wear and surface integrity will be investigated to contrast the effect different cutting tools. Finally, data will be presented that includes the simultaneous measurement of acoustic emission and cutting for potential applications in monitoring tool wear and delaminations when trimming composite laminates. The research specific objectives are summarized as follows:

Dust Emission

- Develop a system for particle collection and analysis from composite machining
    - Safe
    - Captures all dust from the source
    - Closed system
    - Provides consistent results
- Characterize effect of fiber orientation, tool geometry, and process conditions on particles generated.
    - Investigate particle geometry through scanning electron micrsocopy (SEM)
    - Perform gravimetric analysis using cascade impactors
    - Measure particle count and mass concentration through real-time particle analysis instrumentation

Cutting Force

- Quantify effect of fiber orientation, tool geometry, and process conditions on cutting force
    - Characterize mechanisms through cutting force measurement and analysis
    - Develop a methodology to predict cutting force when milling which is applicable to multi-directional laminates at any cutting orientation utilizing a rotating dynamometer.

Process Conditions

- Quantify effect of fiber orientation, tool geometry, and process conditions on tool wear and surface integrity.
    - Characterize effect of cutting conditions through tool wear measurement and analysis.
    - Characterize effect of cutting conditions through surface finish measurement.
- Perform simultaneous measurement of acoustic emission and cutting force.

Limited results have been published on the milling and edge trimming of composite materials. Further, no published work provides a fully self-contained process for particle collection and analysis at the source. Quantifying dust produced at the source when dry machining is essential for design of containments methods to ensure worker and equipment safety. The capabilities of a system that enables rapid evaluation of particles produced from machining in a safe manner can be used can be used to find optimal combinations of cutting tool geometries that yield high material removal rates, provide necessary surface integrity, and minimize production of more hazard sized particles in shorter flow times with lower consumable costs. The importance of this investigation is significant as the use of composite materials requiring milling for secondary processing is only increasing.

CHAPTER 4

EXPERIMENTAL METHOD

4.1 Introduction

The experiments conducted as part of this research concentrate on milling and edge trimming of composite laminates. The effects of machining process parameters and cutting conditions (feed rate, cutting speed, depth of cut), tool geometry, tool material, and laminate fiber orientation have been evaluated with respect to cutting forces, tool wear, acoustic emission signatures, damage mechanisms, and chip formation (dust). Aerosol data collected includes particle sizing and distribution by cascade impactors and real-time instrumentation. SEM micrographs were also captured to characterize physical particle size. The real-time dust sampling instrumentation provides particle mass and count distribution, with as small as 1 second sampling frequency. Data acquired from cutting force experiments are used with mechanistic models for cutting force prediction of multi-directional laminates in any orientation. Data from the dust collection experiments are used in models to describe particle distribution for different cutting conditions. A significant component of the research involved developing techniques for optimal use of instrumentation for cutting force analysis and the design, build and test of a system for fully self-contained and enclosed machining dust collection and analysis directly from the particle source.

The research was performed chronologically in five major phases following *a building block methodology* for continued process refinement. Figure 4.1 summarizes the methodology for the five experimental analysis phases of this research. This building block approach was necessary as there was limited published information on the acquisition and analysis of data from key instruments for cutting force and methods for dust collection and particle analysis in a controlled environment applicable to machining. Techniques ultimately had to be developed to accomplish the planned research objectives.

In the first phase of this investigation, experiments were performed to validate the feasibility of accomplishing the fundamental objectives of the research. In the second phase,

processes were refined, and a number of experiments were conducted to explore the effects of different cutting conditions with preliminary analysis of cutting force and dust particle generation. In the third phase, new instruments were tested and selected for real-time particle analysis, and cutting force comparisons were made to address dynamometer results. In the fourth phase, development was conducted to analyze all particles collected from edge trimming involving many test steps, iterations, and fabrication of a new dust collection system. In the fifth phase, experiments were conducted to support a cutting force prediction model for multi-directional laminates combined with real-time machining dust particle analysis. The experimental method developed as part of this research provides a foundation for further study of cutting force modeling and particle analysis when trimming advanced composite materials. The dust collection system and procedures developed can be applied to almost any manufacturing process that generates particles of interest.

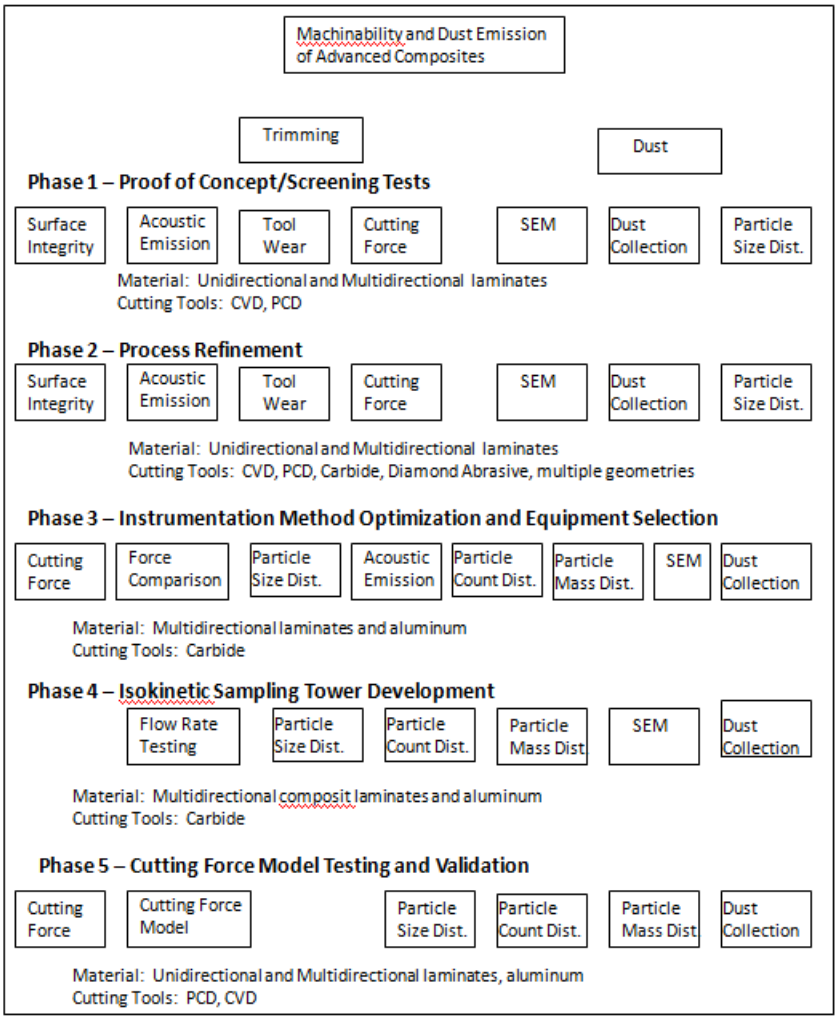

Figure 4.1. Five Test Phase Chronological Summary

The experimental component of this research is structured as shown in table 4.1 for this dissertation. The models and analytical tools developed in conjunction with the experimental work will be discussed in chapters 8 and 9 and recommendations for future work will be addressed in chapter 10.

Table 4.1. Experimental chapter summary

Chapter	Title	Chronological Phases (fig. 4.1)	Topics
4	Experimental Methodology	1-5	Chronological history; materials, cutting tools, and equipment used in experimental research.
5	Preliminary Machinability Investigation	1-2	Phase 1 screening tests, Phase 2 composite machinability assessment, research focus
6	Dust Collection System Development	3-5	Dust collection system and particle analysis development for phases 3-5.
7	Composite Cutting Force Process Development	3,5	Cutting force process and modeling development for phases 3 and 5.

4.2 Materials

The materials used in the research include both unidirectional and multi-directional carbon epoxy laminates, autoclave cured, and manufactured from prepreg unidirectional tape without fiberglass face sheets. The material uses Toray T800H high strength, intermediate modulus yarn, and toughened epoxy resin 3900-2. The laminates specifically constructed for this research are identified in table 4.2. All other cutting tests were performed using conventional 6061-T6 aluminum plate with thicknesses from 6.35 mm to 75 mm.

Table 4.2 Materials used in the research.

#	Qty	Mfg.	Length (in)	Width (in)	Thick (in)	Type	# Plies	Layup
1	1	Toray	48	48	.25	Uni	33	$[100\%/0\%/0\%], [0]_{33}$
2	1	Toray	48	48	.50	Uni	67	$[100\%/0\%/0\%], [0]_{67}$
3	1	Toray	48	48	.75	Uni	100	$[100\%/0\%/0\%], [0]_{100}$
4	1	Toray	48	48	.48	Multi	64	$[(45/90/-45/0)_8]_s$
5	1	Toray	48	48	.08	Multi	10	$[(0/45/90/-45/0)]_s$

4.3 Machining Center and Process Parameters

The machining center used for the experiments conducted as part of this research consists of a HAAS Tool Mill, Model TM 1P shown in figure 4.2. Maximum spindle speed of this 3-axis numerically controlled machine is 6000 rpm. Maximum feed rate in X and Y directions is 10 m/min. Additional specifications are included in table 4.3. Milling was performed dry, without the use of cutting fluid. A specially built containment box equipped with integral vacuum has been fabricated for dust containment during composite machining experiments (figure 4.3).

Modifications made to the vacuum system to improve chip collection and particle analysis efficiency will be discussed in chapters 5 and 6. The containment box is placed within the HAAS machine enclosure and bolted to the machine bed with an internal work holding fixture. They HAAS machine envelope is further sealed with plastic sheet and duct tape to mitigate dust migration as secondary containment.

Figure 4.2. HAAS 3-axis mill.

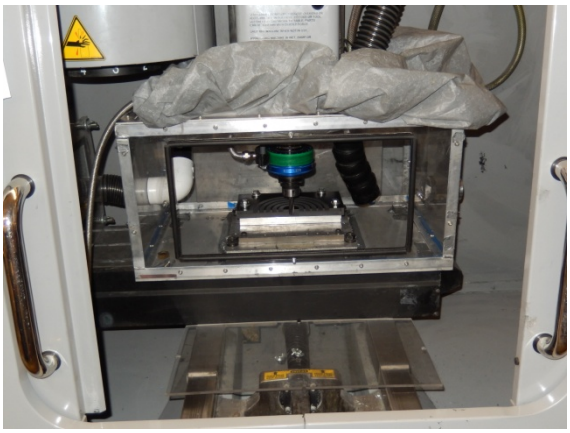

Figure 4.3. Dust containment box.

Table 4.3. HAAS TM1P Milling Machine specifications.

Item	**Value**	**Units**
Tool holder interface	Taper 40	N/A
Maximum speed	6000	rpm
Maximum torque	44.74 @1200 rpm	Nm
Spindle power	5.6	kW
Maximum thrust force (Z)	8900	N
Maximum feed rate	10.16	m/min
Accuracy	.01	mm
Repeatability	.005	mm
Acceleration (per HAAS)	1,600,000	encoder counts/sec^2
Encoder counts/inch (per HAAS)	138,718	encoder counts/inch
Acceleration (derived)	.293	m/sec^2

4.4 Cutting Tools

The cutting tools used for this research are summarized below in table 4.4. The table also summarizes in which phases of the research the cutting tools were used. Figure 4.4 is a

photograph of the cutting tools which are labeled according table 4.4. The polycrystalline diamond (PCD) and chemical vapor deposition (CVD) tools are the most expensive, approximately 10-15 times the cost of the solid carbide tools, thus used to a more limited degree for process development in this research.

Table 4.4 Cutting tools used in the research.

ID	Material	# Flutes	Helix (deg)	Diameter (mm)	Coating	Supplier	Phase
1	Carbide	2	30	12.7	N/A	Niagara	3,4,5
2	Carbide	4	30	12.7	N/A	Niagara	1,2,3,4,5
3	Carbide	2	0	12	PCD	Cajero	1,2,3
4	Carbide	6	0	12	CVD diamond	Mapal	2
5	Carbide	4	0	12	CVD diamond	Mapal	2,3,4,5
6	Carbide	8	0	12	CVD diamond	Mapal	2
7	Carbide	N/A	N/A	12.7	Diamond burr	Cajero	2
8	Carbide	N/A	N/A	12.7	125 grit	Amer. Diamond	2
9	Carbide	N/A	N/A	12.7	40 grit	Amer. Diamond	2
10	Carbide	2	0	12.7	N/A	McMaster-Carr	3

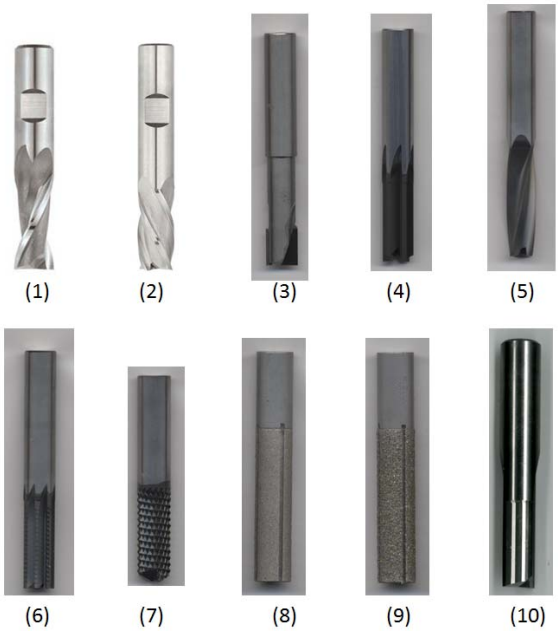

Figure 4.4 Cutting tools used in the research (reference table 4.4)

4.5 Dynamometer

A rotating 4-component dynamometer for measurement of cutting forces and torques was used in this research. The dynamometer is a Kistler 9123C and consists of a four component sensor fitted under high pre-load between a base plate and top plate [102]. The four components are measured practically without displacement. The dynamometer is used for investigation of cutting forces near the tool edge during milling and drilling. Using a dynamometer, the acting force vector on single-edge tools can be directly measured. The rotating cutting force

dynamometer is used for the dynamic and quasistatic measurement of the three force components F_x, F_y, F_z as well as of the drive moment M_z on a rotating tool, with the tangential force, F_t, radial force, F_r, and resultant force, F_a, calculated. The dynamometer has a maximum speed of 10,000 RPM with a sampling rate capacity of 7.8 KHz per the manual (Kistler later confirmed via e-mail that this is actually 7999 Hz). The signal conditioner, type 5223B, is the signal output and supply/control unit for the rotating dynamometer. Signals are transmitted across the air gap from the dynamometer to a stationary stator. Kistler DynoWare DAQ software is used for data processing with input via a PCI DAQ card and ASCII system output format. The rotating cutting force dynamometer has an advantage over fixed dynamometers because the cutting forces can be measured on the rotating tool independent of the size of the workpiece. The schematic of the force measurement system is shown in figure 4.5. Cutting forces are collected with each experimental run and analyzed for profile and magnitude with respect to cutting conditions and process parameters assigned for the test including:

- Laminate type (unidirectional or multi-directional), or other material (e.g. aluminum)
- Fiber orientation (+45, -45, 0, 90 degree)
- Cutting tool (geometry and material)
- Process parameters (feed rate/direction, rpm, axial and radial depth of cut, spindle speed)

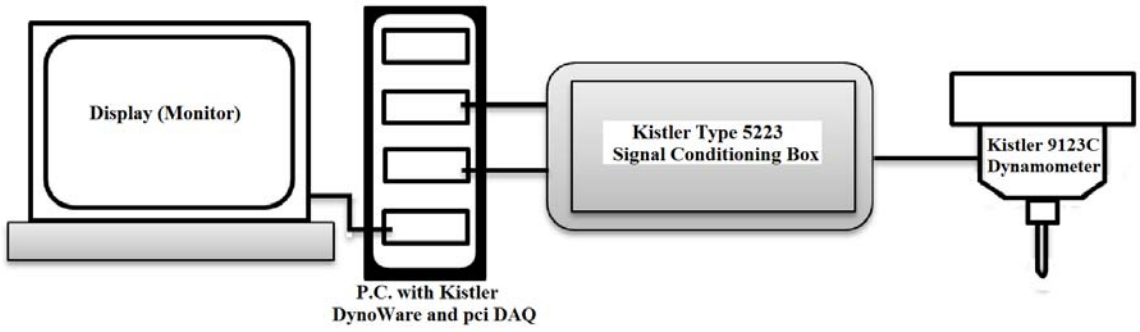

Figure 4.5. Schematic diagram of the force and torque measurement system

4.6 Acoustic Emission Measurements

Acoustic Emission (AE) signals were captured during select edge trimming experiments to investigate applicability for tool wear monitoring, detecting delaminations, and possible correlation to cutting force. AE signals were acquired using a Physical Acoustic PCI-2 AE system with AEwin PCI-2 software and WIN-POST post processing software along with two

WD wideband acoustic sensors and 2/4/6 pre-amplifier [103]. The PCI-2 system is equipped with 2 channels, AE data acquisition and digital signal processing system on a full-size PCI card, 18 bit A/D conversion, 1 Mhz acquisition rate with sample averaging, and automatic offset control. The two-wideband sensors are typically positioned along the edge of the workpiece to be trimmed and attached to the workpiece using Sonotech Ultragell II coupling gel with a mini C-clamp to hold the sensors in place. For edge trimming operations, the AE signal characteristics such as energy, count, rms, power, rise time, average and peak frequency were measured. The schematic diagram of the acoustic emission measurement system is shown in figure 4.6. Acoustic emission data was collected with specific experimental runs and analyzed with respect to the cutting conditions and process parameters assigned for the test, as described for cutting force measurement.

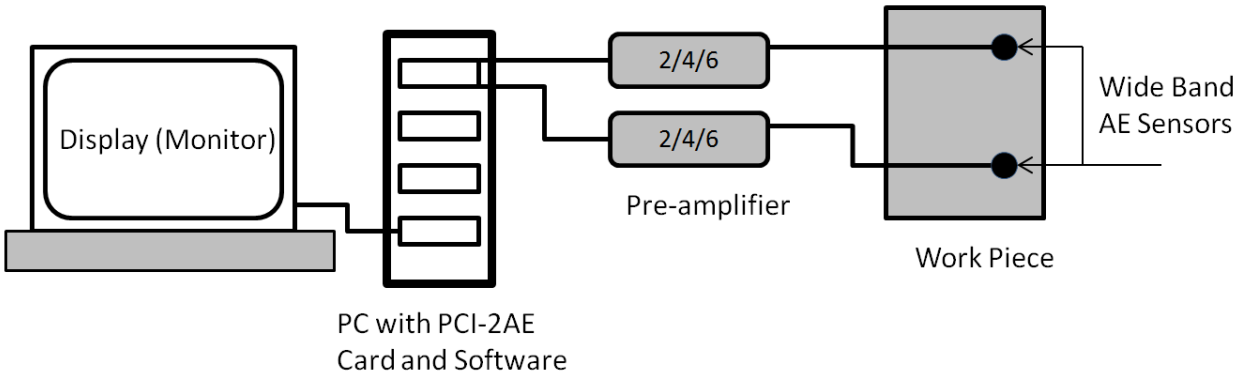

Figure 4.6. Schematic diagram of the acoustic emission measurement system.

4.7 Tool Wear Measurements

Tool wear measurements were made using a Micro-Vu, Model Sol 161 measuring machine as shown in figure 4.7. For specific experimental runs, the cutting edges of a tool were measured for wear from the parent edge of the tool and recorded. This systematic measurement process tracked the amount of tool wear in micrometers relative to the cumulative cutting distance for the tool. This provides an indication of the expected life of a cutter for a set of cutting conditions and process parameters.

Figure 4.7. Micro-Vu Microscope.

4.8 Surface Roughness Measurements

Surface roughness measurements were made using a Mahr MarSurf GD 25 contour measurement machine following each applicable run as shown in figure 4.8. A Wyko – NT 2000 Surface Profiler was used to generate 2D and 3D pictures of select surfaces (figure 4.9).

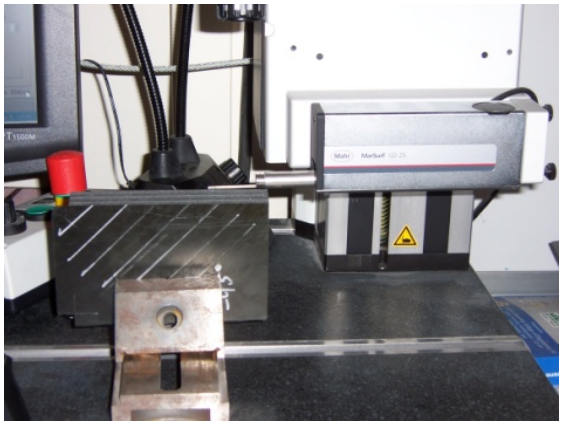

Figure 4.8 Mahr MarSurf GD 25

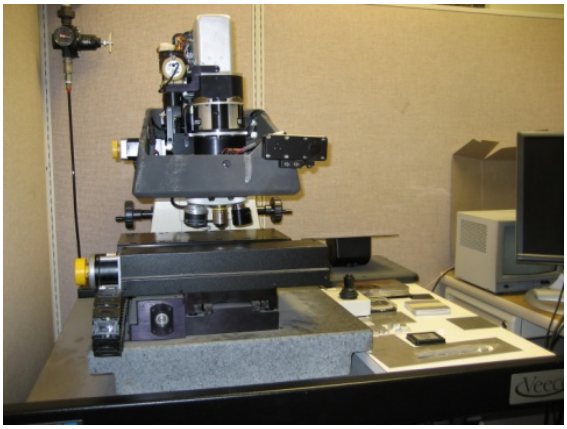

Figure 4.9. Wyko NT-2000

4.9 Dust Collection and Analysis Equipment and Instruments

Several instruments were used as part of the machining dust particle collection and analysis focus of this research and represented a significant development effort to function as a complete system, which is now patent pending. As will be covered in chapter 6, the dust collection and particle analysis system evolved significantly during the research. The system design evolved from initially using only a Sierra Instruments, Series 210 impactor in an open

environment, without local exhaust ventilation, for early screening tests in phase 1, up through a fully self-contained isokinetic sampling tower with real-time instrumentation utilizing sampling at the source in phase 4 and 5. This section will summarize the capabilities and functionality of some of the key instruments used in the system.

4.9.1 Cascade Impactors

Particles from select machining operations were collected through a Sierra Instruments, Series 210 cascade impactor in phase 1 screening tests [104]. Sioutas impactors were used in phase 2 and 3 testing and designed with an isokineic nozzle for future use. Cascade impactors are instruments based on impaction and have been used extensively for the measurement of particle size distributions by mass since the 1960s [79]. All inertial impactors operate on the same principle. An aerosol is passed through a nozzle and the output stream is directed against a flat plate. The flat plate, or impaction plate, deflects the flow to form an abrupt 90° bend in the streamlines. Particles whose inertia exceeds a certain value are unable to follow the streamlines and collide or impact on the flat plate and stick to the surface. Smaller particles can follow the streamlines and avoid hitting the impaction plate. They remain airborne and flow out of the impactor. Thus, an impactor separates aerosol particles into two size ranges; particles larger than a certain aerodynamic size are removed from the air stream and those particles smaller than that size remain airborne and pass through the impactor.

In a cascade impactor, a downstream filter is added so the user can collect all the particles that escape impaction. Sampling an aerosol with such an impactor can provide information about its particle size distribution. The mass of the particles collected on the impactor plate and those collected on the filter are determined by weighing before and after sampling. The impactor separates the sampled particulate mass up to two size ranges: that contributed by particles larger than the cut off size (collected on the impaction plate) and that contributed by particles smaller than the cut off size (collected on the filter). The cut off size is also called cut off diameter, cut point, cut size, cut off, or d_{50}. The most common approach is to operate several impactors in series, arranged in order of decreasing cut off size, with the largest cut off size first. This configuration is called a cascade impactor. Each separate impactor is called an impactor stage.

The cut off size is reduced at each stage by decreasing the nozzle size. Each stage is fitted with a removable impaction plate for gravimetric or chemical determination of the collected particles. The last stage in a cascade impactor is usually followed by a filter that captures all particles less than the cut off size of that stage. In operation, each cascade impactor stage is assumed to capture all particles reaching it that are larger than its cut off size. Because the aerosol flows in sequence through the successive stages, the particles captured on the impaction plate of a given stage represent all particles smaller than the cut off size of the previous stage and larger than the cut off size of the given stage. The sequential separation divides the entire distribution of particles into a series of contiguous groups according to their aerodynamic diameters. From the gravimetric measurements of each stage, the fraction of the total mass of each aerodynamic size range can be determined. The mass median aerodynamic diameter (MMAD) is obtained directly from the cumulative plot. Data reduction is based on the assumption that each stage has the ideal cut off characteristics.

Hard solid particles may bounce when they strike the impaction plate or they may adhere and subsequently blow off. Because of this, some of the mass of certain particles size ends up on a lower stage and thus is attributed to a smaller particle size range. Furthermore, once a particle bounces, it is likely to continue to bounce in subsequent stages because the impaction velocity is greater in the stages. Whether or not a particle bounces depends on its material, its velocity, and the type of impaction surface. Particles can also be deposited in the passageways between the stages of the cascade impactor. This is called interstage loss and represents another operational problem with cascade impactors. For conventional impactors, interstage losses are primarily a problem of large particles being lost in the first two stages. Particles are lost primarily by inertial removal at bends in the flow path. Since these interstage losses depend on particle size and are not included in the collected mass, they distort the size distribution towards smaller sizes.

Processing of the impactor filters requires several steps and is time consuming. First, the filters are carefully removed from packaging, placed in a petri dish or on a foil lined tray, and conditioned in an environmentally controlled weighing chamber for at least 24 hours. Typical humidity in the weighing chamber is approximately 32% RH and temperature 22^{o}C. Second, after conditioning, each filter is individually weighed on Mettler Toledo UMT2 analytical

balance, which first requires calibration using multiple weights. Two readings for each filter are required to be within ± 5 μg, which sometimes takes up to five individual measurements to meet the tolerance. At this point, the unexposed filters can be assembled into the impactor, which is then sealed until use. Following dust collection, which may involve sampling for up to 2 hours, the impactor is returned to the weighing lab and disassembled in a positive pressure chamber. Each exposed filter is then placed in a petri dish and brought to the weighing chamber to be conditioned for at least 24 hours. The exposed filters are then individually weighed using the analytical balance following the same procedure for the unexposed filters. The mass of dust collected at each impactor stage can then be determined by simply subtracting the unexposed filter mass from the exposed filter mass. This data is then used to prepare the log-probability plots to determine MMAD.

The Sierra Instruments Series 210 Impactor is a 10 stage impactor using a radial slot design. This design creates a circumferential air flow between stages, resulting in exceptionally low interstage, or wall losses [104]. The Series 210 directly measures the aerodynamic particle size instead of the geometric size. Prior to each dust collection experiment, the impactor is disassembled and each stage is thoroughly cleaned in deionized water and placed in a Model 1510 Branson Sonicator to remove any particles. The stages are then air dried for several hours prior to assembly. The impactor is then fully assembled using punched Teflon coated quartz fiber filters for stages 1-9, and a Teflon membrane or Teflon coated quartz fiber filter in stage 10. A Teflon membrane is used in stage 10 of the impactor to facilitate removal of the particles for SEM or toxicology analysis. Figure 4.10a-e are labeled photographs of the Sierra Instruments, Series 210 cascade impactor and dust collection system components used in phase 1 testing. This instrument was loaned for the research courtesy of Dr. Michael Kleinman at the University of California, Irvine.

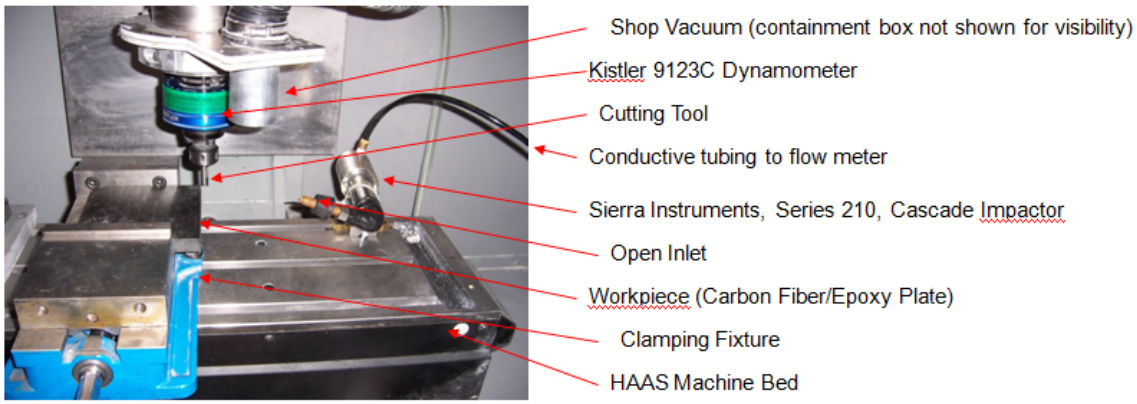

a) Sierra Instruments, Series 210, Cascade impactor set up

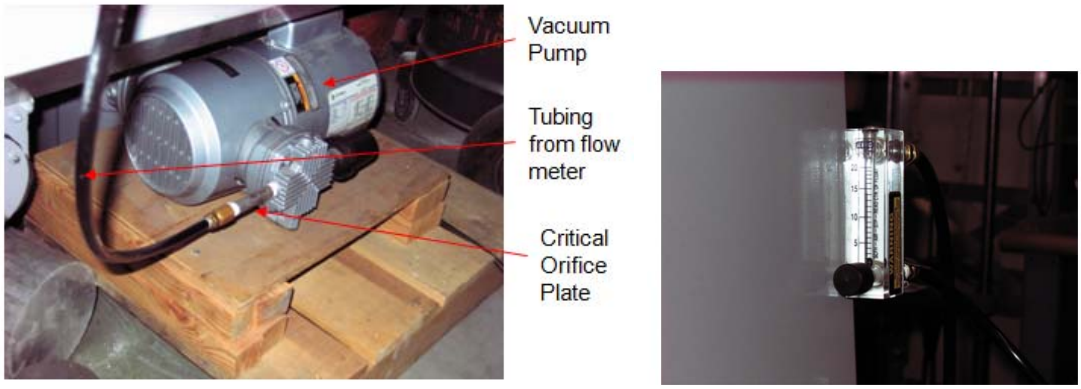

b) Vacuum pump, critical orifice plate

c) Flow meter (rotameter)

d) Mettler Toledo UMT2 Balance

e) Exposed impactor filters

f) Stage assembly

Figure 4.10. Sierra Instruments, Series 210, Cascade Impactor configuration

Sioutas cascade impactors were used for phase 2, 3, and 4 testing. Sioutas impactors have 4 stages with cutpoints at 2.5 µm, 1.0 µm, 0.50 µm, and 0.25 µm, and a backup filter [106].

The Sioutas impactors operate at 9 lpm, and have fittings for 3/8 inch ID tubing at the inlet and vacuum source ends. The fewer stages makes processing much faster than the Sierra Instruments impactor; however, there are significantly fewer cutpoints. The filters are processed in an identical fashion to the process used for the Sierra Instruments, Series 210. The Sioutas impactor stages use 25 mm 0.5 µm PFTE filters and a 37 mm 2.0 µm PFTE backup filter. For several tests, 0.4 µm nuclepore filters were used prior to the backup filter to provide improved visibility with SEM. The Sioutas impactor is shown in 4igure 4.11.

Figure 4.11 Sioutas Cascade Impactor

To support the Sioutas Impactor an improved vacuum system was designed and fabricated. This system utilizes a receiver tank and manifold for capability to run 4 or more instruments simultaneously which require a vacuum source. A Millipore nominal 10 lpm critical orifice was used to create the constant flow from vacuum source for the Sioutas impactors. The critical orifices were mounted in custom machined fittings attached to the manifold. The critical orifice for the Sierra Insruments, Series 210 impactor was also relocated and would later serve to provide 3.5 lpm flow to the Thermo Fisher Scientific PDR DataRam. The system has 3 valves, two of the valves open the air flow at either end of the manifold, while the third valve opens to a 0-60 standard cubic feet per hour (SCFH) rotameter which provides a cumulative flow to the

system to minimize flow disruptions when the valve manifold valves open. A schematic of the revised vacuum flow system is shown in figure 4.12 and photograph of the control panel is shown in figure 4.13.

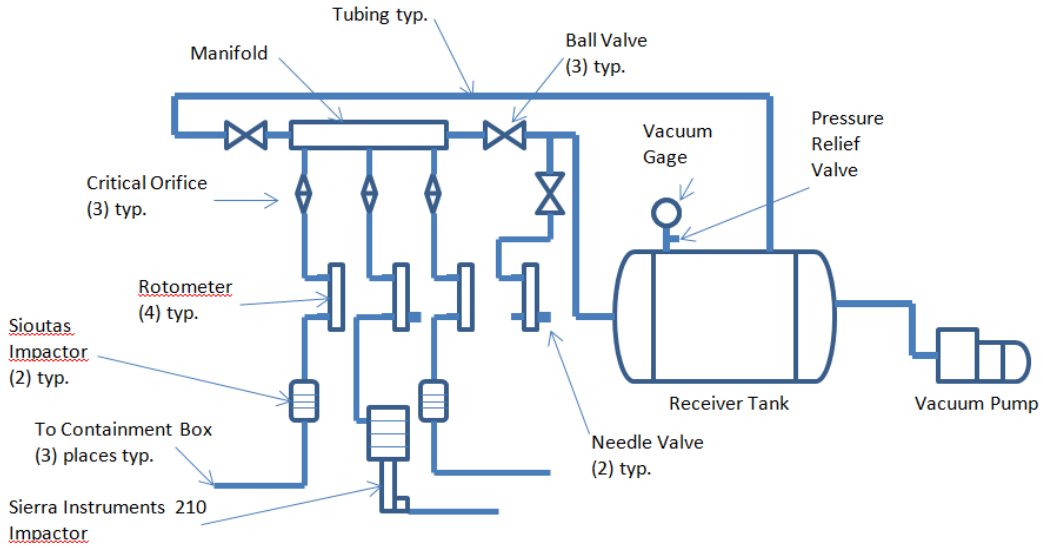

Figure 4.12 Revised vacuum flow schematic

Figure 4.13 Vacuum source control panel

4.9.2 Critical Orifice Meter

Critical orifices were used to provide constant flow to the Sierra Instruments Series 210 impactor, Sioutas impactor, and ThermoFisher Scientific PDR DataRam. For constant flow control during filter sampling, a type of orifice meter called a critical orifice meter or plate can

be used downstream of the filter [77]. The orifice is small enough to provide a downstream pressure less than 0.53 of the upstream pressure, under which conditions the velocity in the constriction reaches the speed of sound; a further reduction in the downstream pressure does not increase the velocity through the system, resulting in a "choked flow." The critical orifice maintains a nearly constant flow under such conditions. For a critical orifice, the flow rate Q (m^3/sec) is proportional to the air pressure P_1 (Pa) and air density, ρ_1 (kg/m^3), at the upstream and is expressed in equation 4.1.

$$Q = 0.58k\gamma^{1/2}(A_o/\rho_a)(\rho_1 P_1)^{1/2} \quad (4.1)$$

P_1 = air pressure

σ_1 = air density

k = discharge coefficient

γ = ratio of specific heats (1.4 for air)

A_o = area of the orifice (m^2)

ρ_a = ambient air density (kg/m^3)

4.9.3 Rotameter

Six rotameters were used in the experiments to ensure controlled air flow to the cascade impactors and real-time sampling instruments.

- King Instruments 0-30 SCFH (qty 2)
- King Instruments 0-20 SCFH with needle valve (qty 1)
- King Instruments 0-60 SCFH with needle valve (qty1)
- Dwyer Instruments 0-10 SCFH, RM-50 (qty 2)

A rotameter is used to monitor the air flow rate through the cascade impactor to ensure constant flow and no clogging. The rotameter consists of a "float" that is free to move up and down in a vertical tapered tube, through which the fluid to measured passes. The tapered tube is larger at the top than the bottom. The gas flows upward, causing the float to rise until the pressure drop across the annular area between the float and the tube wall is just sufficient to support the float, where by its weight balances the upward drag force due to the fluid flowing up through the tube. The height of the float indicates the flow rate. For a rotameter calibrated at an ambient pressure, $P_{a,c}$, and used at a different ambient pressure, $P_{a,i}$, the true volumetric flow rate Q_i at a fixed float position is given by equation (4.2).

$$Q_i = Q_c(P_{a,c}/P_{a,i})^{1/2} \quad (4.2)$$

Q_i = true volumetric flow rate

Q_c = flow rate indicated by the rotameter during calibration

$P_{a,c}$ = ambient pressure at which rotameter was calibrated

$P_{a,i}$ = ambient pressure during use

4.9.4 Pitot Tubes and Magnehelics®

Two Dwyer Series 166-6CF pocket size pitot tubes and two Dwyer Magnehelics ® were used to measure air velocity in the isokinetic ducts for phase 3, 4, and 5 testing [106]. Pitot tubes were located in the ducts according to the guidelines provided by Dwyer.

- Duct diameter should be 30x pitot tube diameter
- Smooth straight duct sections a minimum of 8.5x duct diameter in length upstream
- Smooth straight duct sections a minimum of 1.5x duct diameter downstream
- Centered in duct

The pitot tube enables the direct measurement of dynamic pressure which allows calculation of gas velocity in ducts. Dynamic or velocity pressure is the difference of the total pressure or impact pressure at the nose of the pitot tube and the static pressure of the gas stream at the side ports. The dynamic pressure varies with the square of the gas velocity. Air velocity is determined according to the following equation (4.3).

$$\text{Air Velocity} = 1096.2\sqrt{\frac{Pv}{D}} \qquad (4.3)$$

Where Pv = velocity pressure in inches of H_2O and D = Air density in lbs/ft^3. For these calculations, air density was assumed at .075 lbs/ft^3, which is used for dry air at 70^{o}F and 29.9 inches Hg barometric pressure. Air velocity in feet/min is easily converted into m/sec, by multiplying by 0.0051, as these instruments are more readily available in US customary units.

Differential pressure was measured using Dwyer Magnehelic® gages. Two Dywer Series 2000 Magnehelic gages were flush mounted to custom fabricated mounts with tubing from the two pitot tubes connected to the high and low pressure ports on the Magnehelics® with bronze fittings. The gages are mounted above the HAAS machine so they can be quickly monitored for duct flow velocity during cutting operations. A 0 - .25 in H_20 gage and 0 - .50 in H_20 gage was used in the experiments. Figure 4.14 is a photograph of the Maghelic gages above the HAAS machine, and a typical pitot tube schematic.

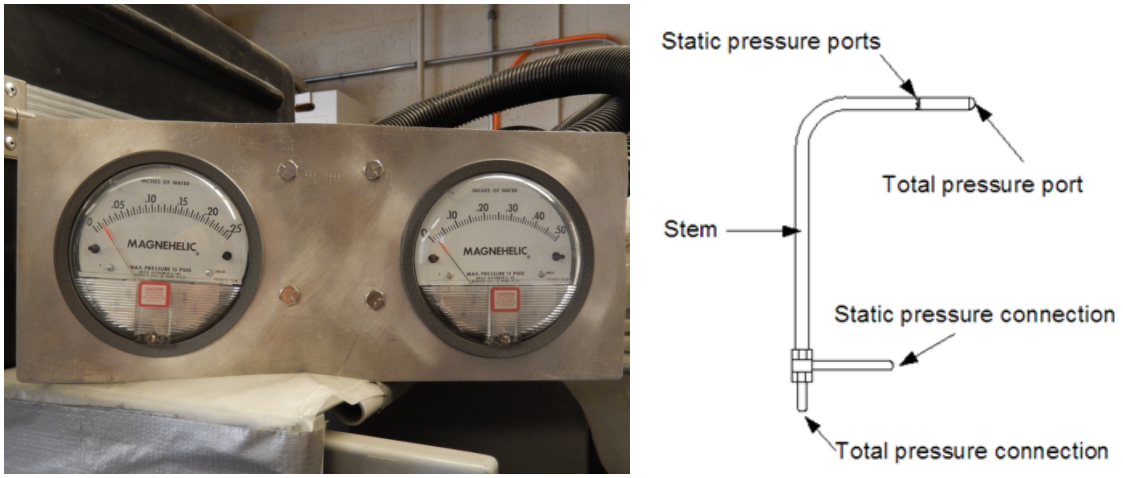

Figure 4.14 Magnehelic® gages and pitot tube schematic

4.9.5 Ultrafine Particle Counter

A TSI PTRAK™ Ultrafine Particle Counter (UPC) was used in this research to measure ultrafine particle concentrations in real-time during the machining experiments in phase 3, 4, and 5 of the research. The PTRAK has a concentration limit of 500,000 particles/cm^3 and a particle size range of 0.02 to 1 μm. The PTRAK has data logging capability for capturing multiple runs within the memory of the instrument and data is acquired, visualized, and exported using TSI TrakPro™ software.

Two types of direct reading instruments include Optical Particle Counters (OPC) and Condensation Particle (CPC) counters. OPCs are routinely used for real-time aerosol characterization in the particle size range of approximately 0.3-20 μm. They are applied to everything from low concentration measurements such as clean room monitoring, monitoring in ambient air, to highly concentrated aerosols for industrial filter testing under realistic conditions [107]. An OPC utilizes a light source, typically a laser diode, to illuminate a selected sample of air that has mechanically controlled flow through precisely configured nozzle. The light beam is positioned at an angle to the air sample. A photo detector then measures the light elastically scattered off of particles by reflection, refraction and diffraction. Based on the intensity of the flash, particles can be counted and sized at the same time. The physical properties of the particles can have an effect on the light scattered as various materials absorb light at different rates which will affect the intensity of the light scattered [108].

A CPC, such as the PTRAK^{TM}-8525 makes measurements in units of particles per cubic centimeter (pt/cm^3) versus traditional aerosol measurements of milligrams per cubic meter (mg/m^3) made by photometers. Particles are drawn through the PTRAK^{TM} UPC using a built in pump. Upon entering the instrument, particles pass through a saturator tube where they mix with an alcohol vapor. The particle/alcohol mixture then passes into a condenser tube where alcohol condenses onto the particles, causing them to grow into a larger droplet. The droplets then pass through a focused laser beam, producing flashes of light which are sensed by a photo-detector. The particle concentration is determined by counting the light flashes. If the particles were not grown into a larger droplets, they would not produce enough scattered light to be detected. The PTRAK^{TM} UPC counts ultrafine particles smaller than 0.1 μm in diameter [109], with a stated particle size range of 0.2 to 1 μm. A picture of the PTRAK is shown in figure 4.15.

Figure 4.15 TSI PTRAK 8525

4.9.6 ThermoFisher Scientific PDR-1200 personal dataRAM^{TM}

The ThermoScientific personal DataRAM (pDR-1200) measures mass real-time concentrations of dust. It is a light scattering photometer incorporating a pulsed, high output, near infrared light emitting diode source, in a silicon detector/hybrid pre-amplifier amplifier, collimating optics, and a source reference feedback detector [110]. This optical configuration responds to particles in the size range of 0.1 to 10 μm. The instrument has a measurement range from 0.001-400 mg/m^3. The unit was gravimetrically calibrated using National Institute of Standards and Technology (NIST) traceable standard Society of Automotive Engineers (SAE) fine dust. It has an integral filter holder downstream of the photometric sensing stage and

accepts 37 mm diameter filters which can be used for gravimetric calibration. The pDR – 1200 incorporates an optional metal cyclone (BGI model GK 2.05). The vacuum system can be operated at specific sampling flow rates to provide precisely defined particle size cuts, such as PM 2.5. The instrument has data logging capability and data is extracted through software which can then be exported into Microsoft Excel for analysis. A custom isokinetic nozzle was also fabricated to enable use of the pDR – 1200 in the isokinetic sampling tower. Figure 4.16 is a photograph the pDR-1200 dataRAM and GK 2.05 cyclone cutpoint curve. The pDR was used in practice with and without the cyclone. This instrument was loaned for the research courtesy of Dr. Michael Kleinman at the University of California, Irvine.

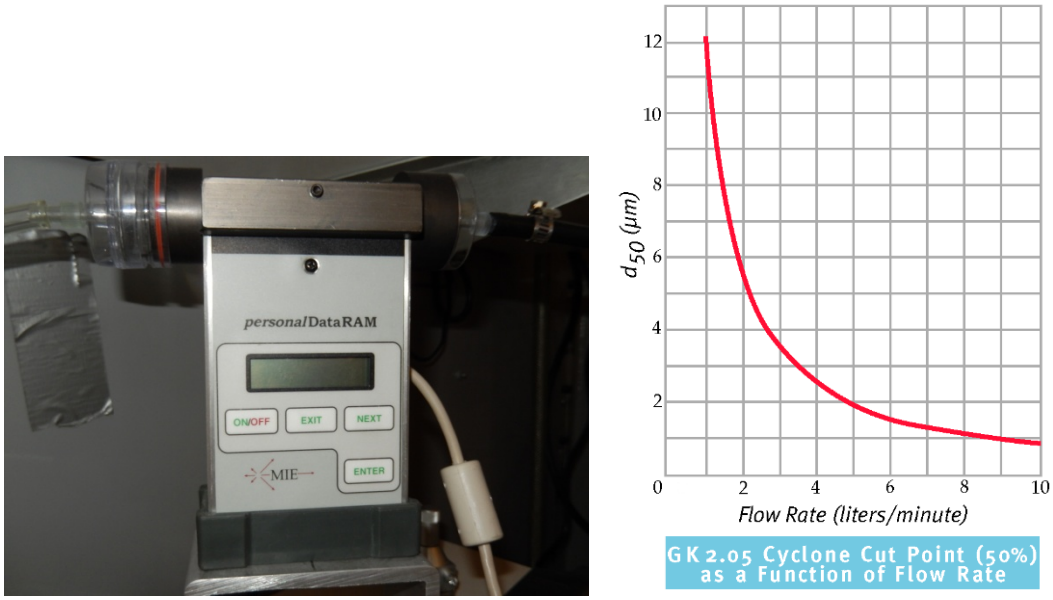

Figure 4.16 ThermoScientific PDR DataRam and Cyclone

4.9.7 Casella CEL-712 Microdust Pro™

The Casella CEL-712 Microdust Pro™ was also used in this research for real-time detection of airborne dusts similar to the pDR–1200. The Microdust Pro is a much newer instrument than the PDR–1200 and has a wider concentration range from 0.001 to 2500 mg/m^3. The instrument uses a modulated light source passing to a measurement chamber which then reaches a laser detector [111]. It also has a removable sampling probe that can be used with either a cyclone or polyurethane foam (PUF) filters. It is factory calibrated using ISO 12103-1 A2 fine test dust (Arizona road dust equivalent), and each unit has its own specific calibration insert which creates a fixed optical scattering effect in the sampling space. This fixed reference

can be used at any time to confirm the factory calibration point for the instrument and probe. Gravimetric calibration can be performed with an optional 37 mm diameter filter holder. A custom isokinetic nozzle was fabricated for the Microdust Pro for use in the isokinetic sampling tower. For isokinetic sampling, the flow rate is calculated from the sample velocity cross-sectional area of the gravimetric inlet tube which is 200 mm. The unit has data logging capability and data can be extracted via the Casella Insight data management software. Figure 4.17 is a photograph of the Casella Microdust Pro CEL-712.

Figure 4.17. Casella Microdust Pro CEL-712

4.9.8 GRIMM 1.109 Portable Aerosol Spectrometer

The GRIMM 1.109 Portable Aerosol Spectrometer was the flagship of real-time instruments used in this research for particle analysis. The instrument measures airborne particles in sizes ranging from 0.25 µm to 32 µm in 31 different size channels in real-time and supplies the measured values as particle number concentration and particle mass. All particles are collected on a 47 mm diameter PTFE filter inside the instrument which can be used for gravimetric calibration and further analysis. Each particle in the aerosol is individually detected by scattered light photometry inside an optical measuring cell. The scattered light impulse of each individual particle is counted based on the intensity of the scattered light signal attributed to a particle size [112]. The aerosol spectrometer collects the particle size distribution of solid aerosol particles in many size classes. The instrument is calibrated with polystyrene latex spheres (PSL). Data is captured real time and displayed on a PC using the GRIMM 1178 LabVIEW software . The data for 31 different size channels can then be exported by either mass

distribution or count distribution. A disadvantage of the GRIMM 1.109 is that it takes 6 seconds to scan 31 channels, requiring longer samples, compared to the other 3 real-time instruments which can scan at 1 second intervals. The GRIMM offers capability to scan half the channels in 1 second intervals but this requires using different dated software (v. 1.177) that is only Windows XP based, or sending commands through a hyper terminal interface. This 1 second sampling capability was verified in a limited series of tests, but not used in the research because of recommendations by GRIMM. A Grimm 1.152 isokinetic sampling probe with four interchangeable nozzles was used with the instrument for isokinetic sampling. This custom isokinetic nozzle utilizes two tubes. One tube is for the dust inlet and the other tube connects to the dust monitor exhaust port to maintain a balanced pressure differential. A Topas DIL 550 aerosol diluter is used in conjunction with the GRIMM 1.109 for isokinetic sampling. The Topas diluter is factory calibrated for a 10:1 dilution ratio at the Grimm flow rate of 1.2 lpm. The diluter removes particles from the aerosol in a definite manner where the aerosol flow split into two streams. One aerosol flow passes through a HEPA filter which removes all particles and then a valve for flow rate adjustment. The second flow passes through a thin capillary tube. The dilution factor is determined by the flow rate ratio between these two streams [113]. Figure 4.18 is a photograph the Grimm 1.09 portable aerosol spectrometer and Topas DIL 550 diluter.

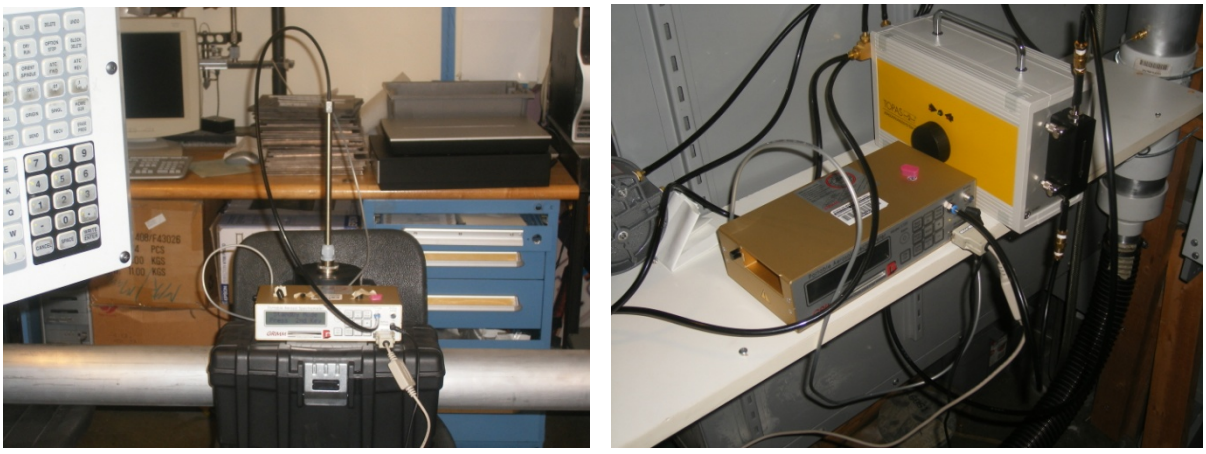

Figure 4.18. GRMM 1.109 and isokinetic nozzle, with Topas Diluter

4.10 Experimental Method Summary

This chapter summarized the materials, cutting tools, equipment, and instruments used to conduct the experimental component of this research. The five phases of development were

discussed showing a progression of technique maturity. Chapter 5 will discuss the screening tests and preliminary machinability experiments conducted for composite materials. Chapter 6 will cover in detail the development and evolution of a unique particle collection and analysis system. This system enables the collection and analysis of particles from dust generating manufacturing processes to be conducted in a safe and controlled environment. Chapter 7 will address the development of cutting force data acquisition processes in support of a cutting force prediction model for multi-directional composite laminates. These techniques can be applied to predict forces when trimming multi-directional composite laminates with just a minimum of calibration tests on a unidirectional laminate of the same material system. The experimental techniques developed as part of this research further enhance the capabilities for understanding the machining of composite materials.

CHAPTER 5

PRELIMINARY MACHINABILITY INVESTIGATION

5.1 Introduction

This chapter presents the experimental investigation and results for phase 1 and 2 of this research. Phase 1 consisted of screening tests that were designed to validate experimental measurement and data acquisition techniques with preliminary results for select cutting conditions. Basic experimental techniques were evaluated for cutting force measurement, acoustic emission signal analysis, surface integrity measurement, tool wear measurement, and composite dust collection using a 10 stage cascade impactor. The Phase 2 experimental investigation expanded the phase 1 screening test dust collection matrix and incorporated new techniques and instruments for particle collection. The results of the phase 2 investigation focused the following phases of this research on development of techniques for real-time self-contained machining dust particle collection and analysis, and cutting force prediction of multi-directional laminates. In particular, the need for machining dust particle collection and analysis is growing in order to ensure the safety of dry machining processes for composites.

5.2 Phase 1 Screening Tests

As discussed in chapter 4, the research was performed in five major phases with specific objectives for each phase. In the first phase of the research, a feasibility study was conducted which included screening experiments to determine representative processing conditions, including cutting speed, feed rate, and depth of cut for selected cutting tools and fiber orientations. Another importance of the screening experiments was to validate the basic experimental configuration for the Dynamometer (cutting forces), Acoustic Emission signal acquisition, tool wear measurement, surface finish measurement, and initial dust collection protocol using a 10 stage cascade impactor. The

phase 1 screening experiments provided valuable insight into experimental details such as cutting force magnitude, cutting tool performance, acceptable feed rates, placement of cascade impactor, filter measurement protocols, and preliminary durations to achieve measurable dust levels. The measurements, instruments, and data derived from the initial screening experiments are summarized in table 5.1. Figure 5.1 is an illustration of the initial dust collection system with a picture of typical results from after an edge trimming test shown in figure 5.2. The design of the machining particle dust collection and analysis system was a significant focus of this research, and evolved from the starting state shown in figure 5.2 to a fully self-contained isokinetic sampling system described in chapter 6.

Table 5.1. Summary of screening experiments performed in phase 1.

Screening Experiment	**Instrument/Process**	**Data Derived (lessons learned)**
Cutting force measurements	Kistler 9123C Dynamometer	Force magnitudes, feedrates, depth of cut, RPM, mechanical setup, fixturing, 0 count usage
Acoustic emission signal acquisition	Physical Acoustic PCI-2 AE	Signal magnitude, sensor location, sensor fixturing
Tool wear measurements	Micro-Vu Sol 161 Microscope	Magnitude over time, process
Surface roughness measurement	Profilometry Mahr MarSurf GD 25	Surface roughness relative to fiber orientation
Damage integrity measurement	Surface Profiler Wyko NT-2000; SEM	Damage relative to fiber orientation
Dust particle collection	Sierra Instruments Series 210 Cascade Impactor; Mettler Toledo UMT2 Analytical Balance	Particle MMAD relative to fiber direction, impactor location, filter weighing protocol
Chip formation (dust) analysis	SEM	SEM photos, cellular toxicity (preliminary)

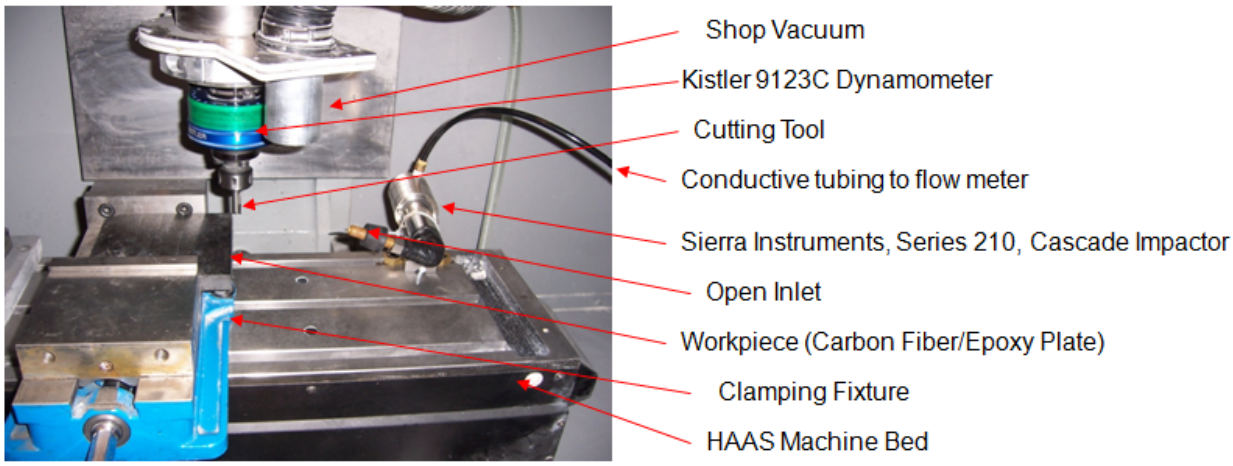

Figure 5.1 Initial dust collection configuration.

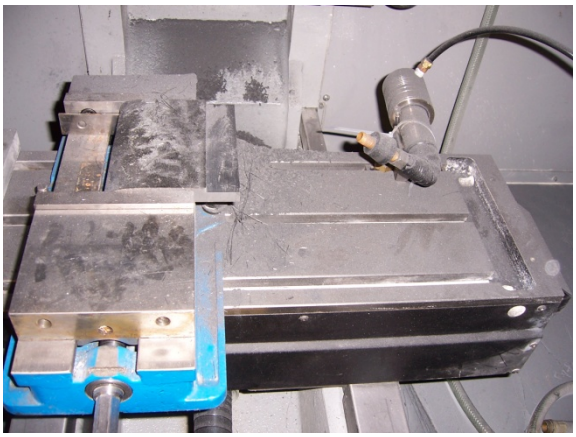

Figure 5.2 Phase 1 dust collection post trimming test

5.3 Phase 1 Screening Test Results

In the first phase, screening experiments were performed to validate the feasibility of accomplishing the fundamental objectives of the research. Screening experiments are necessary to select cutting parameters and conditions (spindle speed, cutting speed, feed rate, and depths of cut). The screening experiments also helped provide insight into dust collection times using a cascade impactor to gather meaningful samples. A total of 57 individual experiments were conducted. The goals of the screening experiments are summarized as follows:

- Develop and validate experimental setup, procedures, and protocols
- Demonstrate all experiment types planned for the research
- Determine acceptable cutting process parameters (feedrate, RPM, depth of cut)
- Validate cutting tool geometry and materials
- Validate cutting force data was in line with published works
- Validate acoustic emission data trended with cutting forces
- Validate preliminary surface finish of different fiber orientations
- Capture preliminary micrographs of dust and machine workpiece surface
- Validate dust particle sizes are in the potentially respirable size range
- Train in use of equipment
- Capture, plot, and analyze preliminary data

5.3.1 Initial Cutting Force Measurements

Cutting forces were measured using the Kistler 9123C rotating dynamometer and Acoustic Emission signals acquired using the PCI-2 AE system as described in chapter 4. Cutting force and acoustic emission measurements were initially made on 53 different combinations of composite laminates, including unidirectional (0, 60, +45, -45, 90), and quasi-isotropic multi-directional laminates. Different cutting tools, feedrates, axial and radial depth of cuts, and cutting methods (climb vs. conventional cutting) were used in the data acquisition. Table 5.2 summarizes the cutting conditions for this first series of screening experiments.

Table 5.2 Phase 1 screening experiment test conditions (no dust measurements).

ID	Material	Cutter Type	Cutter Dia (mm)	# Edge	Cutting Type	Spindle Speed (rpm)	Table Feed rate (mm/min)	Radial Depth of Cut (mm)	Axial Depth of Cut (mm)
2/6-1	0 deg[1]	PCD	19.05	2	climb	6000	508	2.54	6.35
2/6-2	0 deg[1]	PCD	0.75	2	climb	6000	508	2.54	6.35
2/6-3	0 deg[1]	PCD	0.75	2	climb	6000	1016	2.54	6.35
2/6-4	0 deg[1]	PCD	0.75	2	climb	6000	2286	2.54	6.35
2/6-5	0 deg[1]	PCD	0.75	2	conv.	6000	508	2.54	6.35
2/6-6	0 deg[1]	PCD	0.75	2	conv.	6000	1016	2.54	6.35
2/6-7	0 deg[1]	PCD	0.75	2	conv.	6000	2286	2.54	6.35
2/6-8	90 deg[1]	PCD	0.75	2	climb	6000	508	2.54	6.35
2/6-9	90 deg[1]	PCD	0.75	2	climb	6000	1016	2.54	6.35

2/6-10	90 deg[1]	PCD	0.75	2	climb	6000	2286	2.54	6.35
2/6-11	90 deg[1]	PCD	0.75	2	conv.	6000	508	2.54	6.35
2/6-12	90 deg[1]	PCD	0.75	2	conv.	6000	1016	2.54	6.35
2/6-13	60 deg[1]	PCD	0.75	2	climb	6000	508	2.54	6.35
2/6-14	60 deg[1]	PCD	0.75	2	climb	6000	1016	2.54	6.35
2/6-15	60 deg[1]	PCD	0.75	2	climb	6000	2286	2.54	6.35
2/6-16	60 deg[1]	PCD	0.75	2	conv.	6000	508	2.54	6.35
2/6-17	60 deg[1]	PCD	0.75	2	conv.	6000	1016	2.54	6.35
4/30-1	multi[2]	CVD	6.35	4	climb	6000	635	0.762	7.39
4/30-2	multi[2]	CVD	6.35	4	climb	6000	635	0.762	7.39
4/30-3	multi[2]	CVD	6.35	4	climb	6000	635	0.762	7.39
5/3-1	multi[3]	CVD	6.35	4	climb	6000	635	0.762	2.03
5/6-1	multi[3]	CVD	6.35	4	climb	6000	635	0.254	2.03
5/6-2	multi[3]	CVD	6.35	4	climb	6000	635	0.762	2.03
5/6-3	multi[3]	CVD	6.35	4	climb	6000	635	0.762	2.03
5/6-4	multi[3]	CVD	6.35	4	climb	6000	635	0.762	2.03
5/6-5	multi[3]	CVD	6.35	4	climb	6000	635	0.762	2.03
5/6-6	multi[3]	CVD	6.35	4	climb	6000	635	0.762	2.03
5/6-7	multi[3]	CVD	6.35	2	climb	6000	635	0.254	2.03
5/6-8	multi[3]	CVD	6.35	2	climb	6000	635	0.762	2.03
5/6-9	multi[3]	CVD	6.35	2	climb	6000	635	0.762	2.03
5/6-10	multi[3]	CVD	6.35	2	climb	6000	635	0.762	2.03
5/6-11	multi[3]	CVD	6.35	2	climb	6000	635	0.762	2.03
5/6-12	multi[3]	CVD	6.35	2	climb	6000	635	0.254	2.03
5/6-13	multi[3]	CVD	6.35	2	climb	6000	635	0.762	2.03
5/6-14	multi[3]	CVD	6.35	2	conv.	6000	635	0.762	2.03
5/6-15	multi[3]	CVD	6.35	2	conv.	6000	635	0.762	2.03
5/6-16	multi[3]	CVD	6.35	2	conv.	6000	635	0.762	2.03
5/6-17	multi[3]	CVD	6.35	2	conv.	6000	635	0.762	2.03
5/6-18	multi[3]	CVD	6.35	2	conv.	6000	635	0.762	2.03
5/7-1	0 deg[1]	CVD	6.35	4	climb	6000	254	0.762	6.35
5/7-2	0 deg[1]	CVD	6.35	4	climb	6000	381	0.762	6.35
5/7-3	0 deg[1]	CVD	6.35	4	climb	6000	635	0.762	6.35
5/7-4	90 deg[1]	CVD	6.35	4	climb	6000	254	0.762	6.35
5/7-5	90 deg[1]	CVD	6.35	4	climb	6000	381	0.762	6.35
5/7-6	90 deg[1]	CVD	6.35	4	climb	6000	635	0.762	6.35
5/7-7	-45 deg[1]	CVD	6.35	4	climb	6000	254	0.762	6.35
5/7-8	-45 deg[1]	CVD	6.35	4	climb	6000	381	0.762	6.35
5/7-9	-45 deg[1]	CVD	6.35	4	climb	6000	635	0.762	6.35
5/7-10	+45 deg[1]	CVD	6.35	4	climb	6000	127	0.762	6.35
5/7-11	+45 deg[1]	CVD	6.35	4	climb	6000	254	0.762	6.35

5/7-12	+45 deg[1]	CVD	6.35	4	climb	6000	381	0.762	6.35
5/7-13	+45 deg[1]	CVD	6.35	4	climb	6000	508	0.762	6.35
5/7-14	+45 deg[1]	CVD	6.35	4	climb	6000	635	0.762	6.35

[1]33 ply unidirectional laminate.

[2]26 ply multi-directional laminate $[F/(90/-45/0/45)_3]_s$

[3]10 ply multidirectional laminate $[(0/45/90/-45/0)]_s$

As an example of one experiment, ID 5/6-17 from table 5.2, cutting force measurements were taken on both sides of a 10-ply multi-directional prepreg autoclave cured laminate, with layup $[(0/45/90/-45/0)]_s$. A picture of this fixtured laminate is shown in figure 5.3, with summary cutting conditions adjacent to the photograph. Acoustic emission sensors are located at the ends of the workpiece, with mini C-clamps removed for the picture. C-Clamps are used to keep the AE sensors in position so they don't move as a result of vibration during trimming.

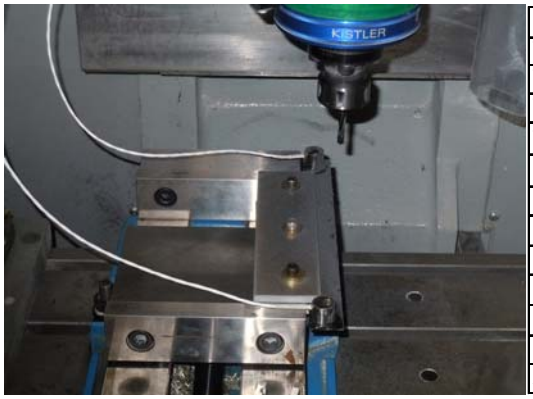

Parameter	Value
Workpiece Material	Carbon/Epoxy 10-ply
Workpiece Length (mm)	250
Workpiece Width (mm)	40
Workpiece Thickness (mm)	0.19
Milling Process	conventional
Cutter Material	CVD
Cuttter Geomerty	2-flute, 0 deg
Cutter ID.	19305011
RPM	6000
Feedrate (mm/min)	635
Radial Depth of Cut (mm)	0.762
Axial Depth of Cut	full thickness

Figure 5.3. Multi-directional laminate cutting force and acoustic emission experiment.

Approximately 30 seconds of force data was acquired. Since the spindle speed is 6000 rpm, 2 complete rotations of the cutter occur in .02 seconds. Typical plots of the forces for both sides of the workpiece are shown in figure 5.4, with the sample taken at 15 seconds, approximately midway through the cut. Force data was collected for the rotating dynamometer Fx, Fy axes and moment, Mz. The tangential, Ft, and radial force, Fr, are derived from these measurements in Kistler DynoWare software and also plotted.

As these were initial screening experiments to assist with first-time usage of the instrument, more details are provided in chapter 7 on data interpretation and improved techniques. The initial graphs show an oscillating pattern for Fx and Fy as expected for the rotating coordinate system and a sinusoidal profile for Ft expected for the trim cut. With the light edge trimming cuts, force magnitudes are very low. The radial force, Fr, is flat with a few small spikes, which is indicative of errors in derivation as these forces should not be zero.

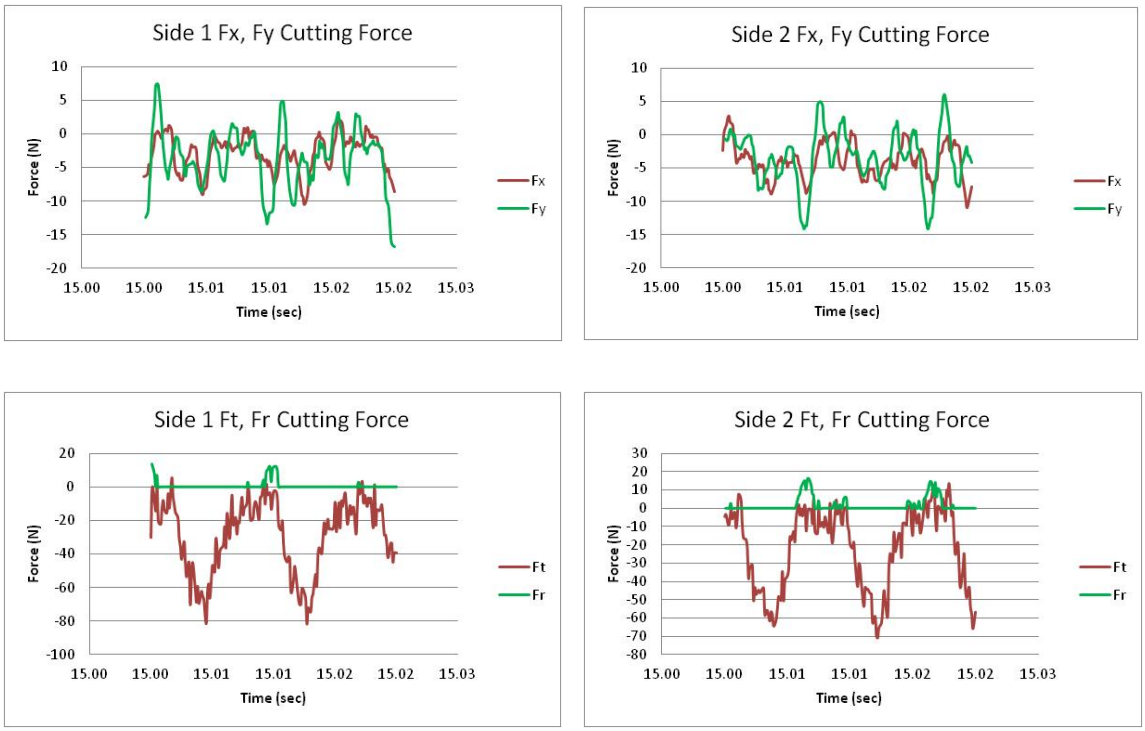

Figure 5.4. Multi-directional laminate cutting forces.

5.3.2 Initial Acoustic Emission Signal Acquisition

In addition to the cutting force measurements, Acoustic Emission (AE) signal data was acquired with the same cutting conditions in table 5.2. The purpose of capturing the acoustic emission signals was to investigate the potential to use AE as an instrument to

monitor tool wear, detect delaminations, and correlate to cutting forces. Related applications were discussed in the literature review in chapter 2. AE data from the same multi-directional laminate milling experiment, ID 5/6-17, from which the cutting forces were captured is plotted in figure 5.5. A .02 second sample of data, corresponding to two cutter revolutions is shown. Signal time vs. voltage is plotted. As with the cuteting force data, the AE data can be plotted down to the actual cutter rotational position. From the AE graphs, a similar pattern to the cutting forces can be seen. Significant analysis is required to demonstrate the potential for correlating AE signals to delaminations, tool wear, and cutting forces for milling of composite material.

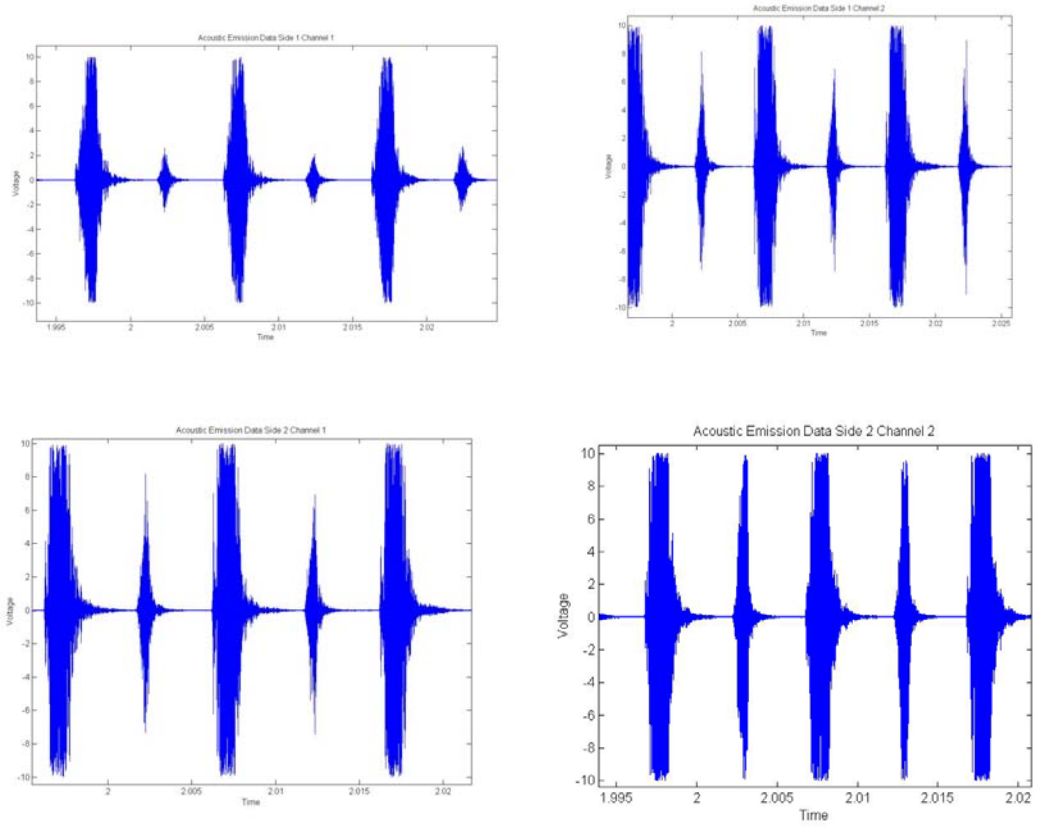

Figure 5.5. Acoustic emission data for sample ID 5/6-17.

5.3.3 Preliminary Surface Finish Measurements

Surface measurements were made for the multi-directional laminate, ID 5/6-17, used in the cutting force and AE experiments using both the Mahr MarSurf GD 25 Surface Profilometer and Wyko NT-2000 Surface Profiler. Figure 5.6 is a photograph of the machined edge of side 2 of the 10-ply laminate. The fiber orientations corresponding to the $[(0/45/90/-45/0)]_s$ layup are clearly visible in the photograph.

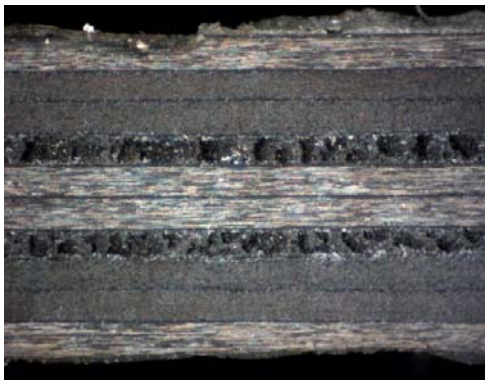

Figure 5.6. Photograph of machined 10-ply multi-directional laminate, ID 5/6-17.

Surface finish readings from the Mahr profilometer are included in Table 5.3.

Table 5.3. Single side surface finish of 10-ply laminate from Mahr profilometer.

	10-Ply Multi-Directional Laminate Side 1, ID 5/6-17		
Point and Direction	**Ra (μm)**	**Rq (μm)**	**Rt (μm)**
Pt 1 Longitundial	0.662	0.892	8.970
Pt 2 Longitudinal	0.557	0.711	6.110
Average Longitudinal	**0.610**	**0.802**	**7.540**
Pt 1 Transverse	1.209	1.770	11.660
Pt 2 Transverse	1.111	1.695	14.270
Average Transverse	**1.160**	**1.733**	**12.965**

In addition to the Mahr profilometer, surface profile data was obtained for the same edge using the Wyko NT-2000 Surface Profiler shown figure 5.7.

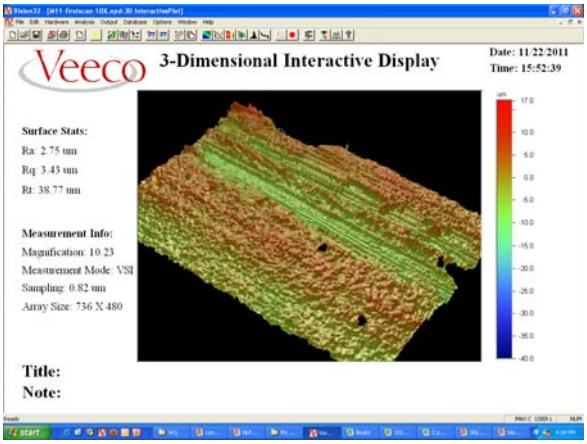

Figure 5.7 10-ply laminate surface profile from Wyko NT-2000 Surface Profiler.

There is a significant difference between the Ra, Rq, and Rt surface finish readings between the Mahr and Wyko. This can likely be explained by measuring different points on the surface of the part.

5.3.4 Preliminary Cellular Toxicity Evaluation of Carbon Fiber Dust

An initial screening test was conducted to look at potential cellular toxicity of composite materials using dust generated from drilling of a CFRP laminate. Dust was collected in a container from drilling a .25" unidirectional laminate using a HSS ¼" diameter drill. From the Cell Viability Graph (figure 5.8), we can see that 10 µg/mil of carbon fibers (CNF), produced the same degree of cell killing as 50 µg/mil of diesel particles. This is loosely equivalent to the diesel exposure of living 100m away from a freeway for several months. In the test, RPMI, which is a medium used to grow cells, was used as a negative control, and had 100% viability as expected. Triton X is a surfactant that breaks up cell membranes and was used as positive control, to kill 50% of the cells (macrophages). Different amounts of carbon material was then added demonstrating a dose response reduction in cell viability. 10 µg/mil of (CNF) killed 50% of the cells. The cells used in the experiment were macrophages removed from a rat lung by lavage and cultured in RPMI fluid.

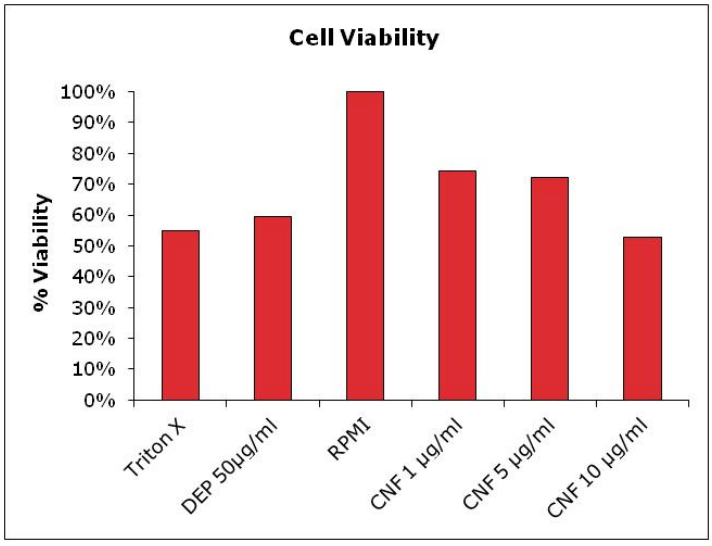

Figure 5.8. Cell viability (courtesy of Dr. Michael Kleinman, UCI).

The Nitric Oxide (NO) Production Graph, figure 5.9, shows that lower concentrations of carbon fiber cause the normal response of producing high levels of nitric oxide. At higher levels of carbon fiber concentration, half of the cells were killed, and the others were damaged and no longer capable of producing nitric oxide as part of the immune defense mechanism.

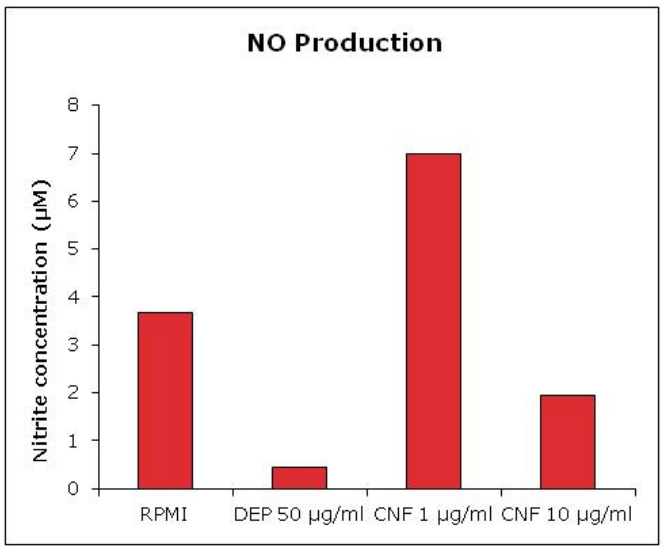

Figure 5.9. Nitric Oxide Production (courtesy Dr. Michael Kleinman, UCI)

The combined results from these very preliminary screening tests indicate potential cellular toxicity of carbon fiber dust in macrophages from laboratory rats. It should be noted that this testing was very limited, and significant further evaluation is necessary and outside of the scope of this research effort.

5.3.5 Effect of Fiber Orientation on Dust Particles

Initial particles were collected by simply capturing the dust in a container, where in follow-on tests, the dust was collected through the use of a Sierra Instruments, Series 210, cascade impactor, with pre- and post- exposure filters weighed using a microgram-scale analytical balance, and photographed using SEM. Initial testing was completed to evaluate the effect of fiber orientation on particle mass distribution using a cascade impactor. Prior to conducting a series of impactor tests on four different unidirectional fiber orientations, a trial run was conducted to validate the experimental set up and functionality of the equipment by visibly verifying dust was collected at each impactor stage. The machining test configuration showing the four fiber orientations (0^o, 90^o, -45^o, $+45^o$), cutting direction, and cutter orientation is illustrated in figure 5.10. This experiment also was used to acquire data on cutting forces, chip formation, workpiece surface finish, surface damage and tool wear as described in the following sub-sections. The machining parameters and conditions used for these four experiments are summarized in table 5.4.

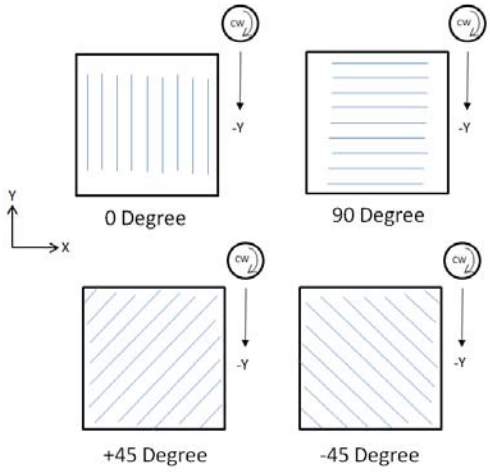

Figure 5.10. Milling test configuration.

Table 5.4. Machining and process conditions for particle size relative to fiber orientation

	Fiber Orientation			
	0 Degree	**90 Degree**	**+45 Degree**	**-45 Degree**
Length of Cut (mm)	153.92	153.92	152.40	152.40
Number of Runs	6	4	3	3
Cutting Direction (climb or conventional)	climb	climb	climb	climb
Total Number of Passes	255	145	123	105
Linear Feedrate (mm/min)	635	635	635	635
RPM	6000	6000	6000	6000
Axial Depth of Cut/Pass (mm)	6.35	6.35	6.35	6.35
Radial Depth of Cut/Pass (mm)	0.762	0.762	0.762	0.762
Total Volume Removed (cm^3)	31.34	17.82	15.12	12.90
Total Cutting Time (est.) (min.)	61.81	35.15	29.52	25.20
Total Air Sampling Time (hr:min:sec)	1:56:06	1:09:50	0:56:22	0:45:46
Critical Orifice Flow Rate (liter/min)	4.75	4.75	4.75	4.75
Total Air Sampling Volume (liter)	551.5	331.7	267.7	217.4

The cutting tool used for all experiments was a 12mm, 2-flute, 0 degree helix angle, PCD end mill. The mass of particulate collected at each impactor stage is included in table 5.5 and graphically illustrated in figure 5.11.

Table 5.5. Sample mass collected at each impactor stage following cutting tests.

	Fiber Orientation			
	0 Degree	**90 Degree**	**+45 Degree**	**-45 Degree**
Stage 1 (mg)	0.312	0.632	0.130	-0.071
Stage 2 (mg)	0.164	0.108	-0.005	-0.010
Stage 3 (mg)	0.118	0.129	-0.002	-0.139
Stage 4 (mg)	0.635	2.215	0.034	-0.005
Stage 5 (mg)	0.565	1.675	0.143	0.076
Stage 6 (mg)	0.281	0.978	0.183	0.157
Stage 7 (mg)	0.443	0.944	0.332	0.278
Stage 8 (mg)	0.707	1.689	0.580	0.474
Stage 9 (mg)	1.333	1.911	2.859	2.053
Stage 10 (mg)	6.122	9.076	2.255	4.728
Total Collected Mass	10.679	19.357	6.512	7.541
Total Air Volume Sampled (liter)	551.500	331.700	267.700	217.400
Particle Mass/Volume mg/m3	19.364	58.356	24.321	34.687

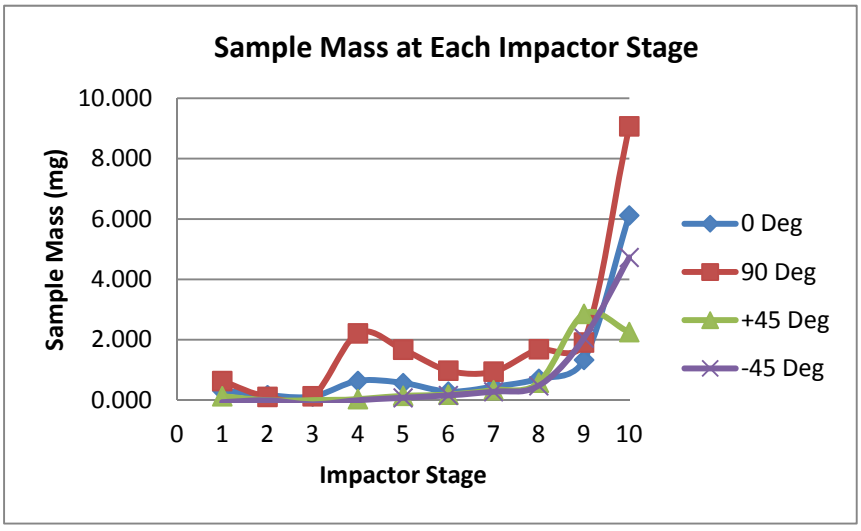

Figure 5.11. Graph of sample mass at each impactor stage.

Log probability plots for the four fiber orientations are shown in Figure 5.12.

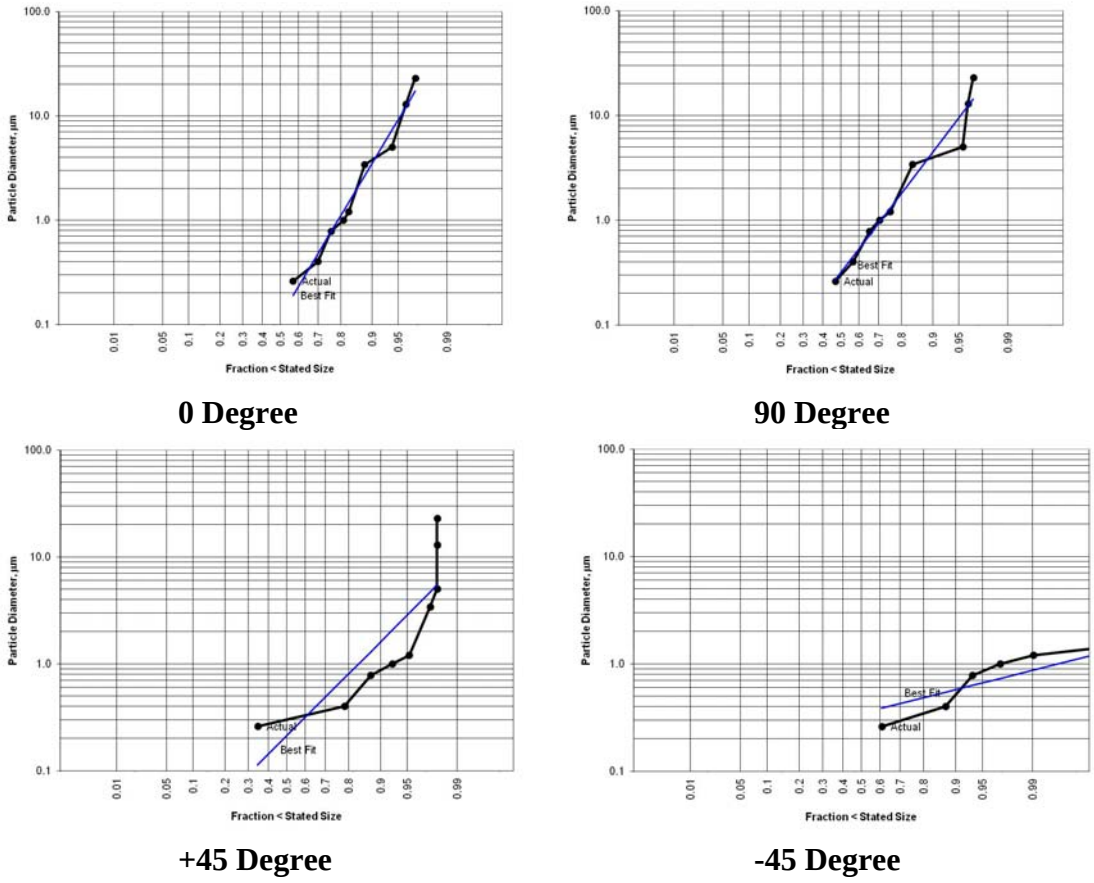

Figure 5.12. Log Probability plot for 0, 90, +45, -45 degree fiber orientations

Table 5.6 includes the Median Diameter data from the Log Probability Plots for the four fiber orientations including r^2, correlation coefficient and σ_g, the geometric standard deviation. According to the data, this indicates that for the 0 degree fiber orientation, 50% of the particles collected are less than .12µm in diameter, and similar for the other fiber orientations. Remember that carbon fiber diameters are approximately 8µm. Due to complexities in dust collection, this data should be considered preliminary, and further analysis is required.

Table 5.6. Log Probability Plot summary data for four fiber orientations.

	Fiber Orientation			
	0 Degree	**90 Degree**	**+45 Degree**	**-45 Degree**
Data from Best Log-Normal Fit				
Median Diameter, d50 (μm)	0.12	0.31	0.21	0.35
σ_g	14.05	7.93	4.87	1.49
r^2	0.974	0.952	0.704	0.853

Sample SEM scans of the impactor stage 10 filters of the collected fibers and particles are shown in figure 5.13-5.15 to provide a representative description of particle formation from carbon fiber composite milling. It appears in the limited initial SEM scans of the 0 degree and 90 degree samples that there is evidence of long fibers, significantly less than 1μm in diameter. These long fibers are likely filter media. Initial micrographs in figures 5.13-5.15 were provided by the University of California, Irvine. All SEM micrographs in figure 5.16 and onwards were made at the University of Washington Nanotechnology User Facility with a FEI Sirion Scanning Electron Microscope and provide much more insightful images.

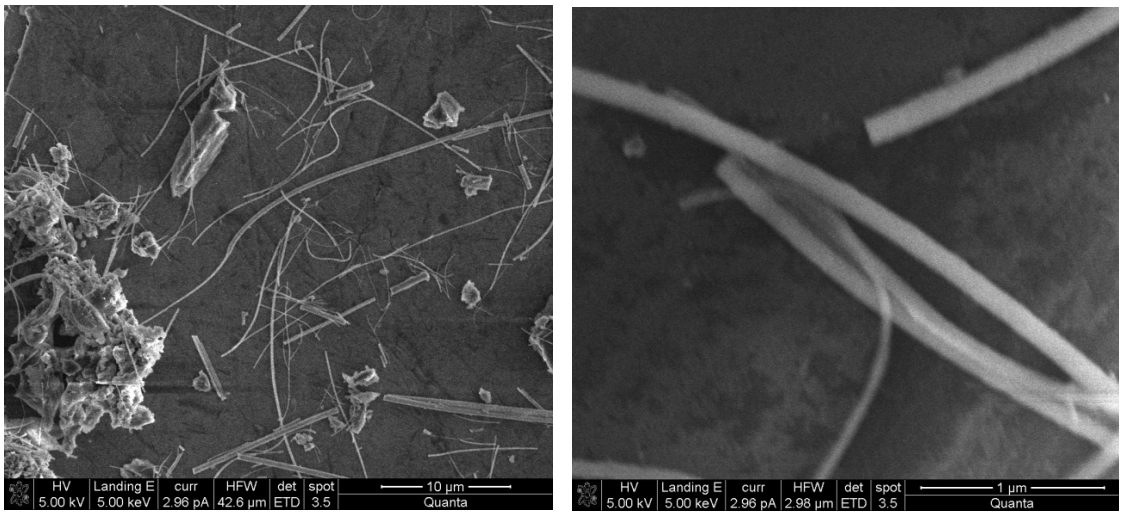

Figure 5.13. SEM micrographs of 0 degree fiber sample from impactor stage 10 filter.

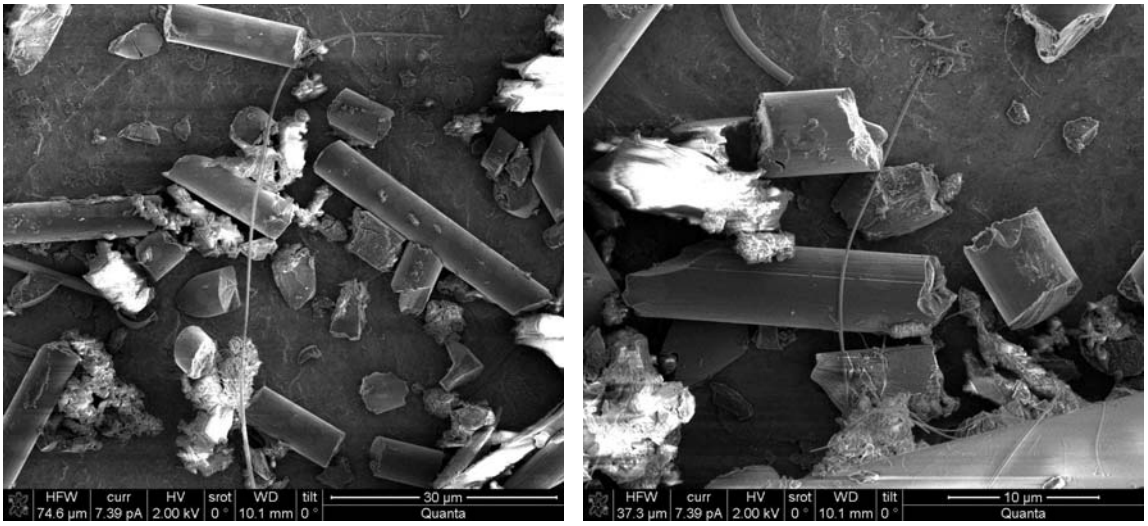

Figure 5.14. SEM micrographs of 90 degree fiber sample from impactor stage 10 filter.

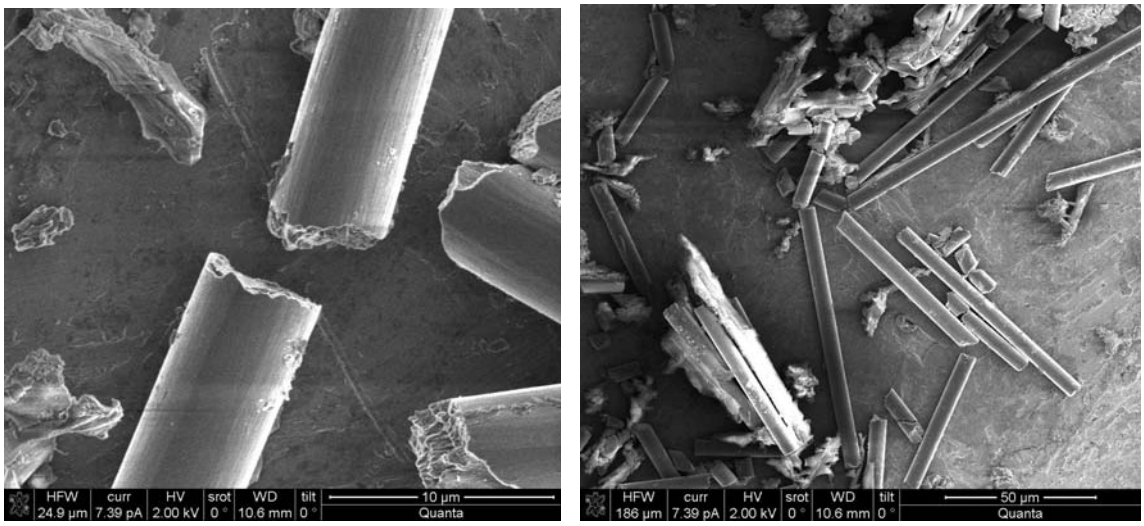

Figure 5.15. SEM micrographs of 45 degree fiber sample from impactor stage 10 filter

SEM micrographs are included of the workpiece in figures 5.16-5.17 where the fibers detached during the milling process.

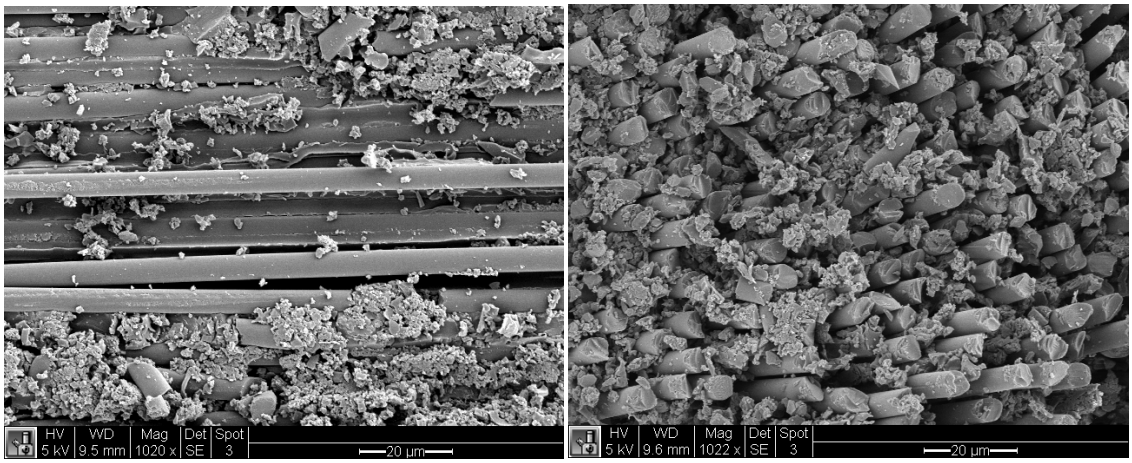

Figure 5.16. SEM micrograph of 0 degree (left) and 90 degree (right) workpiece surface

Figure 5.17. SEM micrograph of +45 degree (left) and -45 degree (right) workpiece surface

5.3.6 Surface Finish

Surface finish of the workpiece for the four fiber orientations used in the dust collection experiments after machining was measured using the Mahr MahrSurf G25 Surface Profilometer as shown in figure 5.18. Ra results for each of the (4) fiber directions are summarized in Table 5.7. The surface finish was measured at two points in

both the longitudinal and transverse direction for each orientation at positions near the center of the work piece. From the results, the 90° fiber orientation had the best finish followed by 0°, +45°, and -45°. A surface profilometer plot of a typical result from the surface finish measurement is shown in figure 5.19 for the 0°, point 1, transverse direction.

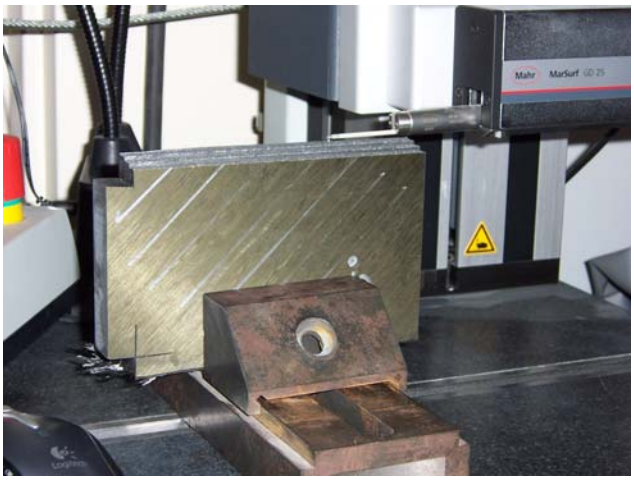

Figure 5.18. Surface profilometry measurements for dust collection workpieces.

Table 5.7. Ra Surface Finish in micrometers (μm) for the four fiber orientations.

	Fiber Orientation			
Point and Direction	**0 Degree**	**90 Degree**	**+ 45 Degree**	**-45 Degree**
Pt 1 Longitundial	2.419	1.932	3.800	15.824
Pt 2 Longitudinal	1.780	1.972	6.019	21.783
Average Longitudinal	**2.100**	**1.952**	**4.910**	**18.804**
Pt 1 Transverse	4.859	3.233	5.800	18.542
Pt 2 Transverse	4.226	2.937	5.272	21.970
Average Transverse	**4.543**	**3.085**	**5.536**	**20.256**

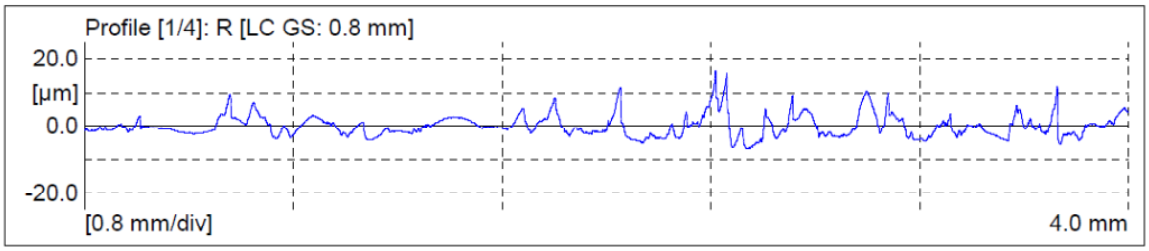

Figure 5.19. Surface profilometer plot for 0^o, point 1, longitudinal direction, Ra (µm)

5.3.7 Tool Wear

Preliminary tool wear measurements were also made during the particle sampling experiments because of the longer machining run time. The cutting tool utilized was a straight, 0-degree helix, 2-flute PCD, 12mm diameter end mill. The same tool was used for the 0^o, 90^o, -45^o, and $+45^o$ fiber orientation milling tests in consecutive order. The tool wear measurements made using the Micro-Vu Sol 121 microscope are summarized in table 5.8.

Table 5.8. Cumulative tool wear summary for 12mm, 0 degree helix, 2-flute, PCD tool.

Cumulative Distance Cut (m)	Fiber Orientation	Passes	Cumulative Cutting Time (min) (est)	Cumulative Volume Removed (m^3)	Tool Wear Measurement (µm)
6.4638	0 Deg	42	10.18	0.0003	N/A
12.7737	0 Deg	41	20.12	0.0006	39.1
19.2375	0 Deg	42	30.30	0.0009	38.4
26.0091	0 Deg	44	40.96	0.0013	38.4
32.6268	0 Deg	43	51.38	0.0016	37.6
39.2445	0 Deg	43	61.80	0.0019	37.6
45.5544	90 Deg	41	71.74	0.0022	53.1
51.5565	90 Deg	39	81.19	0.0025	81.0
56.943	90 Deg	35	89.67	0.0028	138.7
61.56	90 Deg	30	96.94	0.0030	167.6
67.1988	-45 Deg	37	105.82	0.0033	179.1
72.5328	-45 Deg	35	114.22	0.0035	179.1
77.562	-45 Deg	33	122.14	0.0038	205.7
83.9628	+45 Deg	42	132.22	0.0041	205.7
90.2112	+45 Deg	41	142.06	0.0044	205.7
96.3072	+45 Deg	40	151.66	0.0047	221.0

Feedrate = .635 m/min
Radial Depth of Cut=.762mm
Axial Depth of Cut = 6.35 mm
RPM = 6000
Distance per Pass 0, 90 Deg = .1539m. +45, -45 Deg = .1524m.

Cumulative tool wear is plotted in Figure 5.20. An increasing progression in tool wear was expected. Small measurement discrepancies are likely due to difficulties in tool wear measurement as it is performed with an optical microscope and subject to human visual error or inconsistency. Tool wear photos taken on the Micro-Vu Sol 121 microscope are shown in figure 5.21. From the graph, there is an initial increase in tool wear between 6 and 12m. Tool wear remained relatively consistent until about 40 m of cumulative cutting distance and increased significantly to approximately 61m with a rise

of 126µm. This was followed by another increase at approximately 77m where it remained relatively consistent to 90 m. The final measurement at a cumulative cutting distance of 96 m showed another increase in tool wear of approximately 15µm.

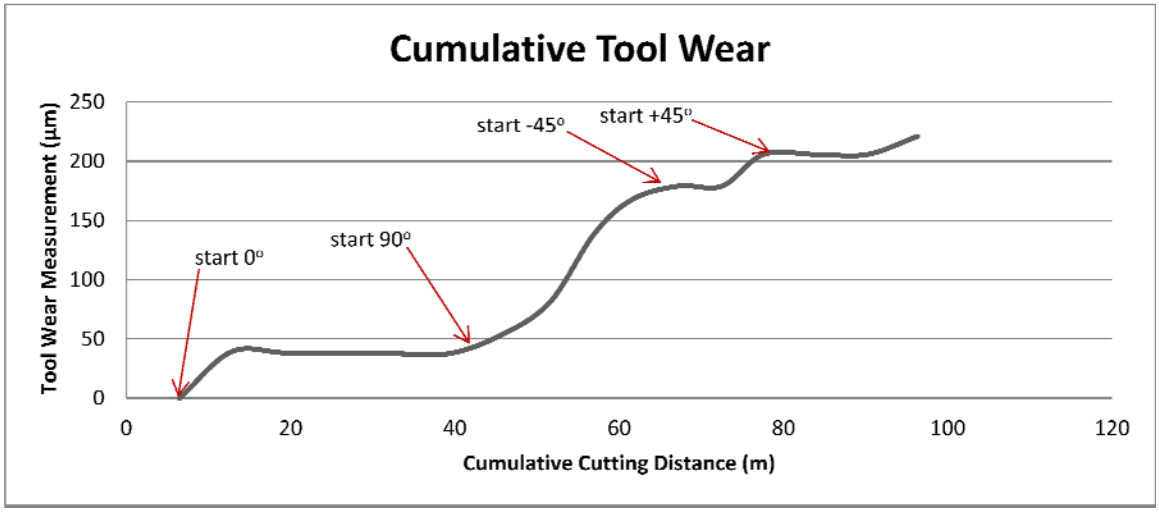

Figure 5.20. Cumulative tool wear measurement for four fiber orientations.

0^o 6.4m 0^o 39.2m 90^o 138.7m -45^o 77.6m $+45^o$ 96.3m

Figure 5.21. Tool wear photos from 0^o and 6.4m cutting distance to $+45^o$ and 96.3m

5.3.8 Cutting Forces for Four Primary Fiber Orientations

Cutting forces were collected for each of the four fiber orientations following each set of machining passes as referenced in table 5.7. A pass is defined as one linear motion along the edge of the workpiece, approximately 15cm. For example, the first 0^o

cutting force measurement was made after 42 passes, and the first 90^{o} cutting measure measurement was made after 41 passes, and so on. With a spindle speed of 6000 rpm, two rotations of the cutting tool occurs in .02 sec. For consistency, cutting forces were compared at 10 seconds through the pass, roughly half way through the cut, as data acquisition start is performed manually. Cutting force plots showing 2 cutter revolutions for the final pass for each of the four fiber orientations are included in figure 5.22 inlcuding Fx, Fy, and the derived resultant force, Fa. A magnification scale factor of 10 was applied to the actual forces due to a set up error. The 90 degree sample had the lowest maximum resultant force (670 N) followed by the -45 degree sample (742 N), + 45 degree (1097 N), and 0 degree (1399 N).

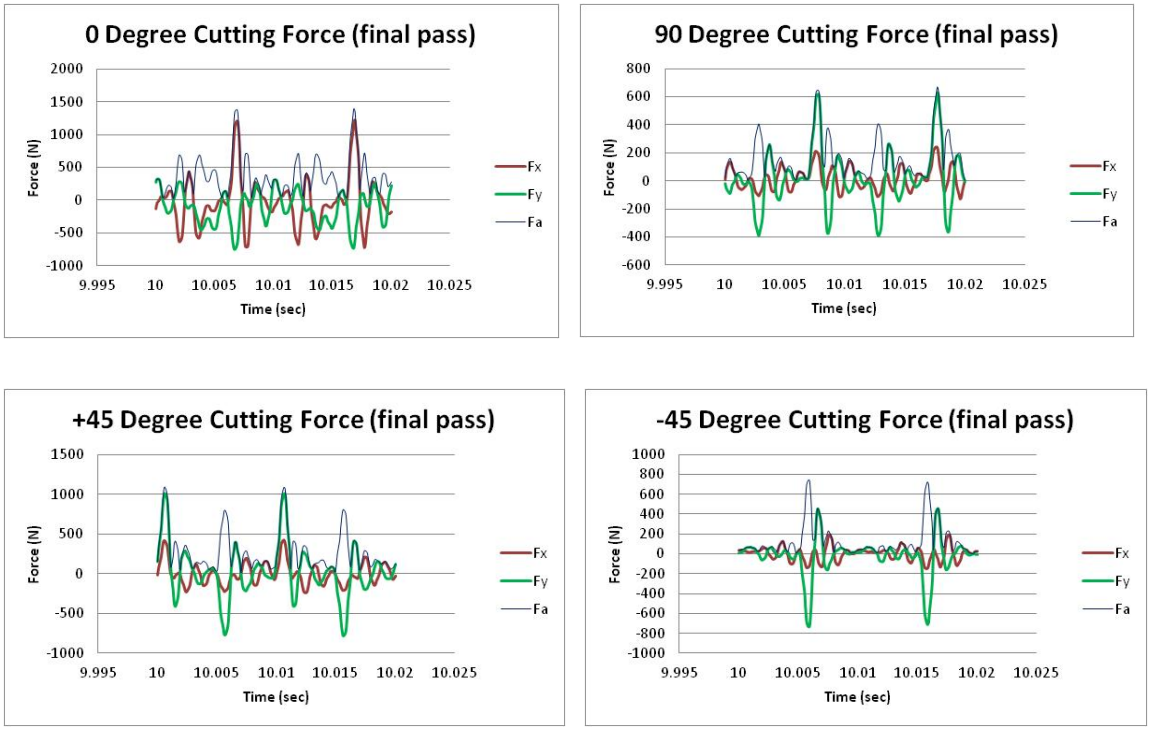

Figure 5.22. Cutting forces from dust collection experiments.

5.3.9 Phase 1 Results Summary

In the phase 1 investigation, a series of screening experiments were conducted to validate the experimental measurement and data acquisition techniques proposed for this research effort. Results were successfully achieved for all proposed experimental methods. The results from the phase 1 experiments indicate that dust particle size, cutting forces and surface finish are clearly dependent on fiber orientation. An opportunity for technique improvement in machining dust particle collection was identified as it was clear more substantial containment was necessary to prevent particle migration from the HAAS milling machine. Consistent with the building block experimental methodology, Phase 2 testing was designed to incorporate the lessons learned from phase 1 and evaluate several more combinations of cutting conditions, including fiber orientation, cutting tool, and cutting direction for composite edge trimming particle collection and analysis.

5.4 Phase 2 Testing

Following the phase 1 screening investigation covered in section 5.2-5.3, changes were made in the experimental protocol, as expected, based on the phase 1 results and incorporated into the phase 2 investigation. The focus of the phase 2 investigation was on enhancing the understanding of the dust particles generated from composite edge trimming as a result of different cutting tools, cutting conditions and fiber orientations. A major improvement in the phase 2 investigation was made through the use of a dust containment system within the working volume of the HAAS machine envelope which included the use of a separate acrylic enclosure, flexible membrane to allow machine motion, stationary vacuum exhaust, and filtered air return. This was done as the working volume of the HAAS TM 1P Mill was not sufficiently sealed in the as-built factory condition to prevent migration of aerosol particles generated from dry composite edge trimming. Interestingly, this confirmed some of the motivation for researching dust generated from dry composite machining, as the dust was found to travel significant

distances. This can be explained by considering the terminal settling velocity of the particles described in equation 2.4.4, where the terminal settling velocity increases with the square of the particle diameter, so for smaller particles, the lower the terminal settling velocity and the farther they can travel, dependent on environmental conditions. The phase 2 experimental design enabled the same tool wear, acoustic emission, and cutting force measurements to be performed as in phase 1.

Dust was fully contained in an acrylic enclosure which is approximately 689 mm x 419 mm x 343 mm (27.125 in. x 16.5 in. x 13.5 in.). The enclosure is supported by an aluminum frame with acrylic sheets on 3 sides. The fourth side is a removable gasketed door held in place with 4 wing nuts for relatively quick access to the fixture, sensors and work piece. The base is an aluminum plate with holes for mounting to the HAAS machine bed and a cutout for a work holding fixture. The top of the enclosure consists of polypropylene membrane which is flexible to allow machine motion in X, Y, and Z directions of the 3-axis mill within the envelope of the enclosure. Travel range in the enclosure is limited to approximately 236 mm (9.3 inch) in X, 145 mm (5.7 inch) in Y by approximately 102 mm (4 inch) in Z motion directions, and care must be used not to drive the machine through the enclosure. The top flexible membrane remains partially inflated during cutting tests. The inflation serves two purposes. The first is to keep the membrane out of the enclosure when the dust exhaust vacuum is on as the membrane gets sucked in, blocks visibility and can interfere with the cutter. The second purpose is to provide a simple visible indication of flow balance between the vacuum exhaust and HEPA filtered air inlet. A partially inflated and stable membrane indicates balance between the inlet and outlet air flows. In the phase 2 test configuration inlet air was provided from the exhaust of the 6.5 HP primary shop vacuum used for dust collection and from the exhaust of a second 6 HP vacuum. The two flows were combined in a wye fitting with a balancing valve and were necessary because of pressure drops. The balancing valve is used to maintain partial inflation of the flexible membrane with any

exhaust vented into the HAAS enclosure. The inlet of the second vacuum was located in the HAAS enclosure to provide a closed loop system. The combined air flow passes through a HEPA filter and then into the enclosure and directed towards the flexible membrane. The HEPA filter used is a SBM BioMax Model H10A3X1, 203.2 mm x 203.2 mm x 149.2 mm deep (8 in. x 8 in. x 5.875 in.), 99.99% efficient, 3 micron, with 1 inch water gage (in wg) pressure drop. The filter is gasketed and compression mounted between 2 acrylic plates with a 63.5 mm (2.5 in) tube stub on either side for hose mounting to both inlet and outlet. The HEPA filtered air is intended to ensure that no particles other than those produced from machining are sampled by the cascade impactor. Figure 5.23 is an illustration of the dust collection and containment system used for phase 2 testing. Figure 5.24 is photograph of the test configuration used for phase 2 testing within the sealed enclosure.

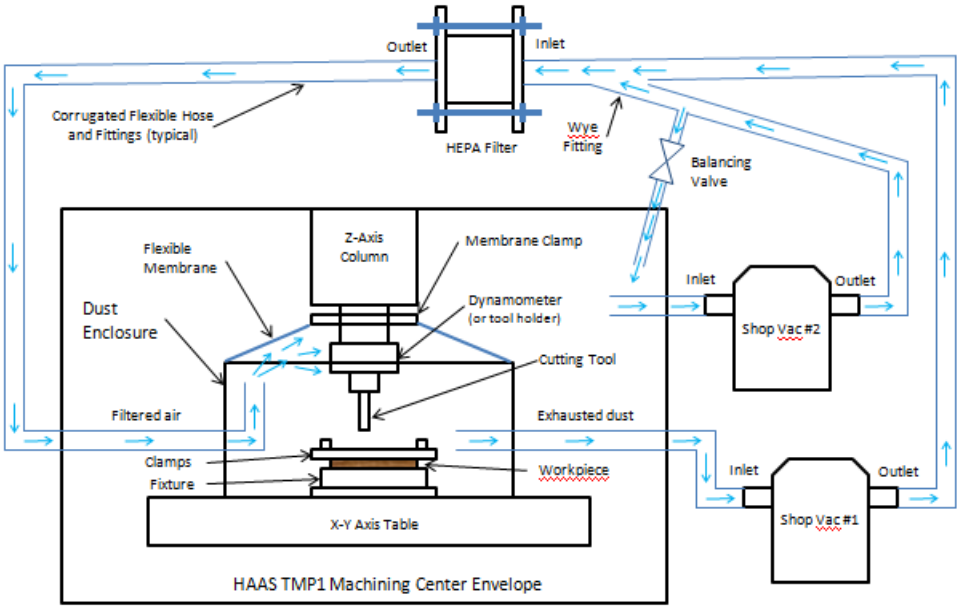

Figure 5.23. Dust collection and containment system for phase 2 testing

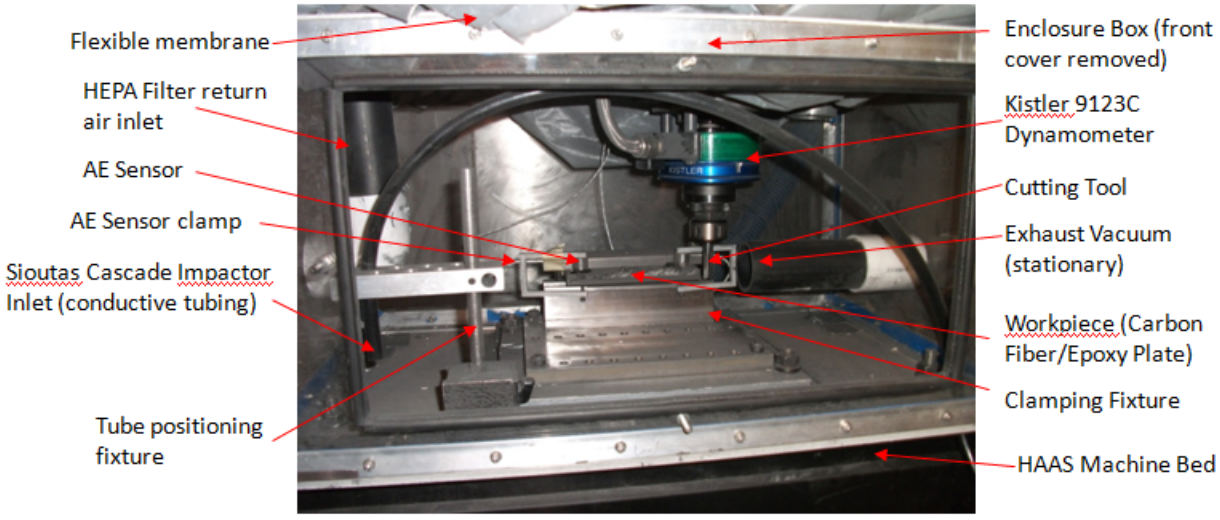

Figure 5.24. Phase 2 testing configuration within the sealed enclosure

For phase 2 testing, the 10 Stage Sierra Instruments 210 cascade impactor, used in phase 1 testing, was replaced with 4 stage Sioutas Impactors for faster filter processing. Two Sioutas impactors were used for improved efficiency as they can be more rapidly cycled for more frequent testing. The Sioutas impactors were also located outside of the enclosure with a conductive tubing inlet inside the box, which facilitated cleaning as the sampling tube could be readily blown out prior to each test by disconnecting from the impactor. The inlet tubing was positioned to try to avoid overloading of the impactor stages. Positioning the tube with the inlet down and away from the cutting source provided the most consistent results. Nuclepore® filters were also used for several experiments with the Sioutas Impactors as a backup filter to capture the smallest particles. Nuclepore® filters are made from polycarbonate material with tiny holes which were used to improve SEM images as the particles could be seen with a background of holes of a known diameter versus a fibrous filter web. For this testing, Nuclepore® filters with holes of 0.4 μm and 0.8 μm were used.

The dust containment system contained all the dust generated from machining and captured the majority of the material with a 6.5HP Sears Craftsman shop vacuum. Depending on the test, some large dust particles may have collected on the base of the enclosure due to some vacuum inefficiencies. The machining time was also reduced as sufficient dust was found to be generated with shorter cutting times. A select number of experiments were performed to contrast the effects of different cutting conditions with results in section 5.5. Table 5.9 summarizes the phase 2 measurements conducted using the dust collection and containment system described.

Table 5.9. Phase 2 measurements

Measurement	Instrument/Process	Data Derived (lessons learned)
Cutting force measurements	Kistler 9123C Dynamometer	Force magnitudes, feedrates, depth of cut, RPM, mechanical setup, fixturing, 0 count usage
Acoustic emission signal acquisition	Physical Acoustic PCI-2 AE	Signal magnitude, sensor location, sensor fixturing
Tool wear measurements	Micro-Vu Sol 161 Microscope	Magnitude over time, process
Surface roughness measurement	Profilometry Mahr MarSurf GD 25	Surface roughness relative to fiber orientation
Dust particle collection	Sioutas Cascade Impactor; Mettler Toledo UMT2 Analytical Balance	Particle MMAD relative to fiber direction, dust collection system efficiency
Chip formation (dust) analysis	SEM	SEM photos, particle sizing, nucleopore filters

5.5 Phase 2 Composite Machinability Test Results

In the second experimental phase, an expanded test matrix was used to evaluate the effects of different cutting tools for edge trimming both unidirectional and multidirectional laminates. In addition, testing was performed using both climb and conventional machining. Most of the same measurements from the phase 1 screening tests were utilized in phase 2. Measurements include, cutting force, acoustic emission, surface integrity, tool wear, particle sizing, and SEM. Sioutas impactors were

incorporated into the particle collection process in place of the Sierra Instruments, Series 210, and used in conjunction with the dust enclosure and return air system. The test matrix for phase 2 is included in table 5.10. Summary results are provided for each measurement for each test ID in the following subsections. Sampled detailed results are also provided with additional data in Appendix A.

Table 5.10 Phase 2 test matrix

Test ID	Laminate Orientation	Cutter	Cutting Orientation	RPM	Feedrate (m/min)	Radial Depth of Cut (mm)	Axial Depth of Cut (mm)
S1	0 Degree	Carbide 4 flute (new),12.7mm	Climb	6000	0.635	0.762	6.35
S2	90 Degree	Carbide 4 flute,12.7mm	Climb	6000	0.635	0.762	6.35
S3	+45 Degree	Carbide 4 flute,12.7mm	Climb	6000	0.635	0.762	6.35
S4	-45 Degree	Carbide 4 flute,12.7mm	Climb	6000	0.635	0.762	6.35
A1	Multidirectional	Carbide 4 flute (new),12.7mm	Climb	6000	0.635	0.762	6.35
A2	0 Degree	PCD 2 flute straight (new),12	Climb	6000	0.635	0.762	6.35
A3	90 Degree	PCD 2 flute straight, 12mm	Climb	6000	0.635	0.762	6.35
A4	+45 Degree	PCD 2 flute straight,12mm	Climb	6000	0.635	0.762	6.35
B1	-45 Degree	PCD 2 flute straight,12mm	Climb	6000	0.635	0.762	6.35
B2	Multidirectional	PCD 2 flute straight,12mm	Climb	6000	0.635	0.762	6.35
B3	Multidirectional	PCD 2 flute straight,12mm	Conventional	6000	0.635	0.762	6.35
B4	Multidirectional	Carbide 4 flute (new),12.7mm	Conventional	6000	0.635	0.762	6.35
C1	Multidirectional	2 st. flute carbide (new),12.7	Climb	6000	0.635	0.762	6.35
C2	Multidirectional	6 flute CVD (new),12mm	Climb	6000	0.635	0.762	6.35
C3	Multidirectional	40 grit diamond (new),12.7mm	Climb	6000	0.635	0.762	6.35
C4	Multidirectional	125 grit diamond (new),12.7	Climb	6000	0.635	0.762	6.35
D1	Multidirectional	4 flute CVD twist (new), 12mm	Climb	6000	0.635	0.762	6.35
D2	Multidirectional	Burr Tool (new),12.7mm	Climb	6000	0.635	0.762	6.35
D3	Multidirectional	Serrated CVD 8 flt (new),12mm	Climb	6000	0.635	0.762	6.35

5.5.1 Phase 2 Cutting Force and Acoustic Emission Results

Table 5.11 summarizes the cutting force and acoustic emission measurements for the phase 2 test matrix.

Table 5.11 Cutting Force and Acoustic Emission measurements

Test ID	Laminate Orient.	Cutter	Cutting Orient.	Fx (Max +) N	Fy (Max +) N	Mz (Max +) Nm	Fa (Max +)	AE RMS Max (ch 1,2)
S1	0 Deg	Carbide 4 fl. (new)	Climb	383.17	349.06	0.603	521.60	0.2533
S2	90 Deg	Carbide 4 flute	Climb	213.05	168.27	0.718	280.13	0.7739
S3	+45 Deg	Carbide 4 flute	Climb	291.11	277.29	0.597	365.32	0.4758
S4	-45 Deg	Carbide 4 flute	Climb	190.62	159.69	0.110	271.22	0.2771
A1	Multi. Dir.	Carbide 4 flute (n)	Climb	90.60	188.56	0.469	288.76	0.5960
A2	0 Deg	PCD 2 fl. st. (new)	Climb	233.15	79.67	0.614	278.37	1.6767
A3	90 Deg	PCD 2 flute st.	Climb	345.21	160.73	0.671	386.78	2.8669
A4	+45 Deg	PCD 2 flute st.	Climb	503.76	376.40	0.973	631.56	1.4319
B1	-45 Deg	PCD 2 flute st.	Climb	300.75	152.56	0.527	344.29	1.4319
B2	Multi. Dir.	PCD 2 flute st.	Climb	503.76	303.21	1.017	639.17	1.1036
B3	Multi. Dir.	PCD 2 fl. St.	Conv	411.70	264.17	0.660	502.31	1.3306
B4	Multi. Dir.	Carbide 4 fl (new)	Conv.	126.99	184.40	0.168	197.59	1.4023
C1	Multi. Dir.	2 st. fl. carbide (n)	Climb	112.74	275.32	0.899	333.22	1.5800
C2	Multi. Dir.	6 fl. CVD (new)	Climb	125.02	119.58	0.477	183.60	2.2440
C3	Multi. Dir.	40 grit dia. (new)	Climb	73.40	52.86	0.418	96.57	1.3400
C4	Multi. Dir.	125 grit dia. (new)	Climb	52.90	121.38	0.624	228.95	1.3880
D1	Multi. Dir.	4 fl. CVD twist (n)	Climb	120.72	103.11	0.759	178.58	2.4040
D2	Multi. Dir.	Burr Tool (new)	Climb	13.16	37.54	-0.089	45.12	1.8560
D3	Multi. Dir.	Serr. CVD 8 flt (n)	Climb	34.82	87.85	0.224	134.21	2.3140

For each test, the data for each dynamometer channel (Fx, Fy, Mz, Fz) and AE waveform was analyzed. An example, Fx, Fy forces for the B2 test using a PCD 2-flute cutting tool, in climb cutting configuration on a multidirectional laminate are provided in figure 5.25. The forces are analyzed with respect to time and rotation which corresponds to the time upper time scale and derived lower cutter rotation position scale. The pulse marks correspond to a zero count signal from channel 6 of the dynamometer. The pulse is generated by an infrared light barrier which senses a groove on the rotator of the dynamometer. This provides improved interpretation as the pulse appears once per cutter rotation. As you can see from the figure, the pulse indicates two rotations which corresponds to the .01 second/rotation time and 360 degree/rotation position. In later phases, the pulse was aligned to a cutter edge and the dynamometer axis for enhanced analysis.

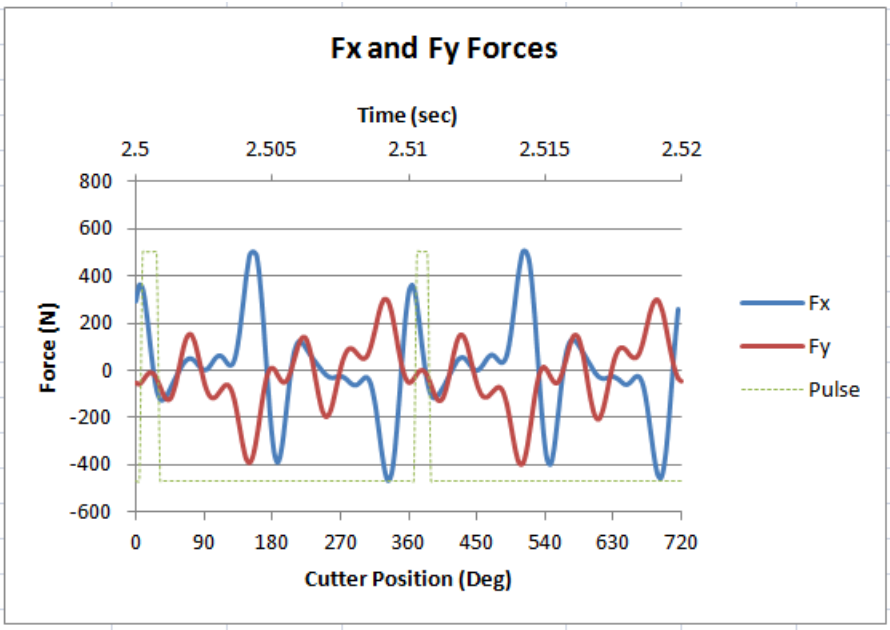

Figure 5.25 Fx, Fy forces for B2 test.

The Ft, Fr forces are shown in a similar manner in figure 5.26. One of the features to note is that Fr, radial force, appears significantly higher than Ft, or cutting force. At the time the phase 2 tests were conducted, the signals were not shifted to correct for offset, so the derived values calculated by the Dynoware software for the radial force (Fr) are plotted. Cutting edges were also not aligned to the dynamometer axes. Extensive experimentation was done in phase 3 and phase 5 to better understand the relationships between tangential (Ft) and radial forces (Fr) to address the difference in magnitude using techniques to be discussed in chapter 7.

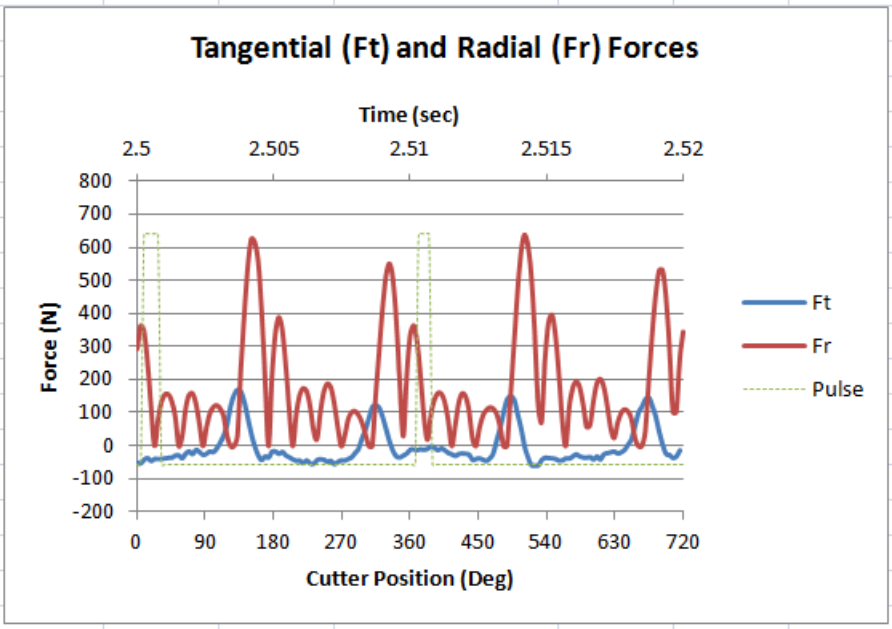

Figure 5.26 Ft, Fr forces for B2 test

Fz, and Mz are plotted on a combined graph in figure 5.27 to illustrate the relationship between thrust force and torque, similar to the use of the dynamometer for a drilling application. Two clear rises in Fz indicate the thrust force when using a 2-flute cutter. Mz corresponds to peaks in torque or moment of the same two flutes in the workpiece. As again should be noted, these tests were conducted at 6000 rpm, with a maximum sampling rate of the dynamometer of 7800 Hz. This only provides 78 samples per rotation, or 1 sample per each 4.6 degrees of cutter rotation.

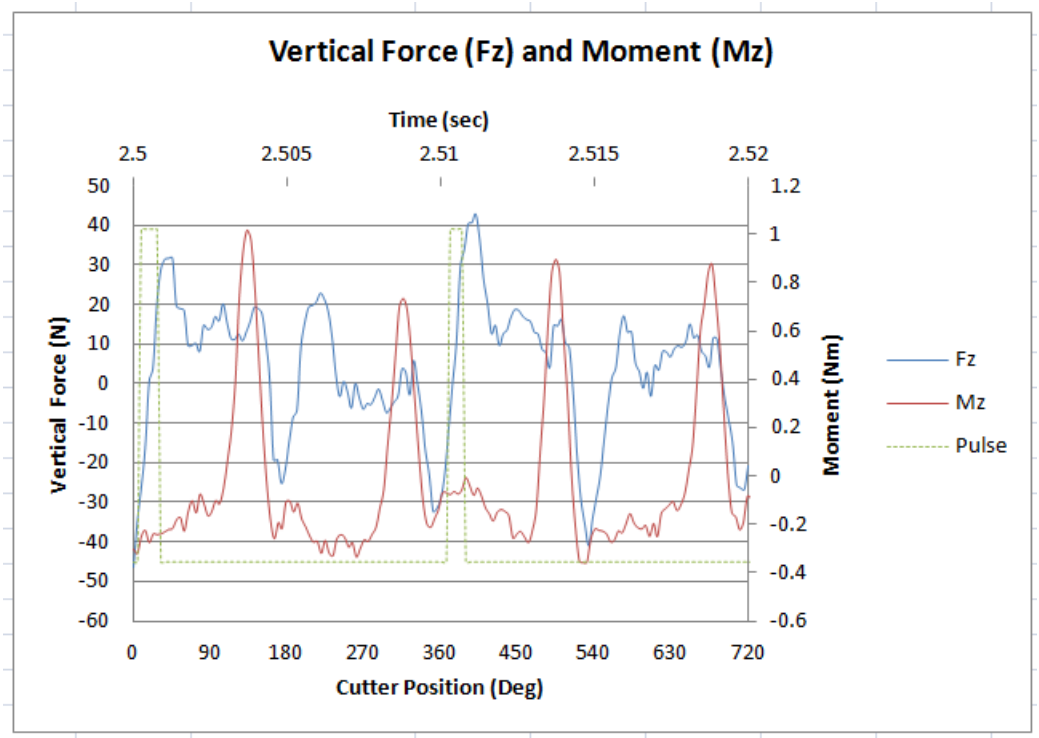

Figure 5.27 Fz and Mz values for B2 Test

The resultant force, Fa, is plotted in figure 5.28. The resultant force is significant as it is also used to calculate Fr, when combined with Mz. These relationships are described in equations 5.1 through 5.4. Fa also has a tendency to provide a more symmetric signal that is sometimes easier to interpret than simply studying Fx, Fy. This is especially true in homogenous materials such as aluminum where more shearing occurs during cutting than brittle failures as with composites.

$$Fa = \sqrt{Fx^2 + Fy^2} \tag{5.1}$$

$$Ft = \frac{Mz}{r} \quad , r \text{ is the cutter radius} \tag{5.2}$$

$$Fr = \sqrt{Fx^2 + Fy^2 - Ft^2} \tag{5.3}$$

and if the independent sensor relationships hold,

$$Fa = \sqrt{Fx^2 + Fy^2} = \sqrt{Ft^2 + Fr^2} \tag{5.4}$$

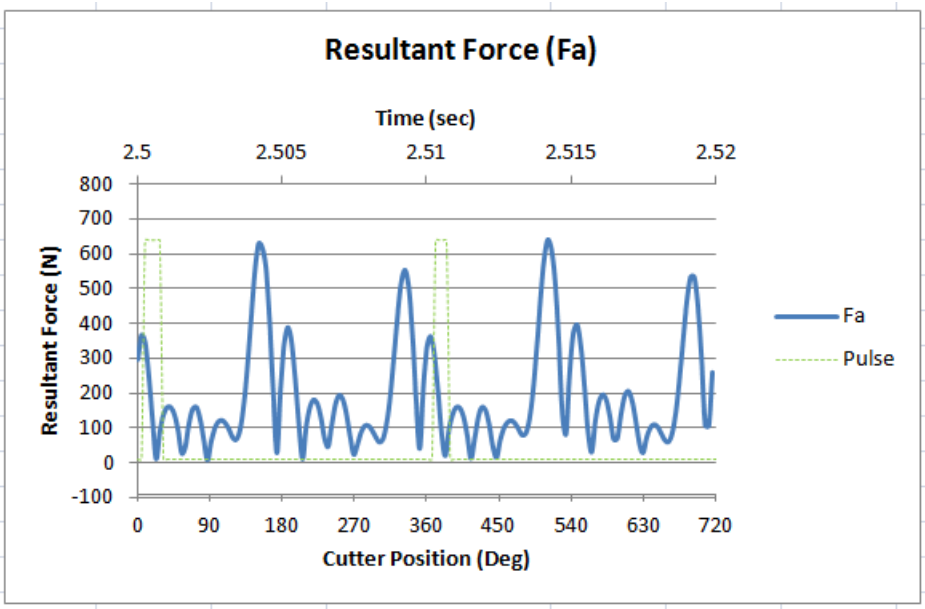

Figure 5.28 Fa values for B2 Test

The stand alone AE waveform was also plotted for each test case as shown in figure 5.29. This is simply the voltage plotted over time in the time domain. What is interesting and relatively consistent is the AE waveform appears to show very significant evidence of cutter engagement in the workpiece. This is further illustrated in figure 5.30, where the AE waveform is shown plotted with the Fa, resultant force, and Ft, tangential or cutting force. Remember that Ft has the same form as Mz, it differs only in magnitude due to division by the cutter radius. A slight offset in timing between the AE waveform and Dynamometer results (Ft, Fa) may be due to an imperfect labview trigger that was used to synchronize timing between the instruments.

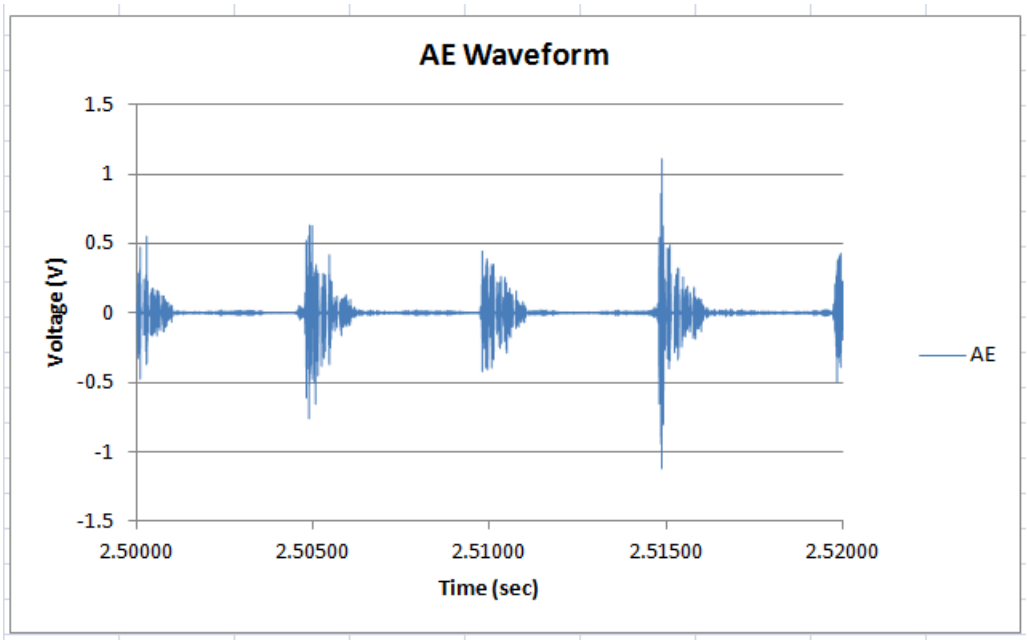

Figure 5.29 AE Waveform for B2 test

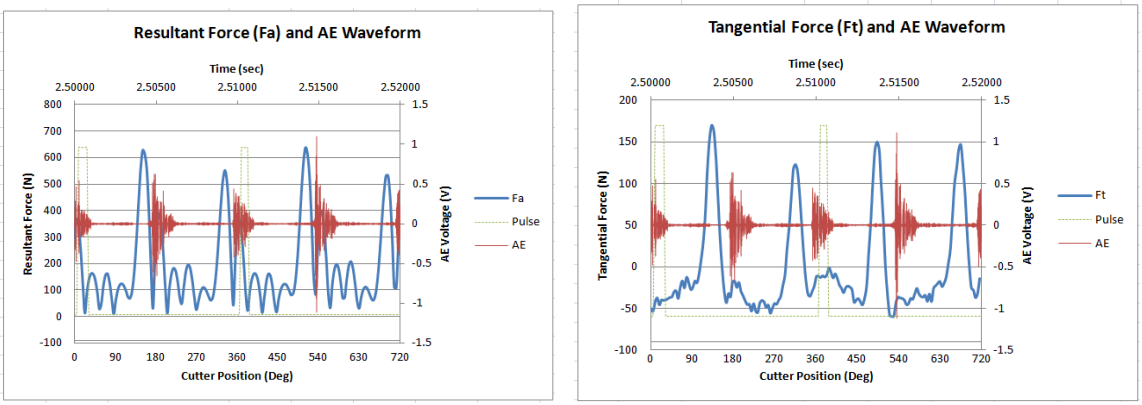

Figure 5.30 AE Waveform plotting with Fa and Ft for B2 test

5.5.2 Phase 2 Tool Wear Results

Table 5.12 summarizes the tool wear measurements for the phase 2 test matrix. The highlighted rows in the table indicate where the same tool was used for multiple tests.

Table 5.12. Tool wear measurements for the phase 2 test matrix.

Test ID	Laminate Orientation	Cutter	Cutting Type	RPM	Cum. Cutting Distance (m)	Cum. Tool Wear (µm)	Δ Tool Wear (µm)
S1	0 Degree	Carbide 4 flute (new)	Climb	6000	4.27	106.43	106.43
S2	90 Degree	Carbide 4 flute	Climb	6000	8.38	117.35	10.92
S3	+45 Degree	Carbide 4 flute	Climb	6000	12.19	150.79	33.44
S4	-45 Degree	Carbide 4 flute	Climb	6000	16.00	202.18	51.39
A1	Multidirectional	Carbide 4 flute (new)	Climb	6000	4.27	86.36	86.36
A2	0 Degree	PCD 2 flute straight (new)	Climb	6000	4.27	59.44	59.44
A3	90 Degree	PCD 2 flute straight	Climb	6000	8.53	80.52	21.08
A4	+45 Degree	PCD 2 flute straight	Climb	6000	12.80	90.93	10.41
B1	-45 Degree	PCD 2 flute straight	Climb	6000	17.07	96.01	5.08
B2	Multidirectional	PCD 2 flute straight	Climb	6000	21.34	97.07	1.06
B3	Multidirectional	PCD 2 flute straight	Conventional	6000	25.45	99.06	1.99
B4	Multidirectional	Carbide 4 flute (new)	Conventional	6000	3.96	85.08	85.08
C1	Multidirectional	2 st. flute carbide (new)	Climb	6000	3.81	162.12	162.12
C2	Multidirectional	6 flute CVD (new)	Climb	6000	3.66	38.29	38.29
C3	Multidirectional	40 grit diamond (new)	Climb	6000	3.81	N/A	N/A
C4	Multidirectional	125 grit diamond (new)	Climb	6000	2.66	N/A	N/A
D1	Multidirectional	4 flute CVD twist (new)	Climb	6000	3.81	11.14	11.14
D2	Multidirectional	Burr Tool (new)	Climb	6000	3.66	N/A	N/A
D3	Multidirectional	Serrated CVD 8 flt (new)	Climb	6000	3.81	7.30	7.30

Tool wear was measured after a cumulative distance using the Micro-Vu Sol 16 microscope. In some cases, the same tool was used for multiple tests due to cost or availability, shown in the highlighted rows. Typical images from the microscope taken under identical conditions are shown in figure 5.31 for experiment ID B4. The wave like wear pattern on the cutting tool is consistent with the fiber orientations and ply thicknesses of the multi-directional laminate used in the experiment. Tool wear is determined by using the microscope's tool kit to pick the maximum wear and measure the distance from the initial condition, generally by establishing parallel lines and finding the perpendicular distance. Several measurements were made for each tooth of the cutting tool and averaged. Some measurement errors may be due to user skill in adjusting the tool correctly within the field of view of the microscope, finding the exact wear limit, averaging method, and lighting adjustment of the microscope.

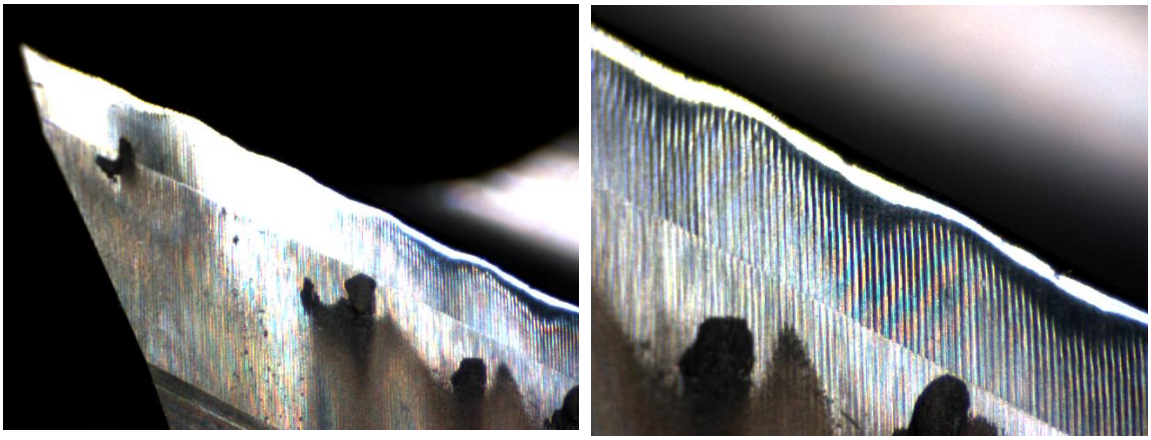

Figure 5.31 Tool wear, 4-flute solid carbide cutter, multi-directional laminate.

In phase 2 testing, there were 2 series of tests that used the same cutting tool. In the first series, tests S1-S4, used the same solid carbide 4-flute cutting tool for edge trimming. The cumulative tool wear results for tests S1 through S4 are plotted in figure 5.32. Descriptions of the tests are found in table 5.11. Each of the data points on the plot represents a corresponding test in order. Tool wear in micrometers is plotted against the cumulative cut length in meters. Figure 5.33 is a plot of the cumulative tool wear for tests A2 through B3 which used a 2-flute PCD cutting tool for the experiments as noted in table 5.11, and following the same methodology as the previous plot. Assuming some consistency in the measurements, it can be shown that different cutting materials and coatings experience different wear patterns.

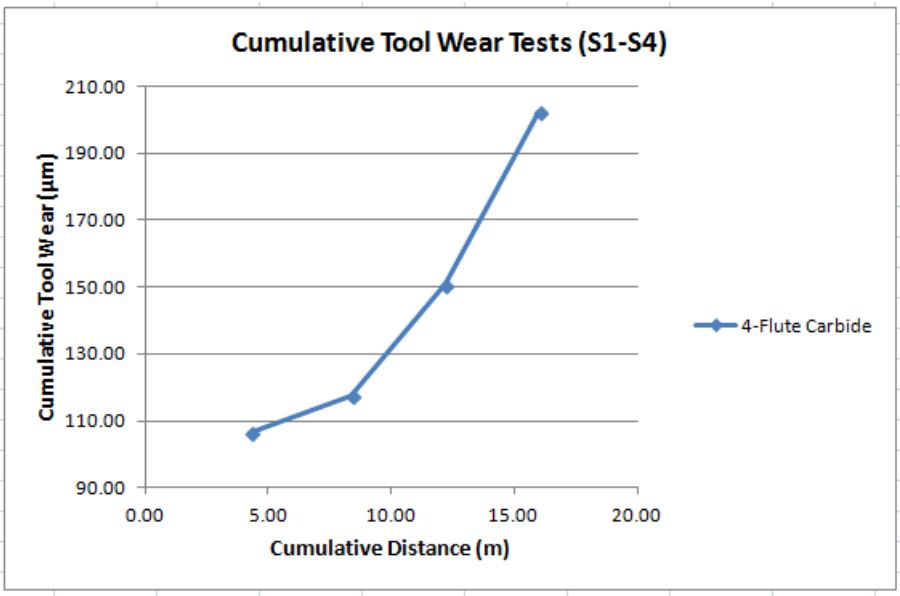

Figure 5.32 Cumulative Tool Wear for Phase 2 tests S1-S4

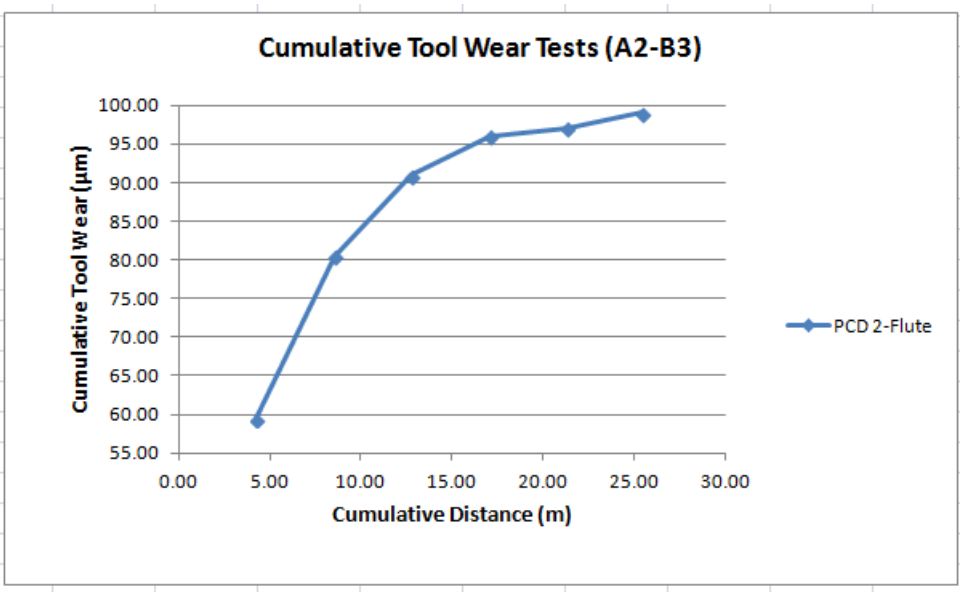

Figure 5.33 Cumulative Tool Wear for Phase 2 tests A2-B3

5.5.3 Phase 2 Surface Finish Results

Table 5.13 summarizes the surface integrity measurements for the phase 2 test matrix.

Table 5.13. Phase 2 Surface Integrity Measurements

Test ID	Laminate Orientation	Cutter	Cutting Orientation	Transverse Ra	Transverse Rz	Trans-verse Rt
S1	0 Degree	Carbide 4 flute (new)	Climb	3.167	20.073	33.900
S2	90 Degree	Carbide 4 flute	Climb	1.186	6.865	8.760
S3	+45 Degree	Carbide 4 flute	Climb	3.965	21.043	33.640
S4	-45 Degree	Carbide 4 flute	Climb	5.751	28.791	46.870
A1	Multidirectional	Carbide 4 flute (new)	Climb	5.644	30.217	48.490
A2	0 Degree	PCD 2 flute straight (new)	Climb	1.783	10.236	13.210
A3	90 Degree	PCD 2 flute straight	Climb	1.004	5.298	7.670
A4	+45 Degree	PCD 2 flute straight	Climb	1.826	9.007	13.960
B1	-45 Degree	PCD 2 flute straight	Climb	6.804	33.508	62.250
B2	Multidirectional	PCD 2 flute straight	Climb	6.443	32.970	57.380
B3	Multidirectional	PCD 2 flute straight	Conventional	3.044	16.523	28.610
B4	Multidirectional	Carbide 4 flute (new)	Conventional	4.400	24.043	44.710
C1	Multidirectional	2 st. flute carbide (new)	Climb	6.853	34.860	60.420
C2	Multidirectional	6 flute CVD (new)	Climb	1.753	10.520	21.160
C3	Multidirectional	40 grit diamond (new)	Climb	4.940	23.983	42.700
C4	Multidirectional	125 grit diamond (new)	Climb	4.414	23.817	38.760
D1	Multidirectional	4 flute CVD twist (new)	Climb	1.301	7.739	13.300
D2	Multidirectional	Burr Tool (new)	Climb	2.776	13.625	25.640
D3	Multidirectional	Serrated CVD 8 flt (new)	Climb	1.958	12.003	24.420

Surface integrity measurements were made for every test using the Mahr MarSurf GD25 profilometer in both longitudinal and transverse directions of the work piece following the peripheral trimming cut. The longitudinal direction is parallel to the cutting direction and the transverse direction is perpendicular to the cutting direction. The transverse direction tends to be of more interest as it crosses multiple plies, or lamina, within the laminate. For each surface integrity measurement, the process is repeated 3 times at a slightly different location on the work piece (generally near the center of cut for consistency). As an example for the B2 test using the 2-flute PC cutter on a multidirectional laminate in a climb cutting configuration, the longitudinal surface profile is shown in figure 5.34. For the same B2 test, the transverse profile is shown in figure 5.35. As can be seen from the data in table 5.12, the surface integrity of the work pieces cut using the 2-flute PCD cutting tool tends to have the lowest profiles, or best finish.

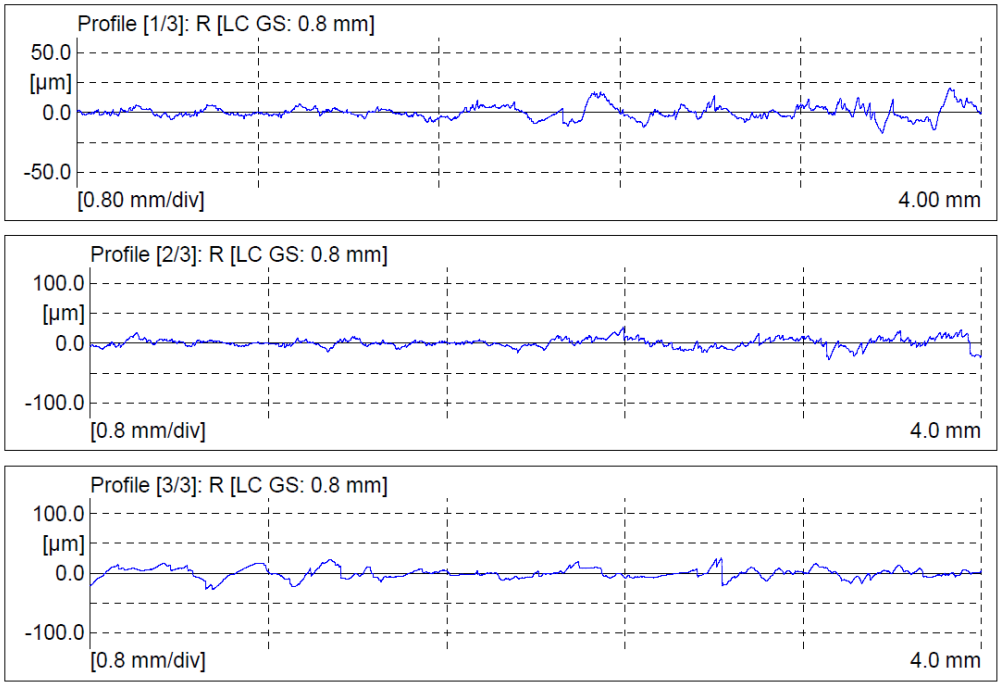

Figure 5.34 Longitudinal surface integrity profile for Test B2.

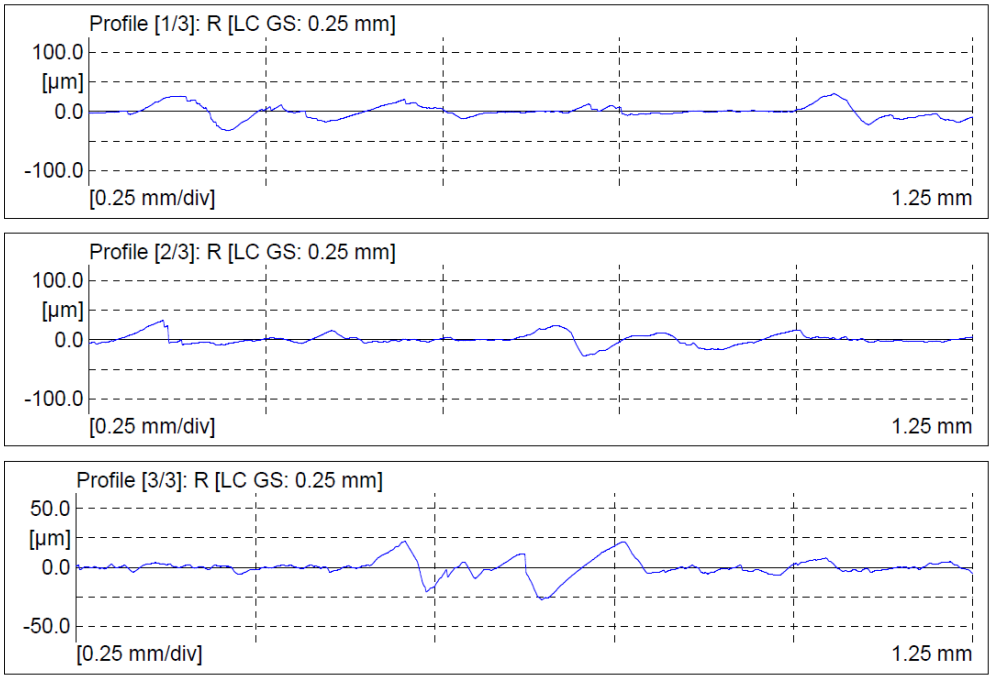

Figure 5.35 Transverse surface integrity profile for Test B2.

5.5.4 Phase 2 Particle Analysis Results

Table 5.14 summarizes the particle analysis information from the Sioutas cascade impactors used for all tests.

Table 5.14. Phase 2 particle analysis results

Test ID	Laminate Orientation	Cutter	Cutting Orientation	MMAD d50 (μm)	Inhalable Particle Conc. mg/m^3	σ_g	r^2
S1	0 Degree	Carbide 4 flute (new)	Climb	1.21	7.667	9.2	0.974
S2	90 Degree	Carbide 4 flute	Climb	1.02	6.485	5.25	0.94
S3	+45 Degree	Carbide 4 flute	Climb	1.15	3.891	4.31	0.831
S4	-45 Degree	Carbide 4 flute	Climb	56.16	4.582	47.12	0.973
A1	Multidirectional	Carbide 4 flute (new)	Climb	1.22	5.108	7.1	0.917
A2	0 Degree	PCD 2 flute straight (new)	Climb	2.46	3.618	5.12	0.954
A3	90 Degree	PCD 2 flute straight	Climb	1.23	10.19	3.94	0.862
A4	+45 Degree	PCD 2 flute straight	Climb	4.53	4.937	12.78	0.898
B1	-45 Degree	PCD 2 flute straight	Climb	7.89	3.262	6.67	0.84
B2	Multidirectional	PCD 2 flute straight	Climb	37.77	4.985	15.35	0.994
B3	Multidirectional	PCD 2 flute straight	Conventional	15.02	4.491	26.26	0.954
B4	Multidirectional	Carbide 4 flute (new)	Conventional	12.3	9.952	50.94	0.928
C1	Multidirectional	2 st. flute carbide (new)	Climb	28.19	4.218	46.56	0.981
C2	Multidirectional	6 flute CVD (new)	Climb	1.74	7.361	4.61	0.936
C3	Multidirectional	40 grit diamond (new)	Climb	1.04	6.622	6.41	0.935
C4	Multidirectional	125 grit diamond (new)	Climb	10.42	10.478	22.92	0.874
D1	Multidirectional	4 flute CVD twist (new)	Climb	7.49	19.669	9.64	0.894
D2	Multidirectional	Burr Tool (new)	Climb	9.5	9.401	12.53	0.92
D3	Multidirectional	Serrated CVD 8 flt (new)	Climb	6.53	11.011	6.94	0.933

This data was compiled through individual aerosol sampling experiments conducted for each test ID. Every experiment required the same extensive procedures described in chapter 4 for processing the impactors and conditioning filters. A sample result is provided for the C2 test where a 6-flute CVD diamond coated cutter was used for the peripheral trim test of a multi-directional laminate. Figure 5.36 is the mass summary for the C2 experiment. This was compiled by using the sample weights calculated at each filter stage by subtracting the mass of each unexposed filter from the exposed filter weights as shown in table 5.15. For the C2 test, 2 backup filters were used. The first was a 0.4 μm diameter etched Nuclepore® filter. The second filter directly behind and downstream is a standard 37 mm PTFE filter. The Nuclepore® filter is placed upstream

to more clearly distinguish small particles for improved SEM micrographs. From early experiments, it was found at the backup stage, small particles (less than approximately 0.50 μm) could get lost in the fibrous filter media and be more difficult to distinguish. The Nuclepore® filters improve the imaging of small particles as they are polycarbonate and have random etched holes of a known diameter (.4 μm). This also provides an additional visual scale factor. The PTFE backup filter is there to catch any tiny particles that may pass through the pores in the Nuclepore® filter so they can be accounted for in the mass measurement. SEMs will be provided in a later subsection and in Appendix A for all tests. The concentration is estimated by first calculating the total sample air volume which is the product of the flow rate through the critical orifice (10.2 lpm) and the sample time (12.33 min). This provides the total air volume sampled in liters (125.8 liters). The total collected mass is found by summing the sample weights of each filter stage which is equal to (926 μg). The mass concentration in mg/m^3 is found by dividing the total sample mass collected by the total sample volume in liters and converting to cubic meters. For the C2 test, the concentration sampled is 7.361 mg/m^3 at PM 2.5, where PM 2.5 is the maximum cut point for the impactor.

Table 5.15 Filter mass summary for C2 test

Ref	Filter (Stage)	Impactor Stage	Unexposed Filter Weights (mg)	Exposed Filter Weights (mg)	Sample Weights (mg)	Sample Weights (μg)
1	C2-1	A	91.8800	92.2303	0.3503	350
2	C2-2	B	87.6038	87.8970	0.2933	293
3	C2-3	C	86.2830	86.4038	0.1208	121
4	C2-4	D	93.5943	93.6250	0.0308	31
5	C2-5	Backup	55.1628	55.1755	0.0127	13
6	C2-6	Nuclepore	9.8368	9.9550	0.1183	118
					0.926	**926**

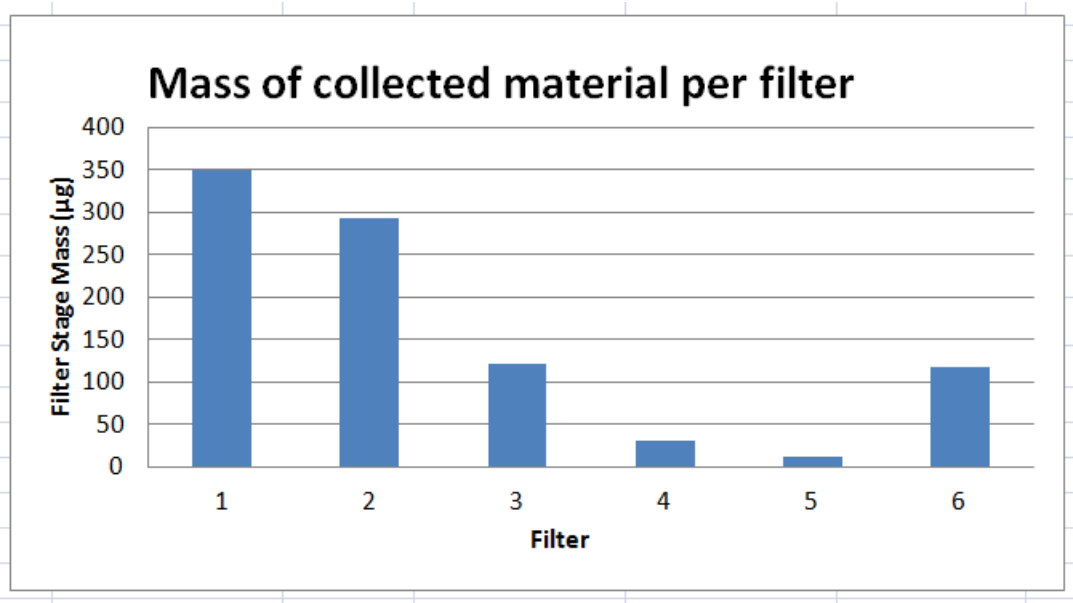

Figure 5.36. Filter mass summary for C2 test.

The results are then plotted on a log probability graph automatically generated in Microsoft Excel from the filter mass data. The log probability plot for the C2 test is included in figure 5.37. From the log probability plot, the geometric standard deviation, σ_g and d_{50} (CMD) are calculated. The r^2 correlation coefficient is also calculated directly from the plot providing an indication of fit. Equations will be discussed in chapter 8 as a section of the particle model. In the case of the C2 impactor test, the log probability provides:

$\sigma_g = 4.61$

d50 = 1.74 µm

$r^2 = .936$

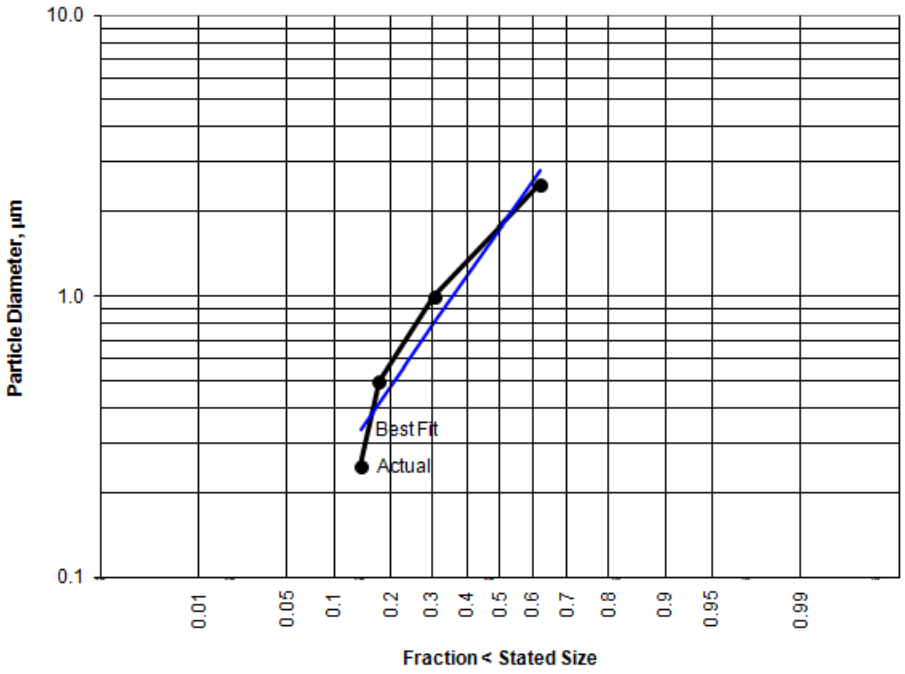

Figure 5.37 Log Probability Plot for C2 impactor test

Extensive SEM micrographs were taken of individual filter samples to provide additional insight into particle geometry at each cut point. Filter sections were carefully cut and placed on SEM mounts attached with carbon tape. Up to 8 filter samples could be imaged on a single rotisserie mount, while some filters were imaged on a single mount. Figure 5.38 provides sample micrographs of the D3 test where a 8-flute CVD coated tool was used to edge trim a multi-directional laminate. Micrographs from each of the impactor stages are provided with increasing magnification. For stages A-D, the first image presents the line of particle build up on the filter stage as the Sioutas impactors utilize a linear slot for separation. Examples of relatively clean fractures perpendicular to the fiber axes are shown in addition to longitudinal cleavage of the fibers. Almost every geometry in between is also illustrated. Images from the backup Nuclepore® filter stage are provided. The diameter of the 400 nm randomly located etched pores is clear when compared to the SEM scale of the micrograph. The polycarbonate material improves the

ability to distinguish between individual particles. When taking the images, the particles sometimes jumped around due to the electron beam, so there may have been more particles in any single location depending on the image. This tended to happen more with piles of particles in a single location. Additional micrographs are included in Appendix A. Future work could include the use of techniques such as Energy Dispersive X-Ray Spectrosocopy (EDS) to distinguish between carbon fiber and resin in the filter samples. Some limited investigation using the capabilities of the Oxford Inca EDS system at the University of California, Irvine was explored for the 90 degree phase 1 sample collected using the Sierra Instruments Series 201 Impactor, backup filter. Carbon fibers obviously have a very high carbon content, greater than 95%, so can be clearly identified as shown in figure 5.39 with spectrums in Appendix B. The resin mixtures are proprietary, so knowing relative percentage content of some key elements helps to distinguish from the high carbon content fibers, filter media and substrate as illustrated in figure 5.40. An example of the elements of a filter filament is shown in figure 5.41 and likely elements of the aluminum sample mounting stub in figure 5.42, evidenced by the high aluminum content.

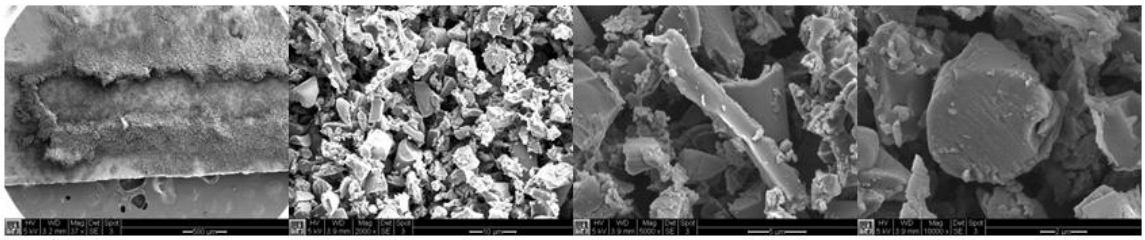

Filter A

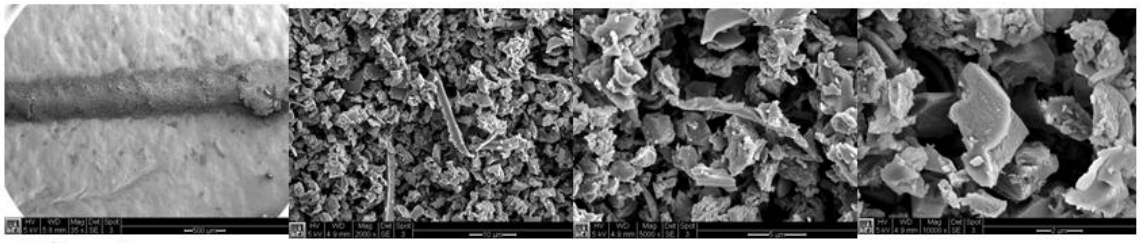

Filter B

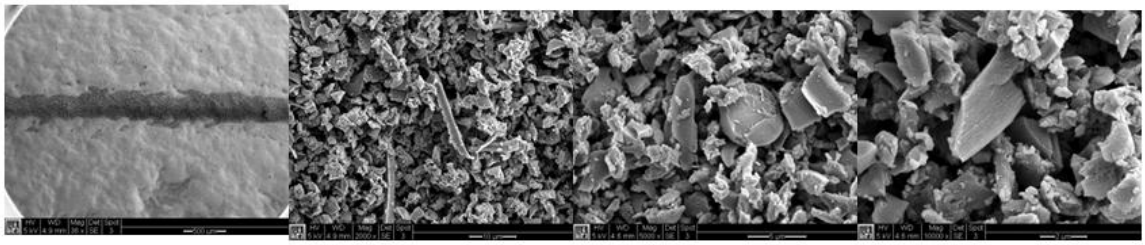

Filter C

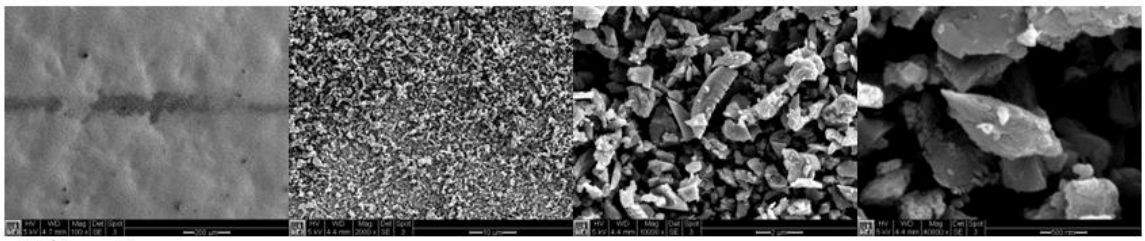

Filter D

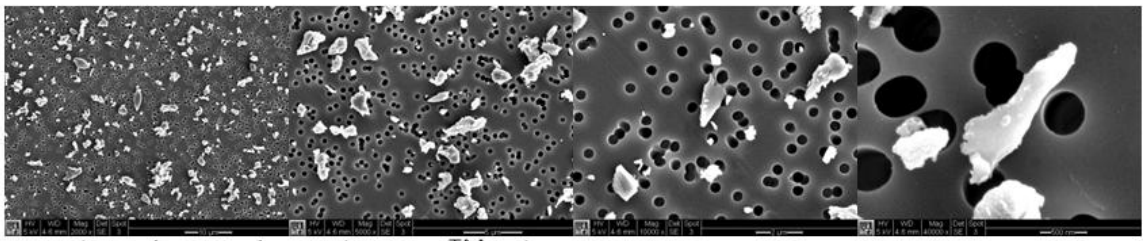

Backup (.4 µm) Nuclepore™ Filter

Figure 5.38. D3 impactor test SEMmicrographs

Spectrum	In stats.	C	O	Mg	Al	Si	S	Total
Sample B One(1)	Yes	98.84	0.83	0.00	0.33	0.00	0.00	100.00
Sample B One(2)	Yes	98.81	0.84	0.00	0.29	0.07	0.00	100.00
Sample B One(3)	Yes	99.11	0.65	0.00	0.25	0.00	0.00	100.00
Sample B One(4)	Yes	99.25	0.51	0.00	0.24	0.00	0.00	100.00
Sample B One(5)	Yes	99.20	0.58	0.00	0.22	0.00	0.00	100.00
Mean		99.04	0.68	0.00	0.27	0.01	0.00	100.00
Std. deviation		0.20	0.15	0.00	0.04	0.03	0.00	
Max.		99.25	0.84	0.00	0.33	0.07	0.00	
Min.		98.81	0.51	0.00	0.22	0.00	0.00	

Figure 5.39. EDS Sample carbon fiber (Sierra Instruments 90 deg)

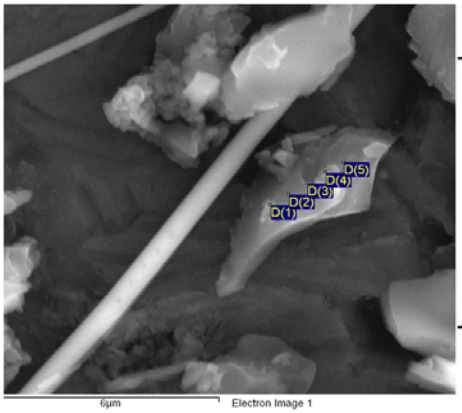

Spectrum	In stats.	C	O	Na	Mg	Al	Si	S	Total
D(1)	Yes	62.36	6.45	0.20	1.50	28.02	0.33	1.14	100.00
D(2)	Yes	61.38	6.79	0.21	1.57	28.39	0.32	1.35	100.00
D(3)	Yes	60.34	5.59	0.17	1.69	30.84	0.24	1.14	100.00
D(4)	Yes	64.19	7.05	0.19	1.37	25.82	0.21	1.17	100.00
D(5)	Yes	62.02	5.78	0.16	1.55	29.28	0.14	1.07	100.00
Mean		62.06	6.33	0.18	1.54	28.47	0.25	1.17	100.00
Std. deviation		1.42	0.63	0.02	0.12	1.84	0.08	0.10	
Max.		64.19	7.05	0.21	1.69	30.84	0.33	1.35	
Min.		60.34	5.59	0.16	1.37	25.82	0.14	1.07	

Figure 5.40. EDS Sample unknown, possibly matrix (Sierra Instruments 90 deg)

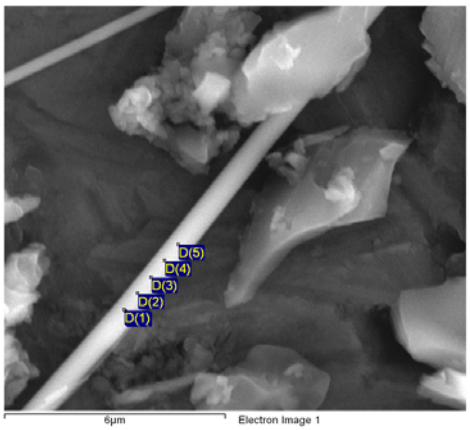

Spectrum	In stats.	C	O	Na	Mg	Al	Si	S	Total
D(1)	Yes	24.68	28.97	0.98	2.03	35.32	7.83	0.19	100.00
D(2)	Yes	23.89	28.95	1.16	2.10	36.10	7.67	0.12	100.00
D(3)	Yes	22.63	28.41	1.18	2.04	37.45	8.09	0.20	100.00
D(4)	Yes	22.55	28.52	1.24	2.03	37.40	8.14	0.11	100.00
D(5)	Yes	23.06	28.77	1.12	2.07	36.78	8.05	0.16	100.00
Mean		23.36	28.72	1.14	2.05	36.61	7.96	0.16	100.00
Std. deviation		0.91	0.25	0.10	0.03	0.91	0.20	0.04	
Max.		24.68	28.97	1.24	2.10	37.45	8.14	0.20	
Min.		22.55	28.41	0.98	2.03	35.32	7.67	0.11	

Figure 5.41. EDS Sample filter media (Sierra Instruments 90 deg sample)

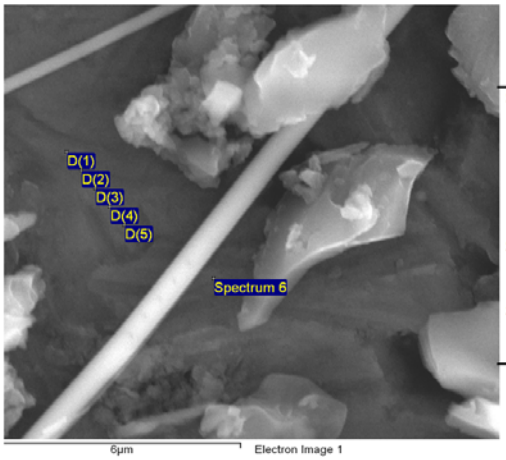

Spectrum	In stats.	C	O	Na	Mg	Al	Si	S	Total
D(1)	Yes	16.43	1.05	0.00	4.12	78.40	0.00	0.00	100.00
D(2)	Yes	15.23	0.99	0.00	3.92	79.86	0.00	0.00	100.00
D(3)	Yes	15.71	1.30	0.00	3.79	79.20	0.00	0.00	100.00
D(4)	Yes	16.18	1.77	0.00	4.02	77.85	0.00	0.18	100.00
D(5)	Yes	13.46	1.39	0.00	4.32	80.84	0.00	0.00	100.00
Spectrum 6	Yes	13.85	5.45	0.00	3.89	76.41	0.40	0.00	100.00
Mean		15.14	1.99	0.00	4.01	78.76	0.07	0.03	100.00
Std. deviation		1.23	1.72	0.00	0.19	1.56	0.16	0.07	
Max.		16.43	5.45	0.00	4.32	80.84	0.40	0.18	
Min.		13.46	0.99	0.00	3.79	76.41	0.00	0.00	

Figure 5.42. EDS Sample aluminum stub (Sierra Instruments 90 deg)

5.5.5 Phase 2 Results Summary

In phase 2 of the research, 19 complete experiments were conducted that utilized the basic experimental methods developed in phase 1 with some refinements. The phase 2 machinability experiments were significant as they provided guidance to steer the focus of the research effort. Clearly, the time consuming nature of the impactor tests, some inconsistency in particle build up on the stages, and other variables make impactor testing impractical for high volume testing of different cutting conditions in the current

laboratory environment, or likely in a production environment. Faster more robust methods are needed to accomplish extensive cutting test experimental plans with many factors and response variables of interest in reasonable times. The dust enclosure was definitely a step in the right direction in providing a controlled safe environment for dust generating experiments as there was no particle migration. AE signal acquisition demonstrated waveforms of similar shape to cutting force data. For milling force data, some discrepancies were found in use of the Kistler 9123C rotating dynamometer that need to be resolved if it is to be used to provide data for models that predict cutting forces.

From the data gathered in the phase 2 composite machinability assessment, the phase 3 experimental efforts were focused on identifying and evaluating real-time particle analysis instrumentation to determine suitability for the application and improving dynamometer techniques and data interpretation for use in a cutting force prediction model. Phase 4 refined the particle collection and analysis technique yielding a patent pending self-contained system that analyzes nearly all exhausted composite dust particles. In phase 5, techniques for a milling force prediction model are developed. The phase 2 machinability experimentation was key to providing the focus for the remainder of this experimental research effort for phases 3-5 which will be discussed in Chapters 6 and 7. Chapter 6 concentrates on dust collection and analysis, and chapter 7 focuses on cutting force processes and prediction.

CHAPTER 6

PARTICLE ANALYSIS SYSTEM DEVELOPMENT

6.1 Introduction

This chapter discusses the development of a dust collection and particle analysis system for dry machining of composite materials. It chronologically picks up after the phase 2 machinability experiments and covers the experimental work performed in phase 3-5 of this research as described in chapter 4. The goal of this effort was to develop a system that is inherently safe for users and the environment, and from a research perspective provides complete insight into the particle sizes and concentrations that are generated from machining and trimming of composite materials. Other objectives were to develop a system that is portable and can be utilized in an industrial environment and moved to multiple machines. Further goals were the capability to perform rapid analysis without necessarily having to be dependent on the time consuming effort of processing cascade impactor filters for multiple experiments. This chapter will provide the experimental methodology and test results for development of a fully self-contained system for real-time isokinetic sampling of dust generated from manufacturing processes.

6.2 Phase 3 Real-Time Instrument Testing

From the experience learned from phase 2 testing, it became clear that flow time for particle analysis was a constraint to performing the types of tests that are desired for industrial use whereby many runs are required for detail study of the effect of cutting conditions (cutter geometry and material, depths of cut, spindle speed, feed rate) on particles produced. While cascade impactors are considered the "gold standard" for aerodynamic particle size distribution, the time required for processing is extensive due to cleaning, assembly, filter conditioning, and weighing. In phase 3, testing was performed to investigate the use of real-time particle measurement instrumentation in this environment to improve flow time and provide additional insight into particle distribution. Limited testing of select instruments was performed to evaluate suitability for the application.

As a result of a industry survey of available systems, literature review and performance goals noted above, the following real-time particle measurement instruments were identified and experimentally evaluated as part of phase 3 to determine suitability for the application. The capabilities of several other instruments were evaluated, but not available for test. Many brands and models of sampling instruments are sold; however, only a few satisfy the performance ranges required for this application and fit within budget constraints. Cascade impactor data from phase 1 and 2 testing was used to estimate necessary performance capabilities for the real-time instrumentation. Key values that were used for performance sizing included MMAD, and PM2.5 concentration. Sample calculations from the impactor data for sizing capabilities for real-time instruments are included in Appendix C in addition to a typical capability comparison table. Real-time instruments tested as part of phase 3 include:

- TSI PTRAK 8525 Ultrafine Optical Particle Counter
- TSI Portacount Respirator Fit Tester 8038
- TSI DustTrak DRX 8533/8534
- TSI OPS 3330 Optical Particle Sizer
- Grimm 1.109 Portable Aerosol Spectrometer
- ThermoScientific PDR DataRam 1200 Personal DataRam Particulate Monitoring
- Casella CEL-712 Microdust Pro Dust Monitor

Real-time instrumentation testing was performed in the phase 2 dust collection configuration for evaluation of potential equipment to be used for further study. Additional holes were placed in the base of the dust containment box and new tube holding fixtures were built. Instrumentation was temporarily placed in front of the HAAS machine, and edge trimming tests were conducted using multi-directional laminates and 4-flute solid carbide cutters with the dust sampled by the respective instruments under test and evaluation. A 101 mm (4 inch) tool holder extension was used in place of the rotating dynamometer to enable use of the same fixturing within the enclosure to avoid damage and wear and tear to the rotating dynamometer, which could be sensitive to fine composite dust. The testing demonstrated that real-time instrumentation could be used to acquire results in a much shorter time which would enable rapid analysis of dust produced by different cutting conditions, which is more desirable for industrial applications, and a key focus of the research. Cutting time could be considerably shortened as collecting sufficient dust for filter mass reading was not necessary, with the exception of optional calibration depending on the instrument. Further, results could be acquired in minutes instead of

days because there was no need to weigh and condition filters as with the cascade impactors. Figure 6.1 are photographs from simultaneous evaluation of 4 real-time instruments (TSI PTRAK 8525, TSI DustTrak 8533, TSI OPS 3330, and PDR DataRAM) and a Sioutas cascade impactor.

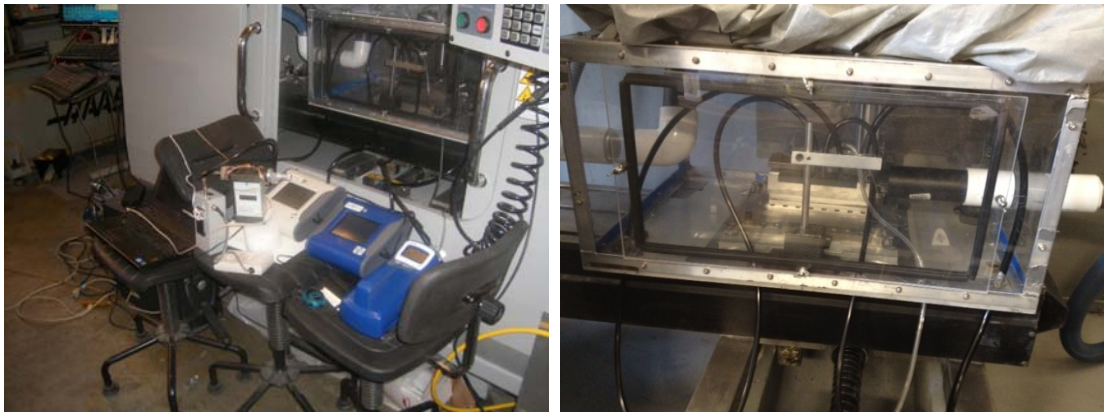

Figure 6.1 Simultaneous testing of real-time instruments and cascade impactor

6.3 Real-Time Dust Analysis Instrumentation Results

Identification and testing of real-time particle analysis instrumentation that could be used to expedite analysis of dust generated from machining operations and provide a wide range of information on particle count and mass distribution was a focus of the phase 3 experimental effort. To evaluate the potential for real-time particle analysis applied to composite machining, several instruments (TSI PTRAK 8525, TSI DustTrak 8533/8534, TSI PortaCount 8038, TSI OPS 3330, PDR DataRAM, GRIMM 1.109) were evaluated as part of phase 3. Applicable instruments were selected as described in section 6.2.

6.3.1 First Round Test Results

The first real-time instrument screening tests were performed using a TSI PortaCount Respirator Fit Tester 8038 and ThermoFisher Scientific PDR-1200 DataRam. The PortaCount was used on loan as it works similar in principle to the TSI PTRAK which was unavailable at the time. Both the DataRam and PortaCount were used without data logging. Initial tests were conducted to evaluate the effectiveness of the vacuum system taking into account the spindle

rotation as it could impact performance. The results are recorded in sequential order and included in table 6.1. Two tests included simultaneous use of Sioutas cascade impactors, D4, E1.

Table 6.1 Initial PortaCount and PDR DataRAM results

Test Condition	**PortaCount (pt/cc)**	**DataRam (mg/m^3)**
Spindle off, door off in chamber, vacuum off	~1700	N/A
Spindle off, door on in chamber, vacuum off	~1000	N/A
Spindle off, door on in chamber, vacuum on	~0-20	N/A
Spindle off, door on in chamber, vacuum off`	~800-1000	N/A
Spindle on, door on in chamber, vacuum off	~24800	N/A
Spindle on, door on in chamber, vacuum on	~490-600	N/A
Spindle on, door on in chamber, vacuum off	~940	0
Spindle off, door on in chamber, vacuum on	0-1	0
3 passes, .762 mm radial cut, 6.35 mm axial cut, 12.7mm diameter, 4-flute, 635 mm/min, multidirectional laminate	~17,000	9
12 passes, .762 mm radial cut, 6.35 mm axial cut, 12.7mm diameter, 4-flute, 635 mm/min, multidirectional laminate	~251,000 peak	2 (avg. 5 min)
12 passes, .762 mm radial cut, 6.35 mm axial cut, 12.7mm diameter, 4-flute, 635 mm/min, multidirectional laminate (D4 Impactor)	~600,000 peak	1.9
11 passes, .762 mm radial cut, 6.35 mm axial cut, 12.7mm diameter, 4-flute, 635 mm/min, multidirectional laminate (E1 Impactor)	~600,00 peak	1.9

Log probability plots and mass analysis from the Cascade impactor tests are in Appendix D. Table 6.2 summarizes the cascade impactor test results. Sample SEM micrographs for the D4 and E1 Sioutas cascade impactors are included figure 6.2 and figure 6.3, respectively.

Table 6.2. D4 and E1 Impactor results

Test ID	**Laminate Orientation**	**Cutter**	**Cutting Orientation**	**MMAD d50 (µm)**	**Inhalable Particle Conc. mg/m^3**	**σ_g**	**r^2**
D4	Multidirectional	Carbide 4 flute	Climb	0.97	4.87	32.37	0.502
E1	Multidirectional	Carbide 4 flute	Climb	1.36	4.14	2.78	0.062

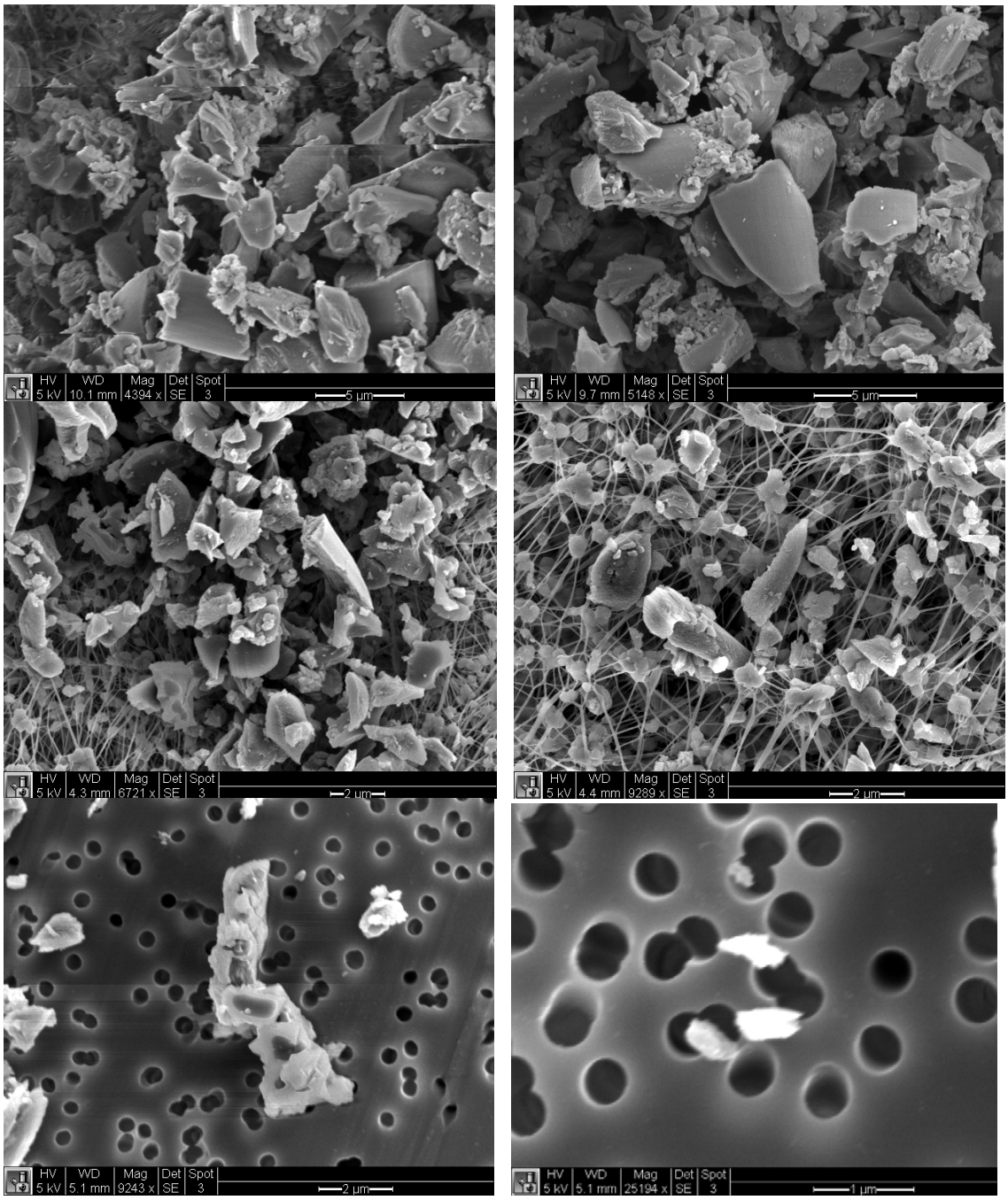

Figure 6.2. D4 Impactor SEMs from L to R and down (Stage A,B,C,D,backup x2)

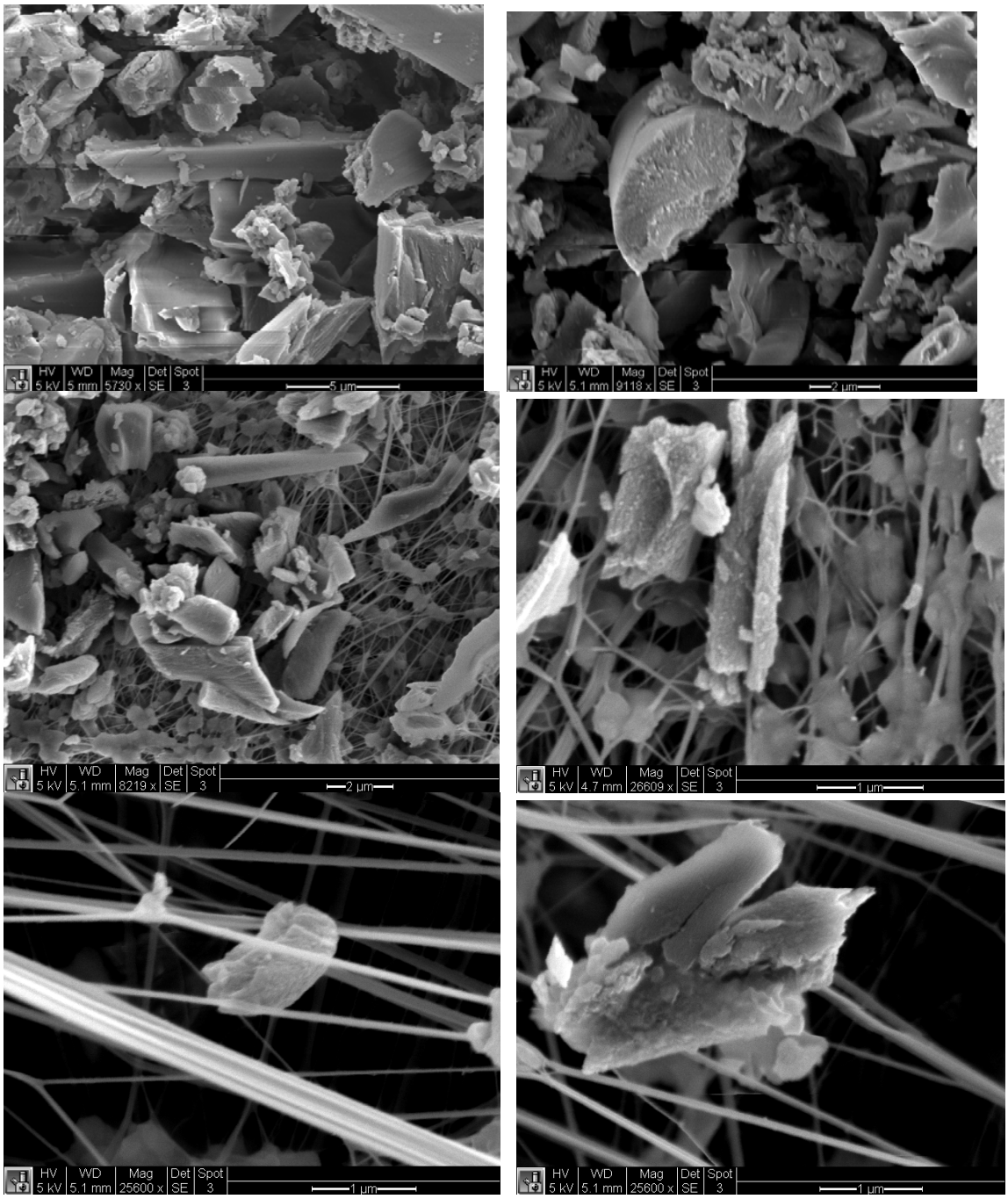

Figure 6.3. E1 Impactor SEMs from L to R and down (Stage A,B,C,D,backup x2)

6.3.2 Second Round Test Results

The next set of experiments used a TSI PTRAK 8525, TSI DustTRAK DRX 8533, and PDR-1200 DataRAM. The TSI DustTRAK DRX 8533 provides real-time dust monitoring. The DustTRAK simultaneously measures size-segregated mass fraction concentrations corresponding to PM1, PM 2.5, respirable, PM 10 in total PM size fractions with data logging capability at

sampling rates as short as 1 second [114]. The particle size range is 0.1 to 15 μm, and concentration limit to 150 mg/m³.

The four milling experiments conducted to test the performance of these instruments are summarized in table 6.3. Sample figures of test results are included in figure 6.4 for the PTRAK, figure 6.5 and figure 6.6 for the DustTRAK, and figure 6.7 for the DataRAM. The pattern identified by each of the instruments clearly shows a peak during each pass of the laminate. In general, the concentration or particle counts starts at zero prior to cutting when there are no particles and finish at approximately zero following the tests indicating that the vacuum system has eliminated the particles from the chamber after cutting is completed. The low point in the graphs represent a short pause between each machining pass of the laminate where the vacuum system catches up and removes particles from the chamber. Additional data for second round experimentation is in Appendix E.

Table 6.3. PTRAK, DataRAM, and DustTRAK test conditions

#	Laminate Orientation	Cutter	Cutting Orient.	# of Passes	RPM	Feedrate (m/min)	Radial Depth of Cut (mm)	Axial Depth of Cut (mm)
1	Multi-directional	Carbide 4 flute 12.7mm	Climb	14	6000	0.635	0.762	6.35
2	Multi-directional	Carbide 4 flute,12.7mm	Climb	11	6000	0.635	0.762	6.35
3	Multi-directional	Carbide 4 flute,12.7mm	Climb	10	6000	0.635	0.762	6.35
4	Multi-directional	Carbide 4 flute,12.7mm	Climb	18	6000	0.635	0.762	6.35

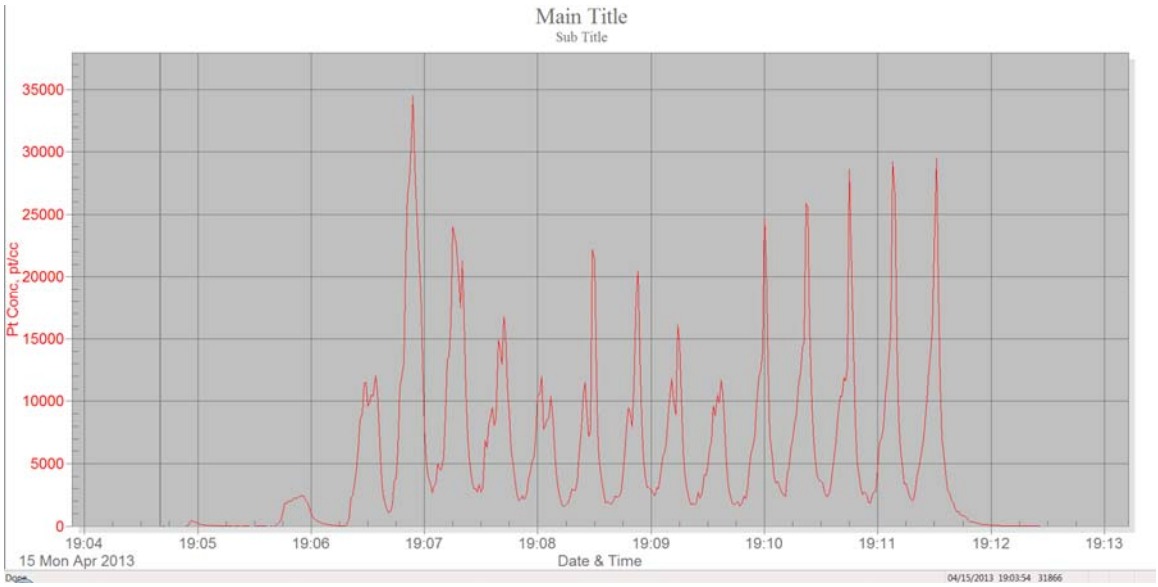

Figure 6.4. PTRAK results test #1.

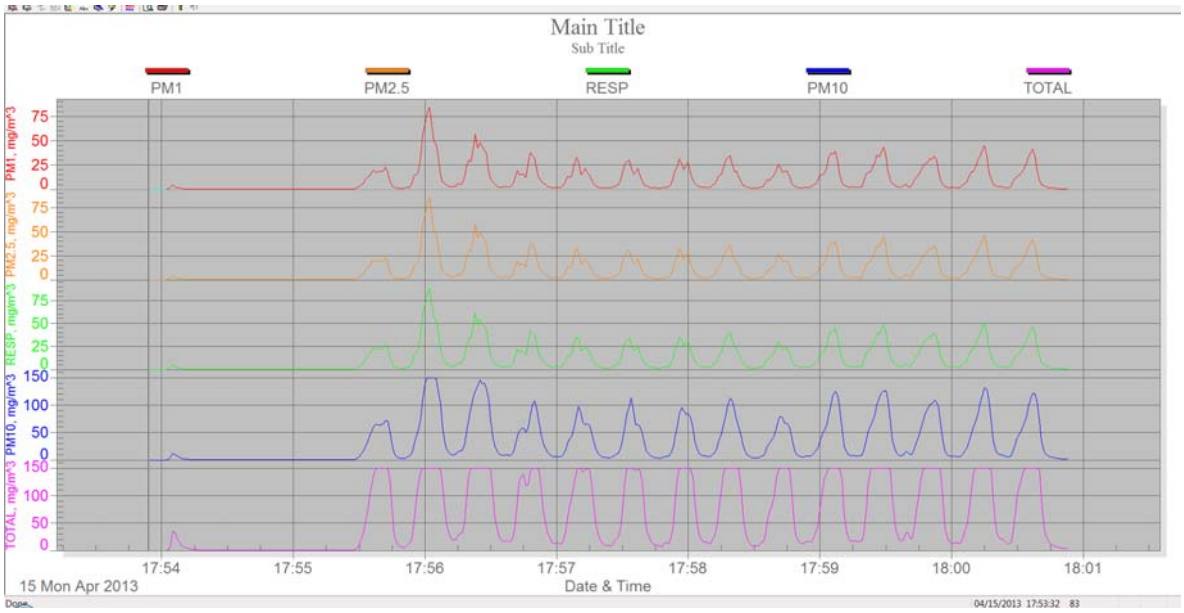

Figure 6.5. DustTRAK results test #1.

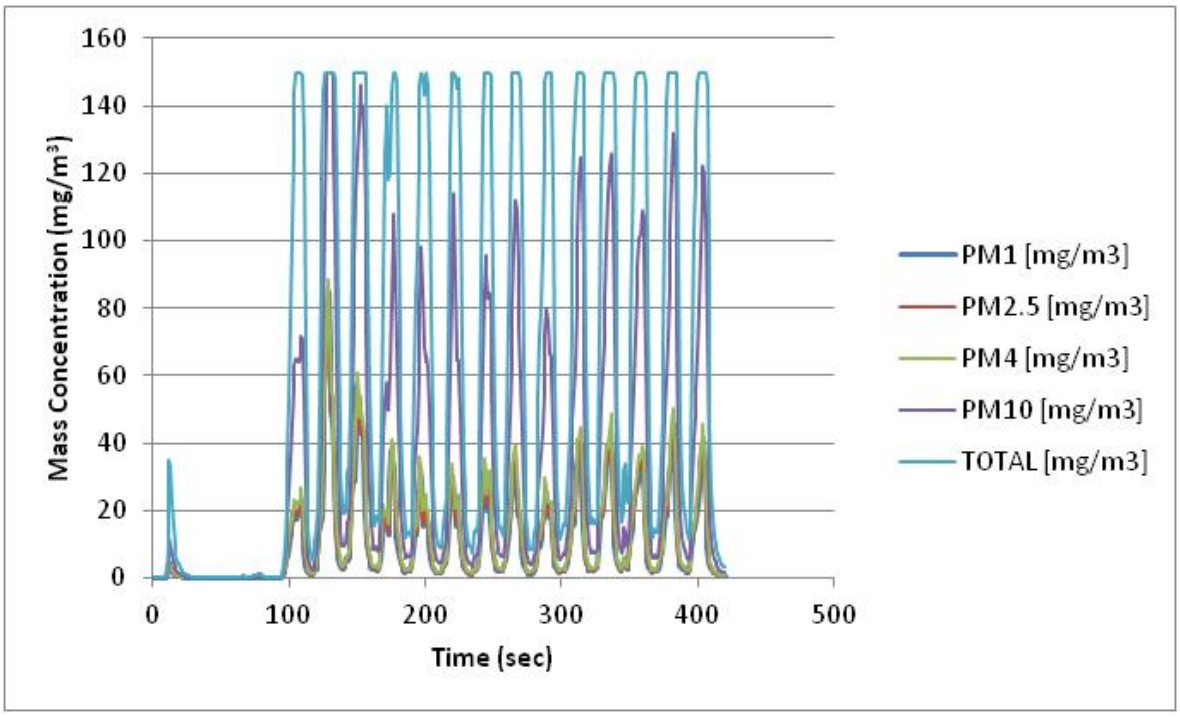

Figure 6.6. DustTRAK results test #1, combined.

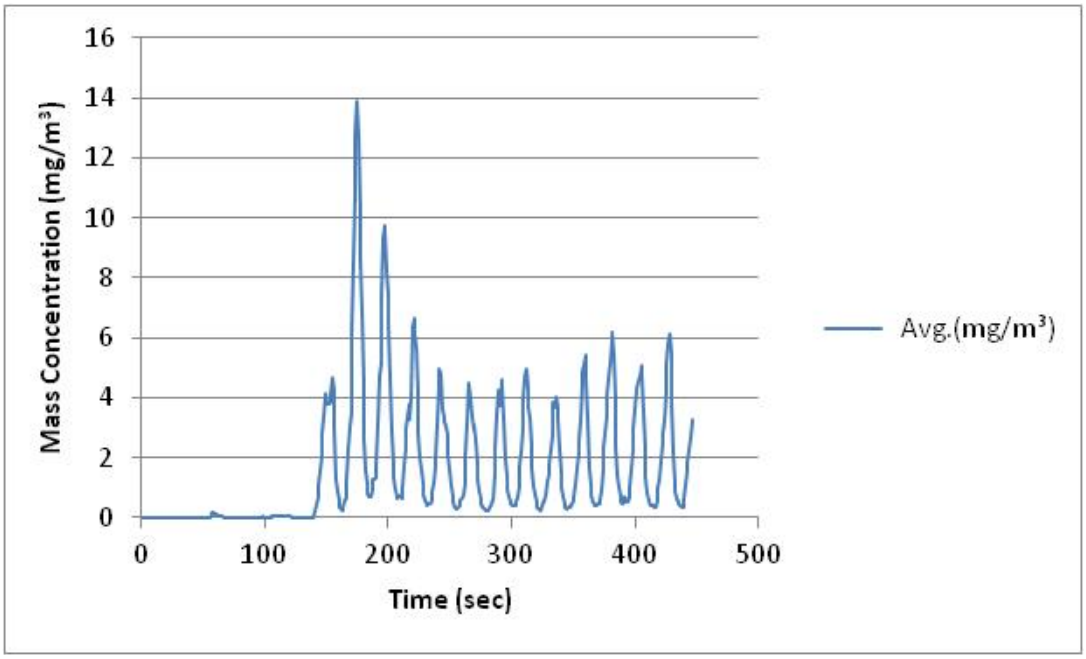

Figure 6.7. pDR DataRAM results, test #1.

6.3.3 Third Round Test Results

A TSI Optical Particle Sizer, OPS 3330 was used in the next series of tests which also included a TSI PTRAK, TSI DustTRAK, and pDR DataRAM. The TSI OPS 3330 provides particle concentration and size distribution over 16 channels. The particle size range is from 0.3

– 10 μm with a maximum count concentration of 3000 particles/cm^3 and a maximum mass concentration of 275,000 μg/m^3 [115]. The software provides datalogging capability with a recommended minimum sampling rate of 6 seconds. Nine tests were performed using this combination of instruments to capture real-time data to evaluate performance and suitability for the application. The test matrix is shown in Table 6.4. For tests 3-9, a size correction factor (SCF) and a photometric calibration factor (PCF) were used with the DustTRAK. The SCF is used to improve the relative accuracy and aerodynamic size difference between the 5 mass channels (PM1, PM2.5, Respirable, PM10) and the PCF is a custom calibration to improve the accuracy for a specific aerosol compared to Arizona Road Test Dust (ISO 12103-A1). The specific methods for determining the SCF and PCF are described in the DustTRAK manual and involve determining concentration through filter weighing and use of a PM2.5 impactor that was furnished with the equipment. The true mass concentration was used to calculate a custom calibration factor for the CFRP dust particles. A SCF of .570 and a PCF of .2068 were input into the instrument and utilized for the concentration measurements. Appendix F includes a table of DustTRAK gravimetric calculations for the calibration factors. Typical results from test 6 of this series of are shown in figure 6.8 for the PTRAK, figure 6.9 for the DustTRAK, figure 6.10 for the OPS 3330, and figure 6.11 for the PDR DataRAM with additional results included in Appendix F.

Table 6.4 Multi-Instrument test.

#	**Laminate Orientation**	**Cutter or Test Description**	**Cutting Orient.**	**Sample Time (min)**	**RPM**	**Feed (mm/ min)**	**Radial Depth of Cut (mm)**	**Axial Depth of Cut (mm)**
1	N/A	Vacuum only for control case	N/A	N/A	N/A	N/A	N/A	N/A
2	N/A	Vacuum with spindle on	N/A	N/A	N/A	N/A	N/A	N/A
3	Multidirectional	Carbide 4 flute,12.7mm, top half of laminate	Climb	4:30	6000	0.635	0.762	6.35
4	Multidirectional	Carbide 4 flute,12.7mm, bottom half of lam.	Climb	10:00	6000	0.635	0.762	6.35
5	Multidirectional	Carbide 4 flute,12.7mm, top half of laminate	Climb	6:00	6000	0.635	0.762	6.35
6	Multidirectional	Carbide 4 flute,12.7mm (new), top, 16 pass	Climb	7:00	6000	0.635	0.762	6.35
7	Multidirectional	Carbide 4 flute,12.7mm, bottom, 14 pass	Climb	6:00	6000	0.635	0.762	6.35
8	Multidirectional	CVD 4-flute, 12mm, top, 15 pass	Climb	6:00	6000	0.635	0.762	6.35
9	Multidirectional	CVD 4-flute, 12mm, bottom, 15 pass	Climb	5:45	6000	0.635	0.762	6.35

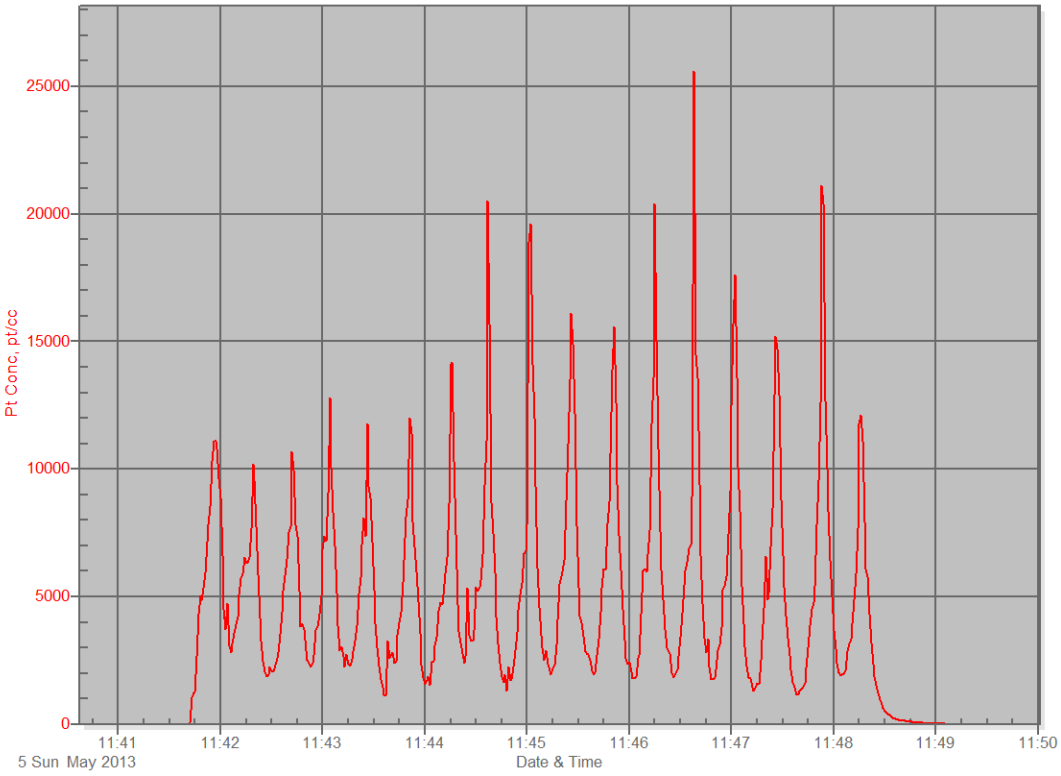

Figure 6.8. PTRAK results, test 6.

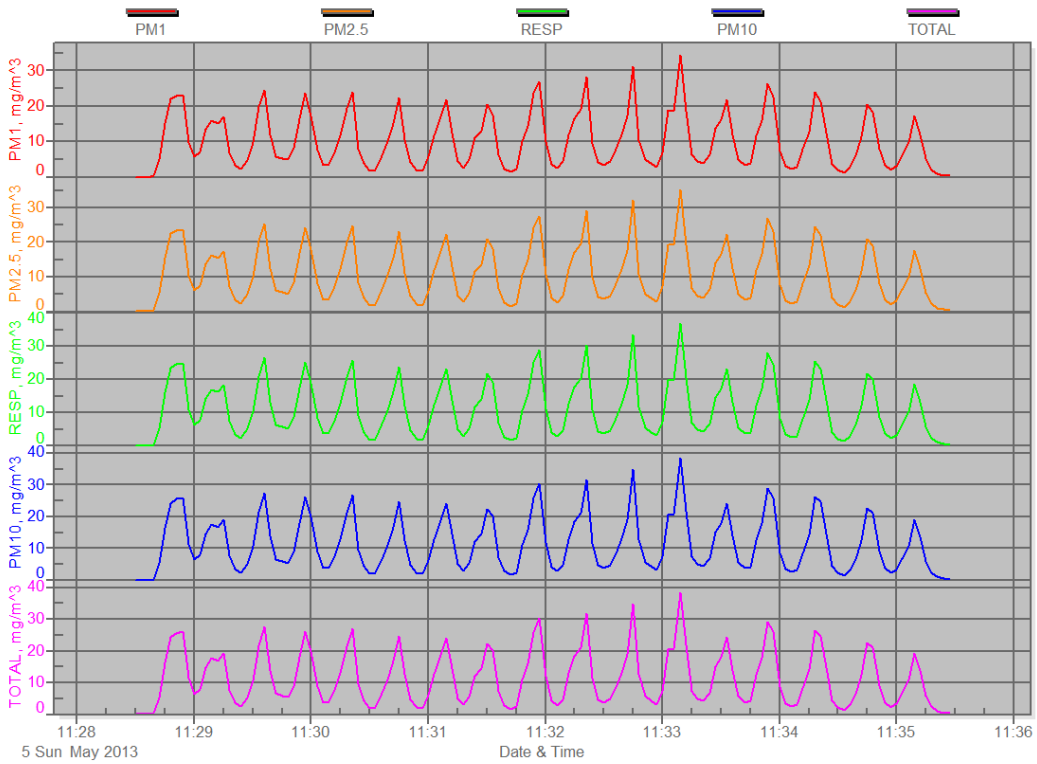

Figure 6.9. DustTRAK results, test 6.

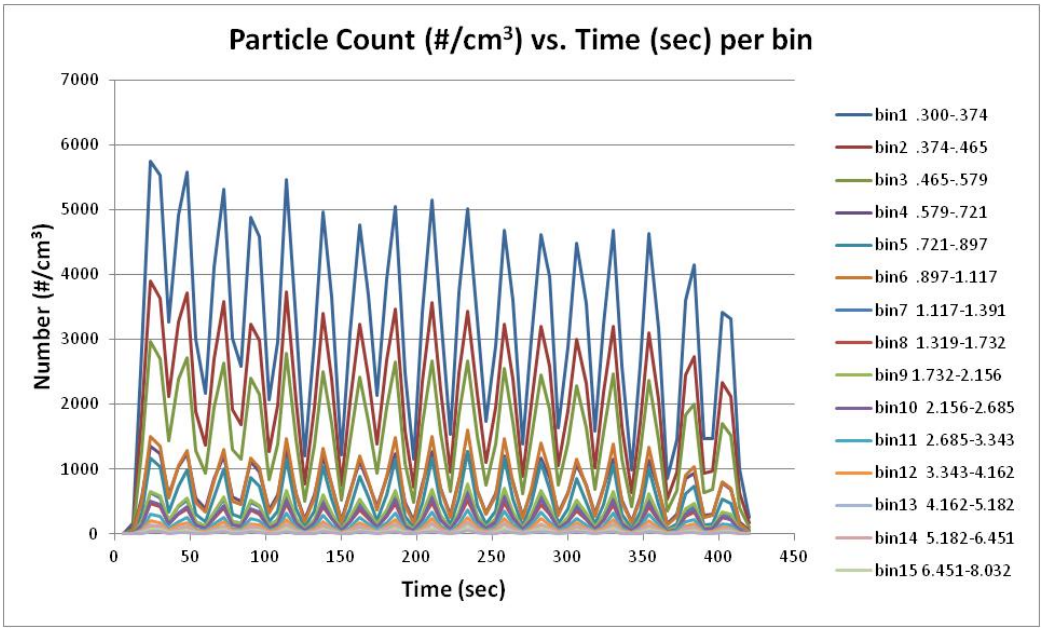

Figure 6.10. OPS 3330 results, test 6.

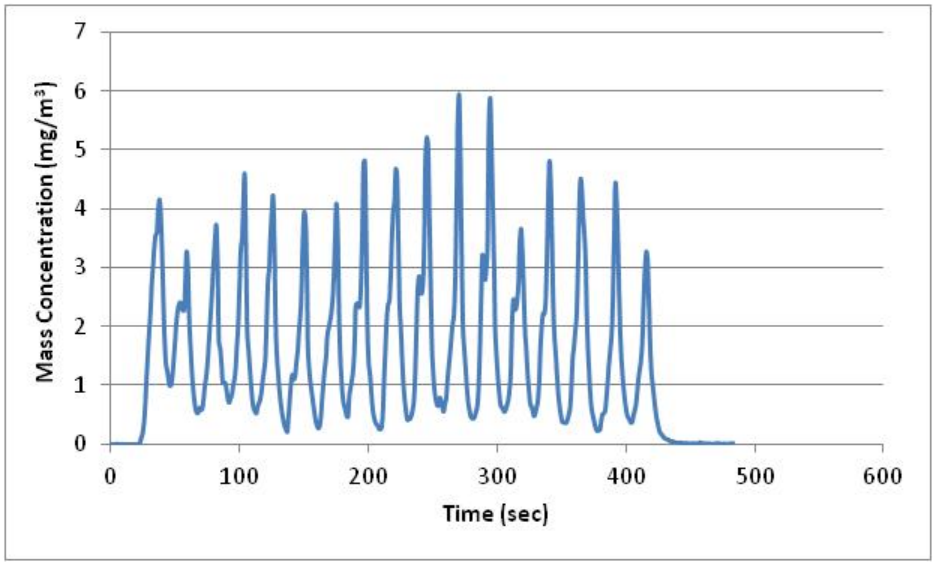

Figure 6.11. pDR DataRAM results , test 6.

6.3.4 Fourth Round Test Results

The final set of tests with real-time instruments in phase 3 testing introduced the GRIMM 1.109 Portable Aerosol Spectrometer. The capabilities and operating principle of the GRIMM were discussed in Chapter 4. A series of experiments were run with the GRIMM and PTRAK to validate GRIMM performance and suitability for this application. In addition, the experiments were also used to evaluate the impact of exhaust pipe placement in the dust containment

chamber. Since the phase 2 and 3 configuration is dependent on measuring residual dust in the chamber, the location and dynamics of the exhaust pipe relative to the cutting tool is significant for measurement consistency. These series of experiments evaluated the stationary side exhaust pipe used for all prior phase 2 and 3 experiments compared to a new exhaust pipe that moves with the cutting tool which utilizes a Loc-Line® flexible vacuum hose for ease of positioning.

The GRIMM was of interest because it was used in other labs at the University of Washington and was cited in a few applicable publications on composite dust [45, 97, 98, 99]. The GRIMM has a particle size range of .25 μm – 32 μm versus 0.3 – 10 μm for the OPS 3330. The GRIMM also has 31 size channels versus 16 for the OPS 3330. However, the OPS 3330 has a count concentration limit 3000 particles/cm^3 and a maximum mass concentration limit of 275,000 μg/m^3 versus 2000 particles/cm3 and 100,000 μg/m^3 for the GRIMM, with higher limits concentration limits being preferred to avoid reaching limits of the instrument. An advantage of the GRIMM is that it has a custom isokinetic kinetic probe available, with 4 nozzle diameters, and two options for diluters. Both of these features would be essential for phase 4 particle collection and analysis development using isokinetic sampling. From testing, the GRIMM software was also less buggy on key features than the OPS 3330. Figure 6.12 are photographs of the initial test configuration for the GRIMM and PTRAK. Five tests using the GRIMM and PTRAK were conducted as described in Table 6.5. Typical results from test 2 of this series are shown in figure 6.13 for the GRIMM and figure 6.14 for the PTRAK with additional results in Appendix G.

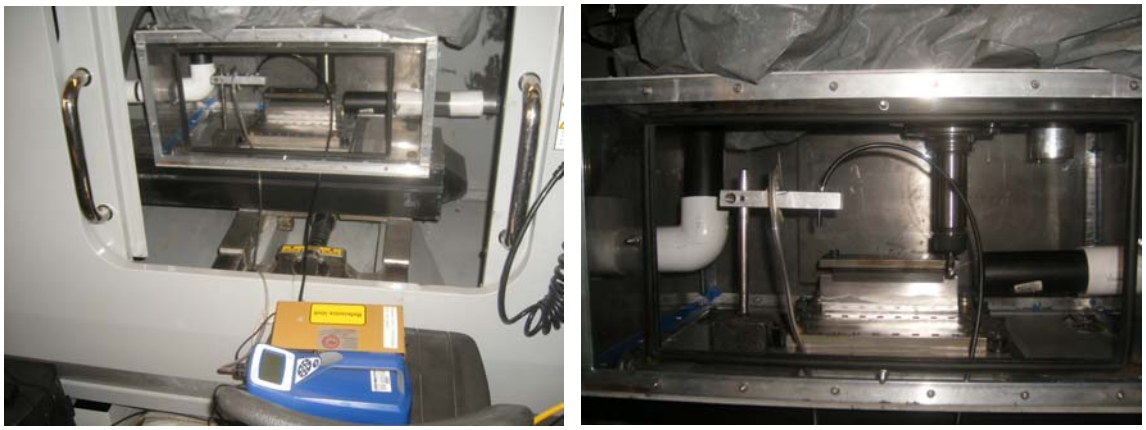

Figure 6.12. Initial GRIMM test configuration

Table 6.5. Initial GRIMM test matrix

#	Laminate Orientation	# Pass	Axial dept of cut (mm)	Experiment Conditions (see Appendix G for additional data)
1	Multidirectional	17	6.35	Fixed side vacuum exhaust, top half of laminate
2	Multidirectional	17	6.35	Fixed side vacuum exhaust, bottom half of laminate
3	Multidirectional	10	12.7	Moving Loc-Line vacuum hose with cutter, full laminate cut
4	Multidirectional	10	12.7	Moving Loc-Line vacuum hose and side vacuum, full laminate cut
5	Multidirectional	5	12.7	Removed 2 links from moving Loc-Line vacuum, no side vacuum
Cutting Conditions and Cutting Tool for all 5 tests below:				
Cutting Conditions: Climb, RPM 6000, Feedrate 0.635 mm/min, Radial depth of cut per pass 0.762 mm,				
Cutting Tool: 4-flute Carbide 12.7 mm diameter, 30 deg helix, new tool for test #1, used for #1-#5 in order				

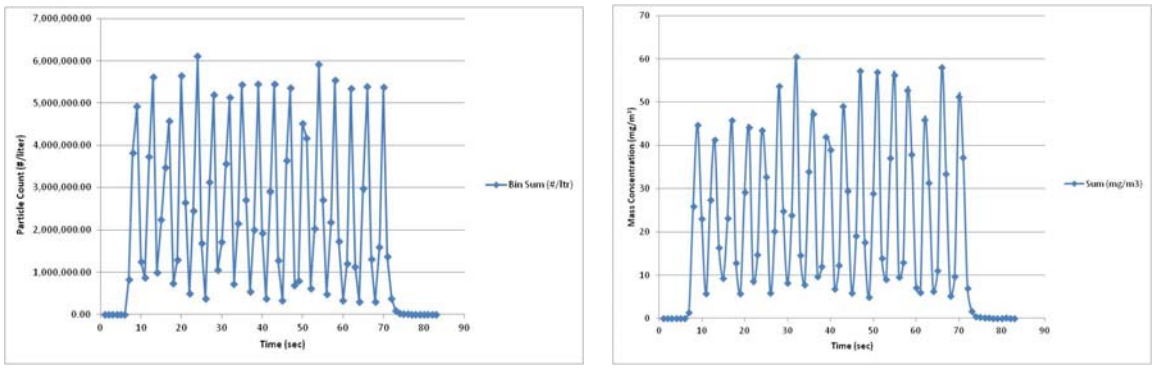

Figure 6.13. Initial GRIMM test results, test 2

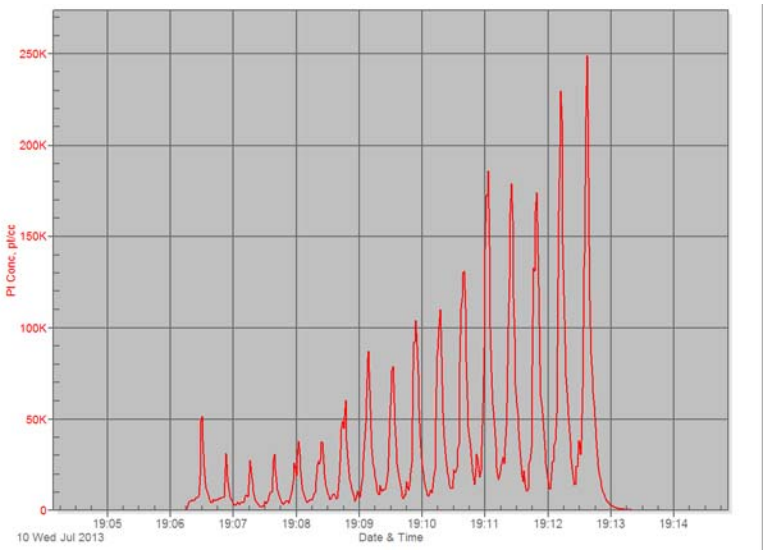

Figure 6.14. Corresponding PTRAK results, test 2

6.3.5 Phase 3 Real-Time Instrument Test summary

The dust collection investigation demonstrated the capability for using real-time instruments within the dust containment system for particle analysis. Consistent trends were found between different instruments that measure particle count and mass distribution demonstrating reliability of the technique. While the profiles between the instruments are very similar for each cutting pass and align well on a time basis, the peak magnitudes differ which may be addressed through calibration to gravimetric standards. Exhaust nozzle placement significantly impacts concentration of background dust in the chamber. PTRAK counts were found to drop from approximately 20,000 cts/cc with a stationary exhaust to less than 500 cts/cc with a moving exhaust that closely follows the cutting tool. Placement of the moving exhaust nozzle relative to the cutting tool also significantly impacts background concentration with PTRAK counts at approximately 7500 cts/cc with removal of two links from the Loc-Line hose. GRIMM mass concentration trends were similar with mass concentration approximately 40-50 mg/m^3 with a stationary exhaust compared to less than 0.5 mg/m^3 for the moving exhaust close to the cutting tool and approximately 5 mg/m^3 with two links removed from the Loc-Line hose.

Preliminary results indicate the geometry of the 4-flute CVD cutting tool produces a higher ultrafine particle count and PM2.5 mass concentration than the 4-flute carbide geometry under the same cutting conditions (6000 rpm, .635 mm/min linear feedrate, 0.762 mm axial depth of cut, 6.35 mm radial depth of cut) and averaged between top and bottom laminate edge trimming. The 4-flute carbide tool was found to have an average mass concentration of approximately 4 mg/m3 when measured using the PDR DataRAM with PM2.5 cyclone and ultrafine particle concentration of 12,500 cts/cc when measured with the PTRAK. The 4-flute CVD cutting tool had an average mass concentration of approximately 6 mg/m3 with the PDR DataRAM and PM2.5 cyclone and average ultrafine particle concentration of 20,000 cts/cc measured with the PTRAK. This may be potentially due to the sharper cutting edge of the CVD tool which is specifically designed for composite laminates and produces a significantly better surface finish than carbide. More experimentation is required to determine relationships between surface integrity, particle size and concentration. In phase 2 experimentation, the CVD tool had a transverse measured surface finish Ra of 1.301 μm with the carbide tool having a transverse measured surface finish Ra of 5.644 μm.

This approach provides a much faster turnaround of data for the extensive testing required to thoroughly evaluate the effect of cutting conditions on particles generated. Further, the multi-channel instruments provide means to evaluate aerosol concentration across several size ranges. With the vacuum exhaust nozzle position relative to the moving cutting tool demonstrated to have a significant impact on particle mass and count concentration, the phase 4 effort will focus on analysis of particles captured through the dust collection system which is more suited to production applications and collects nearly all particles directly from the source.

6.4 Phase 4 Isokinetic System Development

In phase 4, a new dust collection configuration was conceived, designed built and tested to introduce several improvements. The phase 2 and 3 system demonstrated that particles from machining composite laminates could be consistently collected and measured by both cascade impactors (phase 2) and real-time particle analysis instrumentation (phase 3). A limitation of the phase 2 and 3 dust collection test configuration was that sampling consisted of dust that was not collected by the shop vacuum and remained in the enclosure due to vacuum collection inefficiency and likely turbulence in the enclosure from the return air. Another limitation of the phase 2 and 3 configuration was that the vacuum inlet was stationary and distance from the inlet relative to the cutting tool constantly changed as the cutter moved along the part during edge trimming. By changing exhaust vacuum pipe positions, different mass and particle count concentrations were demonstrated to be measured for similar cutting conditions. While mostly consistent results were attained in the phase 2 and 3 configuration, there was an opportunity to come up with a new design that analyzed all dust that was collected by the exhaust vacuum system, and not just the residual dust in the enclosure. Further, the system could be built such that it would be portable and capable of being used on almost any system that collected dust via vacuum. Thus, the phase 4 effort consisted of the design, build, and test of a patent pending isokinetic sampling tower for a completely self contained dust collection and analysis system which can capture and analyze up to 100% of the dust produced from a manufacturing process [116].

6.4.1 Isokinetic System Basic Design

The concept for the isokinetic sampling system came from the observation that with proper vacuum nozzle placement and geometry, the dust collection system could be very efficient and collect a very high percentage of all dust produced. Assuming this could be accomplished, the next step was to design a system that could sample the dust while it moved through a duct toward the vacuum. The sampled dust could then be analyzed using real-time instrumentation and/or by cascade impactor. Vacuum nozzles could be further optimized to workpiece and cut geometry (e.g. edge trimming vs. slots) for highly efficient dust capture. This is easily accomplished for drilling processes due to single axis motion whereas for multi-axis milling it is more complex. The process for collection in a duct relies on the principle of isokinetic sampling. In isokinetic sampling, an inlet probe or nozzle is aligned parallel to gas streamlines in a duct with the gas velocity entering the nozzle equal to the velocity of the gas in the duct. If isokinetic conditions are met, there is no particle loss at the inlet of the nozzle, regardless of the particle size, and the concentration and size distribution of the aerosol entering the nozzle is the same as in the duct. The basic equation is $U = U_o$, where U_o is the free stream velocity in the duct and U is the velocity in the probe or nozzle with proper alignment. This process is typically used for dust and particle measurements in power plants, furnaces, kilns, and scrubbers. This may be one of the first, if not the first published use of isokinetic sampling for analyzing particles produced by manufacturing processes.

As with many developments, the final configuration for the isokinetic sampling system took several iterations to achieve. The starting point for the design leveraged the configuration used for testing in phase 2 and 3. The basic design constraints included use of the same enclosure, tube fitting sizes, and shop vacuums to reduce cost. The duct would be designed to accommodate an isokinetic sampling nozzle (GRIMM 1.152) for the GRIMM 1.109 Aerosol Spectrometer as the initial measuring device. This nozzle was custom built for the GRIMM 1.109 and came with 4 tips designed for different duct flow rates ranging from 2-25 m/sec. The nozzle selection table is included in figure 6.15 and is derived from the 4 ranges provided by GRIMM, nominal nozzle diameter, nominal instrument flow rate of 1.2 lpm, and basic equation of $Q = VA$, where Q is the flow rate in lpm, V is the velocity in m/sec, and A is the nozzle area

calculated from the nozzle diameter. A nozzle should be selected as close as possible to the nominal sampling flow rate of 1.2 lpm to avoid over or under sampling.

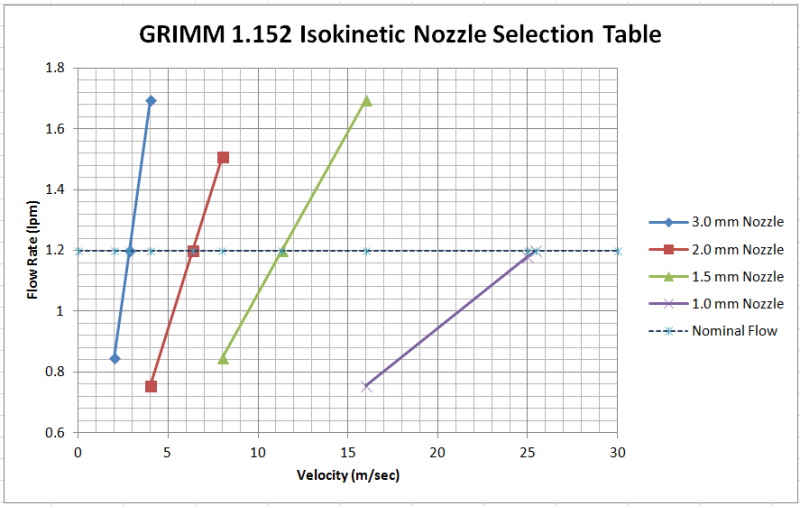

Figure 6.15 GRIMM nozzle selection table

Typical flow rates of a 6.5 HP shop vacuum were estimated at approximately 4.5 m^3/min (160 CFM) from a review of similar vacuums that had published catalog values. Standard 3 and 4 inch (PVC standards are in US customary units) PVC or ABS schedule 40 pipe was initially selected as the duct material and size for testing. This provided an approximate flow rate of 8.250 m/sec in 4 inch PVC which was within the range of the GRIMM nozzle tips using the basic equation of Q = AV. Because of the size of the GRIMM nozzle assembly, a tee fitting was required to mount the nozzle within the tube. The tee fitting is located along the length of the duct and positioned to provide at least 4 duct diameters from the upstream duct inlet. The nozzle fits through a hole in the tee cap and is held in place with a compression fitting. An illustration of the preliminary design concept for the isokinetic sampling system is shown in figure 6.16 with additional figures in Appendix H.

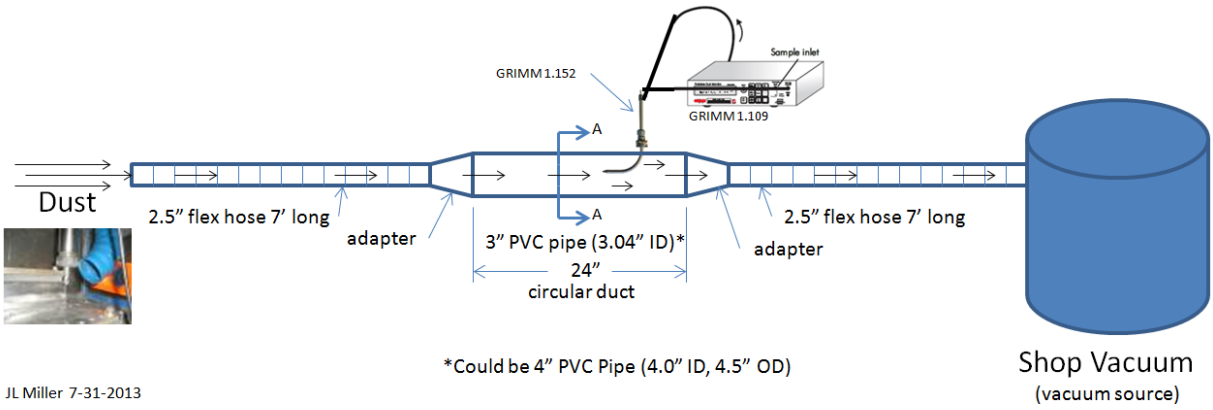

Figure 6.16 Original isokinetic test schematic.

6.4.2 Rigid Duct Flow Testing

Extensive testing was performed to measure velocity in the duct created by the shop vacuum for probe nozzle sizing. An Amprobe TMA40-A data logging vane anemometer was initially used to measure duct velocity. The 70 mm diameter vane was simply located at the open end of the pipe and spun up to steady state speed by the shop vacuum created velocity. Measured velocity values were then recorded. A photo of the duct test is provided in figure. 6.17. Two pitot tube types were soon added to the test configuration to measure differential pressure including a Dwyer DS-300-4 averaging flow sensor and Dwyer 166-6CF pocket size stainless steel pitot tube. Dwyer series 2000 Magnelic® differential pressure gages were used to measure the differential pressure reading from which velocity is calculated. Dwyer Series DM-1000 DigiMag® and Sper Scientific Datalogging Manometer 840098 were also tested, but found to be not as well suited for the application, with too much fluctuation in the data even with the use of pressure snubbers. The original plan was to continuously log the differential pressure/velocity data, however, it was found once the shop vacuums were operating, pressure remained stable through the test and the data logging instruments were not required. The differential pressure gages are used to monitor duct velocity and can also indicate if a vacuum filter becomes clogged by a pressure drop, so they need to be periodically checked. The Dwyer DS-300-4 averaging pitot tube was found to be not well suited to the application as the pressure ranges were at the lower limits of the instrument; however, the Dwyer 166-6CF pitot tubes appeared to work well, providing consistent readings. It was found that the wind vane anemometer appeared to overestimate the velocity in the duct, likely due to the effective duct area being reduced at the vane due to the vane housing. However, the vane anemometer proved

useful for relative performance testing of vacuum system components. 6061-T6 aluminum pipe with 114.3 mm (4.5 inch) OD, 3.17 mm (.125 inch) wall replaced the PVC pipe used for velocity testing to provide a conductive structure to minimize static electricity for reduction of particle build up on the duct walls. Holes were drilled and tapped in the pipe with compression fittings used to center and secure the pitot tubes.

Figure 6.17 Initial isokinetic duct test configuration.

6.4.3 Flexible Duct Flow Testing

Further testing was performed to understand the effect of flexible duct on system velocity losses. Flexible duct is used for the vacuum exhaust system and filtered air return system. As a result, all original 1.5 inch diameter flex hose, used in phase 2 and 3 testing, was replaced by 2.5 inch nominal diameter flex hose and optimized to the minimum length for the configuration. This also included relocation of the inlet HEPA filter to a position within approximately 100 mm of the enclosure such that it traveled with the enclosure on the HAAS machine bed. Losses were studied at points from the inlet nozzle to the shop vacuum source using. Quick measurements for relative performance indication were made using the wind vane anemometer, with pitot tubes used for measurements within the duct. A 20 Amp Variac, variable transformer, was also used to test the effect of shop vacuum performance levels by varying motor speeds. Figure 6.18 includes photographs of some of the typical testing that was performed to optimize system performance. Additional results are included in Appendix I.

Figure 6.18. Typical flow rate testing configurations

To resolve the problem of a stationary vacuum inlet duct, a flexible inlet was attached to the membrane upper support plate on the machine spindle. This serves as a pass through from the enclosure to the outside for the exhaust dust and provides a stationary mounting point for a flexible duct that will travel at a fixed distance relative to the cutting tool. A custom fitting was machined to attach sections of 2.5 inch Loc-Line® modular hose to a tube welded in the membrane upper support plate and secured with a hose clamp. The Loc-Line® modular hose provides flexibility to position the inlet of the exhaust duct at a location adjacent to the rotating cutting tool to capture maximum dust. Care must be used to check machine travel during the cutting operation to avoid hitting the Loc-Line® with the workpiece or fixture. Further opportunities exist to improve inlet geometry of the exhaust vacuum for maximum particle collection efficiency. Using the Loc-Line® hose as-is was found very effective for the edge trimming operation where very little visible dust was left in the chamber, however, it was not as effective for follow-on slot milling tests where sizeable particles and chunks were not captured by vacuum as they tended to get trapped in the slots. Performance can be improved through vacuum inlet nozzle optimization using a variety of additive manufacturing techniques and materials.

Loc-Line Modular hose was connected through a mounting plate in the dust containment box which could be positioned to maintain a fixed distance from the cutting tool at close proximity. The first series of tests focused on measuring air velocity through the Loc-Line Hose shown in figure 6.19 which had an ID at the inlet of 67.56 mm (2.66 in). Through the use of the Amprobe Vane Anemometer, average velocity was found to be approximately 18.5 m/sec.

Figure 6.19. Loc-Line Modular Hose relative to cutting tool

Understanding velocity was the first part of the process to size isokinetic nozzles. Following assembly of the isokinetic sampling duct, the velocity was measured at approximately 12.4 m/sec using the Amprobe Vane Anemometer in the 4 inch schedule 40 duct. Similar testing was conducted measuring the velocity of the return air through the HEPA filter to ensure flows could be balanced in the dust containment chamber. Velocity through the return air system was measured at approximately 24.8 m/sec at the end of 3" ABS pipe with ID of 77.22 mm (3.04 in). The objective was to ensure that the delivered volume of return air would exceed the volume of exhausted air, as the return air system utilized a balancing valve for containment box equilibrium.

6.4.4 Dust Deputy Testing

As an attempt to remove large "boulders" prior to the dust reaching the instruments, a Dust Deputy® from Oneida Air Systems was tested. Boulders are simply large particles. If successful, this system would have been placed in between the enclosure and isokinetic test duct to remove large particles and preserve the HEPA filters in the shop vacuums as the boulders would be captured in a waste bucket. The Dust Deputy® is a cyclone system capable of removing large particles and typically used for wood working applications. Much smaller precision cyclones are used for particle separation for the real-time instrumentation including the PDR DataRam and Casella Microdust Pro. In conversation with Oneida Air Systems, they claimed particles greater than about 50 μm could be captured, but the results were not confirmed.

In the testing performed, the Dust Deputy® captured large particles nicely, but the velocity losses were too significant for the configuration reducing relative flow velocity from about 24 m/sec to 15 m/sec. The Dust Deputy® remains a handy tool for a shop and could possibly be incorporated in a future system with higher flow rates. Figure 6.20 are photographs from the Dust Deputy® testing.

Figure 6.20. Dust Deputy® testing

6.5 Horizontal Isokinetic System Test Results

With the basic flow system analysis and revised configuration complete, a series of initial isokinetic tests using the GRIMM 1.109 and isokinetic nozzle were conducted using the duct in the horizontal configuration, parallel to the floor. A TSI PTRAK® 8525 ultrafine particle counter was placed in the chamber to validate dust enclosure performance and Dwyer 166-6CF pitot and Magnhelic® gages measured differential pressure for determining duct velocity. A multi-directional composite laminate was edge trimmed using two cutter types. The results showed a very consistent particle count for each cutter pass. This indicated that the nozzle traveling with the cutter was helping to provide consistent results. Enclosure particle counts from the PTRAK were very low indicating the enclosure was performing well and the large majority of dust was being captured by the vacuum system. There were no visible particles in the chamber after the experiment. However, there were some issues. First, after the duct was disassembled for inspection following the test, there was a significant coating of fine dust on all components, especially the plastic components (end fittings, tee). There were also some piles of collected dust in the horizontal duct. This indicated a significant amount of static attraction for the particles and some inefficiency of the vacuum system for removing particles along a 2m horizontal duct. More significantly, the GRIMM produced very consistent results; however, they

were at approximately 10,000,000 counts/liter. The GRIMM has a spec concentration limit of approximately 2,000,000 particle/liter so this needed to be addressed. The high concentration could be indicative of coincidence error where a particle enters the sensing zone while the previous particle is still being processed. The coincidence error increases with increasing particle concentration. While a mostly successful series of tests, further work on the test configuration was required. Figure 6.21 is a schematic of the initial horizontal isokinetic test configuration and figure 6.22 are photographs from the first isokinetic test.

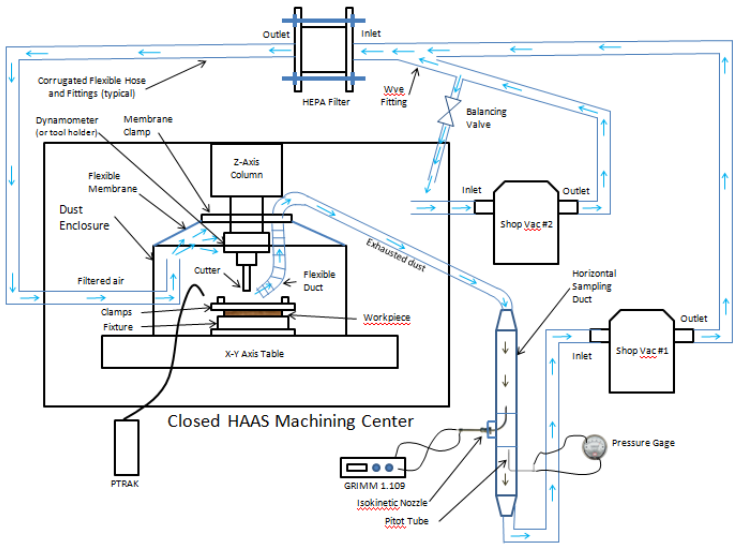

Figure 6.21. Initial isokinetic test configuration (horizontal duct)

Figure 6.22. First horizontal isokinetic test

The first isokinetic tests were conducted with the duct in the horizontal position using the GRIMM 1.109 and GRIMM 1.152 isokinetic probe and 2 mm diameter nozzle with range from 4-8 mm/sec, assuming a duct velocity of 8.2 m/sec. For these series of tests, the duct velocity was calculated from the following procedure using the Amprobe wind vane anemometer:

1) Close dust containment enclosure door
2) Turn on vacuum and return air systems and use balancing valve to achieve flexible membrane equilibrium.
3) Remove dust enclosure door and attach calibration pipe to Loc-Line flexible hose. Calibration pipe diameter is 77.27 mm (3.042 inch). Figure 6.23.
4) Measure air velocity (V) at calibration pipe opening
5) Calculate air flow rate, Q, ($Q=VA$, $A = \pi d^2/4$, d = calibration pipe diameter)
6) Calculate velocity (V) at location of isokinetic nozzle in duct using, Q. Duct diameter is 107.95 mm (4.25 inch). $V = Q/A$
7) Select isokinetic nozzle based on estimated velocity (V) of duct diameter where nozzle is located.
    - 3.0 mm 2 up to 4 m/s
    - 2.0 mm 4 up to 8 m/s
    - 1.5 mm 8 up to 16 m/s
    - 1.0 mm 16 up to 25 m/s

Figure 6.23. Velocity measurement of calibration pipe

The volume of air at the inlet to the exhaust system was assumed to be the same at the isokinetic nozzle position in the duct. This approach to estimate air velocity was initially used due to problems with Sper Scientific 840098 meter and Dwyer DS-300 averaging pitot tube. The final configuration to be discussed in the following paragraphs used Dwyer 166-6-CF pitot tubes

and Magnelic gauges for direct measurement in the duct. The pitot tube air velocity readings were found to be lower than those from the Amprobe.

The TSI PTRAK was used to measure background particle count in the enclosure to evaluate dust collection efficiency using just the standard Loc-Line vacuum tubing open end. No custom exhaust vacuum nozzles were utilized; simply the open end of the Loc-Line hose captures the dust. This proved efficient for edge trimming with typical PTRAK background counts in the dust enclosure less than approximately 600 counts/cc (room background is approximately 3000 counts/cc). However, design of an optimal exhaust nozzle would be a future improvement with the goal of 100% particle capture at the source. Figure 6.24 are photographs of the test configuration. Four tests were conducted using this initial configuration with the conditions noted in table 6.6. These were the same configuration of tests run originally for the GRIMM to compare results of isokinetic testing (probe in a horizontal duct) to those from phase 3, where the GRIMM inlet tube was in the containment box. Results from the four initial isokinetic tests are included in figure 6.25.

Figure 6.24 GRIMM and PTRAK for first isokinetic test

Table 6.6. First isokinetic test conditions

#	Laminate Orientation	Cutter or Test Description	Cutting Orient.	# Pass	RPM	Feed (mm/ min)	Radial Depth of Cut (mm)	Axial Depth of Cut (mm)
1	Multi-directional	Carbide 4 flute,12.7mm, top	Climb	15	6000	0.635	0.762	6.35
2	Multi-directional	Carbide 4 flute,12.7mm, lower	Climb	15	6000	0.635	0.762	6.35
3	Multi-directional	CVD 4 flute,12 mm, top	Climb	11	6000	0.635	0.762	6.35
4	Multi-directional	CVD 4 flute,12 mm, bottom	Climb	11	6000	0.635	0.762	6.35

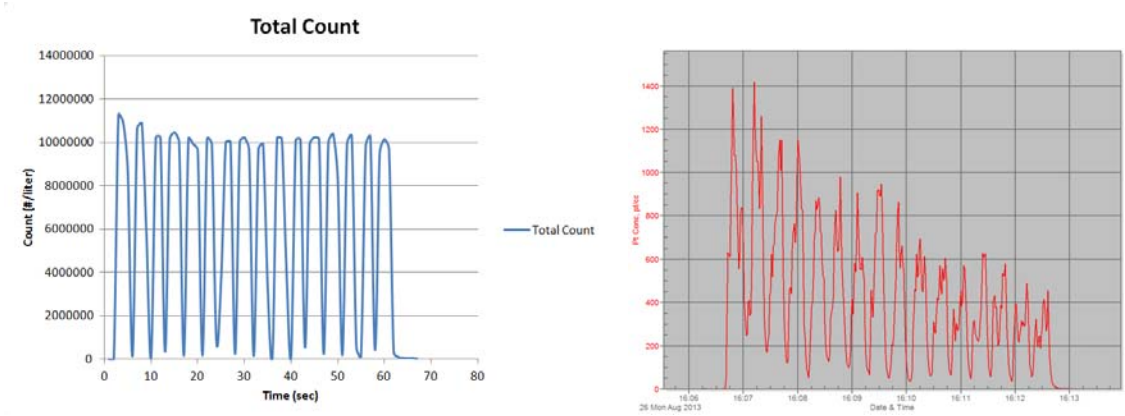

Test 1: GRIMM total particle count, and PTRAK concentration in enclosure

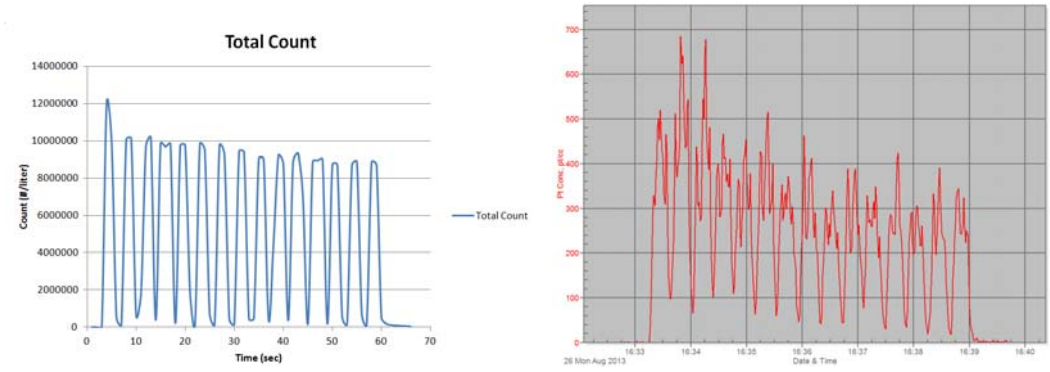

Test 2: GRIMM total particle count, and PTRAK concentration in enclosure

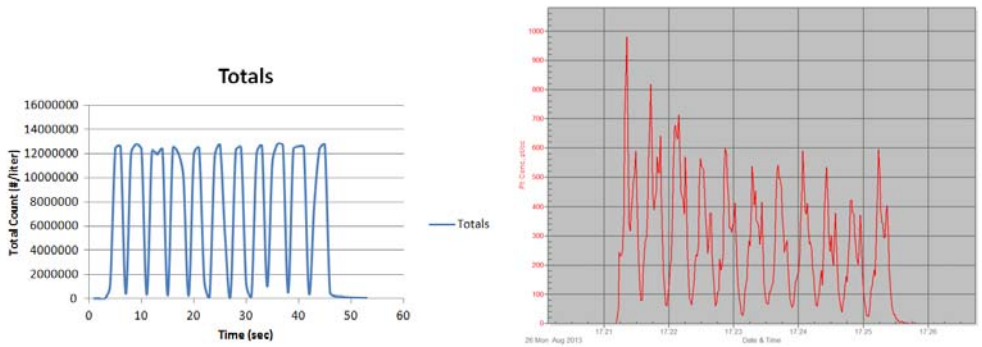

Test 3: GRIMM total particle count, and PTRAK concentration in enclosure

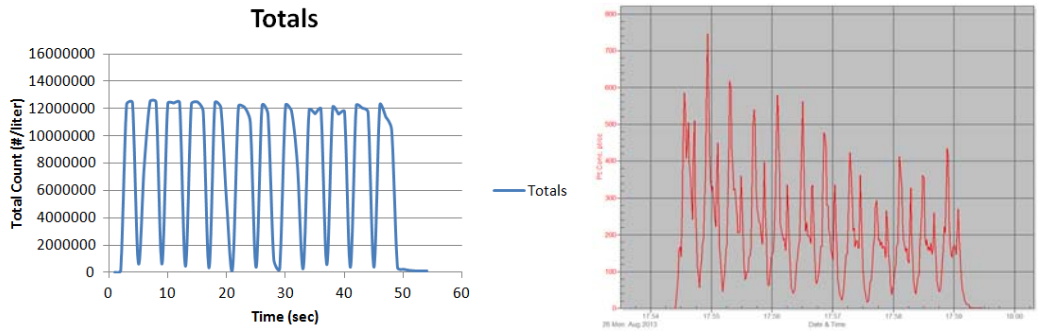

Test 4: GRIMM total particle count, and PTRAK concentration in enclosure

Figure 6.25. Initial GRIMM and PTRAK isokinetic test results.

These tests demonstrate steady peaks at each machining pass of the laminate consistent with the standard containment box testing protocol. Total counts are approximately double in the isokinetic test from the phase 3 containment box tests likely due to a larger number of particles being counted, and the concentration curves appear to be flat, with each peak at a maximum. The background PTRAK counts are very low, less than approximately 2% of the phase 3 containment box tests and between ¼ - $^{1}/_{3}$ of typical ambient tests, indicating the improved efficiency of the Loc-Line nozzle configuration for capturing dust and effectiveness of the HEPA filtered return air for purging the system. An important concern that was validated is that the dust concentrations are very high, exceeding the limits of the GRIMM 1.109 instrument, and indicating the need for dilution to stay within the measurement range of the instrument. A significant amount of dust was found in the duct. This suggested an orientation change for the duct from horizontal to vertical to use gravity to help move the larger particles or "boulders" into to the shop vacuum.

6.6 Vertical Isokinetic System Test Results

Several improvements were identified from the first series of isokinetic tests. First, the entire system was re-designed to be fully electrically conductive to minimize any static build up. The system has 3 PVC components with 2 reducing end fittings and a tee fitting that is used to mount the GRIMM isokinetic nozzle. All 3 PVC fittings were covered in heavy aluminum tape so no plastic is exposed. Brass sheet stock was carefully located in the tee fitting with a close fit hole for the GRIMM nozzle so that it appears as continuous pipe when looking down the end. In addition to providing conductivity, it also removed a possible turbulence condition as there is now no access to the perpendicular volume within the tee fitting. An aluminum riser tube and an aluminum cap were machined to mount the GRIMM nozzle replacing the ABS components. Flexhaust® FlexStat static dissipative vacuum hose was used to connect the aluminum duct to the shop vacuum and the membrane support plate to the aluminum duct. This hose has a smooth interior to minimize material build up and is formulated from a static dissipative thermoplastic polyurethane with an embedded copper grounding wire. All hoses have custom machined aluminum fittings and are attached with stainless steel hose clamps on either end, with geometries optimized for flow in and out of the duct. The Loc-Line® Modular hose was replaced with an anti-static version to minimize particle adhesion at the source.

With the material system revised to address static electricity effects, the next challenge was to address particle build up in the horizontal duct. A support structure was fabricated to mount the entire isokinetic tube assembly vertically at the back of the HAAS mill. Additional flow testing was performed to minimize the required length of the rigid duct. Constraints such as upstream and downstream minimum ratios from pitot tube inlets were design considerations. Two pitot tubes at different locations were installed to ensure consistent flow velocity. With the duct in the vertical orientation, large “boulders” will tend to fall due to gravity and be more easily captured in the shop vacuum. With the duct in the vertical configuration, copper wires were connected at the flexible membrane mounting plate and at the point of connection to the shop vacuum. A Fluke multimeter was used to validate complete system conductivity. Both wire ends were then attached to a building ground. Figure 6.26 is a schematic of the isokinetic sampling tower. The exhaust from the dust collection vacuum and inlet to the blower vacuum

are both located in the HASS machine envelope for closed loop operation, which is not shown to simplify the schematic.

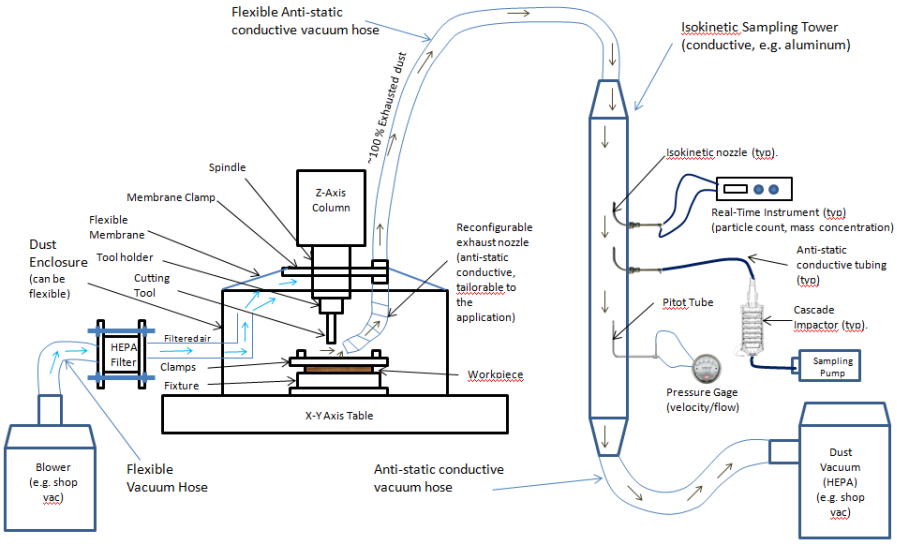

Figure 6.26. Isokinetic sampling tower

To address the high concentration levels with GRIMM 1.109, a diluter was incorporated into the system. A Topas DIL 550 diluter with a 10:1 dilution ratio was factory calibrated and plumbed with conductive tubing and custom machined fittings between the GRIMM isokinetic nozzle and GRIMM aerosol spectrometer. An aerosol diluter reduces the particle concentration of high-concentration aerosols providing a representative sample that meets the requirements of the instrument with minimal particle loss. Calculations were done to estimate the life of the HEPA filter in the diluter. Based on these calculations, filter life was estimated at approximately 500 hrs of use in heavy concentration. The filter life calculations are provided in Appendix J. Diluter testing was conducted to verify that the diluter reduced the particle counts within the specification range of the GRIMM instrument. Figure 6.27 are photographs of the initial diluter tests conducted on the isokinetic sampling tower.

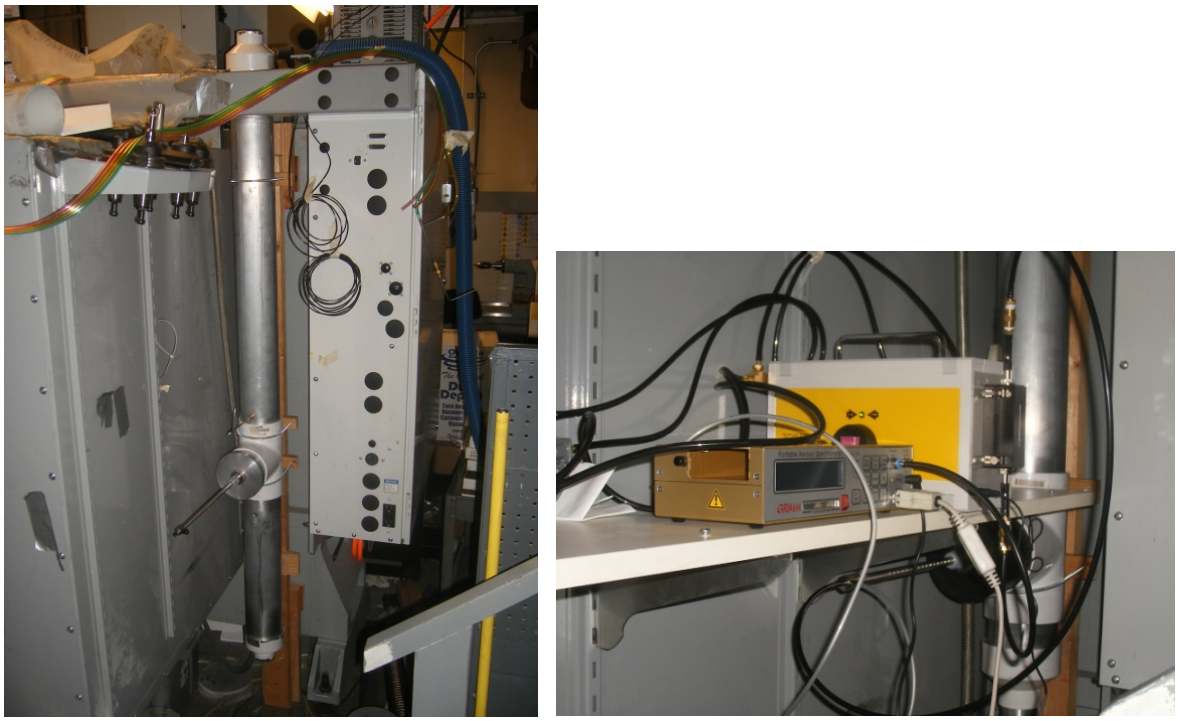

Figure 6.27. Diluter testing in vertical isokinetic configuration

For the next set of tests, a Topas DIL 550 diluter with a 10:1 dilution ratio was used with the GRIMM 1.109 and 1.502 isokinetic probe. The duct was moved from horizontal to vertical and a Dwyer 166-6-CF pitot tube was connected to a Magnelic® gauge for direct velocity measurement in the duct very close to the isokinetic nozzle location. Two tests were conducted repeating, tests 1 and 2 of the initial isokinetic series from table 6.6. In this configuration, the Magnehelic Gage indicated .35 in H_20, corresponding to 12 m/sec, almost 50% higher than the prior test. Because of this higher velocity, a 1.5 mm diameter nozzle with flow velocity range from 8 to 16 m/sec was used with the 1.502 isokinetic probe. The two repeated tests are identified in table 6.7 and the results are provided in figure 6.28. A comparison of the initial two tests from figure 6.25 are included to contrast the effects of dilution. The diluted concentrations are generally less than 2,000,000 particles/liter, within range of the GRIMM 1.109. Also, the trend curves tend to shift, indicating the measurements are not capping out. It should be noted, that these are the diluted values. The diluted particle count and mass concentration values are now multiplied by 10, the dilution ratio, indicating actual particle count concentrations at over 20,000,000 particles/liter. Discussion on the distribution will be covered in Chapter 10 and software for interpreting the results will be presented in Chapter 8.

Table 6.7. Initial diluter test conditions

#	Laminate Orientation	Cutter or Test Description	Cutting Orient.	# Pass	RPM	Feed (mm/ min)	Radial Depth of Cut (mm)	Axial Depth of Cut (mm)
1	Multi-directional	Carbide 4 flute,12.7mm, top	Climb	15	6000	0.635	0.762	6.35
2	Multi-directional	Carbide 4 flute,12.7mm, lower	Climb	15	6000	0.635	0.762	6.35

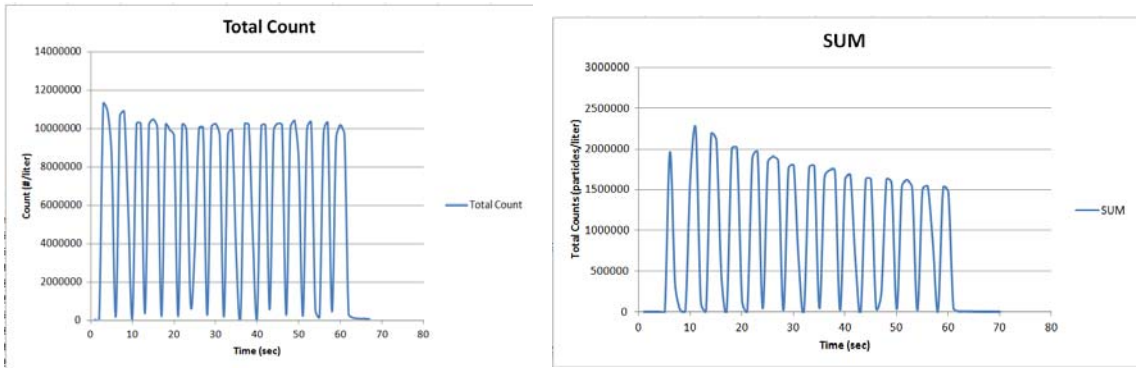

Test 1: No dilution (left) with dilution (right)

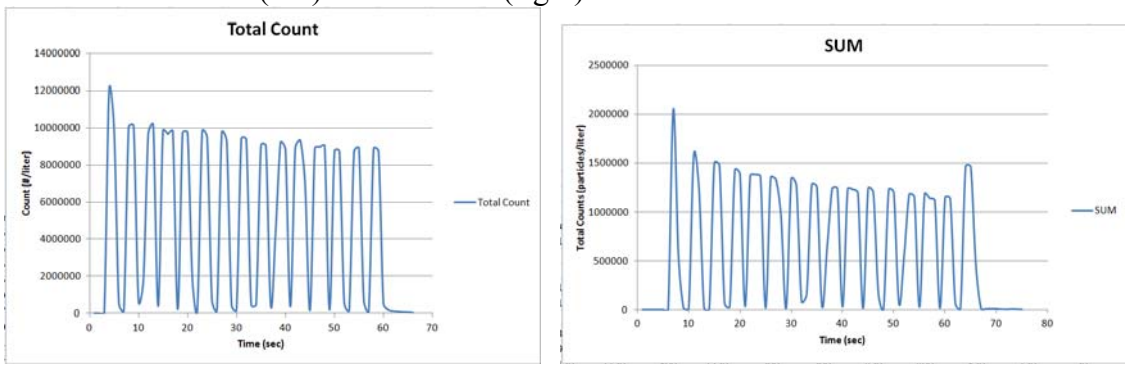

Test 2. No dilution (left) with dilution (right)

Figure 6.28. Isokinetic test comparing dilution to no dilution.

With the GRIMM now performing as expected with the use of a diluter in an isokinetic configuration, the next series of experiments involved incorporating the other real-time particle analysis instruments into the isokinetic sampling system. Some limited manufacturer data was available for using the PDR DataRam and Microdust Pro CEL-712 in an isokinetic configuration with relevant flow rate information provided. Interestingly, in correspondence with the PTRAK manufacturer TSI, I was told that I was the first to use the PTRAK in an isokinetic configuration, and there was no supporting documentation for use of the instrument in this manner.

6.7 Multi-Instrument Isokinetic Testing

To incorporate additional real-time particle analysis instrumentation and cascade impactor in the dust sampling tower, additional isokinetic nozzles were fabricated. Nozzles were designed and built for the Sioutas cascade impactor, TSI PTRAK, Thermoscientific PDR DataRam, and Casella Microdust Pro CEL-712. The primary nozzle diameter is sized to satisfy isokinetic conditions. The flow rate, Q, is determined by the flow requirements of the instrument. The velocity, V, is determined by the duct velocity which in turn is a function of the system, including duct, tubing, and shop vacuum. The velocity was carefully tested several times and measured using two pitot tubes and Magehelic® gages. In its final form, duct velocity was commonly measured at 7.87 m/sec corresponding to 0.15 in H_20 on the Magnehelic® gages. This value was easy to remember because of a certain airplane. Per Dwyer, the equation for calculating air velocity is $V = 1096.2(Pv/D)^{1/2}$, where Pv equals the differential pressure measured in inches of H_20 and D equals air density in lbs/cubic feet. At 70 ^oF and 29.9" barometric pressure, the density of air, Pv, is 1.201 kg/m^3 (0.075 lb/ft^3). With Q = VA, Area, $A = \pi d^2/4$, solving for diameter, d, provides the nozzle diameter. The closest size drill bit was used to bore the nozzle hole. If an exact drill diameter was not available, generally, the closest undersized drill was used. Table 6.8 summarizes the nozzle design parameters for the dust sampling instruments.

Table 6.8. Nozzle design parameters

	Input		Output		Nozzle Hole			Conductive Tubing	
Device	**Flow Rate (lpm)**	**Velocity (m/s)**	Nozzle dia (mm)	Nozzle dia (in)	Drill (ID)	Drill (in)	Drill (mm)	Tube OD (in)	Tube ID (in)
GRIMM	**1.2**	**7.87**	1.799	0.0708	#50	0.07	1.778	0.236	0.157
PTRAK	**0.7**	**7.87**	1.374	0.0541	#54	0.055	1.397	0.236	0.157
Sioutas Impactor	**10**	**7.87**	5.193	0.2044	#6	0.2044	5.19176	0.5	0.375
Casella Microdust Pro	**3.5**	**7.87**	3.072	0.1209	#31	0.12	3.048	0.375	0.25
PDR DataRam	**4**	**7.87**	3.284	0.1293	#30	0.1285	3.2639	0.375	0.25

The tip of the nozzle was nominally angled at 15^o with a knife edge. Similar nozzle designs can be found in ISO 12141 [117]. Nozzle bodies were built from 316 stainless steel tubing. The tubing was sized to accommodate standard threads depending on the nozzle diameter. The threads and nozzles were designed so they could be screwed all the way down into the nozzle body with no gaps, thus requiring thread reliefs. The nozzle body tubing was also designed to fit standard size conductive tubing so the nozzle body ends were machined

accordingly. The length was designed so the nozzles could be radially inserted in the duct without falling all the way in with sufficient length on full insertion so they could be gripped, pulled, turned, and centered in the vertical duct. The nozzle tube bodies were formed with radii determined by available manual tube benders. The tubes were filled with sand during bending to avoid collapsing them and then cleaned. All tube body machining was done prior to forming. Shelves were built on the back side of the HAAS mill to safely store the instruments as well as minimize conductive tubing lengths and paths to the nozzle bodies mounted in the vertical duct from the instruments. Locations for the nozzles in the sampling duct were determined in such a way to provide a minimum of 4 diameters distance from the duct inlet, with linear and radial spacing to minimize flow interference between sampling devices. Nozzles were installed in threaded holes in the duct and held in place by compression fittings. Nozzle spacing and orientation was verified by removing the inlet reducing fitting from the top of the vertical duct, illuminating the inside of the duct with a light and visually inspecting the isokinetic nozzles to ensure they were parallel to the flow of the duct and in the desired position. Figure 6.29 are photographs of the custom isokinetic nozzles and bodies built for the real-time particle counting instrumentation and Sioutas cascade impactor. Figure 6.30 is an illustration of a view looking down the vertical duct at the nozzle tips with typical nozzle tip geometry. Nozzles are located at different vertical positions in the duct and can be adjusted as needed by simply installing additional tapped holes for changing vertical and/or radial positions, pushing or pulling the tube bodies to adjust depth in the duct, and rotation of the tube body for flow path alignment.

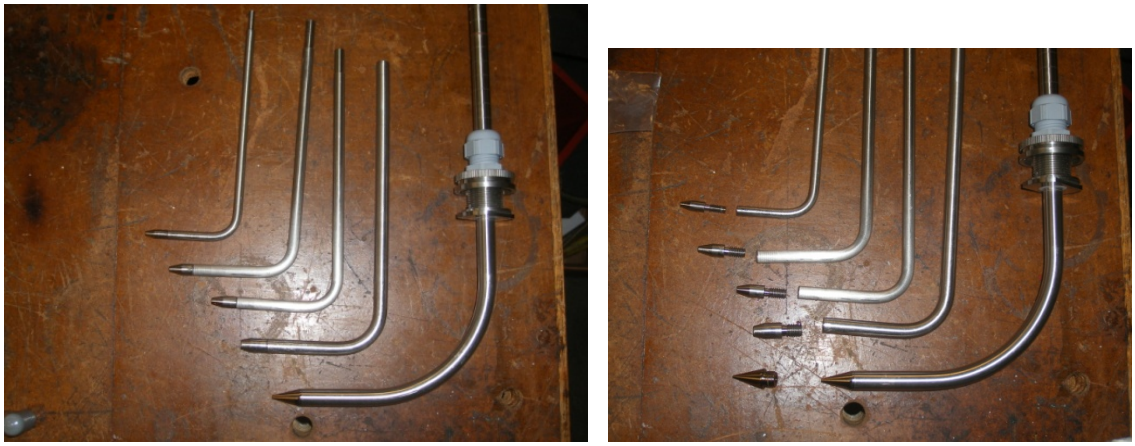

Figure 6.29. Isokinetic nozzles and bodies

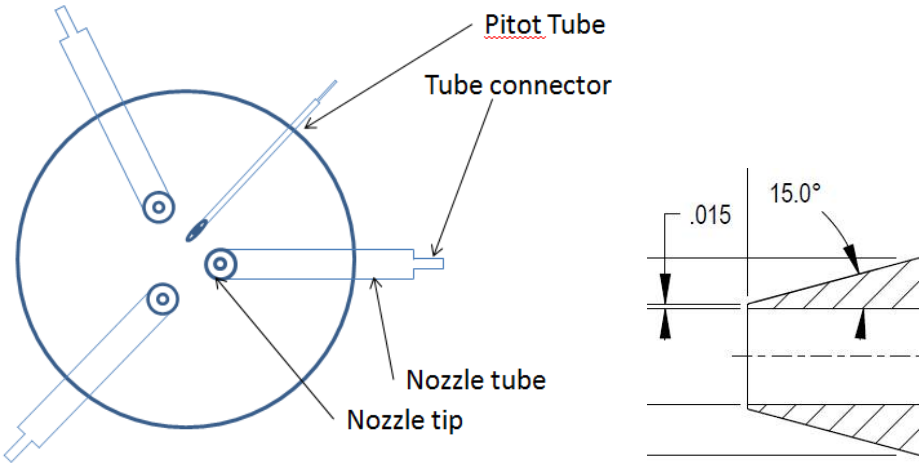

Figure 6.30. View looking down duct at nozzles and typical nozzle tip

Several series of experiments were conducted to verify performance of the real-time instrumentation in the vertical isokinetic sampling configuration. To create the vacuum source for the Casella Microdust Pro and PDR DataRam instruments, the phase 2 vacuum manifold was used. For the Microdust Pro a tube was connected from the vacuum manifold to a needle valve. The needle valve was then connected to a rotameter which was used to monitor the flow rate from the instrument. The rotameter was connected to the filter holder on the instrument. The filters are used to capture dust for subsequent analysis such as SEM as well as prevent dust from entering the vacuum system. The needle valve was adjusted to provide a flow rate of 3.5 lpm for the Casella Microdust Pro. The critical orifice originally used for the Sierra instruments 210 impactor was used to provide a flow rate of 4.4 lpm for the PDR DataRam. Some reorganizing of instruments was necessary to optimize spacing to minimize tube length. It took a few iterations and adjustments to ensure all instruments would function correctly and provide valid data. Factors such as nozzle adjustment, filter replacement, remembering to turn on vacuum pumps, and software configuration are factors in making a successful test. Checklists can help to ensure test readiness. Figure 6.31 are photographs of the configuration used for simultaneous testing of four real-time particle measurement instruments. This represents the final configuration of the equipment for this specific research effort. Several opportunities for improvement exist and will be discussed in Chapter 10.

Figure 6.31. Multi-instrument test using isokinetic sampling tower

The first series of multi-instrument tests with the isokinetic tower utilized the GRIMM 1.109, PTRAK, pDR DataRAM 1200, and a new instrument, the Casella Microdust Pro CEL-712. All instruments used custom designed isokinetic nozzles. The Microdust Pro performs a similar function to the PDR DataRAM by measuring particle concentration. The Microdust Pro is a much newer instrument and has a high concentration limit of 2.5 g/m^3. It also can utilize polyurethane foam (PUF) filters or a cyclone for size segregation. Real-time graphing on the instrument also facilitates use. The incorporation of additional instruments further demonstrates the flexibility of the isokinetic sampling approach for particle analysis by the ability to simply add an additional nozzle to the duct. The test matrix for the first series of tests using all four real-time instruments is described in table 6.9. An example of combined results for test #4 is shown in figure 6.32 with additional results in Appendix K. It is well cited that different instruments may provide different measurements. Some correction is possible through the use of custom calibration factors for each instrument. These tests were performed without any calibration to the specific composite dust aerosol. However, the results can be modified by application of calibration factors. This was also an initial configuration of nozzle locations within the duct. Some refinement of nozzle location may also provide more consistent readings as it is possible that some flow interferences occurred. While the concentration magnitudes of the 3 instruments providing concentration measurements differ, the relative magnitudes and timing were very encouraging. Further testing was performed to improve the configuration.

Table 6.9. First Multi-Instrument Isokinetic test series

#	Laminate Orientation	Cutter or Test Description	Cutting Orient.	# of pass	RPM	Feed (mm/ min)	Radial Depth of Cut (mm)	Axial Depth of Cut (mm)
1	N/A	Vacuum only for control case	N/A	N/A	N/A	N/A	N/A	N/A
2	Multi-directional	Carbide 4 flute,12.7mm, top half of lam. (new)	Climb	10	6000	0.635	0.762	6.35
3	Multi-directional	Carbide 4 flute,12.7mm, bottom half of lam.	Climb	10	6000	0.635	0.762	6.35
4	Multi-directional	Carbide 4 flute,12.7mm, top half of lam.	Climb	10	6000	0.635	0.762	6.35
5	Multi-directional	Carbide 4 flute,12.7mm, bottom	Climb	10	6000	0.635	0.762	6.35
6	Multi-directional	Carbide 4 flute,12.7mm, full laminate	Climb	8	6000	0.635	0.762	12.7
7	Multi-directional	Carbide 4-flute, 12mm, full laminate	Climb	10	6000	0.635	0.762	12.7

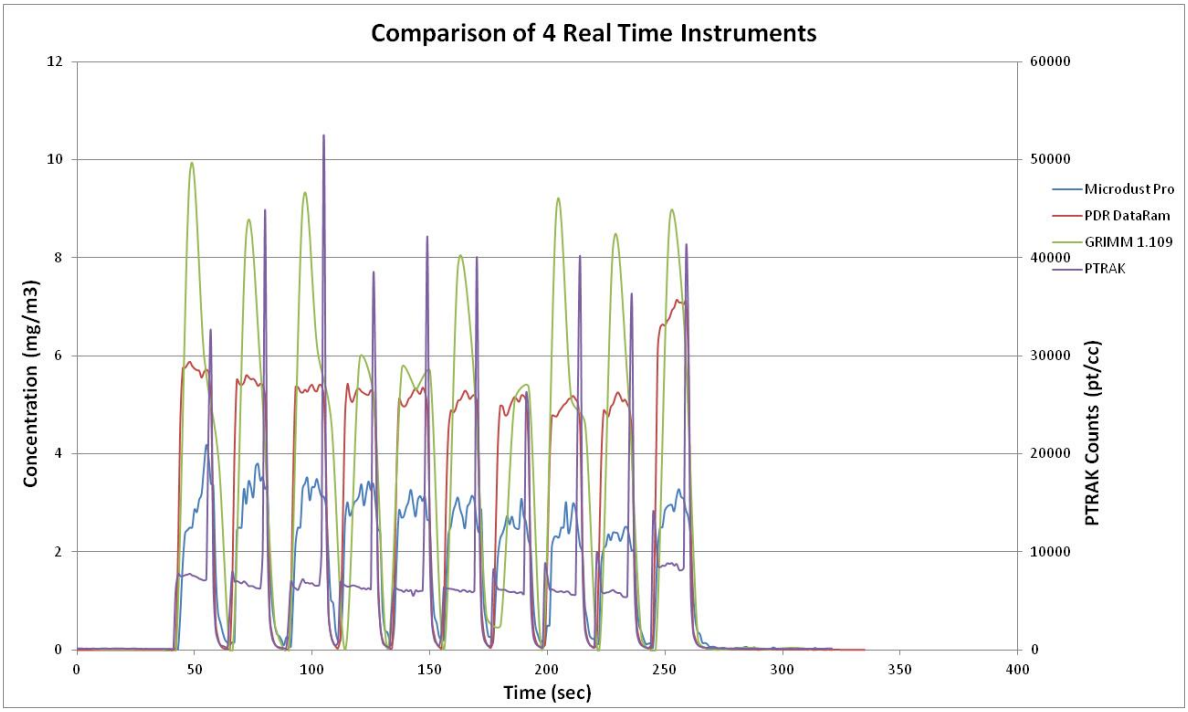

Figure 6.32. Comparison of real-time instruments for test #4.

For the next series of multi-instrument tests, some modifications were made including repositioning of the tower itself to provide more flexibility for nozzle location. By moving the tower, nozzles could be located nearly 270 degrees around the duct. The standard cutting test which had been used for all previous dust generation experiments was replaced by a new cutting

test which automatically performed both a climb and conventional pass. The previous standard test performed either a climb or a conventional pass with the cutting tool returning to the start position, and a manual cycle start executed on the HAAS mill for the following pass. This provided the single dip in the data between each pass. In the new program, a climb pass (left to right) was performed which was immediately following by a conventional pass (right to left) at the same radial depth of cut. This in turn was followed by another climb pass with the cutter advancing by the programmed radial depth of cut. Minimal overshoot of the work piece is programmed. The total number of passes was also programmed, so no manual cycle start interventions were required. The intent of this new cutting test configuration was to generate a relatively steady composite dust aerosol within the limits of the containment box. There is a slight no-cut condition at the start and end of the work piece as the programmed moves were designed to be slightly longer than the work piece. This provides a brief drop in the data as an indicator of end of work piece and change between climb and conventional cutting. Following the first test in this next series, the cyclone was also removed from the PDR DataRAM so full concentration would be measured. The Cyclone was a PM2.5 (BGI GK 2.05). Eight tests were conducted as described in table 6.10. These tests involved different combinations of nozzle positions, instrument positions, and nozzle elevations. For these tests, a cycle includes both a climb and conventional pass at the noted RPM, linear feed rate and respective depths of cut. Figure 6.33 are typical results from the first test of this configuration. From the graphs, the transition between passes is clear with a significant dip in data, and a smaller dip is noted during the change from climb to conventional cutting. The pDR DataRAM, Microdust Pro, and PTRAK, show decreasing trends in particle counts. This will be addressed in Chapter 10 with further analysis of the GRIMM data.

Table 6.10. Climb/Conventional real-time instrument testing (2/27-3/21)

#	Laminate Orientation	Cutter or Test Description	# of cycles (date)	RPM	Feed (mm/ min)	Radial Depth of Cut (mm)	Axial Depth of Cut (mm)
8	Multi-directional	Carbide 4 flute,12.7mm, top of laminate, (new cutter)	7 (2/27)	6000	0.635	0.762	6.35
9	Multi-directional	Carbide 4 flute,12.7mm, bottom, removed cyclone from DataRAM	10 (2/27)	6000	0.635	0.762	6.35
10	Multi-directional	Carbide 4 flute,12.7mm, full laminate, swap Casella, pDR nozzles	9 (3/11)	6000	0.635	0.762	12.7
11	Multi-directional	Carbide 4 flute,12.7mm, (new) , top of laminate	6 (3/20)	6000	0.635	0.762	6.35
12	Multi-directional	Carbide 4 flute,12.7mm, bottom, swap Casella, pDR hoses	6 (3/20)	6000	0.635	0.762	6.35
13	Multi-directional	Carbide 4 flute,12.7mm, full laminate, Casella, pDR at same level	6 (3/20)	6000	0.635	0.762	12.7
14	Multi-directional	Carbide 4 flute,12.7mm, top, (new), Casella moved above GRIMM	2 (3/21)	6000	0.635	0.762	6.35
15	Multi-directional	Carbide 4 flute,12.7mm, bottom, new Casella filter, clean shop vac HEPA	6 (3/21)	6000	0.635	0.762	6.35

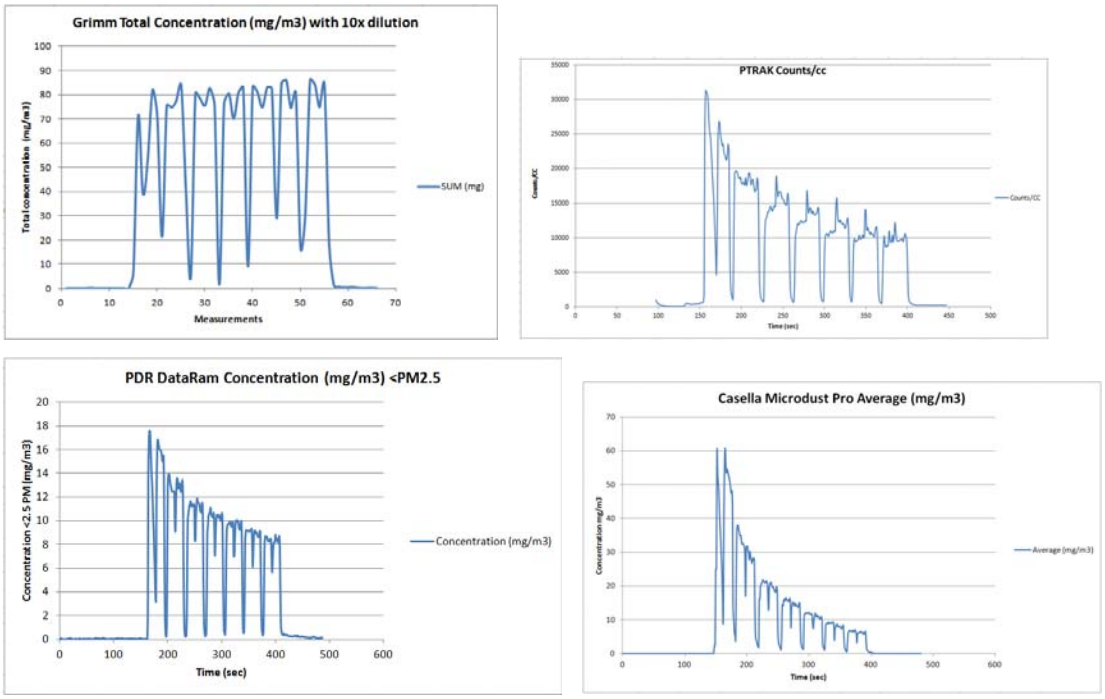

Figure 6.33. Test 6 from climb/conventional instrument test series.

With the isokinetic dust collection system developed in phase 4, primary phase 5 testing returned to focus on the experimental techniques necessary for a model to predict cutting forces when trimming composite materials and is discussed in chapter 7. However, the isokinetic

sampling system developed in phase 4 was used during phase 5 testing to demonstrate the system also worked for composite slot trimming and could be used in parallel to cutting force data acquisition processes. The next section will discuss use of the ioskinetic sampling during phase 5 cutting force development.

6.8 Phase 5 Dust Particle Testing and Results

In phase 5, additional testing of the isokinetic sampling system was performed during the development of the experimental techniques for determining cutting force coefficients which is discussed in great detail in chapter 7. In this test series, five semi-circular slots were machined on a single composite laminate in sequential order from smallest diameter slot to largest with cutting force acquisition by the Kistler rotating dynamometer. Real-time dust collection was performed simultaneously to the cutting force acquisition during three of these tests using both the Casella Microdust Pro CEL-712 and TSI PTRAK with a pause in between each slot on a single workpiece. The purpose was to examine the dust generated from composite slot milling as the previous tests concentrated on peripheral milling or edge trimming. Typical cutting times for these experiments are less than 30 seconds, which provides very few data points for particle analysis. This limited the real-time dust collection instruments to those with 1 second sampling intervals. However, dust collection results were acquired for these short samples, demonstrating the performance of the isokinetic sampling system even with very limited sampling times. Due to the slot geometry, dust collection was not as effective as for peripheral trimming, where there was no slot or "trench" for the dust to collect. This could likely be remedied in the future with a more optimal exhaust nozzle design that is directed at dust removal from relatively narrow slots. Typical nozzle placement for the tests using the black anti-static flexible Loc-Line® 2.5" vacuum hose without any end modifications are shown in figure 6.34. The nozzle was required to be positioned such that it did not interfere with the workpiece, cutting tool, or dynamometer during the tests.

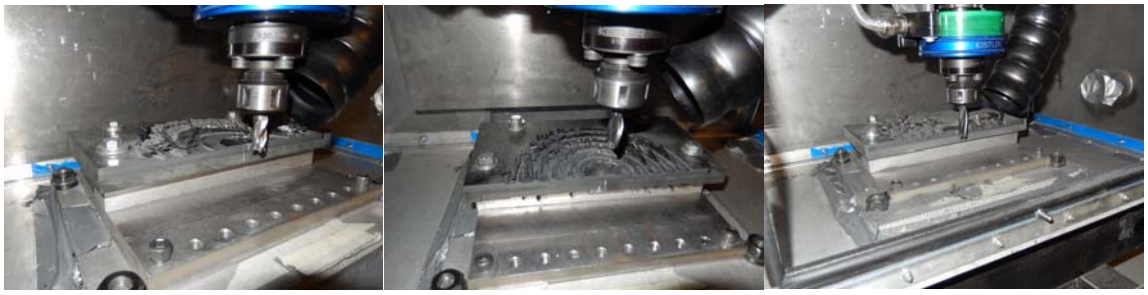

Series 1, 2-flute solid carbide Series 2, 2-flute solid carbide Series 3,4-flute CVD

Figure. 6.34. Typical vacuum nozzle placement for semi-circular slot tests

Data was collected from the PTRAK and Casella Microdust Pro CEL-712 for the first two test series. The units were manually turned on prior to each slot with only the vacuum and return air running to establish a close to zero count (PTRAK) or concentration (Microdust Pro) for approximately 30 seconds prior to starting the cutting experiment. The cutting tests were then conducted which lasted less than 35 seconds. The dust analysis instruments continued to run for up to about minute after the tests to reach close to a zero count which allowed the system to clear out. Data was then logged for each slot experiment. This process was repeated for all five semi-circular slots on the workpiece. The data was then post-processed by first exporting from the instruments in a .txt file and importing into Microsoft Excel. The data from each instrument and respective slot was aligned on a time-basis by first spike which indicated that particles from cutting reached the sensors. The results were then plotted with a separate scale for the PTRAK particle count concentration (pt/cc) and Microdust Pro mass concentration (mg/m^3) on a common graph. Figure 6.35 are results from slot 1 of a 4-flute solid carbide cutter circular slot with 50.8 mm diameter, 2.54 mm depth of cut, 229 mm/min feedrate and total composite cutting time of 27.7 seconds. Figure 6.36 are results from slot 4 of a 2-flute solid carbide circular slot with 146 mm diameter, 2.54 mm depth of cut, 552 mm/min feedrate and total composite cutting time of 27.7 seconds. Results from additional slots of these two test series are in Appendix L. The two figures indicate a similar trend between the real-time instruments where the PTRAK measures count concentration and the Microdust Pro CEL-712 measures mass concentration.

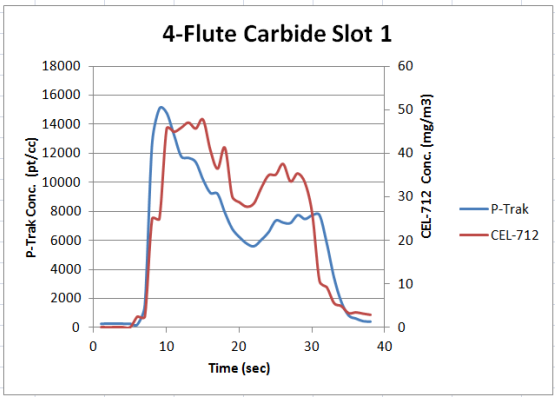

Figure 6.35. 4-flute carbide, slot 1

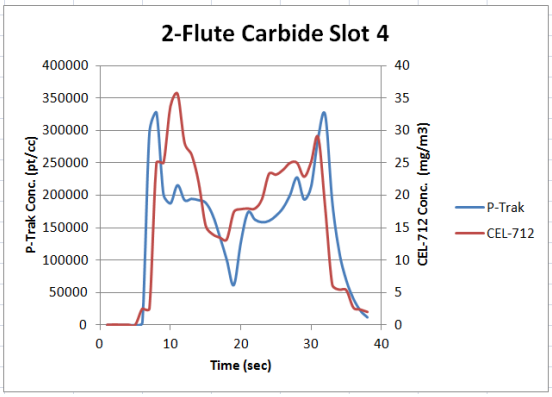

Figure 6.36. 2-flute carbide, slot 4

For the third composite semi-circular slot test series, dust collection was performed in parallel to force data acquisition using the PTRAK as the vacuum source for the Casella Microdust Pro was accidently not turned on, providing no viable data. In this test a Mapal 4-flute CVD diamond coated tool specifically designed for composites was used. The quality of the cut was far better compared to the two prior composite circular slot tests likely because this was a superior cutting tool, which one would hope at about 10x the cost of solid carbide. The higher quality was evidenced by minimal delaminations and uncut fibers compared to the first two series. The time of cut for each of the five slots was also approximately 27.7 seconds, with linear feedrates from 229 mm/min to 660 mm/min with a 5.08mm depth of cut. More details on cutting conditions are in section 7.5 for these tests. PTRAK results from each of the five slots of this series are provided in figure 6.37. As with the first 2 series of composite slot tests, the vacuum was of limited efficiency for clearing all large clumps from the slots. This was even more pronounced as the slots were deeper for this experiment than the prior two. Again, an improved nozzle design, or possibly higher flow rates, could most likely improve efficiency of particle removal for this configuration. A dual peak pattern for the PTRAK was common between the tests. Future experiments could also include a blow out of the tubing and nozzle between slots to ensure no build-up was influencing the results.

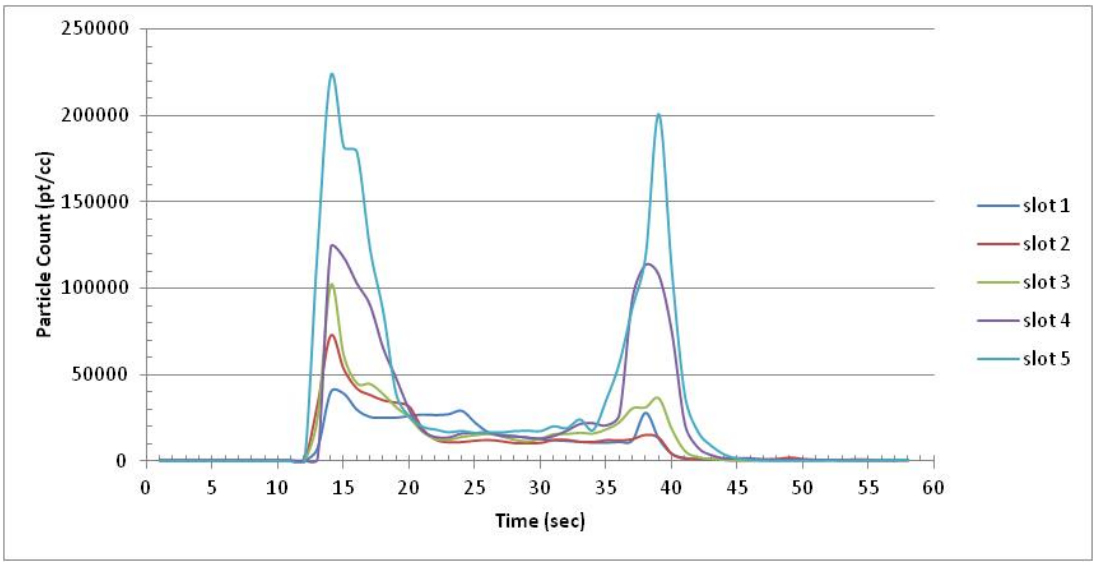

Figure. 6.37. Results from PTRAK for 5 semi-circular slots using 4-flute CVD cutter

6.9 Summary

The results from the development of an isokinetic sampling system for particles produced by dust generating manufacturing processes were presented. This configuration marked a significant change from the initial impactor tests conducted in phase 1 and 2. Phase 3 test results demonstrated that real-time instruments were capable of being used for particle analysis, and provided consistent trends. A limitation of the test configuration was that it likely re-circulated some of the particles and could be influenced by instrument inlet hose location. A further limitation was that the cutter moved relative to the vacuum exhaust inlet position which was another variable for particle distribution in the dust collection containment box. Phase 4 testing consisted of the systematic development of an isokinetic particle collection and analysis system which sampled particles along the exhaust path as they moved from the containment box through a uniform duct to the dust collection vacuum system. Phase 5 testing further demonstrated the capability for dust particle collection and analysis while simultaneously collecting cutting force data for milling of semi-circular slots.

Not only was dust safely contained enabling tests to be performed without risk of exposure, but the development demonstrated the ability to analyze the particles as they travel from the work piece to a dust collection system. This will not only work in a laboratory configuration, but can be applied to almost any machine that utilizes a dust collection system.

This provides the capability to analyze nearly all particles generated from manufacturing processes as well to evaluate dust collection system efficiency. Some challenges were encountered as a result of isokinetic nozzle positioning; however, these can clearly be overcome through nozzle placement tests. Short sampling times using real-time instruments was also demonstrated, with relative consistency between profiles and magnitudes. Further effort is required for individual instrument calibration to specifically match the characteristics of the aerosol. This system configuration provides the opportunity to safely and consistently conduct extensive study regarding the composition of dust generated from composite trimming or other manufacturing processes of interest.

CHAPTER 7

COMPOSITE CUTTING FORCE PROCESS DEVELOPMENT

7.1 Introduction

This chapter discusses the development of experimental techniques for determining milling coefficients used in a cutting force prediction model for multi-directional composite laminates described in chapter 9. Along with the particle collection and analysis development, this one of the two major focus areas for this research effort. Similar to the composite dust focus, the cutting force prediction effort chronologically picks up after the phase 2 machinability experiments and covers the experimental work performed in phase 3-5 of this research as described in chapter 4. The goal of the cutting force development effort was to develop the experimental techniques and mathematical models necessary to predict cutting forces when milling multi-directional composite laminates with a minimum of empirical testing for parameter calibration. Further, the techniques were developed using a Kistler 9123C rotating dynamometer, described in chapter 4, which presented some challenges in providing the level of accuracy and repeatability needed to support the force prediction models. Through extensive testing, techniques were developed that provide relatively consistent data. This chapter will provide the experimental methodology, techniques and test results for development of force prediction capabilities applicable to milling multi-directional composite laminates.

7.2 Phase 3 Cutting Force Testing

From the cutting force data acquired in phase 2 machinability testing, it was evident that there were opportunities for procedural improvements and enhanced analysis for using the Kistler 9123C rotating dynamometer. Obtaining accurate and repeatable data from the dynamometer would be essential to determining accurate milling coefficients to be used in cutting force models for composites. Most published work to date involved the use of stationary dynamometers, so there were few publications for guidance on the Rotating Control Device (RCD) type. In phase 3, testing was performed to compare the results from the rotating dynamometer to a stationary dynamometer and to study the effects of cutter alignment to the rotating dynamometer axes which is intended to correlate 3 different sensors in the unit.

Procedures for tool wear measurement and surface finish measurement were proven out in phase 2 with no further significant effort required on those methods for future work. Acoustic Emission (AE) signals were collected in phase 2 testing and demonstrated alignment to cutting forces; however, further signal processing analysis was determined to be outside of the scope for this specific research effort, but provides an opportunity for further study. For completeness of this research, some additional AE results will be discussed in this chapter to demonstrate consistency of results between composites and aluminum. The focus for phase 3 and following test phases was on refining particle analysis and force modeling processes for edge trimming of composite materials.

Cutting force data from phase 2 testing was analyzed, and while providing insight into differences between varying cutting conditions and fiber orientations, the data was not optimized for use in a model for composite cutting force prediction, or directly comparable to measurements from a stationary dynamometer due to the rotating coordinate system. A series of milling experiments were conducted using aluminum to better understand dynamometer performance and validate relationships for cutting edge alignment relative to dynamometer axes. Aluminum was chosen because it is a homogeneous material and results could be compared to sample data provided by Kistler, the manufacturer. Upon request, Kistler provided laboratory data that was simultaneously acquired using both a 9123C rotating dynamometer and a 9255B stationary plate dynamometer at their facility. This was extremely helpful to test coordinate transformations which were used in later phase testing for cutting force model development. Some additional AE measurements were taken to compare signals from aluminum to those from composite. Figure 7.1 is a photograph of typical aluminum milling tests that were conducted.

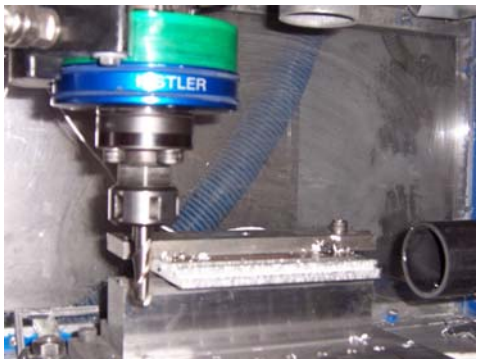

Figure 7.1. Typical phase 3 aluminum milling test configuration.

7.2.1 Cutting Edge Alignment

Cutting forces for all tests were measured using a Kistler 9123C rotating dynamometer. Analysis of the raw data from the phase 1 and 2 investigation showed the tangential cutting forces consistently greater than the corresponding radial forces when edge trimming composite laminates under common cutting conditions. To better understand this, Kistler was contacted, as the tangential cutting force was intuitively expected to be higher than the corresponding radial force. Following some suggestions from Kistler, a series of tests were conducted to compare aluminum and composite results. For the following tests, a 12.7mm diameter, solid carbide, straight, 2-flute cutter was used for both a 6061-T6 aluminum plate and a multidirectional composite laminate. Three conditions were tested for each material including a climb peripheral cut, conventional peripheral cut, and slot cut. The RPM for all tests was 6000. The radial depth of cut for peripheral trim passes was 0.76 mm. The axial depth of cut for the slot test was 2.54 mm. Per suggestion from Kistler, the teeth of the cutter were visually aligned to the Y-Axis of the dynamometer. The raw data from the aluminum cuts and composite cuts are provided in Appendix M. With the cutter aligned to Fy, Fr theoretically equals Fy for a one or two flute cutter, as one tooth is engaged in the workpiece at a time. Since Fr is always positive, the absolute value of Fy is plotted against Fr for both the composite and aluminum cases in figure 7.2. The derived radial force, Fr, approximates the measured Fy value for both aluminum and composites.

Climb Milling

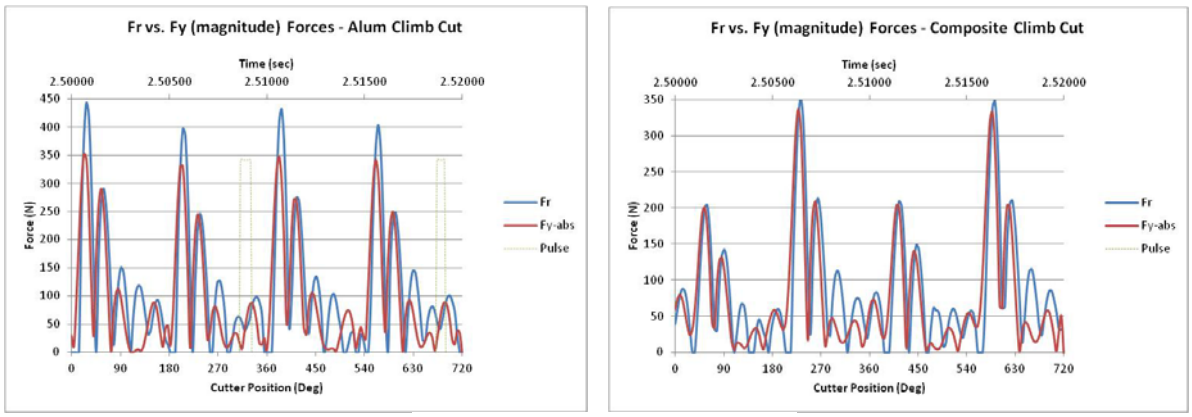

Conventional Milling

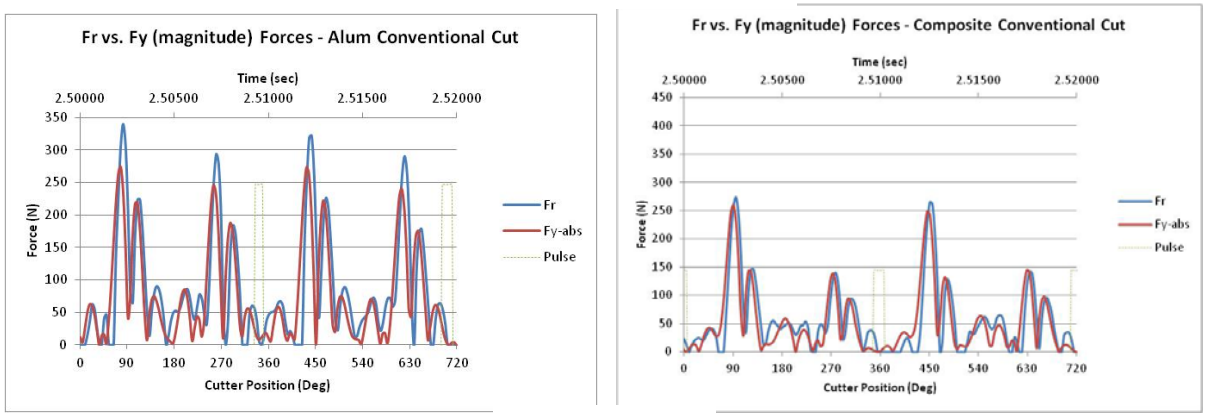

Slot Milling

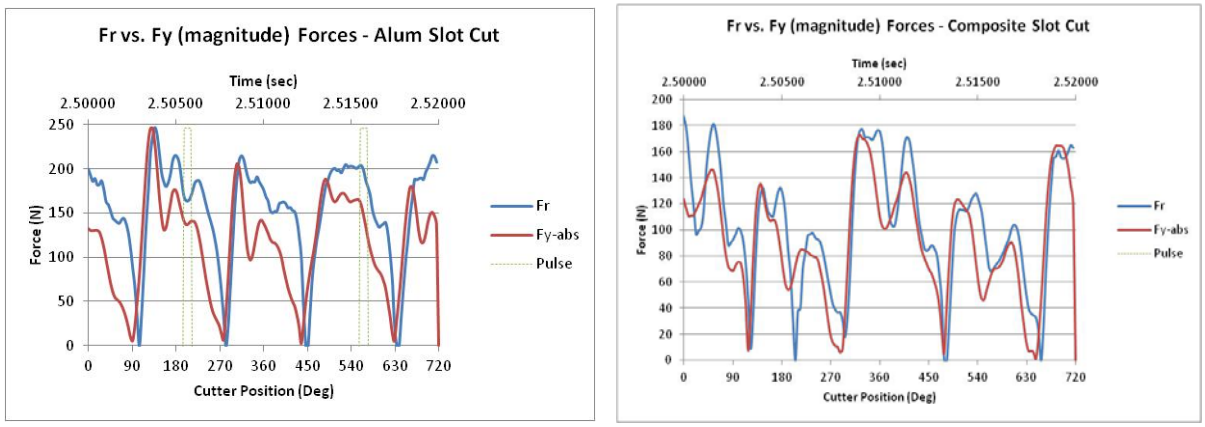

Figure 7.2. Comparison of composite and aluminum cutting forces Fy, Fr

An experiment was conducted to compare results to a published work for machining a 90 degree composite unidirectional laminate under similar conditions to see if a different research group produced similar results when using a Kistler 9123C dynamometer. Karpat [57] used a 2-

flute, 10mm diameter PCD cutter at 3500 rpm with three feedrates including 210, 280, and 350 mm/min on a 90 degree unidirectional composite laminate to mill 3 mm deep slots. Karpat machined under wet conditions to minimize dust. A representative slot milling test was conducted using a 2-flute 12 mm diameter PCD cutter on a 90 degree unidirectional laminate at 2917 rpm, 210 mm/min, with a 3 mm depth of cut. The spindle speed was adjusted to match cutting speeds, since only a 12 mm diameter PCD tool was available at the time, hence the difference between 3500 rpm (10 mm diameter) and 2917 (12 mm diameter). In both cases, a cutting tool edge was aligned to the x-axis of the dynamometer, to follow convention of the paper. The results of the comparison are shown in figure 7.3. The plot on the left are the results from the experiment and the plot on the right is copied from the paper [57]. The results show a similar pattern for Fx, Fy, and Fz, where Fx is several times larger than Fy. With the cutting edge aligned to x-axis, in this configuration, Fx ~ Fr and Fy ~ Ft. This demonstrated that another group was also finding Fr >> Ft. Differences in magnitude can be attributed to different materials and different cutter diameters. Signal drift compensation was not applied to the data.

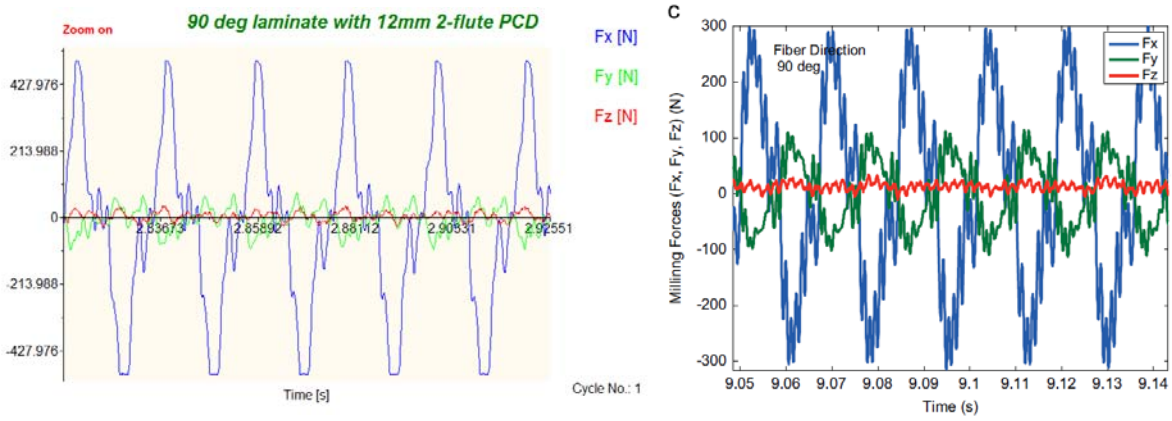

Experiment (left) Karpat [57] right

Figure 7.3. Comparison of 2-flute PCD on unidirectional 90 degree laminate [57].

Acoustic Emission waveforms were also measured as part of this test series for both aluminum and composites. The acoustic emission waveform is plotted with the resultant force for aluminum in figure 7.4 for the three cases. Similar to the results reported in phase 2, the AE waveform peaks at cutter engagement in the work piece.

Climb Milling Conventional Milling Slot Milling

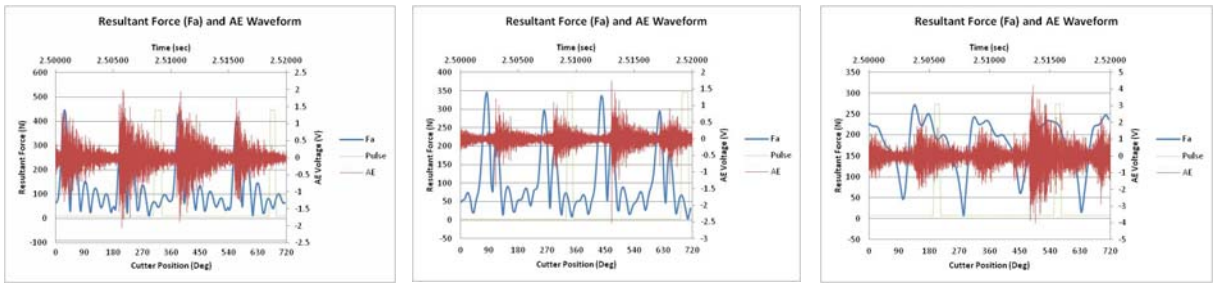

Figure 7.4. AE waveform for aluminum milling

Two sets of additional tests were performed to validate the effect of cutter orientation with respect to the rotating dynamometer coordinate system. Both sets of tests were conducted using 12.7 mm diameter, 2-flute, 30 degree helix, solid carbide end mill. One set of tests was conducted using a 12.7 mm thick aluminum 6061-T6 aluminum plate cantilevered from the workholding fixture using a 12.7 mm diameter, 30 deg Helix, 2-flute high speed steel (HSS) end mill. The other set of tests were conducted using a 76.2 mm thick aluminum block in a Kurt Table Vise using a 12.7 mm diameter, 30 deg Helix, 2-flute solid carbide end mill. Photographs of the fixturing is shown in figure 7.5.

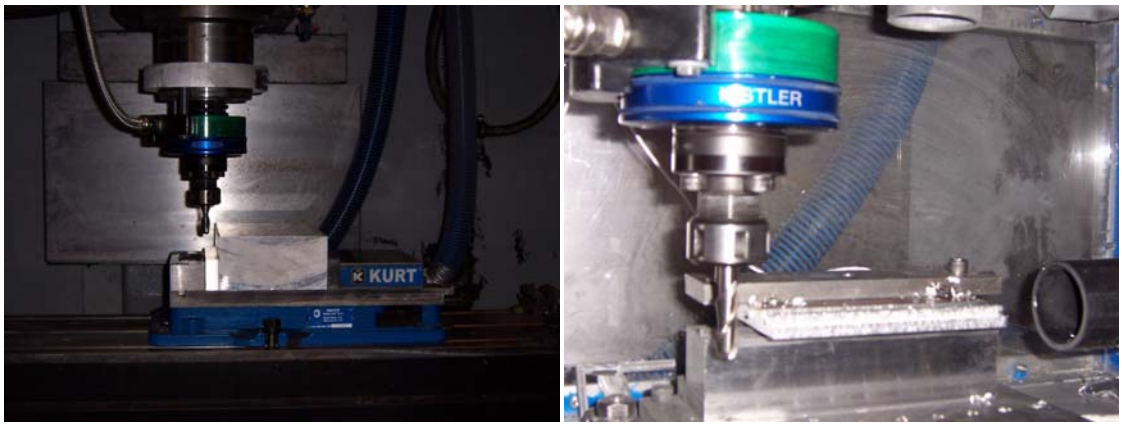

Figure 7.5. Dynamometer cutter alignment testing with aluminum

Milling experiments with combinations of locating the cutting edge to both X, and Y axis of the dynamometer for climb, conventional, and slot cutting were conducted. Figure 7.6 illustrates the cutting edge alignment relative to the dynamometer coordinate system. The tests

demonstrated that when the cutting edge of a 1 or 2-flute cutting tool is aligned to the X or Y axis of the dynamometer, the forces correspond as describe in equations 7.1 through 7.4 such that:

If cutting edge is aligned to dynamometer X-axis then;

$$Fr = abs(Fx) \quad (7.1)$$

$$abs(Ft) = abs(Fy) \quad (7.2)$$

If cutting edge is aligned to dynamometer Y-axis then;

$$Fr = abs(Fy) \quad (7.3)$$

$$abs(Ft) = abs(Fx) \quad (7.4)$$

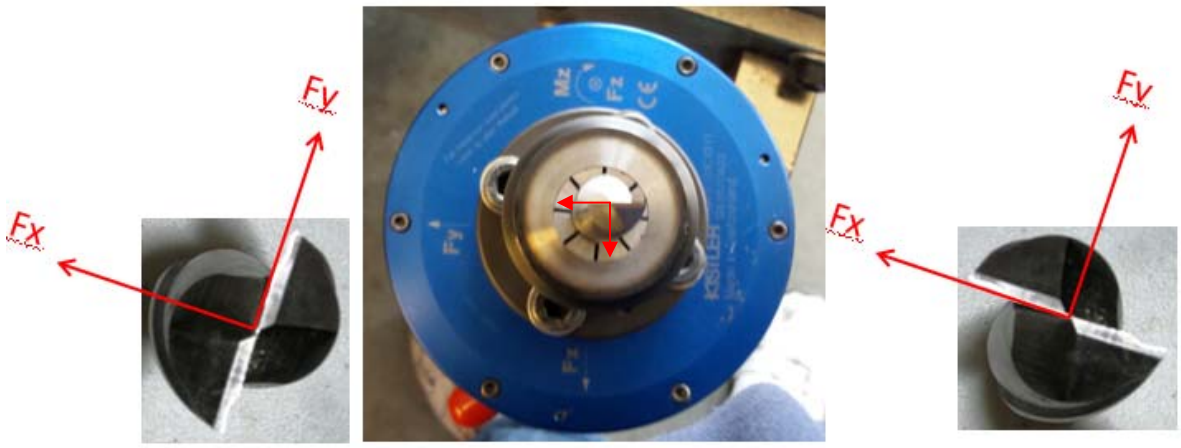

Figure 7.6. Cutting edge relative to dynamometer coordinate system

This is significant as the dynamometer has 3 piezoelectric sensors (Fx, Fy, Mz) that will be used to calibrate the cutting force model. This alignment test provides a way to compare independent sensor measurements during cutting tests. An aluminum peripheral climb milling example where the cutting edge of a two flute cutting tool spinning at 3000 rpm is aligned to either the dynamometer X and Y axis is shown in figure 7.7. Additional examples are included in Appendix N.

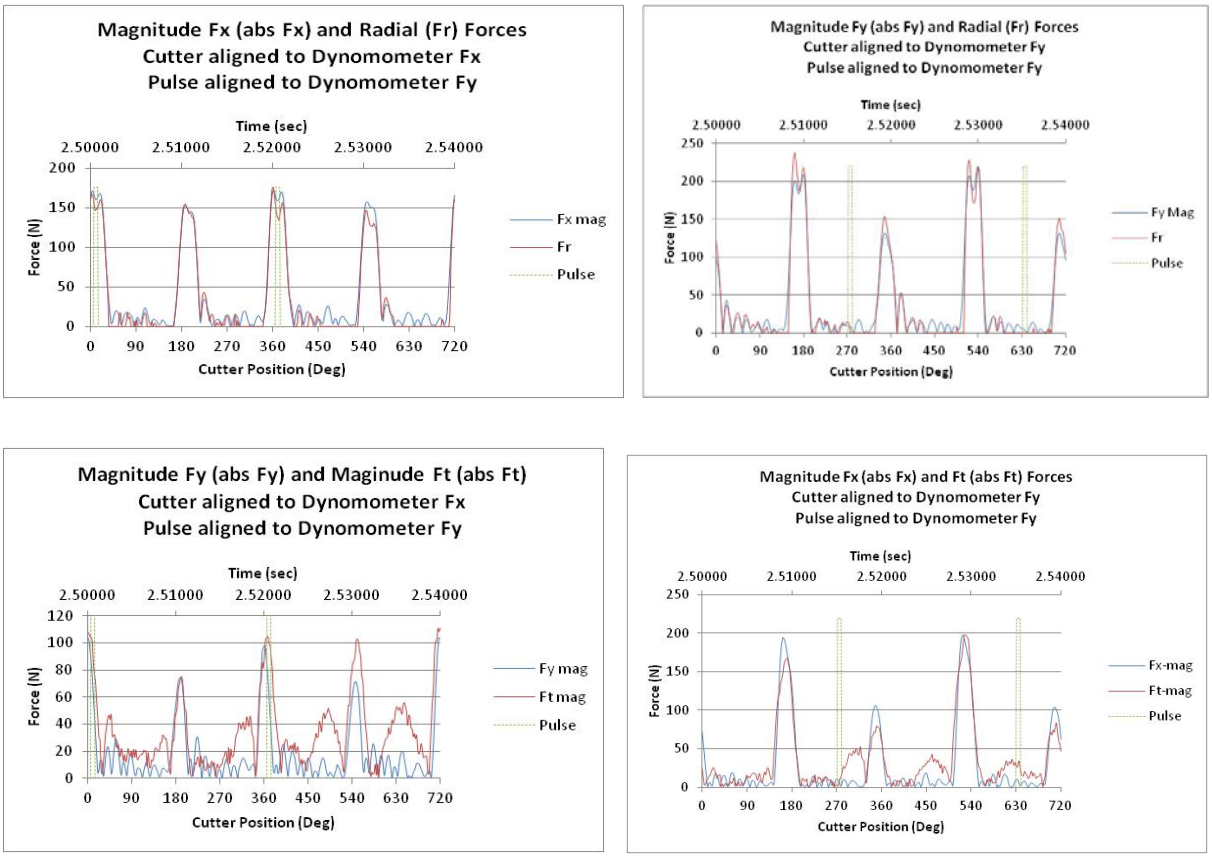

Figure 7.7. Effects of aligning cutting edge to dynamometer axis.

7.2.2 Rotational to Stationary Dynamometer Conversion

Comparing results from a rotating dynamometer with rotating X,Y axes to a stationary dynamometer with fixed X,Y axis is of interest as there is more published data from the use of stationary dynamometers as the rotating types are relatively new. To demonstrate conversion for a limited case, Kistler provided data for a test that was conducted at their facility using both a Kistler 9255B stationary dynamometer and a Kistler 9123C rotating dynamometer simultaneously. Kistler indicated that there was a slight time delay in data acquisition between the instruments. Limited additional information provided was that the test was performed on aluminum using a 12 mm diameter 2-flute cutter rotating at 2000 rpm. Since Kistler previously has aligned a cutting edge with the dynamometer Y-axis, this same relationship was assumed. The first step in the conversion was to find the point in the data by inspection where the 2-flute cutter is perpendicular to the direction of the slot. At this point, Fx, Fy, and the resultant force, Fa, are theoretically zero. This provides a point by which a zero degree angle may be assigned

and the results from the two instruments aligned. The 2000 rpm spindle speed equates to .03 sec/rot. Using this information, each of the 240 measurement points, determined by sampling rate, for one cutter rotation was assigned a corresponding degree. Figure 7.8 is a plot of the raw data from both instruments aligned at the point where Fx, Fy, Fa equals approximately zero. Figure 7.9 is a plot of the resultant forces calculated for both instruments aligned from the same point. The graphs illustrate the different force trends for the same Fx, Fy measurement using different instruments while the resultant forces, Fa, are nearly equal, less the time shift acknowledged by Kistler.

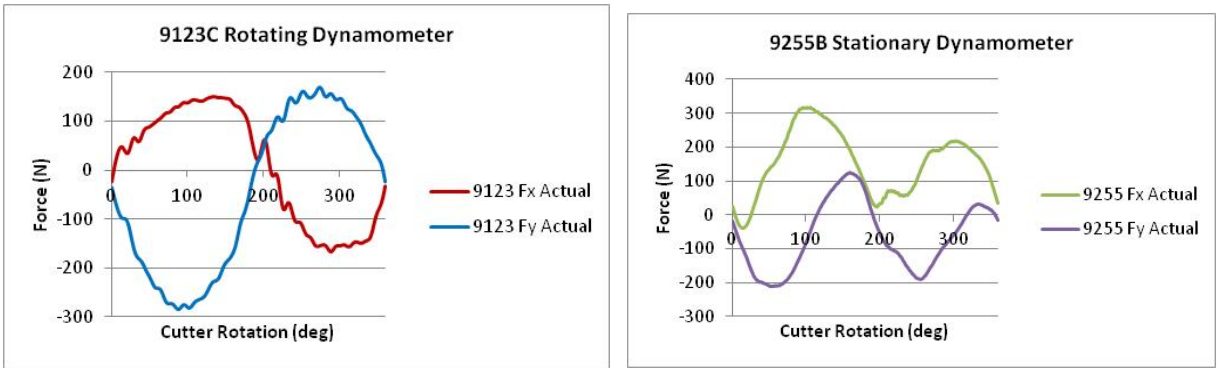

Figure 7.8. Same slot measurement for rotating and stationary dynamometers (Fx,Fy)

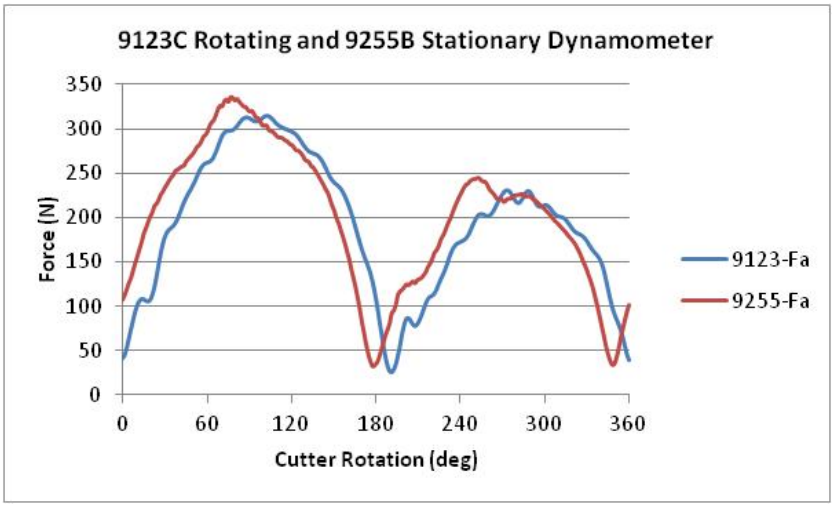

Figure 7.9. Same slot measurement for rotating and stationary dynamometers (Fa)

From a common starting point, the conversion from the rotating coordinate system to the stationary dynamometer coordinate system can be achieved by applying a rotational transformation. In this case, the stationary coordinates remain fixed and the rotational dynamometer coordinates rotate with the cutter. A counter clockwise rotation transformation is

used to convert the rotary dynamometer coordinate system to the stationary system by degree of cutter rotation in equation 7.5. Figure 7.10 is a graphical illustration of the transformation.

$$\begin{bmatrix} x' \\ y' \end{bmatrix} = \begin{bmatrix} cos\theta & -sin\theta \\ sin\theta & cos\theta \end{bmatrix} \begin{bmatrix} x \\ y \end{bmatrix} \tag{7.5}$$

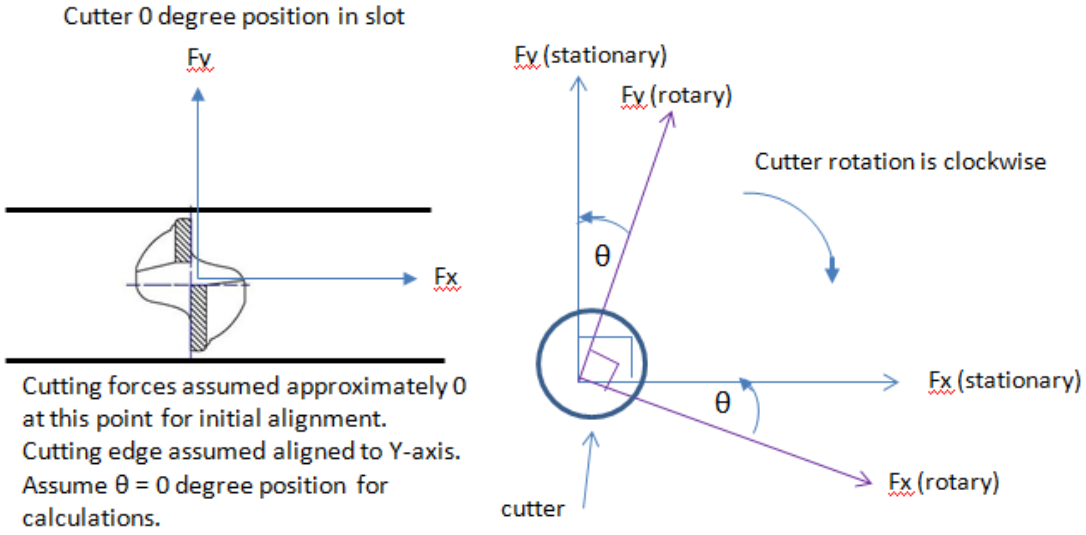

Figure 7.10. Graphical conversion from rotational to stationary coordinates

The results of the applied transformation are shown in Figure 7.11 where the rotating dynamometer coordinates were converted to the stationary dynamometer results for Fx, Fy and in figure 7.12 for Fa. Following the transformation, the shapes and magnitude of Fx, Fy are similar, but the data is shifted. The Fa results are consistent as this is a function of the square root of the sum of the squares of Fx and Fy. The inconsistency of Fx, Fy between the two types of dynamometers makes direct comparison of these force components challenging, leaving a comparison of the resultant forces as a more consistent, but limited, method. This conversion method is further limited to cases where common positions of the cutter can be found through data analysis for angular alignment, such as for 1 or 2 flute cutting tools. While this additional experimentation further enhanced the understanding of the rotating dynamometer performance, still more corrections were applied in phase 5 testing.

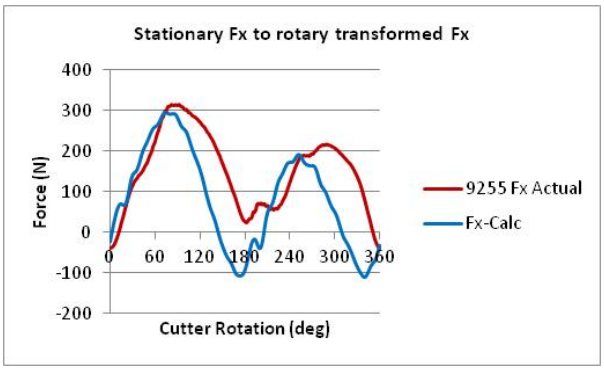

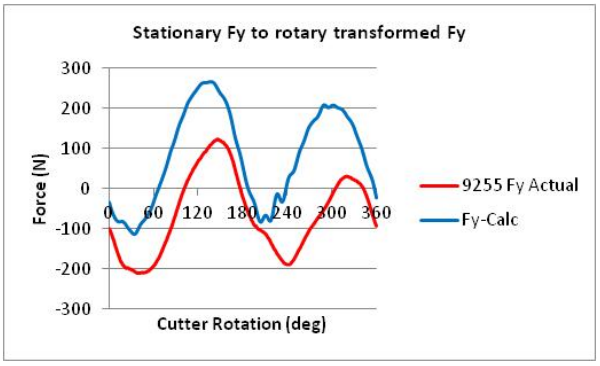

Figure 7.11. Rotary dynamometer system transformed to stationary system (Fx, Fy)

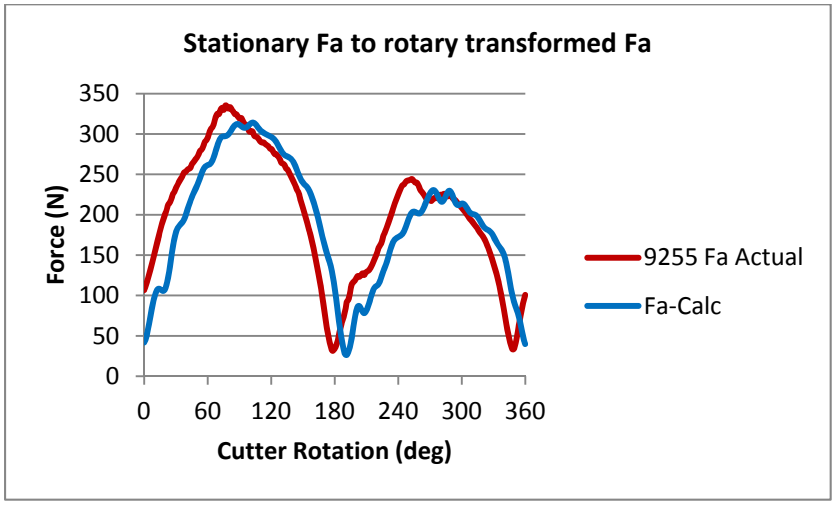

Figure 7.12. Rotary dynamometer system transformed to stationary system (Fa)

7.2.3 Phase 3 Cutting Force Results Summary

The results from milling tests from phase 3 testing were presented. The milling tests demonstrated advantages of aligning cutting teeth with the rotating dynamometer axes as a method to compare independent sensor measurements. Further tests were performed to validate consistency of results found by other researchers. A method for transforming results acquired from a rotating dynamometer to stationary coordinates was also demonstrated, providing a means to compare data obtained through different instruments for limited conditions. In the chronological effort for this research as described in Chapter 4, phase 4 testing was focused on improving the capture and analysis of particles generated from machining of composite materials. The phase 5 experimental effort concentrated on development of a force prediction

model and further improvement of necessary techniques to provide cutting force coefficients using the Kistler 9123C rotational dynamometer.

7.3 Phase 5 Cutting Force Model Experimental Technique and Results

With the dust collection and analysis system in the final form for this research effort through the construction and validation of the isokinetic sampling tower in phase 4, the phase 5 effort focused on developing a milling force prediction model. The mathematical details of the milling model will be discussed in chapter 9. The experimental component of the model conducted in phase 5 consisted of a series of cutting tests and further data acquisition process refinement. For the model, it is first necessary to determine cutting force coefficients. Cutting force coefficients are derived from a series of cutting tests where slots are machined and average force values are acquired for Fx, Fy, and Mz and used to calculate the coefficients. The process was first validated with aluminum and then tested on unidirectional composite material. Experimental process refinements were developed throughout phase 5 testing to improve the accuracy of results.

7.3.1 Linear Milling Model Development

In order to develop a force prediction model for anisotropic multidirectional composites, a simpler case using aluminum was first pursued. Aluminum slot cutting tests were defined to validate the basic cutting force model for a homogeneous material. These experiments were conducted prior to receipt of correct collets, which center and secure the cutting tool about its axis of rotation, so one tooth of the cutter engaged the workpiece and was evaluated. Six slots were defined to determine milling cutting force coefficients from the cutting force data. Table 7.1 identifies the basic cutting conditions for the six slots. Slots were machined parallel to the machine Y-axis with the cutting configuration as shown in Figure 7.13.

Table 7.1. Aluminum milling model initial linear slot cuts

Test ID	Cutter (mm)	Depth of cut (mm)	RPM	Feed rate ipm (mm/min)	Comment
5/3/14-1	12.7, 2fl	2.54	3000	5 (127)	Slot 1, fine
5/3/14-2	12.7, 2fl	2.54	3000	10 (254)	Slot 2, fine
5/3/14-3	12.7, 2fl	2.54	3000	15 (381)	Slot 3, fine
5/3/14-4	12.7, 2fl	2.54	3000	20 (508)	Slot 4, fine
5/3/14-5	12.7, 2fl	2.54	3000	25 (635)	Slot 5, fine
5/3/14-6	12.7, 2fl	2.54	3000	30 (762)	Slot 6, fine

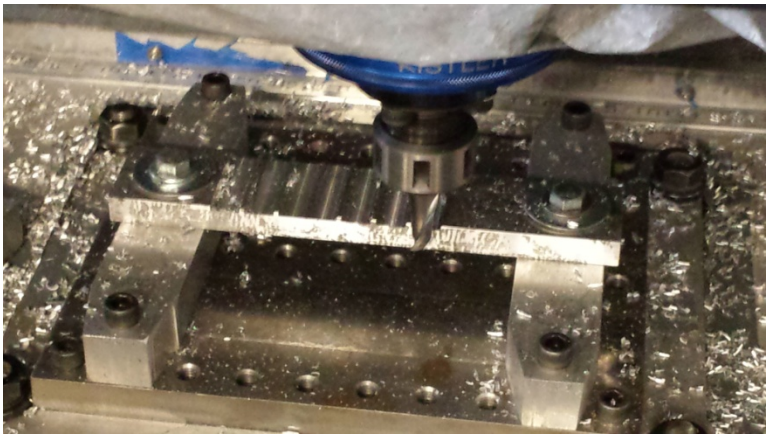

Figure 7.13. Aluminum slot cut configuration for initial milling model validation.

Typical cutting force summary for the 6 slots for Fx, Fy, Ft, Fr as provided by Kistler Dynoware software is shown in figure 7.14. The low forces due to a eccentric cutting tooth, because of the incorrect collet previously discussed, should be quite clear as they appear as a nearly flat valley in between the force peaks.

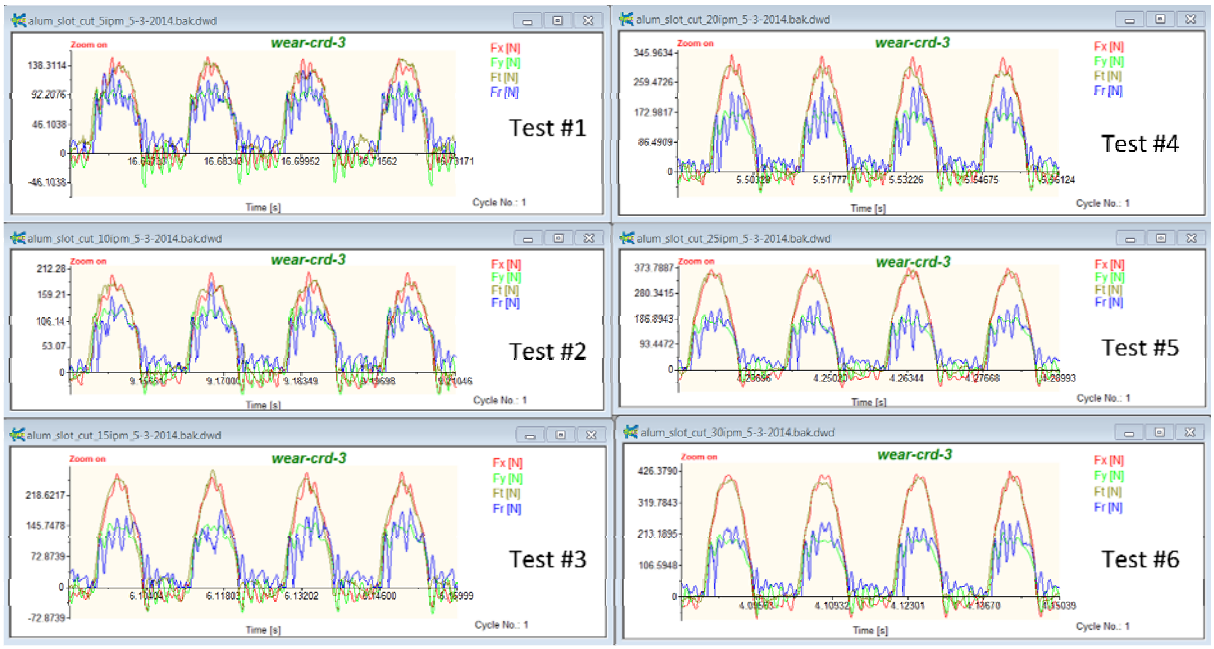

Figure 7.14. DynoWare force summary for aluminum slot cut tests.

To validate the basics of the force prediction model, half of one cutter revolution was evaluated for each of the six linear slots. For a two flute cutting tool, these are the forces associated with one of the teeth while the tool is engaged in the work piece. To acquire the data, graphs from the Kistler DynoWare were analyzed. The first step was to review the data and identify a single cutting tool rotation of interest for each of the six slots. The second step was to determine the time at which the cutting forces at the start and end of the cut are zero. In a slot test using a two flute cutting tool, the cutting forces are theoretically zero when the cutting tool is exactly perpendicular to the center of the slot as shown in figure 7.15. As illustrated in the figure, 0 degrees is assumed to be the degree location at cutter entry into the workpiece and 180 degree is assumed to be the exit position. The cutting force data for one tooth is then exported from DynoWare in a .txt file and imported into Microsoft Excel for manipulation. This process is repeated for each of the six slots. The cutting tool tooth entry and exit times for this experiment are shown in table 7.2.

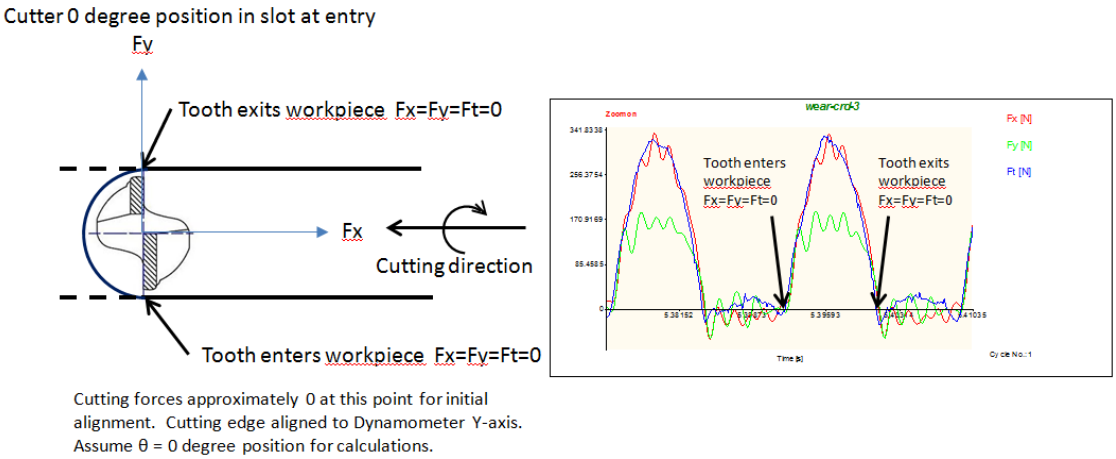

Figure 7.15. Cutting tool alignment in linear slot

Table 7.2. Cutting tool tooth entry and exit times

Slot (#)	Feed rate (mm/min)	Entry time (sec)	Exit time (sec)	Δ time (sec)
1	127	12.11540	12.12660	0.0111933
2	254	7.08776	7.09781	0.0100484
3	381	8.08293	8.09298	0.0100479
4	508	4.19092	4.20097	0.0100484
5	635	2.81837	2.82842	0.0100484
6	762	5.062960	5.073010	0.010048

In the third step, the time values for each slot test are converted to a degree equivalent from 0 to 180, with 0 being entry and 180 being exit. The spindle speed for each slot test was kept at 3000 rpm which provided approximately the same number of data points when sampled at 7800 Hz, the maximum rate for the dynamometer. At this spindle speed and sampling rate, 79 data points were collected for one tooth engagement in the workpiece (0-180 degrees), at an interval of approximately 2.3 deg/data point. This resolution gets worse (lower) at higher spindle speeds. Plots of the measured Fx, Fy forces are shown in figure 7.16 and the DynoWare derived Ft, Fr forces in figure 7.17.

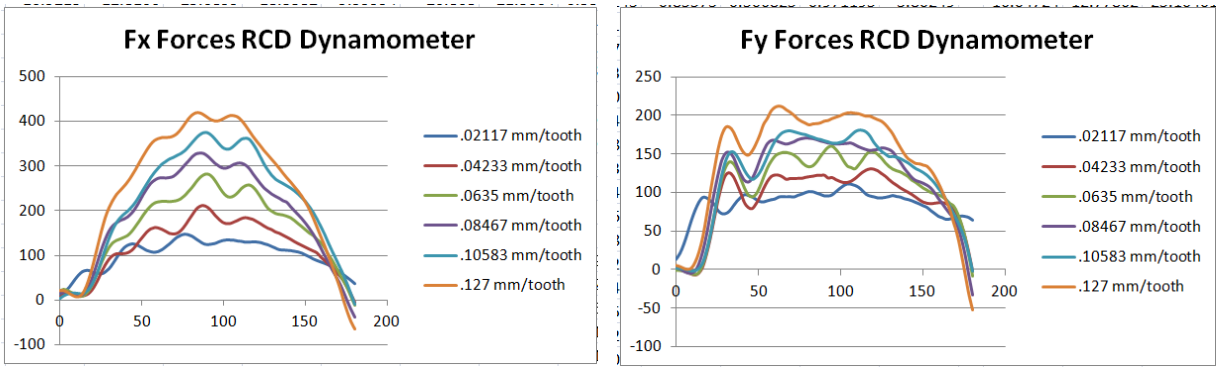

Figure 7.16. Dynamometer, Fx, Fy forces for slot test at single rotation.

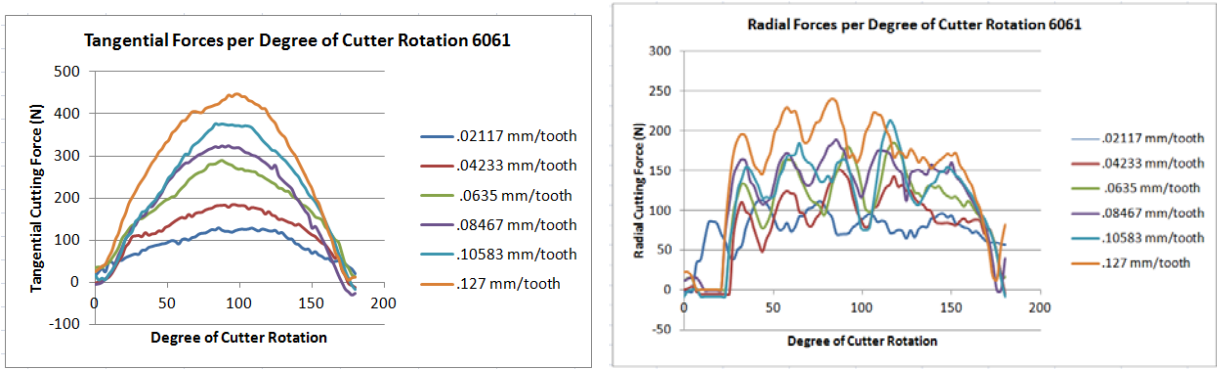

Figure 7.17. Dynamometer, Ft, Fr forces for slot test at single rotation.

With the acquired data now in a suitable format for analysis, cutting force coefficients can be calculated. Three different approaches were used in the case of the linear slot tests to calculate the cutting force coefficients to compare results. The derivation for the equations and method for calculating cutting force coefficients is explained in chapter 9 and the coordinate transformation from rotational to stationary dynamometer was discussed in section 7.2. The rotating dynamometer relationship between cutting tools and edge alignment was also discussed where Ft~Fx and Fr~Fy when the cutting edge is aligned to the rotating dynamometer Y-axis for a 2-flute cutter. These three techniques were used to calculate the cutting force coefficients for the linear slot tests.

In the first method, the cutting force coefficients were calculated using the approach described by Karpat [58] and covered in detail in Chapter 9. Tangential and radial force data from the dynamometer was directly used to calculate K_{tc}, K_{te}, K_{rc}, and K_{re} from equations (6.30 – 6.33) for each of the 180 degree positions of rotation of the single tooth. Regression analysis

was performed at each position so 720 total coefficients were calculated. A plot of the data is shown in figure 7.18.

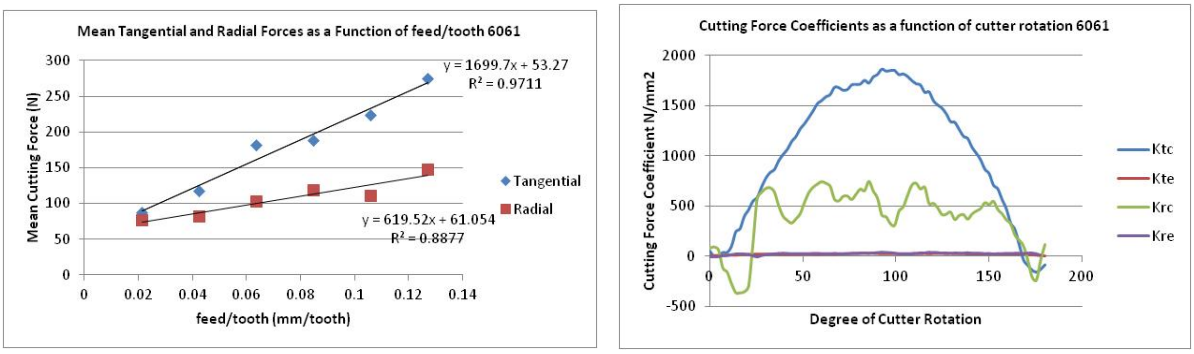

Figure 7.18 Cutting force coefficients using Karpat [58], Ft, Fr method

In the second method, the approach described by Karpat was used again; however, Fx was substituted for Ft and Fy was substituted for Fr. This is because of the relationship of a 2-flute cutter and the rotating dynamometer with alignment of the cutting edge to the Y-axis of the dynamometer. Figure 7.19 is a plot of the four cutting force coefficients using this approach.

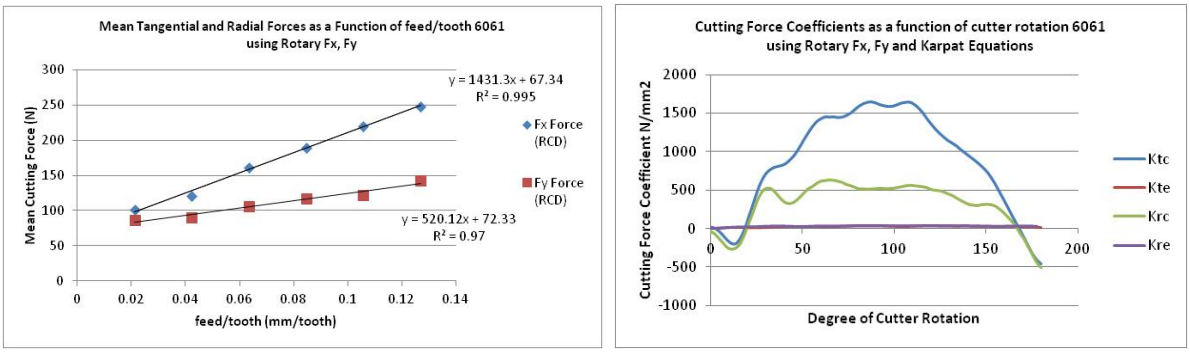

Figure 7.19. Cutting course coefficients using Karpat [58], Fx, Fy method

In the third method, the rotational dynamometer Fx and Fy values were first converted to their respective stationary values using a transformation as shown in figure 7.20. The Budak and Altintas [118,119] method described in chapter 9 was used to determine the 4 cutting force coefficients for a stationary dynamometer. These results are plotted in figure 7.21.

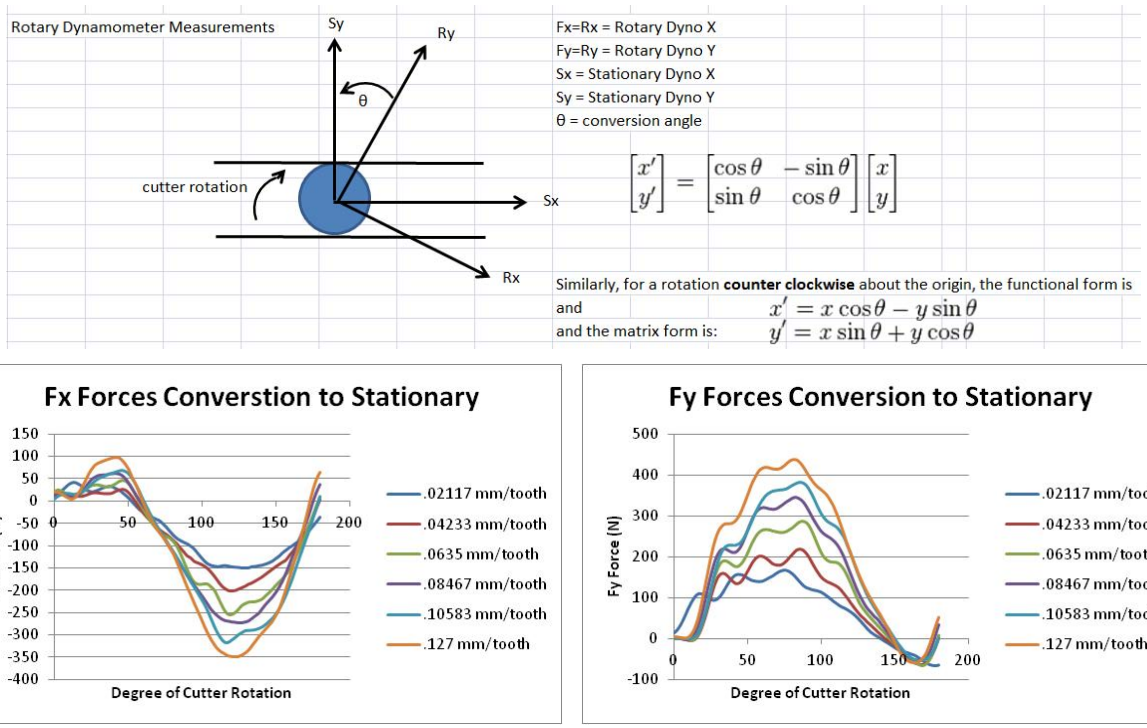

Figure 7.20. Conversion to stationary dynamometer values.

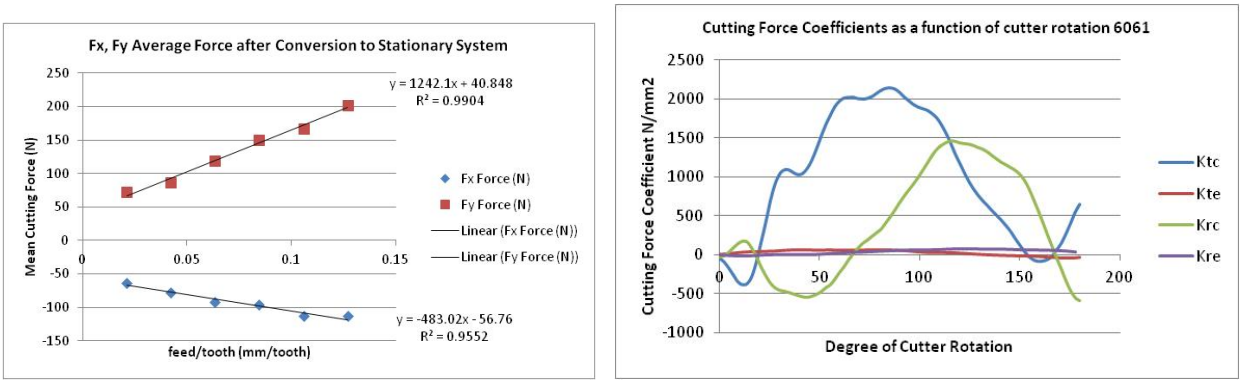

Figure 7.21. Cutting force coefficients using Altintas [119] , Fx, Fy after conversion

In the milling model for a linear slot, the average forces of a single tooth are used to determine the cutting force coefficients, and one set of coefficients is used in the model for cutting force prediction. A comparison of the cutting force coefficients using the 3 methods is shown in table 7.3. In the cutting force model, K_{tc} and K_{rc} have the largest impact on force magnitude and ranged approximately 19% for the 3 methods used for these conditions. A higher difference was found for the edge coefficients; however, these have less of an impact on force prediction results.

Table 7.3. Cutting force coefficients from 3 methods for aluminum linear slots.

Method	Description	K_{tc}	K_{te}	K_{rc}	K_{re}
1	Karpat (Ft, Fr)	1051.121	20.97255	383.1261	24.03719
2	Karpat (Fx,Fy)	885.1303	26.51191	321.6556	28.47657
3	Altintas (Fx,Fy)	978.0029	25.26112	380.3326	35.1015
	Range difference	165.9907	5.53936	61.4705	11.06431
	% difference	18.75	26.41	19.11	46.03

Six additional test cuts were made to generate data for model validation. These were performed using 6.35 mm (.25 in.) thick aluminum 6061-T6 plate. A combination of peripheral climb and conventional cuts were made. Two of the cuts were half immersion cuts (6.35 mm diameter), or half of the cutting tool diameter. The cutting conditions and configurations for the model verification tests are described in Table 7.4 with a photograph of the cantilevered mounting configuration for the tests in figure 7.22. The milling force prediction model was tested using the cutting force coefficients from all 3 methods. The coefficients from the 3 methods were imported into the MATLAB force prediction model described in chapter 9, with input parameters configured for a homogeneous material. The verification tests were conducted to provide additional data so the results predicted by the model could be compared to actual cutting results to check the model force prediction accuracy on a well understood homogeneous material system prior to moving to the far more complex case of composite laminates.

Table 7.4. Initial linear slot milling model verification tests for aluminum.

Test ID	Cutter (mm)	Axial Depth of cut (mm)	Radial Depth of Cut (mm)	RPM	Feedrate ipm (mm/min)	Comment
5/3/14-7	12.7, 2fl	6.35	.762	3000	10 (254)	Peripheral, conv
5/3/14-8	12.7, 2fl	6.35	.762	3000	20 (508)	Peripheral, conv
5/3/14-9	12.7, 2fl	6.35	6.35	3000	5 (127)	Peripheral, conv
5/3/14-10	12.7, 2fl	6.35	.762	3000	10 (254)	Peripheral, climb
5/3/14-11	12.7, 2fl	6.35	.762	3000	20 (508)	Peripheral, climb
5/3/14-12	12.7, 2fl	6.35	6.35	3000	5 (127)	Peripheral, climb

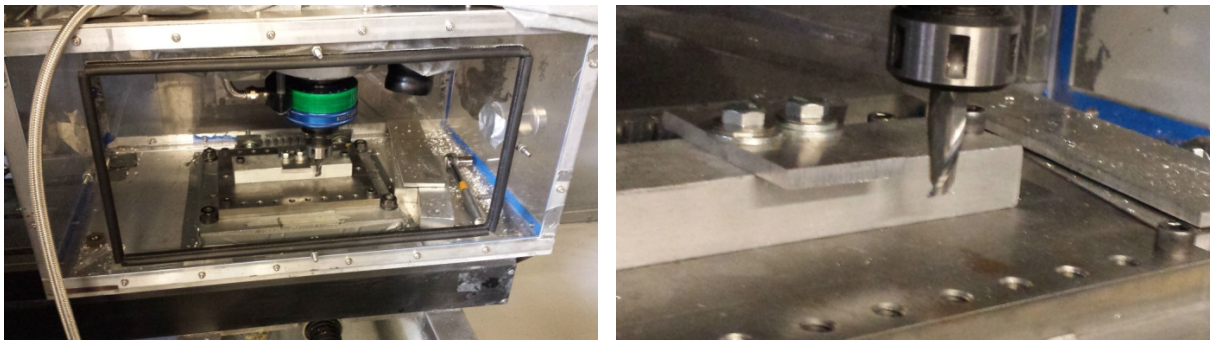

Figure 7.22. Peripheral trim verification test configuration.

The force prediction model was run 18 times using the three different sets of cutting force coefficients and the six verification test configurations. Input data to the model will be described in detail in chapter 9, and includes the cutting tool geometry (helix angle, number of teeth), cutting conditions (axial and radial depths of cut, feed rate/tooth), and other necessary set up parameters. Data from select tests is provided which compare results predicted by the model to a sample of the DynoWare output in figure 7.23. The results predicted by the model demonstrated consistency with the profile of actual force curves for all cases. Force magnitudes were predicted within approximately 10% for half cutter diameter peripheral climb and conventional cutting. The forces for peripheral climb and conventional cuts with .762 mm radial depths of cut were overestimated by approximately 100% by the model. The higher error magnitude for the predicted forces for the lighter peripheral cuts may be partially attributed to the cutter runout discussed earlier that was not caught and understood until after this round of testing was completed.

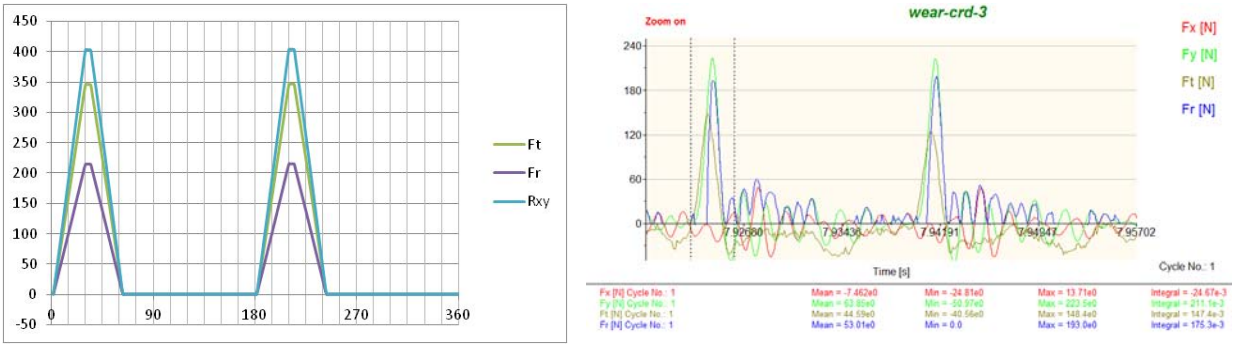

d) Peripheral conventional milling, Karpat method, Ft, Fr

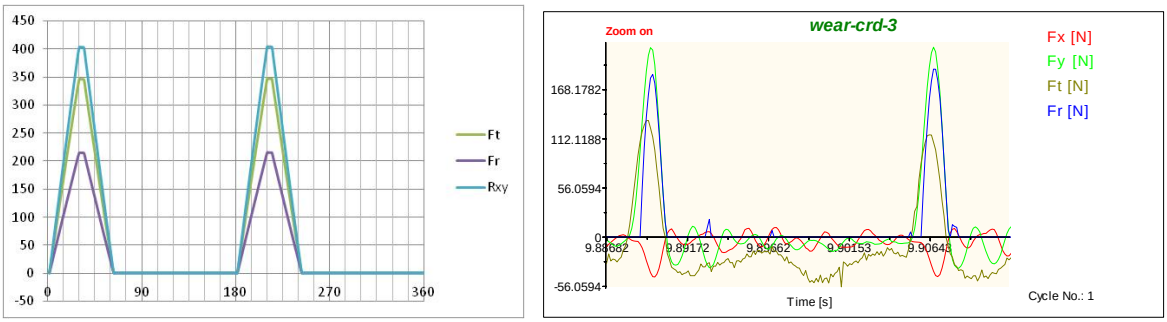

c) Peripheral climb milling, Karpat method, Ft, Fr

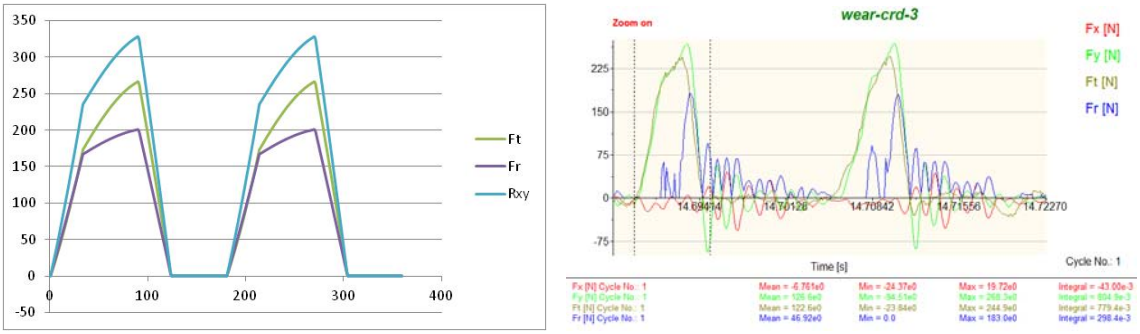

b) Half slot conventional milling, Karpat method, Ft, Fr

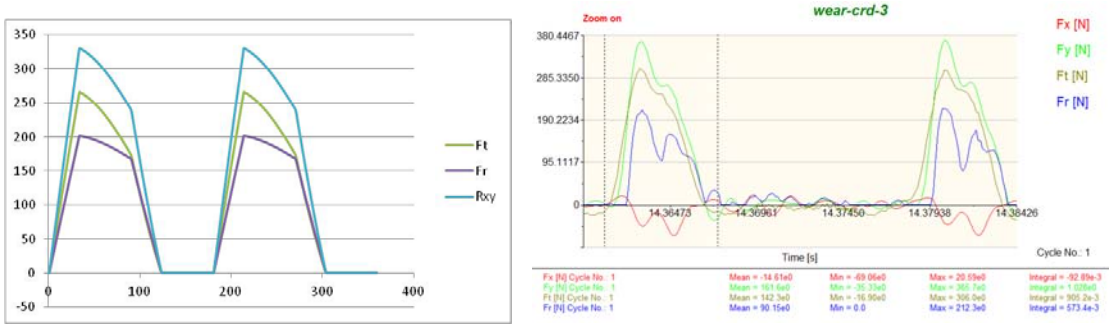

a) Half slot climb cutting, Karpat method, Ft, Fr

Figure 7.23. Predicted results to actual results for aluminum milling.

7.3.2 Linear Milling Model for Composites

With the basic milling model established, the next step was to test it with composite laminate data. Composite linear slot cuts were conducted using a 33 ply unidirectional laminate with a new solid carbide 2-flute, 30 degree helical cutter. Cutting was performed parallel to the fiber direction. Table 7.5 summarizes the composite slot milling conditions. A 6000 rpm spindle speed was used on the composite slot test series where 3000 rpm was used for the aluminum series. This was done to reduce the theoretical chip thickness for composites. With a fixed sampling rate of 7800 Hz, there are half as many data points for the composite slot tests at these spindle speeds. Figure 7.24 is a photograph from the composite slot cutting tests with results in figure 7.25.

Table 7.5. Composite linear slot cutting tests

Test ID	Cutter (mm)	Depth of cut (mm)	RPM	Feedrate ipm (mm/min)	Comment
5/19/14-1	12.7, 2fl	2.54	6000	5 (127)	Slot 1, fine
5/19/14-2	12.7, 2fl	2.54	6000	7.5 (190.5)	Slot 2, fine
5/19/14-3	12.7, 2fl	2.54	6000	10 (254)	Slot 3, fine
5/19/14-4	12.7, 2fl	2.54	6000	12.5 (317.5)	Slot 4, fine
5/19/14-5	12.7, 2fl	2.54	6000	15 (381)	Slot 5, fine
5/19/14-6	12.7, 2fl	2.54	6000	17.5 (444.5)	Slot 6, fine

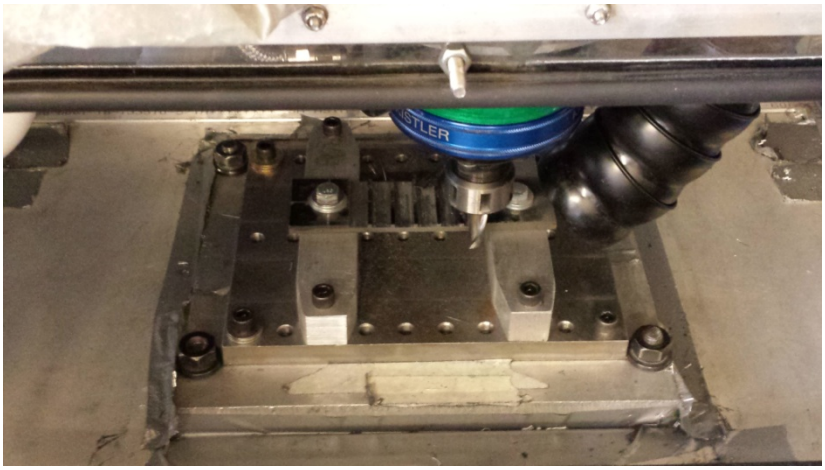

Figure 7.24. Composite slot cut tests

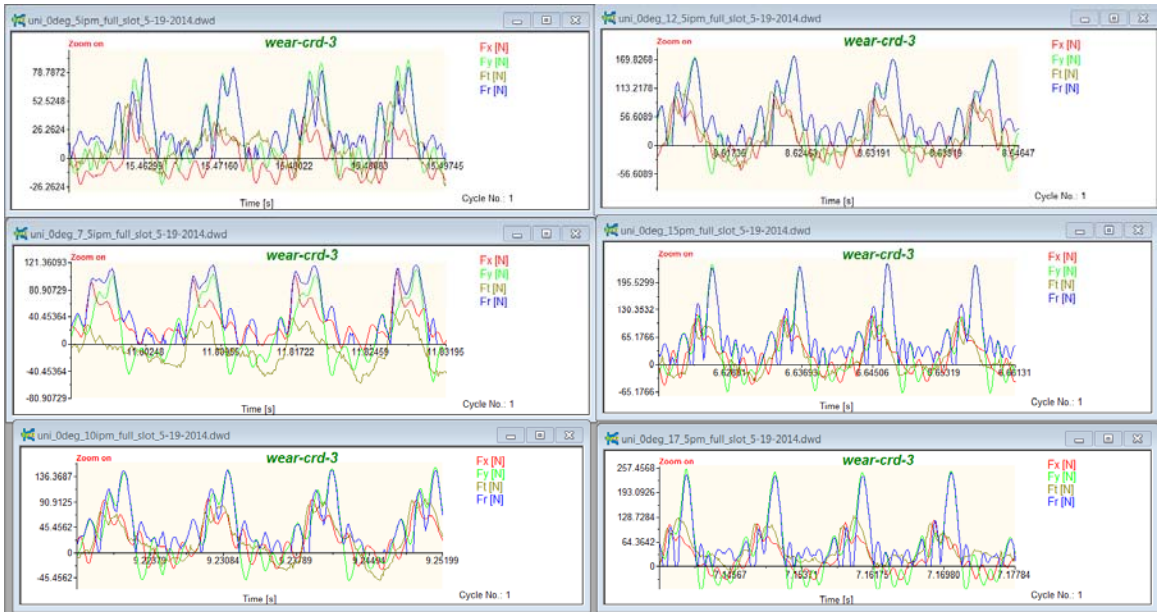

Figure 7.25. Composite slot cutting test results

With composites, higher cutting speed and lower feed rates have been shown to produce better finishes with an appropriate cutting tool. At the 6000 rpm spindle speed and sampling rate, 43 data points were collected for one tooth engagement in the workpiece, at an interval of approximately 4.6 deg/data point. Plots of the measured Fx, Fy forces are shown in figure 7.26 and the DynoWare derived Ft, Fr forces in figure 7.27. These values are not corrected for signal drift.

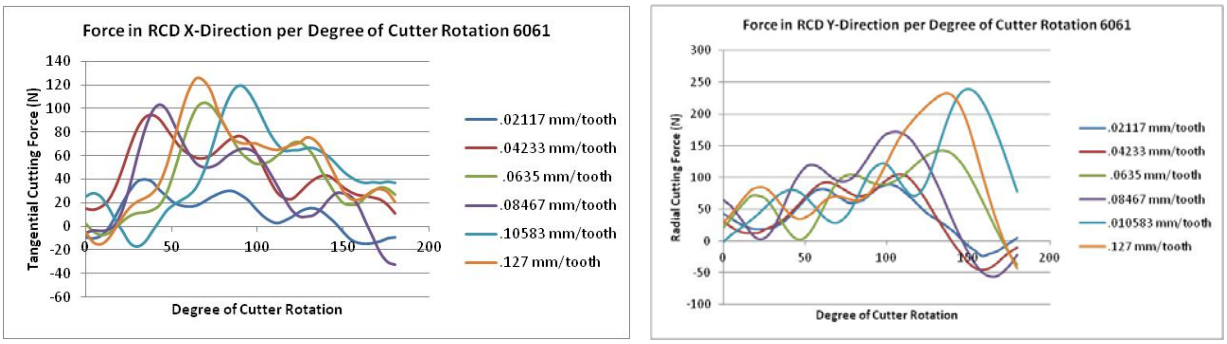

Figure 7.26. Dynamometer, Fx, Fy forces for composite slot test with single rotation.

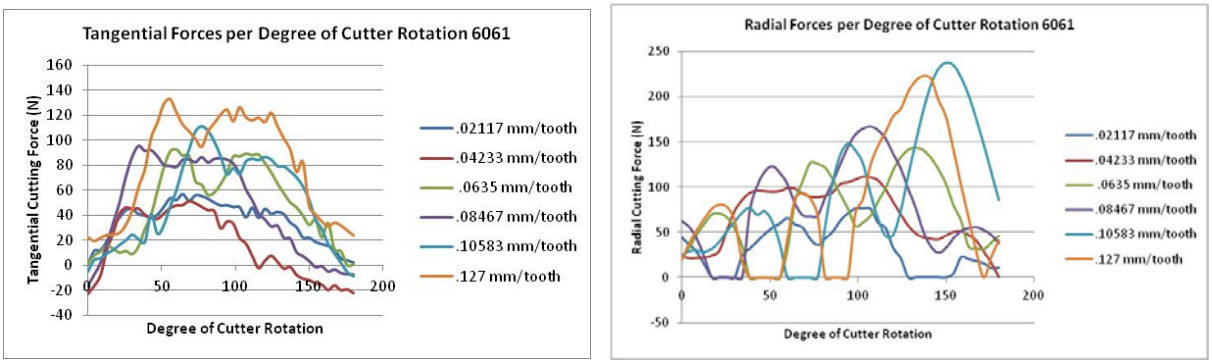

Figure 7.27. Dynamometer, Ft, Fr forces for composite slot test with single rotation.

The results from the aluminum slot tests in figures 7.16 and 7.17 are clearly more uniform and consistent than those for the composite slot tests in figures 7.26 and 7.27. The tangential forces for the composite slots have some consistency, but the radial forces drop to zero at several locations. This can be caused by several issues to be explained shortly. Using the process described for the aluminum slot, the cutting force coefficients were calculated using the approach described by Karpat with a plot of the data shown in figure 7.28.

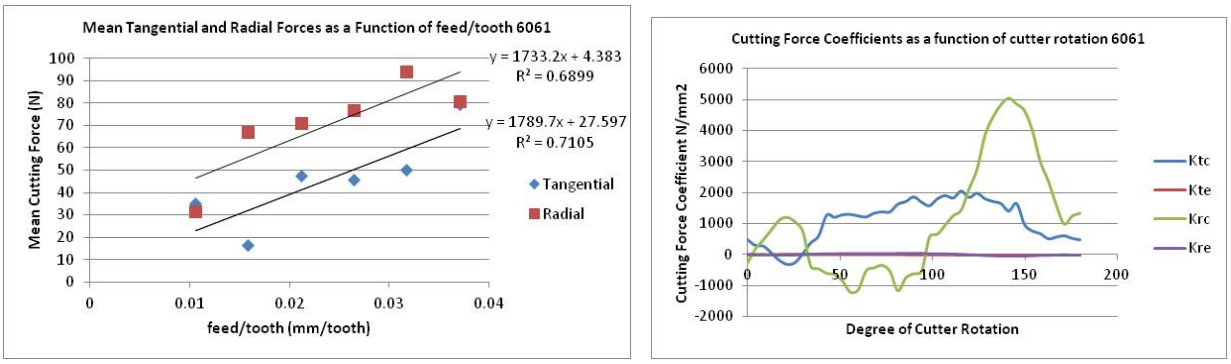

Figure 7.28. Cutting force coefficients using Karpat [58], Ft, Fr method

In figure 7.29 Fx was substituted for Ft and Fy was substituted for Fr which did not improve the tangential cutting force prediction. The third method of converting rotational coordinates to stationary coordinates was tested, but yielded even worse results likely due to inconsistencies to be discussed and is not included in table 7.6, which summarizes the cutting force coefficients for the composite linear slot tests.

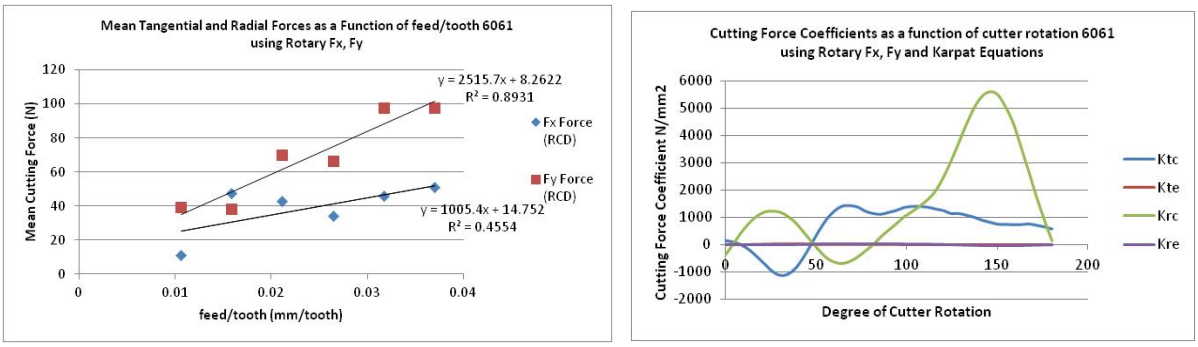

Figure 7.29. Composite cutting force coefficients using Karpat, Fx, Fy method

Table. 7.6. Cutting force coefficients for linear composite slot test.

Method	**Description**	**K_{tc}**	**K_{te}**	**K_{rc}**	**K_{re}**
1	Karpat (Ft, Fr)	1051.121	20.973	383.126	24.037
2	Karpat (Fx,Fy)	621.740	5.808	1555.787	3.253

Several factors likely contributed to the inconsistent prediction of cutting force coefficients for this composite slot test and include:

- Cutting tool design not optimized for composite materials
- Large cutting tool runout
- Signal drift and centering
- Lower data fidelity at higher spindle speeds due to sampling rate limitation

To address concerns with the experimental techniques which are essential to acquiring accurate cutting force data for calculation of milling coefficients needed for the force prediction model, additional aluminum slot cutting tests were conducted as shown in table 7.7. Further tests for both composite and aluminum slots were conducted as shown in Table 7.8.

Table 7.7. Aluminum slot cutting tests.

Test ID	Cutter (mm)	Depth of cut (mm)	RPM	Feedrate ipm (mm/min)	Comment
5/27/14-1	12.7, 2fl	2.54	3000	5 (127)	Slot 1, fine
5/27/14-2	12.7, 2fl	2.54	3000	15 (381)	Slot 2, fine
5/27/14-3	12.7, 2fl	2.54	3000	5 (127)	Slot 3, fine
5/27/14-4	12.7, 2fl	2.54	3000	15 (381)	Slot 4, fine
5/27/14-5	12.7, 2fl	2.54	3000	25 (635)	Slot 5, fine
5/27/14-6	12.7, 4fl	2.54	3000	15 (381)	Slot 6, fine

Table 7.8. Aluminum and composite slot tests

Test ID	Material	Cutter (mm)	Depth of cut (mm)	RPM	Feedrate ipm (mm/min)	Comment
5/28/14-1	Alum.	12.7, 2fl	2.54	3000	5 (127)	Slot 1, fine
5/28/14-2	Alum.	12.7, 2fl	2.54	6000	10 (254)	Slot 2, fine
5/28/14-3	Alum.	12.7, 2fl	2.54	3000	20 (508)	Slot 3, fine
5/28/14-4	0 deg Uni	12.7, 2fl	2.54	3000	5 (127)	Slot 4, fine
5/28/14-5	0 deg Uni	12.7, 2fl	2.54	6000	10 (254)	Slot 5, fine
5/28/14-6	0 deg Uni	12.7, 4fl	2.54	3000	7.5 (190.5)	Slot 6, fine

Figure 7.30 illustrates the increasing Fx, Fy force magnitude for aluminum with increasing feedrate, where forces corresponding to the minimum feedrate of 127 mm/min are compared to a maximum feedrate of 635 mm/min. Figure 7.31 are plots of common conditions of feedrate of 127 mm/min and spindle speed 3000 rpm for the composite and aluminum slots. Figure 7.32 are plots of common conditions of feed rate of 254 mm/min and spindle speed 6000 rpm for the composite and aluminum slots. In both cases, Fy is of larger relative magnitude for the composite than the aluminum case. Further, the aluminum case has a more sinusoidal profile than the composite, with the profile clearer at a lower spindle speed of 3000 rpm due to more sampling points.

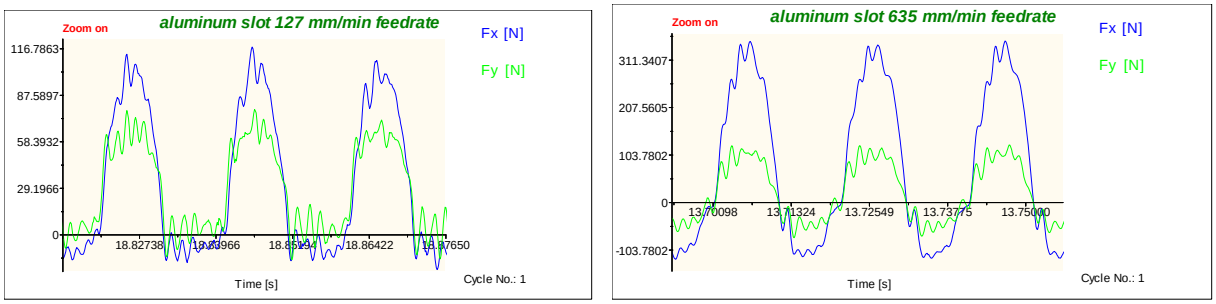

Figure 7.30. Aluminum slot cutting force comparison based on feedrate.

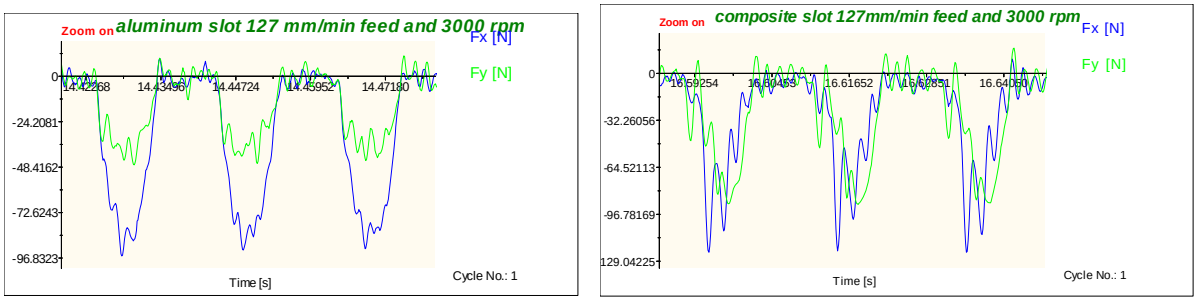

Figure 7.31. Aluminum and composite comparison at 127 mm/min, 3000 rpm

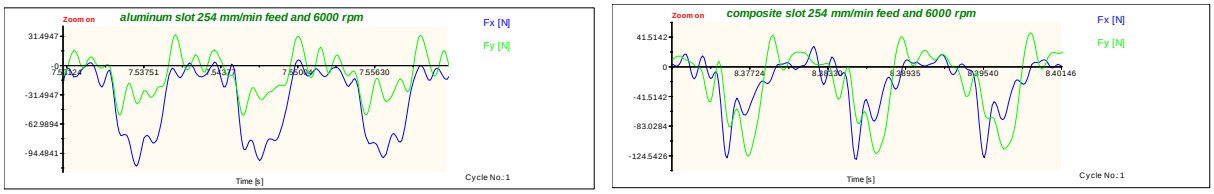

Figure 7.32. Aluminum and composite comparison at 254 mm/min, 6000 rpm

These tests indicate that it is possible to improve the quality of data acquired from the cutting tests. An example is shown in figure 7.33, where the same cutting conditions are used for milling a slot in both aluminum and composites. The plots were enhanced using the limited signal drift compensation and smoothing capabilities in DynoWare, but illustrate the potential for improving data quality.

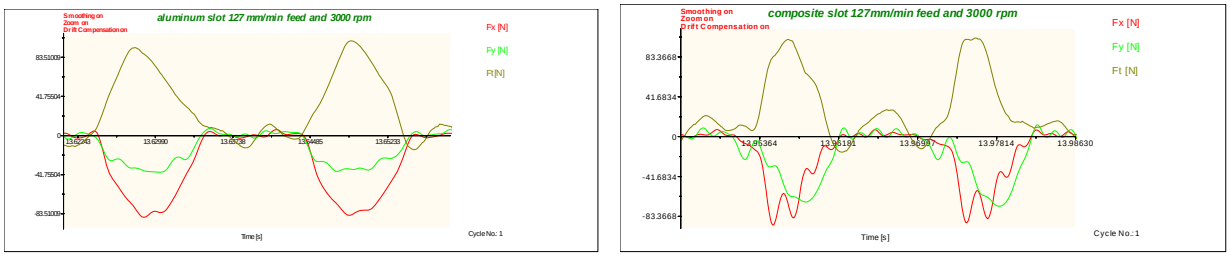

Figure 7.33. Comparison of data between composite and aluminum slot.

The linear slot force prediction model testing demonstrated the capability of the linear model to predict cutting forces. The basic capability was demonstrated for composites, and significant effort was made to improve the experimental techniques. The next step is development of a force prediction model that would be capable of predicting forces in a multi-directional composite laminate at any relative orientation of the cutting tool. However, prior to moving to this more complex model that will utilize a series of semi-circular slot tests in unidirectional composite laminates, several additional experimental process improvements were necessary to obtain better data quality. Four focus areas for experimental technique improvement will be discussed in the next section.

7.4 Cutting Process improvements

Due to the way data is acquired with the Kistler 9123C rotating dynamometer, 5223B signal conditioner, and DynoWare data acquisition software, in some cases it is possible to post-process data that was previously acquired and apply developed process improvements, in other cases new cutting tests are required as key elements from previously collected raw data may be missing. The process improvements identified and developed as part of phase 5 testing include:

- Use of correct collets to minimize runout
- Use of coarse vs. fine settings
- Signal drift and shift correction
- Zoom magnification for Mz

This section will discuss the process improvements identified and developed throughout the phase 5 testing followed by the force model testing conducted using several of these techniques in the next section.

7.4.1 Collet Runout

An analysis of the cutting force data from the linear slot experiments showed that only a single tooth of the two flute cutter appeared to be engaging the workpiece. This was at first attributed to cutter grinding quality as these were lower cost cutting tools. Figure 7.34 shows a cutting force diagram of a relatively clean cut, but with a tooth not engaging the work piece. After another cutter was tested and showed similar results, the spindle runout on the dynamometer was checked using a 12.7mm (0.5 inch) diameter ground shaft. Runout was

measured at approximately .1143 mm (.0045 inch). It was found that the wrong collets had been used with the dynamometer. A ER 25 DIN 6499 collet with a taper of 8 degrees was used instead of a Perske DIN 6388 size 16 collet with a 1:10 taper (5.71 deg), as specified in the Kistler manual [102]. After disassembly, it was evident by a marked ring in the ER collet where it hit the tapered bore opening. While the ER 25 collet fit due to similar dimensions and worked for dust collection testing, for detailed force measurements, it was not acceptable as the cutter was not rotating concentric to spindle center line. It was not noticed during phase 4 dust collection experiments as cutting forces were not captured. The dynamometer had been sent to Switzerland for repair sometime after phase 3 testing and collets may have been misplaced. Proper ER 16 collets were ordered in 6.35, 10, 12, and 12.7 mm diameters. Runout was again measured for the correct collets using a 12.7 mm diameter ground shaft and was less than .0127 mm (.0005 in). Figure 7.35 is a photograph of a typical spindle runout test.

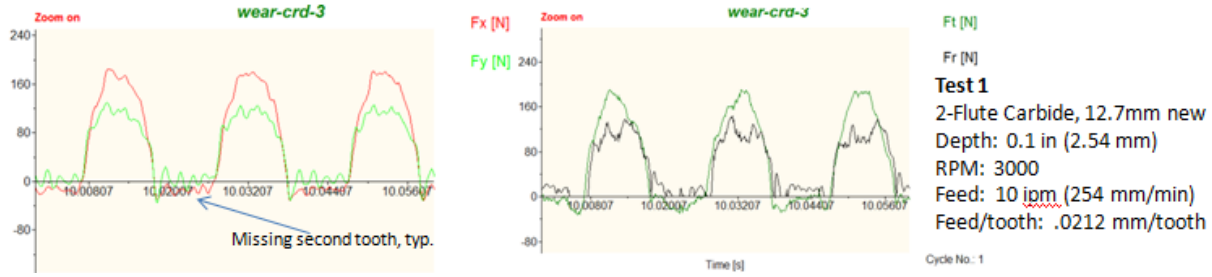

Figure 7.34. Cutting force data indicating missing tooth.

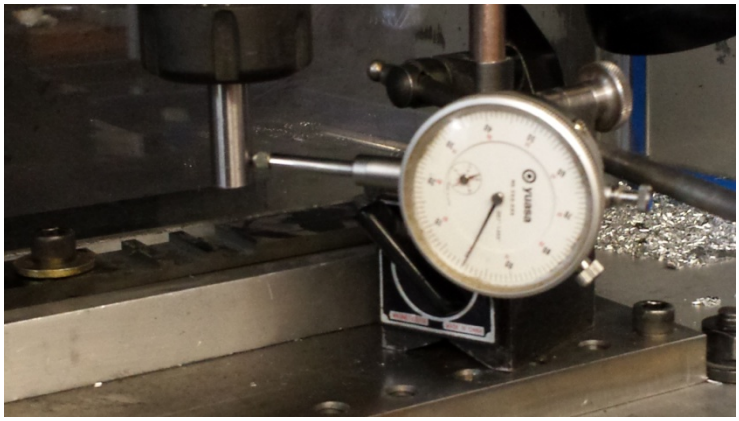

Figure 7.35. Typical spindle runout test

To avoid further mechanical alignment issues that would affect cutting force measurements, a calibrated Gorbar 100TH 20-100Nm (15-80 ft lbs) torque wrench was used to

tighten the Perske collets to 61 Nm (45 ft lbs) with a TTTO 40-43 wrench adapter. Hand wrenches designed for the Perske size EOC 16 nut were used to loosen collets to avoid damage to the torque wrench. Four collet holder screws were torqued to Kistler's recommendation of 26 Nm (19 ft lbs) and the Taper 40 retention knob was torqued to 100 Nm (74 ft lbs). This was the extent of steps that could be taken to mitigate dynamometer alignment issues in the MSTL lab at the University. All prior cutting experiments, including the linear slot investigation, were conducted under these conditions prior to discovery of the incorrect collets. While a single tooth of a 2-flute tool was used for cutting force analysis, the raw data was impacted by the amount of runout. It is interesting to note that for each re-installation of the cutter in the collet, the runout randomly shifted towards positive or negative directions, as indicated in the force measurements, because the collet did not seat consistently in the holder. This was a disappointing lesson learned, but one that was easy to correct for future tests.

7.4.2 Coarse vs. Fine Range Settings

The dynamometer has 2 ranges (coarse and fine) with specific limits for each channel shown in table 7.9. The ranges are set both on the 5223B Signal Conditioner and within the DynoWare software. The cutting conditions for testing done to date were generally well inside of Range 2 with maximum Fx, Fy forces less than the fine range maximum of 500 N, for the majority of tests, and using a significant portion of the available range. Several cutting experiments were specifically conducted to evaluate the effect of using the coarse and fine range settings of the instruments and software in terms of signal to noise. A summary description of tests is shown in table 7.10 with photographs of the test configuration in Figure 7.36. These experiments were conducted prior to correcting the collet runout issue; however, that would likely not have affected the outcome. Figure 7.37 illustrates the results for fine versus coarse range settings where for the same 2 cutting conditions, the top 2 graphs were captured in the fine range and the lower 2 in the coarse range. For lower force values, the coarse range appears to distort the data due to more noise than signal. The Range choice is set prior to data acquisition in both the Signal Conditioner and Dynoware software and cannot be modified after the fact. As a result of the experiments, efforts were made to generate forces that consume a significant amount of the fine range to minimize noise.

Table 7.9. Dynamometer ranges

Channel	Range 1 (coarse)	Range 2 (fine)	Channel
Fx	-5000 to 5000 N	-500 to 500 N	1
Fy	-5000 to 5000 N	-500 to 500 N	2
Fz	-20000 to 20000 N	-2000 to 2000 N	3
Mz	-200 to 200 Nm	-20 to 20 Nm	4
Zoom	N/A	N/A	5 (for Fx,Fz, or Mz)

Table 7.10. Coarse and fine range test matrix

Test ID	Cutter (mm)	Depth of cut (mm)	RPM	Feedrate ipm (mm/min)	Comment
4/26/14-1	12.7, 2fl	2.54	3000	10 (254)	Missing tooth, fine
4/26/14-2	12.7, 2fl	2.54	3000	20 (508)	fine
4/26/14-3	12.7, 2fl	2.54	3000	30 (762)	fine
4/26/14-4	12.7, 2fl	2.54	3000	40 (1016)	Fx exceeded 500 N, fine
4/26/14-5	12.7, 2fl	2.54	3000	35 (889)	Fx exceeded 500N, fine
4/30/14-6	12.7, 2fl	2.54	3000	15 (381)	fine
4/30/14-7	12.7, 2fl	2.54	3000	25 (635)	fine
4/30/14-8	12.7, 2fl	2.54	3000	10 (254)	coarse
4/30/14-9	12.7, 2fl	2.54	3000	35 (889)	coarse
4/30/14-10	12.7, 2fl	2.54	3000	40 (1016)	coarse
4/30/14-11	12.7, 2fl	2.54	3000	25 (635)	coarse

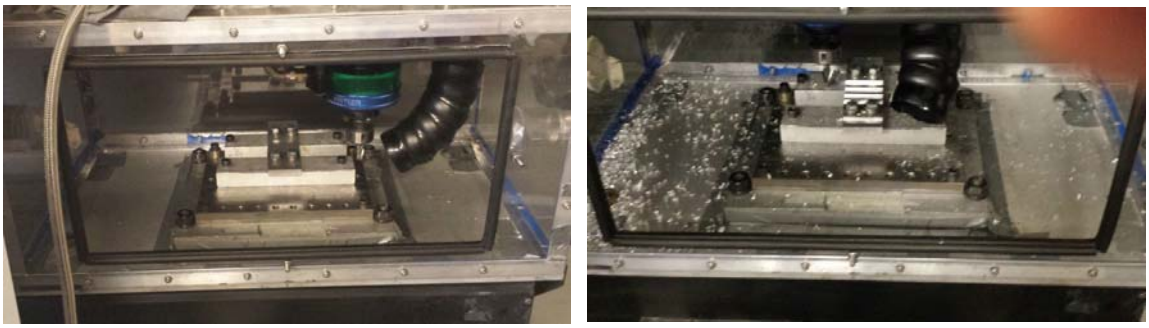

Figure 7.36 Aluminum slot test configuration for course and fine range tests.

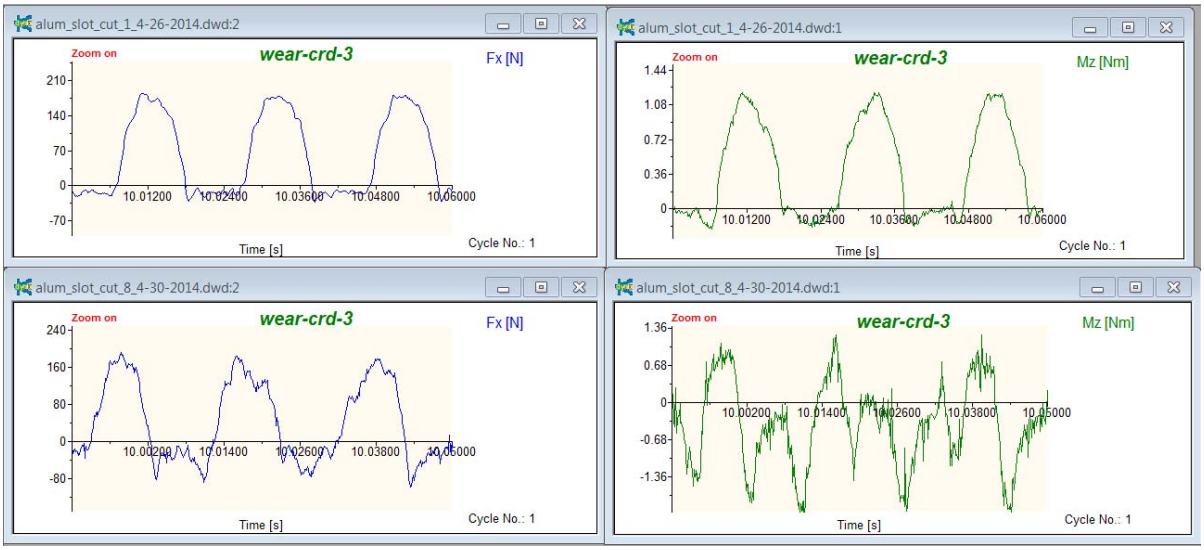

Figure 7.37 Fine (top) vs. Course (bottom) dynamometer measurements

7.4.3 Signal Drift and Shift

A significant amount of varying signal drift was noticed during experiments for the key parameters of interest including Fx, Fy, Mz. The slot cutting tests are designed with approximately 3-5 seconds of no load cutting at the start and end of each cut. No load cutting is where the spindle rotates without contacting the workpiece. If the signal shift is zero, the noise during the no load cutting will be centered around the 0 N (Fx, Fy, Fz, Ft) or 0 Nm (Mz) axis of the plot. After several tests and consultation with Kistler, it was discovered that there was no technique to avoid signal shift and/or drift. Kistler stated that the signal drift should not be more than 1 N/min of cutting for Fx and Fy. This is the left to right vertical shift from start of signal acquisition. The issue found was that the signal could be significantly vertically shifted from the start of data acquisition regardless of care taken with the instrument. Any drift or shift after that

would just compound the problem of accurate force or moment interpretation. The concern is the relationship between sensors on the rotating dynamometer. The forces of interest for the cutting force model are Ft, Fr, which are both derived and related. Fx, Fy, and Mz are directly measured by the dynamometer and are used to derive Ft, Fr in equations 7.6 and 7.7.

Ft = Mz/r, where Mz is the moment, and r is the cutter radius. (7.6)

$$Fr = \sqrt{Fx^2 + Fy^2 - Ft^2} \quad (7.7)$$

If Fx, Fy, and Mz are independently and randomly shifted, the value for Fr will be off, cutting force plots will not make sense, and cutting force coefficients for the model will be in error. An example of typical signal drift and shifts is shown in Figure 7.38. While the Kistler DynoWare software has a Signal Drift Compensation feature, a bug was found and acknowledged by Kistler when trying to save a modified file with the corrections. An algorithm was developed and tested as part of this research to handle the signal shifting offline. The algorithm works by looking at both ends of the cutting force data acquisition. On the left side, Force (N) or Moment (Nm) no-load values are averaged from time 0 to the time the cutting tool first contacts or enters the workpiece. The time the cutter enters the work piece is found by inspection of the data. This could also be automated in a future version. A jump in forces or moment occurs at the first instance of the cutter entering the work piece. An example is shown in Figure 7.39. On the right side, the time the cutter exits the workpiece can be found by inspection, similar to the example, or as deployed, through estimation. This is accomplished by using the programmed velocity of the machine and length of cut prior to the cutter exiting the workpiece from time when cutter contacts the workpiece, simply, $t_e = V(\Delta s + d) + t_o$, where V is the velocity of the machine, Δs is the distance length of the cut, d is the cutter diameter, t_o is the time the cutter first contacts the workpiece, and t_e the time the cutter exits the workpiece. The right side no-load values are then averaged from the time the cutter exists the workpiece to the end of data acquisition. The average shift and/or drift values from the left and right side no-load cutting conditions are then compared. For Fx and Fy, Kistler states that a drift of no more than 1 N/min is to be expected. If this is found valid through comparison of the left and right no-load force averages, then the acquired Fx, Fy data is shifted by subtracting the left no-load force average from all data points. For a 35 second cut at a sample rate of 7800 Hz, this is nearly

275,000 points. For Mz, Kistler states that the maximum drift is 0.2 Nm/min. This can be significant in terms of tangential cutting force. For a 12 mm diameter cutting tool, this equates to 33.3 N in tangential force. Fortunately, the Mz shift in this testing has been less than 0.02 Nm, or about 3.2 N, in most cases. If the left to right shift is less than 0.02 Nm we subtract the left no-load moment average from all data points. If the left to right shifts for Fx, Fy, or Mz exceed thresholds, an angular drift correction can be performed for all data for each of the sensors. Shift and Drift correction can be applied after raw data is captured which enables previously collected data to be post-processed. The Microsoft Excel spreadsheet tool developed for performing the signal drift compensation is included in Appendix O.

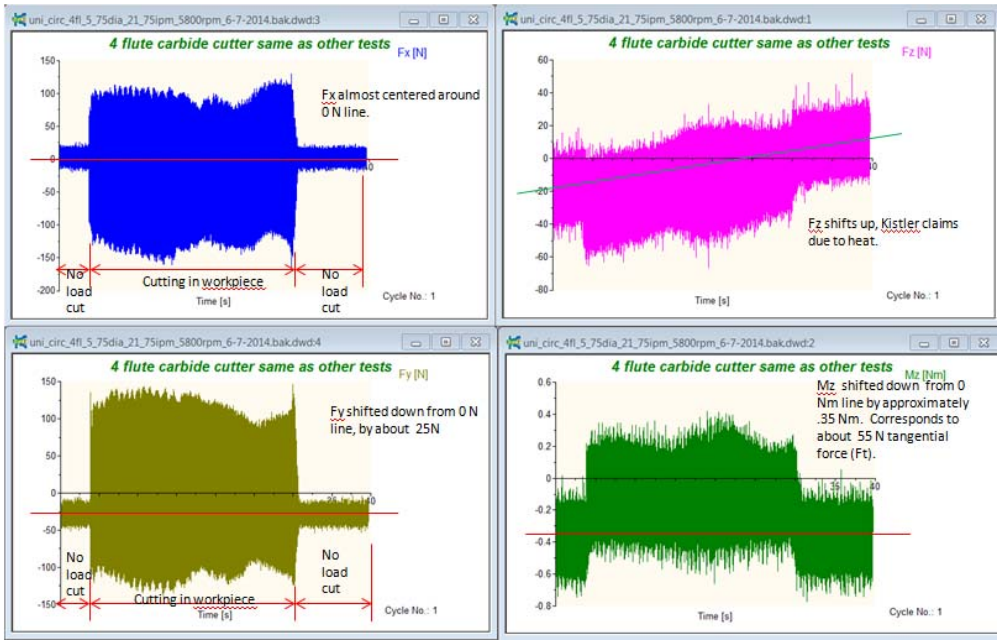

Figure 7.38. Data illustrating typical signal shift and drift

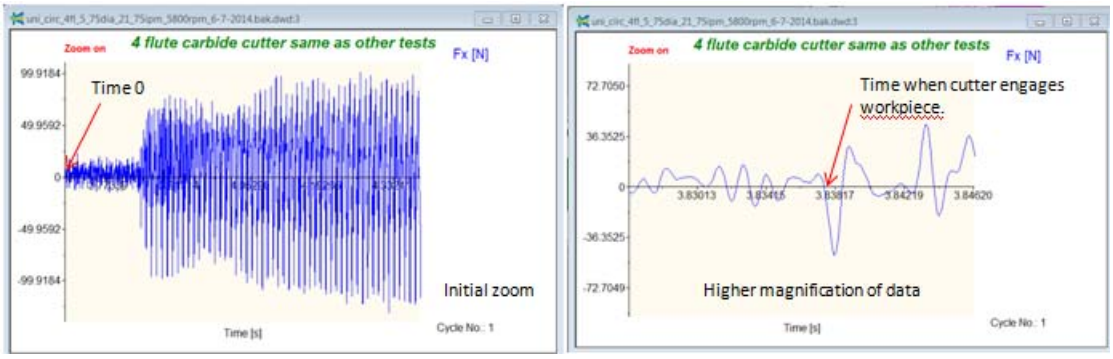

Figure 7.39. Finding time when cutter engages workpiece

7.4.4 Zoom Channel Magnification for Mz

Another opportunity for data improvement is with the moment measurement, Mz. The dynamometer has 2 ranges (coarse and fine) with specific limits for each channel as shown previously in Table 7.9. As discussed, Fx and Fy generally consume a significant portion of the 500 N fine range setting of the dynamometer for the cutting performed. However, for most cutting conditions used to date, Mz, is generally less than 1.5 Nm or less than 10% of the 20 Nm fine range. The Kistler 9123C is both a milling and drilling dynamometer so it has wide ranges, especially with Mz and Fz, as Mz and Fz will be considerably higher for drilling than milling. To address the significantly lower Mz values, an optional zoom amplifier was tested. The zoom magnification is a factor of 10x which magnifies both signal and noise. Experimentation was conducted to compare the results of Mz (Channel 4), and Mz using the zoom amplifier, Channel 5. With zoom amplification, the results are divided offline by a factor of 10. Hand testing results of this capability are included in Appendix P which show the effects of zoom amplification by simply rotating the dynamometer by hand and comparing Channel 4, Mz, to zoom Channel 5. More significant cutting tests were also conducted to evaluate the capability of using this feature. Figure 7.40 is a comparison of Mz with and without zoom amplification for a circular slot cut using a new 4-flute Mapal CVD cutter. The curve represents average values for each degree of the 180 degree semi-circular slot. There are 12 cutter rotations per each degree of the semi-circular slot from the cutting conditions included with the figure. Tangential force is calculated by dividing Mz by half the diameter of the 12 mm cutting tool used for this composite slot trimming test. As is evident, the average values for each degree of the semi-circular slot are nearly equivalent; however, if you look at a single degree of the semi-circular slot, the individual measurements differ as shown in Figure 7.41 which shows 2 cutter rotations from the 90 degree point. The zoomed channel 5 curve for Mz appears smoother than the unzoomed Mz channel 4 curve as a result of the amplification. The zoom channel data is only available if the 5223B Signal Conditioner, and DynoWare software is properly configured to capture the channel of choice at time of test. If the data has been properly captured, the signal drift compensation method described can be applied at any time to this data, further improving the accuracy.

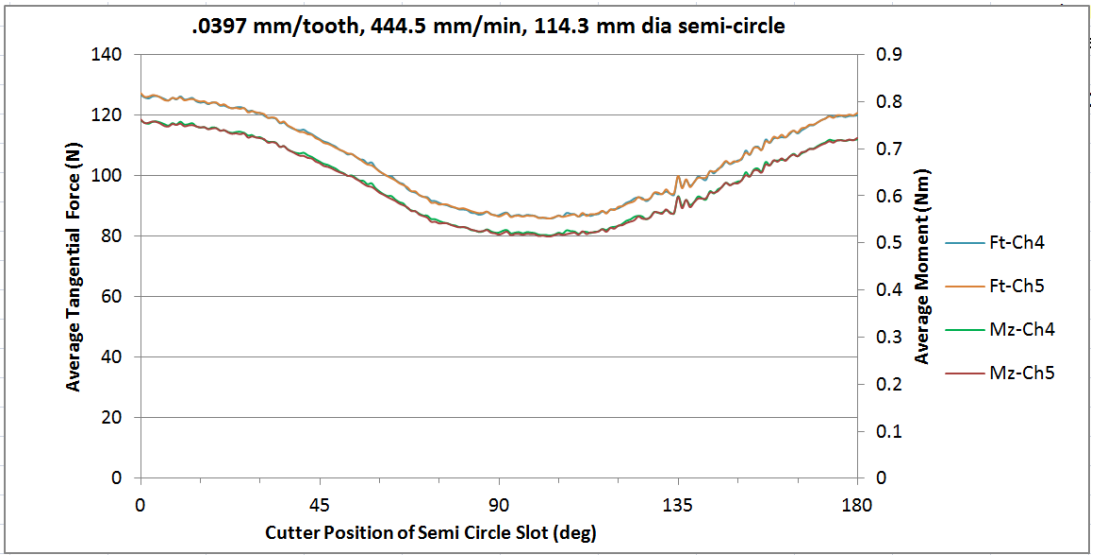

Figure 7.40. Comparison of Mz (Ch 4) and Mz with amplification (Ch 5)

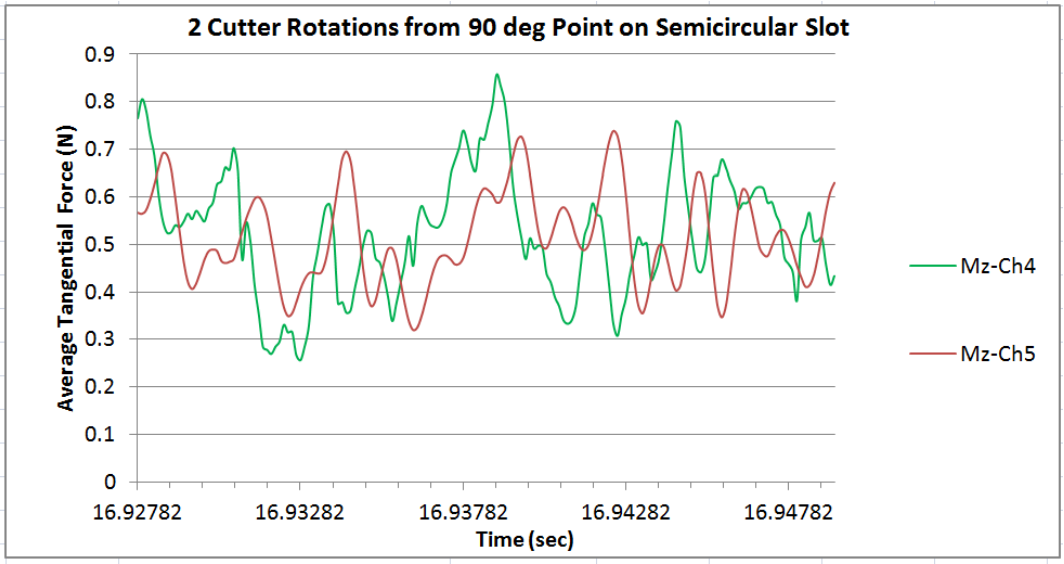

Figure 7.41. Two cutter rotations from the 90 degree point

Filtering provides another opportunity for data improvement. Limited testing was performed with the Butterworth filter capability inside of DynoWare. Benefits were not as obvious with other methods discussed in this section; however, filtering is used by other researchers and may have significant value. The four process improvement areas discussed significantly enhance the consistency and data quality of cutting force acquisition from the rotating dynamometer. With experimental technique process improvements identified and

tested, the effort moved to determination of cutting force coefficients using semi-circular slots in unidirectional laminates that can be applied to a force prediction model applicable to multi-directional composite laminates of the same material system described in the next section.

7.5 Semi-Circular Milling Model Development

A fundamental objective of this research is to develop a cutting force prediction model that requires minimal cutting experiments on a unidirectional laminate to obtain necessary parameters that can be used to predict cutting forces for a multi-directional composite laminate at any orientation for a given cutting tool, material system, and cutting conditions. While a purely analytical or numerical approach that could predict cutting forces for any cutting tool and material system with no physical testing required would be highly preferred, this capability is very difficult to accomplish. Current published techniques for composite milling force prediction utilize linear slot tests as previously described for obtaining basic milling model parameters. While this technique can provide approximate results, and is heavily leveraged for the proposed model in this research, it has been mostly limited to cutting relative to the four primary fiber orientations with unidirectional composites. In practice, large parts are not necessarily trimmed relative to the primary fiber orientations (0^o, 45^o, -45^o, 90^o) nor are they unidirectional. Using this method to capture parameters for accurate prediction of cutting forces relative to the fiber direction at non-standard angles could then potentially require dozens of additional tests, or high reliance on estimates. This is further compounded with multi-directional laminates, where there are different fiber orientations at each ply. Therefore, a more generic approach that can be used for cutting force prediction for multi-directional laminates at any known relative fiber orientation has been developed as part of this research. With linear slot tests complete to the point that feasibility has been established, a semi-circular slot configuration is proposed to acquire data from 0 to 180 degrees relative to fiber orientation for cutting force coefficients at each degree. Mathematical details of the model will be discussed in Chapter 9. The experimental method and design is described in the following section.

7.5.1 Experimental design

The semi-circular slot configuration is designed under the assumption that cutting relative to any fiber orientation can be approximated by a tangent on a circle as illustrated in figure 7.42.

While not perfectly linear at each degree position, the cutter follows a path that is sufficiently close to measure cutting forces at each position at a changing angle relative to fiber orientation. Further, symmetry provides that only a half the circle is required for measurements at each degree position, as a slot cut provides both a conventional and climb edge within the slot, which is used for cutting force coefficient calculation. Instead of a separate linear slot for each desired cutting angle relative to fiber orientation, the circular pattern captures all angles. With between 3-6 slots needed for each angle in the cutting model, only 3-6 circular slots are required versus 540-1080 linear slots if data was required for every angle. This can consume quite a lot of expensive material and cutters, and be very time consuming to conduct. The data from cutting a unidirectional laminate will also be used to predict the cutting forces for the multi-directional laminate case in this model.

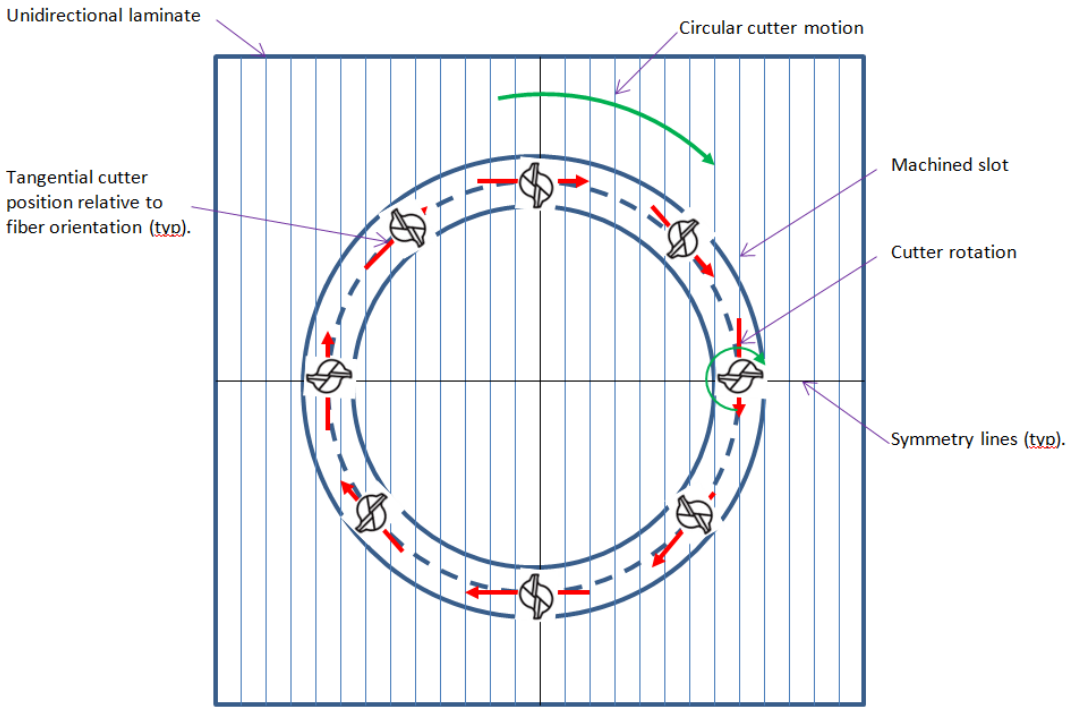

Figure 7.42. Circular slot illustration

With this approach, experimental details are then defined. A test part sizing model was built to facilitate calculations. The goal is to have at least 5 semi-circular slots in a single work piece, for a single set up, and fit the workpiece within the working envelope of the existing dust containment system for dust capture and analysis. The part also had to utilize the machine travel limits within the enclosure and the existing fixturing base. Exceeding these limits would require a new enclosure and new tooling. Further, each slot requires a different feed rate in terms of feed

per tooth for regression analysis in the cutting model which is determined by spindle speed, linear feed rate, and number of teeth on a cutter. To keep file sizes within reason, cutting tests should be kept within approximately 35 seconds. For modeling purposes, each cut had to be performed at a constant velocity so affects of machine acceleration needed to be addressed. Diametric sizing of the slots was also important as this determines slot cutting distance. The longer the circular slot along the arc length, the more cutter rotations per degree, depending on spindle speed. More rotations provides more data for sampling. Further because of the 7800 Hz limit of the dynamometer, higher spindle speed provides fewer measurements per cutter rotation. The HAAS machine also has a spindle speed limit of 6000 rpm. Two part sizing models were built with one having a lead in parallel to the machine X-axis and the other parallel to the machine Y-axis. To work within enclosure and machine travel limits, the Y-Axis version has been used for the experiments. Circular slot model input sizing parameters include the following:

- Cutter diameter
- Number of teeth on the cutter
- Fixed spacing between circular slots
- Diameter of the first inner slot
- Axial depth of cut
- Linear feed rate (separate for each slot)
- Spindle speed (separate for each slot)
- Ply thickness (for reference calculations)
- Lead in/out slot length (to account for machine acceleration)

The semi-circular slot model output includes the following data for each slot and work piece:

- Feed/tooth
- Feed/revolution
- Cutting speed
- Cutting length (total; semi-circle, lead-in, lead out)
- Cutting time (total; semi-circle, lead-in, lead out)
- Number of cutter rotations (total; semi-circle, lead-in, lead-out)
- Dynamometer measurements (total; each degree of semi-circle, each rotation)
- Material removal rate (total; semi-circle, lead-in, lead-out
- Work piece part size and graphic

The input parameters are adjusted to find an optimal combination of output parameters prior to conducting a test. For aluminum testing, axial depth of cut, cutting speed and feed/tooth are targeted for established parameters in the Machining Data Center Handbook [120], while

providing a reasonable spread in feed/tooth for subsequent regression analysis across five slots. For composite laminate testing, guidelines including a feed/revolution at approximately ½ to $^{1}/_{3}$ of a ply thickness while achieving a reasonable spread in feed/tooth across five slots. The feed/tooth targets in composite laminates are considerably lower than for aluminum driving higher spindle speeds, thus delivering fewer data points per revolution. Typical feed/tooth per aluminum in a slot cut may be approximately 0.13 - 0.15 mm/tooth, where for composites it may be approximately 0.01 - .03 mm/tooth. The figure produced by the Microsoft Excel Circular Slot parameter sizing model developed as part of this research is shown in Figure 7.43 with more details in Appendix Q. The figure illustrates the geometry to be cut during the circular slot tests. Some excess material around the minimum slot boundaries is used in the actual work piece for fixturing. Fixturing is accomplished with 2 aluminum riser bars in the front and back below the work piece and 4 bolts which go through the workpiece and riser bars into a steel subplate with tapped holes.

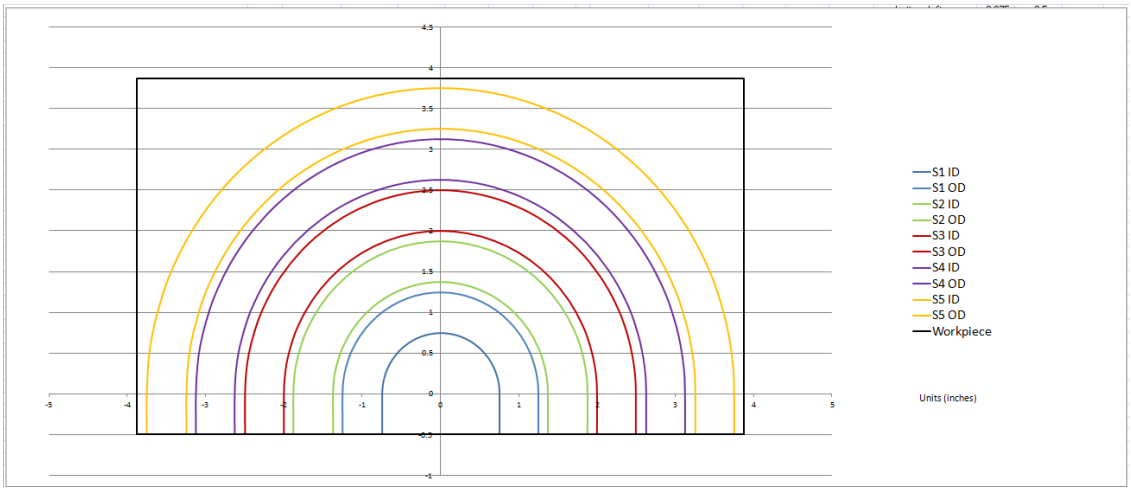

Figure 7.43. Graphical output from circular slot parameter model

A key element for ensuring the cutter position is known relative to any given radial degree position on the semi-circle is timing of the slot cutting process. Precise timing is required to ensure accurate cutter location for this model. This is accomplished through several techniques. First, prior to the circular slot cutting test, the work piece boundary at the linear lead-in and lead-slot locations are faced to establish the exact machine Y-coordinate of the workpiece. This facing cut is made parallel to the machine X-Axis. Next, the cutter is offset by a pre-determined amount that is incorporated into the sizing model. This is done to account for

machine acceleration time, or the time it takes for the machine to get to the programmed velocity. According to HAAS, the machine has a minimum acceleration of 1,600,000 encoder steps/sec^2, with the encoder providing a resolution of 138,718 steps/inch. This gives an acceleration of 11.534 in/sec^2 or 0.293 m/sec^2. Using basic equations of motion, a programmed velocity at 1016 mm/min (maximum used in testing) would take 0.75 sec to get to the part with a 12.7 mm offset (typical). The time to accelerate to 1016 mm/min is 0.058 sec at an acceleration of 0.293 m/sec^2. Since the time to get the programmed velocity is less than the time to get to the part, a 12.7mm offset is acceptable. The timing when the cutter contacts the part is found through an inspection of the data as described earlier. The nearly exact time the cutter contacts the part is found by identifying the time the force data first increases. This can be accomplished to within approximately 0.001 sec. accuracy by inspection. With the time at part contact identified; lead in distance, semi-circle diameter, and programmed velocity known, the time to the start of the semi-circle cut can be calculated. Using the semi-circle diameter, programmed velocity, calculating the arc length and diving into 180 degree segments provides a time position for each degree. With the time position for each degree known, the associated forces and moments can be captured and processed. The force data can be further analyzed to check if the predicted time for exit from the work piece matches the actual time. At cutter exit, the forces should return to the no-load conditions. Appendix R provides an illustration of the cutter offset and timing.

7.5.2 First Aluminum Semi-Circular Slot Test

To test the concept on a homogeneous material, the first circular slot test was performed with a 95.25 mm thick 6061-T6 aluminum plate using a 12.7 mm diameter, new 2-flute solid carbide cutting tool with 30 degree helix. The cutting conditions for each of five semi-circular slots are summarized in table 7.11. Detailed analysis is in Appendix S. Figure 7.44 are photographs of the part on the machine and completed part. Following the tests that were designed using the part parameter set up tool, the raw data from each slot is exported from Kistler DynoWare software. The raw data included time, Fx, Fy, Mz. Prior versions exported Ft directly, but newer versions of the software developed for this research derive Ft from Mz as well as can handle the amplified channel. The amplified or zoom channel was not used in calculations. This raw data is then merged into a analysis tool with a separate file for each slot.

Future versions can consolidate some of these functions. Similar input parameters as described earlier are used with one addition being the time of first cutter contact with the work piece which is easily found from a quick analysis of the cutting force data in DynoWare or looking at a plot of the raw data. The data analysis tool first performs signal drift compensation as described earlier and adjusts the three channels (Fx, Fy, Mz), by centering around the left-side, no-load cutting signal. It then calculates Ft, Fr, Fx (abs), Fy (abs), and Fa both by using Fx, Fy and by using Ft, Fr. Timing analysis is then performed by using the time of first cutter contact, velocity, lead-in length, and slot diameter, to calculate the time and position of each degree of the semi-circular slot. The integer value of the number of complete cutter revolutions between degree point is calculated. Using the number of complete cutter revolutions, average values for Fx(abs), Fy(abs), Ft, Fr, and Fa(x,y), and Fa(t,r) are calculated and plotted for each of 180 degrees of the semicircular slot cut. Further analysis is also performed by looking at the number of instances of where Fr equals 0 at each degree. If this occurs for greater than about 10-15% of the data analyzed, there is a high likelihood of data issues. This may be due to excessive chatter because of improper cutting conditions. Figure 7.45 is a typical summary of data provided from the analysis tool following the processes described for 3 slots of the series. Additional plots are included in Appendix S. In this figure the approximate average forces for each degree position are plotted. As expected, for a homogeneous material like aluminum the data is relatively flat as shown in slot 3. However, the testing was not fully consistent as perfectly flat curves were not achieved for all 5 slots. The data from this tool for all five slots is then imported into a separate tool to calculate cutting force coefficients for use in the milling model which is described in detail in chapter 9.

Table 7.11. Cutting conditions for aluminum circular slot test

Test ID	**Cutter (mm)**	**Depth of cut (mm)**	**Slot Dia in (mm)**	**RPM**	**Feedrate ipm (mm/min)**
6/7/14-1	12.7, 2fl	2.54	2 (50.8)	3500	10 (254)
6/7/14-2	12.7, 2fl	2.54	3.25 (82.55)	3500	15 (381)
6/7/14-3	12.7, 2fl	2.54	4.5 (114.3)	3500	20 (508)
6/7/14-4	12.7, 2fl	2.54	5.75 (146.05)	3500	25 (635)
6/7/14-5	12.7, 2fl	2.54	7 (177.8)	3500	30 (762)

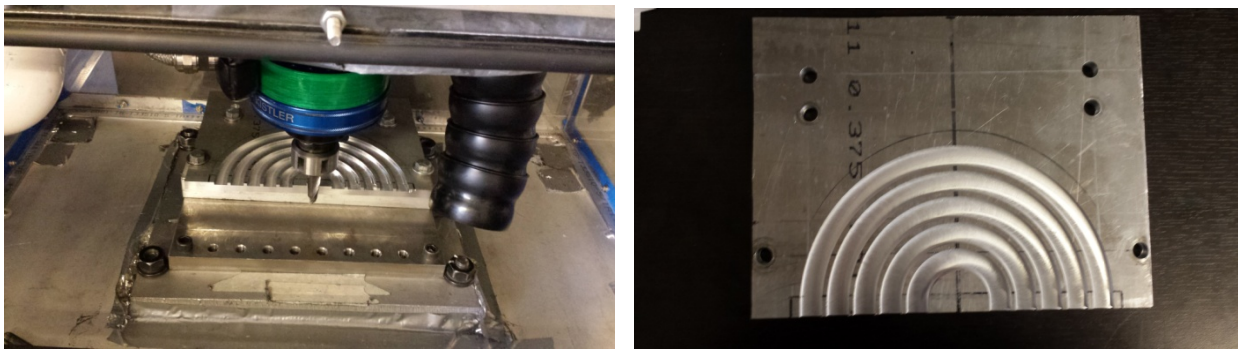

Figure 7.44. Aluminum circular slot test

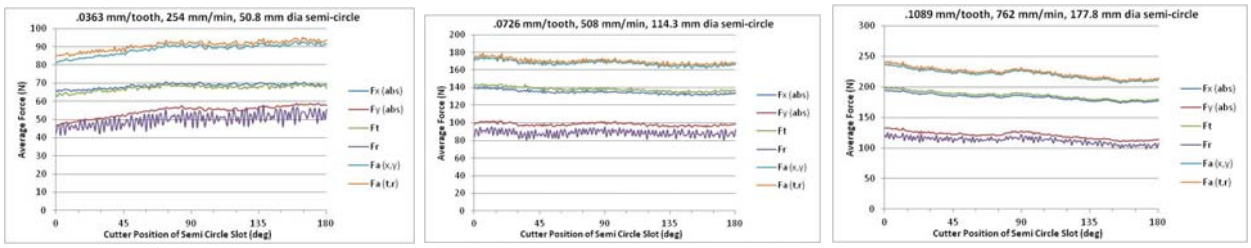

Figure 7.45. Aluminum circular slot data slot 1 left, slot 3 middle, slot 5 right.

Plots of the average cutting forces used to determine the cutting force coefficients for this aluminum test are provided in figure 7.46 for five positions on the circular slot, corresponding to primary fiber orientations of a composite (0^o, 45^o, 90^o, 135^o, 180^o). With the cutting edge of the 2-flute cutter in these experiments aligned to the y-axis of the dynamometer, relatively linear tangential force and X-axis force plots were obtained. The radial force and Y-axis force plots are not quite as linear.

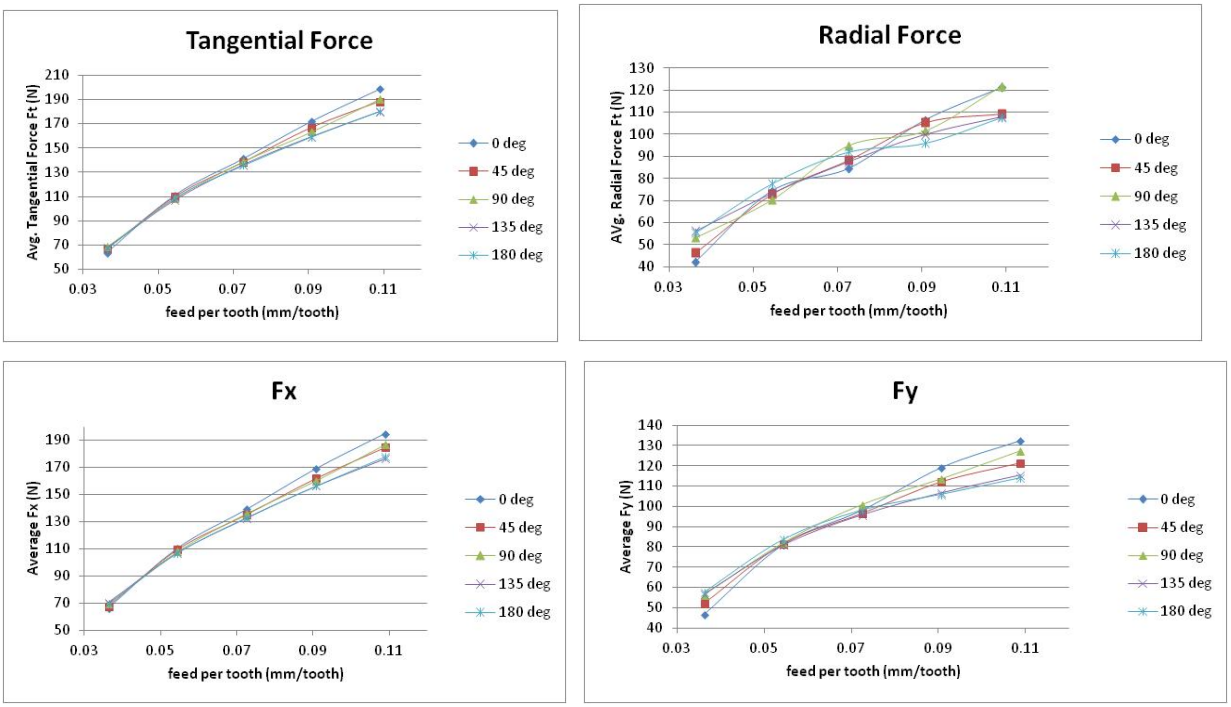

Figure 7.46. Force vs. feed plots for first aluminum semi-circular slot test

Similar to the linear models, cutting force coefficients were calculated at each degree position based on the average cutting forces. These were determined using two of the methods discussed for linear slots including the Karpat [58] with Ft, Fr and Karpat with Fx, Fy. The plot for the Karpat method using Ft, Fr is shown in figure 7.47 and the plot for the Karpat method using Fx, Fy is included in figure 7.48.

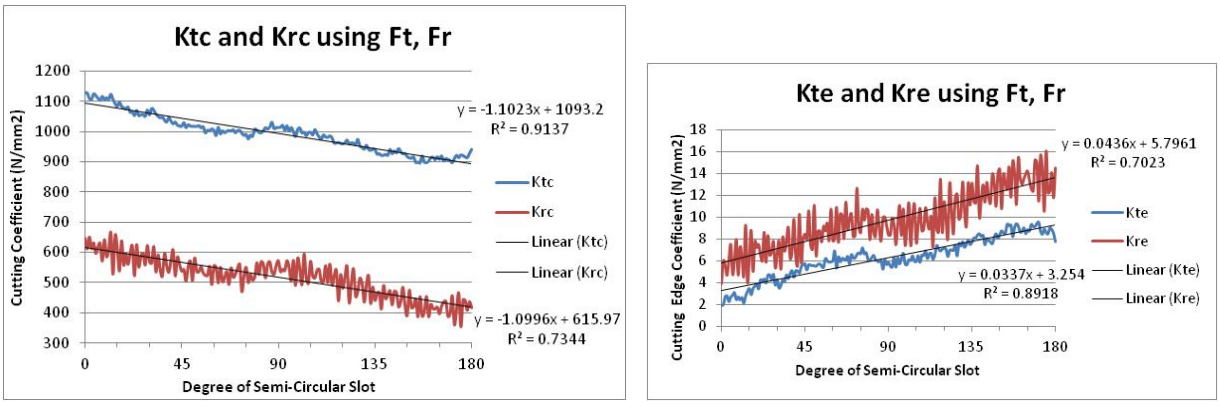

Figure 7.47. Cutting force coefficients using Ft, Fr and Karpat method

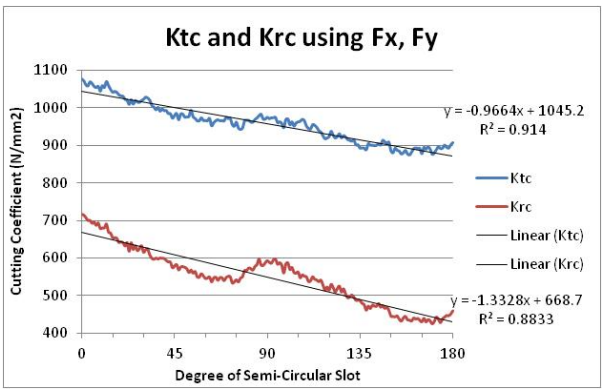

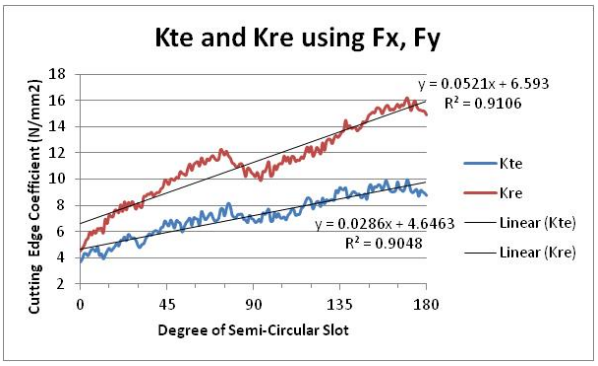

Figure 7.48. Cutting force coefficients using Fx, Fy and Karpat method

Since the milling coefficients are determined through linear regression, a comparison of the correlation coefficients are plotted for the two methods in figure 7.49 to provide an assessment of linearity at each degree position.

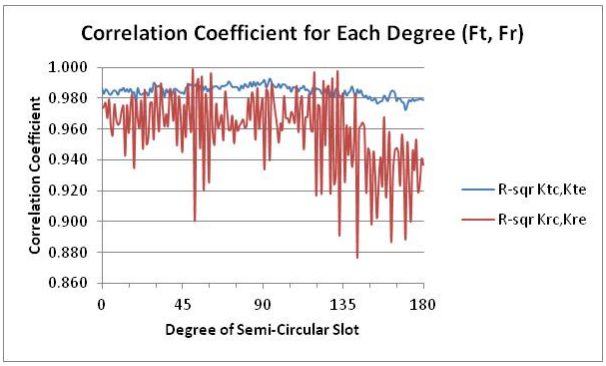

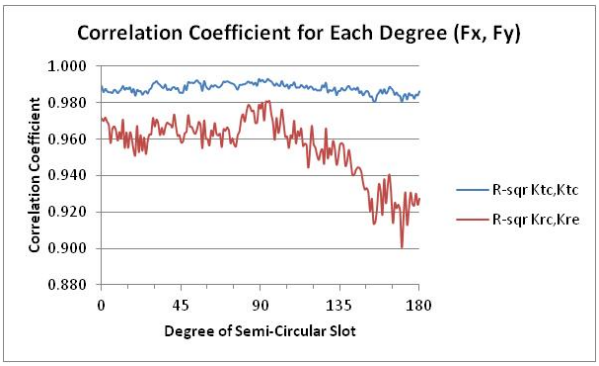

Figure 7.49. Plot of correlation coefficients for two methods.

With the basic fundamentals established for the semi-circular slot method using a homogeneous aluminum test case, the next phase involved testing on unidirectional composite laminates. The force prediction model will use the milling coefficients from the unidirectional laminate to predict cutting forces for multi-directional laminates of the same material system and cutting tool.

7.5.3 First Semi-Circular Composite Slot Tests

Following the same approach for the aluminum slot, composite semi-circular slot experiments were then performed using a 99 ply unidirectional laminate. The first semi-circular

slot test used a new 4-flute solid carbide 30 degree helix cutter, but due to a programming error, there were only 4 of 5 usable slots for data. Results for this test are included in Appendix T. For the next semi-circular slot test, a new solid carbide 2 flute helical cutter was used. Table 7.12 summarizes the cutting conditions for this test. The quality of the finish on this test had many uncut fibers with significant delamination. This was likely due to the choice of cutting tool. The solid carbide 2-flute, 30 degree helical cutter works well with aluminum, but is not designed for composites. Figure 7.50 is a photograph of the 2-flute solid carbide test.

Table 7.12 Cutting conditions for 2-flute composite slot cutting test

Test ID	Cutter (mm)	Depth of cut (mm)	Slot Dia in (mm)	RPM	Feedrate ipm (mm/min)
6/14/14-6	12.7, 2fl	2.54	2 (50.8)	4800	9 (228.6)
6/14/14-7	12.7, 2fl	2.54	3.25 (82.55)	5300	13.25 (336.5)
6/14/14-8	12.7, 2fl	2.54	4.5 (114.3)	5600	17.5 (444.5)
6/14/14-9	12.7, 2fl	2.54	5.75 (146.05)	5800	21.75 (552.4)
6/14/14-10	12.7, 2fl	2.54	7 (177.8)	5943	26 (660.4)

Figure 7.50. 2-flute carbide circular slot cutting test

Similar to the aluminum slot test results, average force results from three slots are provided in figure 7.51 for each degree of cutter rotation, with results from the two additional slots in Appendix U. Plots of the average cutting forces used to determine the cutting force coefficients are provided in figure 7.52 for the primary fiber orientations.

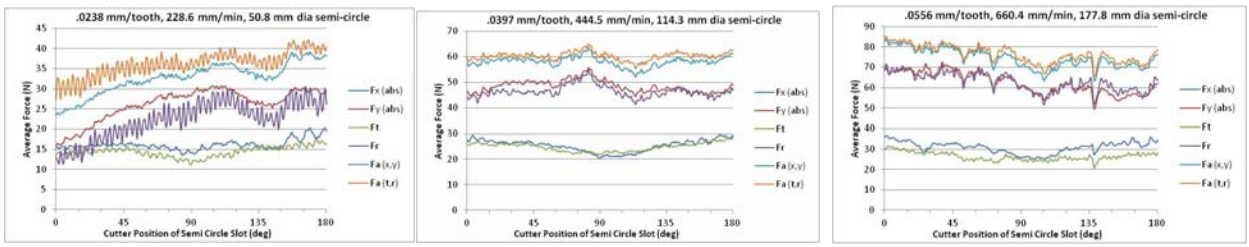

Figure 7.51. Composite slot data: slot 1 left, slot 3 middle, slot 5 right.

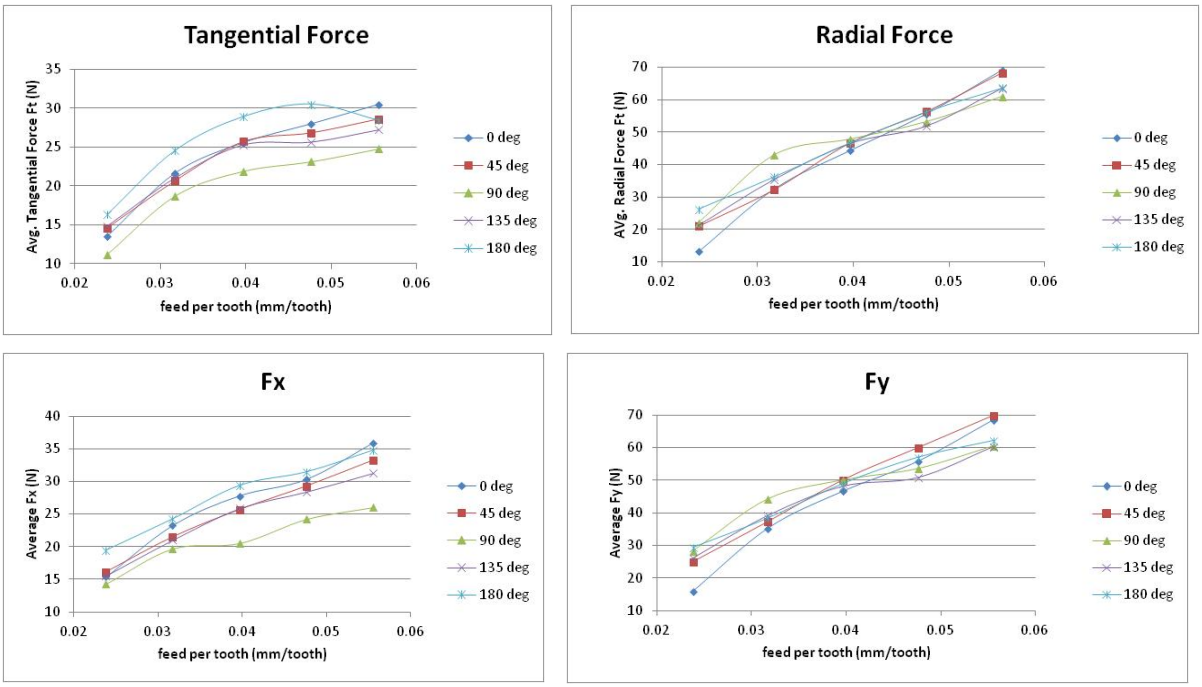

Figure 7.52. Force vs. feed plots for composite 2-flute semi-circular slot test

The calculated cutting force coefficients are plotted in figure 7.53 and 7.54 for each degree position using the two methods described for the aluminum semi-circular slot. Correlation coefficients at each degree position for the cutting forces are shown in figure 7.55 to compare the results of the two methods with respect to linearity. Again, the Fx, Fy method can be used for this case because of the 2-flute cutting tool.

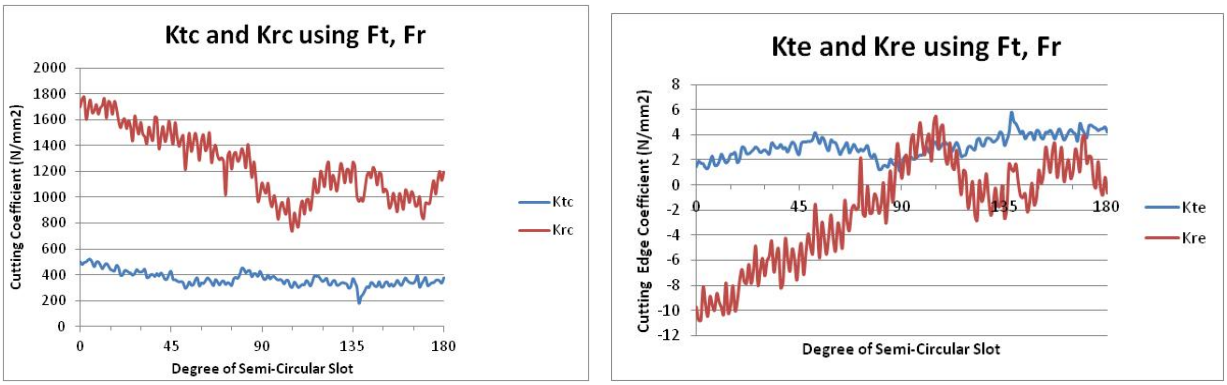

Figure 7.53. Cutting force coefficients using Ft, Fr and Karpat method

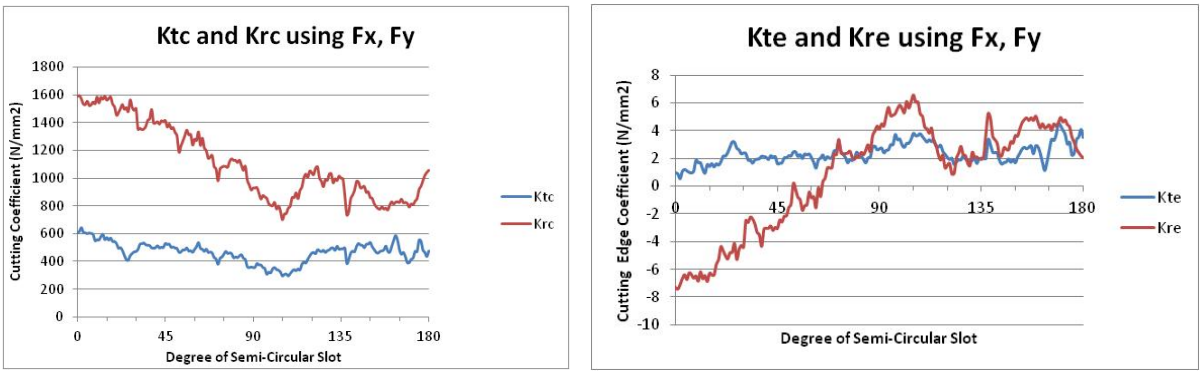

Figure 7.54. Cutting force coefficients using Fx, Fy and Karpat method

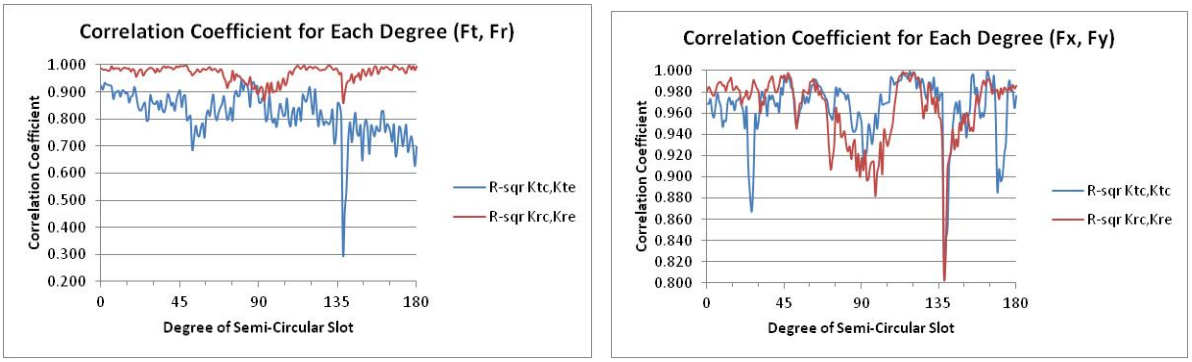

Figure 7.55. Plot of correlation coefficients for two methods.

7.5.4 Semi-Circular Composite Slots Test Using 4-Flute CVD Tool

The next composite circular slot test was conducted with a new 4-flute Mapal CVD coated cutting tool designed for composite materials. A deeper depth of cut at 5.08 mm was selected to drive up the cutting forces to use more of the dynamometer fine range. Parameters for this test are included in table 7.13. Photographs of this circular slot cutting test are shown in

figure 7.56. As can be seen from the right photograph, the quality of the cutting tool makes a big difference in the quality of the milled slot. These slots had minimal defects compared to all other composite slot tests. Very little uncut fibers were detected, with the exception of a small amount at around the 90 degree position of the inner wall of slot 4.

Table 7.13. Cutting conditions for Mapal 4-flute CVD tool

Test ID	Cutter (mm)	Depth of cut (mm)	Slot Dia in (mm)	RPM	Feedrate ipm (mm/min)
7/19/14-1	12, 4fl	5.08	2 (50.8)	4800	9 (228.6)
7/19/14-2	12, 4fl	5.08	3.25 (82.55)	5300	13.25 (336.5)
7/19/14-3	12, 4fl	5.08	4.5 (114.3)	5600	17.5 (444.5)
7/19/14-4	12, 4fl	5.08	5.75 (146.05)	5800	21.75 (552.4)
7/19/14-5	12, 4fl	5.08	7 (177.8)	5943	26 (660.4)

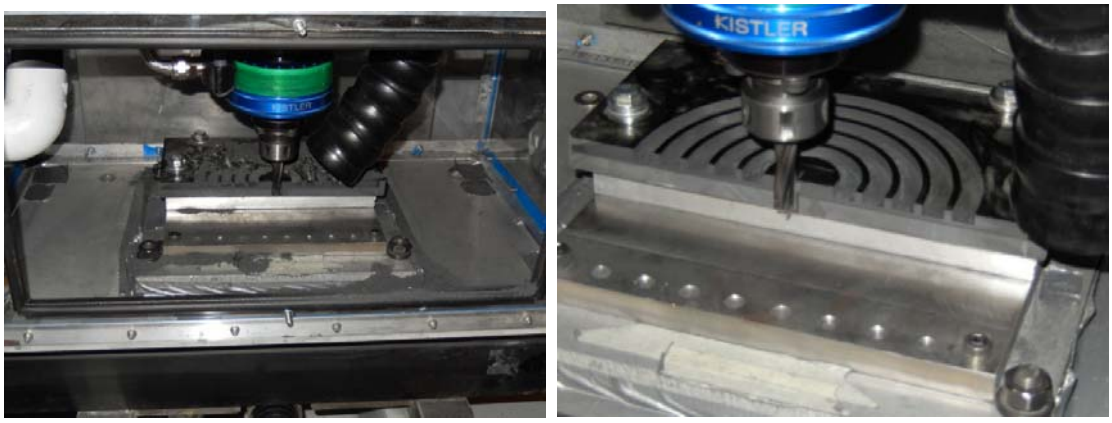

Figure 7.56. Mapal 4-flute CVD composite cutting test

The quality of the tangential cutting force data was also significantly better. Consistent with the other semi-circular slot examples in this section, figure 7.57 includes the average force profiles for each degree of cutter rotation. All 5 slots were provided to show the relative consistency of data. It should be noted that the resultant force plots, Fa, calculated from Fx,Fy and Ft,Fr align well consistently between 45-90 degrees, but diverge at either end. Since a 4-flute cutting tool was used, separate plots for Fx and Fy are not plotted as cutting force coefficients will be calculated from Ft, Fr. With the exception of the first slot, the resultant force curve is relatively smooth when determined by Ft, Fr. This could be due to a poor combination

of cutting conditions for the first slot or chatter. This test was designed to uniformly verify increments of feed rate ranging from $^1/_3$ to ½ of a ply thickness per revolution, with one increment below and one above.

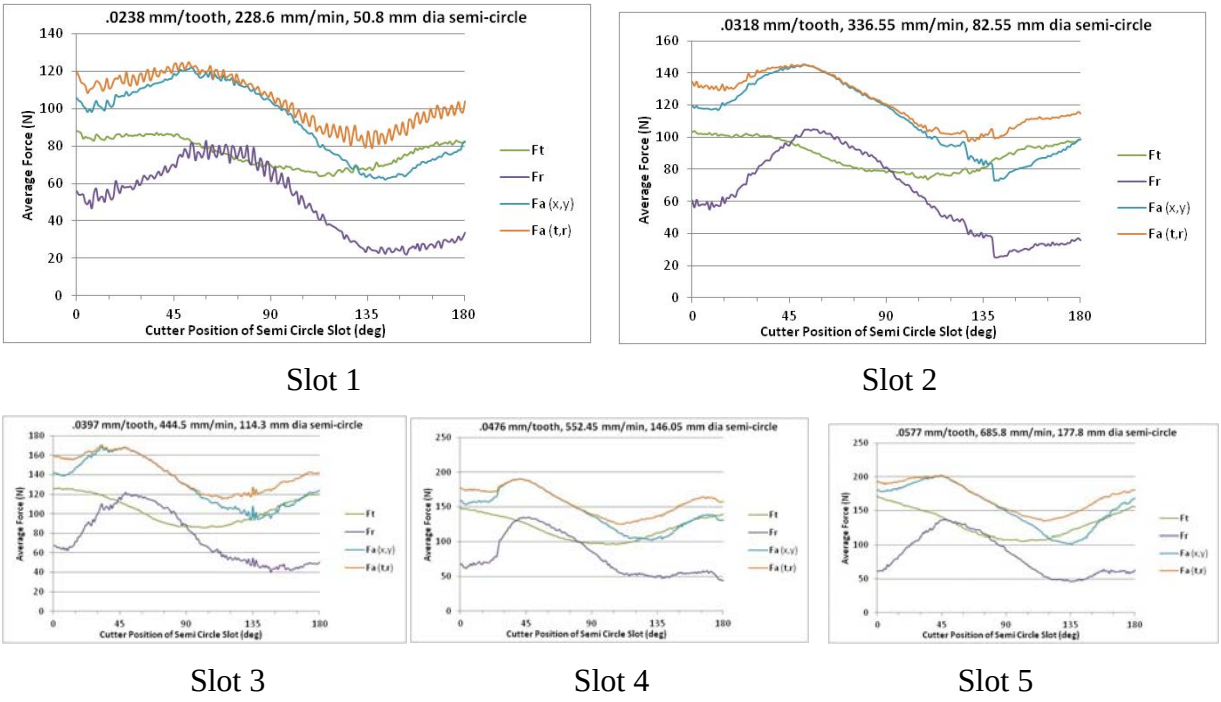

Figure 7.57 Mapal 4-flute CVD tool cutting force test results.

Tangential and radial forces are plotted in figure 7.58 for the primary fiber orientations. The tangential force plot relative to feed per tooth for the five slot tests are mostly linear at each primary fiber orientation, with the radial forces not following quite as linear a trend. The cutting force coefficients are plotted in figure 7.59 for each relative position of the semi-circular slot. The cutting force coefficients were calculated only by the Karpat Ft,Fr method as the Fx,Fy method is not applicable for the 4-flute cutter as more than one tooth is engaged in the work piece at any point in time. Correlation coefficients for each degree of the semi-circular slot are plotted in figure 7.60. The cutting force coefficients (Ktc, Kte) derived from the tangential cutting force are exceptionally linear across all degree positions of the semi-circular slot. This is not the case for the milling coefficients (Krc, Kre) calculated from the radial force. The radial force is again derived from the Mz, Fx, and Fy sensors of the dynamometer. While the steps taken to improve data quality, including using the correct collets, maximizing force values in the

dynamometer fine range, and signal drift correction appears to have significantly helped, it is still not enough to correct the radial force derivation so that the cutting force coefficients follow a linear trend. This also could be the nature of circular slot milling unidirectional composite laminates.

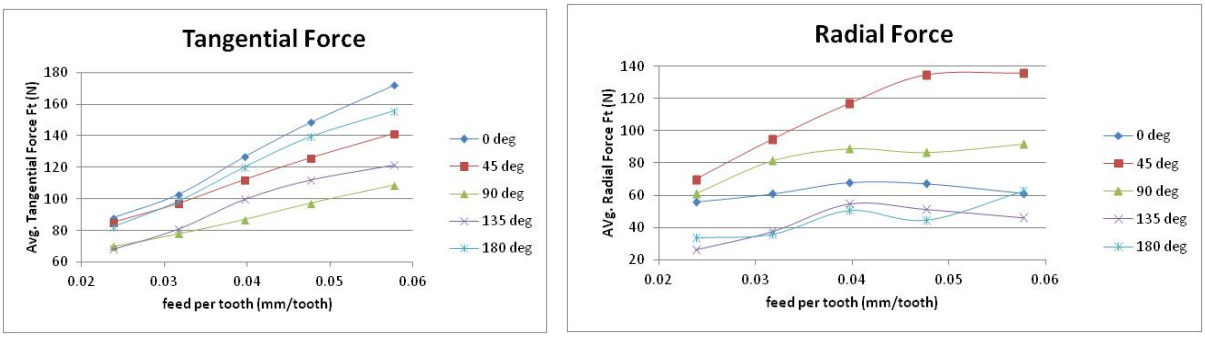

Figure 7.58. Tangential and radial forces for 4-flute Mapal CVD cutter test.

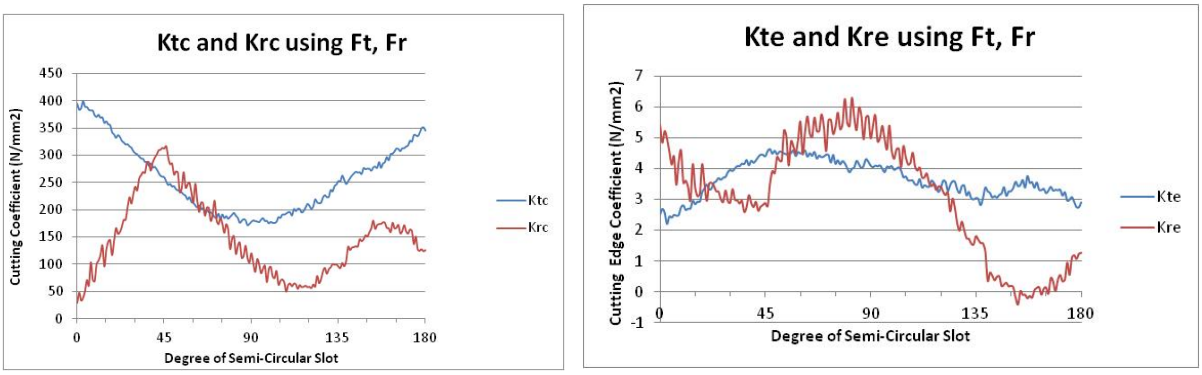

Figure 7.59. Cutting force coefficients for 4-flute Mapal CVD cutter test.

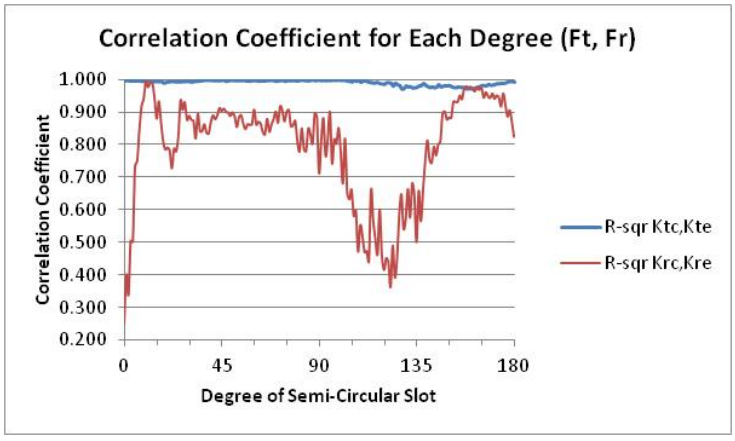

Figure 7.60. Correlation coefficients for 4-flute CVD cutter test.

7.6 Summary

This chapter addressed the development of experimental techniques for determining milling coefficients to be used in the force prediction model for trimming of multi-directional composite materials which will be discussed in chapter 9. Data from milling aluminum as a homogeneous control case was compared to that from milling composite laminates. From this comparison, several experimental technique improvements were accomplished to address the challenges in working with the rotating dynamometer. Tests were performed on linear slots which established viability of the method to determine milling force coefficients which are integral to the model for predicting cutting forces. This served as a building block for conducting the semi-circular milling slot tests which are ultimately used in the force prediction model for multi-directional composite laminates. The use of high quality cutting tools designed for composites under appropriate cutting conditions appeared to improve the quality of the cutting force data when milling the semi-circular slots. Chapter 9 will discuss the mathematics of the cutting force prediction model which utilizes the milling coefficients determined through the experimental effort described in this chapter.

CHAPTER 8

PARTICLE ANALYSIS AND MODELING

8.1 Introduction

This chapter will discuss the models and tools developed for analysis and presentation of dust generated from machining of composite materials. A combination of software tools including Microsoft Excel, Matlab, and Mathematica were used to create elements of the models as will be described. Data used in the particle models was acquired from the GRIMM 1.109 Portable Aerosol Spectrometer and 1178 LabVIEW Software. Comparative and supporting data was acquired from the PTRAK 8525, Casella Microdust Pro CEL-712, ThermoFisher Scientific PDR DataRAM and respective accompanying software. Additional data used for comparative purposes was collected using the Sioutas Cascade Impactor with results provided from custom-built Excel analysis tools. The purpose of these models is to provide tools and techniques that can be applied in an industrial or lab environment for analysis of particles generated from trimming composite materials. Only a few studies have been published which address the dust generated by milling of composites covered in the literature review. Certain key observations prepared using these models will be compared to some of the limited published literature. Techniques for calibration to a specific aerosol will also be addressed.

8.2 Particle Analysis Tools and Models

Tools and models to assist in analyzing the particles generated from milling operations were developed as part of this research. Several simple tools incorporate inspection data from multiple instruments by comparing particle concentration and count in single plots. The purpose of these tools is to compare results of different instruments to establish consistency in measurement and validate performance of the closed-loop isokinetic sampling system. The models are time based so that they are aligned based on initial concentration during milling testing. All dust collection tests are performed with the vacuum and return air system on prior to cutting to normalize the results. Both particle count and mass concentration are generally close to zero levels when the air return system and vacuum is on as no dust is being generated from

cutting and only filtered air is entering the chamber serving as a purge. Synchronization becomes possible by alignment to initial spikes in count or concentration as the initial dust from cutting experiments reaches the instruments. This enables direct comparison of results, which are easily plotted. Examples of combined plots from multiple air sampling instruments were provided in Chapter 6.

Other tools developed as part of this research include custom spreadsheets that are used for providing results from cascade impactor tests. For these tools, the mass of conditioned unexposed filters are measured and recorded prior to sampling, with the mass of conditioned exposed filters after sampling also recorded. The tool than proceeds to calculate mass summaries by filter stage and automatically produces a log-probability plot, calculating median diameter, geometric standard deviation, and the correlation coefficient. Examples of log-probability plots from Sioutas cascade impactors were also provided in Chapter 6.

8.2.1 Log Probability Plots for GRIMM Aerosol Spectrometer

A model was built using data from the GRIMM 1.109 Portable Aerosol Spectrometer to generate log-probability plots and determine mass median diameter, geometric standard deviation, and the correlation coefficient for each sample. This instrument provides 31 channels of data so it enables flexibility in collection and separation of data compared to the other instruments used in Phase 3, 4 and 5 of this research. Samples are taken at 6 second intervals for all channels or bins of the instrument. The objective of the model is to compare concentration data to that collected by the cascade impactor for particle sizing analysis. The same approach can also be used with the other mass and count concentration instruments that can size separate particles using cyclones or polyurethane foam filters. However, since only one cut point is used at a time, utilizing these other instruments in this manner could be very time consuming. Point results from these instruments can be useful to check consistency which can be acquired in parallel during the same cutting experiment, as was deployed in this research.

The basic model is illustrated in figure 8.1 with each section to be described identified by a bracketed letter. Section [A] of the model is the input block. For rapid development and quick modifications, the basic model was developed in Microsoft Excel. However, the same logic can be executed in a number of different environments. For the initial model input, particle count

data is copied directly from the GRIMM 1.178 LabVIEW software Excel Output and directly pasted into a preformatted spreadsheet input tab. The user can then identify a single density for each bin range, or single density for all bins. GRIMM actually uses 1.67 g/cm^3 as a common density within their software for all bins except bin midranges .58μm and .65μm which use 1.76 and 1.75 g/cm^3, respectively. GRIMM considers this proprietary, but it can be determined from the LabVIEW 1178 software Excel output by using the count and mass tabs assuming a spherical geometry with bin midrange as the diameter and solving for density. In the model built for this research, the user also enters a dilution ratio which serves as a multiplier. Dilution was utilized in the experiments as the concentrations from milling of composites were found to exceed the instrument limits. The GRIMM software does not have this feature. The user also enters a very small correction factor which simply prevents some Excel functions from crashing with zero values without impacting results.

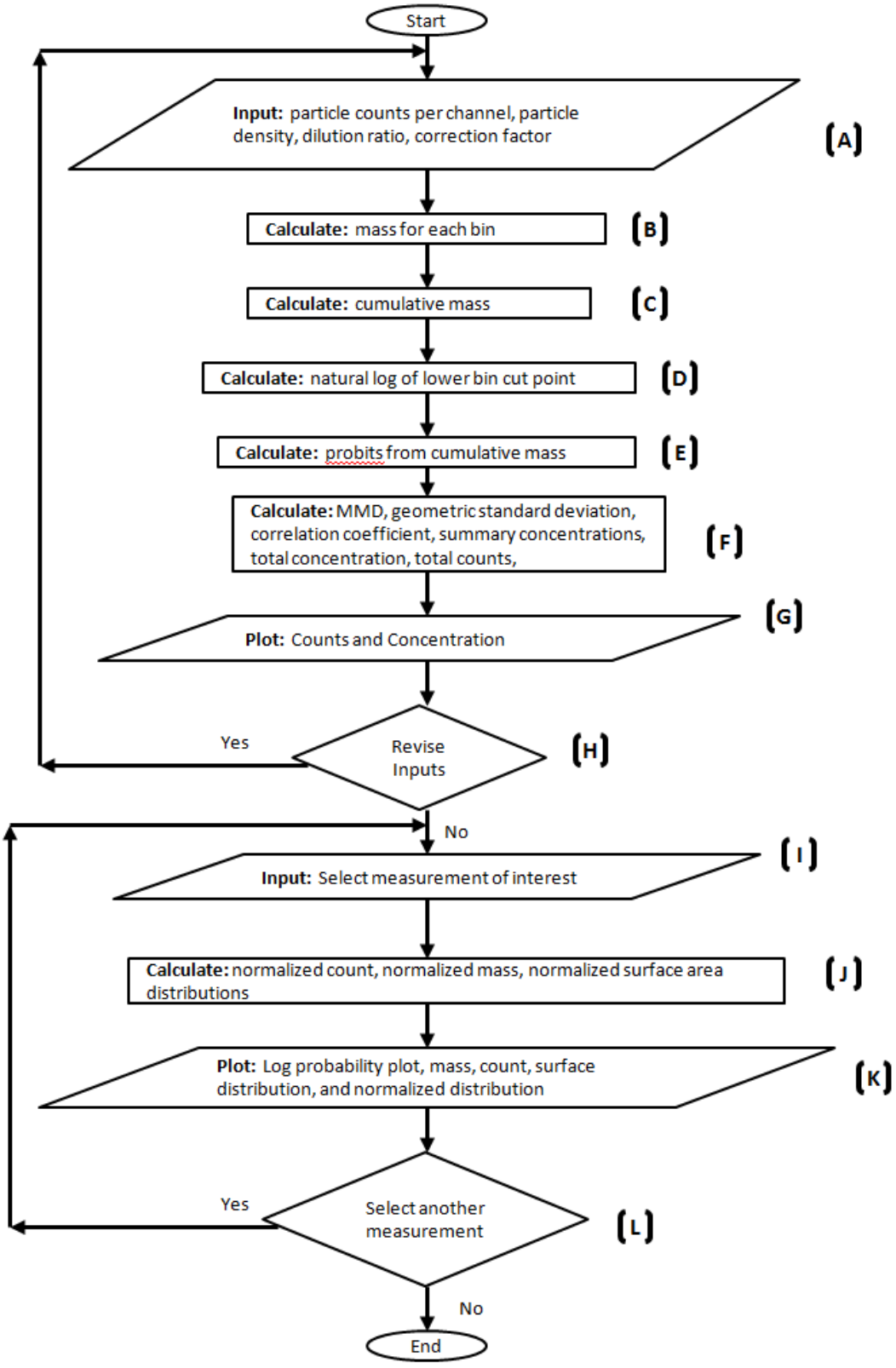

Figure 8.1 GRIMM Particle Model

Mass for each bin is then calculated and recorded in a separate tab identified in section [B]. Mass for each bin sample is simply calculated as follows:

$$mass = \rho \frac{1}{6} \pi {d_{mp}}^3 \mathrm{f} \qquad (8.1)$$

where ρ is the particle density, $d_{mp,}$ is the bin midpoint diameter, and, f, is the dilution ratio. Cumulative mass is calculated in section [C] and recorded in a separate tab. Cumulative mass is simply the increasing mass consisting of the sum of each successive bin size from smallest to largest. The natural log for the lower bin cut point for each size is calculated in section [D] and recorded in a separate tab. This is used in conjunction with the probit table calculated in section [E] to build the log-probability plot. To build the probit table, the Excel NORMSINV function is applied to the cumulative mass calculated in section [C], which is the inverse of the standard normal cumulative distribution. In section [F] results are calculated in a new tab for the following values with graphs for the cumulative data values for each sample automatically plotted in section [G].

- d_{50} mass median diameter
- σ_g geometric standard deviation
- R^2 correlation coefficient
- Cumulative mass concentration
- Total mass concentration
- Total counts

The values for d50, σ_g, and R^2 are determined from the data determined in sections [B] – [E] and extracted using Excel functions described in Appendix V. Calculations for σ_g and d_{50} are presented in equations 8.2 and 8.3, respectively. The geometric mean diameter, d_g, is described by equation 8.4 and is equivalent to the count median diameter (CMD) for lognormal distributions. In lognormal distributions, the log of the particle size distribution is symmetrical, so the mean and median are equal. Lognormal distributions are used extensively for aerosol size distributions because they fit observed size distributions reasonably well and are mathematically convenient. The geometric standard deviation (GSD), σ_g, replaces the linear standard deviation, σ, for a aerosol lognormal distribution in which the log of the particle diameter is normally distributed. Of particular interest is the cumulative mass concentration which is simply the sum for each set of bin ranges of interest for comparison to other instruments. For example, the

Sioutas impactor has cut points at .25 µm, .5 µm. 1.0 µm, and 2.5µm. Other cumulative cut points of interest may include 4.0 µm (respirable), 5.0 µm, 10.0 µm, and total. These are user definable depending on the ranges of interest. The cumulative concentration values are approximated as the fixed bin size ranges of the GRIMM do not exactly match these values, which may drive some interpolation as desired.

$$\sigma_g = exp\left[\left(\frac{\sum n_i(\ln d_i - \ln d_g)^2}{N-1}\right)^{1/2}\right] \quad (8.2)$$

$$MMD = d_{50} = \frac{\sum nd^3 \ln d}{\sum nd^3} \quad (8.3)$$

$$d_g = CMD = exp\left[\frac{\sum n_i \ln d_i}{N}\right] \quad (8.4)$$

N = total number of particles
d = particle diameter

Since this is a spreadsheet based model, section [H] simply allows the user to go back and change input parameter assumptions and re-calculate. In section [I], the user can select a sample of interest to review. Again, these are taken at 6 second intervals for 31 channels of the GRIMM 1.109. With this selection, normalized distributions are calculated in section [J] for count, mass, and surface area of the selected sample. Spherical geometry is assumed for the mass and surface area calculations. The normalized distribution provides a distribution that is independent of bin width which is useful when comparing results from different instruments. Normalized distribution enables a display of the differential particle size distribution which is normalized to logarithmic channel width. The equations for normalized distributions of count, mass, and surface area are provided in equations 8.5, 8.6, and 8.7, respectively.

$$dN/d\log D_p = \frac{dN}{logD_{pu} - logD_{pl}} \quad (8.5)$$

$$dM/d\log D_p = \frac{dM}{logD_{pu} - logD_{pl}} \quad (8.6)$$

$$dS/d\log D_p = \frac{dS}{logD_{pu} - logD_{pl}} \quad (8.7)$$

dN = particle concentration, count
dS = particle surface area

dM = particle mass, $dM = \frac{\pi}{6} d^3 \rho$, ρ is density

dS = surface area, $dS = \pi d^2$

D_p = midpoint particle diameter

D_{pu} = upper channel diameter

D_{ul} = lower channel diameter

A log probability plot and plots of the cumulative and normalized cumulative distributions are then graphed in section [K] for the sample of interest. The user can then select another sample of interest in section [L] or export the data as needed. The method described by this model enables a variety of analysis of to be performed on particles captured from the dust collection system. While some limited similar analysis capabilities exist in the existing GRIMM 1.178 LabVIEW software, this model provides far more flexibility to modify inputs and is designed to enable comparison between results of the other instruments used in this research. Further, it provides for the use of a dilution ratio and generates log probability plots and particle statistics not found in the GRIMM software. The next section describes the process to modify the bin ranges of this model for conversion to aerodynamic diameter which is useful when comparing results from the GRIMM 1.109 to a cascade impactor.

8.2.2 Aerodynamic Diameter Solver

As an enhancement to the particle model described in section 8.3.1, the capability to calculate aerodynamic particle diameter was developed. This is useful to support comparison to cascade impactor results, as the cascade impactor utilizes aerodynamic separation to measure aerodynamic particle size. The optical particle counter sees an effective or direct diameter at each bin size whereas the aerodynamic diameter is the diameter of a sphere with density at 1000 kg/m^3 that has the same settling velocity as the particle of interest. The aerodynamic diameter standardizes for shape and density, which is equivalent to the density of a droplet of water. The aerodynamic diameter is the key particle property for characterizing respiratory disposition. Figure 6.8 illustrates the tool and process for this calculation with each section to be described identified by a bracketed letter.

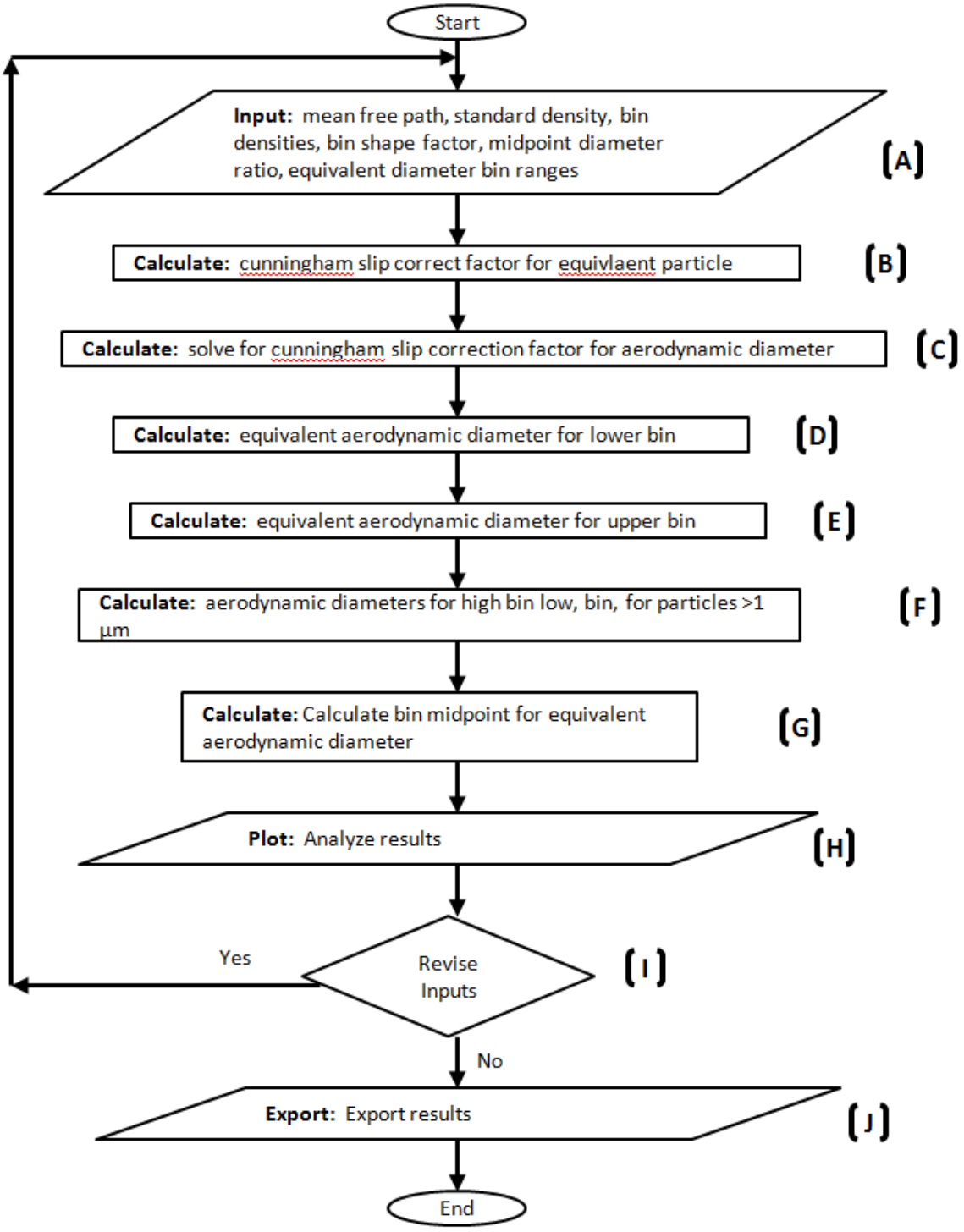

Figure 8.2. Aerodynamic particle calculation process

Section [A] of the model is the input block. For this block, the mean free path, λ, standard density, ρ_a, estimated particle density, ρ_e, shape factor, χ, and midpoint factor are

entered. Because this model uses data from the GRIMM 1.109, the upper and lower bin size ranges are entered for each of the 31 channels. This model was also developed in Microsoft Excel to facilitate data entry and manipulation. However, Matlab is used to solve for the Cunningham Slip Correction Factor with its "solve" function. Data from Excel is used in a Matlab program by copying a designated matrix from Excel and directly placing it into a predefined matrix in Matlab. A matrix containing all the calculated values is then returned to Excel using the same method for further processing. A future version could perform all functions in Matlab if desired. The Cunningham Slip Correction Factor, C_e, for direct particle measurement is calculated in Section [B] using equation (8.8) with, d_e, being the low bin range diameter for a directly measured particle. The Cunningham Slip Correction factor is used to account for gas slip that is significant for particles less than 1μm in diameter which causes the settling velocity to be faster than predicted by Stoke's law. For particles less than 1μm, slip increases rapidly as size decreases. Stoke's law assumes that the relative velocity of the gas at the particle surface is zero which is true with a continuous medium. However, when the particle gets smaller, the medium is no longer continuous to the particle and each molecule is no longer invisible to the particle. This causes slip, whereby gas molecules moving around the particle may miss the particle so the velocity of the gas right at the particle surface is no longer zero due to the missing collision. Because the collision is a source of drag, the particle's settling velocity becomes faster than predicted by Stoke's law due to the smaller than expected resistance. The Cunningham Slip Correction Factor is always greater than one and reduces the Stoke's drag force. Equation (8.8) is valid for particles between 0.1 μm and 1 μm in diameter and used in this model as the GRIMM can measure particles to 0.25μm.

$$C_e = 1 + \frac{2.52\lambda}{d_e} \tag{8.8}$$

For particles less than 0.1 μm in diameter equation (8.9) is utilized [79].

$$C_c = 1 + \frac{\lambda}{d}\left[2.34 + 1.05exp\left(-0.39\frac{d}{\lambda}\right)\right] \tag{8.9}$$

In Section [C], the following equations are combined in 8.10 and 8.11 to solve for the Cunningham Slip Correction Factor at the aerodynamic diameter.

$$d_a = d_e\sqrt{\frac{C_e\rho_e}{C_a\rho_a\chi}} \tag{8.10}$$

$$d_a = \frac{2.52\lambda}{C_a - 1} \tag{8.11}$$

The combination yields equation 8.12.

$$\frac{2.52\lambda}{C_a - 1} = d_e\sqrt{\frac{C_e\rho_e}{C_a\rho_a\chi}} \tag{8.12}$$

And finally rearranging terms to configure for use with a numeric solver in Matlab yields equation 8.13.

$$\frac{d_e\sqrt{\frac{C_e\rho_e}{C_a\rho_a\chi}}(C_a - 1)}{2.52\lambda} = 1 \tag{8.13}$$

This enables the Matlab Solver to find the Cunningham Slip Correction Factor, C_a, for the aerodynamic diameter. For testing purposes, the solutions were also checked in Wolfram Mathematica to ensure this was a unique solution and further verified by using the solved values for C_a, in the equation. The low bin aerodynamic diameter is then calculated in Section [D] using the same equation in (8.14).

$$d_a = \frac{2.52\lambda}{C_a - 1} \tag{8.14}$$

The upper bin aerodynamic diameter, calculated in Section [E], is simply an alternating substitution of the lower bin aerodynamic diameter as the upper bin diameter of a preceding bin is the same as the lower bin diameter of the following bin. For bin ranges with the lower bin greater than 1 μm, the equivalent aerodynamic lower and upper bin diameters are calculated using the following equation in Section [F] provided in equation 8.15. Half of the GRIMM 1.109 bin sizes are less than 2.5μm.

$$d_a = d_e\sqrt{\frac{\rho_e}{\rho_a\chi}} \tag{8.15}$$

The midpoints for all bin sizes are calculated in Section [G] and are simply the average of the upper and lower bin ranges. Results are then tabularized and plotted in Section [H]. An

example of a plot using a shape factor, χ, of 1.5 and assumed particle density, ρ_e, of 1.67 g/cm^3 is shown in figure 8.3 for the upper and lower GRIMM bin ranges.

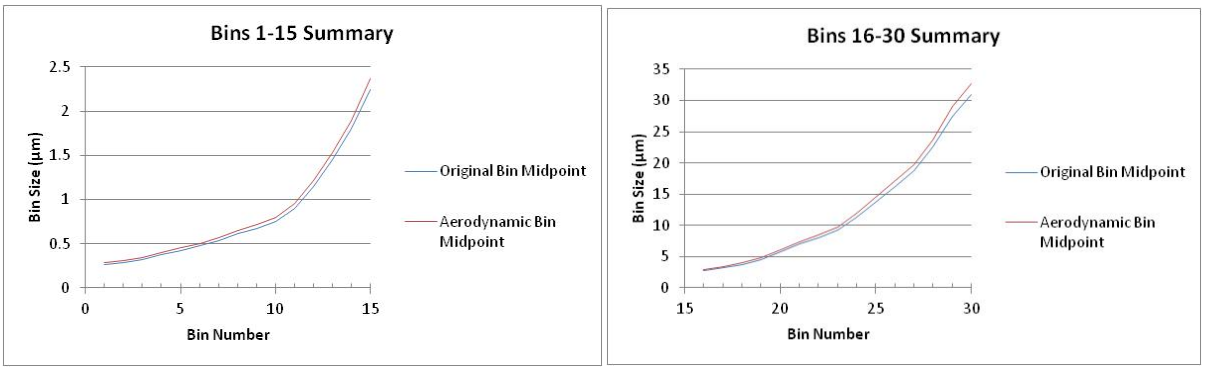

Figure 8.3. Effect of aerodynamic diameter on bin midpoint.

Only a slight difference between the direct particle diameter and equivalent aerodynamic diameter is shown for this combination of parameters. However, the assumptions may make a difference when combining bins for comparison to a cascade impactor using different parameters. The process can be iterated as shown in Section [J] to evaluate the effects of different shape factors, χ, and different densities, ρ_e. Results can then be exported and used in the particle model described in section 6.3.1 as shown in Section [J]. This capabilities described in this section were included to enable comparison of the data acquired by the GRIMM 1.109 to a cascade impactor and improve model accuracy through the use of the Cunningham Correction Factor to correct for slip when applying Stoke's law.

8.3 Dust Collection and Particle Analysis

The phase 1 screening tests explored basic techniques for assessing machinability of composite materials including cutting force acquisition, AE signal acquisition, tool wear measurement, surface finish measurement, and particle analysis using cascade impactors. From the cascade impactor results, the particle d50 mass median aerodynamic diameter (MMAD) range from the phase 1 testing was from .12 µm for edge trimming parallel to the 0 degree fiber orientation to .35 µm for trimming at -45 deg relative to the fibers. There was a larger percentage of total weight at the smaller cutpoints with the 10-stage Sierra Series 210 impactor used in this study than the 7 Anderson Impactor used by Kwan [91]. However, it is not clear the exact cutting tools or cutting conditions used in Kwan's study. Boatman [86] found that the

machining processes studied generated few particles of respirable size and did not observe longitudinal cleaving. A weakness in this study was that particles were collected by a vacuum with several stages, and only the particulates in the bag filter of the vacuum were analyzed. Thus particles from the filter vacuum stages were discounted in the analysis. Results from these early publications combined with the phase 1 dust results indicate that particle size generated from machining was determined by material, cutting tool, cutting conditions and process used to sample. Open machining without dust containment was also not an acceptable solution and led to the system described in this investigation.

In the phase 2 machinability assessment, MMAD ranges for particle sampling were from 1.02 μm to 56.6 μm. Clearly there is an overload condition at the larger sizes likely due to the sampling technique. Nine of the 19 samples performed using the Sioutas 4-stage impactors in phase 2 testing had MMAD greater than 7 μm, which is the midrange of the fiber diameters. This was indicated by excessive build up on the impactor stages as well as by large piles of particles in the SEM micrographs. This was a challenge with the dust containment configuration used in this phase of testing. However, eight of the MMAD values from this series experiments were less than 2.5 μm. Yon [97] provided results of a machining operation monitored by several real-time instruments with a range of mass median diameter (MMD) from 6.4 μm to 268.3 μm. This seems to support findings that placement and technique of instruments is essential for consistent results.

A series of papers were published by Haddad [45,98,99], which discussed dust collection analysis when milling composites with 4 cutting tool types using a GRIMM 1.209. The authors found as similar to this research that particles generated from machining exceeded the Occupational Safety & Health Administration (OSHA) 1910.1000 Table Z-3 exposure limits of 5 mg/m^3 for nuisance dust [121]. Their study was limited to 4 cutting tool types each at 6mm diameter with three cutting speeds and two feed rates and performed in an open environment with the GRIMM dust monitor stationary relative to machining such that distance to the cutting tool is not constant. The authors used a 2mm depth of cut with climb milling configuration. Dust collection did not appear to be performed based on the large quantity of build up on the work piece and fixture. The authors claim that reducing the theoretical chip thickness reduces the amount of harmful portion of dust generated claiming that 90% of the particles in the

atmosphere reach the pulmonary alveoli. It appears from the graphs provided that the authors may be exceeding the particle count limits of the GRIMM which was also experienced in performing this research effort. The particle counts at the lower bin sizes appear greater than 2 million, which is the limit for the GRIMM. A typical graph of results from these papers for a 4-flute, 6mm diameter cutter, at 2 mm radial depth of cut is provided in figure 8.4.

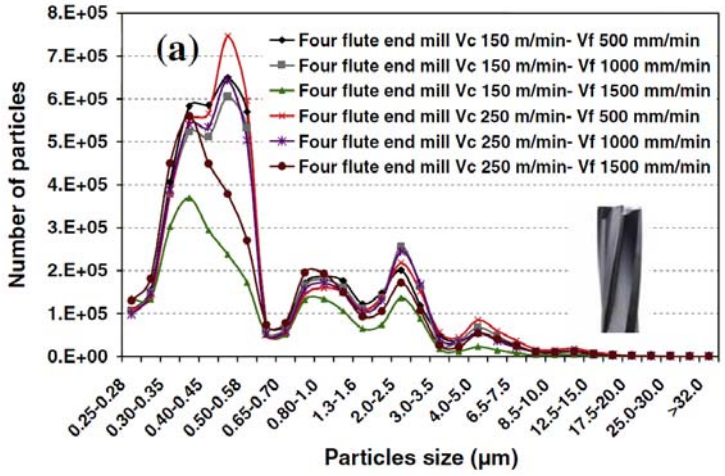

Figure 8.4. 4-flute dust results from Haddad [99]

A comparison of tests performed in this research using a 12.7 mm diameter 4-flute solid carbide cutter and 12 mm diameter 4-flute CVD cutter at 6000 rpm, linear feedrate 635 mm/min, with radial depth of cut of .762 mm is shown in figure 8.5. This test was performed using isokinetic sampling without dilution and exceeds the 2 million particle ct/liter limits of the GRIMM. The top and bottom references simply mean trimming the top or bottom half of the laminate. Figure 8.6 are test results using the 4-flute solid carbide with dilution.

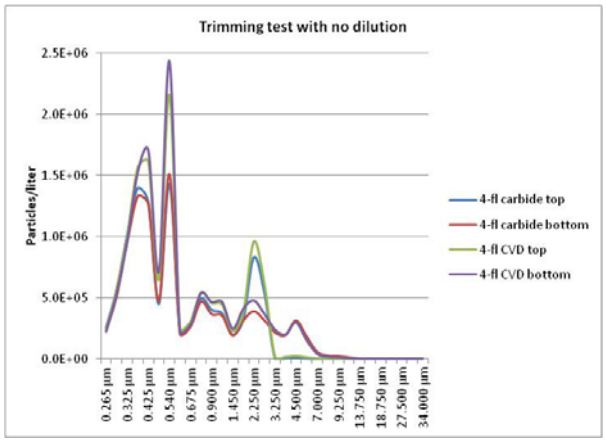

Figure 8.5. Cutting test with no dilution

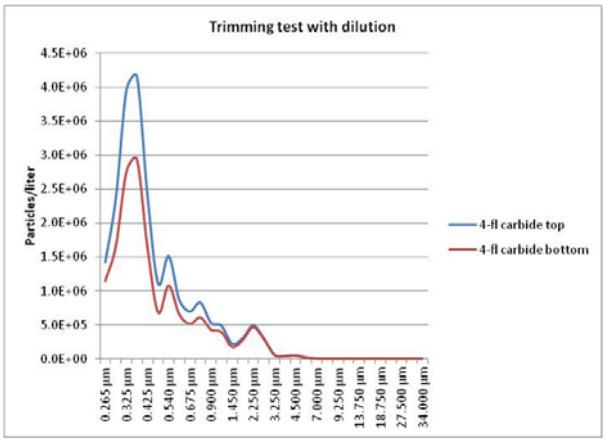

Figure 8.6. Cutting test with dilution

Results are also dependent on which sample is selected from the run. The previous figures represent just one six second sample that may or may not reflect nominal conditions. Further, it is not clear the effect of distance or tool movement relative to the instrument sampling inlet. The authors claim that 90% of the particles will reach the alveoli is also not correct and an over simplification. Figure 8.7 is a typical graph of the deposition probability of inhaled particles in the respiratory tract according to particle size and contradicts the authors claim [79].

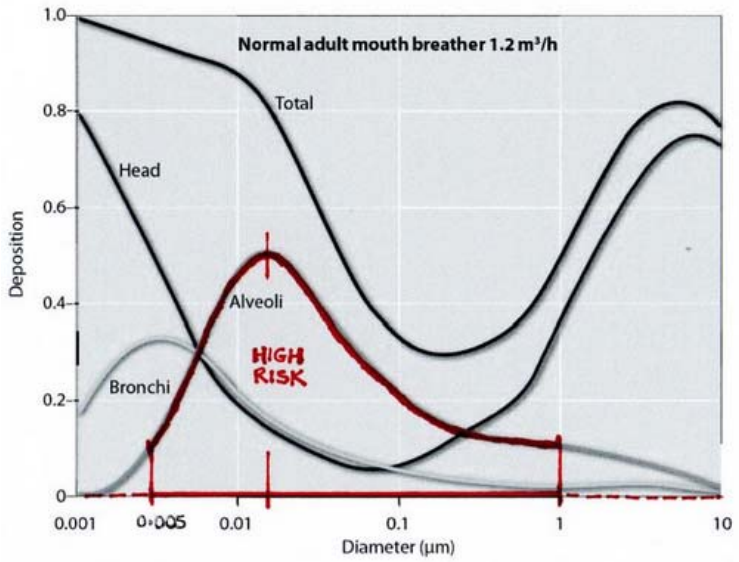

Figure 8.7 Deposition probability of inhaled particles in the respiratory tract [79].

A software package called MMPD or Multiple-Path Particle Dosimetry Model developed by the CIIT Centers for Health Research, USA in collaboration with the National Institute of Public Health and the Environment, Netherlands calculates the deposition and clearance of monodisperse and polydisperse aerosols in the respiratory tract of rats and human adults and children for particles ranging from 0.01 µm to 20 µm [122]. The models are based upon methods for tracking air flow and calculating aerosol disposition in the lung. Figure 8.8 is a plot of the regional deposition fraction generated from the MMPD V2.0 from the following input parameters taken from composite machining results. The deposition fraction is the fraction of the inhaled aerosol mass that is deposited in a given respiratory tract region. In the plot, the total deposition fraction as well as the deposition fraction in the head, pulmonary and tracheobronchial is shown.

Model input parameters

- Density 1.60 g/cm^3 (typical for carbon fiber)
- Diameter 1µm (MMAD)
- GSD 3 (geometric standard deviation)

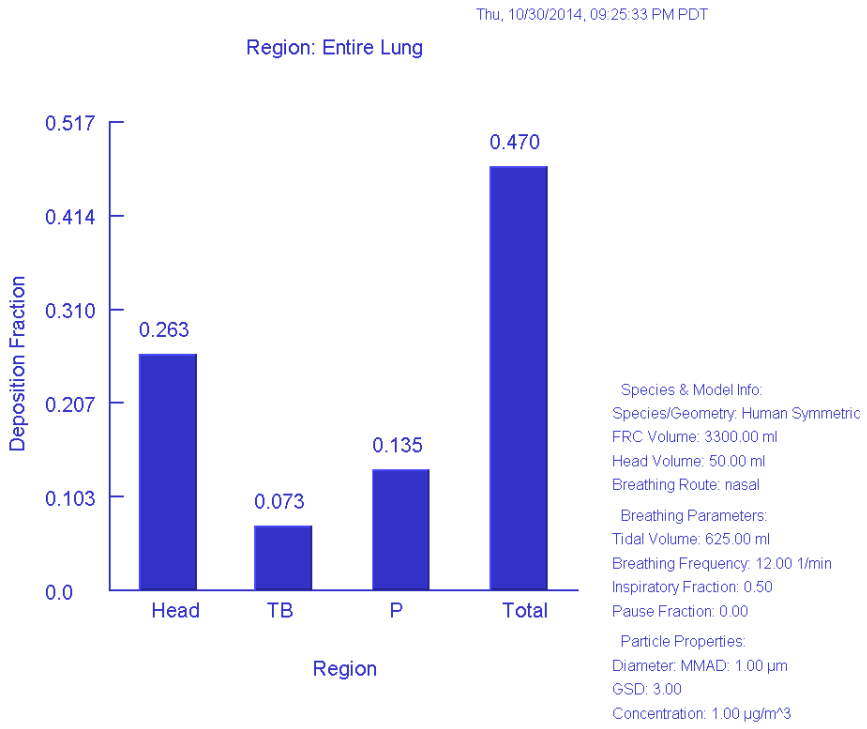

Figure 8.8. Typical regional deposition fraction for composite dust.

The models and tools discussed in this chapter support inputs for the MMPD tool to determine regional deposition fraction and other reports of interest by using key parameters calculated from GRIMM data. Figure 8.9 is a log probability plot generated from the first dilution test for sample 57. From this plot, we get MMD which can be converted to MMAD using the aerodynamic particle conversion process described in this chapter and the geometric standard deviation, σ_g. Either MMD and MMAD are acceptable inputs to the MPPD model. Concentrations are also calculated which can be used to compare to established limits. OSHA defines respirable dust as those dust particles that are small enough to penetrate the nose and upper respiratory system and deep into the lungs. The Mine Health and Safety Administration (MHSA) defines respirable dust as the fraction of airborne dust that passes a size selecting device, having the characteristics in table 8.1. The Environmental Protection Agency (EPA) describes inhalable dust as that size fraction of dust which enters the body, but is trapped in the nose throat and upper respiratory tract. The median aerodynamic diameter of inhalable dust is about 10 μm. Total dust includes all airborne particles, regardless of their size or composition.

Table 8.1 MSHA definition of respirable dust.

Aerodynamic diameter (μm) unit density sphere	Percent passing selector
2.0	90
2.5	75
3.5	50
5.0	25
10.0	0

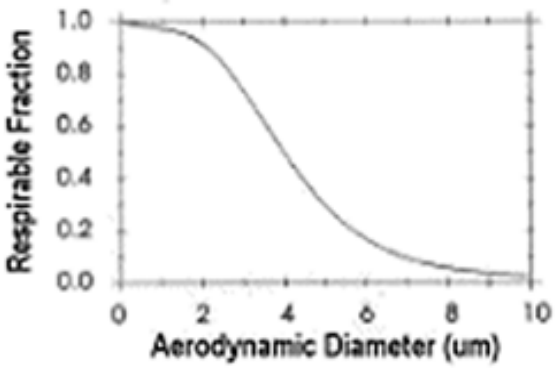

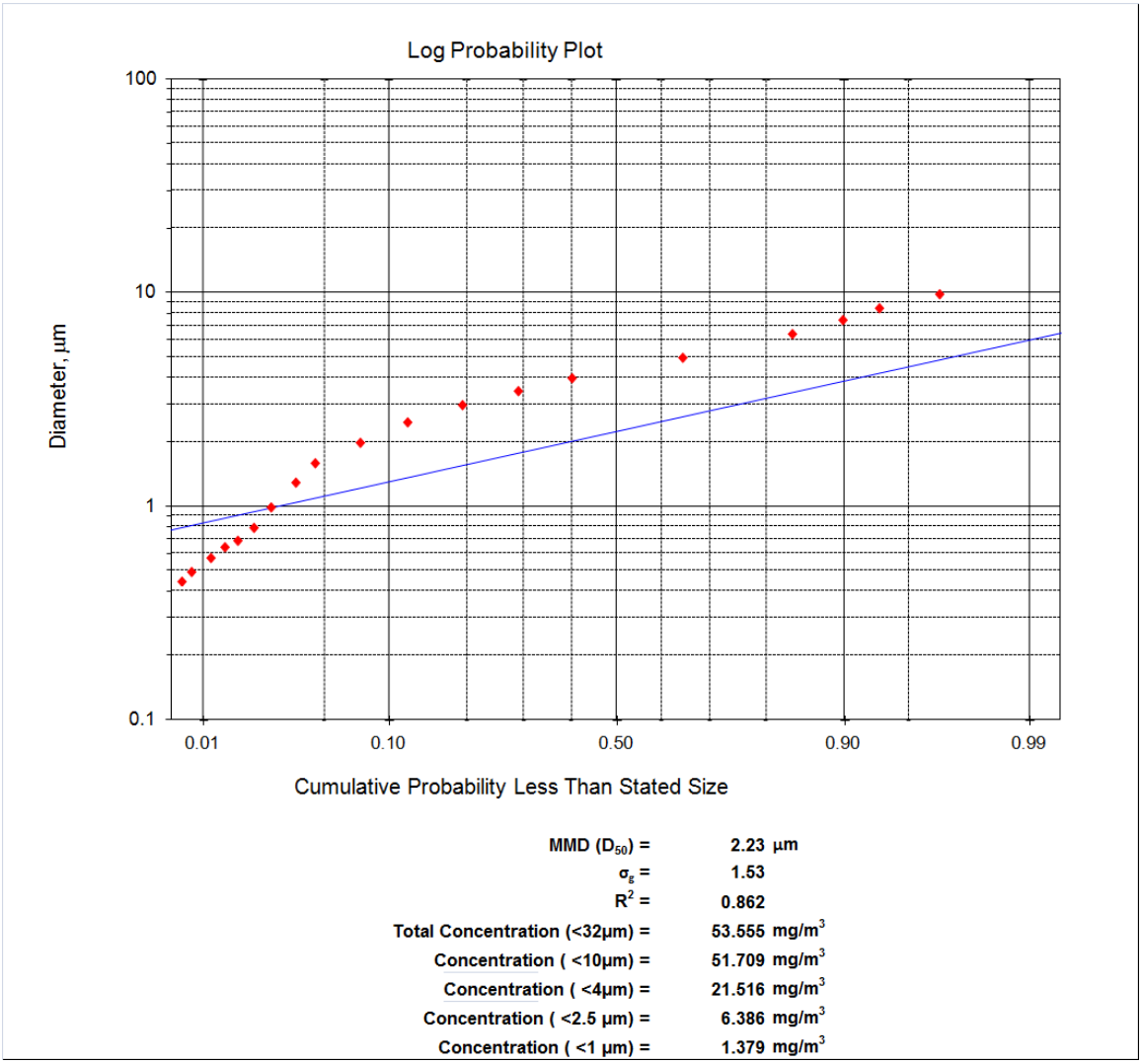

Figure 8.9 Log Probability plot from first dilution test, sample #57.

Additional data is calculated for the same sample including count distribution and normalized count distribution. This provides insight into how the particles are distributed across the bin sizes. Figure 8.10 is the graph for normalized count distribution with count plotted on logarithmic scale. The particle count can further be combined with PTRAK data or equivalent ultrafine particle counter to count particles below the limits of the GRIMM .25 µm. For approximation, GRIMM counts can be subtracted from PTRAK counts between the ranges of approximately .25µm-1µm. There is some interpolation required as the nearest GRIMM bin range upper limit is 1.15 µm so the lower particle count would at best be an approximation. Normalized mass distribution is plotted in figure 8.11. This plot is useful when comparing

GRIMM concentration measurements to the mass concentration determined by other instruments. Graphs for surface area distribution and normalized surface area distribution are included in Appendix V. Mass and surface area in these models is calculated assuming the particles have a spherical geometry. This does not represent the actual geometry of the particles as the shapes vary considerably as evidenced by study of extensive SEM micrographs. For modeling purposes, the bin midrange diameter was used to calculate the spherical volume and surface area. In the Haddad [99] paper, the authors assumed the volume of each particle to be a cube.

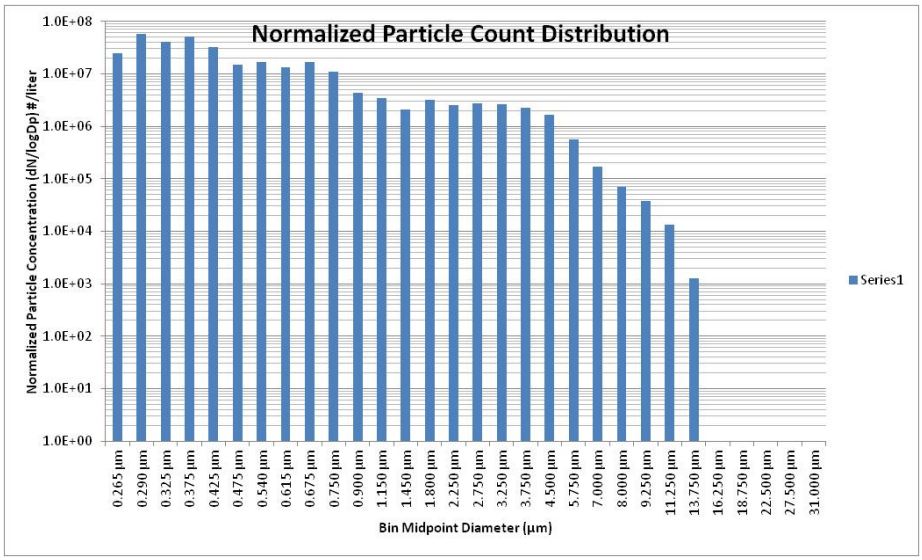

Figure 8.10. Normalized particle count distribution.

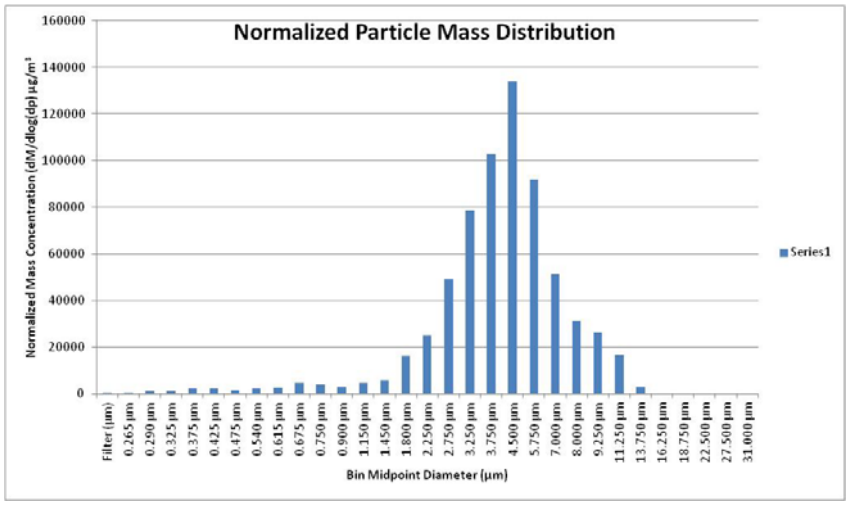

Figure 8.11. Normalized mass distribution.

The SEM micrographs also provide a method to directly measure particle size. This can be used to help calibrate the models where the diameter is assumed. Using this approach, a representative particle is sized based on its two-dimensional projected image. Because the particles from machining composites are irregularly sized, an equivalent diameter used. The most commonly used equivalent diameter is the projected area diameter, d_{PA} which is the diameter of a circle that has the same projected area as the particle silhouette [79]. Software such as ImageJ by the National Institutes of Health (NIH) can provide the particle area, A, by importing the micrograph in a .tiff format or equivalent and setting the scale factor from the image [123]. From this, projected particle area diameter, d_{pa}, can easily be calculated from equation 8.15.

$$d_{PA} = \sqrt{\frac{4A}{\pi}} \tag{8.15}$$

An illustrative example is shown in figure 8.12. In this figure, an SEM micrograph from the D3 impactor, stage 6 is provided, as described in chapter 5. In this example, the maximum particle length is longer than the projected area diameter. The equivalent projected area diameter, d_{PA}, can then be used to calculate the volume of the particle, υ_p, using a volume shape factor, α_v, which as shown in equation 8.16, for a sphere. The equivalent diameter, d_e, is related to the projected area diameter, d_{PA}, as shown in equation 8.17 and 8.18. The aerodynamic diameter, da, is related to the equivalent diameter, de, in equation 8.19 for particles larger than 1 μm and in equation 8.20 for particles between 0.1 and 1 as discussed in chapter 8. Hinds [79] describes the ratio of d_a/d_{PA} which combines the volume shape factor, α_v, the dynamic shape factor, χ, and particle density, ρ_e. This ratio is close to 1 for most materials and is described in equation 8.21 for particles larger than 1 μm and in equation 8.22 for particles between 0.1 and 1. The model in this research calculates the volume for a particle bin using equation 8.23 with initial particle diameter assumed to be the bin midpoint diameter. Total mass for the bin is then calculated in equation 8.24. This can be done for both the measured diameter (optical) and aerodynamic diameter.

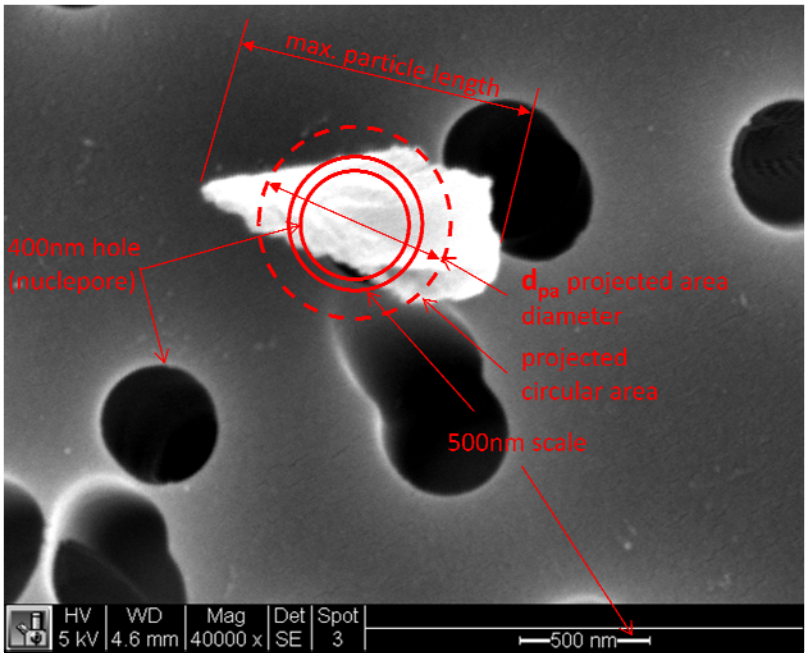

Figure 8.12. Equivalent area diameter illustration (D3-6-pic5)

If measured mass, m_i, from corresponding impactor stages is available, an aerodynamic particle diameter, d_a, using the number of particles measured by the real-time instrument of a corresponding range can be determined as in equation 8.25. The aerodynamic particle diameter can then be used in equations 8.19 and 8.20 to find the equivalent diameter, d_e. The projected area diameter, d_{PA}, can then be determined in equation 10.4 and compared to the equivalent diameter, d_e. Equations 8.21 and 8.22 can be used to evaluate selection of the volume shape factor, α_v, and dynamic shape factor, χ. While the number of equations may be a little confusing, the objective is to find the appropriate particle diameter, dynamic shape factor, and density for each bin size to use for mass calculation so the mass concentrations of the real-time instrument match those of an impactor for accurate direct gravimetric measurement. This calibration method provides more flexibility and is more specifically tailored than the built-in functions of the instruments which simply provide an option of a single calibration factor that is applied to all bin sizes as a scale factor. The approach described and supporting models developed enable each bin size to be individually calibrated, assuming availability of corresponding gravimetric data.

$$v_p = {d_{PA}}^3 \alpha_v \qquad (8.16)$$

$$d_e = d_{PA}\sqrt[3]{\frac{6\alpha_v}{\pi}} \tag{8.17}$$

$$d_{PA} = \frac{d_e}{\sqrt[3]{\frac{6\alpha_v}{\pi}}} \tag{8.18}$$

$$d_a = d_e\sqrt{\frac{\rho_e}{\rho_a \chi}} \tag{8.19}$$

$$d_a = d_e\sqrt{\frac{C_e\rho_e}{C_a\rho_a \chi}} \tag{8.20}$$

$$\frac{d_a}{d_{PA}} = \sqrt{\frac{\rho_e}{\rho_a \chi}}\sqrt[3]{\frac{6\alpha_v}{\pi}} \sim 1 \tag{8.21}$$

$$\frac{d_a}{d_{PA}} = \sqrt{\frac{C_e\rho_e}{C_a\rho_a \chi}}\sqrt[3]{\frac{6\alpha_v}{\pi}} \sim 1 \tag{8.22}$$

$$v_B = \sum P_{N/B}\frac{\pi}{6}{d_B}^3 \tag{8.23}$$

$$m_B = v_B\rho \tag{8.24}$$

$$d_a = \sqrt[3]{\frac{6m_i}{\sum P_{N/B}\,\rho_a\pi}} \tag{8.25}$$

With a calibrated model for real-time particle instruments, the contribution for each bin size relative to volume of total material removed can then be determined. This is accomplished by first determining the volume of material removed which is calculated by multiplying total length of cut by both axial and radial depths of cut. Since particle sampling is performed isokinetically by the system developed in this investigation, the total air volume for the time of cut is determined by multiplying the time of cut by the vacuum system flow rate derived from the Magnehelix® differential pressure reading recorded during each experiment. The mass of any particle size or range of particle size is then determined by multiplying mass concentration by total air volume for the length of cut of interest. Ranges of interest may include PM1, PM2.5, PM3.5 (respirable), PM10, and total. The estimated mass of particles removed for each bin size and cumulative percent of total material removed is plotted in figure 8.13 for sample 57 with log probability plot shown in figure 10.6. In this example the cumulative mass climbs considerably after bin midpoint 1.45μm with an asymptote at bin midpoint 9.25 μm. Further studies can associate the specific contributions by each fiber orientation to the total concentration.

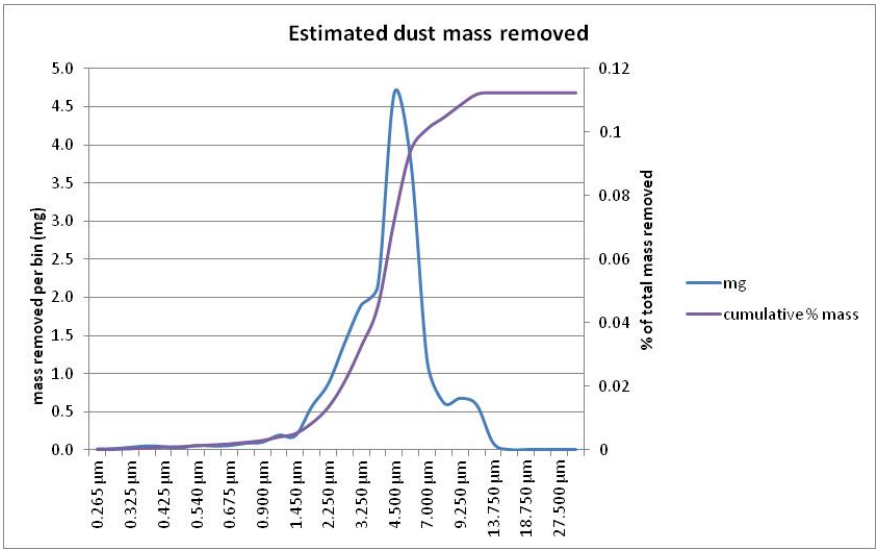

Figure 8.13 Mass of particles removed

8.4 Summary

This chapter presented tools and techniques developed in this research for particle analysis of the dust generated when trimming composites and are intended to be used in conjunction with the isokinetic sampling system. The tools present a method to calculate the mass median aerodynamic diameter for comparison to cascade impactors. Key parameters determined from these tools can be used in models such as MPPD to determine the deposition of aerosols in the respiratory tract. The tools also facilitate the comparison of results from different real-time particle analysis instruments for both count and mass concentration. Further, the tools provide flexibility to customize the analysis by providing the option to quickly modify many input parameters, including dilution factor, shape factor, and density for each bin size. The tools can be calibrated at each bin size using data from corresponding impactors to improve the results of the real-time instruments to match those which are determined gravimetrically for the specific composite dust aerosol of interest. The flexibility of the particle analysis tools developed for this research can help further the understanding of the relationship between cutting conditions, tool geometry, and material system on the particles that are generated to help achieve processes that provide the desired quality (surface integrity), maximize material removal, and minimize risk to the environment and workers.

CHAPTER 9

CUTTING FORCE PREDICTION MODEL

9.1 Introduction

This chapter will discuss the models developed for cutting force estimation for composite materials using a semi-circular slot technique for determination of milling coefficients. A combination of software tools including Microsoft Excel, Matlab, and Mathematica were used to create elements of the models to be described. Data used in the cutting force model was acquired using the Kistler 9123C dynamometer and DynoWare software. The focus of these models are to present tools and techniques that can be applied in a lab or industrial environment for cutting force prediction of multi-directional composite laminates while cutting at any angle relative to fiber direction. The cutting force prediction model developed is intended to enable the user to determine cutting force coefficients through a minimum of cutting tests on a unidirectional laminate that can then be utilized in the model for cutting force prediction of a multi-directional laminate based on the same material system and cutting tool. Select results predicted by the model will be compared to experimentally acquired forces along with applicable comparison to cutting force trends from relevant publications.

9.2 Cutting Force Model

The mechanistic model deployed is largely based on specific cutting energy, also known as specific cutting pressure, which is a material property that describes the amount of energy consumed in removing a unit volume of the work piece. The cutting forces are the product of the undeformed chip thickness area and specific cutting energy. For metals, the specific cutting energy is dependent on chip thickness, cutting speed, and tool wear. For composite materials, specific cutting energy is also dependent on fiber orientation. For this model, a milling test is used to generate specific cutting energies at all fiber orientations for unidirectional laminates.

9.2.1 Cutting Force Coefficients

Chapter 7 described the circular slot test utilized to derive cutting force coefficients which are an essential input to the cutting force model. From this method, five slots were

defined that each utilized a different feed/tooth while also satisfying several constraints determined by the instruments, cutting envelope, and distribution objectives for linear regression analysis. The slots are made in a unidirectional composite with the material system and cutting tool the same as intended for a multidirectional laminate. The objective is to use a minimal number of tests performed on a unidirectional laminate to predict the cutting forces on any laminate of the same material system using the same cutting tool. For different material systems or different cutting tools on the same material system, a new set of calibration tests is required. Unidirectional laminate testing enables the cutting force coefficients specific to the cutting orientation for that fiber direction to be determined. These in turn are individually utilized in the cutting force model for predicting the cutting forces of a multidirectional laminate. Further, since a semi-circular slot is utilized, cutting force coefficients are easily calculated at each degree position. This is a benefit since prior work has clearly demonstrated that for composites, cutting forces are also a function of cutting orientation relative to fiber direction.

The method by which cutting force coefficients are calculated for the semi-circular slot are similar to methods for calculation using a linear slot. The cutting forces are modeled in terms of two fundamental phenomena, an edge force component due to rubbing or plowing at the cutting edge, represented by K_{te} and K_{re} for a unit width of cut, and a cutting component due to shearing at the shear zone and friction at the rake face, represented by K_{tc}, K_{rc} on a unit area of cut basis [118,119]. The subscript, (r) and (t) represent the radial and tangential components, with (e) and (c) representing the edge and cutting component, respectively. The elemental tangential, dF_t, and radial, dF_r, cutting forces acting on flute j of an ideal system consisting of a rigid cutter with zero eccentricity around the axis of rotation are described in equations 9.1 and 9.2.

$$dF_{tj}(\phi,z) = [K_{te} + K_{tc}h_j(\phi,z)]dz \quad (9.1)$$

$$dF_{rj}(\phi,z) = [K_{re} + K_{rc}h_j(\phi,z)]dz \quad (9.2)$$

$$h_j(\phi,z) = c*\sin \phi_j(z) \quad (9.3a)$$

$$\phi_j(z) = \phi + j\,\phi_p - k_i z \quad (9.3b)$$

$$\phi_p = 2\pi/N \quad (9.3c)$$

$k_i = \tan i/R$ (9.3d)

Equation 9.3 is the uncut chip thickness and, c, is the feed rate per tooth. ϕ is the immersion angle measured clockwise from the positive y-axis to a reference flute, j, which has immersion, ϕ, at its tip z = 0. On flute, j, a differential chip element at axial location z has an immersion angle $\phi_j(z) = \phi + j\,\phi_p - k_i z$, where $\phi_p = 2\pi/N$ is the flute angular pitch, N is the number of teeth on the cutter. At an axial depth z, the angular helix lag of the differential element on tooth j from the leading point on the tooth's cutting edge (z = 0) is $k_i z$, where $k_i = \tan i/R$, where i and R are the cutter helix angle and cutter radius, respectively.

In order to determine the milling force coefficients, a set of slot milling experiments at different feeds per tooth for each cutting tool geometry and material system are required to be conducted. The calculated coefficients are valid only for the specific cutter geometry and material combination tested, such that a different set of milling tests is required for each cutter geometry and material combination. The cutting force coefficients are evaluated from a comparison of the linear equations relating the average force components per tooth period to the feed per tooth established by the slot milling experimental data and derived from mechanistic analysis. The average cutting forces can be expressed by a linear function of feed rate,c, in feed/tooth and an offset contributed by the edge for components in equation 9.4.

$$\bar{F}_q = \bar{F}_{qe} + c\bar{F}_{qc} \quad (q \approx x, y, z) \tag{9.4}$$

The average forces at each feed rate are measured, and edge cutting force components ($\bar{F}_{qe}$, $\bar{F}_{qc}$) are estimated by linear regression of the data. The cutting force coefficients are evaluated from linear regression of the data. The elemental forces are resolved into feed (x) and normal (y) using the transformation equations in 9.5 and 9.6.

$$dF_{x,j}(\theta_j(z)) = -dF_{t,j}\cos\phi_j(z) - dF_{r,j}\sin\phi_j(z) \tag{9.5}$$

$$dF_{y,j}(\theta_j(z)) = +dF_{t,j}\sin\phi_j(z) - dF_{r,j}\cos\phi_j(z) \tag{9.6}$$

Substituting equations 9.1, 9.2, and 9.3 into 9.5 and 9.6 yields equations 9.7 and 9.8 as follows.

$$dF_{x,j}(\phi_j(z)) = \{c/2[-K_{tc}\sin 2\phi_j(z) - K_{rc}(1-\cos 2\phi_j(z))] + [-K_{te}\cos\phi_j(z) - K_{re}\sin\phi_j(z)]\}dz \tag{9.7}$$

$$dF_{y,j}(\phi_j(z)) = \{c/2[(1-\cos 2\phi_j(z))-K_{rc}\sin 2\phi_j(z)]+[-K_{te}\sin\phi_j(z)-K_{re}\cos\phi_j(z)]\}dz \quad (9.8)$$

Replacing dz = a, $\phi_j(z) = \phi$ and integrating over one cutter revolution and dividing by the pitch angle, ϕ_p, yields the average milling forces per tooth in equation 9.9 where the flute only cuts within the immersion zone between the entry and exit angles ϕ_{st} to ϕ_{ex}.

$$\bar{F}_q = \frac{1}{\phi_p}\int_{\phi_{st}}^{\phi_{ex}} F_q(\phi)d\phi \quad (q = x, y, z) \quad (9.9)$$

Integrating the instantaneous cutting forces yields 9.10 and 9.11 for x and y.

$$\bar{F}_x = \{\frac{Nac}{8\pi}\left[K_{tc}cos2\phi - K_{rc}[2\phi - sin2\phi]\right] + \frac{Na}{2\pi}[-K_{te}sin\phi + K_{re}cos\phi]\}_{\phi_{st}}^{\phi_{ex}} \quad (9.10)$$

$$\bar{F}_y = \{\frac{Nac}{8\pi}[K_{tc}(2\phi - sin2\phi) + K_{rc}\cos 2\phi] - \frac{Na}{2\pi}[K_{te}cos\phi + K_{re}sin\phi]\}_{\phi_{st}}^{\phi_{ex}} \quad (9.11)$$

Utilizing slot milling experiments where entry angle ϕ_{st} is 0 degree and the exit angle ϕ_{ex} is 180 degrees (π) applied to equations 9.10 and 9.11 yields the following average forces per tooth in equations 9.12 and 9.13.

$$\bar{F}_x = -\frac{Na}{4}K_{rc}c - \frac{Na}{\pi}K_{re} \quad (9.12)$$

$$\bar{F}_y = +\frac{Na}{4}K_{tc}c + \frac{Na}{\pi}K_{te} \quad (9.13)$$

The average cutting forces are expressed as a linear function of feed rate, c, and an offset contributed by the edge forces in equation 9.14.

$$\bar{F}_q = \bar{F}_{qe} + c\bar{F}_{qc} \quad (q = x, y, z) \quad (9.14)$$

Average forces at each feed rate are measured with the cutting force and edge coefficients determined by linear regression of the data with the cutting force coefficients derived from equations 9.12, 9.13 and 9.14 yielding equations 9.15 through 9.18 below.

$$K_{tc} = \frac{4\bar{F}_{yc}}{Na} \text{ (N/mm}^2\text{)} \qquad K_{te} = \frac{\pi\bar{F}_{ye}}{Na} \text{ (N/mm)} \quad (9.15, 9.16)$$

$$K_{rc} = \frac{-4\bar{F}_{xc}}{Na} \text{ (N/mm}^2\text{)} \qquad K_{te} = \frac{-\pi\bar{F}_{xe}}{Na} \text{ (N/mm)} \quad (9.17, 9.18)$$

$\bar{F}_{xc}$, $\bar{F}_{yc}$ are the slope and $\bar{F}_{xe}$, $\bar{F}_{ye}$ are the y-intercept of the cutting force curves where feed rate, c, in mm/tooth is plotted on the X-axis and cutting force, Fx, Fy, in Newtons, is plotted on the Y-axis for a stationary dynamometer following a series of slot cutting tests for a given cutting tool and material system.

9.2.2 Cutting Force Coefficients for a Rotating Dynamometer

For a rotating dynamometer such as the Kistler 9123C, Karpat [58] proposes the following derivation described in this section. Figure 9.1 illustrates the cutting forces acting on a 4-flute cutting tool during slot milling. Equation 9.19 represents the cutting forces during the slot milling process where tangential forces, Ft, are directed in the opposite direction of cutting and the radial forces, Fr, act toward the center of the tool.

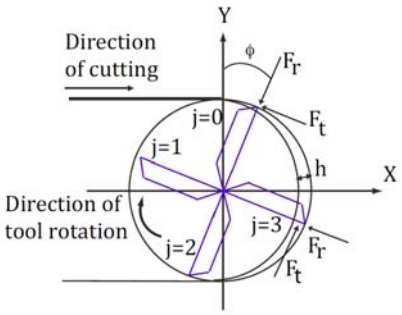

Figure 9.1 Cutting forces during slot milling

$$\begin{bmatrix} F_r \\ F_t \end{bmatrix} = a_p \sum_{j=0}^{s-1} g_j \left(\left(f \sin(\phi_j) \right) \begin{bmatrix} K_{rc}(\theta) \\ K_{tc}(\theta) \end{bmatrix} + \begin{bmatrix} K_{re}(\theta) \\ K_{te}(\theta) \end{bmatrix} \right) \tag{9.19}$$

$$\phi_j = \phi_0 - j\frac{2\pi}{s}, \quad j = 0, 1, \ldots, s-1$$

$$g_j(\phi_j) = \begin{cases} 1 & \phi_s \le \phi_j \le \phi_e \; and \; h_j > 0 \\ 0 & elswhere \end{cases}$$

a_p: is the axial depth of cut
f: is the feed rate per tooth
$f \sin(\phi_j)$: is the instantaneous chip thickness
s: is the number of teeth on the tool
j: is an index for the number of teeth on the tool
g: is a control function that indicates whether the tooth is engaged in the workpiece

The average tangential and radial forces during a slot test can be expressed as follows in equations 9.20 and 9.21.

$$\bar{F}_t = \frac{s \cdot a_p}{2\pi} \int_{\phi_s}^{\phi_e} (K_{tc}(\theta) f sin(\phi) + K_{te}(\theta)) d\phi \quad (9.20)$$

$$\bar{F}_r = \frac{s \cdot a_p}{2\pi} \int_{\phi_s}^{\phi_e} (K_{rc}(\theta) f sin(\phi) + K_{re}(\theta)) d\phi \quad (9.21)$$

For a slot test the entry angle, ϕ_s, is 0 deg and the exit angle, ϕ_e, is 180 deg (π radians). Solving the integrals with these conditions provides the following expressions for the average tangential and radial forces in equations 9.22 and 9.23.

$$\bar{F}_t = \frac{s \cdot a_p \cdot f}{\pi} K_{tc} + \frac{s \cdot a_p}{2} K_{te} \quad (9.22)$$

$$\bar{F}_r = \frac{s \cdot a_p \cdot f}{\pi} K_{rc} + \frac{s \cdot a_p}{2} K_{re} \quad (9.23)$$

Similar to the stationary dynamometer case, average tangential and radial cutting forces can be expressed by a linear function of feed rate, f, and an offset contributed by the edge forces in equations 9.24 and 9.25.

$$\bar{F}_t = \bar{F}_{tc} f + \bar{F}_{te} \quad (9.24)$$

$$\bar{F}_r = \bar{F}_{rc} f + \bar{F}_{re} \quad (9.25)$$

Thus, from linear regression analysis, $\bar{F}_{tc}$, $\bar{F}_{rc}$ and $\bar{F}_{te}$, $\bar{F}_{re}$ are the respective slope and y-intercept terms of the curves resulting from milling slot tests conducted at consistent depths of cut, a_p, and varying, feed rate (mm/tooth), f, for the same cutting tool and material system using tangential and radial force measurements from a rotating dynamometer in equations 9.26 – 9.29, where $\bar{f}$, $\bar{F}_t$, and $\bar{F}_r$ are the average feed rate, average tangential and average radial forces, respectively. Similar to the stationary dynamometer case, feed rate, c, in mm/tooth is plotted on the X-axis and cutting force, Ft, Fr, in Newtons, is plotted on the Y-axis for a rotational dynamometer following a series of slot cutting tests for a given cutting tool and material system.

	Slope	Y-Intercept	
Tangential Force	$\bar{F}_{tc} = \frac{\sum(f-\bar{f})(F_t-\bar{F}_t)}{\sum(f-\bar{f})^2}$	$\bar{F}_{te} = \bar{F}_t - \bar{F}_{tc}\bar{f}$	(9.26, 9.27)

Radial Force $\bar{F}_{rc} = \frac{\sum(f-\bar{f})(F_r-\bar{F}_r)}{\sum(f-\bar{f})^2}$ $\bar{F}_{re} = \bar{F}_r - \bar{F}_{rc}\bar{f}$ (9.28, 9.29)

The tangential and radial cutting and edge coefficients are then calculated as follows in equations 9.30 – 9.33.

	Cutting coefficient	Edge coefficient	
Tangential Force	$K_{tc} = \frac{\pi \cdot \bar{F}_{tc}}{s \cdot a_p}$	$K_{te} = \frac{2 \cdot \bar{F}_{te}}{s \cdot a_p}$	(9.30, 9.31)
Radial Force	$K_{rc} = \frac{\pi \cdot \bar{F}_{rc}}{s \cdot a_p}$	$K_{re} = \frac{2 \cdot \bar{F}_{re}}{s \cdot a_p}$	(9.32, 9.33)

This approach is desirable for a rotating dynamometer where Ft is directly derived from the Mz measurement, and Fr is derived from the rotating Fx, Fy force values and Mz such that no dynamic transformations are necessary when using this type of instrument. The Altintas [118,119] derivation is applicable to a stationary dynamometer and directly uses stationary Fx, Fy coordinates to calculate the cutting force coefficients. In this investigation, both methods were used, however; for the semi-circular slot cutting force model, the Karpat approach was directly applicable for the 9123C rotational dynamometer. The semi-circular slot configuration is illustrated in figure 9.2. Each circular slot is made at a constant depth of cut, but different feed rate, as described in chapter 7. At the same angular position for each of the five slots, the average tangential and radial forces are calculated which support helical cutting tools with any number of teeth. Regression analysis is then performed to calculate $\bar{F}_{tc}$, $\bar{F}_{rc}$, $\bar{F}_{te}$, and $\bar{F}_{re}$. The tangential and radial cutting and edge coefficients are then calculated using these values in combination with the number of cutting teeth and axial depth of cut from equations 9.30 – 9.31. It is important to keep track of fiber direction relative to cutting orientation so this information can be consistently imported into the milling model and used to estimate cutting forces for multidirectional laminates.

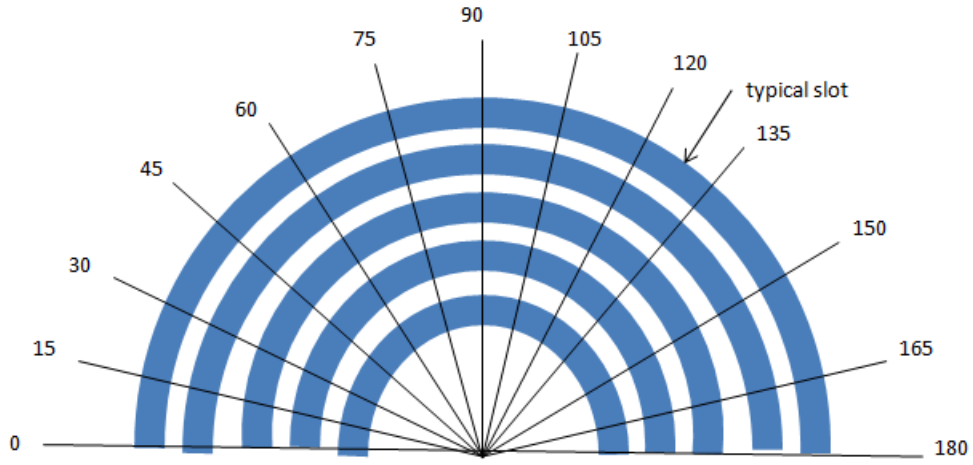

Figure 9.2. Slot configuration with common angular positions

9.2.3 Cutting Force Model

The cutting force simulation model developed for this investigation is derived from a mechanistic model for metal cutting using helical end mills. The core of the model is derived from pseudo code provided by Altintas [119]. In the core model, the cutter is rotated with small incremental angles. At each incremental rotation position, the cutting forces are integrated axially along sliced differential elements from the bottom of the flute toward the final axial depth of cut. The core model input variables include, cutter helix angle, entry angle, exit angle, axial depth of cut, number of teeth, feed rate, spindle speed, cutter diameter and cutting force coefficients for a homogeneous material. This model was modified for composite laminates where a fundamental difference includes a unique set of cutting force coefficients for each cutting orientation relative to fiber angle, empirically determined for a unidirectional laminate. Cutting forces for a multidirectional laminate are then determined by superposition using the forces predicted for each unidirectional lamina in the full laminate for the same material system. The flow chart for the simulation model for calculating milling forces using a helical tool in a multidirectional composite laminate is shown in figure 9.3. The simulation model will be described in the following paragraphs with each section of the model having a unique identification letter, as shown in the figure. The Matlab code and typical input files for the model are included in Appendix W.

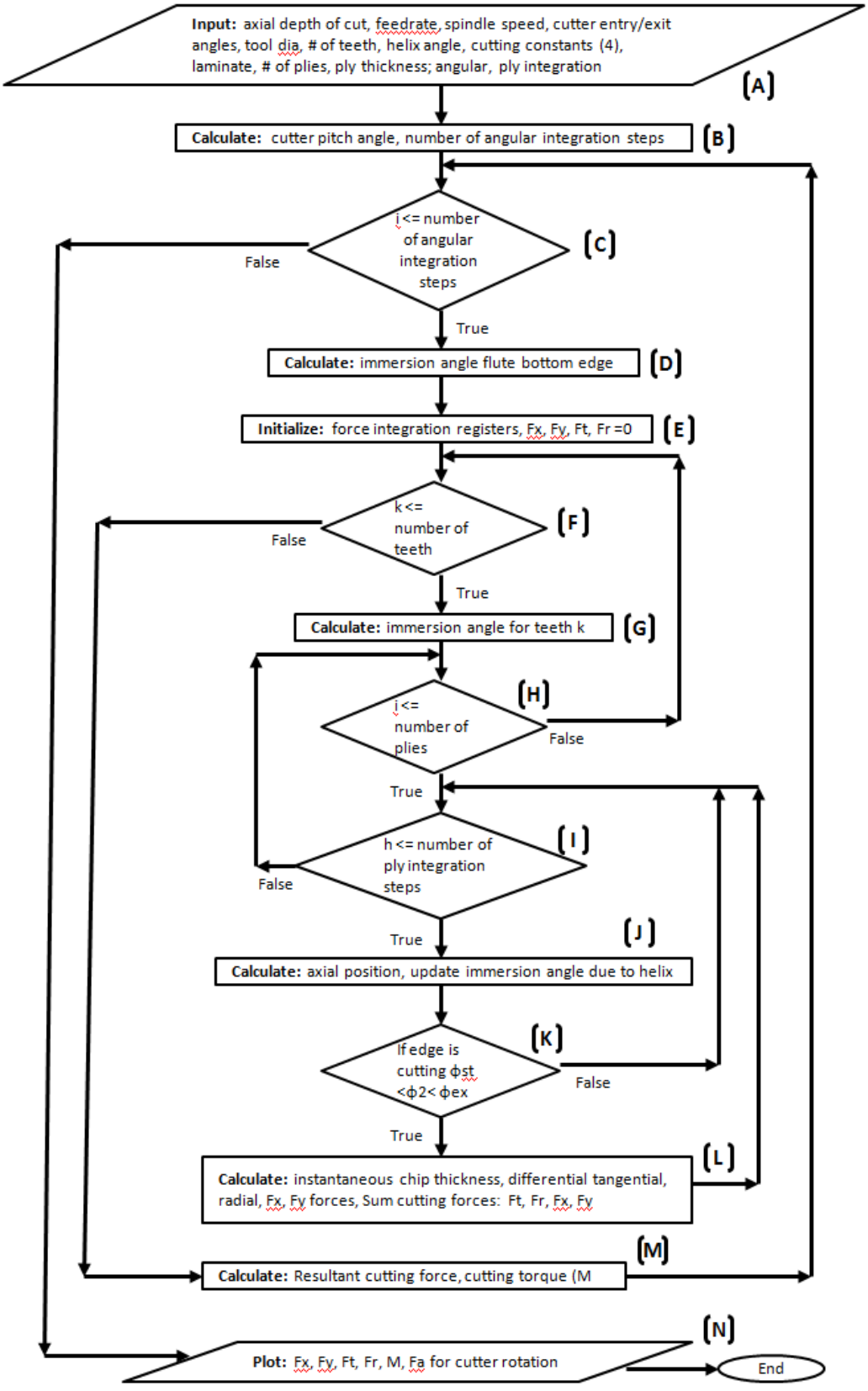

Figure 9.3 Flowchart for milling model.

Section [A] of the model is the input block. The first set of input variables include those for cutting conditions to be predicted by the model:

- Axial depth of cut (mm)
- Feed rate (mm/tooth)
- Spindle speed (rpm)
- Cutter entry angle, ϕ_{st}, (deg)
- Cutter exit angle, ϕ_{ex}, (deg)

The second set of input variables describes the cutting tool.

- Cutter diameter (mm)
- Number of cutting teeth (#)
- Helix angle (deg)

The cutter entry and exit angles are used to determine the type of cutting to be simulated which may be one of three fundamental types including:

- peripheral climb milling
- peripheral conventional milling
- full immersion slot milling.

The radial depth of cut may be used to determine the cutter entry and exit angles for climb or conventional edge trimming. Figures 9.4 and 9.5 illustrate calculations for entry and exit angles for conventional and climb cutting, respectively. Full immersion slot cutting has an entry angle of 0 deg and exit angle of 180 deg (π radians). Slot cutting consists of both climb and conventional cutting so it is orientation independent for purposes of this model.

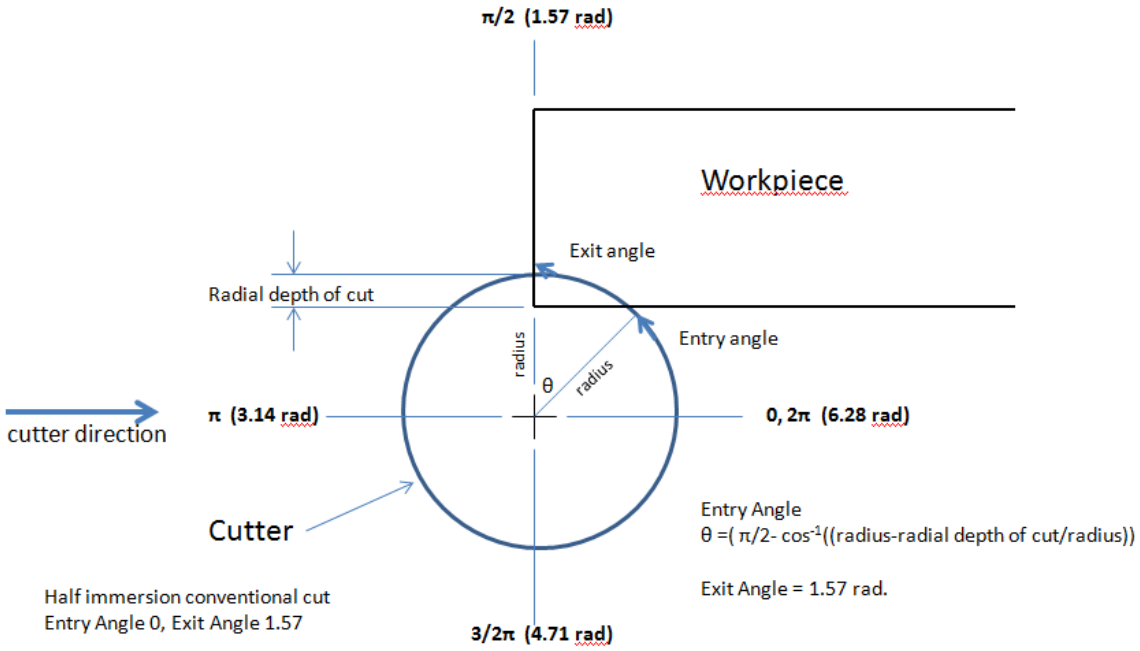

Figure 9.4 Conventional cutting illustration

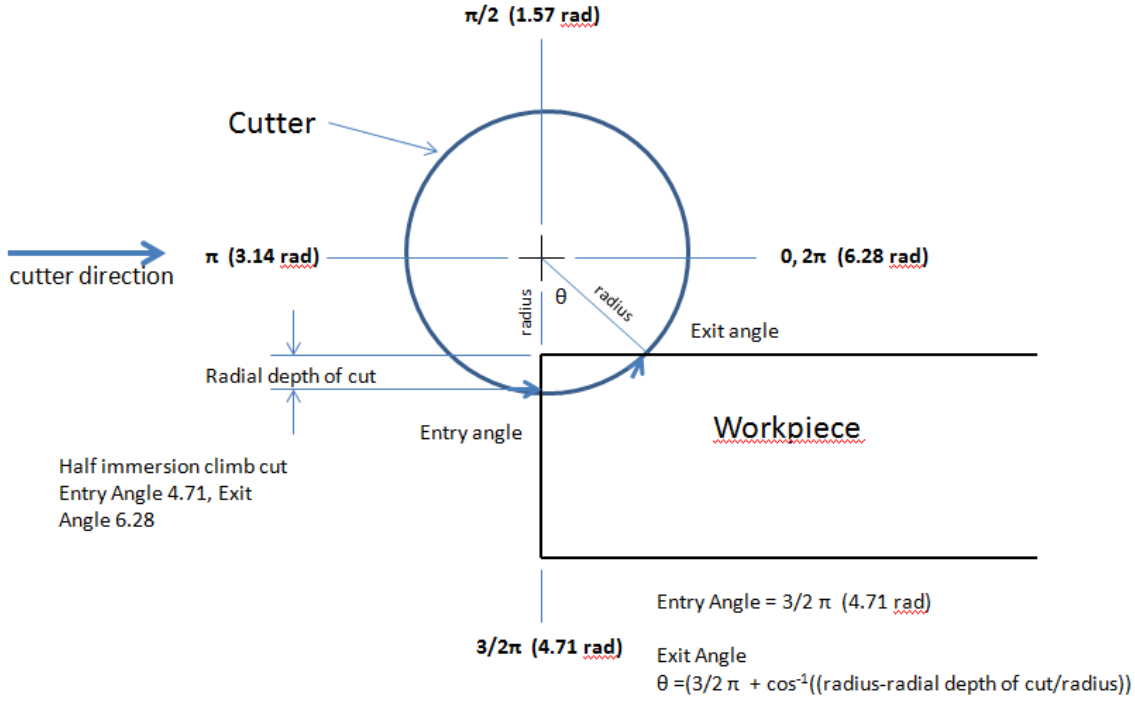

Figure 9.5 Climb cutting illustration

The third set of input variables are the cutting force coefficients or cutting constants. Each model utilizes cutting constants empirically derived for a common cutting tool and material system. A new combination of cutting tool and material system requires new cutting constants. For this research, a unique milling force coefficient is used for each of 180 degrees of cutting relative to fiber orientation, or 720 total constants for a given combination of cutting tool and material system. Fortunately, these are automatically calculated by tools in the model. The cutting force coefficients were empirically derived using the process described by Karpat [58] in section 9.2.1 from a series of five semi-circular milled slots. The four cutting force coefficients include:

K_{tc} = Tangential cutting force coefficient (N/mm^2)
K_{rc} = Radial cutting force coefficient (N/mm^2)
K_{te} = Tangential edge force coefficient (N/mm)
K_{re} = Radial edge force coefficient (N/mm)

The fourth and final set of input variables describe the composite laminate to be milled. The laminate may be unidirectional or multidirectional consisting of any orientations.

- Number of plies in the laminate (#)
- Ply thickness, constant for this model (mm)
- Ply table, from bottom of cutter up (ply, angle)
- Ply integration constant (#) or integration steps per ply
- Rotational integration angle (deg)

The ply integration constant enables each ply of the laminate to be axially integrated in more than one step if desired by the user. Any partial ply thickness as a result of the axial depth of cut exceeding an integer multiplier of ply thickness is also figured in the vertical integration. The rotational integration angle determines the number of angular elements in each rotation of the cutter to be simulated. The ply table allows the user to enter the laminate description where the cutting angle relative to fiber direction is entered for each ply. Figure 9.6 is an illustration of the laminate description adjacent to the helical cutting tool showing the stacking sequence of each ply including the full and partial plies. This provides the user flexibility to estimate cutting forces with the work piece at any planar orientation in the milling machine.

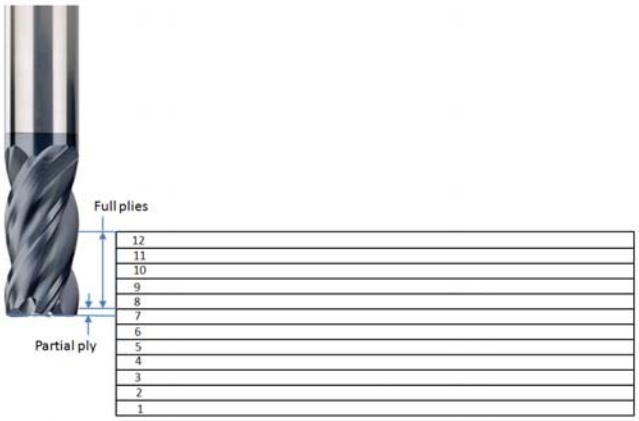

Figure 9.6. Laminate plytable stacking sequence.

In practice, a Numerical Control (NC) program may not be written to cut relative to the fiber orientation used in the circular slot cutting tests for the same laminate. By applying a simple rotational offset to each ply, this table can be easily adjusted to reflect actual work piece orientation relative to cutter motion on the machine tool. In this manner, forces at any position along a NC cutting path can be estimated as long as a reference angle is known for the actual cutting direction relative to ply orientation. For example, if the actual cutting direction is off 10 degrees relative to the 0 degree fiber orientation, all lamina can be shifted by 10 degrees to account for the actual cutting direction of the machine tool. Since cutting coefficients have been empirically determined for all cutting orientations, the appropriate cutting coefficients will be used that address this angular offset for cutting direction relative to ply orientation. An illustration of angular offset correction is shown in figure 9.7.

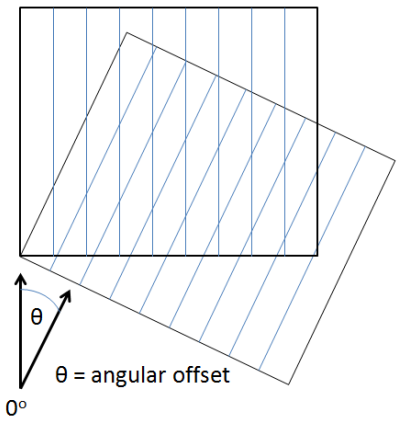

Figure 9.7 Angular offset correction.

After the input block, the cutter pitch and number of angular integration steps is calculated in Section [B] of the code. The cutter pitch angle, ϕ_p, is simply $2\pi/N$, where N is the number of cutting teeth. The number of angular integration steps is simply the number of cycles that will be integrated for one rotation of the cutter. This is used in Section [C] of the code to set the set the number of iterations for the angular integration loop. In Section [D], the immersion angle of the flute's bottom edge is calculated which is the sum of the cutter entry angle and angular integration increment. Force integration registers are initialized in Section [E] for Fx, Fy, Ft, Fr. A loop for the number of teeth in the cutter is initialized in Section [F]. The immersion angle for the tooth is calculated in Section [G] which is the sum of the cutter pitch angle and angular integration increment.

Section [H] sets the loop to step through the number of plies for axial integration. This also provides the ply index value to select the correct cutting constants from the ply table for a multi-directional laminate. Section [I] sets the loop for axial integration within a single ply which may include as many steps or increments as entered by the user. The axial integration position and update to immersion angle is calculated in Section [J]. The axial integration position is the distance from the bottom of the cutter and includes any partial ply thickness. The immersion angle is updated by the cutter helix angle. Section [K] determines whether the cutter tooth being analyzed is cutting. The tooth is considered to be cutting if the updated immersion angle is between the cutter entry angle and cutter exit angle. If the tooth is cutting, differential tangential, radial, feed, and normal forces are calculated in Section [L]. In addition, the cutting forces for all active edges are summed. The differential tangential and radial forces are directly calculated using the cutting force coefficients, where the differential feed (Fx) and normal (Fy) forces are derived as follows in equations 9.34 – 9.37:

$$\Delta F_t = a(K_{tc}h + K_{te}) \quad (9.34)$$

$$\Delta F_r = a(K_{rc}h + K_{re}) \quad (9.35)$$

$$\Delta F_x = -\Delta F_t \cos(\phi) - \Delta F_r \sin(\phi) \quad (9.36)$$

$$\Delta F_y = \Delta F_t \sin(\phi) - \Delta F_t \cos(\phi) \quad (9.37)$$

Where, ϕ, is the immersion angle, a, is the axial integration height, and, h, is the instantaneous chip thickness defined by $h = c*\sin(\phi)$, and, c, is the feed/tooth.

Unique cutting force coefficients are associated with each angle for a multi-directional laminate and found using the current ply number as the index in the ply table to find the angle of each ply. The angular orientation is the index used in the cutting force coefficient table to find the cutting force coefficients used in the equations. If the tooth is not cutting, the next axial position is checked for edge engagement. The resultant force and cutting torque or moment is calculated in Section [M] after the force contribution of all teeth has been determined for each angular cutter position. The results are plotted in Section [N] after the simulation has cycled through all cutter angular positions for one rotation of the cutter. Output of the model includes:

- Ft (Tangential Force)
- Fr (Radial Force)
- Fx (Stationary Fx)
- Fy (Stationary Fy)
- Fx (Rotational Fx)
- Fx (Rotational Fy)
- Fa (Resultant Force)
- Mz (Spindle moment)

9.3 Cutting Force Modeling

Extensive work in calibrating the Kistler 9123C rotating dynamometer for use in the model to predict cutting forces for multi-directional composite laminates began in phase 3 of this research. The techniques discussed in chapter 7 provided sufficient process understanding to conduct a series of tests for the model discussed in this chapter. A few authors have developed force prediction models for milling and edge trimming of composites including Karpat [56,57,58], Puw [46,47,48], Zaghbani [62], Sheikh-Ahmad [50,51,52,53,54,55]. All utilize specific cutting energy as a key component for force prediction and conduct cutting tests to provide data for their respective models. Specific cutting energy is the machining power per unit volume of material removed which can vary depending on the material cutting speed, axial and radial depths of cut, tool geometry. The basis for these models dates to work performed by Martellotti [124,125], Tlusty [126] and Devor [127], among others. Germain [128] provides an extensive review of the work performed in the area of force modeling for metal cutting processes. The model proposed herein leverages similar approaches, but utilizes a semi-circular slot to determine the cutting force coefficients for all fiber orientations in unidirectional laminate

for a given cutter and material system, and superposition of these results to address multi-directional laminates. This approach is intended to address the effect of cutting mechanisms described by Wang [14,15] for different fiber orientations and tool geometries without the need for more complex prediction capabilities. The cutting force coefficients at all orientations are determined through linear regression (slope, y-intercept) which may have some limitations as other authors used more complex approaches. Linear regression was used for simplicity as a starting point which can be modified as needed should more complex curve fits be necessary for prediction accessory. Zaghbani [62] proposed a third-order polynomial equation for determining the coefficients where Kalla [51] proposed an artificial neural network for determining the milling coefficients. From what is available in publications, Karpat [58] showed very clear linearity for tangential and radial force slot milling of a 45 deg laminate using a 4-flute helical end mill with 3 data points as shown in figure 9.8 using a Kistler 9123C rotating dynamometer. Tangential force linearity appears relatively close for the other 3 fiber directions. Radial force appears slightly off for the other 3 directions. With only 3 data points it is difficult to assess true linearity. Zaghbani [62] provided data for machining laminates of 0^o, 75^o, and 100^o with a 2-flute straight solid carbide cutter using a Kistler 9255B stationary dynamometer shown in figure 9.9. There is clear linearity for the y-component, with some variation in the x-component with more variation in the x-component for the composite material compared to aluminum. The x and y components for 6061-T6 aluminum appear very linear as expected.

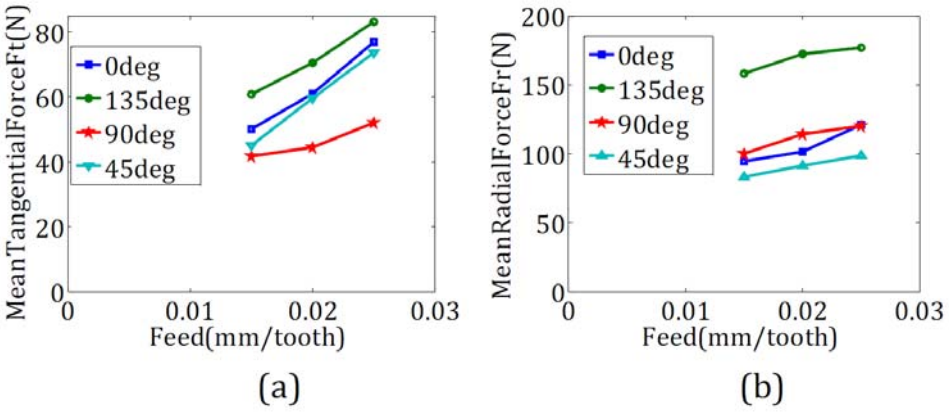

Figure 9.8 Karpat [58], figure 5. Mean tangential and radial forces.

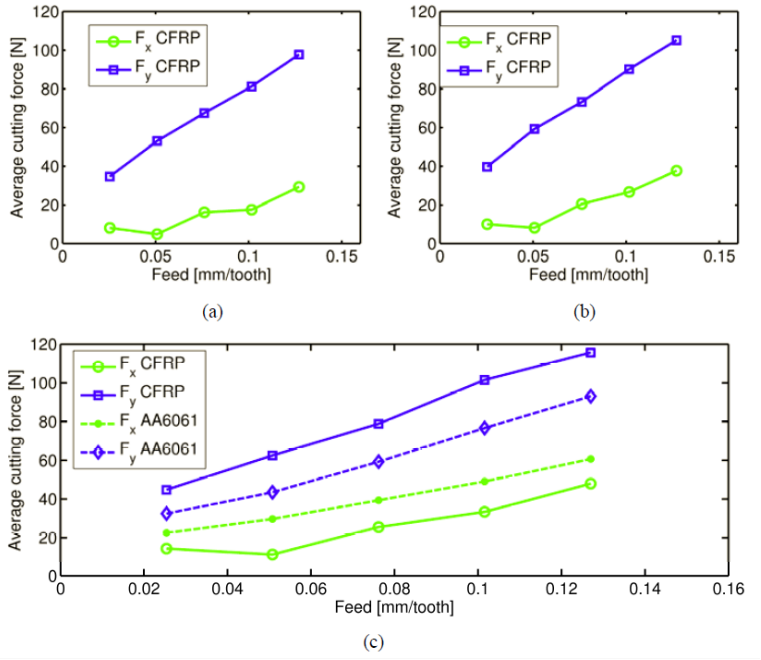

Figure 9.9 Zaghbani [62], figure 12. Mean X,Y forces. a, 0°, b. 75°, c. 100°

The method in this work differs from other researchers in that a series of semi-circular slot test are used to provide milling coefficients for all cutting orientations relative to fiber direction in lieu of linear tests for each angle of interest. This reduces the number of cutting tests required and the need to interpolate between angles as measured values for all angles are empirically provided. The method uses average force and the tangential and radial components of a rotating dynamometer assuming a linear fit at each angular position to accommodate any number of teeth on a helical cutting tool. Analysis of the linearity of each degree position of the semi-circular slots is performed by assessing the correlation coefficients at each radial position. As an example, an analysis of the correlation coefficients for the 4-flute CVD composite circular slot test is shown in table 9.1. The tangential components for Ftc and Fte for the tangential cutting coefficients for every fiber orientation between 0 and 180 degrees were very linear; however, that is not the case for the radial components. It is not fully clear if this fully due to inherent non-linearity of the composite or with use of the dynamometer as discussed in chapter 7, or some combination. Zaghbani [62] describes the radial force as the resistance of the material to the penetration of the cutting tool where Karpat [58] claims the larger radial forces compared to the tangential forces is due to contact between fibers and the tool's edge radius and flank face.

For purposes of this investigation, a linear fit for both tangential and radial forces was assumed. Future work could more specifically tailor the fit, should the true difference merit.

Table 9.1 Correlation coefficients for 4-flute CVD circular slot test.

Statistic	**R^2 for F_{tc}, F_{te}**	**R^2 for F_{rc}, F_{re}**
min	0.9906	0.1820
max	1.0000	0.9969
range	0.0094	0.8149
average	0.9975	0.7743
std dev	0.0014	0.2110

With the rationale of approach from both the specific cutting energy basis and linearity assumptions, the model was first tested with a homogeneous material and compared to published results. Figure 9.10 compares results from the Matlab model used in this research to those provided by Altintas [119] for conditions summarized in table 9.2. Since the model was designed for composite materials, the number of plies was set to 1 and the ply thickness was set to the axial depth of cut. One orientation and one set of cutting force coefficients were used. Other than that, it was run the same as for a multi-directional laminate. As shown in figure 9.10 the results are nearly identical, providing some confidence that the core of the algorithms based upon the guidance provided by Altintas [119] were correctly coded. Further examples for predicting forces from the aluminum tests were provided in chapter 7.

Table 9.2 Model calibration homogeneous material test

Model Parameter	**Value**
Number of teeth (#)	4
Axial depth of cut (mm)	2
Feed per tooth (mm/tooth)	.1
Tangential Cutting Coefficient, Ktc (N/mm^2)	1800
Tangential Edge Coefficient, Kte (N/mm)	0
Radial Cutting Coefficient, Krc (N/mm^2)	.3
Radial Edge Coefficient, Kre (N/mm)	0

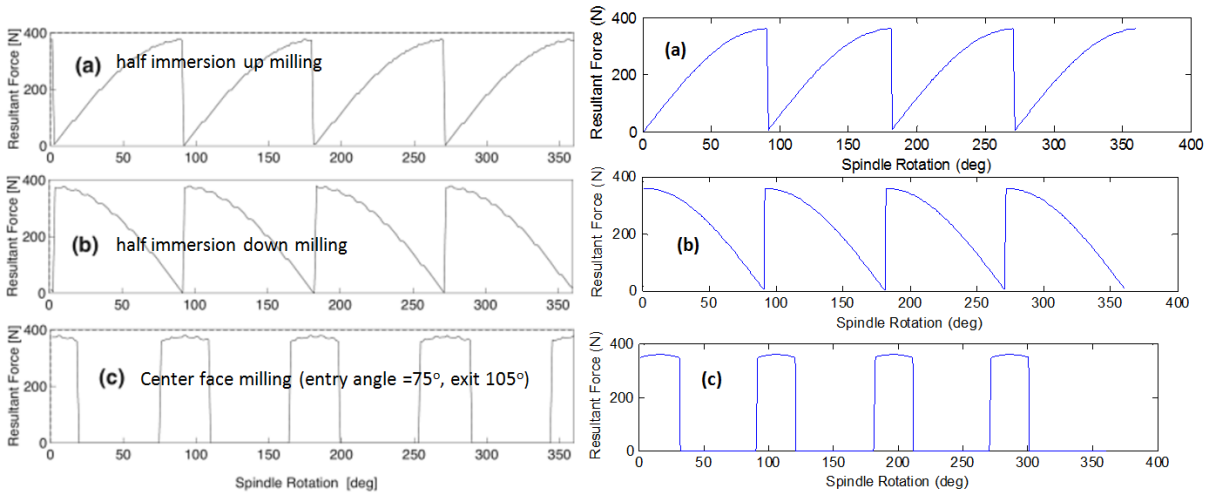

Figure 9.10 Model results comparison: left Altintas [119], right model.

As one of several examples tested, the model was run for five slot tests described in table 9.3. Milled slots 1 through 4 were simulated using unidirectional laminates. The slot 5 test used a multidirectional laminate modeled with 64 plies and configured as $[(45/90/135/0)_8]_s$. Each laminate was loaded into the model "plytable" variable and has a 0.19 mm ply thickness. The software was set to integrate with 4 steps per ply, and includes the height of partial plies in the total vertical integration. The cutting force coefficients (Ktc, Kte, Krc, Kre) from the semi-circular slot test were loaded into the "cutcoef" variable, even though only 4 of the 180 sets were used for these tests and automatically pulled during running of the model for calculations at the corresponding ply orientation. Other setup parameters were loaded into the "circinput" variable, including feed per tooth, cutter entry and exit angle (π, 2π), cutter diameter, number of teeth, helix angle, total plies, ply thickness, and number of integration steps per ply. For this set of tests the model was run 5 times. Sample results are plotted in figure 9.11 showing two full cutter rotations (720 degrees) for a 4-flute cutter. With two rotations of a 4-flute cutter there are 8 peaks as shown.

Table 9.3. Simulated composite slot test configuration for 4-flute CVD cutter

Slot	Feed	Teeth	Helix	Dia.	Depth	Ply	Ktc	Kte	Krc	Kre
#	mm/tooth	#	deg	mm	mm	Deg	N/mm^2	N/mm	N/mm^2	N/mm
1	.02	4	30	12	5.08	0	394.21	2.50	28.95	5.41
2	.02	4	30	12	5.08	45	259.90	4.41	313.05	2.88
3	.02	4	30	12	5.08	90	178.63	4.10	120.26	4.98
4	.02	4	30	12	5.08	135	253.09	3.04	95.83	1.80
5	.02	4	30	30	5.08	Multi	all above	all above	all above	all above

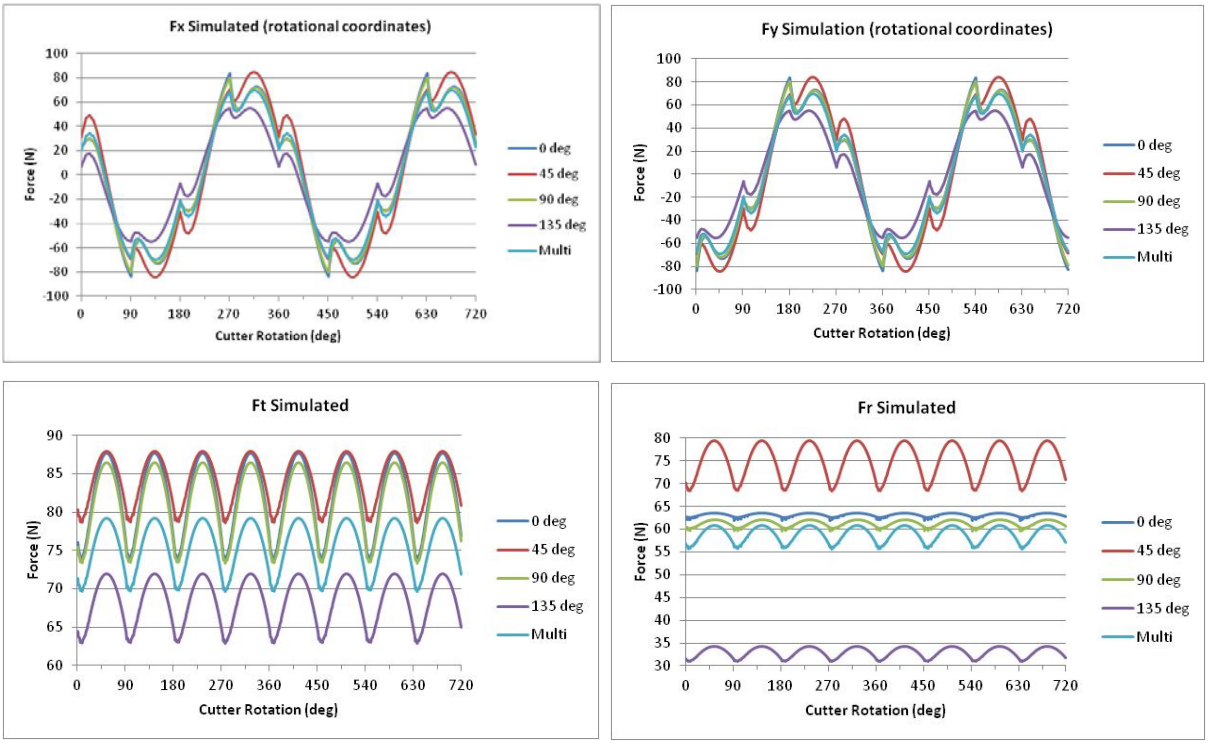

Figure 9.11. Simulated results for composite slot tests using 4-flute CVD cutter.

Figure 9.11 clearly shows the influence of the cutting coefficients derived from the unidirectional laminate on the force prediction of the multi-directional laminate. The superposition used during the cutting force calculation for the multidirectional laminate estimates the forces in between the 4 primary orientations as expected. Values for Fx and Fy for a rotational coordinate system common to the Kistler 9123C rotating dynamometer were calculated using a clockwise transformation in equation 9.38 as the model initially determines Fx and Fy for a stationary dynamometer system. This enables the model to be used for either

rotational or stationary dynamometers, as the cutting force coefficients can be independently determined using either type of device.

$$\begin{bmatrix} \overline{Fx_{rot}} \\ \overline{Fy_{rot}} \end{bmatrix} = \begin{bmatrix} cos\theta & sin\theta \\ -sin\theta & cos\theta \end{bmatrix} \begin{bmatrix} \overline{Fx_{sta}} \\ \overline{Fy_{sta}} \end{bmatrix} \tag{9.38}$$

To validate the models, the simulated results were compared to acquired forces from actual cuts for the 4 unidirectional laminate cases in table 9.4. The acquired data comes from a milled semi-circular slot at the start of each applicable degree position. This data is acquired through a time based calculation that determines the precise degree position in the semi-circle as described in chapter 7. Two cutter rotations were captured and compared to the cutting forces predicted by the model. At 5600 rpm, the resolution is one data point per each 4.33 degrees at a sampling rate of 7800 Hz, which limits the fidelity. An example of the Fx and Fy forces are shown in figure 9.12 for slot #2, 45 degrees.

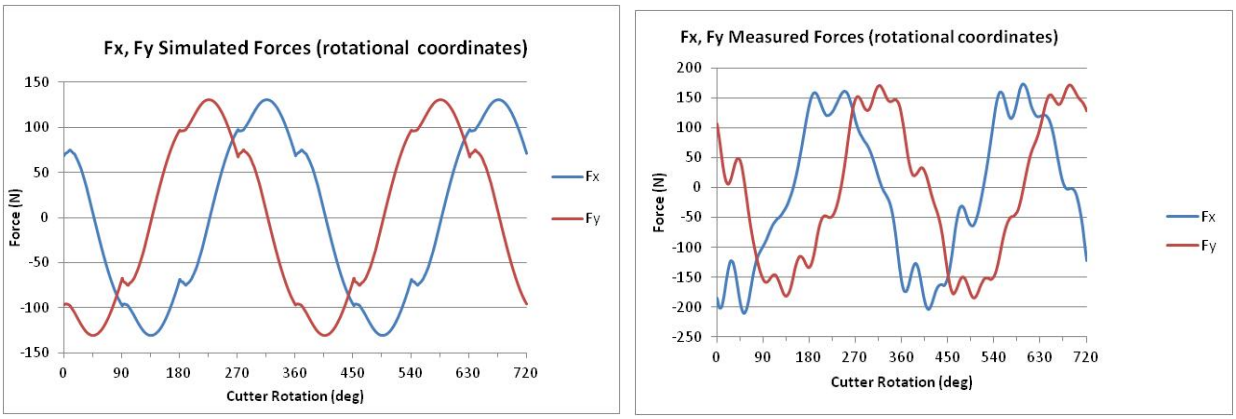

Figure 9.12. Results from slot #2, 45 degrees for Fx, Fy compared to model

It is encouraging that the shapes for the Fx and Fy plots for the measured and simulated forces are similar especially considering that they were derived from cutting force coefficients determined from tangential and radial forces and transformed from stationary to radial coordinates. However, the magnitudes are not the same. Table 9.4 summarizes the maximum force for Fx, Fy, Ft, Fr, and Fa (resultant force) between the simulation and actual acquired data.

Table 9.4. Model prediction versus actual measurements for 4-flute CVD test

Slot		Model	Actual		Model	Actual	
#		Fx max	Fx max	Ratio	Fy max	Fy max	Ratio
1	0 deg	127.73	186.04	1.46	127.23	187.61	1.47
2	45 deg	130.58	172.76	1.32	130.57	170.63	1.31
3	90 deg	93.72	132.78	1.42	93.73	139.85	1.49
4	135 deg	84.94	141.25	1.66	84.94	134.24	1.58
	Average			1.46			1.46

Slot		Model	Actual		Model	Actual		Model	Actual	
#		Ft max	Ft max	Ratio	Fr max	Fr max	Ratio	Fa max	Fa max	Ratio
1	0 deg	149.26	211.92	1.42	67.95	223.59	3.29	164.00	233.91	1.43
2	45 deg	128.34	180.82	1.41	128.88	200.72	1.56	181.88	220.18	1.21
3	90 deg	100.03	142.62	1.43	90.32	153.18	1.70	134.77	175.92	1.31
4	135 deg	113.02	205.49	1.82	49.82	156.98	3.15	123.51	165.71	1.34
	Average			1.52			2.42			1.32

From table 9.4 the ratio of actual to predicted force ranges from an average of 1.32 to 1.52 for all cases except for the radial force, Fr, which has a ratio of 2.42. As these are initially determined from linear regression and then multiplied as described in chapter 8, the difference between predicted and measured forces is larger than desired. More testing is required to determine if the prediction accuracy can be improved by a simple scale factor of the cutting force coefficients and applicability to all immersion angles and cutting orientations, or if there is an incorrect assumption in the fundamental derivation. Other work can be pursed as discussed in chapter 8 for further improvement of the experimental technique especially for acquiring accurate radial forces using a rotating dynamometer. From the work of other researches and this effort, the specific cutting energy approach appears to capture the general trends in cutting force prediction in milling composites. The semi-circular slot technique appears to have potential to provide milling coefficients at all fiber orientations and the capability to be used with superposition to predict cutting forces for multi-directional composite laminates. Additional fine tuning and experimentation is required to ensure general validity of the approach.

9.4 Summary

This chapter presented the model developed to predict cutting forces in multi-directional laminates based on tests conducted on a unidirectional laminate of the same material system and helical cutting tool combination. The model utilizes cutting force coefficients determined through a series of semi-circular slot tests on unidirectional laminate using a common helical cutting tool. The cutting force coefficients are determined for each degree position of the semi-circle. This provides milling coefficients for the cutting direction at any angle relative to fiber orientation which is a significant savings in the number of tests required compared to linear slot tests, where one test series is required for each cutting direction of interest relative to fiber orientation. The model utilizes these milling coefficients, layup configuration of a multi-directional laminate, and proposed cutting conditions to predict cutting forces at a specified cutting orientation by decomposing each ply, depending on depth of cut, and determining the differential forces which are then summed through superposition. The method offers an approach for cutting force prediction that greatly reduces the number of test cuts required for a material and cutting tool combination which has been specifically configured for multi-directional laminate composites. The initial results show general consistency; however, accuracy of the predictive model may be improved by further analysis of the underlying assumptions and additional experimentation to ensure applicability for all conditions. Further study is needed to refine the cutting force model for peripheral cutting and contour milling with realistic conditions.

CHAPTER 10

CONCLUSIONS AND RECOMMENDATIONS

10.1 Conclusions

Methods were presented for evaluating milling and edge trimming of composite materials. The techniques used for experimental evaluation including established methods of surface integrity measurement, tool wear measurement, SEM, cutting force, and AE acquisition. Models were developed to predict cutting forces within a multidirectional laminate using a specific energy approach and empirically determined cutting coefficients through simple semi-circular slot tests in unidirectional laminates. Very limited work has been published on particle collection techniques for dust generated from composite materials. The limited published work involved sampling in uncontrolled conditions where the local environment was exposed to the dust generated, thus limiting extensive experimentation without risk of creating unsafe conditions. A technique was developed and validated that provides a controlled environment for dust collection and analysis using isokinetic sampling with simultaneous instrumentation. This approach enables the fully controlled evaluation of nearly all particles generated by composite edge trimming from the source, and can be used for virtually any process that generates dust of interest.

Extensive testing was done to develop techniques for using the Kistler 9213C rotating dynamometer, as very little published work discussed optimal usage. This effort improved the fidelity and usability of the data to support the cutting force prediction model. A semi-circular slot technique for determining cutting force coefficients at all fiber orientations in unidirectional composite laminates for a material system and cutting tool combination was developed that utilizes data acquired from a rotating dynamometer leveraging the enhanced experimental techniques. The tests conducted demonstrated that using this approach provides mostly linear cutting force coefficients and constant cutting forces when milling aluminum. The data acquired when slot cutting composites demonstrated that cutting coefficients are dependent on fiber orientation as described by previous researchers.

The particle collection and analysis system developed demonstrated that isokinetic sampling could be used as a method for particle analysis for dust generated from the source of machining operations in safe and self-contained environment. Test after test demonstrated consistent patterns in the dust which is influenced by cutting conditions. This validated that short cutting tests could be used with real-time instruments to quickly analyze particle characteristics for evaluation of cutting conditions providing an effective tool and process for safely conducting extensive experimentation. The testing quantified the need for dilution because of high particle concentrations that exceeded the limits of the real-time instruments used in the study. Testing also demonstrated that dust generated at the source from composite milling appears to exceed OSHA permissible limits thus meriting careful consideration in design of dust collection systems for dry machining.

The conclusions from the experiments and analysis performed as part of this research includes:

Dust Emission

Gravimetric Particle Analysis and Scanning Electron Microscopy (SEM)

- Extensive study of SEM micrographs indicate that fiber fracture is random and independent of tool type when edge trimming with evidence of longitudinal cleaving, symmetric shearing, and various chipping resulting in many geometries. Many sharp edges are produced. Evidence of particles with at least one dimension as small as 500 nm are frequently observed.
- Energy dispersive X-ray spectroscopy (EDS) is capable of distinguishing carbon fiber particles produced as a result of edge trimming carbon fiber composite laminates.
- The MMAD for the four primary fiber orientations of unidirectional composite laminates was less than 0.4 μm when edge trimmed using a 2-flute, 0 degree PCD cutting tool in climb cutting orientation under the same conditions measured using a 10 stage cascade impactor, with 0 degree unidirectional laminates the lowest and -45 degree unidirectional laminates the highest. Difference range between low and high MMAD was just 0.23 μm.
- Mass concentration from the four primary fiber orientations of unidirectional composite laminates was between 19.4 and 58.4 mg/m^3 when edge trimmed using a 2-flute, 0 degree PCD cutting tool in climb cutting orientation under the same conditions measured using a

10 stage cascade impactor, with 0 degree unidirectional laminates the lowest and 90 degree unidirectional laminates the highest.

- The MMAD for 0, 90, +45 degree orientations of unidirectional composite laminates was less than 1.21 μm when edge trimmed using a 4-flute, 30 degree helix solid carbide cutting tool in climb cutting orientation under the same conditions measured using a 4 stage Sioutas cascade impactor, with 90 degree unidirectional laminates the lowest and 0 degree unidirectional laminates the highest. Difference range between low and high MMAD was just 0.19 μm.
- Average PM2.5 mass concentration measured with Sioutas cascade impactors is 6.997 mg/m^3 for 21 composite edge trimming dust collection tests with a range from 3.262 mg/m^3 for a 2-flute PCD cutting tool climb cutting a -45 degree laminate to 19.669 mg/m^3 for a 4-flute CVD tool trimming a multidirectional laminate. This seems to indicate through gravimetric analysis that the mass concentration of dust generated from composite edge trimming can be well above the OSHA limit for respirable dust of 5 mg/m^3 when measured at the source for the conditions evaluated. Results also demonstrate that larger axial and radial depths of cut will increase the particle mass concentration.

Real-Time Particle Collection and Measurement

- Composite dust profiles collected using real-time particle analysis instruments in both a dust enclosure and through isokinetic sampling demonstrate a common profile on a time-basis for both particle count and mass concentration. Magnitudes differ between instruments for the same or similar parameters but the profiles remain consistent on a time basis.
- The use of a shop vacuum system in an enclosure with balanced HEPA filtered return air quickly reduces composite dust count to below 500 cts/cc on a consistent basis after cutting completes in a matter of seconds where particle concentration during trimming could be greater than 25,000 cts/cc. This demonstrates dust can be quickly captured with an appropriate collection system.

- A 4-flute CVD cutting tool produced higher ultrafine particle count by approximately 40% and a higher PM2.5 mass concentration by approximately 50% than a 4-flute carbide cutting tool under the same cutting conditions.
- Exhaust nozzle position relative to the cutting tool significantly impacts particle mass and count concentration measurements under the same cutting conditions. A dust exhaust nozzle that closely follows the cutting tool while edge trimming captures the large majority of dust with minimum background particle count concentration less than approximately 500 cts/cc. Background particle count concentration with a fixed stationary nozzle was approximately 20,000 cts/cc. Background particle count concentration with a moving nozzle relative to the cutting tool but approximately 8 cm away was approximately 7,500 cts/cc. Exhaust nozzle position, design and flow rate is critical for efficient particle capture.
- Particle counts measured isokinetically using real-time instrumentation consistently exceed more than 10,000,000 particles/liter when edge trimming composites using 4-flute carbide cutting tools for particles ranging between 0.25μm to 32 μm using a aerosol spectrometer. Because of the high particle counts, dilution may be required for instruments with total particle count limits below this range to avoid under estimation.
- Mass concentration when edge trimming composites can exceed 30 mg/m^3 for respirable dust measured using real-time instrumentation, well above the OSHA limit for respirable dust of 5 mg/m^3 when measured at the source. While the concentration differs, the patterns are consistent to those measured gravimetrically using cascade impactors.
- Mass concentration when edge trimming composites can exceed 50 mg/m^3 for total dust using real-time instrumentation, well above the OSHA limit for total dust of 15 mg/m^3 when measured at the source.

Cutting Force

Cutting Force Comparison

- A diamond burr tool had the lowest maximum directly measured resultant cutting force (without any signal shift compensation) from a rotating dynamometer for a edge trimmed multidirectional composite laminate compared to eight other cutting tool types under the same cutting conditions.

- Unidirectional laminates with 0 degree fiber orientation had the lowest average resultant cutting force and +45 degree orientation the highest compared to 0, +45 and -45 degree unidirectional laminates trimmed with a 2-flute, 0 degree PCD cutting tool in climb cutting orientation under the same conditions directly measured using a rotating dynamometer without any signal shift compensation.

Milling Force Prediction

- Tangential cutting forces measured when using a 4-flute CVD cutting tool had a average correlation coefficient of .99 at every degree position when feed rate in mm/tooth was plotted against tangential force in Newtons. Radial forces had a average correlation coefficient of .77 for the same tool and material system.
- Average correlation coefficients using a 2-flute cutting tool in aluminum for a semi-circular slot with cutting edge aligned to the y-axis of a rotating dynamometer were nearly identical at all degree positions whether using combinations of Fx, Fy or Ft, Fr to calculate, where feed per tooth (mm/tooth) is plotted against force (N). Average correlation coefficients were greater than .98 for Ft, Fx and greater than .95 for Fr, Fy combinations following the edge alignment convention.
- Average cutting forces for a semi-circular slot test are very linear for aluminum and vary with fiber orientation for unidirectional composite laminates. Average cutting force is determined by averaging the force at an integer number of rotations at each degree position in the semi-circular slot.
- Signal shift in a rotating dynamometer can significantly impact the magnitude and accuracy of derived resultant and radial forces as well as comparison of forces. The amount of impact is proportional to the amount of signal shift for each measured force or moment component (Fx, Fy, Mz). Measured force output should be carefully evaluated to determine the amount of signal shift prior to using for assessment and in calculations. Further, cutting tests should ideally have a no-load cutting condition at either end of the test for centering of the signal.
- Cutter runout can have a significant impact in cutting force measurement. A cutter runout of .114 mm was found to provide a full force profile for a single tooth of a 2-flute

cutting tool and near zero for the second tooth in both aluminum and composite full immersion slot experiments using a rotating dynamometer for a single cutter rotation.

- Cutter force magnitudes that use a significant percentage of the measurement range of the rotating dynamometer appear to improve the signal to noise ratio. Cutter forces greater than approximately 40% of the dynamometer fine range had lower error when comparing resultant forces calculated using measured Fx and Fy forces and those determined by using measured Mz (moment), Fx, Fy for a 2-flute solid carbide cutter in aluminum. Similar trends were found with 4-flute CVD, 4-flute carbide, and 2-flute carbide cutters in composites.

Process Conditions

Tool Wear

- A 4-flute solid carbide cutter experienced approximately twice the total tool wear compared to a 4-flute PCD cutter when edge trimming the same sequence of 0, 90, +45, -45 degree unidirectional composite laminates under the same cutting conditions and climb cutting orientation.

Surface Integrity

- Unidirectional laminates with 90 degree fiber orientation had the lowest average surface finish, Ra, when measured perpendicular to the trimming direction compared to 0, +45 and -45 degree unidirectional laminates trimmed with a both a 2-flute, 0 degree PCD cutting tool and 4-flute carbide cutting tool in climb cutting orientation under the same conditions.
- Unidirectional composite laminates edge trimmed using a 2-flute, 0 degree PCD cutting tool had lower average surface finish, Ra, for all four primary fiber orientations when measured perpendicular to the trimming direction compared to a 4-flute solid carbide cutting tool with 30 degree helix tool in climb cutting orientation under the same conditions.
- A multidirectional laminate edge trimmed with both a 2-flute 0 degree PCD cutting tool and 4-flute solid cutting tool with 30 degree helix in *conventional* cutting orientation had a lower lowest average surface finish, Ra, when measured perpendicular to the trimming

direction, compared to a multidirectional laminate under the same conditions and cutting tool but with *climb* edge trimming.

- A 4-flute CVD coated cutting tool had the lowest average lowest average surface finish, Ra, when measured perpendicular to the trimming direction compared for a multidirectional composite laminate compared to eight other cutting tools under the same conditions and cutting with climb cutting.

Acoustic Emission

- Acoustic Emission (AE) signal profile consistently aligned on a time-basis to resultant cutting forces with multi-tooth helical cutting tools, when edge trimming carbon fiber composite unidirectional and multidirectional laminates independent of cutting orientation and conditions.

10.2 Recommendations for Future Study

This research focused on developing new and updated techniques for cutting force modeling of composite laminates and particle analysis from the milling process. Often, research will generate more questions than answers. In the case of this work, the focus of the effort was to develop techniques that have industrial and production applicability. Thus, there are many opportunities for future study applying the techniques developed to gain further understanding and perform process optimization and model refinement.

10.2.1 Acoustic Emission

Acoustic emission (AE) studies were conducted as part of this research. The preliminary analysis demonstrated that the AE signal profile timing, shape, and relative magnitude was similar to that of the resultant cutting forces. This trend was tested and found consistent with cutting tools designed with different number of teeth when trimming in both composites and aluminum. Further studies in this area may include:

- Effects of location of AE sensors
- Effects of clamping on AE sensors
- Monitoring AE signal for tool wear
- Monitoring AE signal for surface integrity and delamination

10.2.2 Cutting Force Model

A specific energy derived predictive cutting force model and enhanced method to acquire cutting force coefficients was developed as part of this research. This method had an industrial focus and attempted to demonstrate that a simple set of semi-circular slot tests on a unidirectional laminate could be used to predict cutting forces for the same cutting tool and on a multidirectional laminate of the same material system in any configuration. With only limited testing performed as part of this research, there is opportunity for additional study for the following objectives.

- Validating general case applicability and fundamental derivation
- Determining model accuracy for a wider range of cutting tools
- Conducting rotating dynamometer technique refinement including filtering
- Testing with a stationary dynamometer
- Testing the model for process optimization using full factorial design of experiments
- Integrating the model with a CAD/CAM NC programming package for cutting force analysis along a tool path with changing cutting orientation relative to fiber angles

10.2.3 Particle Analysis

Methods were developed as part of this research to analyze data from multi-channel particle analyzers and to present the information in a variety of usable formats, including log-probability plots and calculation of numerous statistics. Several opportunities exist to expand the basic methodology developed. This ranges from thorough analysis of actual particle sizing from SEM micrographs to improve mass concentration estimates and comparison to gravimetric impactor results for model calibration. Topics for future study include:

- SEM image sizing and statistical volumetric analysis
- Optimum density determination for all size ranges
- Calibration to gravimetric impactor measurements
- Distinguishing matrix from fibers at the submicrometer scale using techniques such as EDS
- Structured data collection using cyclones at different flow rates
- Combining data and sizing from multiple instruments
- Particle analysis for insight into fracture modes

10.2.4 Particle Collection

Limited test cases were conducted as part of this research with respect to analyzing dust generated from many cutting conditions, as the emphasis was on development of a safe and controlled means for particle collection and analysis from milling operations using dust directly

generated from the source. With the techniques developed for closed-loop particle collection and analysis that can be accomplished through a series of short tests, study opportunities exist to look at a variety of materials, cutting geometries, and process conditions. The system and techniques developed enable rapid testing to allow full factorial test matrices to be conducted. A variety of factors can be studied. Future study and development opportunities include, but are not limited to:

- Nozzle optimization for slot cutting and improved encapsulation for edge trimming using additive manufacturing techniques
- Full factorial studies changing cutting conditions, cutter geometry, axial depth of cut, radial depth of cut, feed rate, and spindle speed on particle concentration and count generated for different cutting operations
- Process optimization for a given cutting geometry and material system to maximize material removal rates, minimizing hazardous dust concentrations, and maintaining surface integrity
- Correlating surface finish to particle size and concentration
- Studying the effects of tool wear on different cutting geometries and impact on dust count and concentration
- Development of an environmental factor rating system to describe and quantify the dust produced from dry cutting for material, tool, and cutting condition combinations
- Support to toxicity studies on environmental effects of generated particles

10.3 Final Words

Particle size and mass concentration generated from the source should be considered when dry machining composite laminates to ensure a safe operation. It is the hope that the techniques, tools, and processes developed as part of this research can be used to contribute to further the understanding of machinability of composite materials and make their way into production use.

REFERENCES

1. "ASM Handbook, Volume 21 Composites.", ASM International, Materials Park, OH, 2001.

2. Campbell, F.C., "Manufacturing Process for Advanced Composites.", Elsevier Ltd., New York, 2004.

3. Creese, Robert C., "Introduction to Manufacturing Processes and Materials.", Marcel Dekker, Inc., New York, 1999.

4. Oberg, E., Jones, F., Horton, H., Ryffel, "Machinery's Handbook, 24th Edition.", Industrial Press, NY, 1992.

5. Boothroyd, G, Knight, W., "Fundamentals of Machining and Machine Tools.", CRC Press, Boca Raton, FL, 2005.

6. Ramulu, M., 2008. ME 599 Machining of composites. Course pack. University of Washington, Seattle.

7. ASME B94.19-1997, Milling Cutters and End Mills, An American National Standard, American Society of Mechanical Engineers, NY, 1997.

8. ANSI B212.4-1995, American National Standard for Cutting Tools – Indexable Inserts-Identification System, ANSI, 1995.

9. Carboloy, General Electric, Milling Handbook of High-Efficiency Metal Cutting, General Electric Company, CT, 1980.

10. Merchant, M. Eugene, "Basic Mechanics of the Metal Cutting Process.", Journal of Applied Mechanics, September, (1944), pp. A168-A175.

11. ASME B46.1-2002, An American National Standard, Surface Texture (Surface Roughness, Waviness, and Lay), American Society of Mechanical Engineers, NY, 2002.

12. Gordon, S., Hillery, M.T., "A review of the cutting of composite materials.", *Proc. Instn. Mech. Engrs.,Vol. 217, Part L., J. Materials Design and Applications*, (2003), pp. 35-45.

13. Koenig, W.,Wulf, Ch. Graß, Willerscheid, H., "Machining of Fibre Reinforced Plastics.", *Annals of the CIRP*, Vol. 34/2/1985, (1985), pp. 537-548.

14. Wang, D.H., Ramulu, M., Arola, D., "Orthogonal Cutting Mechanisms of Graphite/Epoxy Laminate. Part 1: Unidirectional Laminate.", *International Journal of Machine Tools and Manufacturing*, Vol. 35, No. 12, (1995), pp. 1623-1638.

15. Wang, DH., Ramulu, M., Arola, D., "Orthogonal Cutting Mechanisms of Graphite/Epoxy Laminate. Part II: Multi-Directional Laminate.", *International Journal of Machine Tools and Manufacturing*, Vol. 35, No. 12, (1995), pp. 1639-1648.

16. Colligan, K. and Ramulu, M., "The Effect of Edge Trimming on Composite Surface Plies.", *Manufacturing Review*, Vol. 5, No.4, December (1992), pp. 274-283.

17. Hocheng, H., Puw, H.Y., Huang, Y., "Preliminary study on milling of unidirectional carbon fibre-reinforced plastics.", *Composites Manufacturing*, Vol. 4, No. 2, (1993), pp. 103-108.

18. Puw, H.Y., Hocheng, H., "Machinability Test of Carbon Fiber-Reinforced Plastics in Milling.", *Materials & Manufacturing Processes*, 8(6), (1993), pp. 717-729.

19. Müller-Hummel, P, Lamba, S., Schwarz, R., "New Economic Solutions for Drilling and Milling of Carbon Fiber Reinforced Plastics for Aerospace Applications", SME Composites Manufacturing Conference, San Diego, CA, April 2010.

20. Hintze, W., Hartmann, D., Schütte, C., "Occurrence and propagation of delamination during the machining of carbon fibre reinforced plastics (CFRP)-An experimental study.", *Composites Science and Technology*, (2011), doi:1016/j.compscitech.2011.08.002.

21. Hintze, W., Hartmann, D., "Modeling of delamination during milling of unidirectional CFRP.", *14th CIRP Conference on Modeling of Machining Operations (CIRP CMMO), Procedia CIRP 8*, (2013), pp. 444-449.

22. Pecat, O., Rentsch, R., Brinksmeier, E., "Influence of milling process parameters on the surface integrity of CFRP.", *Procedia CIRP 1, 5th CIRP Conference on High Performance Cutting 2012*, (2012), pp. 466-470.

23. Meshreki, M., Sadek, A., Attia, M.H., "High Speed Routing of Woven Carbon Fiber Reinforced Epoxy Laminates.", *Proceedings of the ASME 2012 International Mechanical Engineering Congress & Exposition*, IMECE2012, Houston, Texas, November 9-15, 2012, IMECE2012-88616.

24. Wang, Y.G., Yan, X.P, Chen, X.G., Sun, C.Y., Liu, G., "Cutting Performance of Carbon Fiber Reinforced Plastics Using PCD Tool.", *Advanced Materials Researc*h, Vol. 215, (2011), pp. 14-18.

25. Yashiro, T., Ogawa, T., Sasahara, H., "Temperature measurement of cutting tool and machined surface layer in milling of CFRP.", *International Journal of Machine Tools & Manufacture*, 70, (2013), pp. 63-69.

26. Geis, T., Klingelhöller, C., Hintze, W, "Constant depth scoring of fibre reinforced plastic structures to prevent delamination", *6th CIRP International Conference on High Performance Cutting (CIRP CMMO), HPC2014, Procedia CIRP 14*, (2014), pp. 205-210.

27. Hintze, W., Cordes M., Koerkel, G., "Influence of weave structure on delamination when milling CFRP.", *Journal of Materials Processing Technology*, 216, (2015), pp. 199-205.

28. Hagino, M., Inoue, T., Serra, "Effect of carbon fiber orientation and helix angle on CFRP cutting characteristics by end-milling.", *International Journal of Automation Technology*, Vol. 7, No. 3, (2013), pp. 292-299.

29. Inoue, T., Hagino, M., "Cutting characteristics of CFRP materials with carbon fiber distribution.", *International Journal of Automation Technology*, Vol. 7, No. 3, (2013), pp. 285-291.

30. Kohkonen, K.E., Anderson, S., Strong, A.B., "Machining Graphite Composites with Polycrystalline Diamond End Mills.", *23rd International SAMPE Technical Conference*, October 21-24, (1991), pp. 1036-1046.

31. Chao, P.Y. and Hwang, Y.D., "An improved Taguchi's method in design of experiments for milling CFRP composite.", *International Journal of Production Research,* Vol. 35, No. 1, (1997), pp. 51-66.

32. Rahman, M., Ramakrishna, S., Thoo, H.C., "Machinability Study of Carbon/PEEK Composites.", *Machining Science and Technology*, 3(1), (1999), pp. 49-59.

33. Davim, J.P., Reis, P., António, C.C., "A study on milling of glass fiber reinforced plastics manufactured by hand-layup using statistical analysis (ANOVA).", *Composite Structures*, 64, (2004), pp. 493-500.

34. Davim, J. Paulo and Reis, Pedro, "Multiple regression analysis (MRA) in modeling milling of glass fibre reinforced plastics (GFRP).", *International Journal of Manufacturing Technology and Management*, Vol. 6, Nos. 1/2, (2004), pp. 185 -197.

35. Davim, J. Paulo and Reis, Pedro, "Damage and dimensional precision on milling carbon fiber-reinforced plastics using design experiments.", Journal of Materials Processing Technology, 160, (2005), pp. 160-167.

36. Ucar, M. and Wang, Y., "End-milling Machinability of a Carbon Fiber Reinforced Laminated Composites.", *Journal of Advanced Materials*, Volume 37, No. 4, October (2005), pp. 46-52.

37. Sheikh-Ahmad, J. and Sridhar, G., "Edge Trimming of CFRP Composites with Diamond Coated Tools: Edge Wear and Surface Characteristics.", *SAE Technical Paper Series,*

2002-01-1526, General Aviation Conference and Exhibition, Wichita, Kansas, April 16-18, (2002).

38. Colligan, K., and Ramulu, M., "Edge Trimming of Graphite/Epoxy with Diamond Abrasive Cutters.", *Journal of Manufacturing Science and Engineering*, Vol. 121, November 1999, (1999), pp. 647-655.

39. Janardhan, P., Sheikh-Ahmad, J., Cheraghi, H., "Edge Trimming of CFRP with Diamond Interlocking Tools.", *SAE Technical Paper Series, 2006-01-3173*, Aerospace Manufacturing and Automated Fastening Conference & Exhibition, Toulouse, France, September, 12-14, 2006, (2006).

40. López De LaCalle, L.N., Lamikiz, A., Campa, F.J., Valdivielso, A.F., "Design and Test of a Multitooth Tool for CFRP Milling.", *Journal of Composite Materials*, Vol. 0, No. 00, (2009), pp. 1-16.

41. Lopez de Lacalle, L.N., Lamikiz, A., "Milling of Carbon Fiber Reinforced Plastics.", *Advanced Materials Research*, Vols. 83-86, (2010), pp. 49-55.

42. Ghidossi, P., Mansori, P.E., Pierron, F., "Edge machining effects on the failure of polymer matrix composite coupons", *ICCM-14*, July 14-18, 2003, San Diego, California, SME, TP04PUB108, (2003).

43. Ghidossi, P., Mansori, P.E., Pierron, F., "Edge machining effects on the failure of polymer matrix composite coupons", Composites: Part A, 35, (2004), pp. 989-999.

44. Ghidossi, P., Mansori, P.E., Pierron, F., "Influence of specimen preparation by machining on the failure of polymer matrix off-axis tensile coupons", *Composites Science and Technology*, 66, (2006), pp. 1857-1872.

45. Haddad, M., Zitoune, R., Eyma, F., Castanie, B., "Influence of tool geometry and machining parameters on the surface quality and the effect of surface quality on compressive strength of carbon fibre reinforced plastic.", *Materials Science Forum*, Vol. 763, (2013), pp. 107-125.

46. Puw, H.Y., Hocheng, H., "Milling Force Prediction for Fiber Reinforced Thermoplastics.", *Machining of Advanced Composites, The 1993 ASME Winter Annual Meeting, November 28-December 3, 1993*, MD-Vol. 45, PED-Vol. 66, (1993), pp. 73-88.

47. Puw, H.Y., Hocheng, H., "Milling Force Prediction for Fiber Reinforced Plastics.", *Proceedings of the ASM 1993 Materials Congress, Pittsburgh, PA, October 17-21, 1993,* (1993), pp. 97-108.

48. Puw, H.Y., Hocheng, H., "Anisotropic Model of Milling Force Prediction for Fiber Reinforced Plastics.", PD-*Vol. 75, Engineering Systems Design and Analysis, Volume 3, ASME*, (1996), pp. 11-20.

49. Jahanmir, S., Ramulu, M., Koshy, P., Machining of Ceramics and Composites., Marcel Dekker, Inc., New York, NY, 1999. (Chapt. 9, Puw, H.Y., Hocheng, H., "Milling of Polymer Composites.", pp. 267-294.)

50. Sheikh-Ahmad, J. and Yadav, R., "Force Prediction in Milling of Carbon Fiber Reinforced Polymers.", *IMECE2005-81909*, Proceedings of IMECE2005, November 5-11, Orlando, Florida, (2005), pp. 429-436.

51. Kalla, D., Lodhia, P., Bajracharya, B., Twomey, J., Sheikh-Ahmad, J., "CN Force Prediction Model in Milling of Carbon Fiber Reinforced Polymers.', *Intelligent Systems in Design and Manufacturing VI, Proceedings of SPIEE, Vol. 5999, 59990S*, (2005).

52. Sheikh-Ahmad, J., Twomey, J., Kalla, D., Lodhia, P., "Multiple Regression and Committee Neural Network Force Prediction Models in Milling FRP.", *Machining Science and Technology*, 11, (2007), pp. 391-412.

53. Sheik-Ahamd, Jamal, "Model for predicting cutting forces in machining CFRP.", *International Journal of Materials and Product Technology*, Vol. 32, Nos. 2/3, (2008), pp. 152-167.

54. Sheikh-Ahmad, Jamal Y., Machining of Polymer Composites, Springer, New York, NY, (2009).

55. Kalla, D., Sheikh-Ahmad, Twomey, J., "Prediction of cutting forces in helical end milling fiber reinforced polymers.", *International Journal of Machine Tools & Manufacture*, 50, (2010), pp. 882-891.

56. Karpat, Y., Bahtiyar, O., Değer, B., "Milling Force Modelling of Mulidirectional Carbon Fiber Reinforced Polymer Laminates.", *Procedia CIRP 1, 5th CIRP Conference on High Performance Cutting 2012*, (2012), pp.460-465.

57. Karpat, Y., Bahtiyar, O., Değer, B., "Mechanistic force modeling for milling of unidirectional carbon fiber reinforced polymer laminates.", *International Journal of Machine Tools & Manufacture*, Vol. 56, (2012), pp. 79-93.

58. Karpat, Y., Polat, Naki, "Mechanistic force modeling for milling of carbon fiber reinforced polymers with double helix tools.", *CIRP Annals – Manufacturing Technology*, 62, (2013), pp. 95-98.

59. Sen, A.K., Litak, G., Syta, A., Rusinek, R., "Intermittancy and multiscale dynamics in milling of fiber reinforced composites.", *Mecannica*, 23 October 2012.

60. Rusinek, Rafal, "Cutting process of composite materials: An experimental study.", *International Journal of Non-Linear Mechanics*, 45, (2010), pp. 458-462.

61. Rusinek, Rafal, "Dynamics of Composite Materials Cutting.", *Advances in Manufacturing Science and Technology*, Vol. 35, No. 3, (2011), pp. 31-37.

62. Zaghbani, I., Chatelain, J-F., Berube, S., Songmene, V., and Lance, J., "Analysis and modeling of cutting forces during the trimming of unidirectional CFRP composite laminates.", *Int. J. Machining and Machinability of Materials*, Vol. 12, No. 4, (2012), pp. 337-357.

63. Arola, D. and Ramulu, M., "Orthogonal Cutting of Fiber-Reinforced Composites: A Finite Element Analysis." *Int. J. Mech. Sci*., 39(5), (1997), pp. 597-613.

64. Ramesh, M.V., Seetharamu, K.N., Ganesan, N., and Sivakumar, M.S., "Analysis of machining FRPs using FEM." *Int. J. of Machine Tools & Manufacture*, 38, (1998), pp. 1531-1549.

65. Mahdi, M. and Zhang, L., "A finite element model for the orthogonal cutting of fiber-reinforced composite materials." *J. of Materials Processing Technology*, 113, (2001), pp. 373-377.

66. Arola, D., Sultan, M.B., Ramulu, M., "Finite Element Modeling of Edge Trimming Fiber Reinforced Plastics.", *J. of Manufacturing Science and Engineering*, Vol 124, (2002), pp. 32-41.

67. Nayak, D., Bhatnagar, N., and Mahajan, P., "Machining Studies of UD-FRP Composites Part 2: Finite Element Analysis.", *Machining Science and Technology*, 9, (2005), pp. 503-528.

68. Nayak, D., Singh, I., Bhatnagar, N., and Mahajan, P., "Finite Element Analysis of Effect of Machining Direction on Fibre Orientation of FRP Composites.", *IE(I) Journal-PR*, Vol. 85, (2005), pp. 64-67.

69. Lasri, L., Nouari, M., and EL Mansor, M., "Stiffness degradation concept for modeling the induced-cutting damage and chip formation of a Fiber-Reinforced Polymer (FRP) composite during machining," Manuscript Number JCOMA-07-468 (assumed 2007).

70. Dornfeld, D., "Application of acoustic emission techniques in manufacturing.", *NDT&E International*, Volume 25, Number 6, (1992), pp. 259-269.

71. Ramulu, M., Kim, D., Choi, G., "Frequency Analysis and Characterization in Orthogonal Cutting of Glass Fiber Reinforced Composites" *Composites Part A: Applications and Manufacturing*, Vol.34, No.10, (2003), pp. 949-962.

72. Mascaro, B., Gibiat, V., Bernadou, M., Esquerre, Y., "Acoustic Emission of the drilling of carbon/epoxy composites", *Forum Acusticum, Budapest*, *Hungary*. 4th, (2005), pp. 2823-2827.

73. Arul, S., Vijayaraghavan, L., Malhotra, S.K., "Online Monitoring of Acoustic Emission for Quality Control in Drilling of polymeric Composites", *Journal of Materials Processing Technology*, Vol. 185, (2007), pp. 184-190.

74. Chibane, H., Morandeau, A., Serra, R., Bouchou, A., Leroy, R., "Optimal milling conditions for carbon/epoxy composite material using damage and vibration analysis", *International Journal of Advanced Manufacturing Technology*, Vol. 68, (2013), pp. 1111-1121.

75. Marinescu, I., Axinte, D.A., "A critical analysis of effectiveness of acoustic emission signals to detect tool and workpiece malfunctions in milling operations.", *International Journal of Machine Tools and Manufacture*, Vol. 48, (2008), pp. 1148-1160.

76. European Commission – Environment – Chemicals, "Recommendation on the definition of a nanomaterial", http://ec.europa.eu/environment/chemicals/nanotech/#definition, 18 October 2011.

77. Kulkarni, P., Baron, P., Willeke, K., "Aerosol Measurement: Principles, Techniques, and Applications, 3rd edition." Wiley, Hoboken, NJ, 2011.

78. Burke, W.A., Esmen, N., "The inertial behavior of fibers.", *American Industrial Hygiene Association Journal*, 17, 39, May, (1978), pp. 400-405.

79. Hinds, William C., "Aerosol Technology: Properties, Behavior, and Measurement of Airborne Particles, 2nd Edition.", John Wiley & Sons, Inc., Hoboken, NJ, 1999.

80. Holt, P.F., Horne, M., "Dust from Carbon Fibre.", *Environmental Research*, 17, (1978), pp. 276-283.

81. Holt, P.F, "Submicron Dust in the Guinea Pig Lung.", *Environmental Research*, 28, (1982), pp. 434-442.

82. Wagman, J., Berger, H.R., Miller, J.L., Conner, W.D., "Dusts and Residues from Machining and Incinerating Graphite/Epoxy Composites: A Preliminary Study.", *Environmental Technology Letters*, Vol 3, (1982), pp. 469-478.

83. Siebert, John F. "Dimunition and Longitudinal Splitting of Carbon Fibers due to Grinding.", MS Thesis, University of Pittsburgh, AFIT/CI/NR 88-70, 1987.

84. Mazumder, M.K., Chang, R.J., Bond, R.L., "Aerodynamic and Morphological Properties of Carbon-Fiber Aerosols.", *Aerosol Science and Technology*, 1, (1982), pp. 427-440.

85. Owen, P.E., Glaister, J.R., Ballantyne, B., Clary, J.J., "Subchronic Inhalation Toxicology of Carbon Fibers.", *Journal of Occupational Medicine*, Vol. 28, No. 5, May, (1986), pp. 373-376.

86. Boatman, E.S., Covert, D., Kalman, D., Luchtel, D., Omenn, G.S., "Physical, Morphological, and Chemical Studies of Dusts Derived from the Machining of Composite-Epoxy Materials.", *Environmental Research*, 45, (1988), pp. 242-255.

87. Luchtel, D.L., Martin, T.R., Boatman, ES., "Response of the Rat Lung to Respirable Fractions of Composite Fiber-Epoxy Dusts.", *Environmental Research*, 48, (1989), pp. 57-69.

88. Martin, T.R., Meyer, S.W., Luchtel, D.R., "An Evaluation of the Toxicity of Carbon Fiber Composites for Lung Cells in Vitro and in Vivo.", *Environmental Research*, 49, (1989), pp. 246-261.

89. Bourcier, Denis, "Exposure Evaluation of Composite Materials with Emphasis on Cured Composite Dust.", *Applied Industrial Hygiene*, Special Issue, 12/89, (1989), pp. 40-46.

90. Siebert, John F., "Composite Fiber Hazards.", AFOEHL Report: 90-226E100178MGA, Air Force Occupational and Environmental Health Laboratory, Brooks Air Force Base, Texas, December 1990.

91. Kwan, Joseph Kai-cho, "Health hazard evaluation of the postcuring phase of graphite composite operations at the Lawrence Livermore National Laboratory, Livermore, California.", PhD Thesis, University of California, Los Angeles, 1990.

92. Warheit, D.B., Hansen, J.F., Carakostas, M.C., Hartsky, M.A., "Acute inhalation toxicity studies in rats with a respirable-sized experimental carbon fibre: Pulmonary biochemical and cellular effects.", *Annals Occupational Hygiene*, Vol 38, Supplement 1, (1994), pp. 769-776.

93. Burr, Gregory A., Health Hazard Evaluation Report No. 89-0001, NIOSH, HETA 1989-0001-2436, General Electric Corporation, Evendale, OH, July, 1994.

94. Jahanmir, S., Ramulu, M., Koshy, P., Machining of Ceramics and Composites., Marcel Dekker, Inc., New York, NY, 1999. (Chapt. 12, Klocke, F., Koenig, W., Wuertz, C., Dietz, C., "Environmental Effects and Safety in Machining Fibrous Composites.", pp. 411-425.)

95. Darne, C., Terzetti, F., Coulais, C., Fournier, J., Guichard, Y., Gate, L., Binet, S., "In Vitro Cytotoxicity and Transforming Potential of Industrial Carbon Dust (Fibers and Particles) in Syrian Hamster Embryo (SHE) Cells.", *Annuls Occupational Hygiene*, Vol. 54, No. 5, (2010), pp. 532-544.

96. Ramulu, M., Kramlich, J., "Machining of Fiber Reinforced Composites: Review of Environmental and Health Effects.", *International Journal of Environmentally Conscious Design & Manufacturing*, Vol. 11, No. 4, (2004), pp. 1-19.

97. Yon, Richard E., "Characterization of Graphite Composite Material Particulates from United States Air Force Aircraft Maintenance Operations.", Thesis, AFIT/GIH/ENV/11-M04, Air Force Institute of Technology, Wright-Patterson Air Force Base, OH, 2011.

98. Haddad, M., Zitoune, R., Eyma, F., Castanie, B., Bougherara H., "Surface quality and dust analysis in high speed trimming of CFRP.", *Applied Mechanics and Materials*, Vol. 232, (2012), pp. 57-62.

99. Haddad, M., Zitoune, R., Eyma, F., Castanie, B., "Study of the surface defects and dust generated during trimming of CFRP: Influence of tool geometry, machining parameters and cutting speed range.", *Composites: Part A*, Vol. 66, (2014), pp. 142-154.

100. Bello, D., Wardle, B.L., Yamamoto, N., deVilloria, R., Garcia, E.J., Hart, A.J., Ahn, K., Ellenbecker, M., Hallock, M., "Exposure to nanoscale particles and fibers during machining of hybrid advanced composites containing carbon nanotubes.", *Journal of Nanoparticle Research*, (2008).

101. Toray, http://www.toray.com/ir/individual/ind_012.html

102. Kistler, Instruction Manual: Rotating Cutting Force Dynamometer 9123C, 9123C_002-042e09.10, Kistler Instrumente, AG, Switzerland.

103. Physical Acoustics Corporation, PCI-2 Based AE System User's Manual, Rev 3, Part#: 6301-1000, April 2007.

104. Sierra Instruments, Series 210, Ambient Cascade Impactor Instruction Manual, Bulletin No. 7-79-210IM.

105. SKC Incorporated, Sioutas Cascade Impactor, Operating Instructions, Form 40086 Rev. 1402. http://www.skcinc.com/instructions/40086.pdf

106. Dwyer, Series 160 Stainless Steel Pitot Tubes, Specifications - Installation and Operating Instructions, Bulletin H-11, FR# 440226-00, Rev. 8. www.dwyer-inst.com

107. Heim, M., Mullins, B., Umhauer, H., Kasper, G., "Performance evaluation of three optical particle counters with an efficient "multimodal" calibration method.", *Aerosol Science*, 39, (2008), pp. 1019-1031.

108. "Choosing an Optical Particle Counter.", TSI Application Note ITI-095, TSI Corporation.

109. "P-TRAK® Ultrafine Particle Counter Theory of Operation", TSI Application Note ITI-071, TSI Corporation.

110. Thermo Electron Corporation "Models PDR-1000AN & PDR-1200S Personal DataRam Particulate Monitoring – Instruction Manual", January 2004.

111. Casella CEL Inc. “CEL-712 Microdust Pro Real-tme Dust Monitor – User Manual”, HB4048-01.

112. GRIMM Aerosol, Technik GmbH & Co., Portable Laser Aerosol Spectrometer and Dust Monitor Model 1.108/1.109 Manual.

113. Topas, GmbH, “TOPAS Dilution System DIL 550 Instruction Manual”

114. “TSI DustTRAK DRX Aerosol Monitor Model 8533/8534/8533EP Operation and Service Manual”, P/N 6001898 Rev. J, 2013.

115. TSI “Model 3330 Optical Particle Sizer Spectrometer-Operation and Service Manual”, P/N 6004403, Revision E, April 2011.

116. US Patent Application 14/311,655, Miller, J.L., “Methods and Systems for Particle Collection and Analysis”, 23 June 2014.

117. International Standard ISO 12141, “Stationary source emissions- determination of mass concentration of particulate matter (dust) at low concentrations – manual gravimetric method.” First edition, November 1, 2002.

118. Budak, E., Altintas, Y., Armarego, E.J.A.,“Prediction of Milling Force Coefficients from Othroghogonal Cutting Data.”, *Transactions of the ASME*, Vol. 118, May, (1996), pp. 216-224.

119. Altintas, Yusuf., Manufacturing Automation: Metal Cutting Mechanics, Machine Tool Vibrations, and CNC Design, Cambridge University Press, New York, NY, (2000).

120. Machinability Data Center Handbook, Metcut Research Associates, Inc.. Cincinnati, OH, (1980).

121. Occupational Safety & Health Administration, Regulations, 1910.1000 Table Z-3, Mineral Dusts.

122. Multiple-path Particle Model, MPPD V2.0 2002-2006, Centers for Health Research (CIIT), USA, National Institute of Public Health and the Environment (RIVM), Netherlands.

123. Image Processing and Analysis in Java, ImageJ, Wayne Rasband, National Institutes of Health, USA, Rev 1.48e.

124. Martellotti, M.E., “An analysis of the milling process.”, *Transactions of the A.S.M.E*, November, (1941), pp. 677-700.

125. Martellotti, M.E., “An analysis of the milling process, Part II – Down milling.”, *Transactions of the A.S.M.E*, May, (1945), pp. 233-251.

126. Tlusty, J., “Dynamics of cutting forces in end milling.”, *Annals of the CIRP*, Vol. 24/1/1975, (1975), pp. 21-25.

127. Devor, R.E., Kline, W.A., Zdeblick, W.J., “A mechanistic model for the force system in end milling with application to machining airframe structures.”, Proceeding of the 8th North American Manufacturing Research Conference, (1980), pp. 297-303.

128. Germain, D., Fromentin, G., Poulachon, G., Bissey-Breton, “From large-scale to micromachining: A review of force prediction models.”, *Journal of Manufacturing Processes*, Vol. 15, (2013), pp. 389-401.

APPENDIX A

Phase 2 Tests: Sample S1 Results

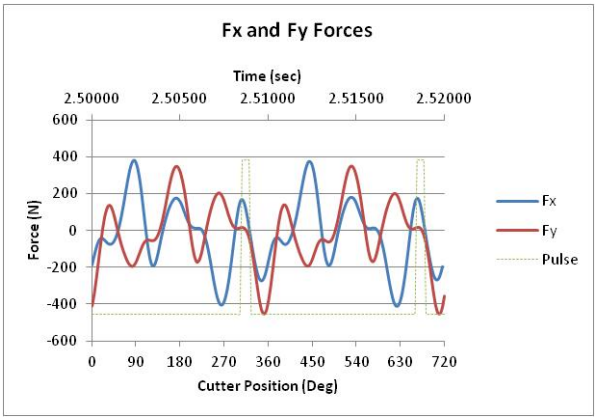

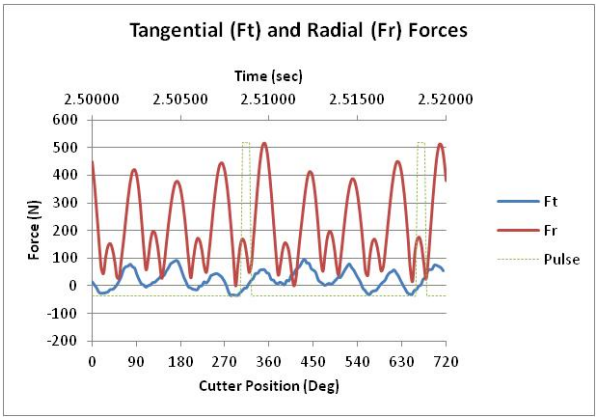

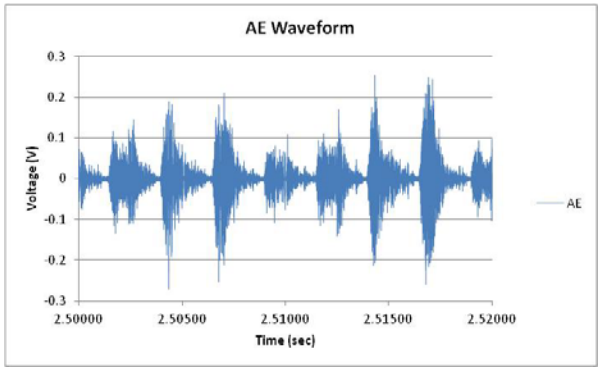

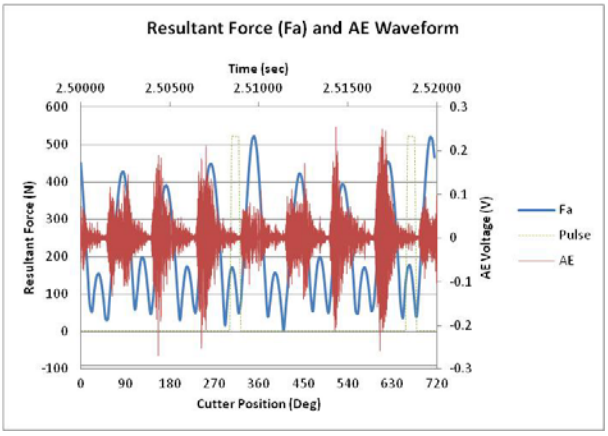

Meas. Instrum.:	Mahr Data Acquisition Board
Drive Unit:	GD 25
Pick-up:	MFW-250 [8.2 %]

Lt:	5.60 mm [N=5]
Ls:	2.5 µm
VB:	±250 µm
Vt:	0.50 mm/s
Points:	22400 [2]

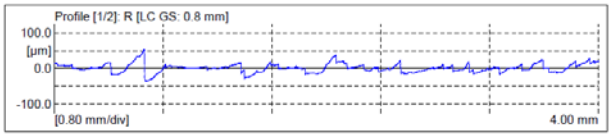

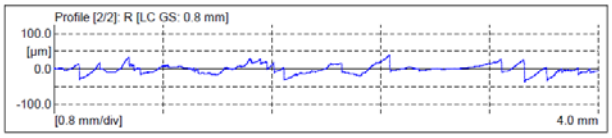

	Ra µm	Rq µm	Rz µm	Rmax µm	Rt µm	Rp µm	Rv µm	R Sm µm	R S µm	R Sk	R Ku
1:	8.734	12.016	55.681	90.47	90.47	32.75	22.93	295.05	207.35	0.56	4.64
2:	9.492	12.368	55.248	64.26	77.11	30.39	24.86	315.86	234.84	0.06	3.15
Xb:	9.113	12.192	55.465	77.37	83.79	31.57	23.89	305.45	221.10	0.31	3.89
S:	0.536	0.248	0.306	18.53	9.45	1.67	1.36	14.72	19.44	0.35	1.05
Max:	9.492	12.368	55.681	90.47	90.47	32.75	24.86	315.86	234.84	0.56	4.64
Min:	8.734	12.016	55.248	64.26	77.11	30.39	22.93	295.05	207.35	0.06	3.15
R:	0.758	0.351	0.433	26.21	13.36	2.36	1.93	20.82	27.49	0.50	1.49

Longitudinal Surface Finish

Meas. Instrum.:	Mahr Data Acquisition Board
Drive Unit:	GD 25
Pick-up:	MFW-250 [8.2 %]

Lt:	1.75 mm [N=5]
Ls:	2.5 µm
VB:	±250 µm
Vt:	0.10 mm/s
Points:	7000 [2]

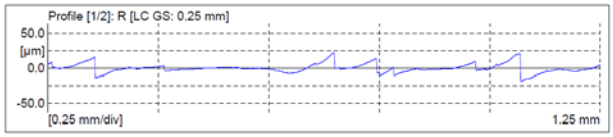

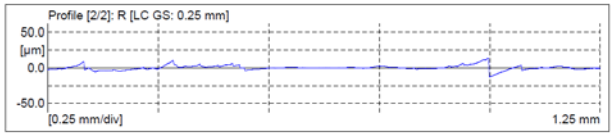

	Ra µm	Rq µm	Rz µm	Rmax µm	Rt µm	Rp µm	Rv µm	R Sm µm	R S µm	R Sk	R Ku
1:	4.174	6.099	25.111	39.43	40.92	14.32	10.79	247.88	137.63	0.63	4.92
2:	2.159	3.230	15.035	26.88	26.88	7.72	7.31	218.50	154.78	0.33	6.63
Xb:	3.167	4.665	20.073	33.16	33.90	11.02	9.05	233.19	146.20	0.48	5.78
S:	1.425	2.029	7.125	8.87	9.92	4.66	2.46	20.77	12.13	0.21	1.21
Max:	4.174	6.099	25.111	39.43	40.92	14.32	10.79	247.88	154.78	0.63	6.63
Min:	2.159	3.230	15.035	26.88	26.88	7.72	7.31	218.50	137.63	0.33	4.92
R:	2.015	2.869	10.076	12.55	14.03	6.59	3.48	29.38	17.15	0.30	1.72

Transverse Surface Finish

Phase 2 Tests: Sample S1 Results (cont.)

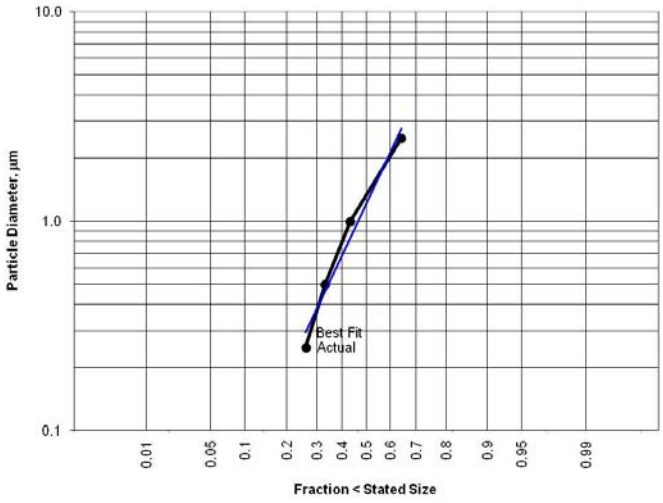

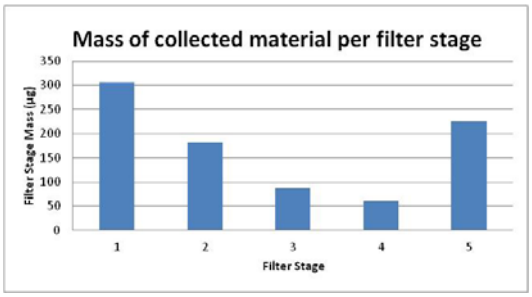

	Data from Best Log-Normal Fit			Data from Plot		
Median diameter, d50	1.21	µm	Median diameter, d50	1.33	µm	
σ_g	9.20					
r^2	0.974					

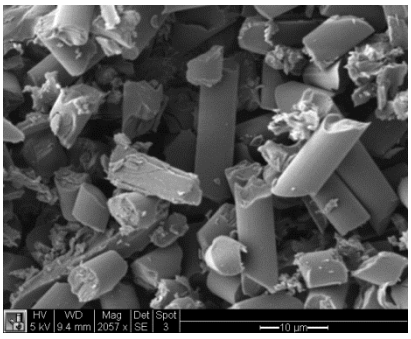

Stage 1(A)

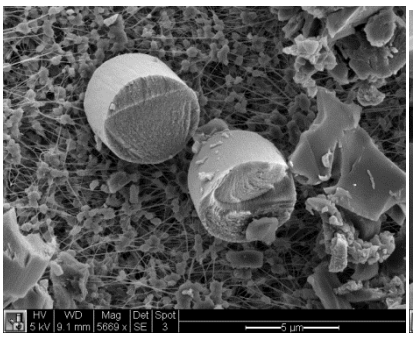

Stage 2(B)

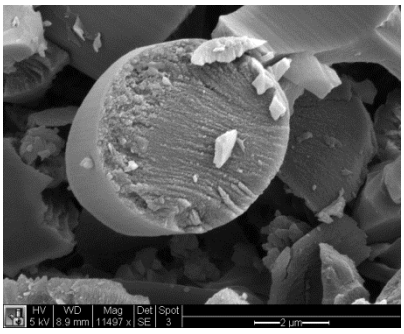

Stage 3(C)

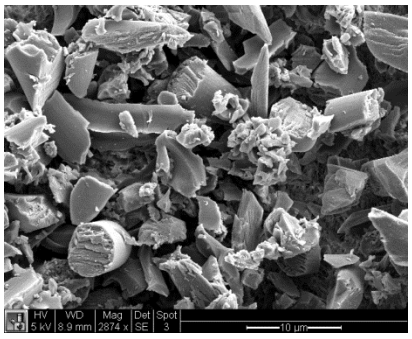

Stage 3 (C)

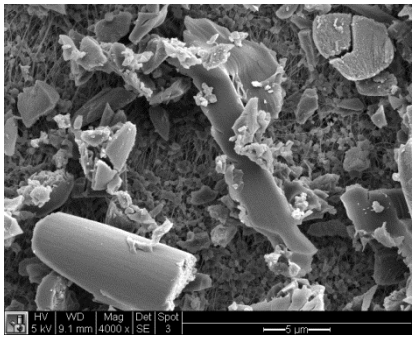

Stage 4 (D)

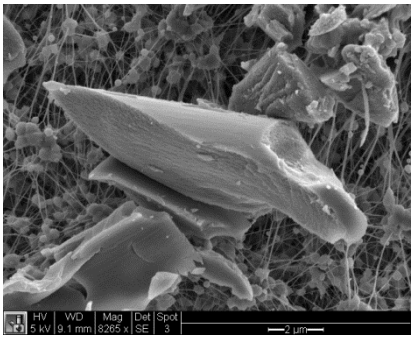

Stage 4 (D)

APPENDIX A

Phase 2 Tests: Sample S2 Results

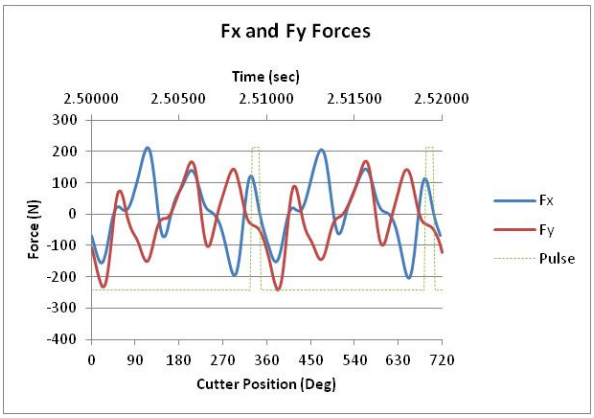

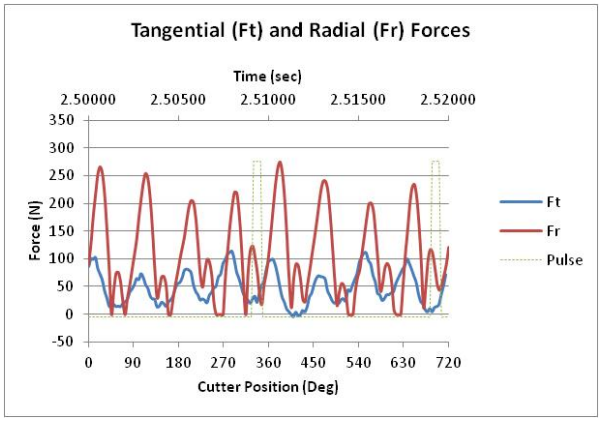

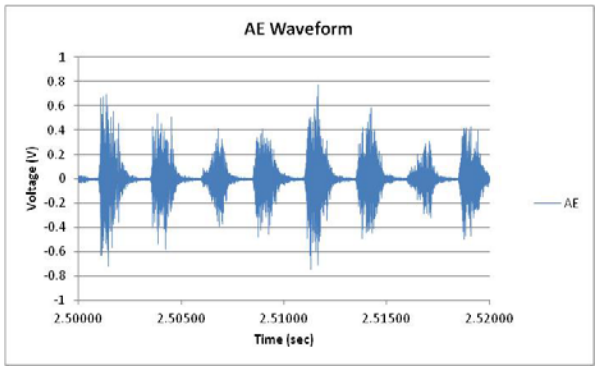

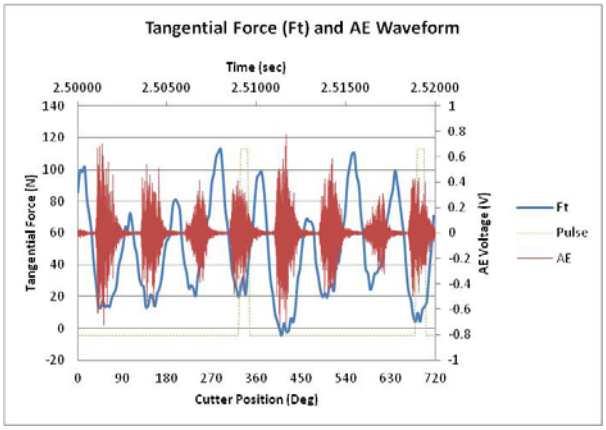

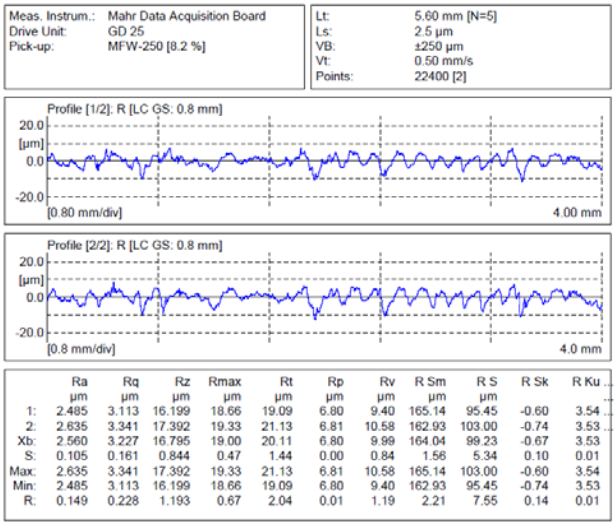

	Ra µm	Rq µm	Rz µm	Rmax µm	Rt µm	Rp µm	Rv µm	R Sm µm	R S µm	R Sk	R Ku
1:	2.485	3.113	16.199	18.66	19.09	6.80	9.40	165.14	95.45	-0.60	3.54
2:	2.635	3.341	17.392	19.33	21.13	6.81	10.58	162.93	103.00	-0.74	3.53
Xb:	2.560	3.227	16.795	19.00	20.11	6.80	9.99	164.04	99.23	-0.67	3.53
S:	0.105	0.161	0.844	0.47	1.44	0.00	0.84	1.56	5.34	0.10	0.01
Max:	2.635	3.341	17.392	19.33	21.13	6.81	10.58	165.14	103.00	-0.60	3.54
Min:	2.485	3.113	16.199	18.66	19.09	6.80	9.40	162.93	95.45	-0.74	3.53
R:	0.149	0.228	1.193	0.67	2.04	0.01	1.19	2.21	7.55	0.14	0.01

Longitudinal Surface Finish

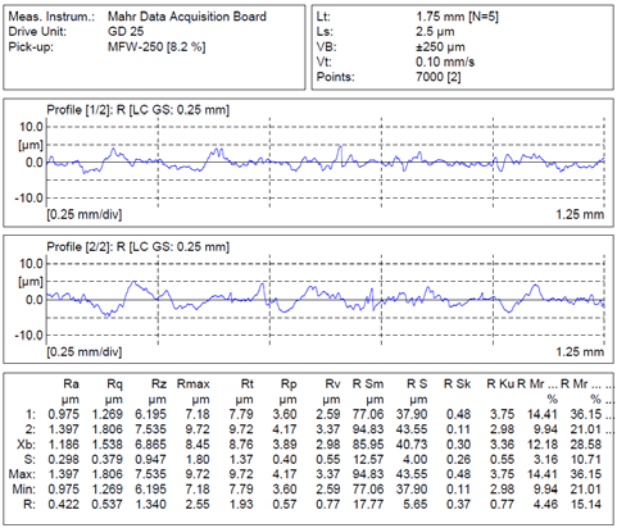

	Ra µm	Rq µm	Rz µm	Rmax µm	Rt µm	Rp µm	Rv µm	R Sm µm	R S µm	R Sk	R Ku	R Mr ... %	R Mr ... %
1:	0.975	1.269	6.195	7.18	7.79	3.60	2.59	77.06	37.90	0.48	3.75	14.41	36.15
2:	1.397	1.806	7.535	9.72	9.72	4.17	3.37	94.83	43.55	0.11	2.98	9.94	21.01
Xb:	1.186	1.538	6.865	8.45	8.76	3.89	2.98	85.95	40.73	0.30	3.36	12.18	28.58
S:	0.298	0.379	0.947	1.80	1.37	0.40	0.55	12.57	4.00	0.26	0.55	3.16	10.71
Max:	1.397	1.806	7.535	9.72	9.72	4.17	3.37	94.83	43.55	0.48	3.75	14.41	36.15
Min:	0.975	1.269	6.195	7.18	7.79	3.60	2.59	77.06	37.90	0.11	2.98	9.94	21.01
R:	0.422	0.537	1.340	2.55	1.93	0.57	0.77	17.77	5.65	0.37	0.77	4.46	15.14

Transverse Surface Finish

Phase 2 Tests: Sample S2 Results (cont.)

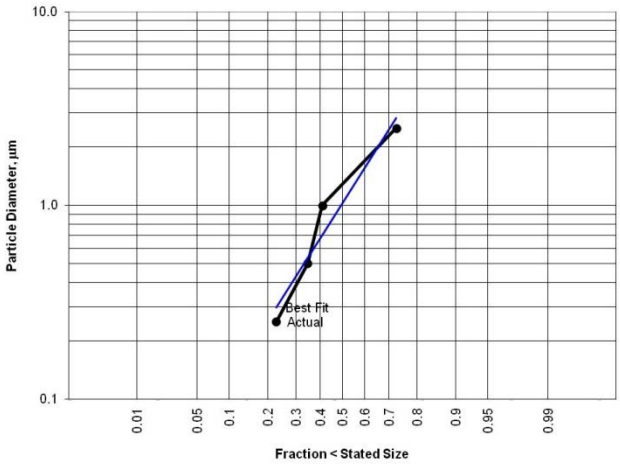

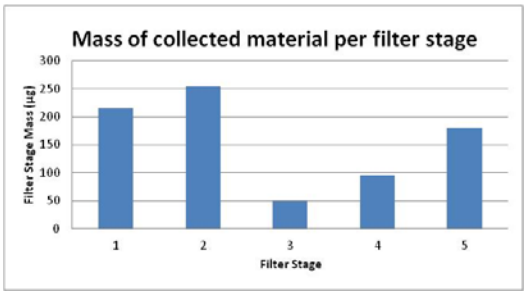

	Data from Best Log-Normal Fit			Data from Plot		
Median diameter, d50	1.02	µm	Median diameter, d50	1.28	µm	
σ_g	5.25					
r^2	0.940					

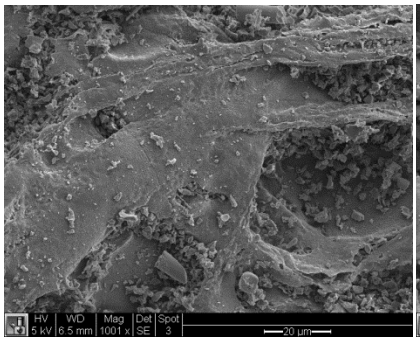

Stage 2 (B)

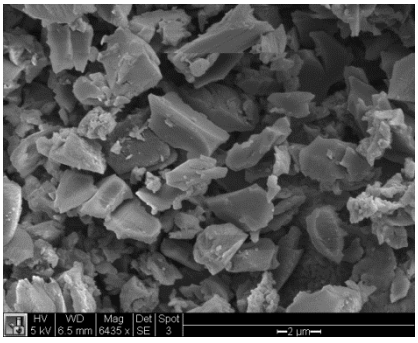

Stage 2 (B)

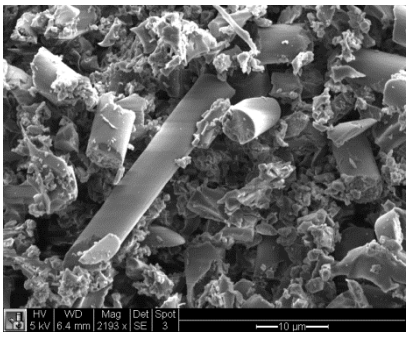

Stage 5 (backup)

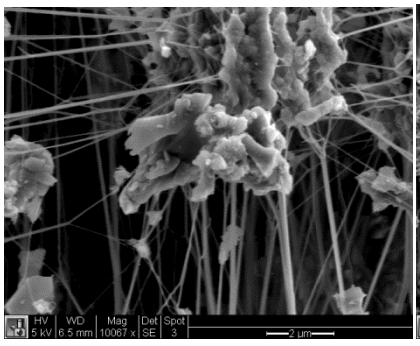

Stage 5 (backup)

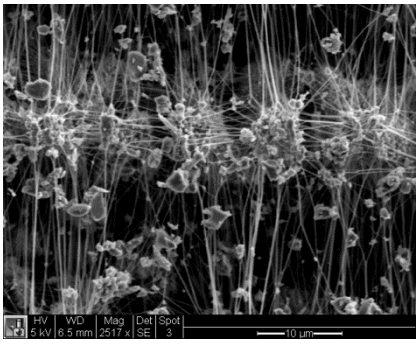

Stage 5 (backup)

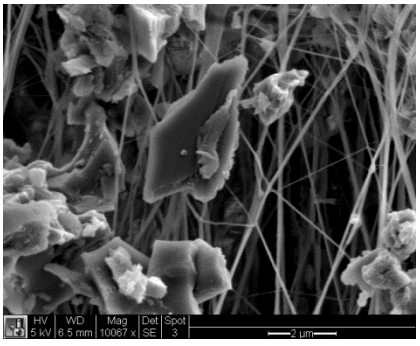

Stage 5 (backup)

APPENDIX A

Phase 2 Tests: Sample S3 Results

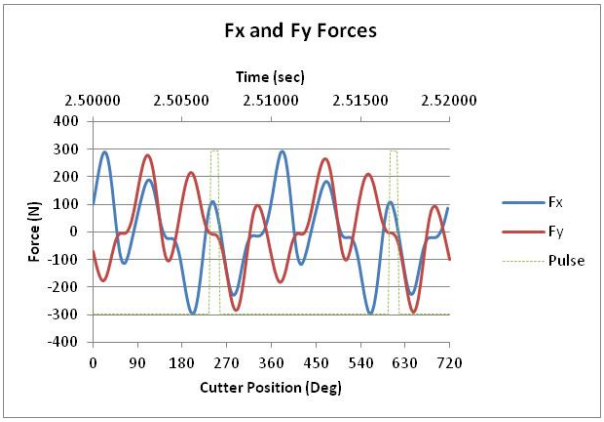

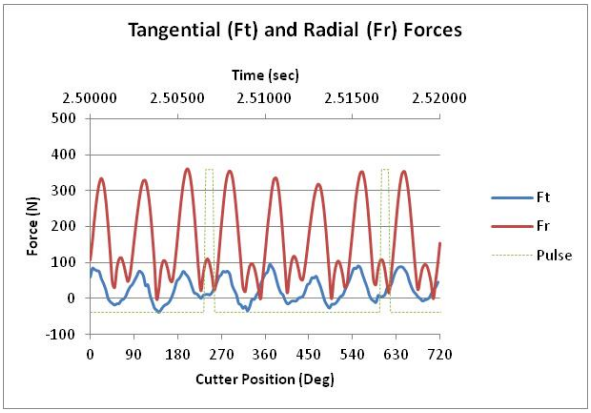

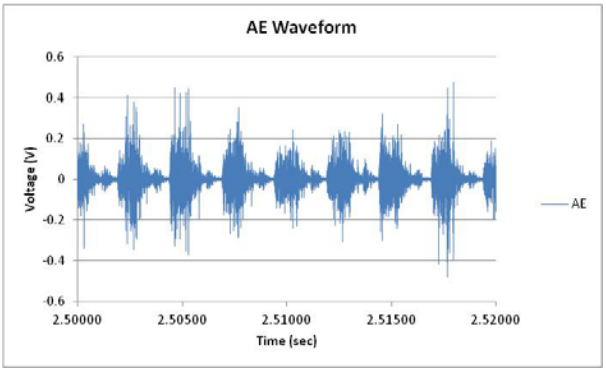

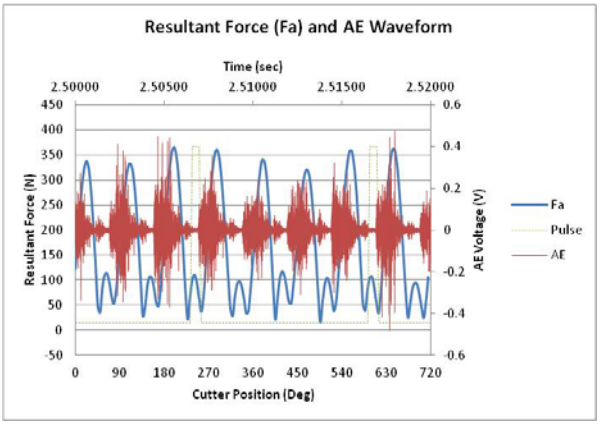

Meas. Instrum.:	Mahr Data Acquisition Board
Drive Unit:	GD 25
Pick-up:	MFW-250 [7.5 %]

Lt:	5.60 mm [N=5]
Ls:	2.5 µm
VB:	±250 µm
Vt:	0.50 mm/s
Points:	33600 [3]

	Ra µm	Rz µm	Rt µm	Rp µm
1:	8.846	50.646	77.33	22.27
2:	9.637	59.935	104.28	32.80
3:	9.869	61.491	106.69	34.53
Xb:	9.451	57.357	96.10	29.87
S:	0.536	5.864	16.30	6.64
Max:	9.869	61.491	106.69	34.53
Min:	8.846	50.646	77.33	22.27
R:	1.023	10.845	29.36	12.26

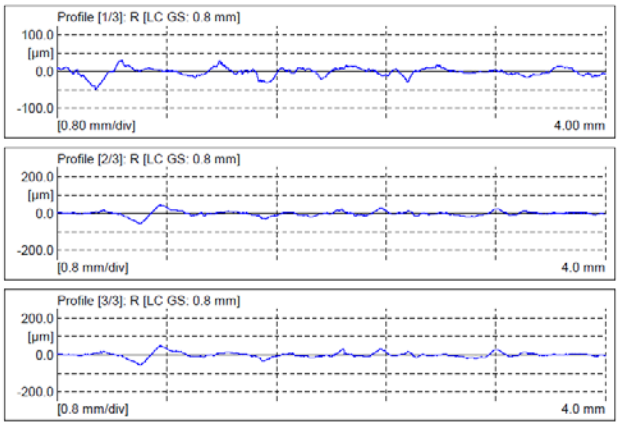

Meas. Instrum.:	Mahr Data Acquisition Board
Drive Unit:	GD 25
Pick-up:	MFW-250 [7.5 %]

Lt:	1.75 mm [N=5]
Ls:	2.5 µm
VB:	±250 µm
Vt:	0.10 mm/s
Points:	10500 [3]

	Ra µm	Rz µm	Rt µm	Rp µm
1:	2.983	14.612	21.86	6.12
2:	5.086	28.427	51.12	16.08
3:	3.826	20.090	27.93	10.99
Xb:	3.965	21.043	33.64	11.06
S:	1.059	6.957	15.44	4.98
Max:	5.086	28.427	51.12	16.08
Min:	2.983	14.612	21.86	6.12
R:	2.104	13.815	29.26	9.96

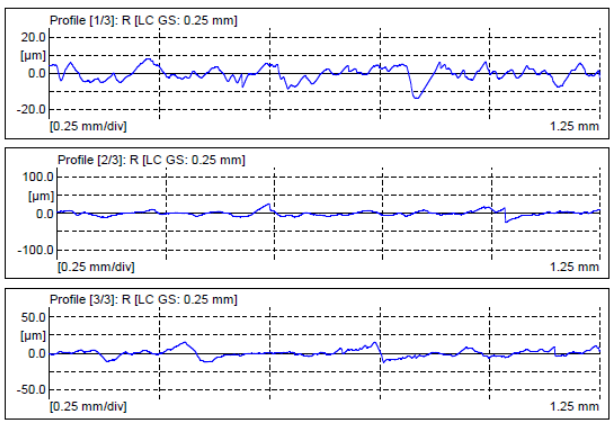

Longitudinal Surface Finish

Transverse Surface Finish

Phase 2 Tests: Sample S3 Results (cont.)

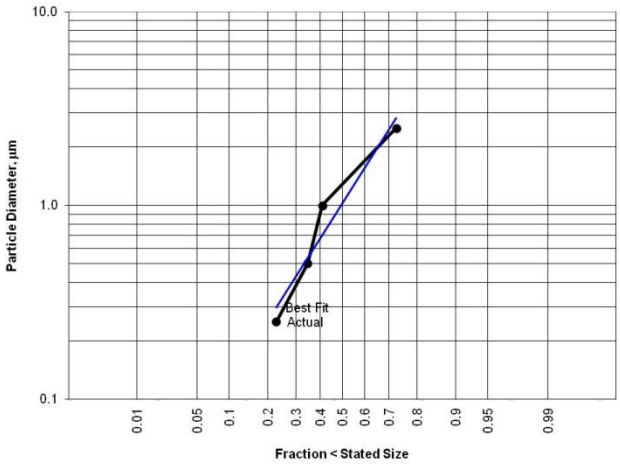

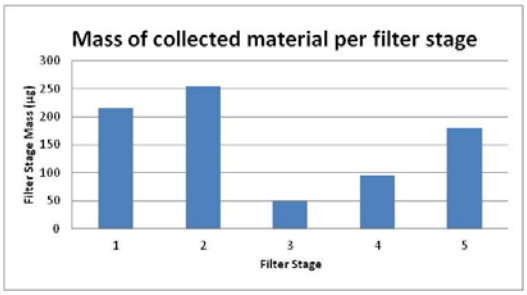

	Data from Best Log-Normal Fit			Data from Plot		
Median diameter, d50	1.02	µm	Median diameter, d50	1.28	µm	
σ_g	5.25					
r^2	0.940					

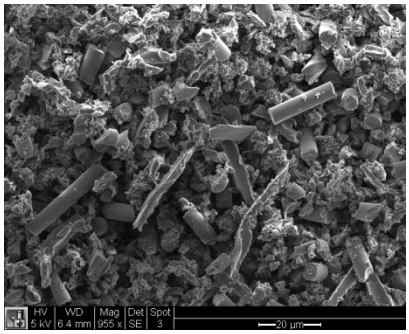

Stage 2 (B)

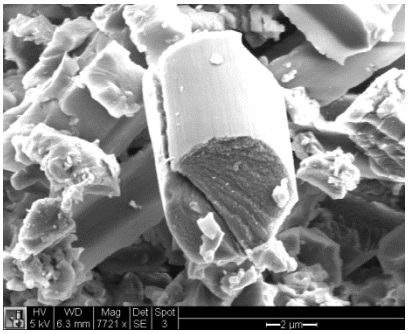

Stage 2 (B)

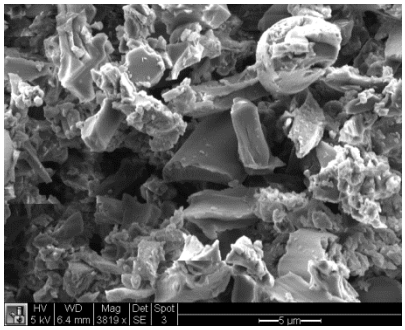

Stage 2 (B)

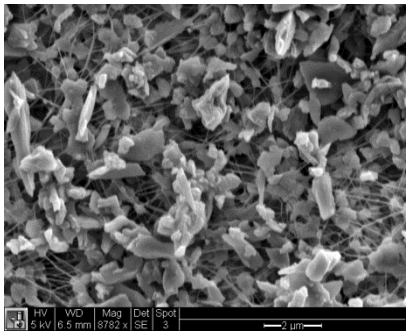

Stage 4 (D)

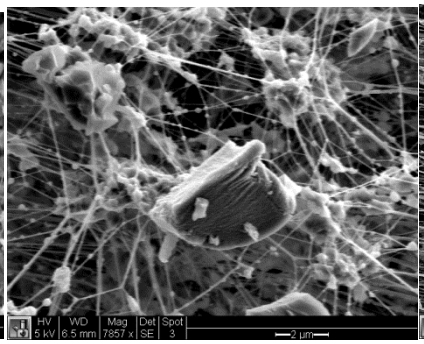

Stage 5 (backup)

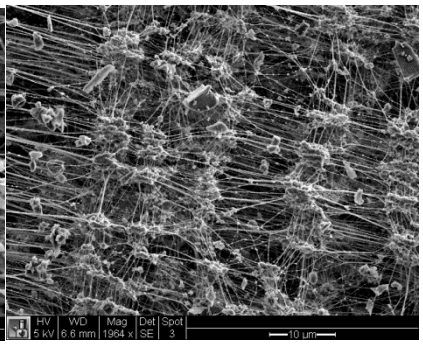

Stage 5 (backup)

APPENDIX A

Phase 2 Tests: Sample S4 Results

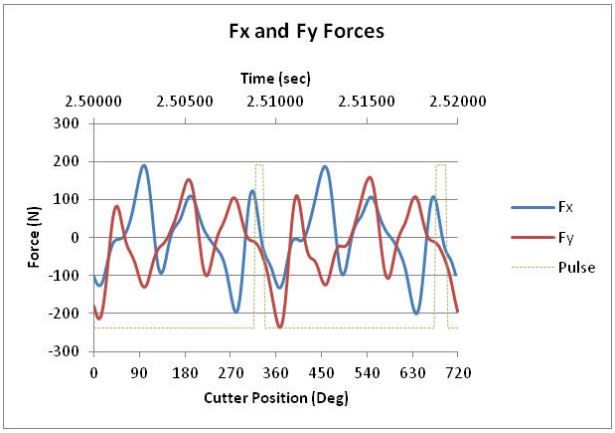

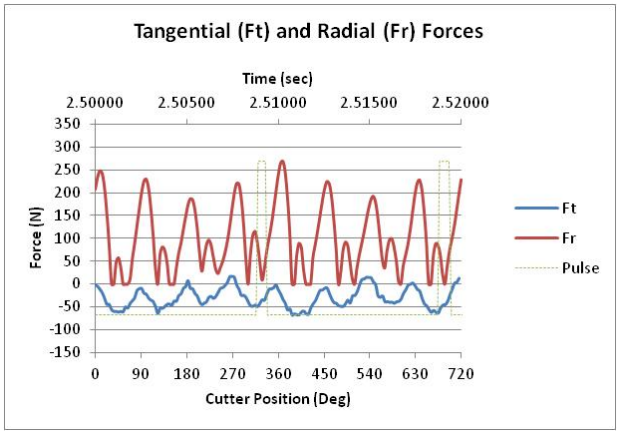

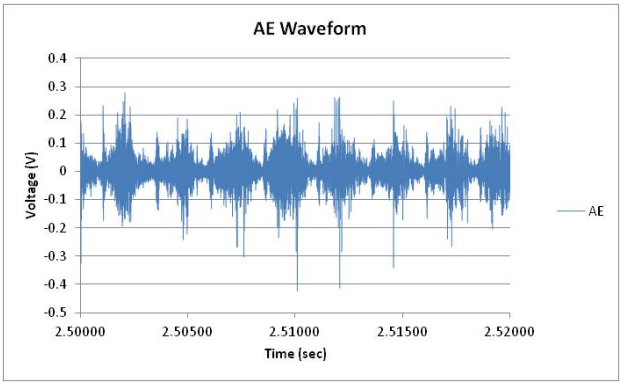

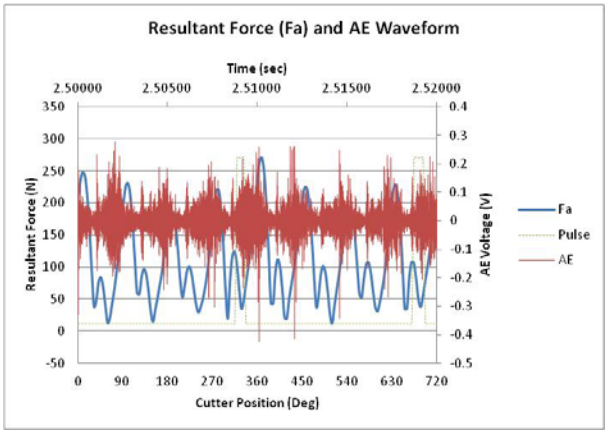

Meas. Instrum.:	Mahr Data Acquisition Board
Drive Unit:	GD 25
Pick-up:	MFW-250 [7.4 %]

Lt:	5.60 mm [N=5]
Ls:	2.5 µm
VB:	±250 µm
Vt:	0.50 mm/s
Points:	33600 [3]

	Ra µm	Rz µm	Rt µm	Rp µm
1:	8.481	50.273	68.95	23.24
2:	11.588	62.763	93.52	25.15
3:	19.077	106.325	129.70	56.63
Xb:	13.049	73.120	97.39	35.01
S:	5.447	29.426	30.56	18.75
Max:	19.077	106.325	129.70	56.63
Min:	8.481	50.273	68.95	23.24
R:	10.597	56.052	60.74	33.39

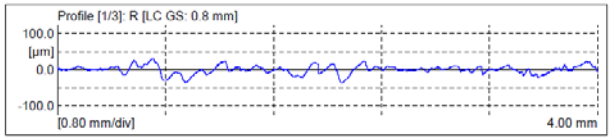

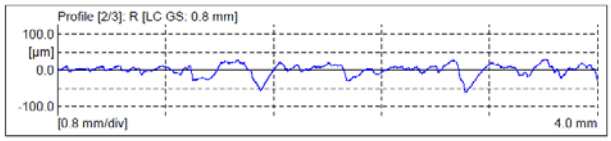

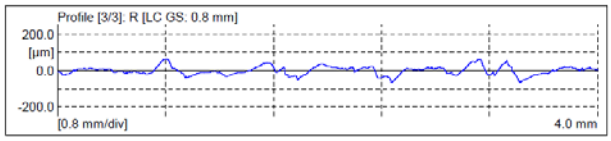

Meas. Instrum.:	Mahr Data Acquisition Board
Drive Unit:	GD 25
Pick-up:	MFW-250 [7.4 %]

Lt:	1.75 mm [N=5]
Ls:	2.5 µm
VB:	±250 µm
Vt:	0.10 mm/s
Points:	10500 [3]

	Ra µm	Rz µm	Rt µm	Rp µm
1:	5.578	25.513	42.51	10.98
2:	4.540	23.290	42.24	13.60
3:	7.135	37.572	55.85	18.59
Xb:	5.751	28.791	46.87	14.39
S:	1.306	7.685	7.78	3.86
Max:	7.135	37.572	55.85	18.59
Min:	4.540	23.290	42.24	10.98
R:	2.595	14.282	13.61	7.61

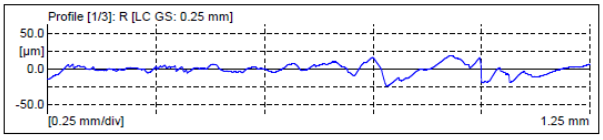

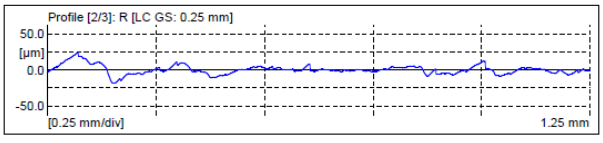

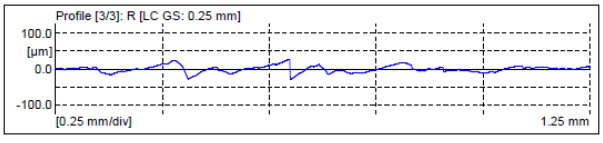

Longitudinal Surface Finish

Transverse Surface Finish

Phase 2 Tests: Sample S4 Results (cont.)

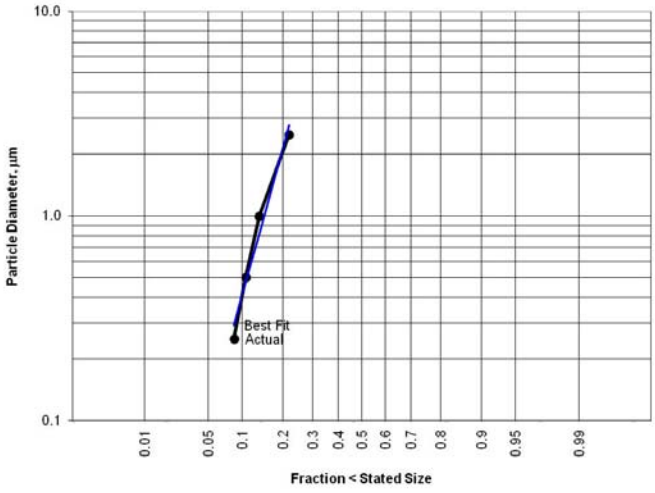

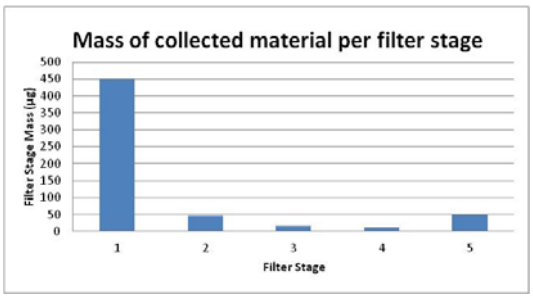

	Data from Best Log-Normal Fit			Data from Plot		
Median diameter, d50	56.16	µm	Median diameter, d50	#DIV/0!	µm	
σ_g	47.12					
r^2	0.973					

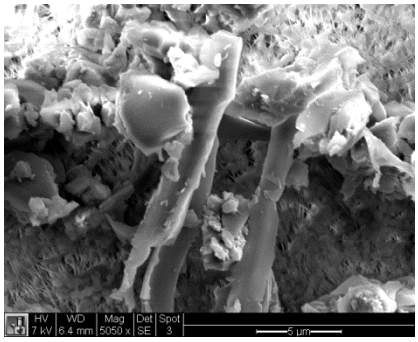

Stage 1(A)

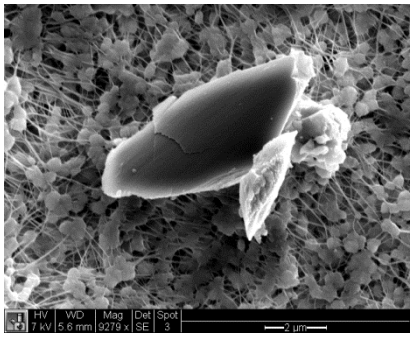

Stage 4 (D)

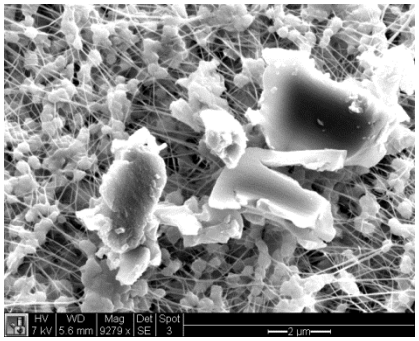

Stage 4 (D)

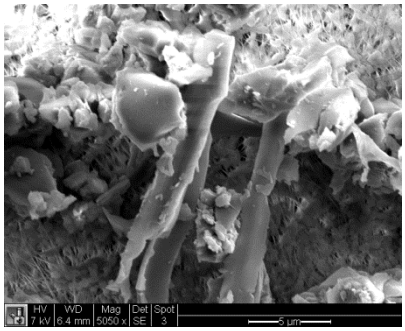

Stage 4 (D)

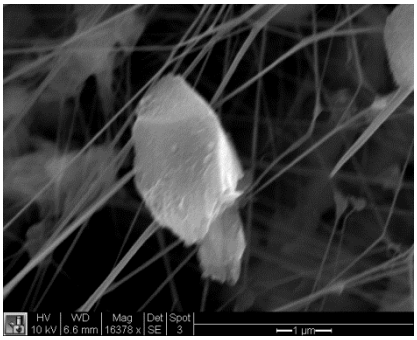

Stage 5 (backup)

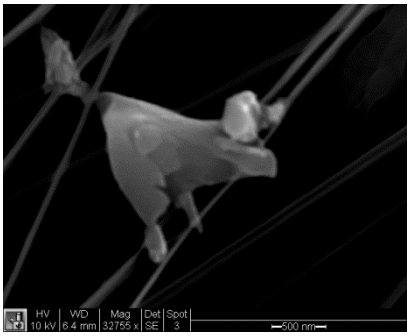

Stage 5 (backup)

APPENDIX A

Phase 2 Tests: Sample A1 Results

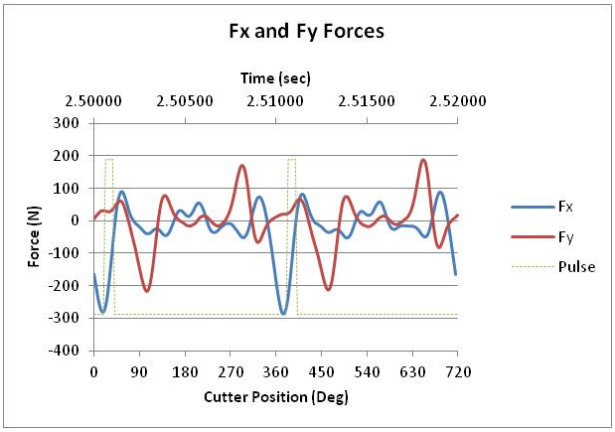

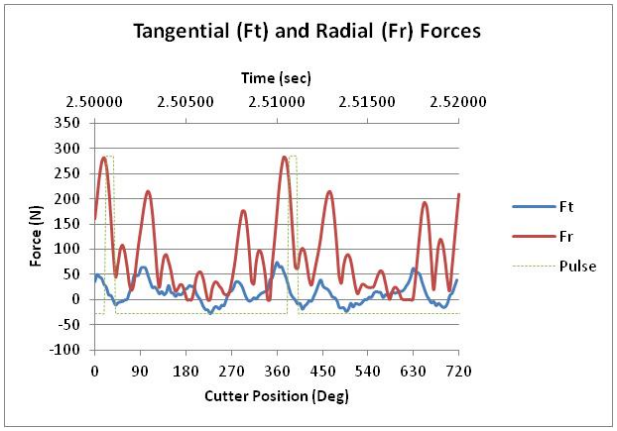

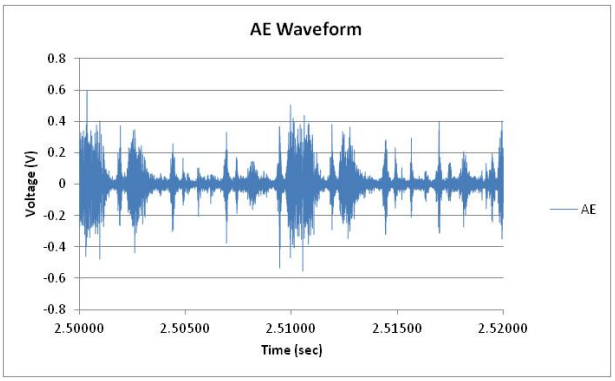

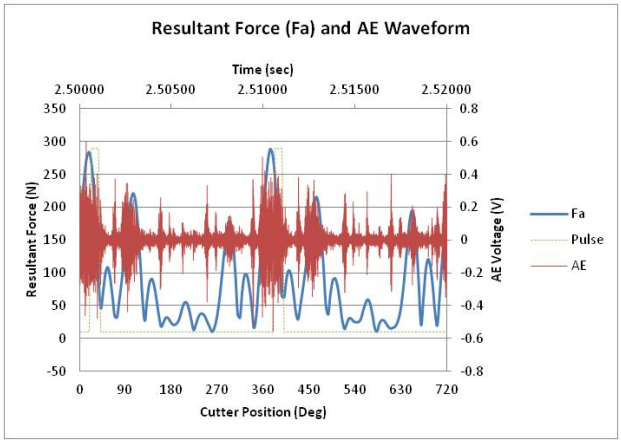

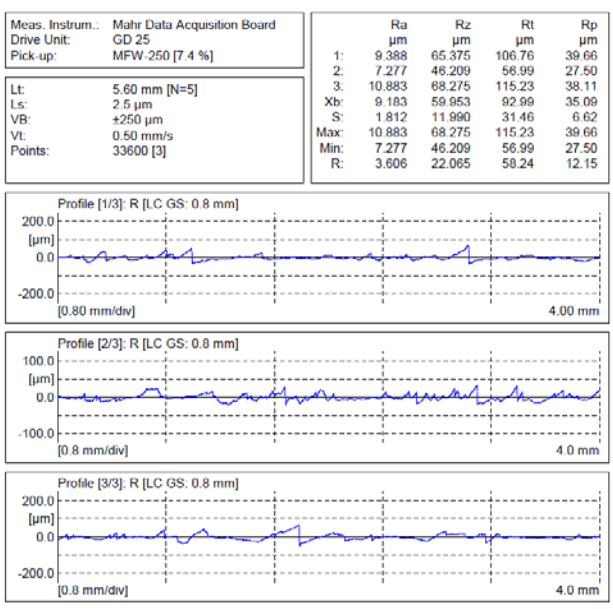

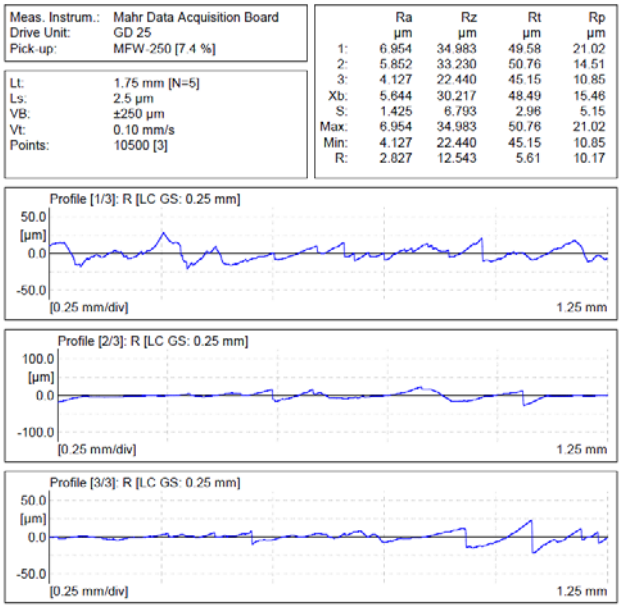

Longitudinal Surface Finish

Transverse Surface Finish

Phase 2 Tests: Sample A1 Results (cont.)

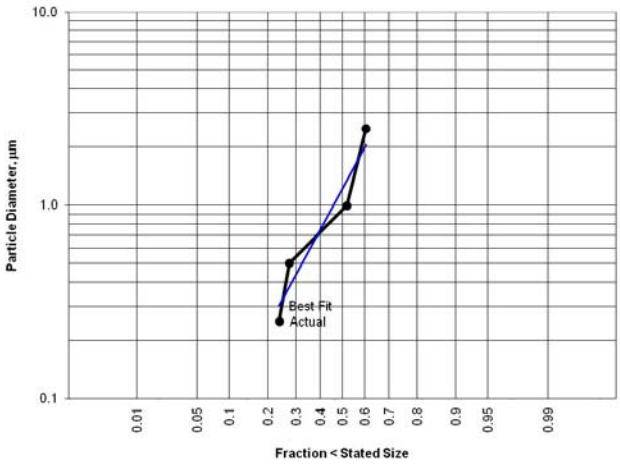

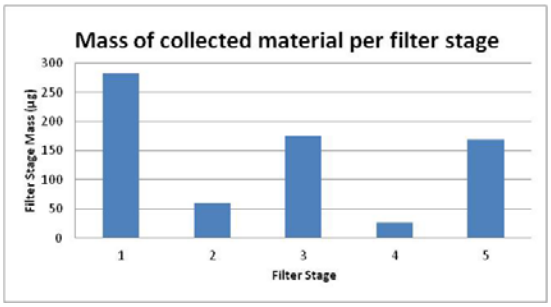

	Data from Best Log-Normal Fit			Data from Plot		
Median diameter, d50	1.22	µm	Median diameter, d50	0.95	µm	
σ_g	7.10					
r^2	0.917					

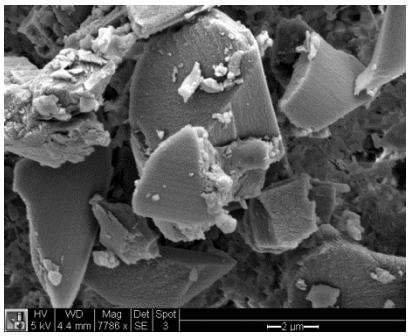

Stage 1 (A)

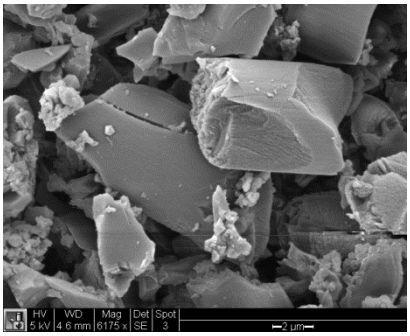

Stage 2 (B)

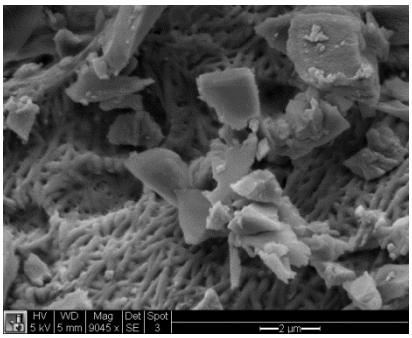

Stage 3 (C)

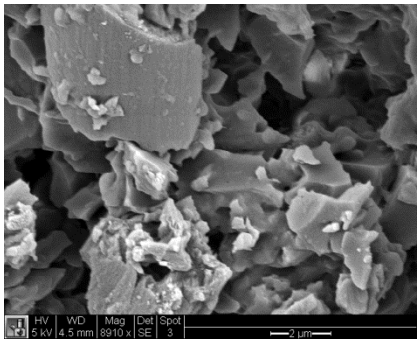

Stage 4 (D)

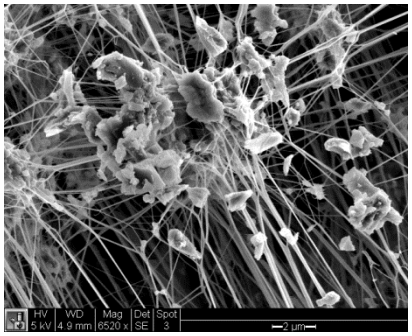

Stage 5 (backup)

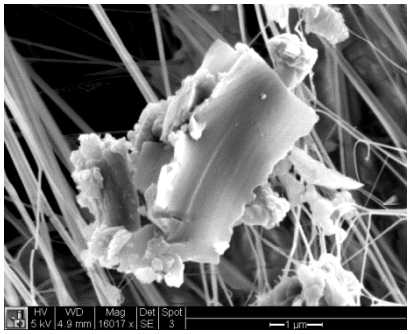

Stage 5 (backup)

APPENDIX A

Phase 2 Tests: Sample A2 Results

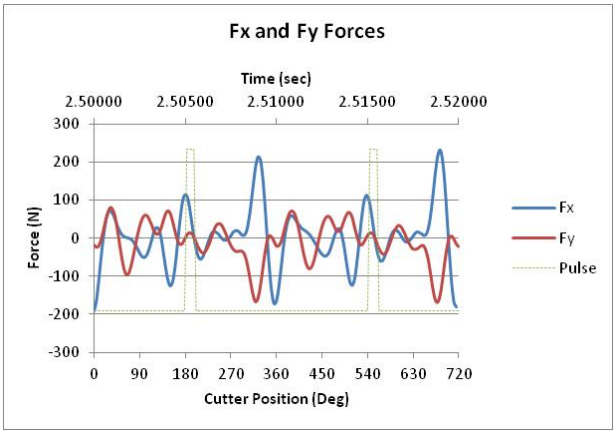

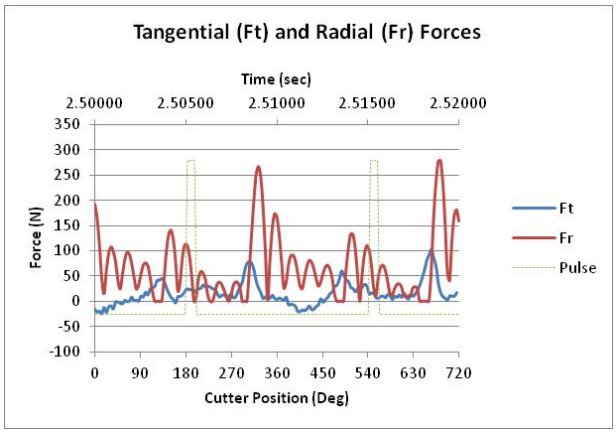

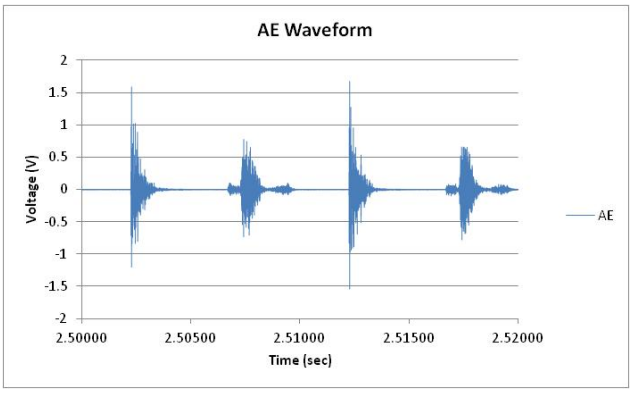

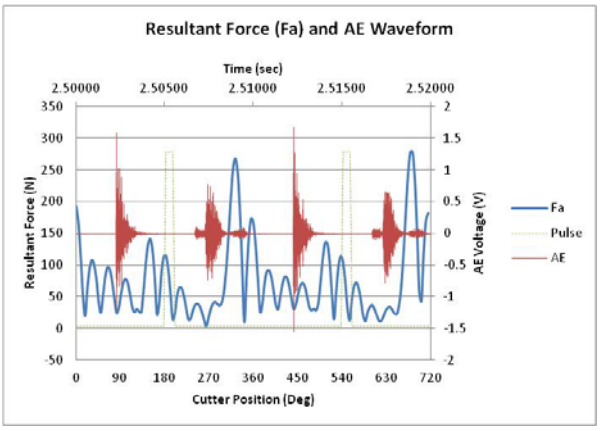

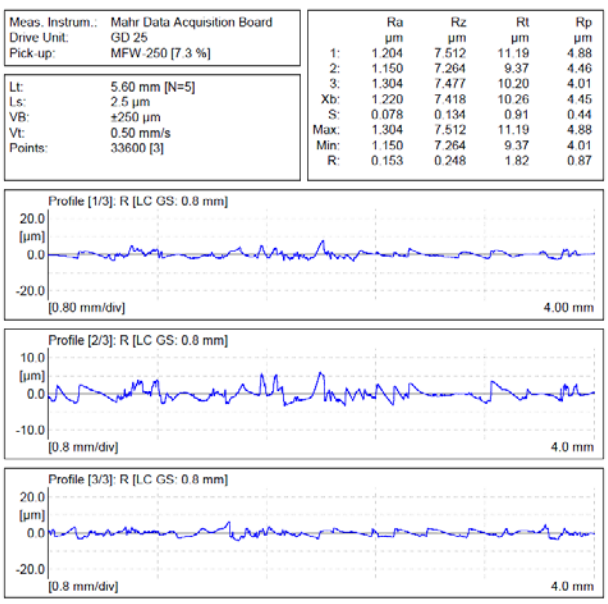

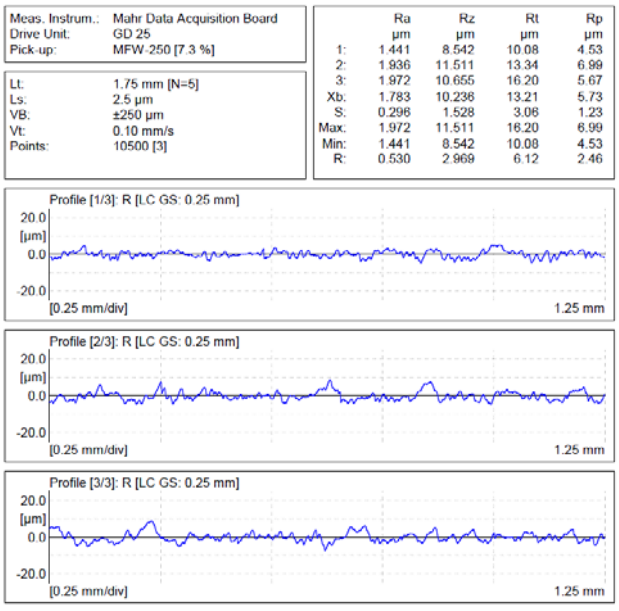

Longitudinal Surface Finish

Transverse Surface Finish

Phase 2 Tests: Sample A2 Results (cont.)

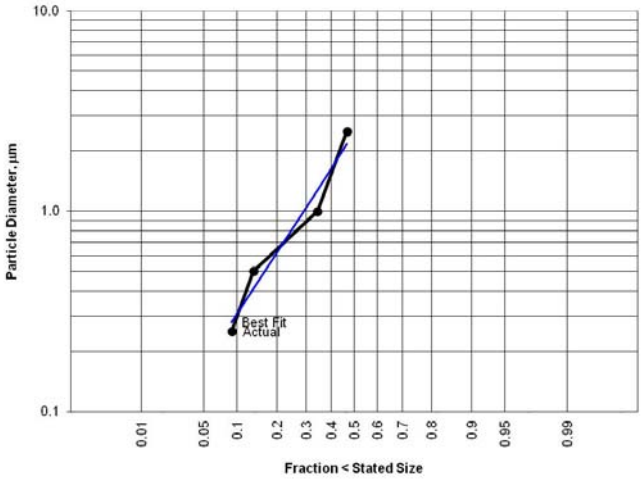

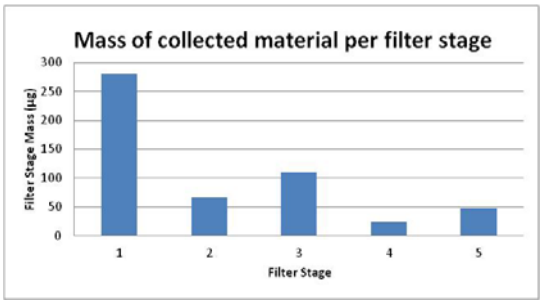

	Data from Best Log-Normal Fit				Data from Plot		
Median diameter, d50	2.46	µm		Median diameter, d50	#DIV/0!	µm	
σ_g	5.12						
r^2	0.954						

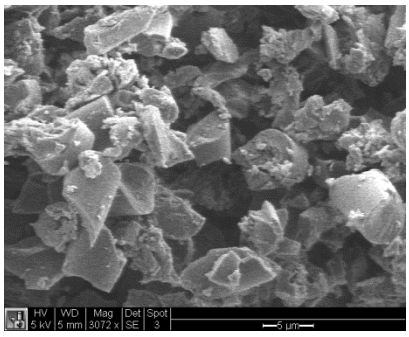

Stage 1 (A)

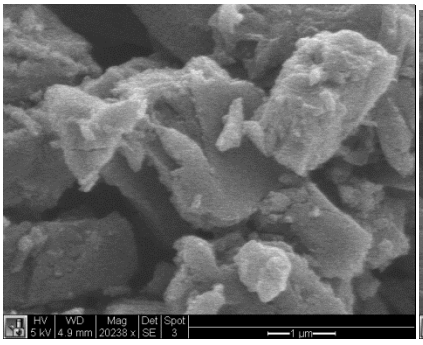

Stage 2 (B)

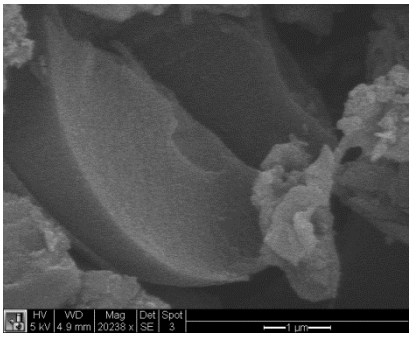

Stage 2 (B)

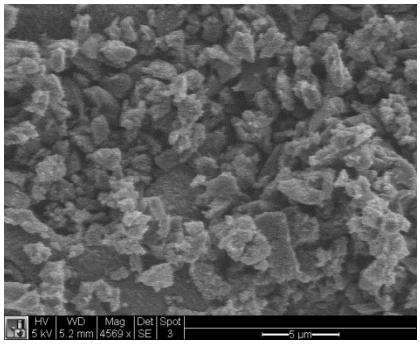

Stage 3 (C)

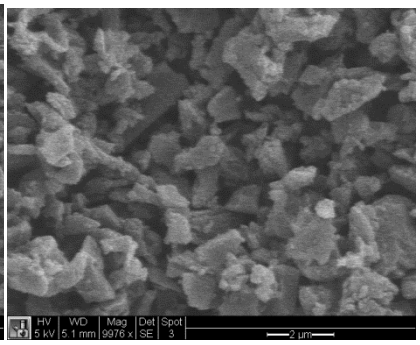

Stage 4 (D)

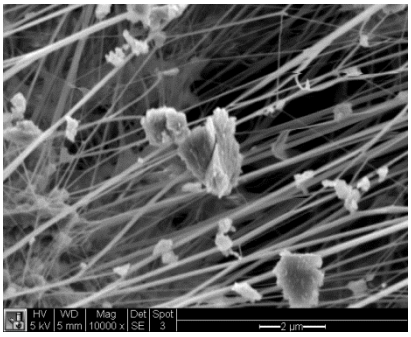

Stage 5 (backup)

APPENDIX A

Phase 2 Tests: Sample A3 Results

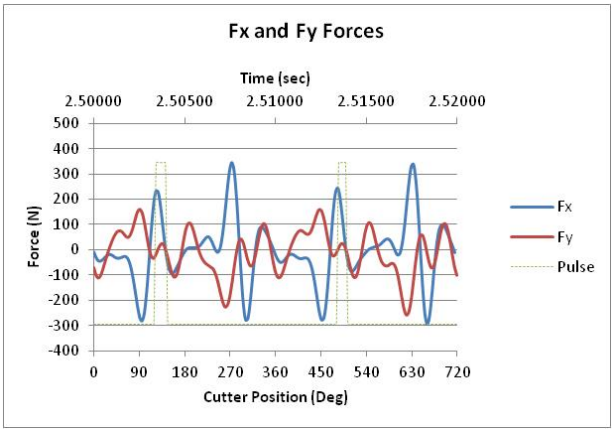

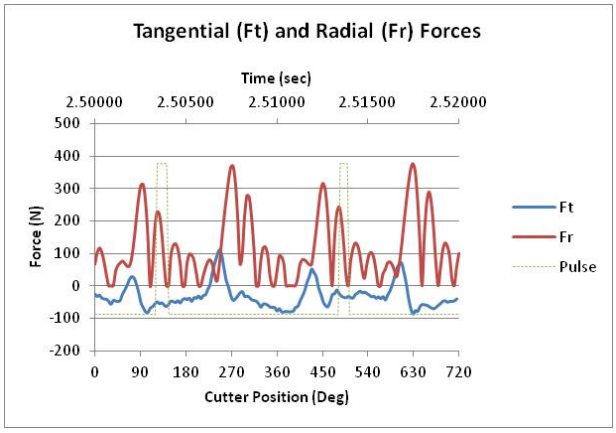

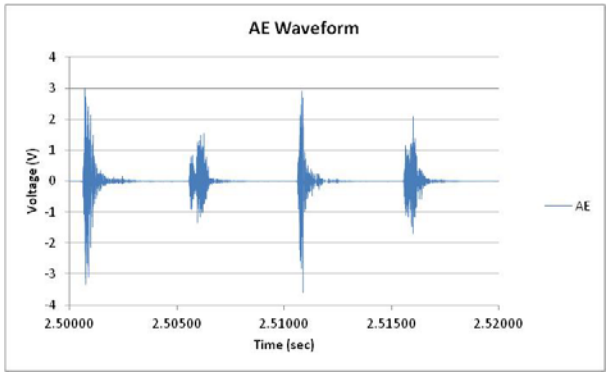

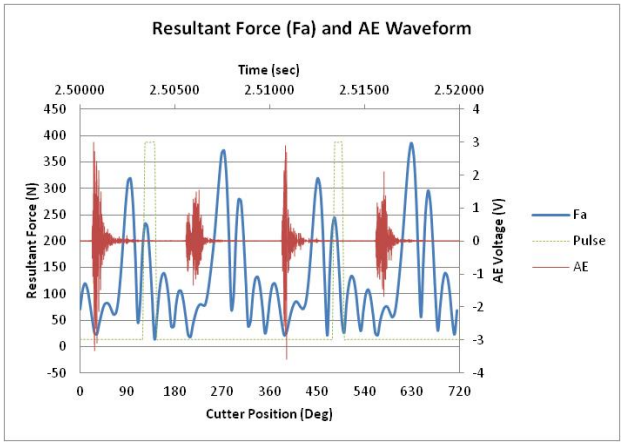

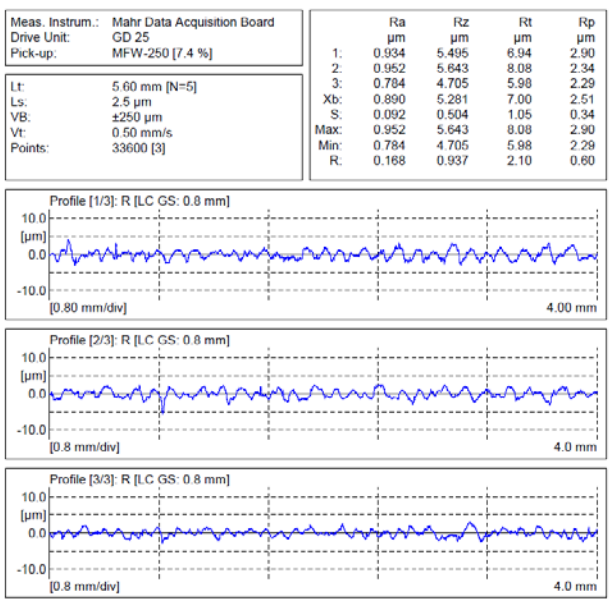

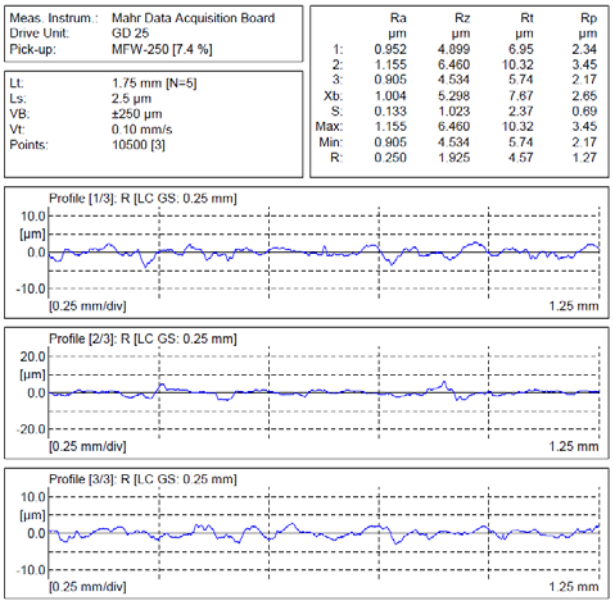

Longitudinal Surface Finish

Transverse Surface Finish

Phase 2 Tests: Sample A3 Results (cont.)

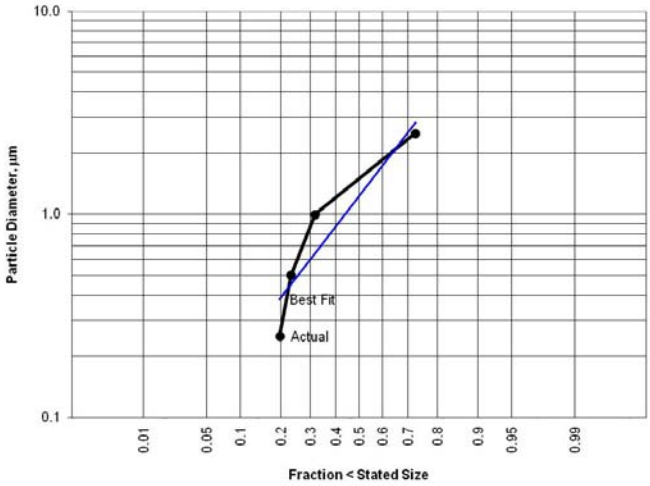

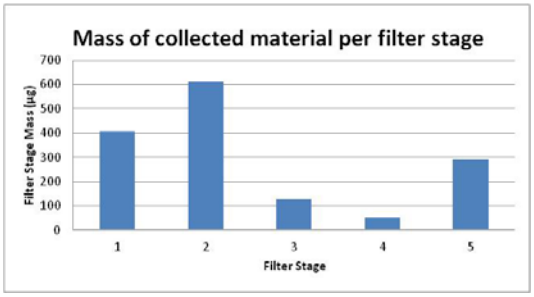

	Data from Best Log-Normal Fit			Data from Plot		
Median diameter, d50	1.23	µm	Median diameter, d50	1.50	µm
σ_g	3.94				
r^2	0.862				

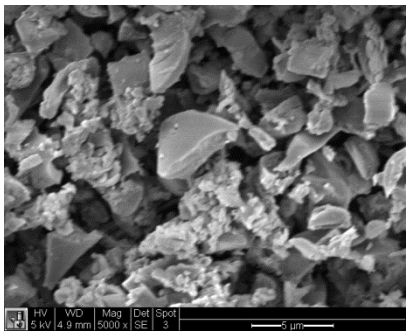

Stage 1 (A)

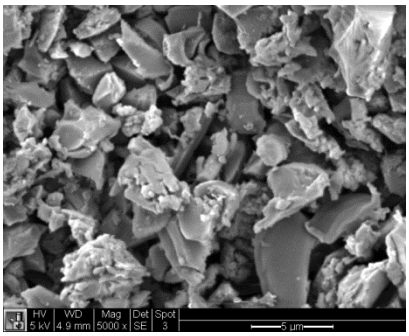

Stage 2 (B)

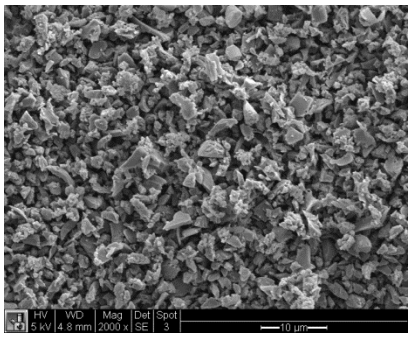

Stage 3 (C)

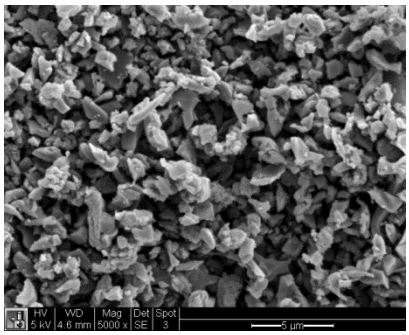

Stage 4 (D)

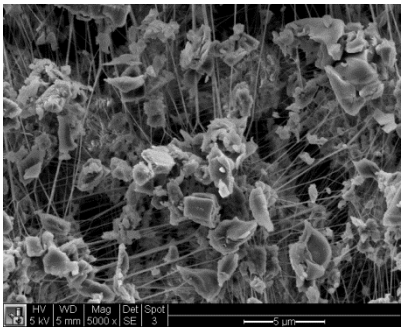

Stage 5 (backup)

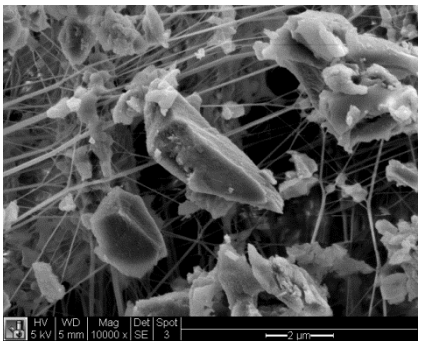

Stage 5 (backup)

APPENDIX A

Phase 2 Tests: Sample A4 Results

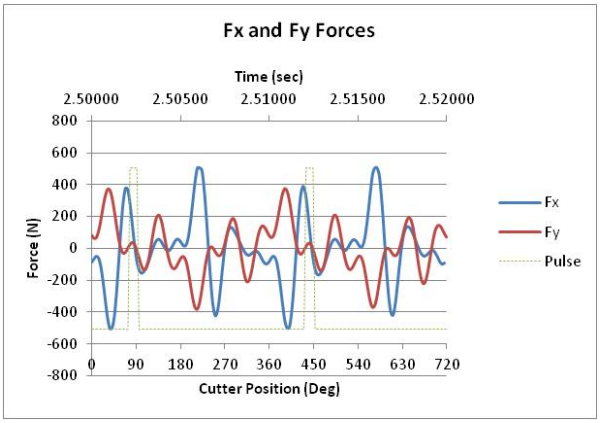

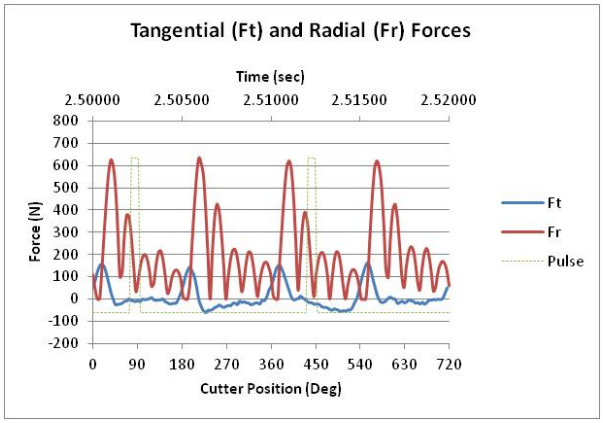

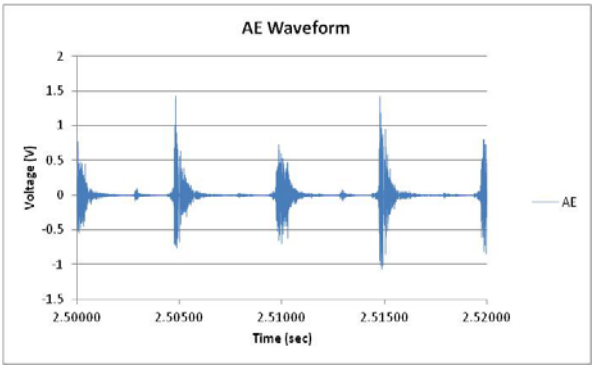

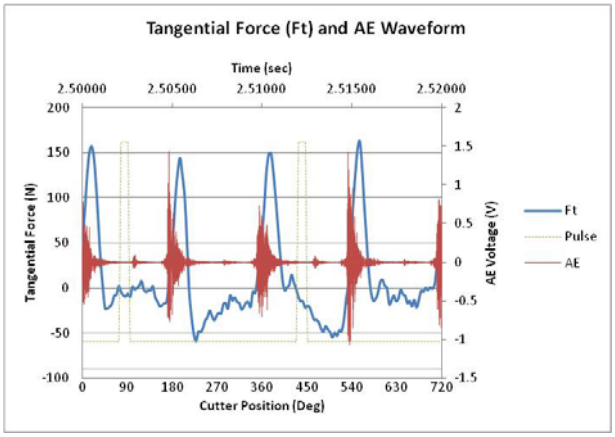

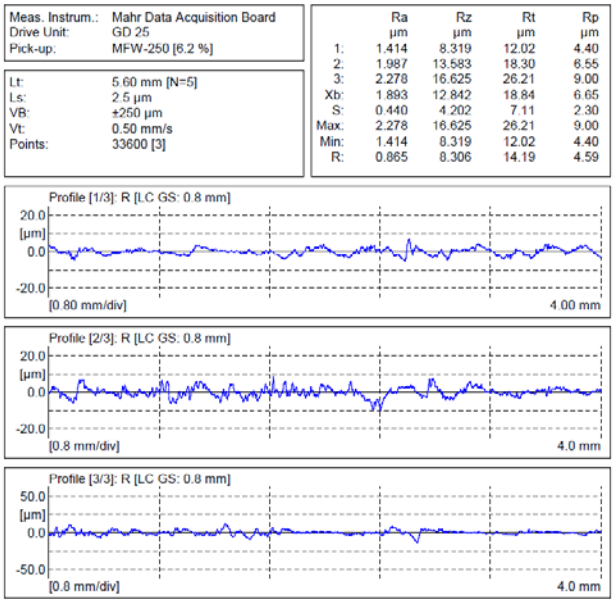

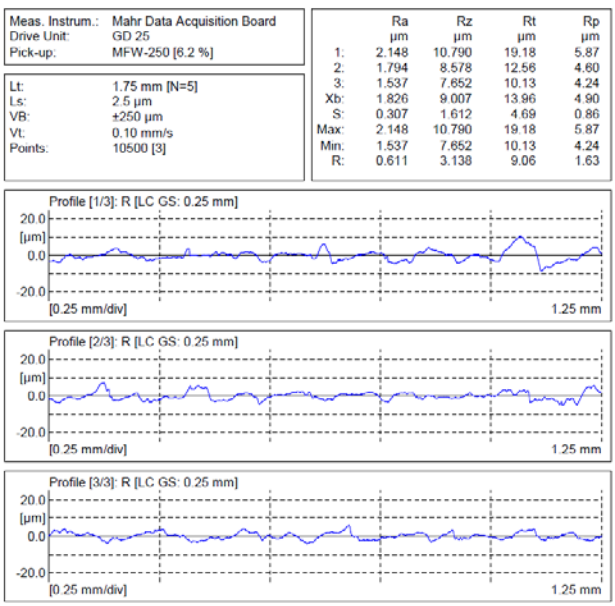

Longitudinal Surface Finish

Transverse Surface Finish

Phase 2 Tests: Sample A4 Results (cont.)

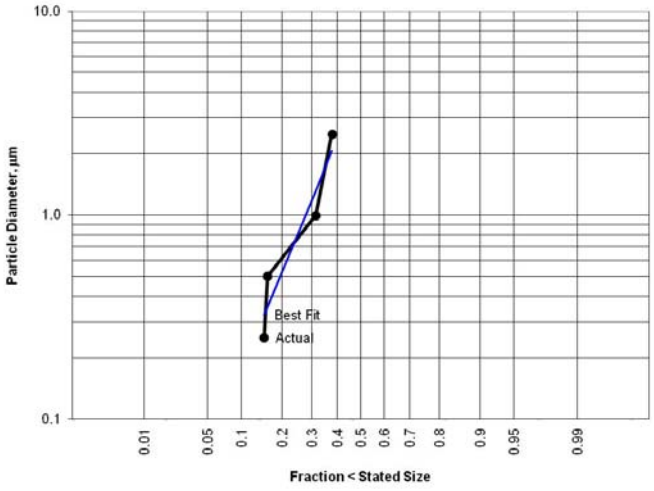

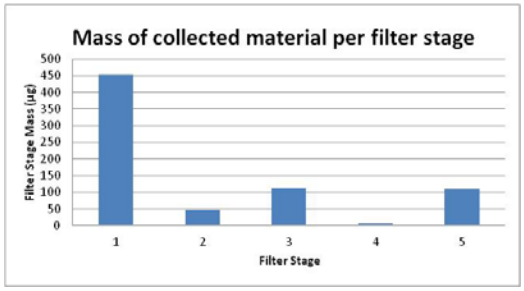

	Data from Best Log-Normal Fit				Data from Plot		
Median diameter, d50	4.53	µm		Median diameter, d50	#DIV/0!	µm	
σ_g	12.78						
r^2	0.898						

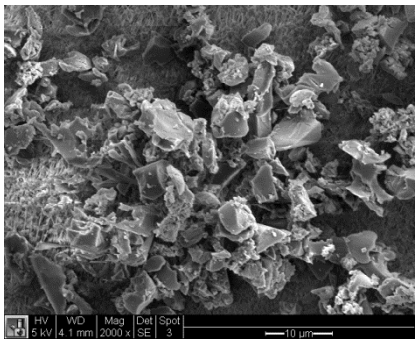

Stage 1 (A)

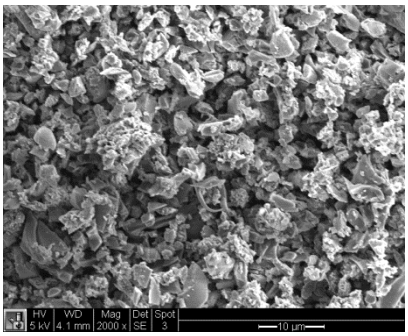

Stage 2 (B)

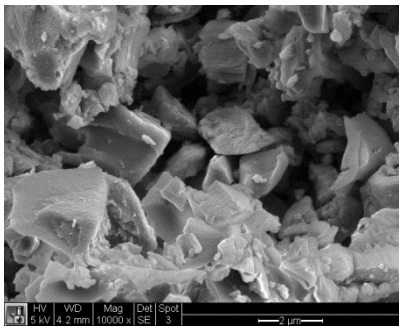

Stage 3 (C)

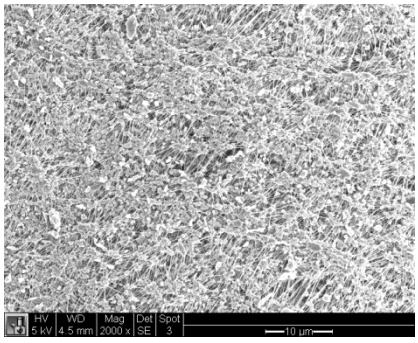

Stage 4 (D)

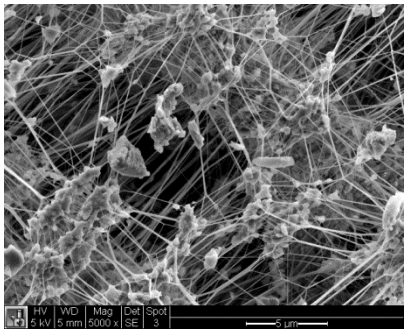

Stage 5 (backup)

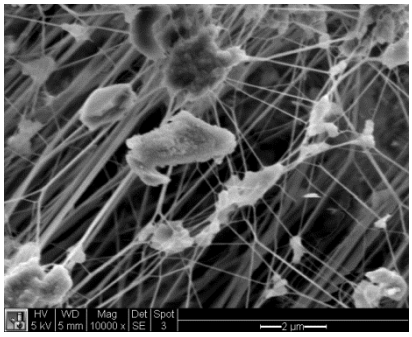

Stage 5 (backup)

APPENDIX A

Phase 2 Tests: Sample B1 Results

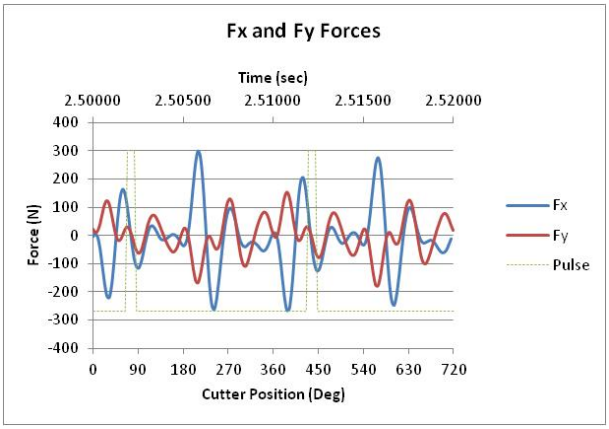

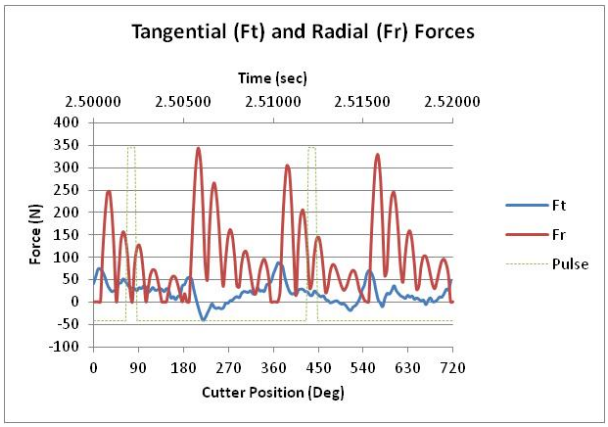

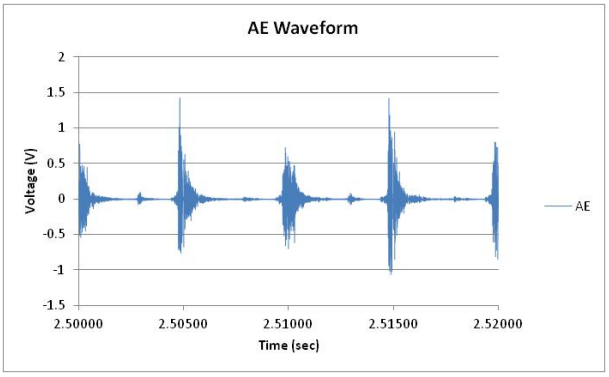

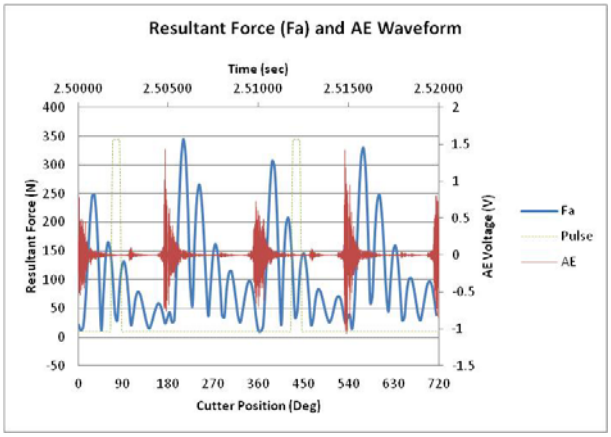

Meas. Instrum.:	Mahr Data Acquisition Board
Drive Unit:	GD 25
Pick-up:	MFW-250 [6.2 %]

Lt:	5.60 mm [N=5]
Ls:	2.5 µm
VB:	±250 µm
Vt:	0.50 mm/s
Points:	33600 [3]

	Ra µm	Rz µm	Rt µm	Rp µm
1:	11.293	62.730	117.70	30.73
2:	12.208	62.638	84.60	24.43
3:	8.068	45.436	66.46	18.55
Xb:	10.523	56.935	89.59	24.57
S:	2.175	9.958	25.98	6.09
Max:	12.208	62.730	117.70	30.73
Min:	8.068	45.436	66.46	18.55
R:	4.140	17.294	51.24	12.18

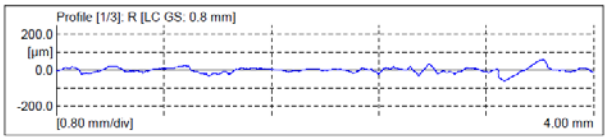

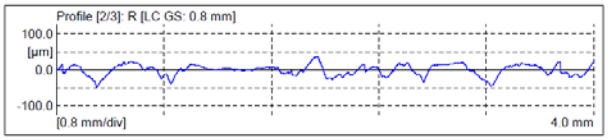

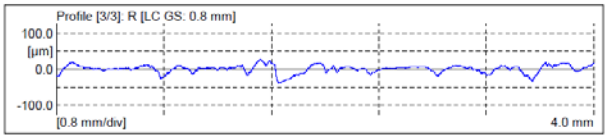

Longitudinal Surface Finish

Meas. Instrum.:	Mahr Data Acquisition Board
Drive Unit:	GD 25
Pick-up:	MFW-250 [6.2 %]

Lt:	1.75 mm [N=5]
Ls:	2.5 µm
VB:	±250 µm
Vt:	0.10 mm/s
Points:	10500 [3]

	Ra µm	Rz µm	Rt µm	Rp µm
1:	7.822	39.487	66.81	18.36
2:	7.956	38.432	80.73	16.33
3:	4.633	22.606	39.19	9.58
Xb:	6.804	33.508	62.25	14.75
S:	1.881	9.456	21.14	4.60
Max:	7.956	39.487	80.73	18.36
Min:	4.633	22.606	39.19	9.58
R:	3.322	16.881	41.54	8.78

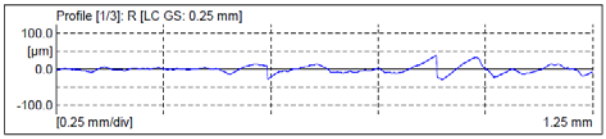

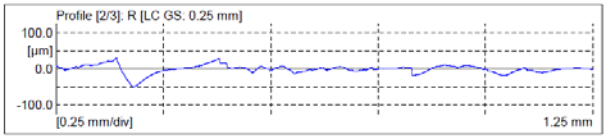

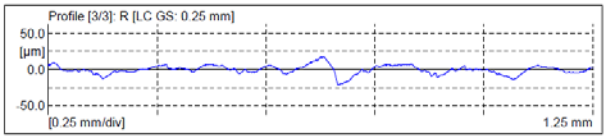

Transverse Surface Finish

Phase 2 Tests: Sample B1 Results (cont.)

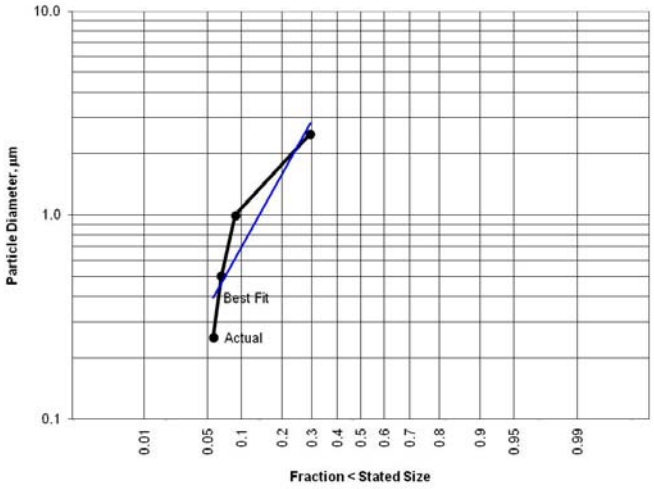

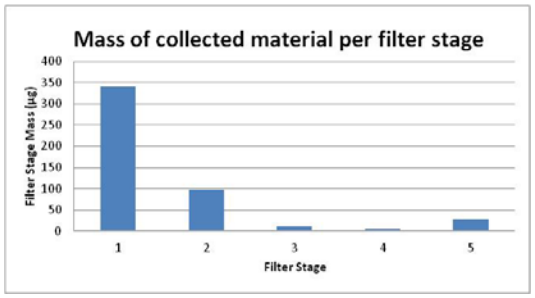

	Data from Best Log-Normal Fit			Data from Plot		
Median diameter, d50	7.89	µm	Median diameter, d50	#DIV/0!	µm	
σ_g	6.67					
r^2	0.840					

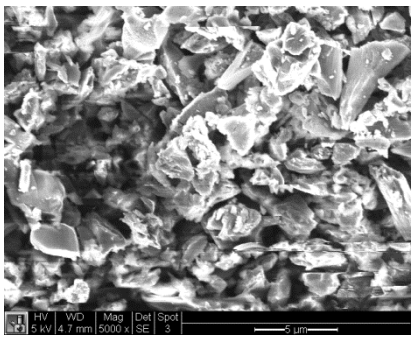

Stage 2 (B)

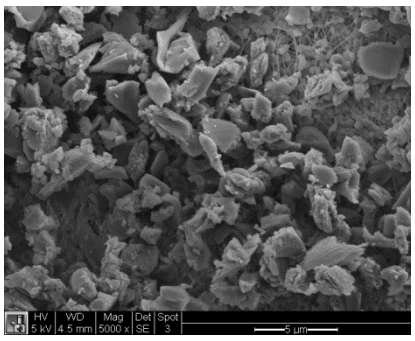

Stage 3 (C)

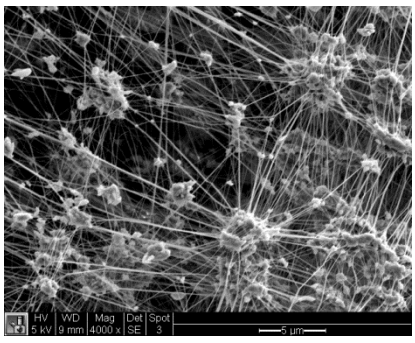

Stage 5 (backup)

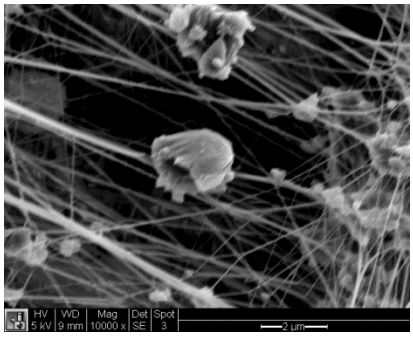

Stage 5 (backup)

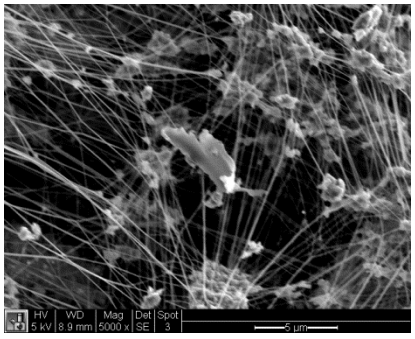

Stage 5 (backup)

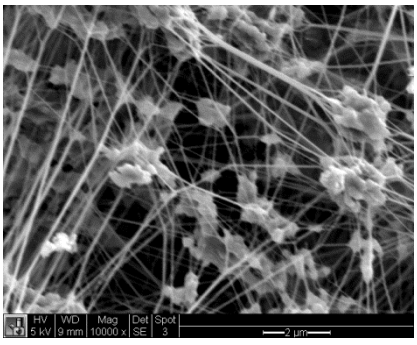

Stage 5 (backup)

APPENDIX A

Phase 2 Tests: Sample B2 Results

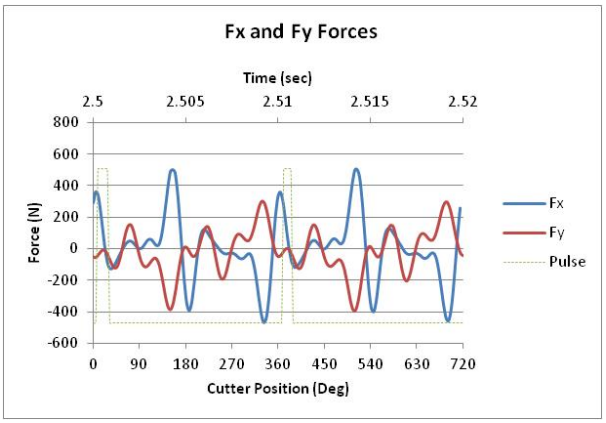

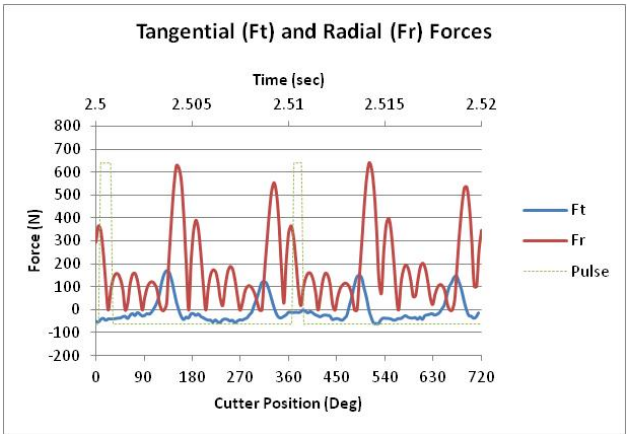

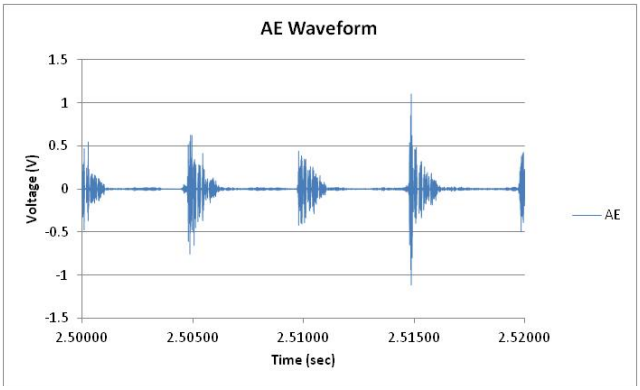

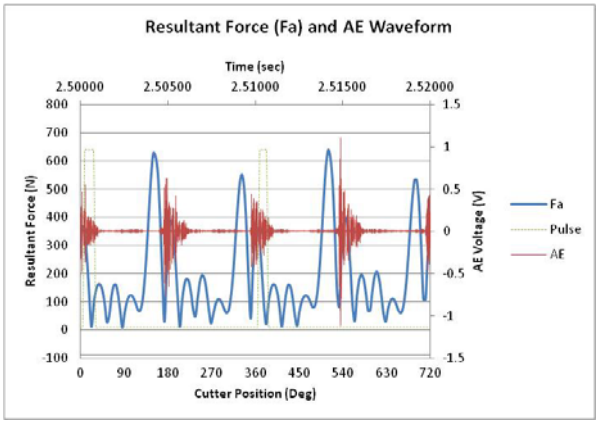

Meas. Instrum.:	Mahr Data Acquisition Board
Drive Unit:	GD 25
Pick-up:	MFW-250 [6.2 %]

Lt:	5.60 mm [N=5]
Ls:	2.5 µm
VB:	±250 µm
Vt:	0.50 mm/s
Points:	33600 [3]

	Ra µm	Rz µm	Rt µm	Rp µm
1:	4.044	24.127	37.83	13.01
2:	5.791	35.688	55.00	18.64
3:	6.653	40.192	52.86	20.39
Xb:	5.496	33.335	48.56	17.34
S:	1.329	8.287	9.36	3.86
Max:	6.653	40.192	55.00	20.39
Min:	4.044	24.127	37.83	13.01
R:	2.609	16.065	17.17	7.39

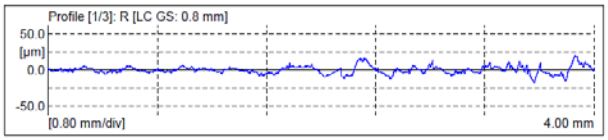

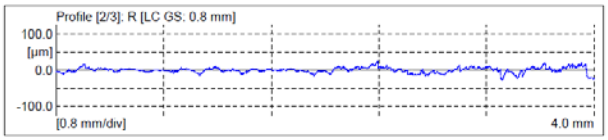

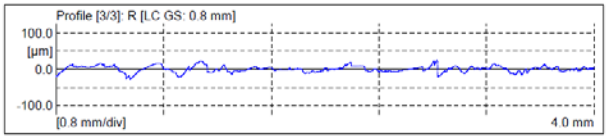

Longitudinal Surface Finish

Meas. Instrum.:	Mahr Data Acquisition Board
Drive Unit:	GD 25
Pick-up:	MFW-250 [6.2 %]

Lt:	1.75 mm [N=5]
Ls:	2.5 µm
VB:	±250 µm
Vt:	0.10 mm/s
Points:	10500 [3]

	Ra µm	Rz µm	Rt µm	Rp µm
1:	7.998	37.474	62.99	19.07
2:	6.615	33.736	60.04	20.85
3:	4.717	27.701	49.12	14.78
Xb:	6.443	32.970	57.38	18.23
S:	1.647	4.931	7.30	3.12
Max:	7.998	37.474	62.99	20.85
Min:	4.717	27.701	49.12	14.78
R:	3.281	9.773	13.86	6.06

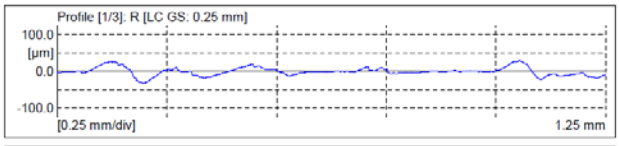

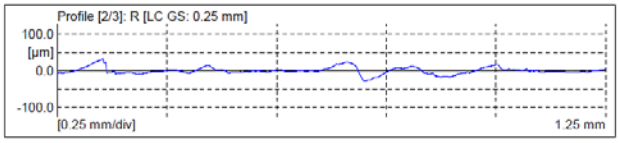

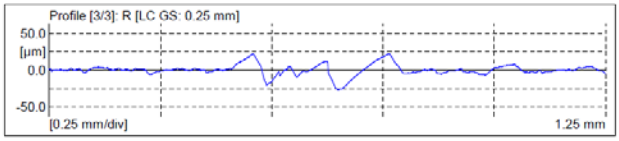

Transverse Surface Finish

Phase 2 Tests: Sample B2 Results (cont.)

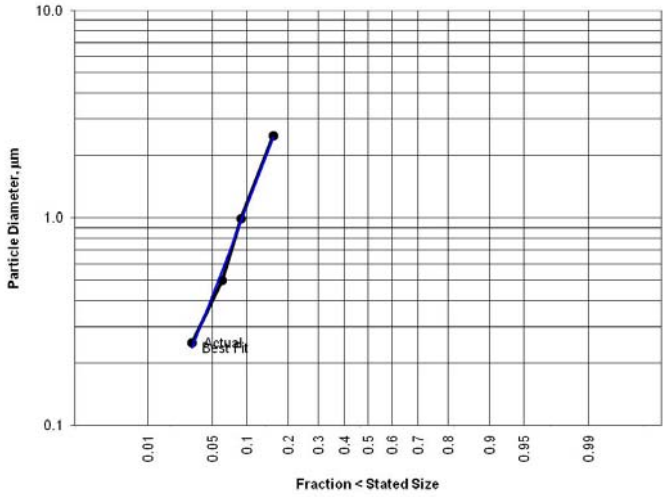

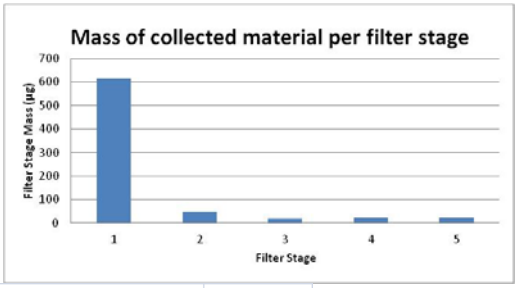

	Data from Best Log-Normal Fit			Data from Plot		
Median diameter, d50	37.77	µm	Median diameter, d50	#DIV/0!	µm	
σ_g	15.35					
r^2	0.994					

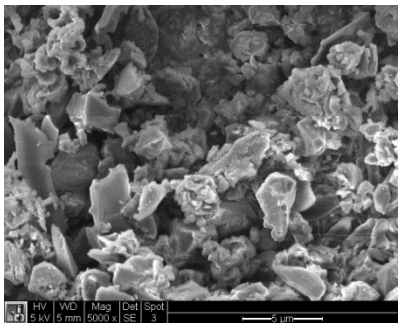

Stage 2 (B)

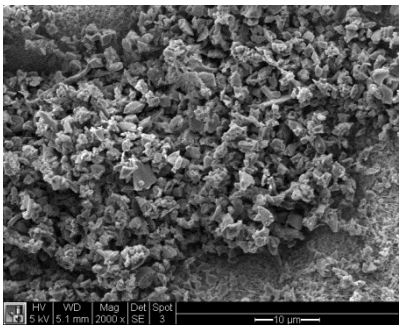

Stage 3 (C)

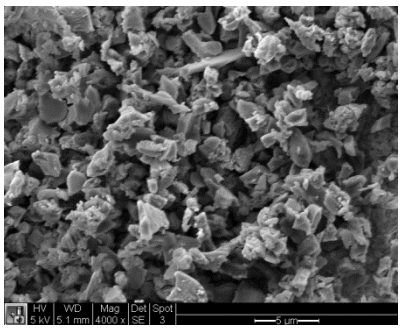

Stage 3 (C)

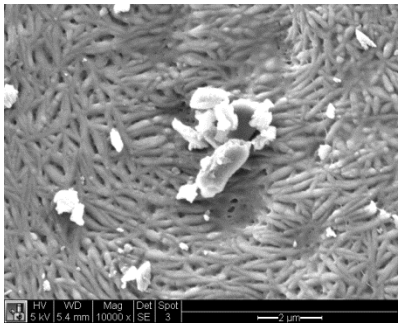

Stage 4 (D)

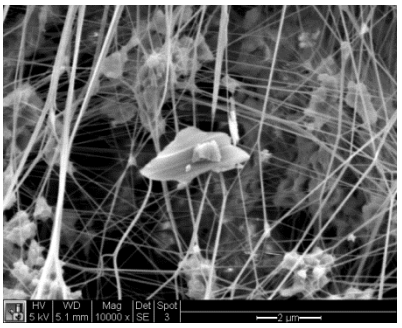

Stage 5 (backup)

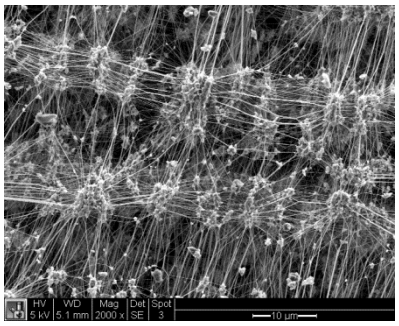

Stage 5 (backup)

APPENDIX A

Phase 2 Tests: Sample B3 Results

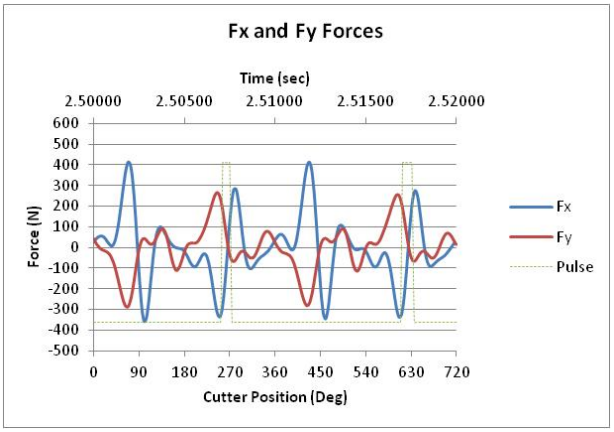

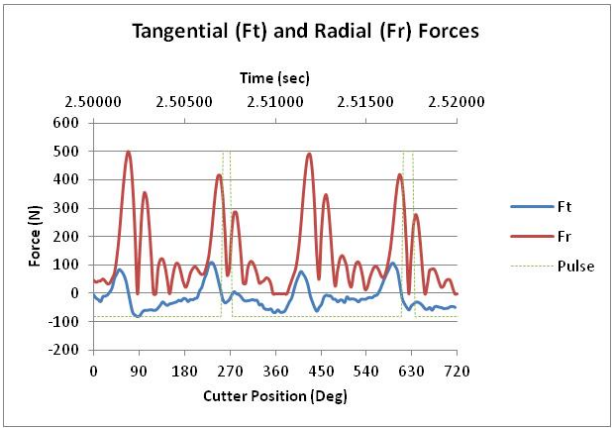

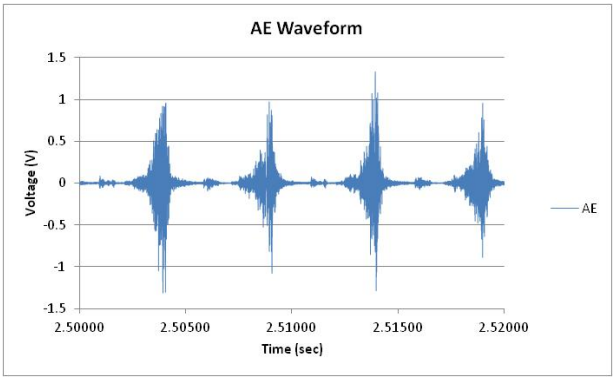

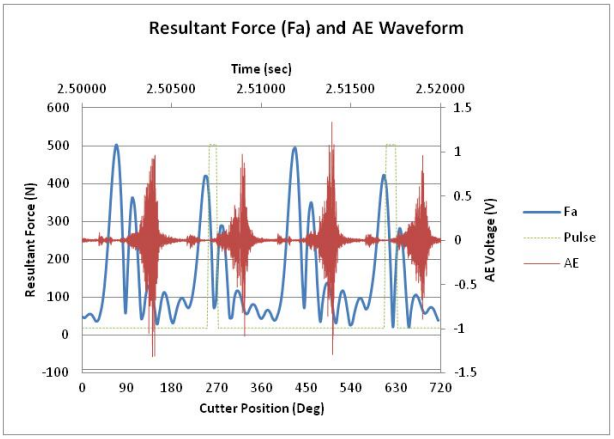

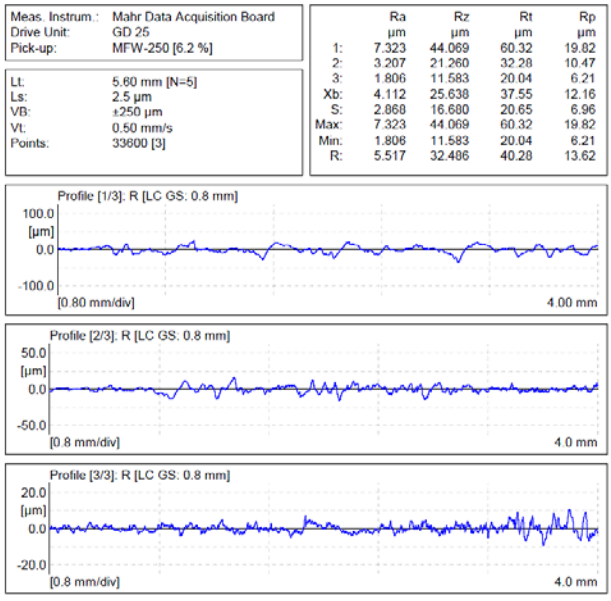

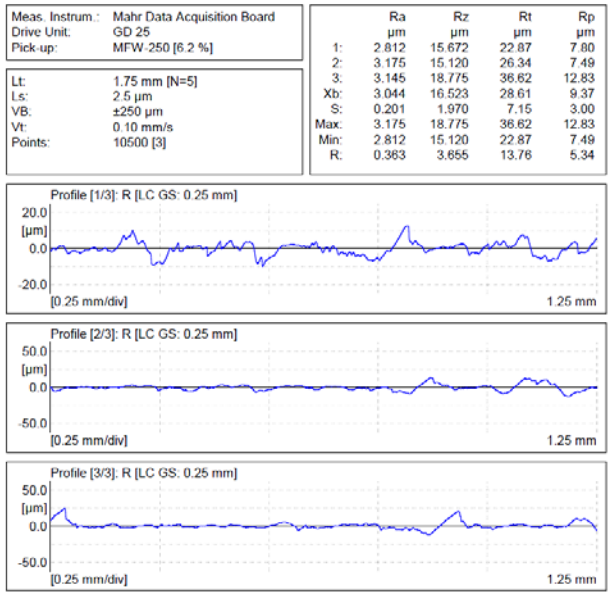

Longitudinal Surface Finish

Transverse Surface Finish

Phase 2 Tests: Sample B3 Results (cont.)

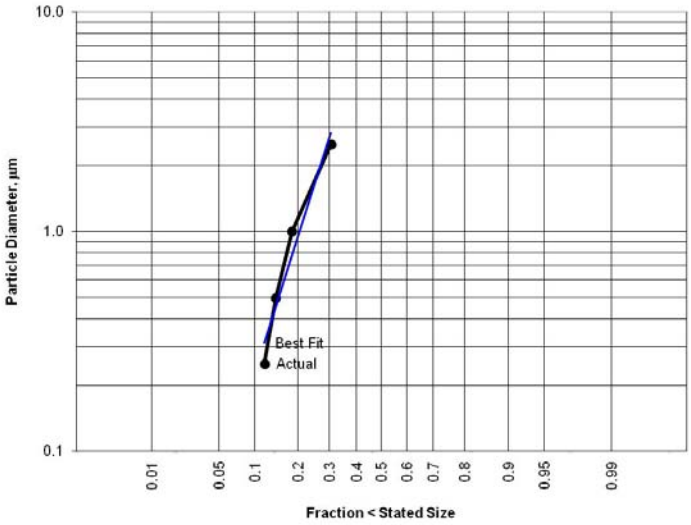

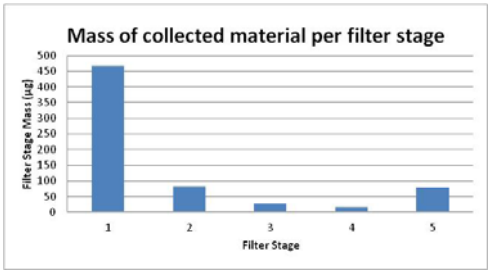

	Data from Best Log-Normal Fit				Data from Plot		
Median diameter, d50	15.02	µm		Median diameter, d50	#DIV/0!	µm	
σ_g	26.26						
r^2	0.954						

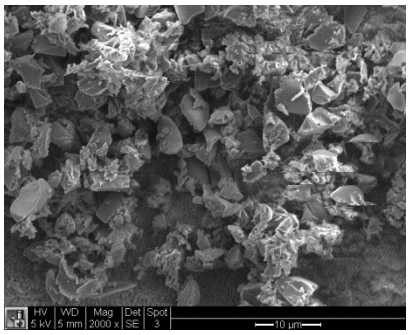

Stage 1 (A)

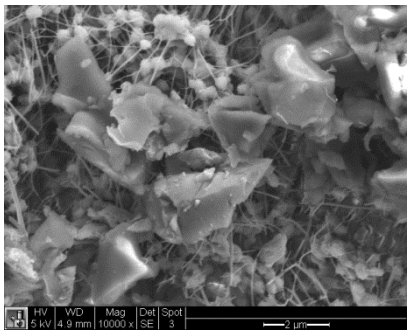

Stage 2 (B)

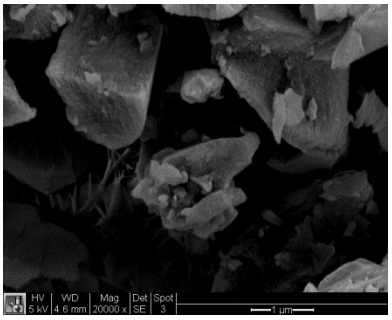

Stage 3 (C)

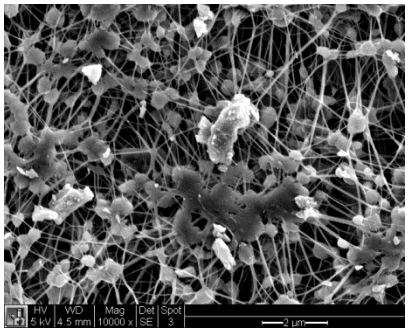

Stage 4 (D)

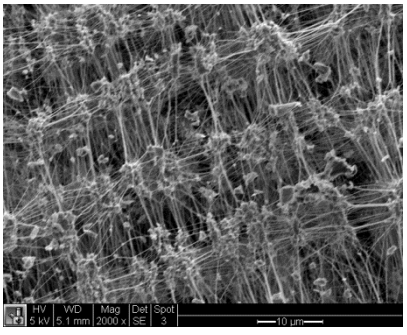

Stage 5 (backup)

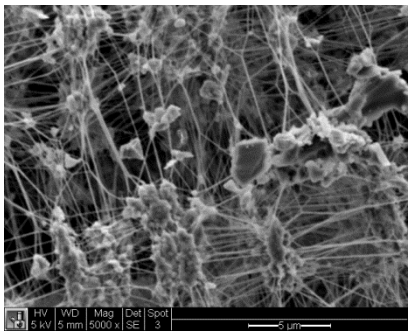

Stage 5 (backup)

APPENDIX A

Phase 2 Tests: Sample B4 Results

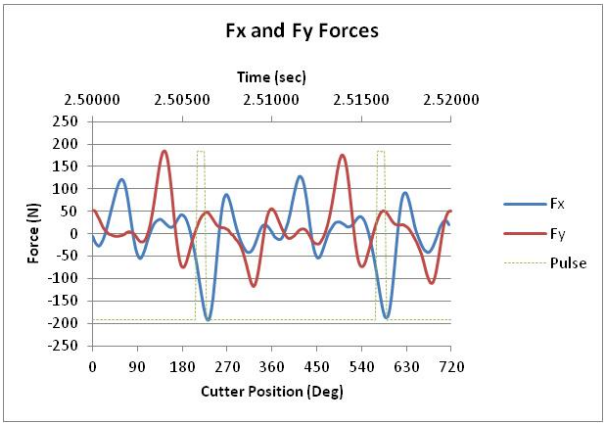

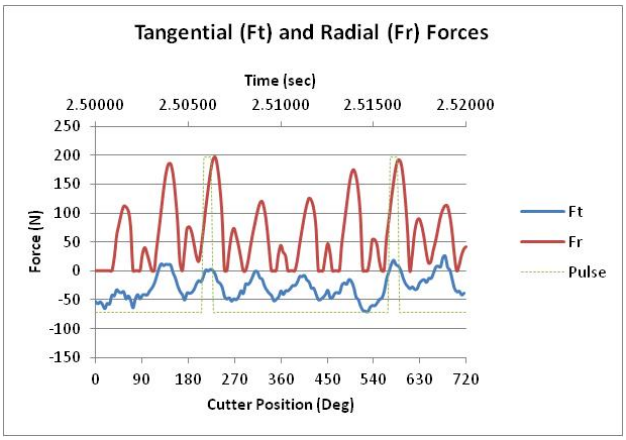

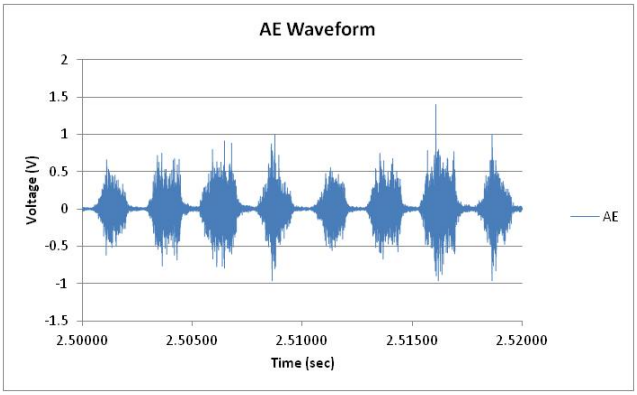

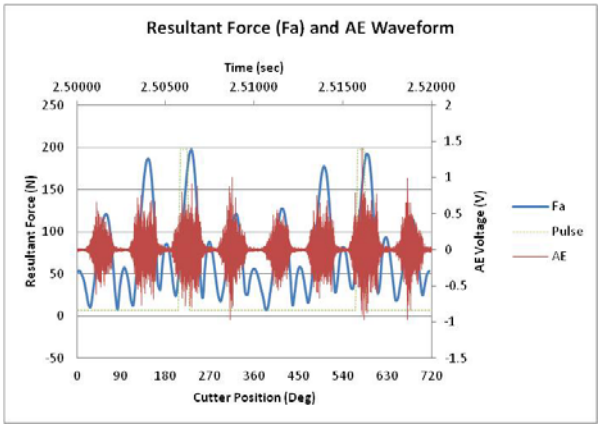

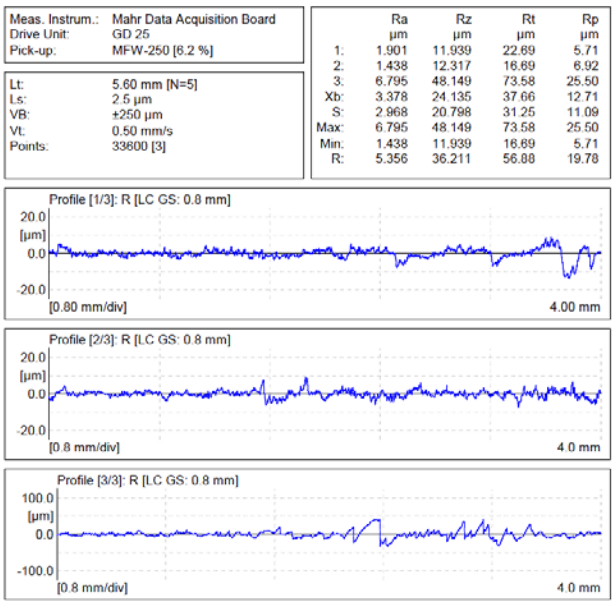

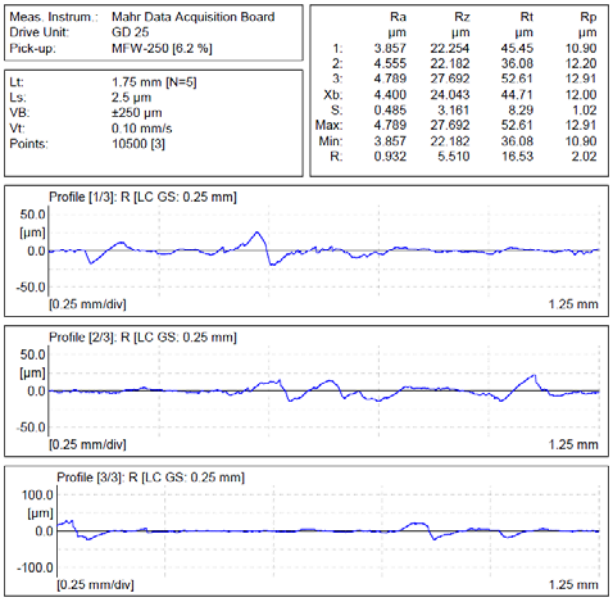

Longitudinal Surface Finish

Transverse Surface Finish

Phase 2 Tests: Sample B4 Results (cont.)

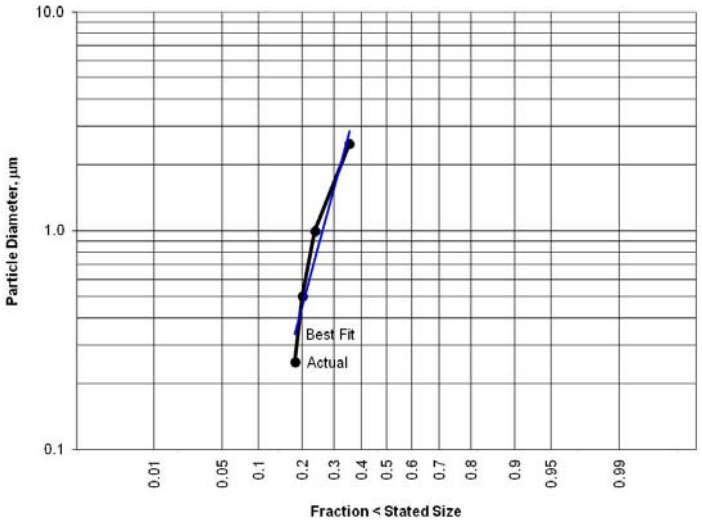

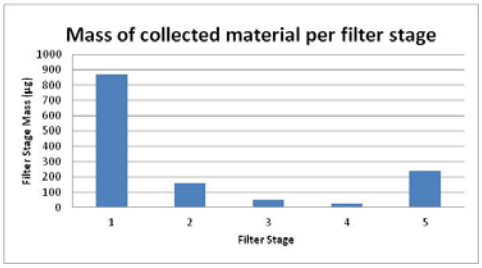

	Data from Best Log-Normal Fit			Data from Plot		
Median diameter, d50	12.30	µm	Median diameter, d50	#DIV/0!	µm	
σ_g	50.94					
r^2	0.928					

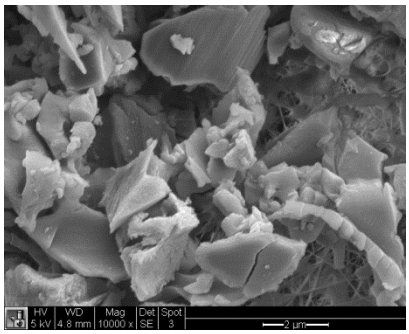

Stage 1 (A)

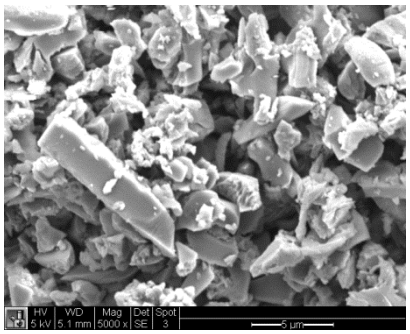

Stage 2 (B)

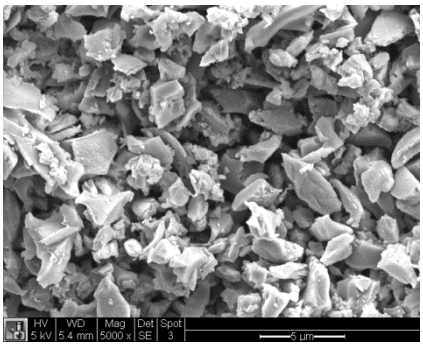

Stage 3 (C)

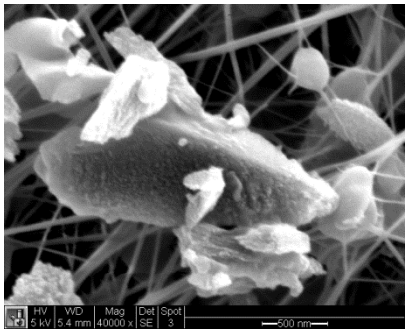

Stage 4 (D)

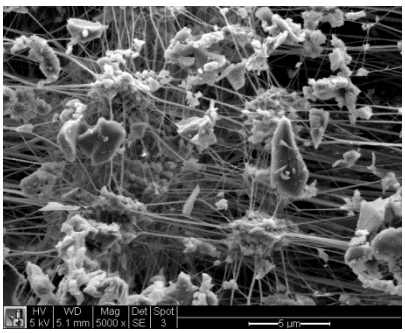

Stage 5 (backup)

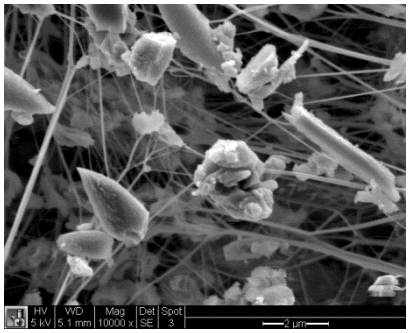

Stage 5 (backup)

APPENDIX A

Phase 2 Tests: Sample C1 Results

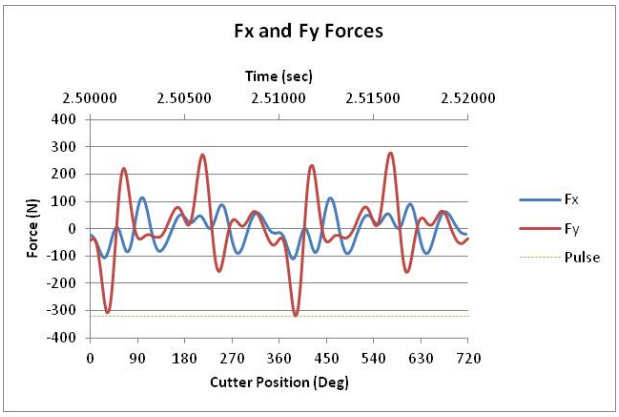

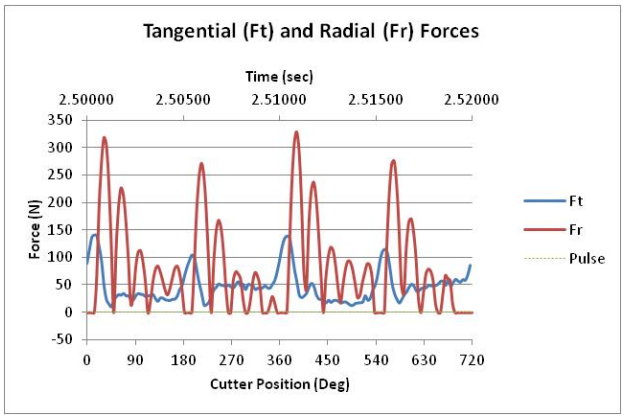

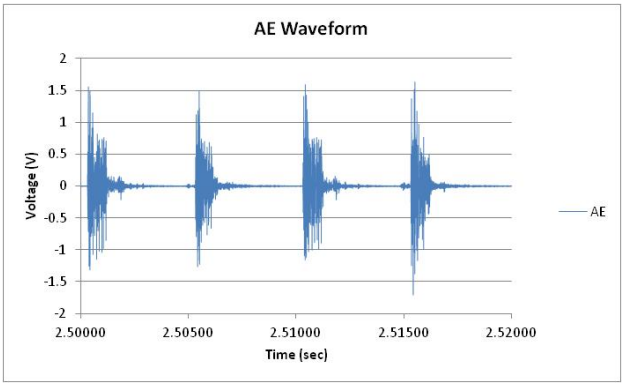

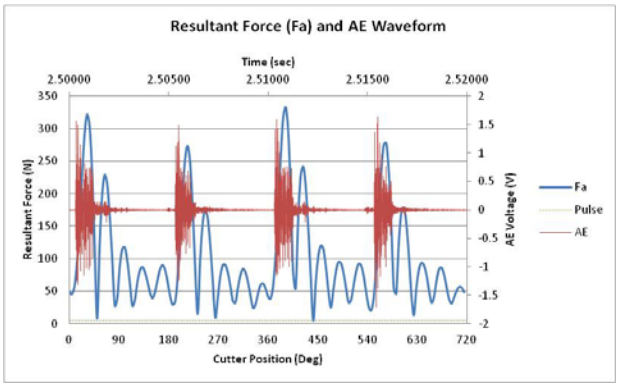

	Ra µm	Rq µm	Rz µm	Rz1 max µm	Rmax µm	RzJ µm	Rt µm	Rp µm	Rv µm	R3z µm	R Sm µm
1:	4.700	6.413	31.323	53.48	53.48	18.458	53.79	18.69	12.63	16.679	216.68
2:	4.616	6.185	29.769	44.36	44.36	18.705	46.15	17.23	12.54	19.866	167.11
3:	4.801	6.391	31.213	47.95	47.95	19.604	50.72	17.99	13.22	17.119	193.34
Xb:	4.706	6.330	30.768	48.60	48.60	18.922	50.22	17.97	12.80	17.888	192.38
S:	0.092	0.126	0.867	4.59	4.59	0.603	3.84	0.73	0.37	1.727	24.80
Max:	4.801	6.413	31.323	53.48	53.48	19.604	53.79	18.69	13.22	19.866	216.68
Min:	4.616	6.185	29.769	44.36	44.36	18.458	46.15	17.23	12.54	16.679	167.11
R:	0.184	0.229	1.553	9.11	9.11	1.146	7.63	1.46	0.69	3.187	49.56

	Ra µm	Rq µm	Rz µm	Rz1 max µm	Rmax µm	RzJ µm	Rt µm	Rp µm	Rv µm	R3z µm	R Sm µm
1:	7.115	8.920	31.828	46.16	46.16	22.229	46.16	16.00	15.82	-.--	288.50
2:	7.283	10.506	36.861	68.85	68.85	30.037	74.89	19.91	16.95	-.--	230.90
3:	6.163	8.949	35.891	60.20	60.20	23.714	60.20	15.64	20.25	-.--	134.50
Xb:	6.853	9.458	34.860	58.41	58.41	25.326	60.42	17.19	17.67	217.97	
S:	0.604	0.907	2.670	11.45	11.45	4.146	14.37	2.37	2.30	77.81	
Max:	7.283	10.506	36.861	68.85	68.85	30.037	74.89	19.91	20.25	288.50	
Min:	6.163	8.920	31.828	46.16	46.16	22.229	46.16	15.64	15.82	134.50	
R:	1.120	1.585	5.033	22.70	22.70	7.807	28.73	4.28	4.43	154.00	

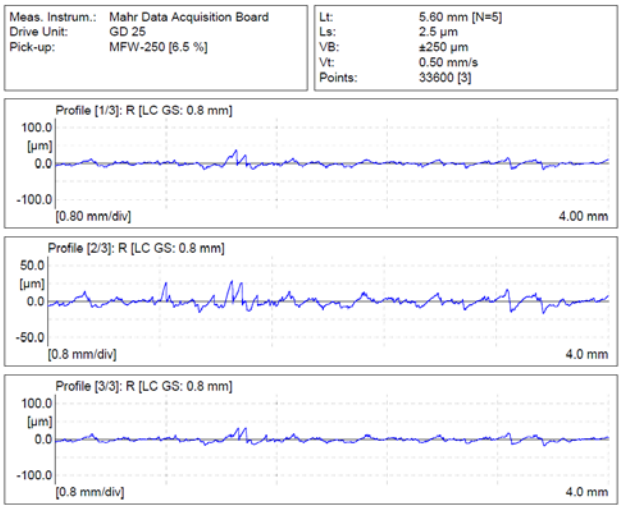

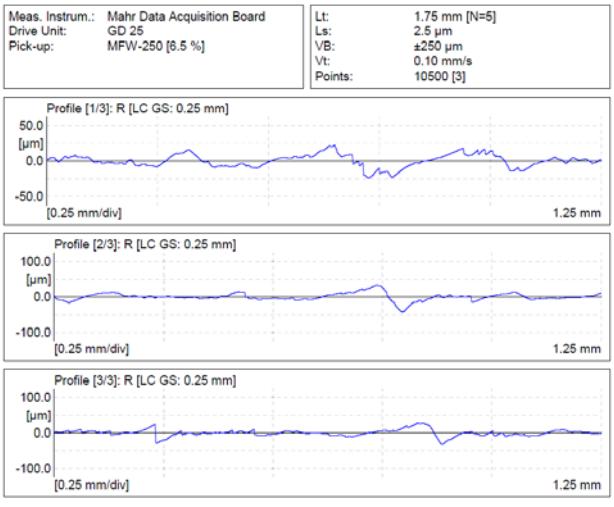

Longitudinal Surface Finish

Transverse Surface Finish

Phase 2 Tests: Sample C1 Results (cont.)

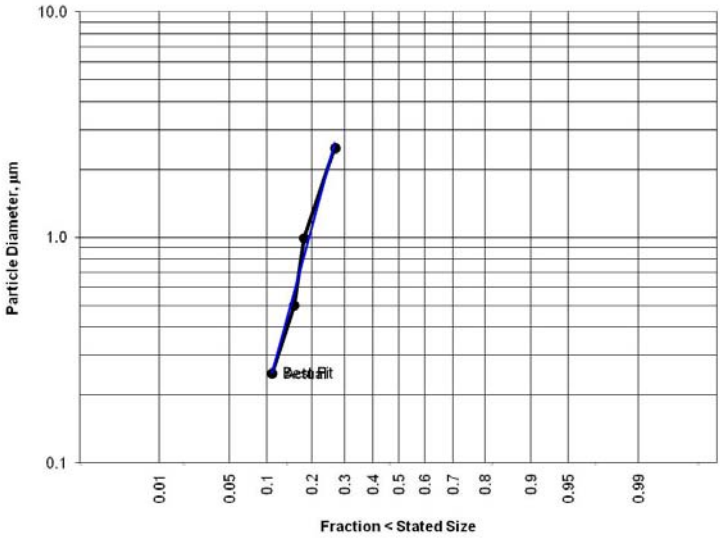

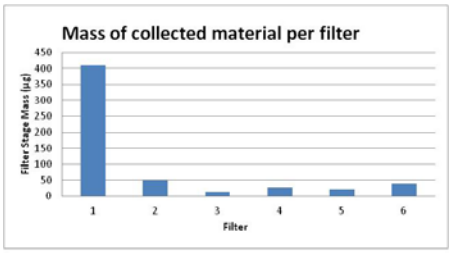

	Data from Best Log-Normal Fit				Data from Plot		
Median diameter, d50	28.19	µm		Median diameter, d50	#DIV/0!	µm	
σ_g	46.56						
r^2	0.981						

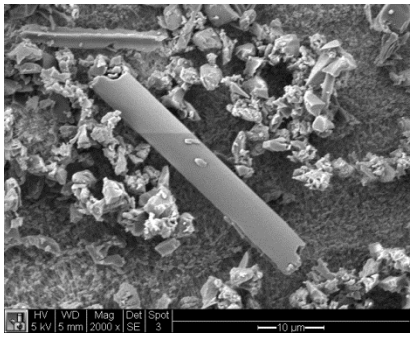
Stage 1 (A)

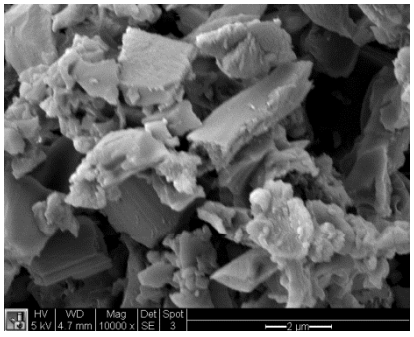
Stage 2 (B)

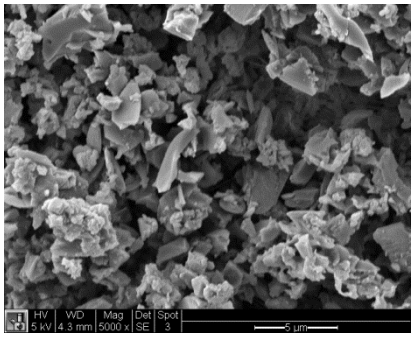
Stage 3 (C)

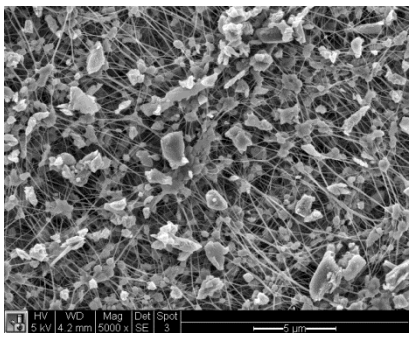
Stage 4 (D)

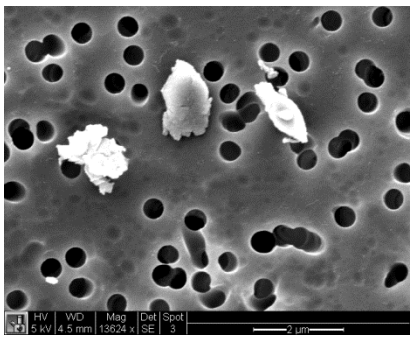
Stage 6 (backup)

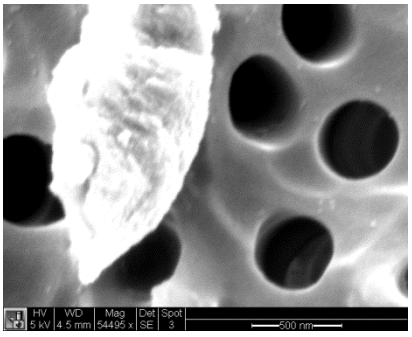
Stage 6 (backup)

APPENDIX A

Phase 2 Tests: Sample C2 Results

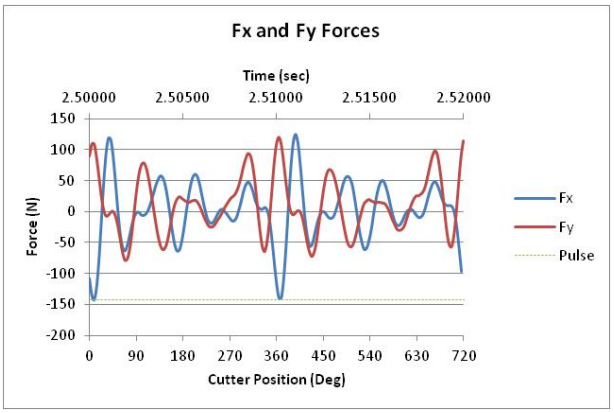

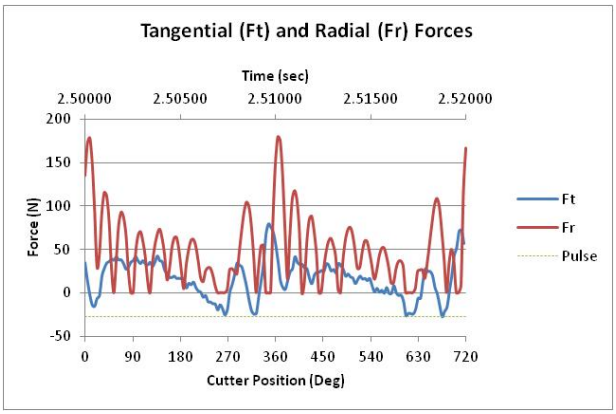

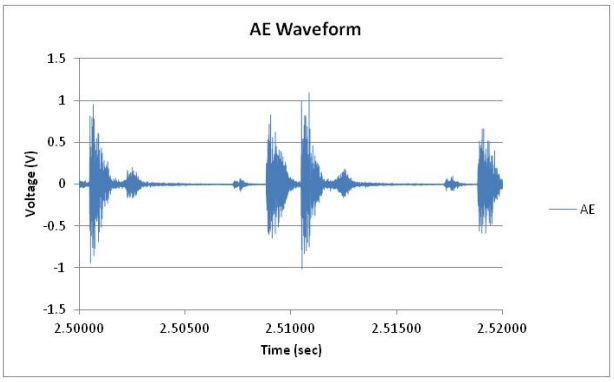

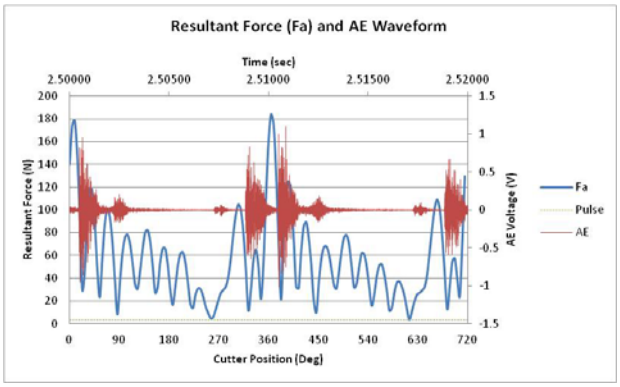

	Ra µm	Rq µm	Rz µm	Rz1 max µm	Rmax µm	RzJ µm	Rt µm	Rp µm	Rv µm	R3z µm	R Sm µm
1:	0.465	0.592	3.551	4.85	4.85	1.719	4.85	1.71	1.84	2.628	57.70
2:	0.481	0.622	3.714	5.29	5.29	1.840	5.29	1.75	1.96	2.817	59.47
3:	0.488	0.635	3.891	5.78	5.78	1.913	5.78	1.78	2.11	2.837	58.58
Xb:	0.478	0.616	3.718	5.30	5.30	1.824	5.30	1.75	1.97	2.761	58.58
S:	0.012	0.022	0.170	0.45	0.45	0.098	0.45	0.03	0.14	0.115	0.88
Max:	0.488	0.635	3.891	5.76	5.76	1.913	5.76	1.78	2.11	2.837	59.47
Min:	0.465	0.592	3.551	4.85	4.85	1.719	4.85	1.71	1.84	2.628	57.70
R:	0.023	0.042	0.340	0.91	0.91	0.194	0.91	0.07	0.28	0.208	1.77

Meas. Instrum.:	Mahr Data Acquisition Board
Drive Unit:	GD 25
Pick-up:	MFW-250 [6.5 %]

Lt:	5.60 mm [N=5]
Ls:	2.5 µm
VB:	±250 µm
Vt:	0.50 mm/s
Points:	33600 [3]

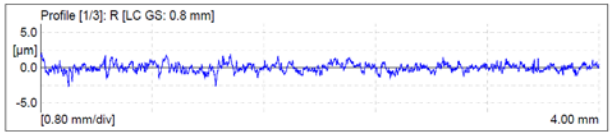

Longitudinal Surface Finish

	Ra µm	Rq µm	Rz µm	Rz1 max µm	Rmax µm	RzJ µm	Rt µm	Rp µm	Rv µm	R3z µm	R Sm µm
1:	1.061	1.509	6.029	9.94	9.94	3.254	9.94	2.90	3.13	2.677	71.88
2:	1.864	3.164	11.312	25.49	25.49	8.364	25.49	5.21	6.10	2.641	118.44
3:	2.334	3.926	14.218	23.79	23.79	9.546	28.05	5.29	8.93	4.168	151.21
Xb:	1.753	2.866	10.520	19.74	19.74	7.055	21.16	4.47	6.05	3.162	113.84
S:	0.644	1.236	4.152	8.53	8.53	3.344	9.80	1.36	2.90	0.871	39.86
Max:	2.334	3.926	14.218	25.49	25.49	9.546	28.05	5.29	8.93	4.168	151.21
Min:	1.061	1.509	6.029	9.94	9.94	3.254	9.94	2.90	3.13	2.641	71.88
R:	1.273	2.417	8.189	15.55	15.55	6.292	18.12	2.39	5.80	1.526	79.33

Meas. Instrum.:	Mahr Data Acquisition Board
Drive Unit:	GD 25
Pick-up:	MFW-250 [6.5 %]

Lt:	1.75 mm [N=5]
Ls:	2.5 µm
VB:	±250 µm
Vt:	0.10 mm/s
Points:	10500 [3]

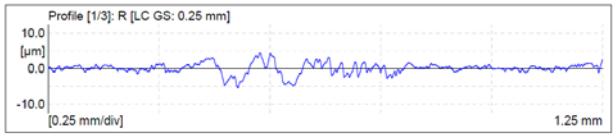

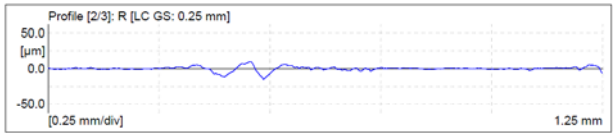

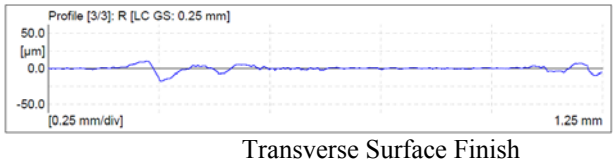

Transverse Surface Finish

Phase 2 Tests: Sample C2 Results (cont.)

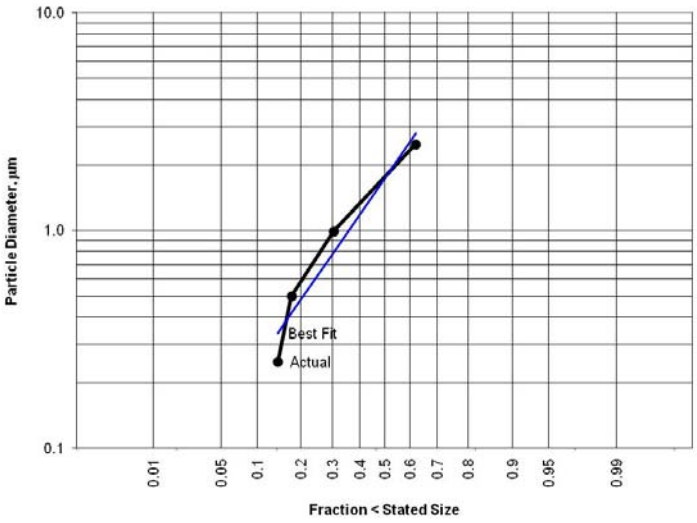

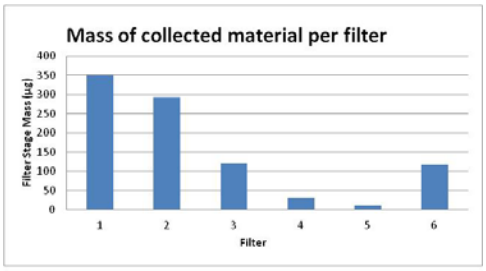

	Data from Best Log-Normal Fit			Data from Plot		
Median diameter, d50	1.74	µm	Median diameter, d50	1.77	µm	
σ_g	4.61					
r^2	0.936					

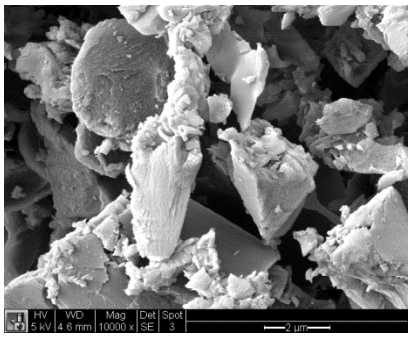

Stage 1 (A)

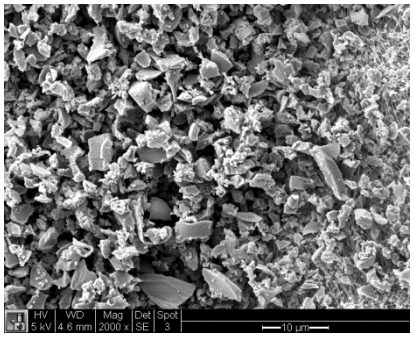

Stage 2 (B)

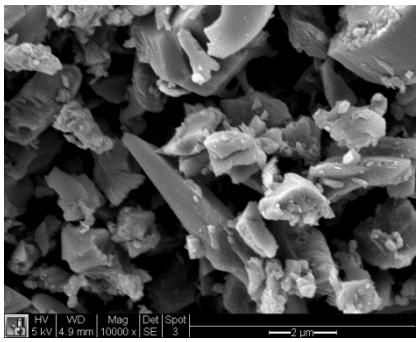

Stage 3 (C)

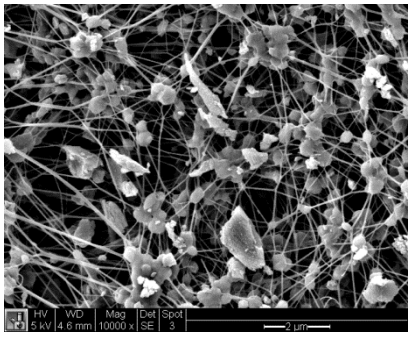

Stage 4 (D)

Stage 6 (backup)

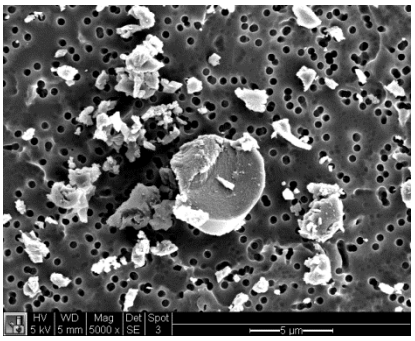

Stage 6 (backup)

APPENDIX A

Phase 2 Tests: Sample C3 Results

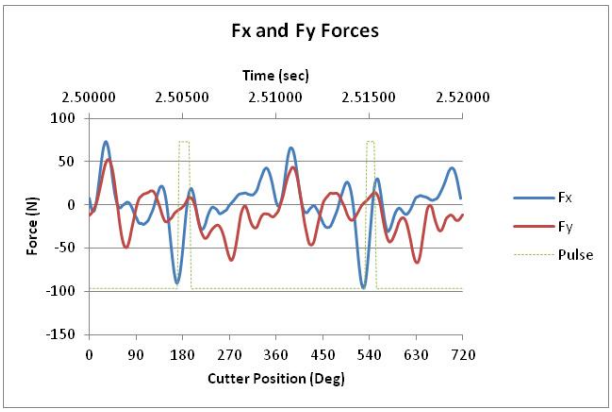

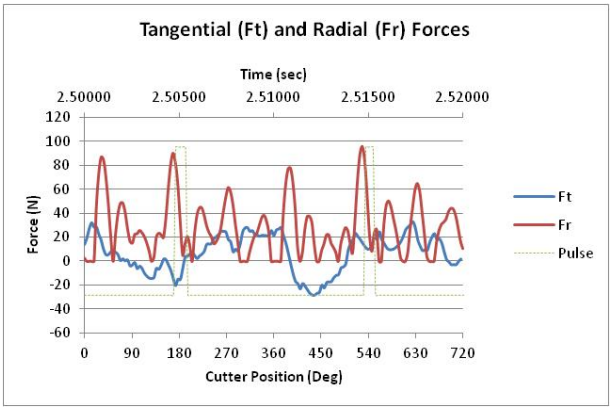

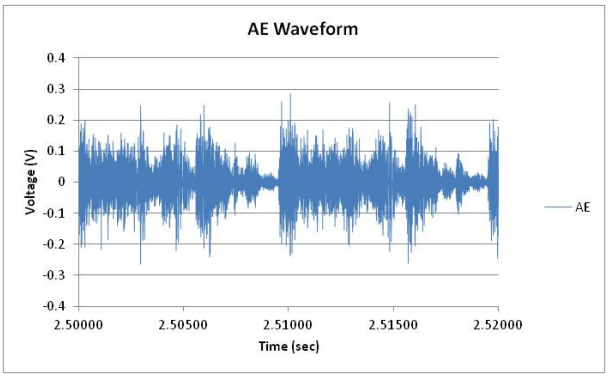

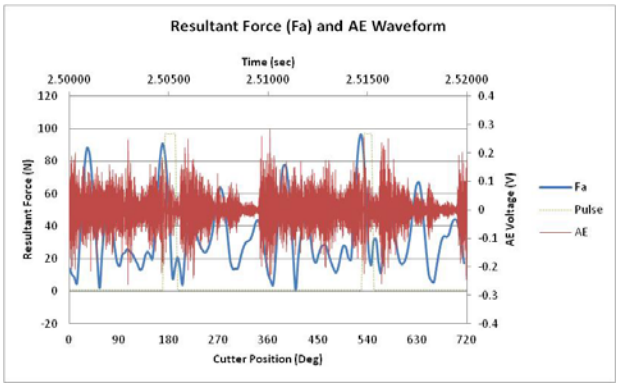

Meas. Instrum.:	Mahr Data Acquisition Board
Drive Unit:	GD 25
Pick-up:	MFW-250 [7.2 %]
Lt:	5.60 mm [N=5]
Ls:	2.5 µm
VB:	±250 µm
Vt:	0.50 mm/s
Points:	33600 [3]

	Ra µm	Rz µm	Rt µm	Rp µm
1:	6.743	40.777	55.45	22.02
2:	2.144	13.300	18.00	7.05
3:	0.924	7.160	10.13	3.89
Xb:	3.270	20.412	27.86	10.98
S:	3.068	17.901	24.22	9.69
Max:	6.743	40.777	55.45	22.02
Min:	0.924	7.160	10.13	3.89
R:	5.818	33.616	45.32	18.13

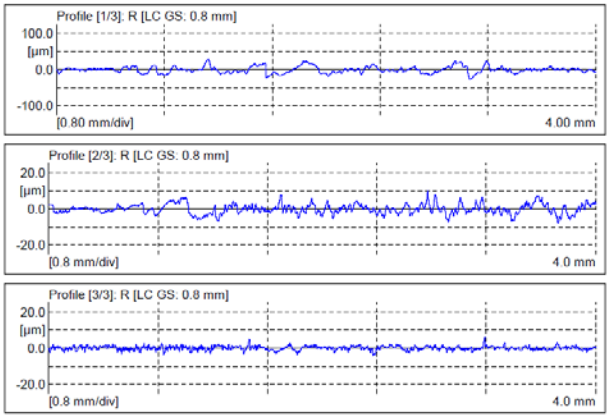

Meas. Instrum.:	Mahr Data Acquisition Board
Drive Unit:	GD 25
Pick-up:	MFW-250 [7.2 %]
Lt:	1.75 mm [N=5]
Ls:	2.5 µm
VB:	±250 µm
Vt:	0.10 mm/s
Points:	10500 [3]

	Ra µm	Rz µm	Rt µm	Rp µm
1:	4.364	23.408	37.02	11.53
2:	5.239	26.085	44.65	12.21
3:	5.218	22.456	46.44	11.85
Xb:	4.940	23.983	42.70	11.86
S:	0.499	1.882	5.00	0.34
Max:	5.239	26.085	46.44	12.21
Min:	4.364	22.456	37.02	11.53
R:	0.875	3.629	9.42	0.69

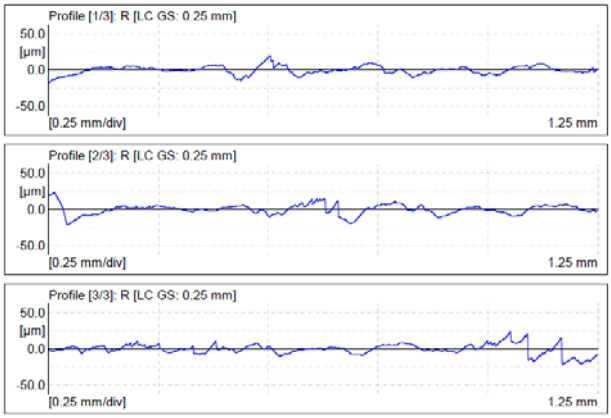

Longitudinal Surface Finish

Transverse Surface Finish

Phase 2 Tests: Sample C3 Results (cont.)

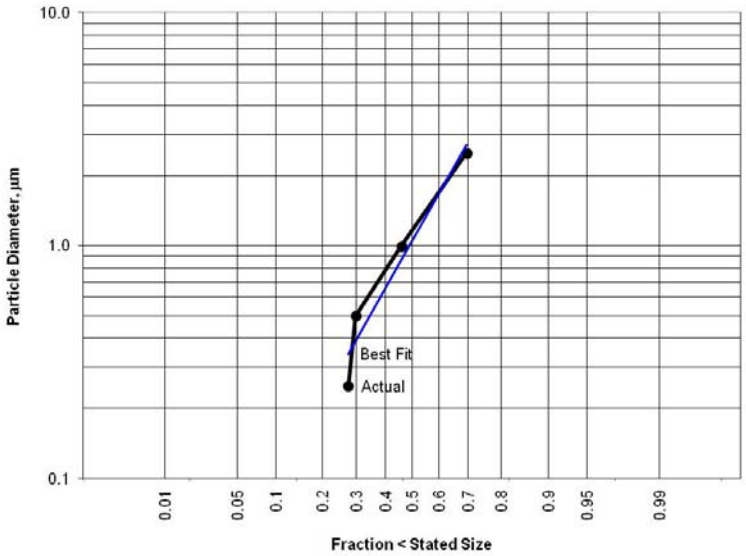

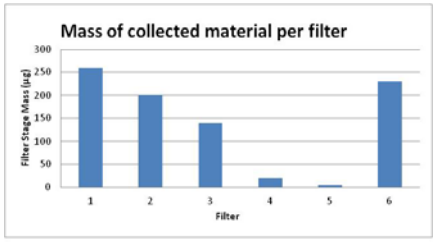

	Data from Best Log-Normal Fit			Data from Plot		
Median diameter, d50	1.04	µm	Median diameter, d50	1.16	µm
σ_g	6.41				
r^2	0.935				

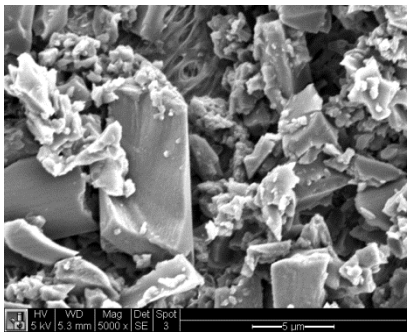

Stage 1 (A)

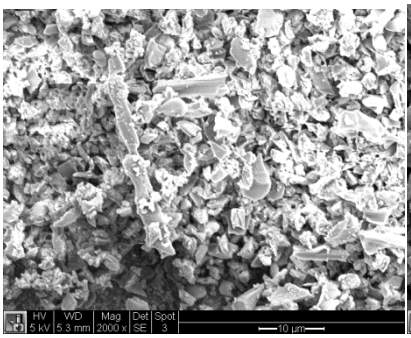

Stage 2(B)

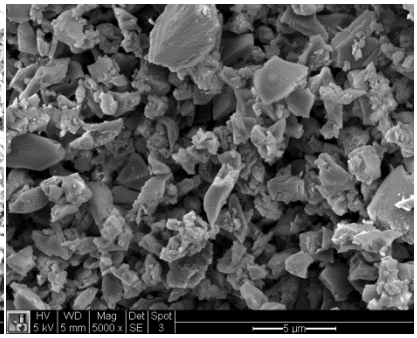

Stage 3 (C)

Stage 4 (D)

Stage 6 (backup)

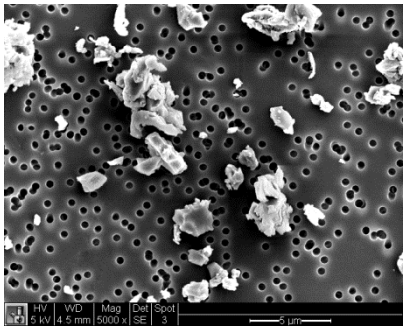

Stage 6 (backup)

APPENDIX A

Phase 2 Tests: Sample C4 Results

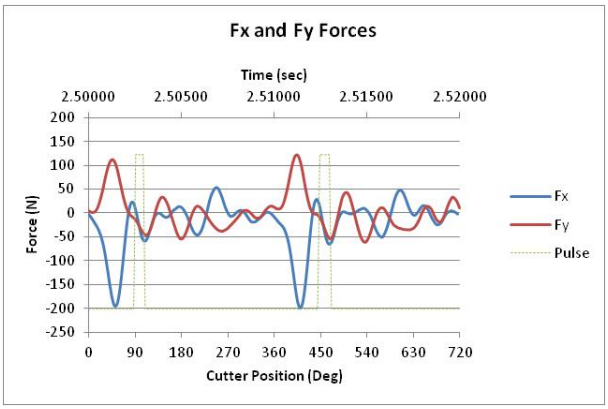

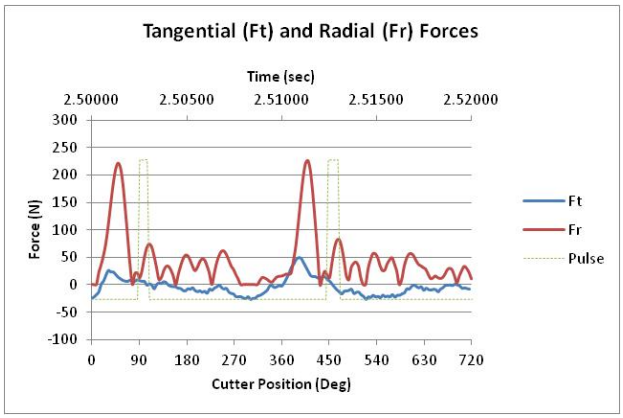

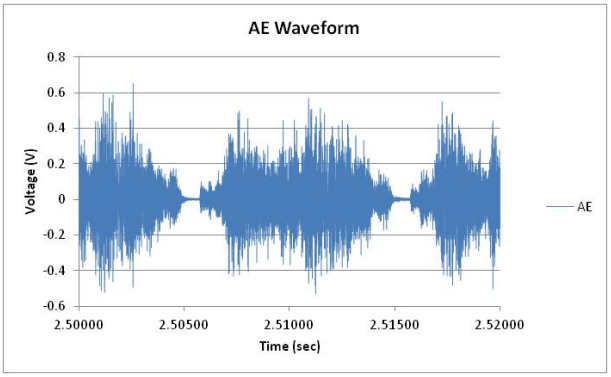

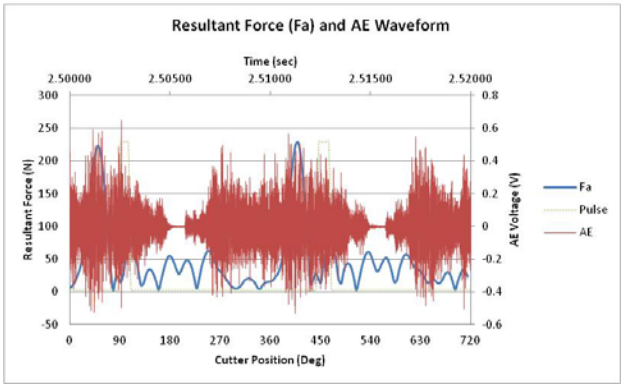

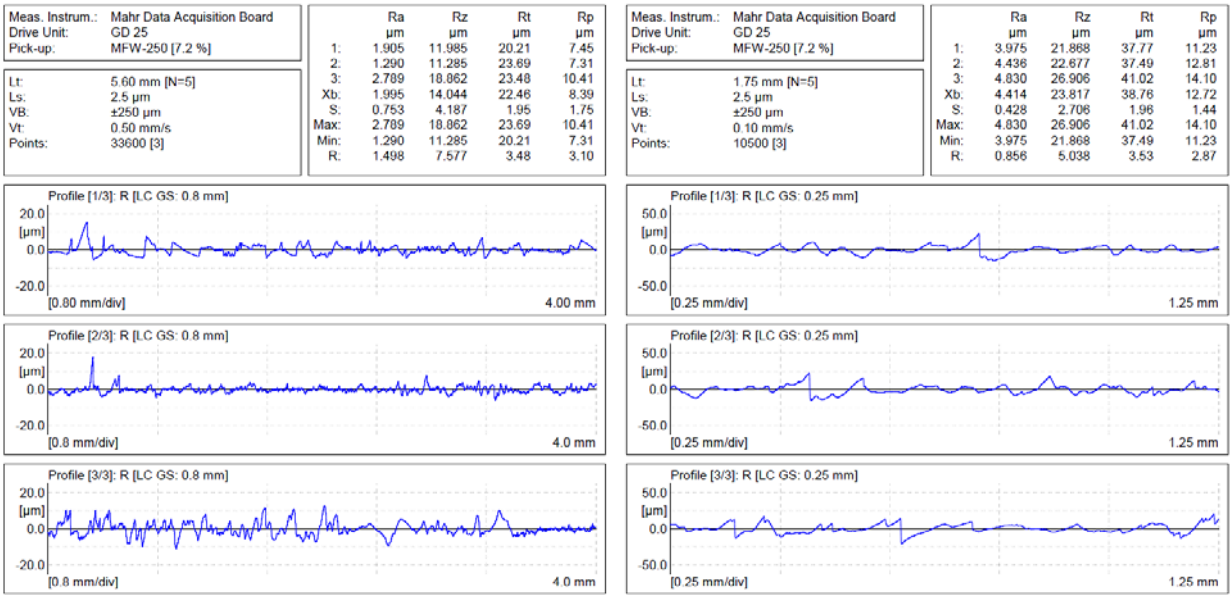

Longitudinal Surface Finish

Transverse Surface Finish

Phase 2 Tests: Sample C4 Results (cont.)

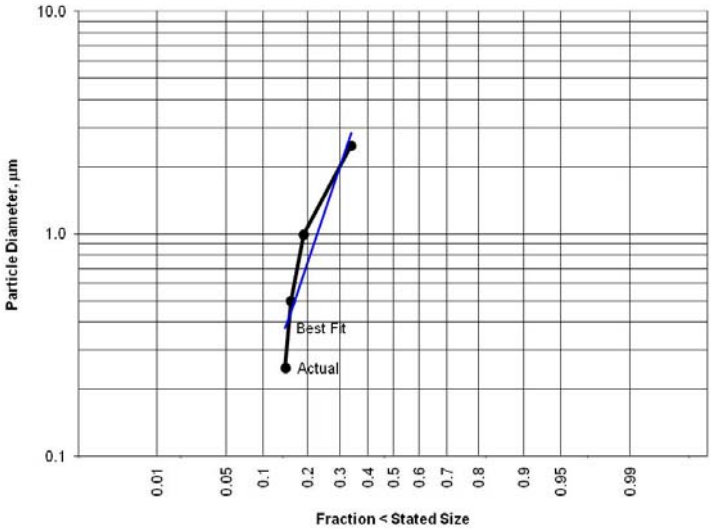

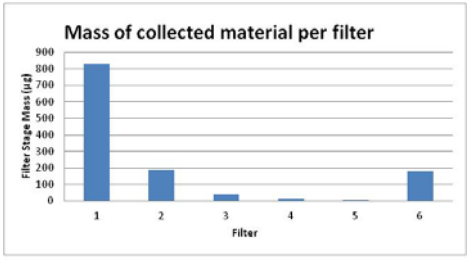

	Data from Best Log-Normal Fit			Data from Plot		
Median diameter, d50	10.42	µm	Median diameter, d50	#DIV/0!	µm	
σ_g	22.92					
r^2	0.874					

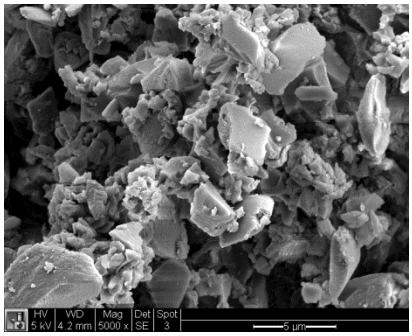

Stage 1 (A)

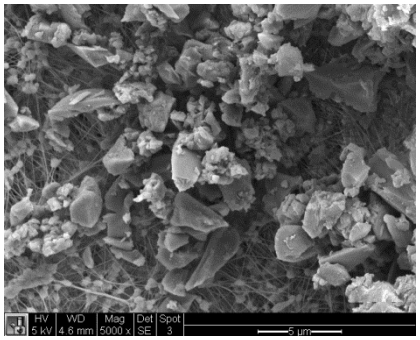

Stage 2(B)

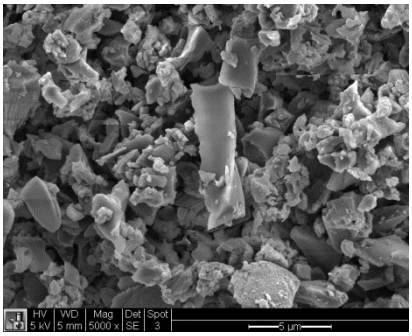

Stage 3 (C)

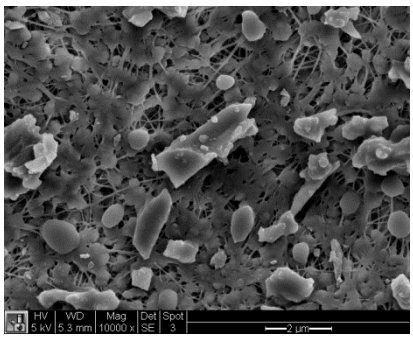

Stage 4 (D)

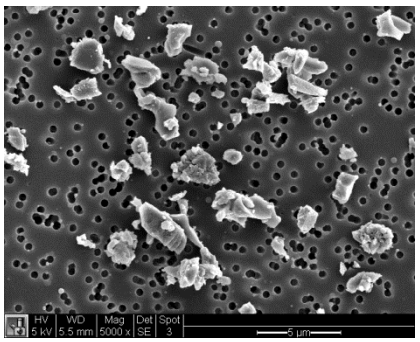

Stage 6 (backup)

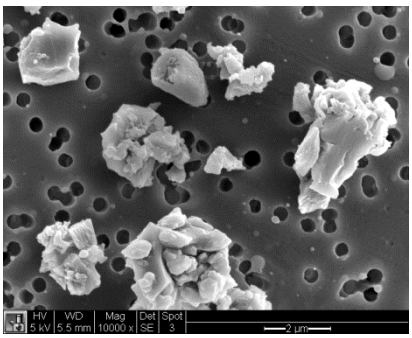

Stage 6 (backup)

APPENDIX A

Phase 2 Tests: Sample D1 Results

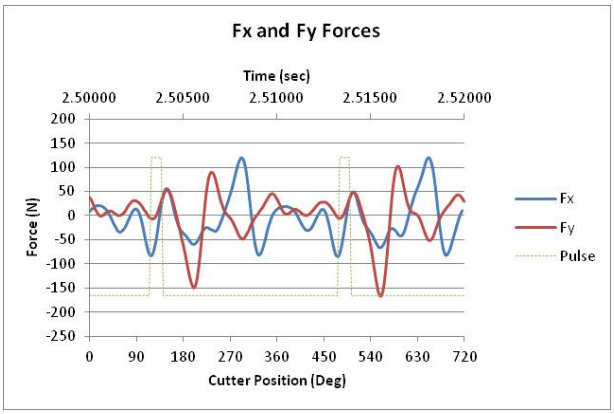

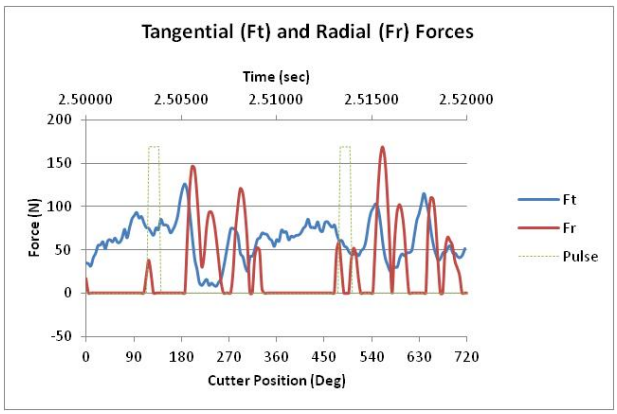

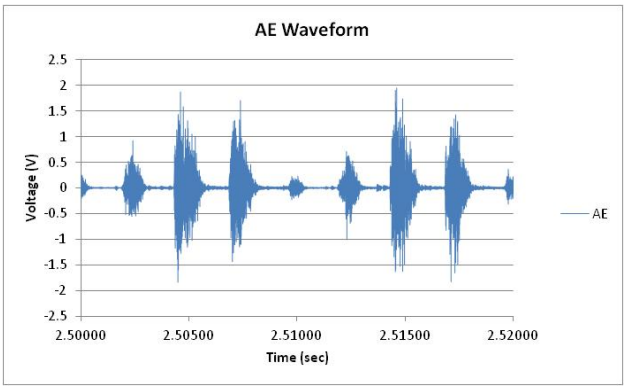

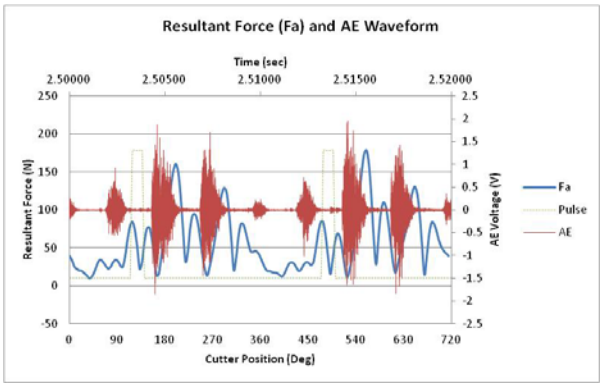

Meas. Instrum.:	Mahr Data Acquisition Board
Drive Unit:	GD 25
Pick-up:	MFW-250 [7.2 %]

Lt:	5.60 mm [N=5]
Ls:	2.5 µm
VB:	±250 µm
Vt:	0.50 mm/s
Points:	33600 [3]

	Ra µm	Rz µm	Rt µm	Rp µm
1:	0.377	3.232	3.54	1.43
2:	5.416	31.208	37.90	9.87
3:	0.459	3.527	4.58	1.89
Xb:	2.084	12.656	15.34	4.40
S:	2.886	16.068	19.55	4.74
Max:	5.416	31.208	37.90	9.87
Min:	0.377	3.232	3.54	1.43
R:	5.040	27.976	34.36	8.43

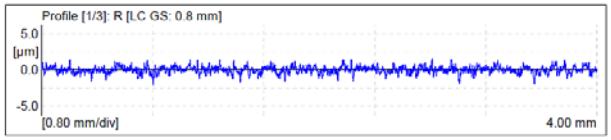

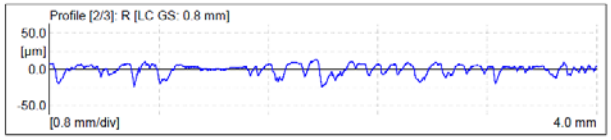

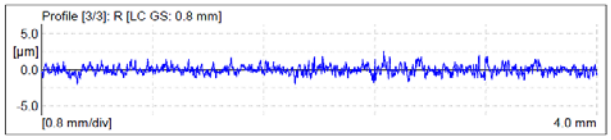

Longitudinal Surface Finish

Meas. Instrum.:	Mahr Data Acquisition Board
Drive Unit:	GD 25
Pick-up:	MFW-250 [7.2 %]

Lt:	1.75 mm [N=5]
Ls:	2.5 µm
VB:	±250 µm
Vt:	0.10 mm/s
Points:	10500 [3]

	Ra µm	Rz µm	Rt µm	Rp µm
1:	1.488	8.063	17.17	3.20
2:	1.112	7.693	9.48	2.21
3:	1.303	7.459	13.25	2.76
Xb:	1.301	7.739	13.30	2.73
S:	0.188	0.305	3.84	0.50
Max:	1.488	8.063	17.17	3.20
Min:	1.112	7.459	9.48	2.21
R:	0.376	0.604	7.69	0.99

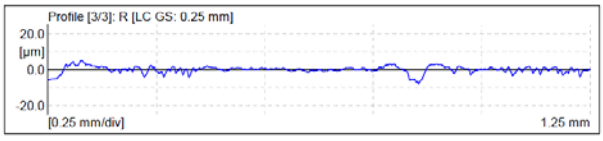

Transverse Surface Finish

Phase 2 Tests: Sample D1 Results (cont.)

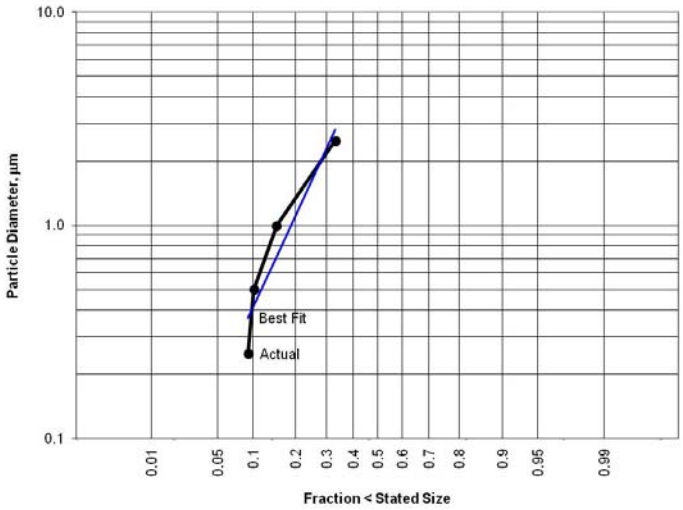

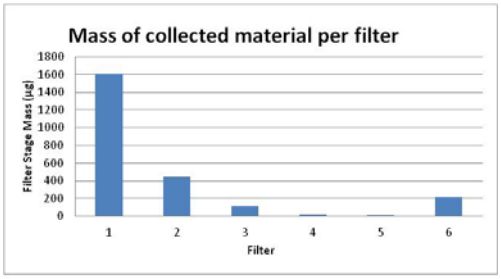

	Data from Best Log-Normal Fit			Data from Plot		
Median diameter, d50	7.49	µm	Median diameter, d50	#DIV/0!	µm	
σ_g	9.64					
r^2	0.894					

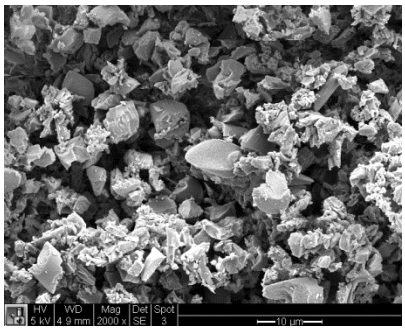
Stage 1 (A)

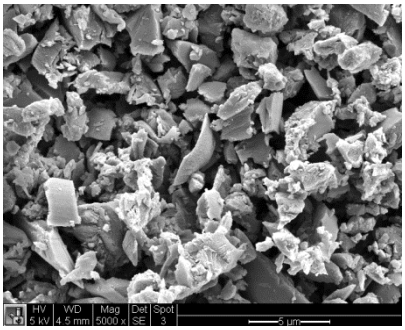
Stage 2(B)

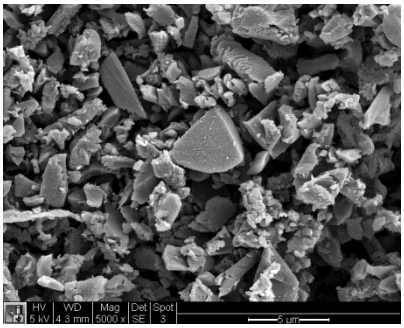
Stage 3 (C)

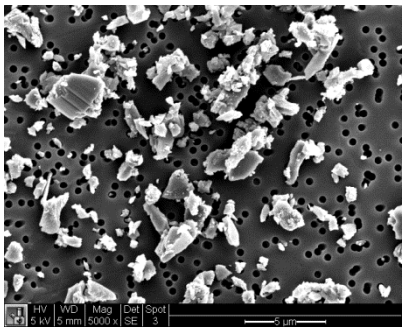
Stage 6 (backup)

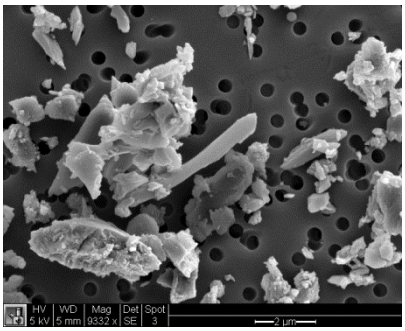
Stage 6 (backup)

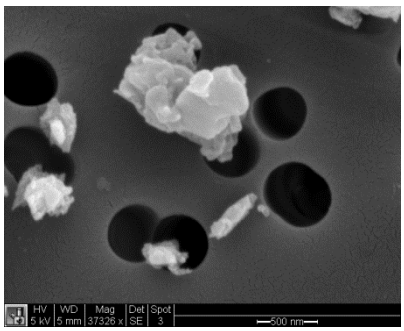
Stage 6 (backup)

APPENDIX A

Phase 2 Tests: Sample D2 Results

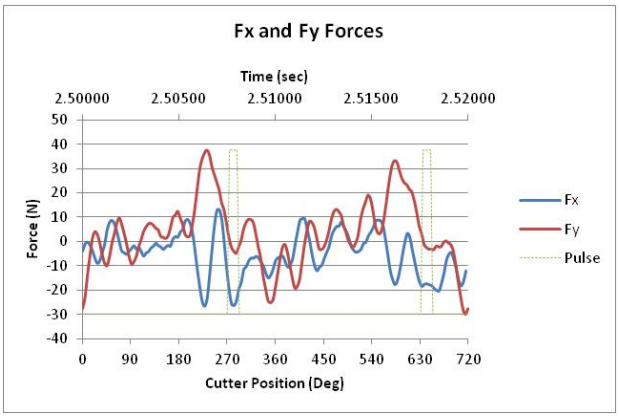

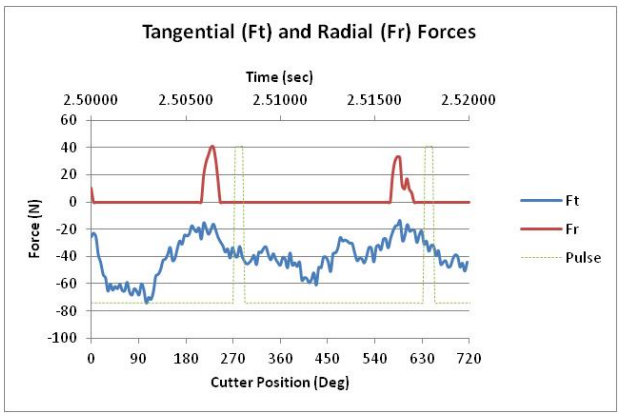

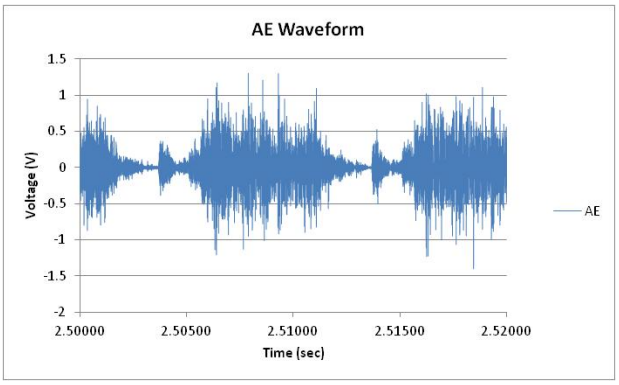

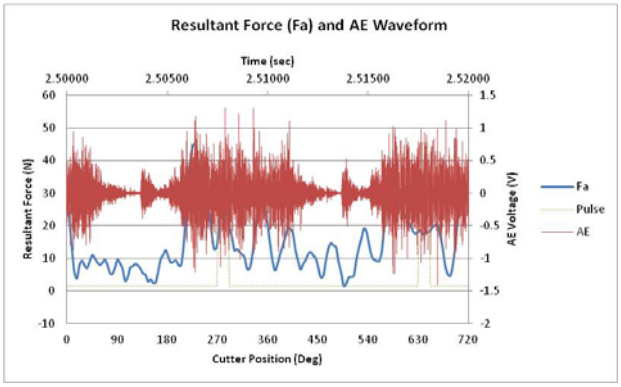

Meas. Instrum.:	Mahr Data Acquisition Board
Drive Unit:	GD 25
Pick-up:	MFW-250 [7.2 %]
Lt:	5.60 mm [N=5]
Ls:	2.5 µm
VB:	±250 µm
Vt:	0.50 mm/s
Points:	33600 [3]

	Ra µm	Rz µm	Rt µm	Rp µm
1:	0.762	5.456	7.00	2.71
2:	0.428	3.621	4.26	2.10
3:	6.912	34.825	41.47	11.81
Xb:	2.700	14.634	17.58	5.54
S:	3.651	17.510	20.74	5.43
Max:	6.912	34.825	41.47	11.81
Min:	0.428	3.621	4.26	2.10
R:	6.484	31.204	37.20	9.70

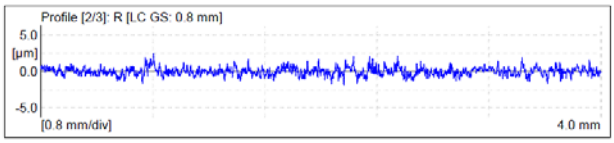

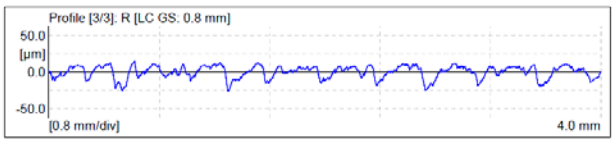

Longitudinal Surface Finish

Meas. Instrum.:	Mahr Data Acquisition Board
Drive Unit:	GD 25
Pick-up:	MFW-250 [7.2 %]
Lt:	1.75 mm [N=5]
Ls:	2.5 µm
VB:	±250 µm
Vt:	0.10 mm/s
Points:	10500 [3]

	Ra µm	Rz µm	Rt µm	Rp µm
1:	2.366	12.960	25.46	6.17
2:	2.941	14.083	27.14	6.34
3:	3.020	13.833	24.32	5.51
Xb:	2.776	13.625	25.64	6.01
S:	0.357	0.590	1.42	0.44
Max:	3.020	14.083	27.14	6.34
Min:	2.366	12.960	24.32	5.51
R:	0.655	1.124	2.82	0.83

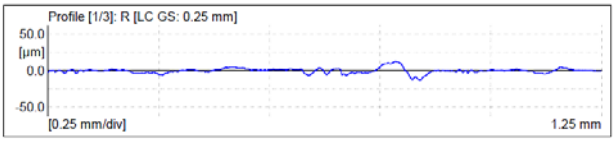

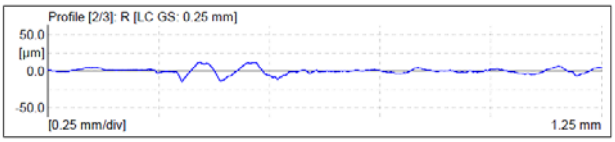

Transverse Surface Finish

Phase 2 Tests: Sample D2 Results (cont.)

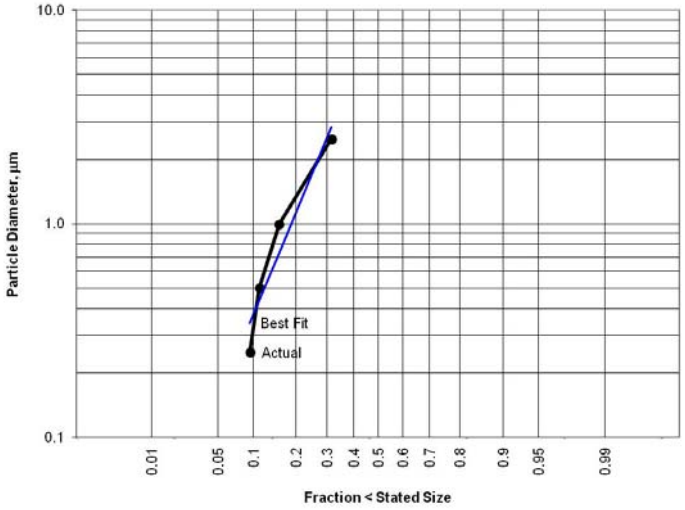

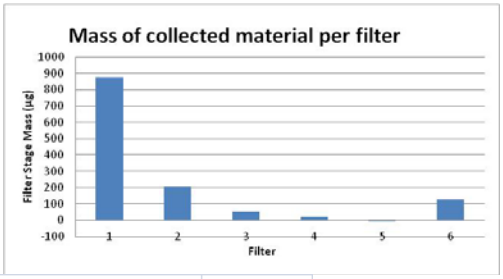

	Data from Best Log-Normal Fit			Data from Plot		
Median diameter, d50	9.50	µm	Median diameter, d50	#DIV/0!	µm	
σ_g	12.53					
r^2	0.920					

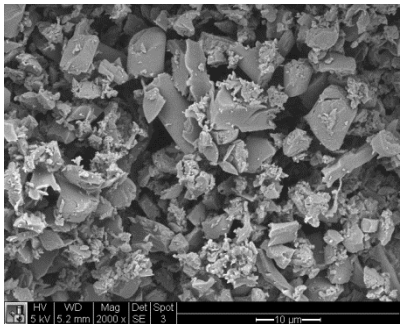

Stage 1 (A)

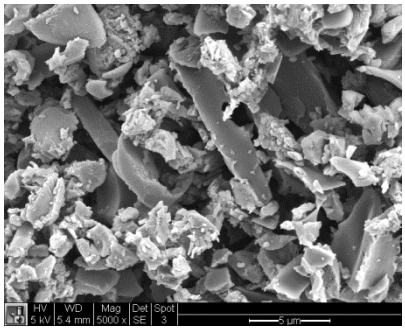

Stage 2(B)

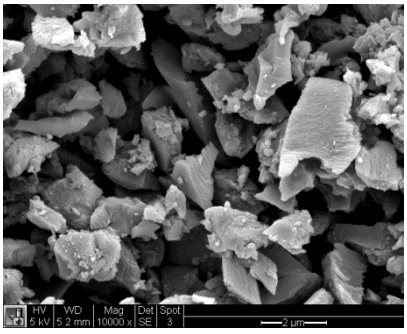

Stage 3 (C)

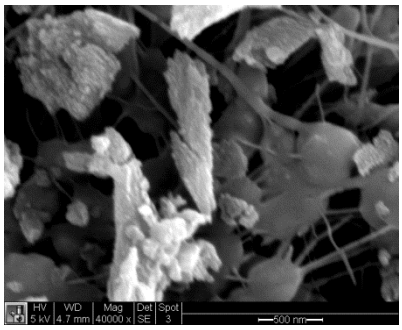

Stage 4 (D)

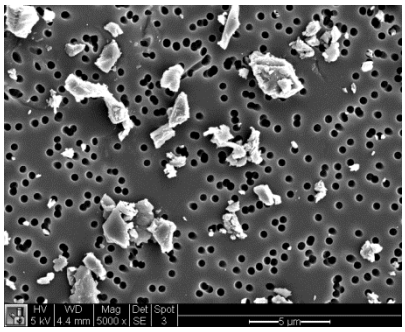

Stage 6 (backup)

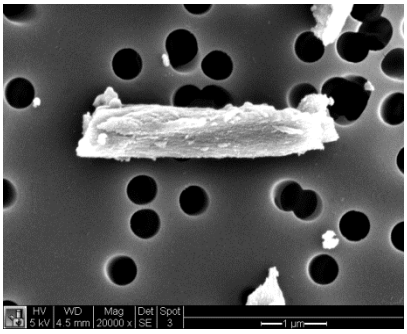

Stage 6 (backup)

APPENDIX A

Phase 2 Tests: Sample D3 Results

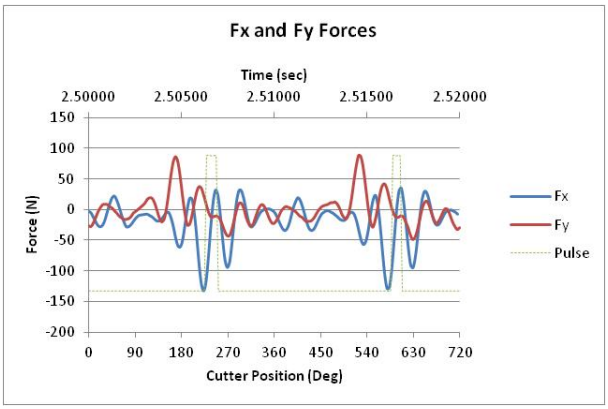

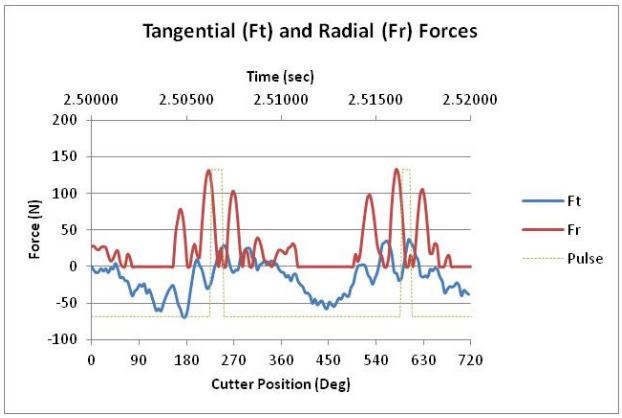

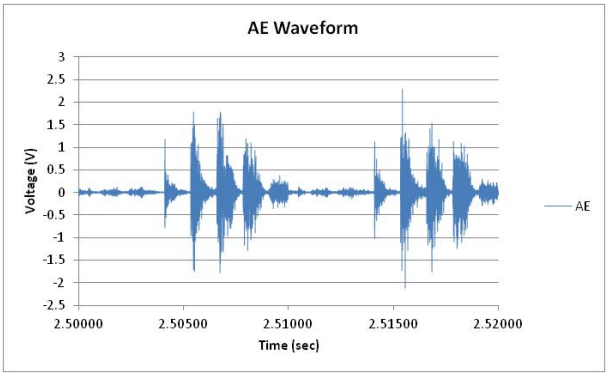

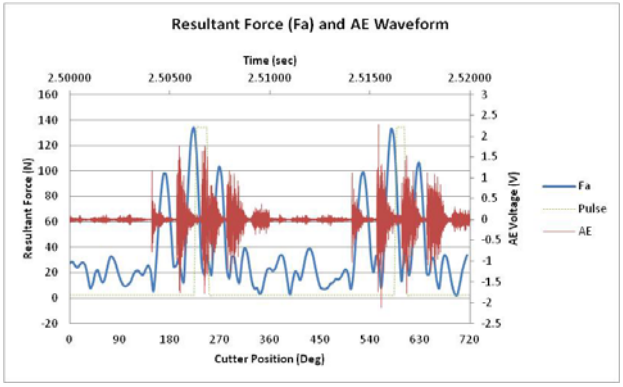

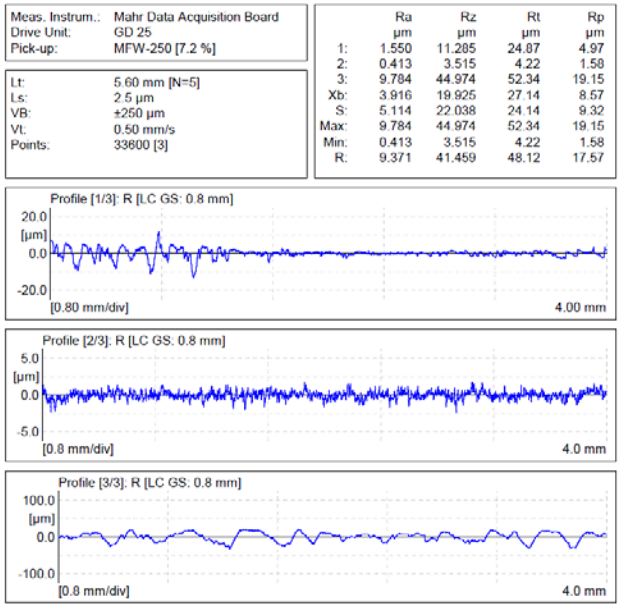

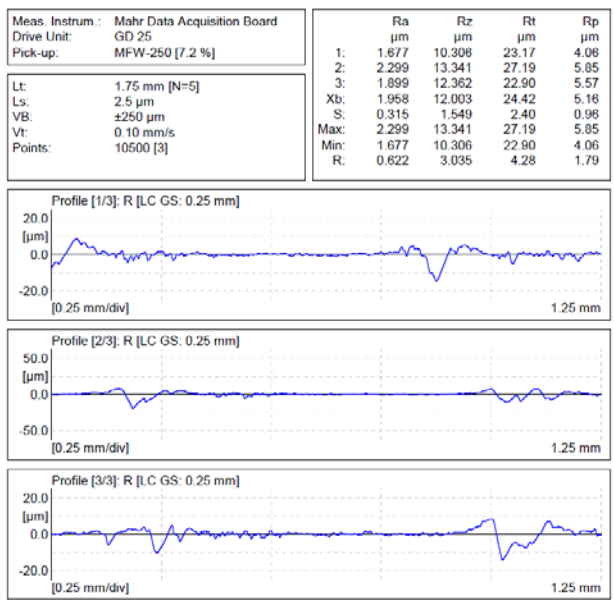

Longitudinal Surface Finish

Transverse Surface Finish

Phase 2 Tests: Sample D3 Results (cont.)

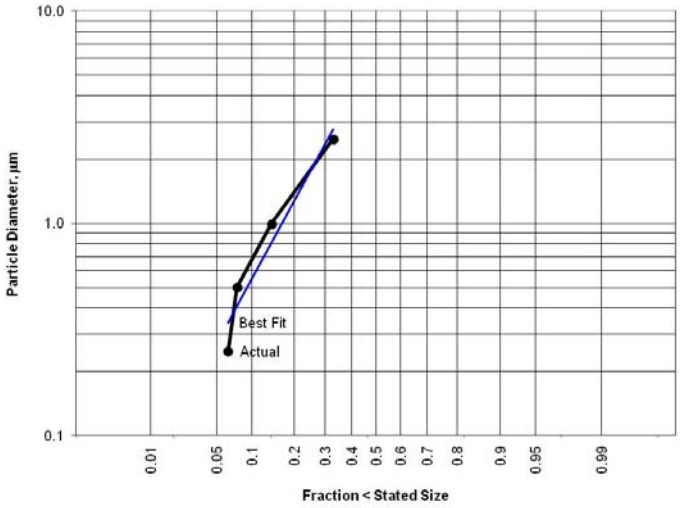

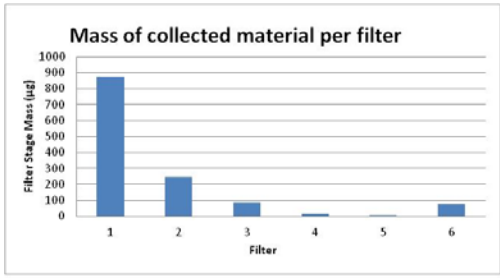

	Data from Best Log-Normal Fit			Data from Plot		
Median diameter, d50	6.53	µm	Median diameter, d50	#DIV/0!	µm	
σ_g	6.94					
r^2	0.933					

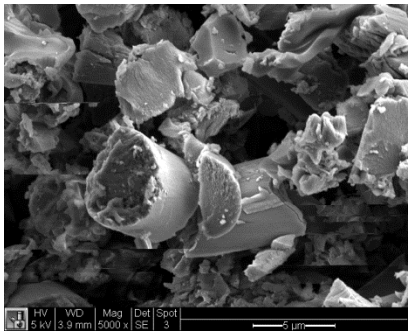
Stage 1 (A)

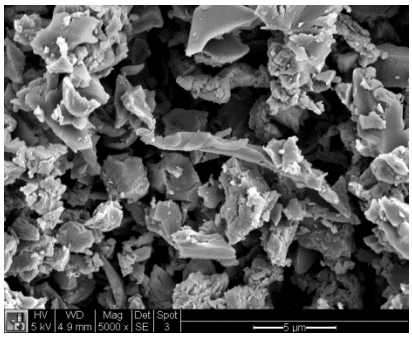
Stage 2(B)

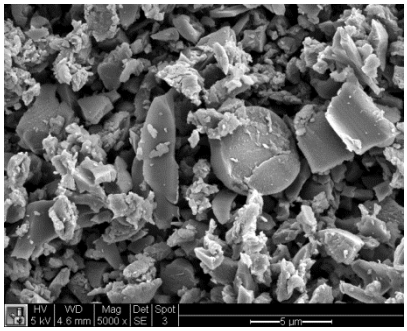
Stage 3 (C)

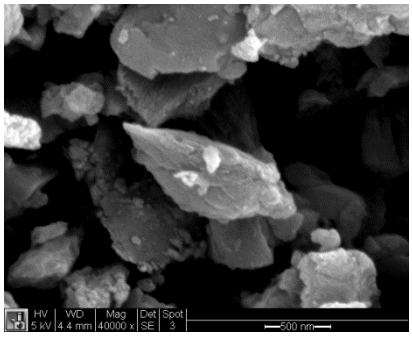
Stage 4 (D)

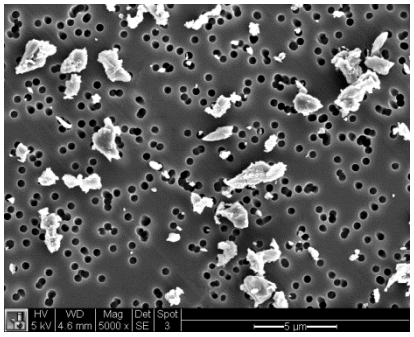
Stage 6 (backup)

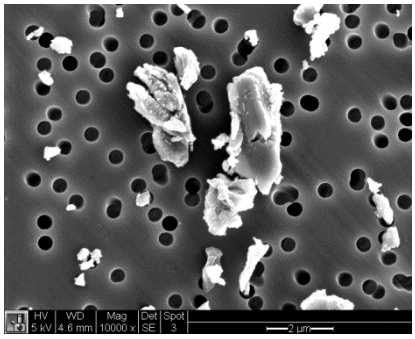
Stage 6 (backup)

APPENDIX B

Energy Dispersive X-Ray Spectroscopy Results

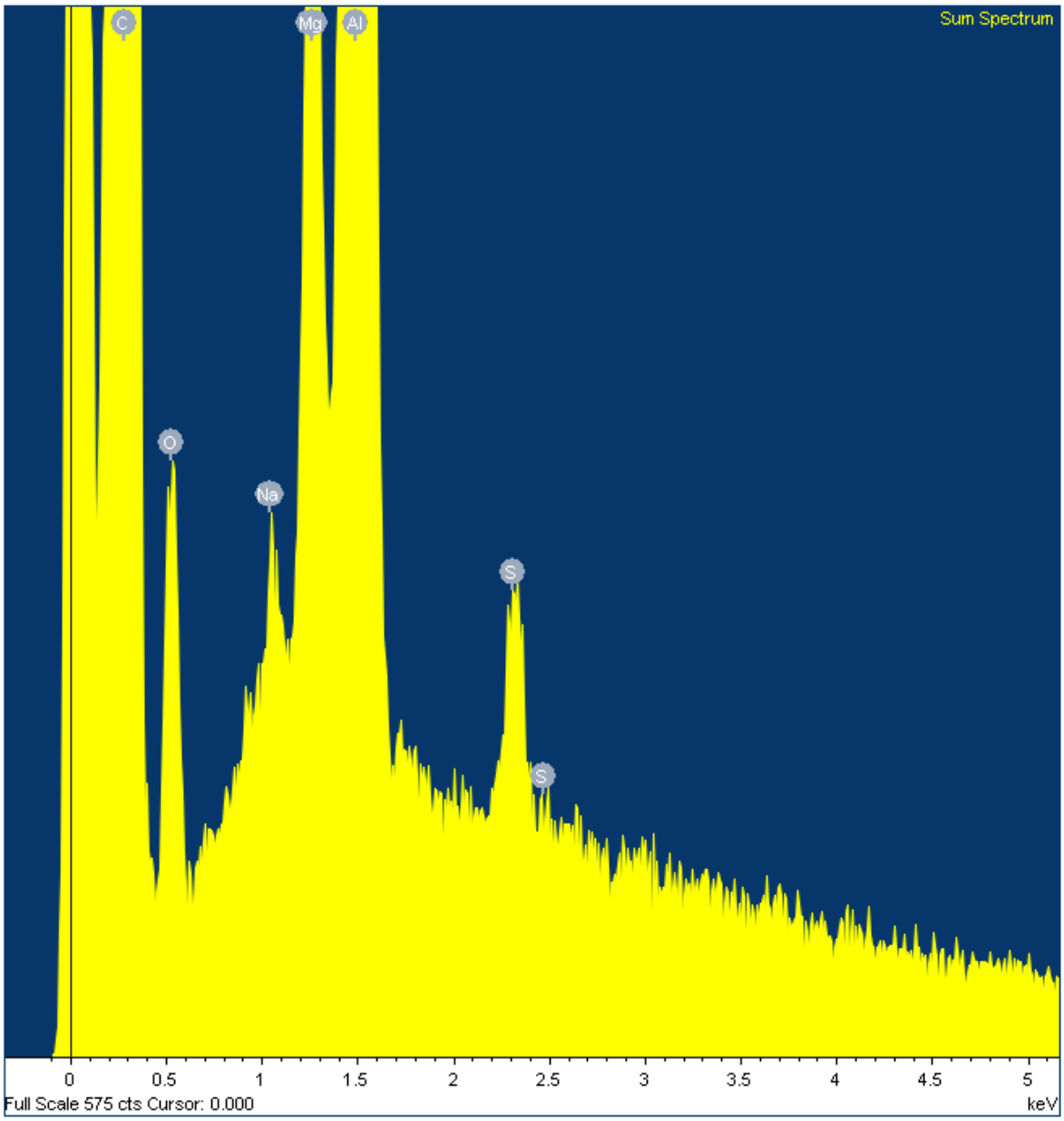

APPENDIX B

Phase 1 Tests: Energy Dispersive X-Ray Spectroscopy Results

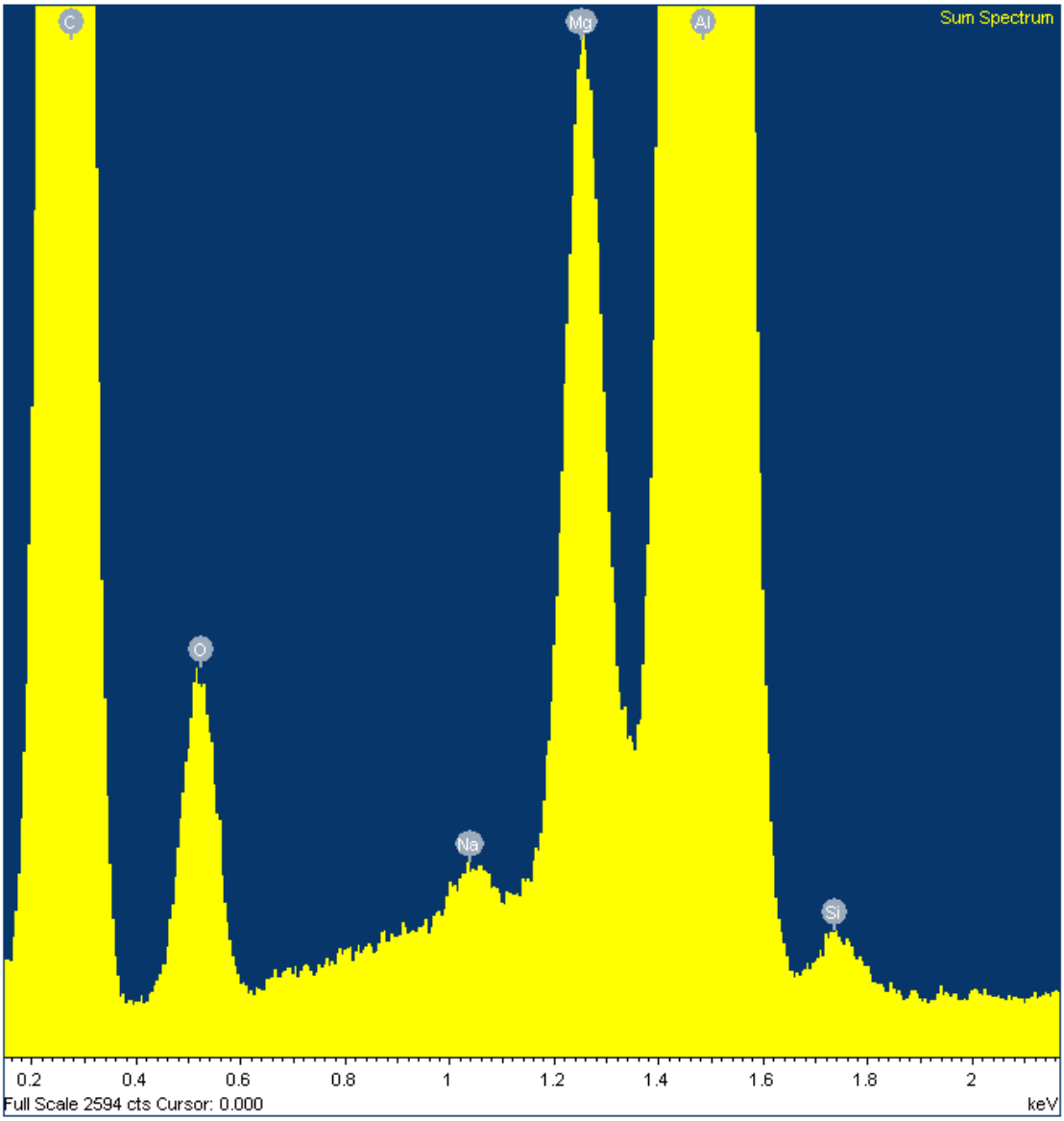

APPENDIX B

Phase 1 Tests: Energy Dispersive X-Ray Spectroscopy Results

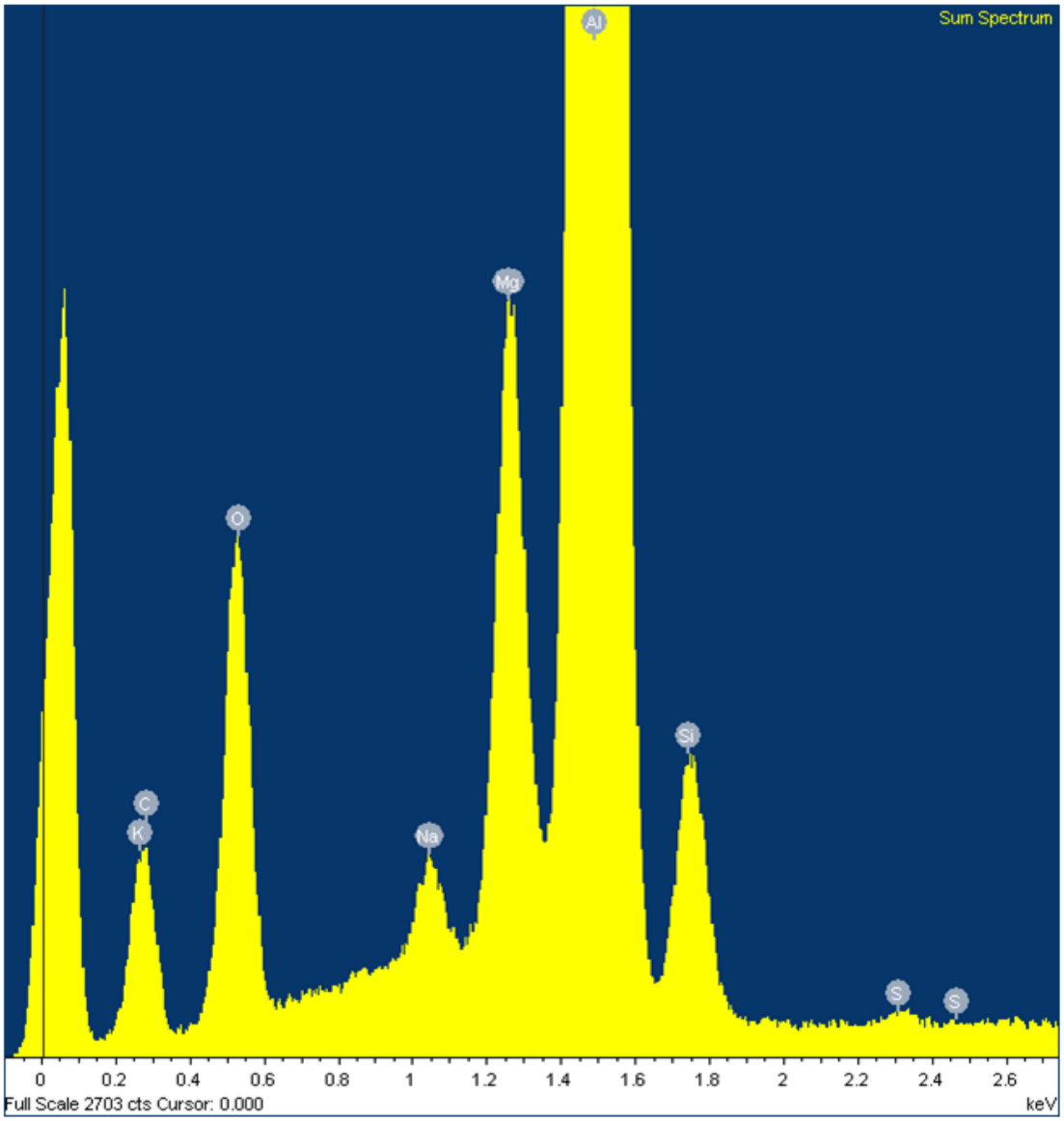

APPENDIX B

Phase 1 Tests: Energy Dispersive X-Ray Spectroscopy Results

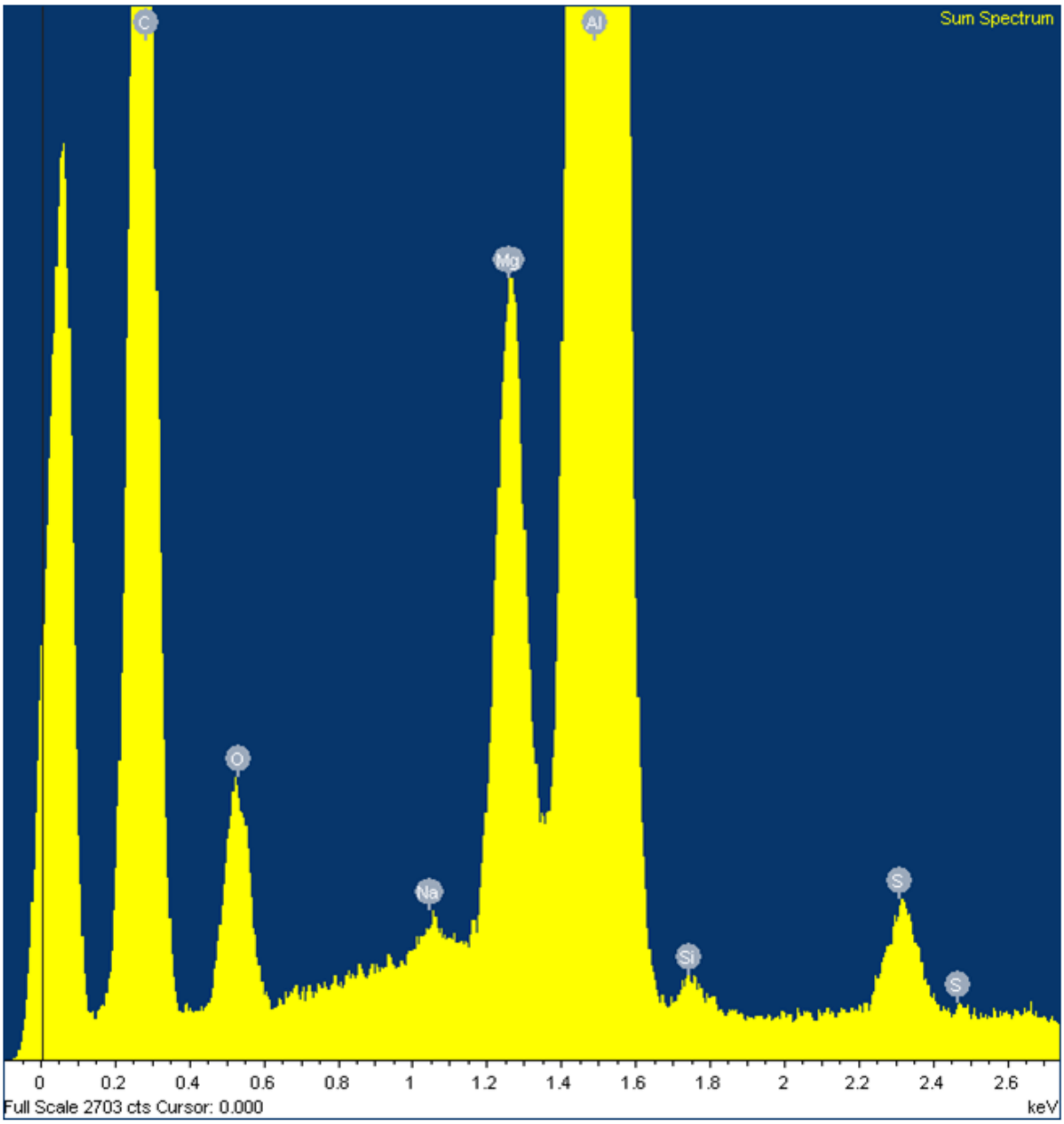

APPENDIX C

Real-time instrument estimation tool

The spreadsheet in Appendix B was developed to estimate potential particle count for sizing of real-time particle analysis instruments. Mass concentration estimates are provided directly by impactor test results. The user enters data directly from impactor experiments including an assumption for particle diameter which can be the MMAD. Output includes a range of particle count estimates depending on the number of impactor samples. This data is then used to evaluate the particle count range of the real-time analysis instrument. The estimated number of particles should not exceed the count capability of the instrument for the size ranges of interest. Sensitivity studies can be performed by modifying the input variables.

Date	4/14/2012	4/14/2013	4/14/2013
Impactor	A1	D4	E1
Input			
Impactor Sample Mass (µg)	282	115.25	73
Particle Density (g/cm3)	1.81	1.81	1.81
Particle Diameter (µm)	1	1	1
Sample Air Volume (liter)	139.4	55.3	52.4
Calculations (Output)			
Single Particle Volume (μm^3)	0.523598776	0.523598776	0.523598776
Particle Density ($\mu g/\mu m^3$)	0.00000181	0.00000181	0.00000181
Single Particle Mass (µg)	9.47714E-07	9.47714E-07	9.47714E-07
Total # of Particles in Sample Mass (#)	297558192	121608445	77027475
Sample Air Volume (cm^3)	139400	55300	52400
Number of Particles (#/cm^3)	**2,135**	**2,199**	**1,470**
Number of Particles (#/liter)	**2,134,564**	**2,199,068**	**1,469,990**

APPENDIX C

Comparison of real-time particle counters

The table in Appendix C is an example of the comparison performed when evaluating suitability of real-time particle counters for use in this application.

Parameter	**TSI OPS 3330**	**TSI DustTrak DRX 8533**	**GRIMM 1.109**	**PALAS PROMO 2000**	**TSI PTRAK 8525**
Measurement Principle	120 deg light collection (90 +/- 60 deg) laser	90 deg light scatter (total area and single particle detection) laser	90 degree light scatter, laser	White light and 90 deg light scatter (light bulb), not laser	
Particle Concentration Limit	3,000 particles/cm^3	Unknown	2,000 particles/cm^3	1,000,000 particles/cm^3, or min 200,000 particles/cm^3	500,000 particles/ cm^3
Mass Concentration Limit	275 mg/m^3	150 mg/m^3	100 mg/m^3	unknown	N/A
Particle Size Range	.3 to 10 micrometer	.1 to 15 micrometer	.25 to 32 micrometer	.2-10, .3-17.5, .6-40	.02 – 1 micrometer
Flow Rate	1 lpm + 1 lpm sheath	3 lpm (1 lpm is sheath)	1.2 lpm	5 lpm	.1 lpm, .7 lpm total
Factory Calibration	PSL spheres	Arizona Road Dust (A1 Test Dust)	PSL spheres	PSL spheres	Not sure
Channels	16 (.3 – 10 micrometer) by bin. selective	5 (PM1, PM2.5, PM4, PM10, Total) cumulative	32 (.25 – 32) fixed	32??	1
User Calibration Options	Dilution, refractive index, shape factor, density	Photometric Calibration Factor, Size Calibration Factor	C-Factor (mass)	Curve fit?	Zero count
Ease of User Calibration (opinion)	(refractive index and shape factor are complicated) No straight answers on how to do this.	SCF, PCF standard calibration is easy. Advanced calibration requires a PM2.5 and PM10 impactor, filters, and separate flow.	C-factor mass calibration appears easy using supplied 47mm filters.	Not sure.	N/A, zero count only
Output	Count, Mass Concentration, Surface Area (mass and surface area are derived by equations) by bin size	Mass Concentration by PM1, PM2.5, PM4, PM10, Total (cumulative). No count or surface area.	Count, Mass Concentration	Count, Mass Concentration	Counts, no size differential
Software	AIM (requires export of all samples for plots.)	TrakPro (graphs all samples, easy export)	Grimm 1178, not personally tested, UW happy with it.	PALAS PDcontrol	TrakPro (graphs all samples, easy export)
Price	$14,300 + tax = $15,658	$9,889.15 + tax	$16,950	$24,905	$5451 + tax
Warranty	1 year?, annual calibration	2 year	1yr, (used, 13hrs)	6 months (used)	2 year
PROs	Channels flexibility	Designed for dust	Range, C-factor, UW happy	Concentration limit	Easy
CONs	Concentration limit may require dilution, user calibration	Mass concentration only for 5 ranges. Calibration may not be accurate	Concentration limit may require dilution	Price, used, unknowns	Only .02 – 1 micron, no size differentiation

APPENDIX D

Impactor D4 results

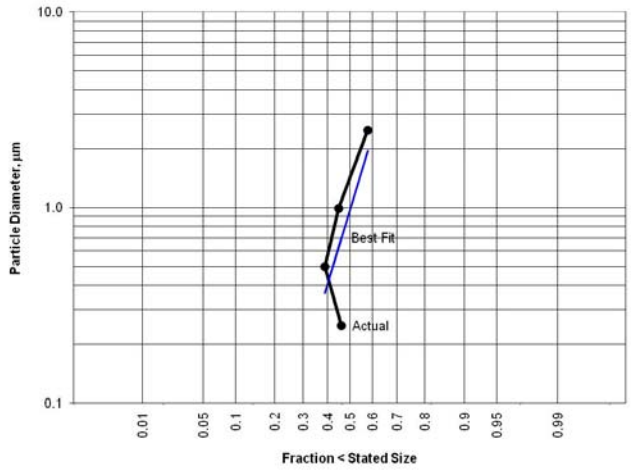

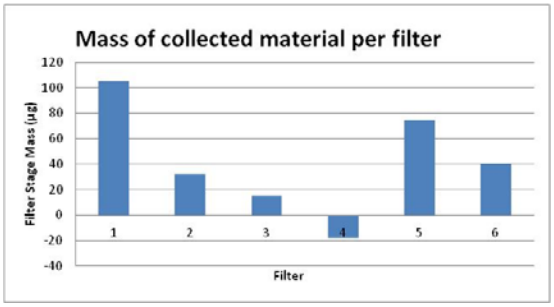

	Data from Best Log-Normal Fit			Data from Plot		
Median diameter, d50	0.97	µm	Median diameter, d50	1.43	µm	
σ_g	32.37					
r^2	0.502					

Mass Conc. **4.871 mg/m^3**

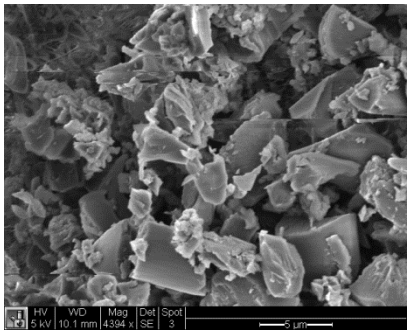

Stage 1 (A)

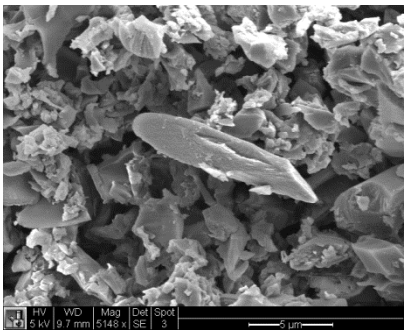

Stage 2 (B)

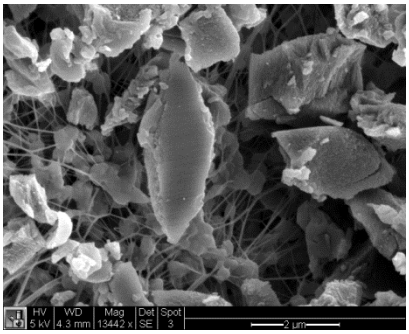

Stage 3 (C}

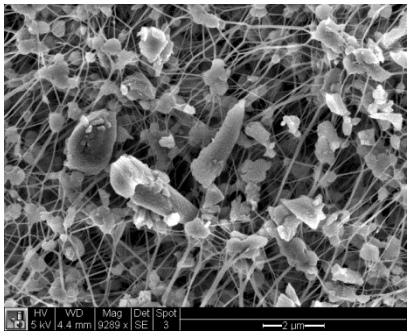

Stage 4 (D)

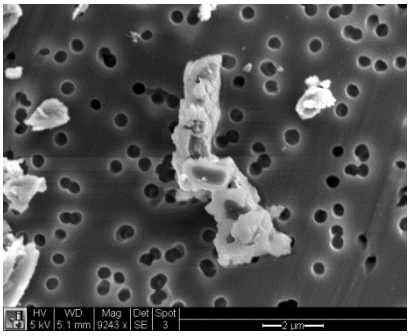

Stage 6 (backup)

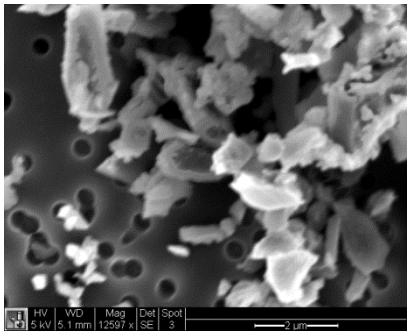

Stage 6 (backup)

APPENDIX D

Impactor E1 results

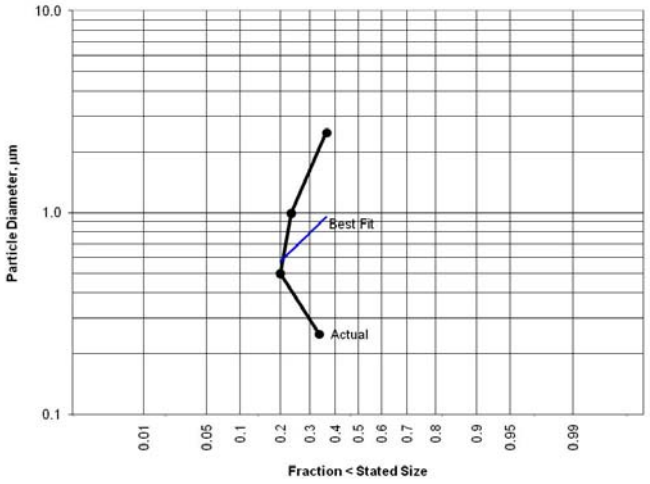

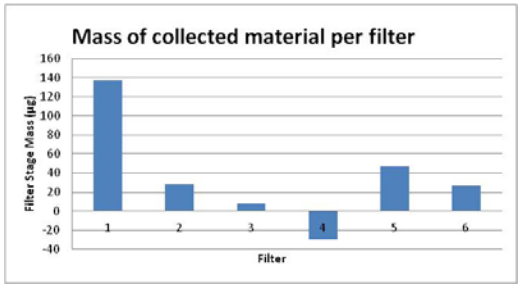

	Data from Best Log-Normal Fit			Data from Plot		
Median diameter, d50	1.36	µm	Median diameter, d50	#DIV/0!	µm	
σ_g	2.78					
r^2	0.062					

Mass Conc. **4.140 mg/m^3**

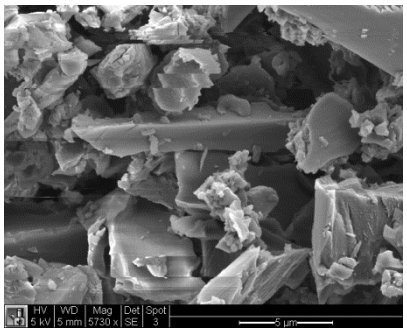

Stage 1 (A)

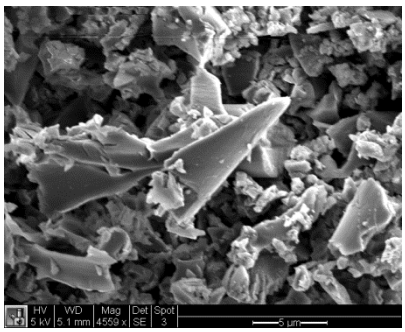

Stage 2 (B)

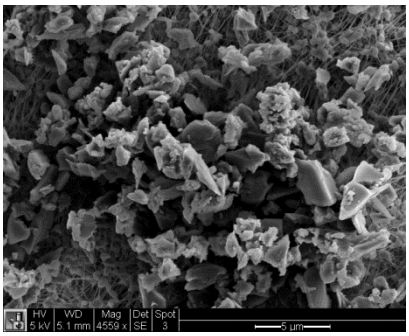

Stage 3 (C)

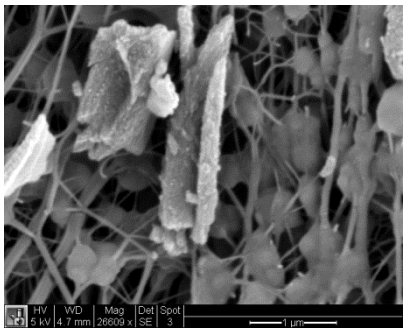

Stage 4 (D)

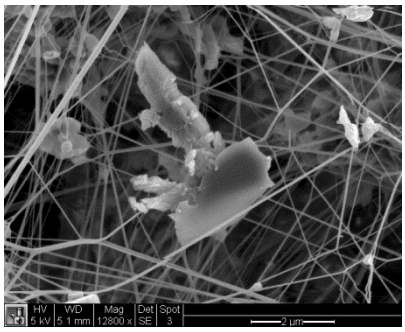

Stage 5 (backup)

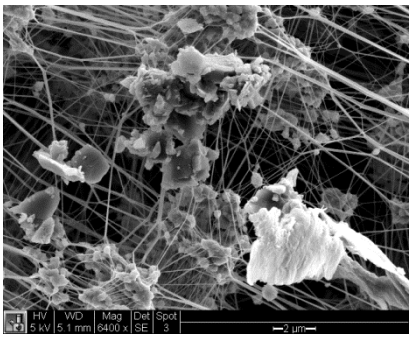

Stage 5 (backup)

APPENDIX E

Second round test results: test 1

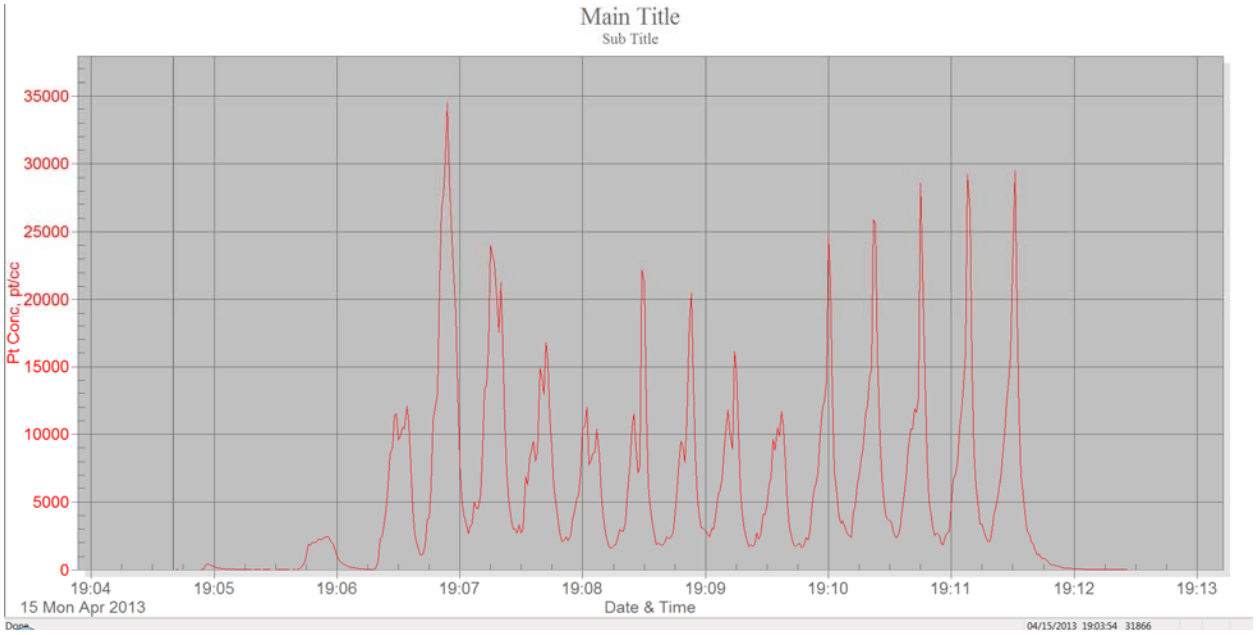

PTRAK 8525 results

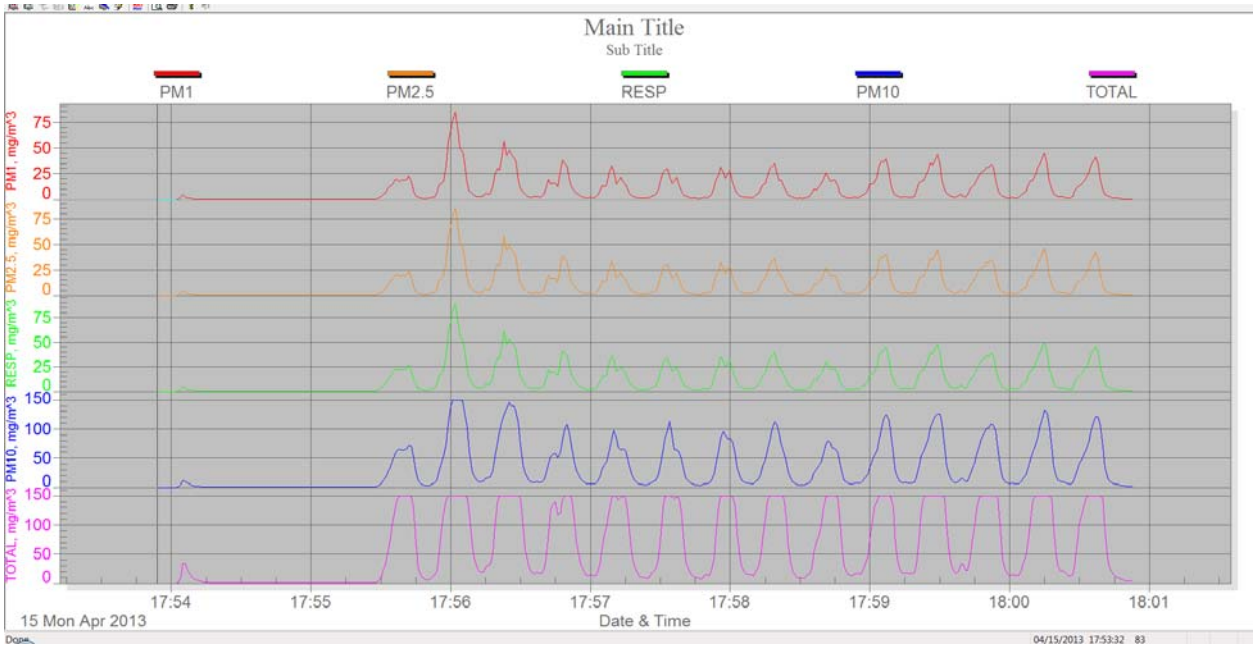

DustTRAK 8534 results

APPENDIX E

Second round test results: test 2

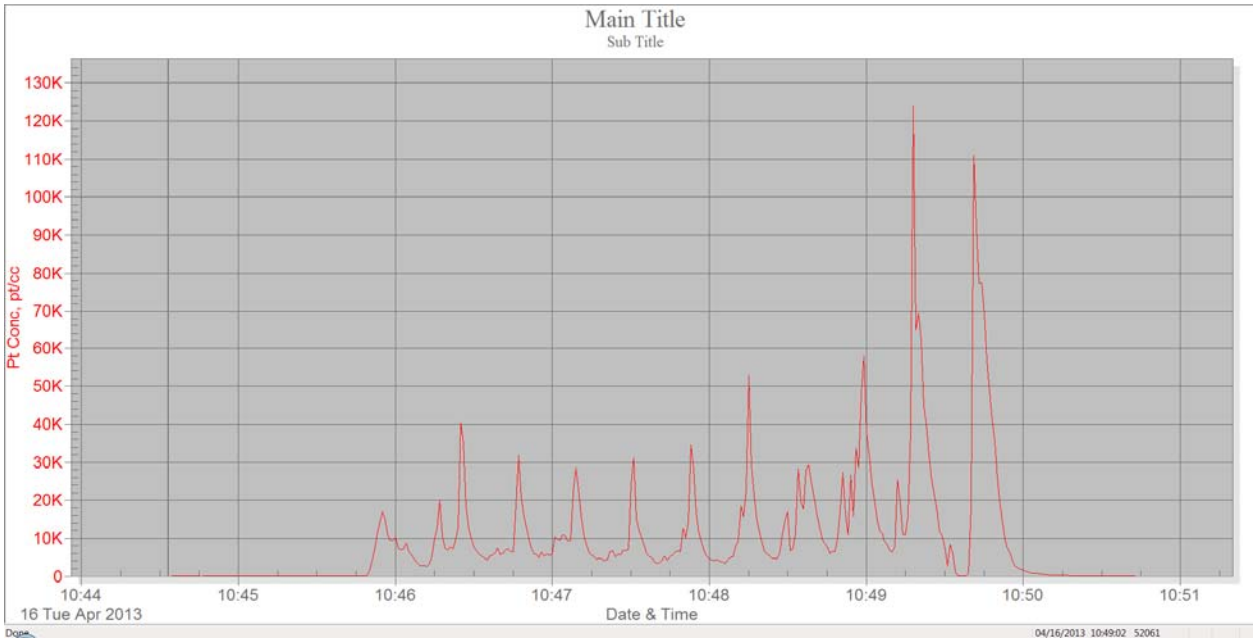

PTRAK 8525 results

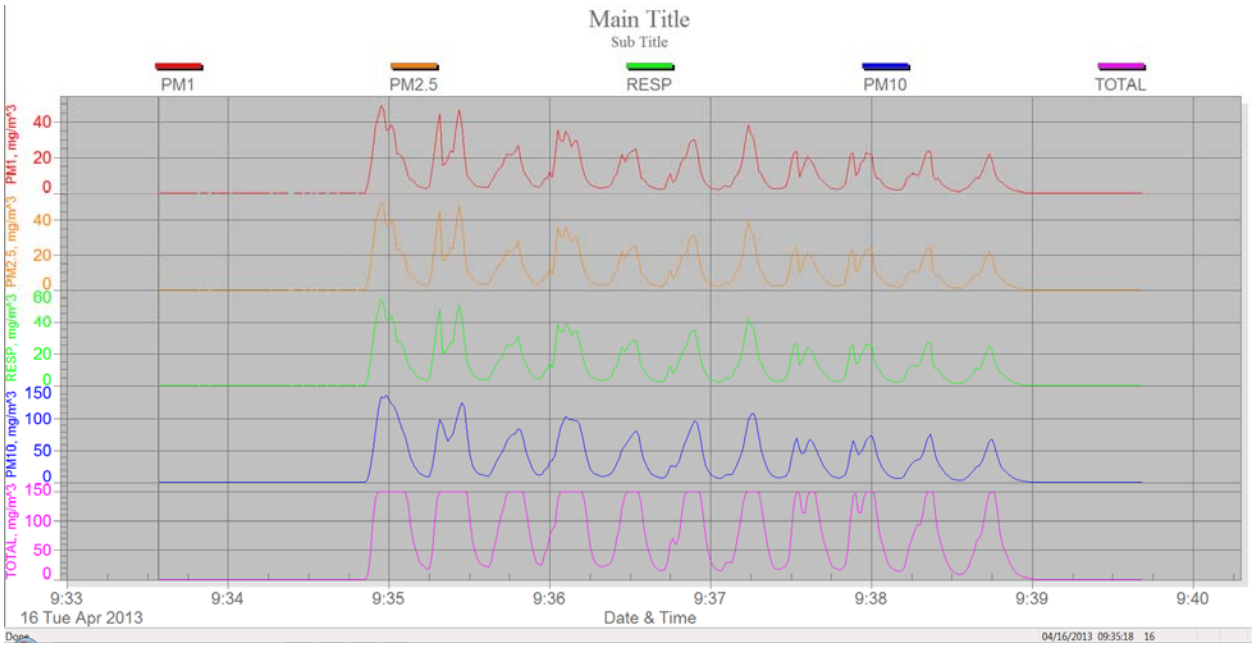

DustTRAK 8534 results

APPENDIX E

Second round test results: test 3

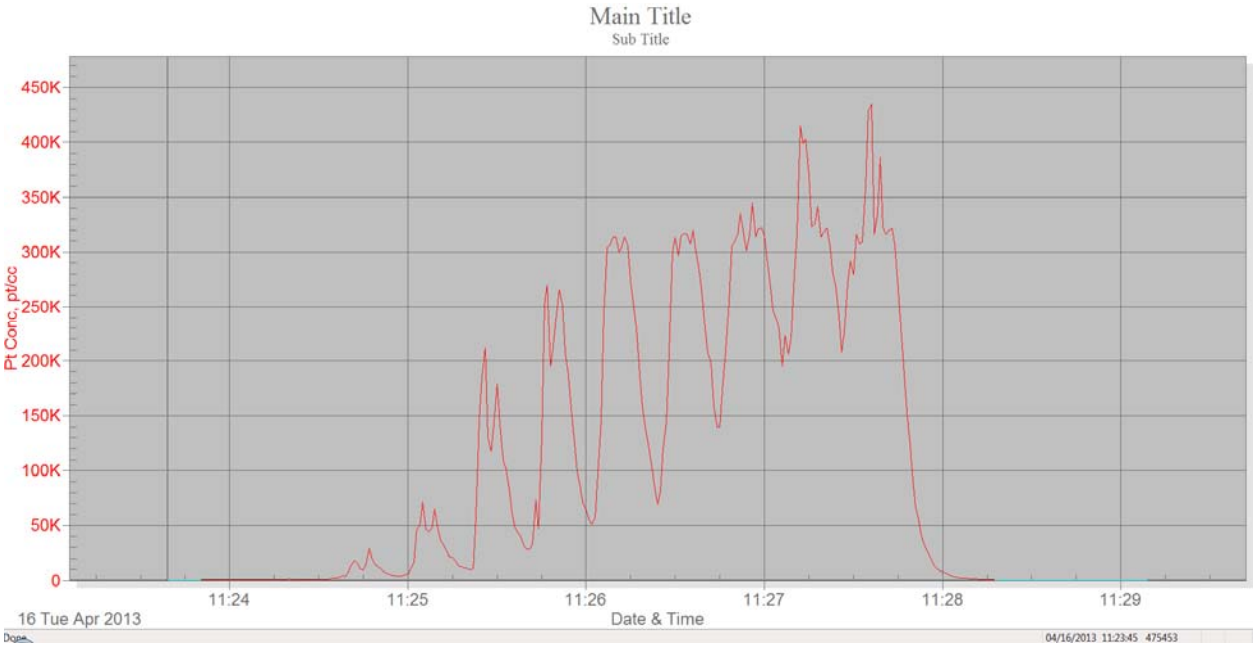

PTRAK 8525 results

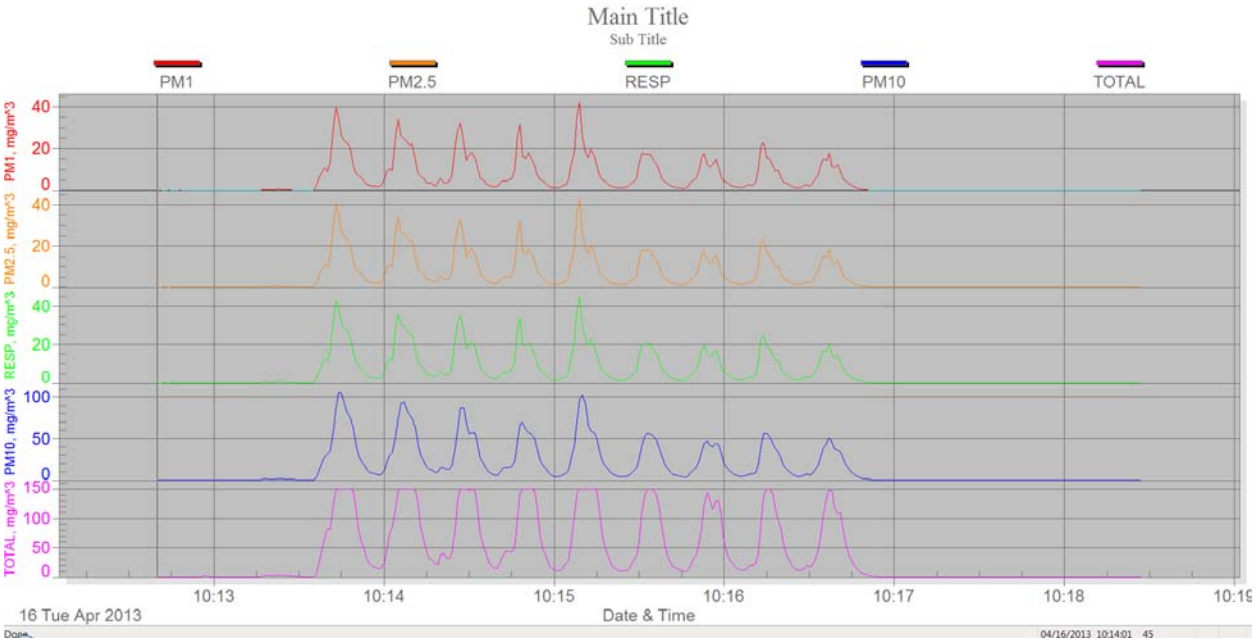

DustTRAK 8534 results

APPENDIX E

Second round test results: test 4

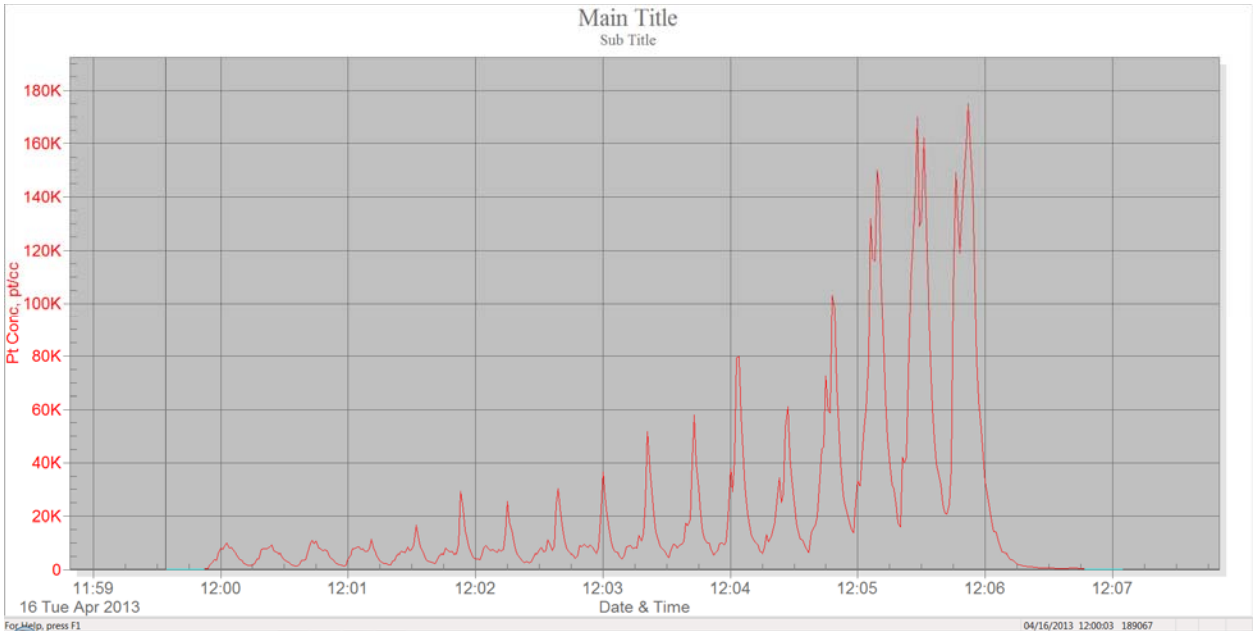

PTRAK 8525 results

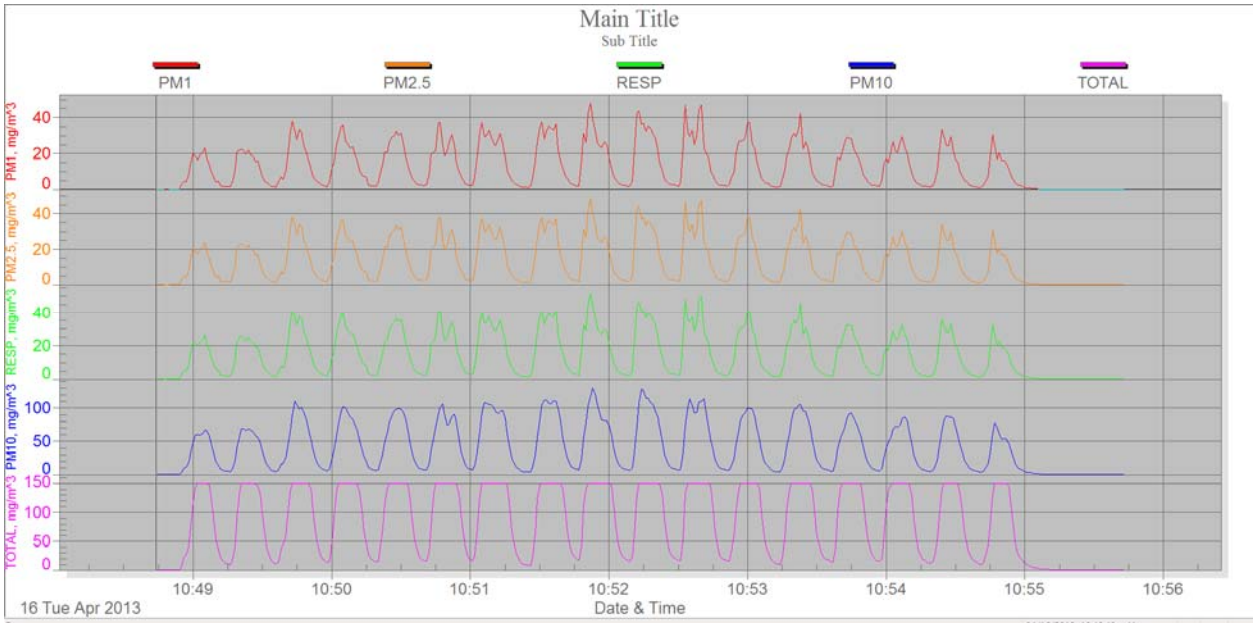

DustTRAK 8534 results

APPENDIX F

Third round test results: summary table

DATE	TEST	DESCRIPTION	P-TRAK	DUST-TRAK	OPS 3330	PDR-DataRam	Comment
5/3/2013	1	Vacuum Only: (Test chamber with vacuum only)	001: OK 105 pts avg: 25 max: 401	001: OK 3 min Avg: .064	Vacuum Only: OK 30 samples		No cutting
5/3/2013	2	Spindle On with Vacuum: (Test chamber with vacuum and spindle on at 6000rpm)	002: OK 213 pts avg: 962 max: 1660	002: OK 3 min Avg: .024	Spindle On: OK 30 samples	?? 0 Possible prob.	No cutting
5/3/2013	3	Set Size Correction Factor (SCF) on DustTrak	003: OK 463 pts avg: 5097 max: 45100	No data since SCF calibration	SFFdusttrak: OK 30 samples	SCF5-13: OK Avg: 1.510	New 4-flute carbide cutter Multi laminate Top half
5/4/2013	4	Photometric Correction Factor (PCF) for DustTrak	004: OK 652 pts Avg: 116856 Max: 500000	003: error Max 150 Resp max: 71.2 Avg2.5: 17.00	PCF Run 1: bad 1 sample only	PCFA413: OK Avg: 2.8	Same cutter as 3 Bottom and full laminate
5/4/2013	5	Photometric Correction Factor (PCF) for DustTrak	005: OK 412 pts Avg: 279179 Max: 500000	004: OK Max: 61.7 Resp Max: 56.5 Avg 2.5: 14.9	PF Run 2: OK 60 samples	PCFB413: OK Avg: 1.49	Same cutter as 3 .5 inch full cut multi lam.
5/5/2013	6	Use SCF=.570 PCF = 2.068 on DustTrak + 2.5 impactor on Dust	006: OK 471 pts Avg: 4839 Max: 25600	005: OK Max: 38.5 Resp Max: 36.8 Avg 2.5: 10.6	Impactor2.5run1: OK 70 samples	IMPA5-5: OK Avg. 1.619	New cutter top multi laminate
5/5/2013	7	Use SCF=.570 PCF = 2.068 on DustTrak + 2.5 impactor on Dust	008: OK 471 pts Avg: 35187 Max: 313000	007: OK Max: 35.8 Resp Max: 33.8 Avg 2.5: 9.990	Impactor2.5run2: OK 60 samples	IMPB5-5: OK Avg. 1.149	Same cutter as 6 bottom of laminate
5/5/2013	8	Use 4Fl Mapal Cutter from D1 impactor test	009: OK 411 pts Avg: 9670 Max: 106000	008: OK Max: 86.8 Resp Max: 84.4 Avg 2.5: 12.2	Mapal 4fl D1: OK 60 samples	D4RUN1: OK Avg. 1.34	Top half of multi laminate
5/5/2013	9	Use 4Fl Mapal Cutter from D1 impactor test	010: OK 457 pts Avg: 7885 Max: 30000	009: OK Max: 79.5 Resp Max: 75.3 Avg 2.5: 23.1	Mapal 4fl D1 run 2: OK 60 samples	D4RUN2: OK Avg: 2.47	Bottom half of multi laminate same cutter as 8

APPENDIX F

Third round test results: observations

- OPS 3330 will not provide mass concentration with coincidence errors, which happens frequently. Concentration may be an issue.
- PDR DataRam seems to consistently provide concentrations at 1/10 of the DustTrak.
- P-Trak has significantly higher counts when compared to OPS 3330. This is may be because particles are less than .3 µm, which is the lower bound of the OPS 3330. The P-Trak has a lower bound of .02 µm.
- Impactor concentration values are lower than DustTrak and higher than PDR DataRam.
- All instruments seem to pick up consistent dust profile.

Possible Solutions

- Use a diluter on the OPS 3330. Grimm 1108 or 1109 will likely have the same issues.
- Reposition inlet tubing to reduce concentration.
- Review PDR DataRam settings (I can't seem to find a problem)

APPENDIX F

Third round test results: test 1

- Purpose: Record efficiency of chamber
- Conditions: Vacuum only
- Other: New shop Vac HEPA Filters
- **PTRAK 8525 Results**

Test 001

Instrument		Data Properties	
Model	P-Trak	Start Date	05/03/2013
Meter S/N	8525-02130002	Start Time	17:54:49
		Stop Date	05/03/2013
		Stop Time	17:56:34
		Total Time	0:00:01:45
		Logging Interval	1 seconds

Statistics	
	Pt Conc
Avg	25 pt/cc
Max	401 pt/cc
Max Date	05/03/2013
Max Time	17:54:50
Min	0 pt/cc
Min Date	05/03/2013
Min Time	17:55:30
TWA (8 hr)	
TWA Start Date	
TWA Start Time	
TWA End Time	

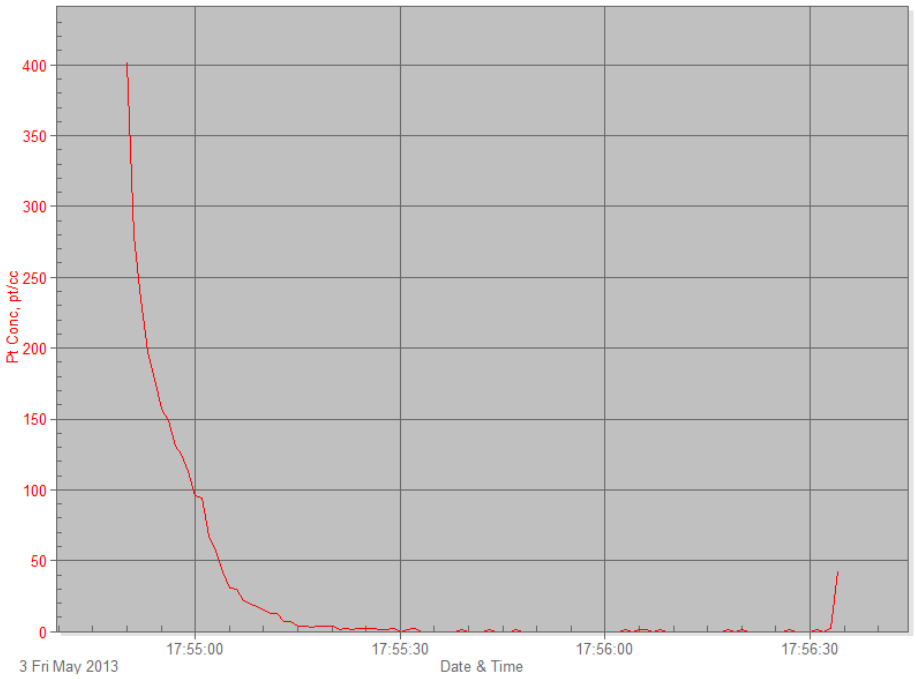

APPENDIX F

Third round test results: test 1

- Purpose: Record efficiency of chamber
- Conditions: Vacuum only
- Comment: Values are cumulative per TSI
- **DustTRAK 8533**

Test 001

Instrument		Data Properties	
Model	DustTrak DRX	Start Date	05/03/2013
Instrument S/N	8533101508	Start Time	17:26:57
		Stop Date	05/03/2013
		Stop Time	17:29:57
		Total Time	0:00:03:00
		Logging Interval	3 seconds

Statistics					
	PM1	PM2.5	RESP	PM10	TOTAL
Avg	0.017 mg/m^3	0.018 mg/m^3	0.020 mg/m^3	0.045 mg/m^3	0.064 mg/m^3
Max	0.188 mg/m^3	0.193 mg/m^3	0.219 mg/m^3	0.565 mg/m^3	0.834 mg/m^3
Max Date	05/03/2013	05/03/2013	05/03/2013	05/03/2013	05/03/2013
Max Time	17:27:33	17:27:33	17:27:33	17:27:33	17:27:33
Min	0.001 mg/m^3	0.001 mg/m^3	0.001 mg/m^3	0.001 mg/m^3	0.001 mg/m^3
Min Date	05/03/2013	05/03/2013	05/03/2013	05/03/2013	05/03/2013
Min Time	17:29:45	17:29:45	17:29:57	17:29:57	17:29:57
TWA (8 hr)	N/A	N/A	N/A	N/A	N/A
TWA Start Date	05/03/2013	05/03/2013	05/03/2013	05/03/2013	05/03/2013
TWA Start Time	17:26:57	17:26:57	17:26:57	17:26:57	17:26:57
TWA End Time	17:29:57	17:29:57	17:29:57	17:29:57	17:29:57

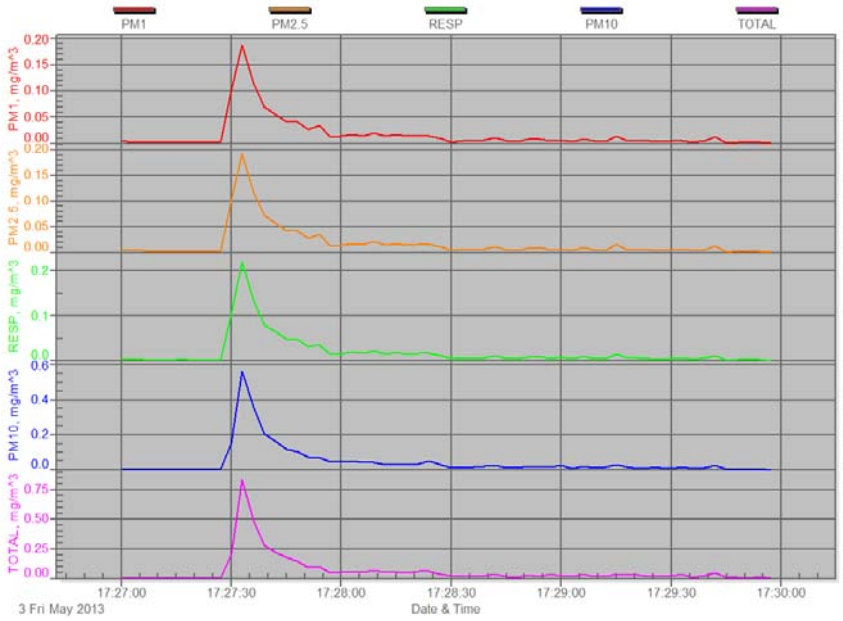

APPENDIX F

Third round test results: test 1

- Purpose: Record efficiency of chamber
- Conditions: Vacuum only
- Other: New shop Vac HEPA Filters
- **TSI OPS 3330**

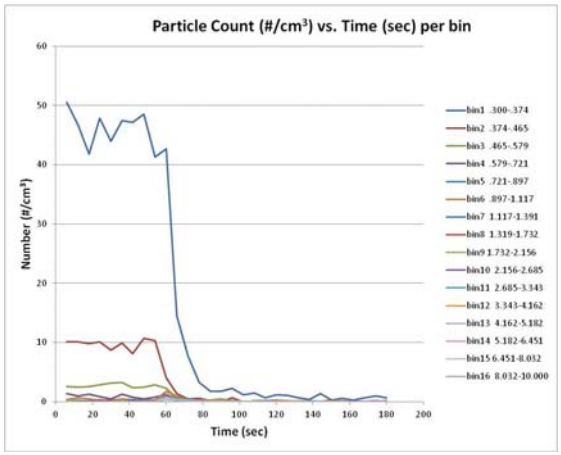

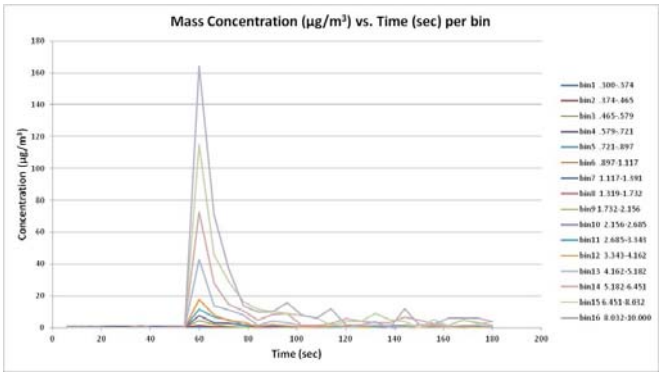

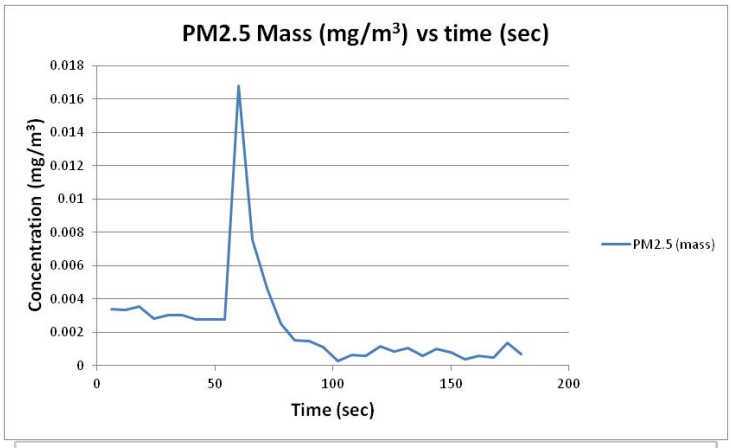

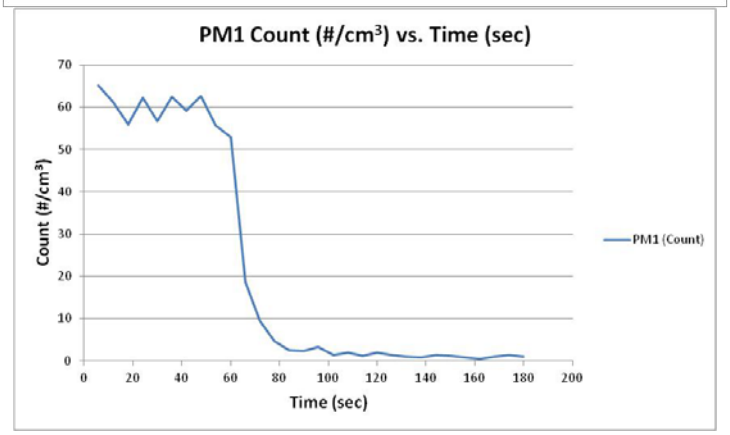

APPENDIX F

Third round test results: test 2

- Purpose: Record efficiency of chamber with spindle running at 6000 rpm
- Conditions: Vacuum on, Spindle on at 6000RPM
- **PTRAK 8525**

Instrument		Data Properties	
Model	P-Trak	Start Date	05/03/2013
Meter S/N	8525-02130002	Start Time	18:04:07
		Stop Date	05/03/2013
		Stop Time	18:07:40
		Total Time	0:00:03:33
		Logging Interval	1 seconds

Statistics	
	Pt Conc
Avg	962 pt/cc
Max	1660 pt/cc
Max Date	05/03/2013
Max Time	18:04:36
Min	391 pt/cc
Min Date	05/03/2013
Min Time	18:04:12
TWA (8 hr)	
TWA Start Date	
TWA Start Time	
TWA End Time	

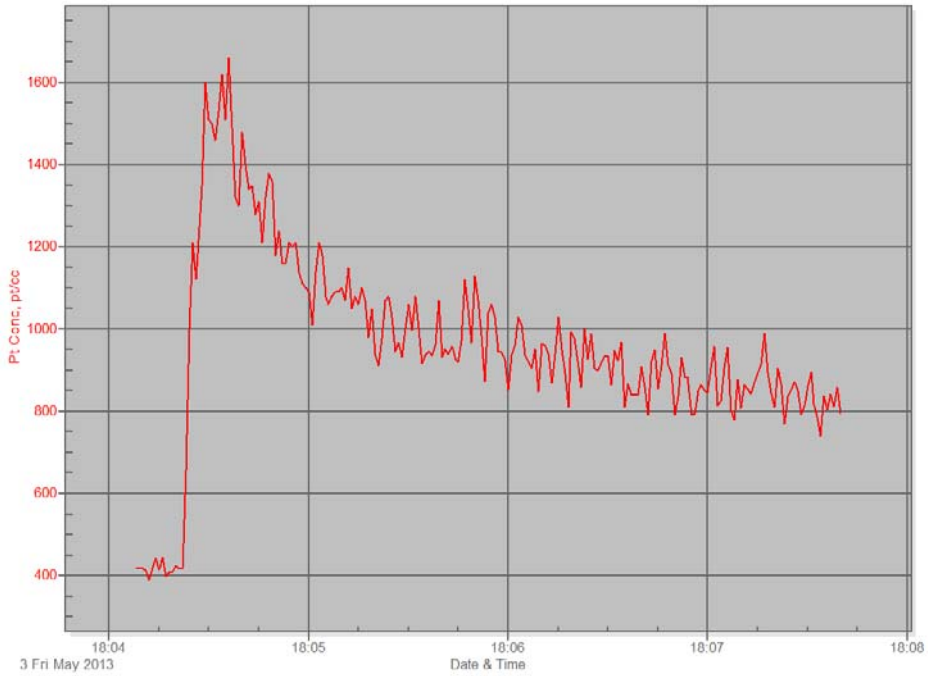

APPENDIX F

Third round test results: test 2

- Purpose: Record efficiency of chamber with spindle running at 6000 rpm
- Conditions: Vacuum on, Spindle on at 6000RPM
- Comment: Values are cumulative per TSI
- **DustTRAK 8533**

Test 002

Instrument		Data Properties	
Model	DustTrak DRX	Start Date	05/03/2013
Instrument S/N	8533101508	Start Time	17:51:21
		Stop Date	05/03/2013
		Stop Time	17:54:21
		Total Time	0:00:03:00
		Logging Interval	3 seconds

Statistics					
	PM1	PM2.5	RESP	PM10	TOTAL
Avg	0.017 mg/m^3	0.017 mg/m^3	0.018 mg/m^3	0.021 mg/m^3	0.024 mg/m^3
Max	0.066 mg/m^3	0.070 mg/m^3	0.071 mg/m^3	0.080 mg/m^3	0.103 mg/m^3
Max Date	05/03/2013	05/03/2013	05/03/2013	05/03/2013	05/03/2013
Max Time	17:51:45	17:51:45	17:51:45	17:51:45	17:53:06
Min	0.001 mg/m^3	0.001 mg/m^3	0.001 mg/m^3	0.001 mg/m^3	0.001 mg/m^3
Min Date	05/03/2013	05/03/2013	05/03/2013	05/03/2013	05/03/2013
Min Time	17:51:24	17:51:24	17:51:24	17:51:24	17:51:24
TWA (8 hr)	N/A	N/A	N/A	N/A	N/A
TWA Start Date	05/03/2013	05/03/2013	05/03/2013	05/03/2013	05/03/2013
TWA Start Time	17:51:21	17:51:21	17:51:21	17:51:21	17:51:21
TWA End Time	17:54:21	17:54:21	17:54:21	17:54:21	17:54:21

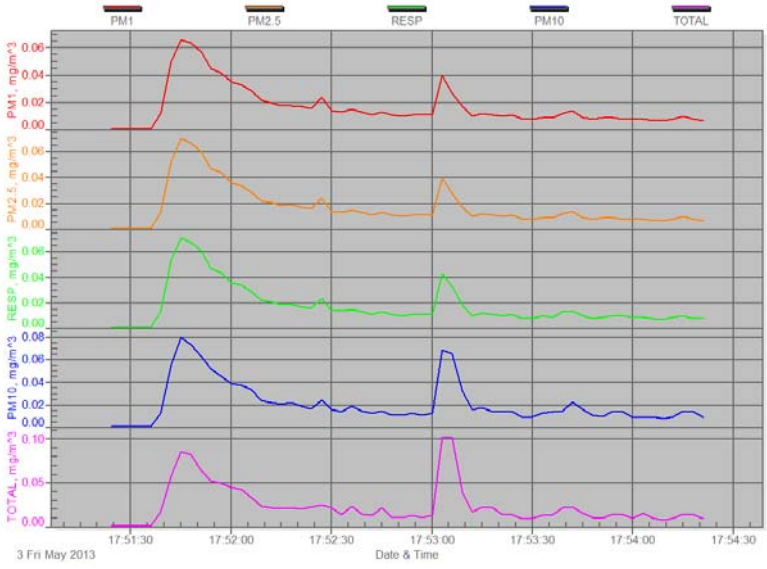

APPENDIX F

Third round test results: test 2

- Purpose: Record efficiency of chamber with spindle running at 6000 rpm
- Conditions: Vacuum on, Spindle on at 6000RPM
- **OPS 3330**

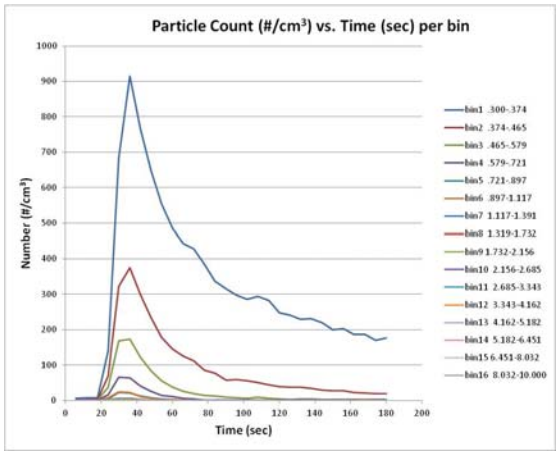

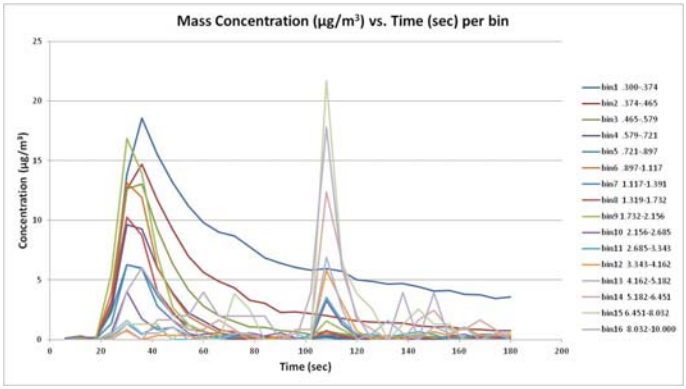

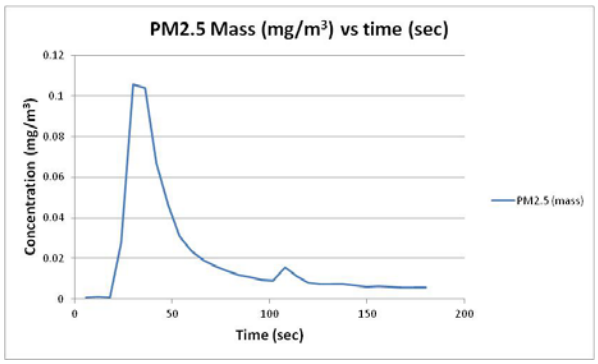

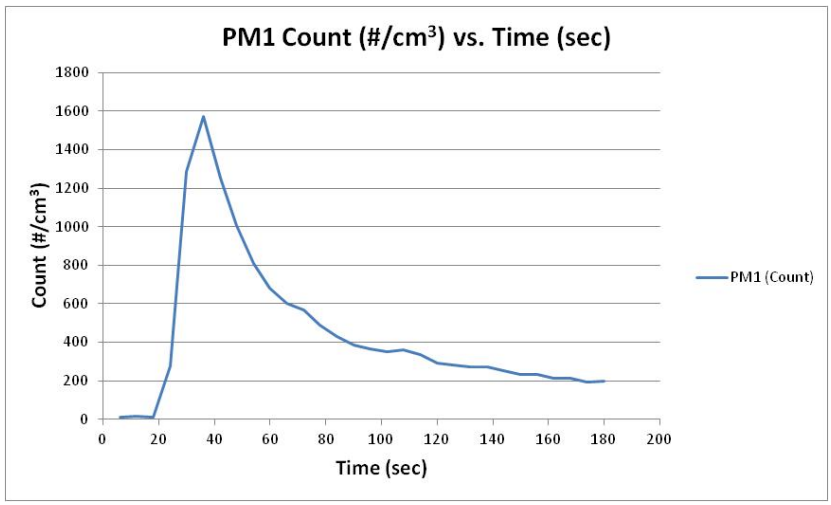

APPENDIX F

Third round test results: test 3

- Purpose: Size Correction Factor (SCF) Runs for Dust-Trak per manual
- Conditions: New carbide cutter, 6000 rpm, 635 mm/min feed, .762 radial depth of cut, 6.35mm axial depth of cut, climb multi-directional laminate, top half.
- Comment: Double peaks because 2, 2 minute runs per instructions, with a 30sec – 1min pause during changeover
- **PTRAK 8525**

Instrument		Data Properties	
Model	P-Trak	Start Date	05/03/2013
Meter S/N	8525-02130002	Start Time	18:54:13
		Stop Date	05/03/2013
		Stop Time	19:01:56
		Total Time	0:00:07:43
		Logging Interval	1 seconds

Statistics	
	Pt Conc
Avg	5097 pt/cc
Max	45100 pt/cc
Max Date	05/03/2013
Max Time	19:00:25
Min	3 pt/cc
Min Date	05/03/2013
Min Time	18:58:43
TWA (8 hr)	
TWA Start Date	
TWA Start Time	
TWA End Time	

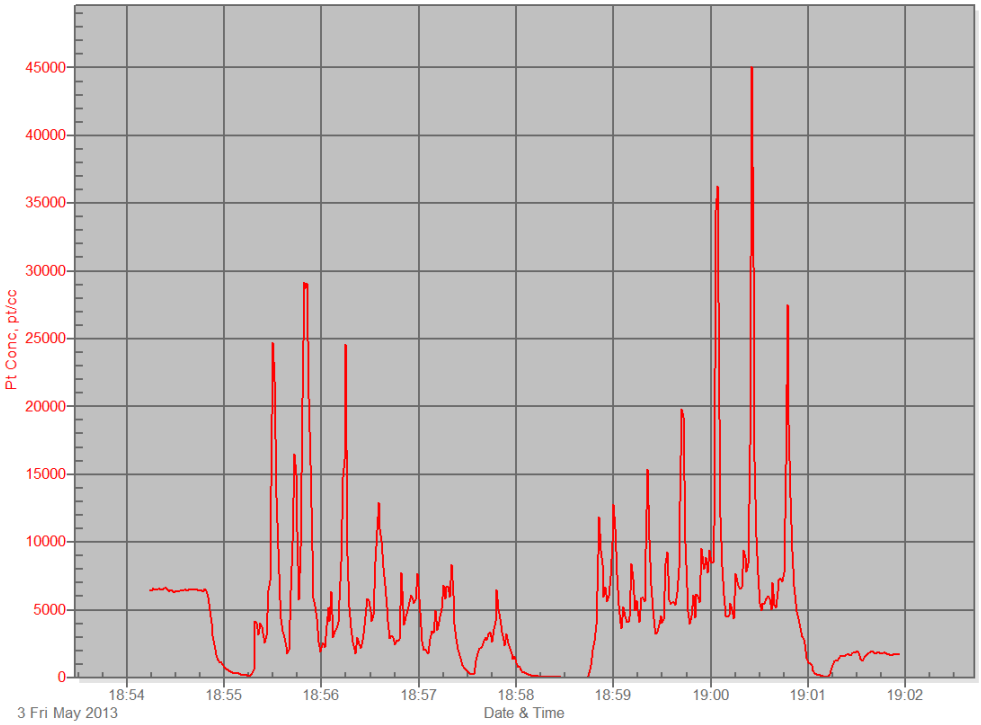

APPENDIX F

Third round test results: test 3

- Purpose: Size Correction Factor (SCF) Runs for Dust-Trak per manual
- Conditions: New carbide cutter, 6000 rpm, 635 mm/min feed, .762 radial depth of cut, 6.35mm axial depth of cut, climb multi-directional laminate, top half.
- Comment: Double peaks because 2, 2 minute runs per instructions, with a 30sec – 1min pause during changeover
- **PDR DataRAM**

pDR-1000
Tag Number: 05
Number of logged points: 438
Start time and date: 16:30:07 03-May
Elapsed time: 00:07:18
Logging period (sec): 1
Calibration Factor (%): 100
Max Display Concentration: 9.573 mg/m³
Time at maximum: 16:31:43 May 03
Max STEL Concentration: 0.492 mg/m³
Time at max STEL: 16:37:07 May 03
Overall Avg Conc: 1.133 mg/m³
Logged Data:

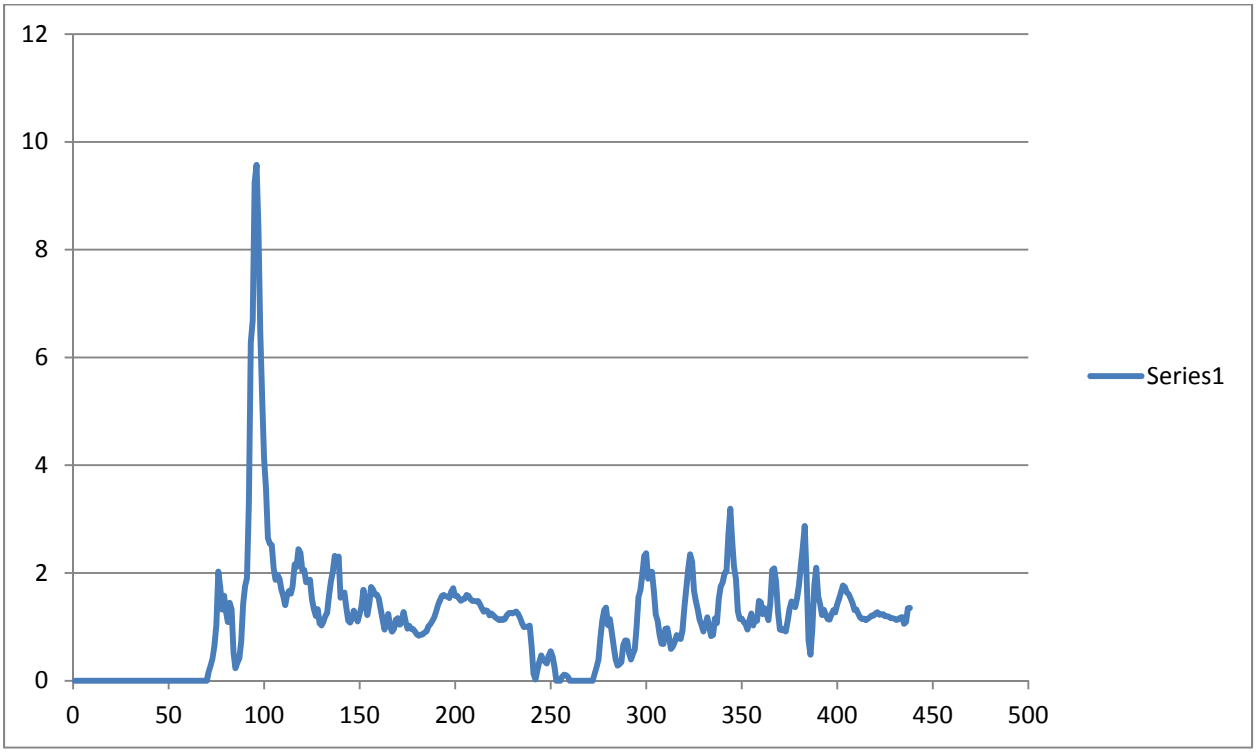

APPENDIX F

Third round test results: test 3

- Purpose: Size Correction Factor (SCF) Runs for Dust-Trak per manual
- Conditions: New carbide cutter, 6000 rpm, 635 mm/min feed, .762 radial depth of cut, 6.35mm axial depth of cut, climb multi-directional laminate, top half.
- Comment: Double peaks because 2, 2 minute runs per instructions, with a 30sec – 1min pause during changeover
- **OPS 3330**

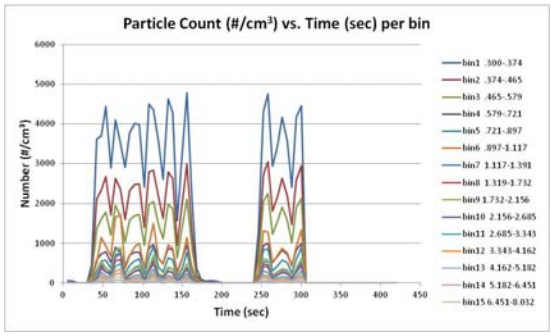

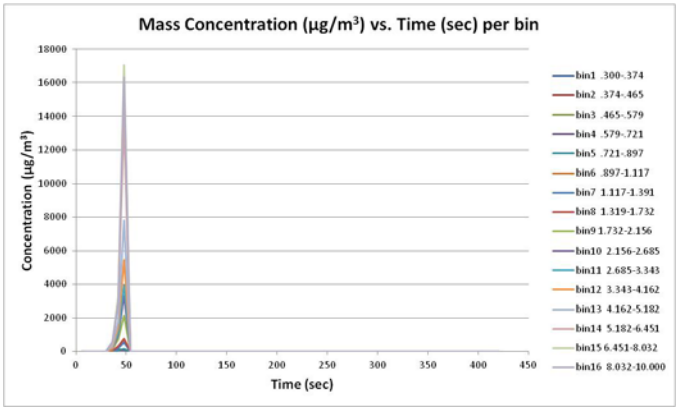

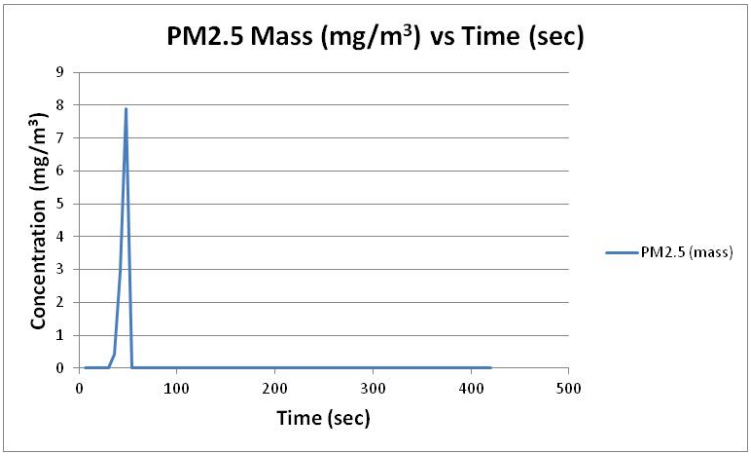

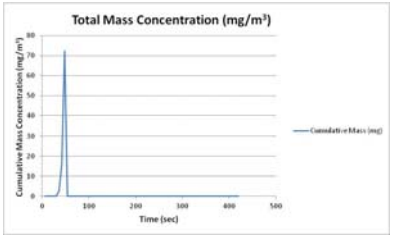

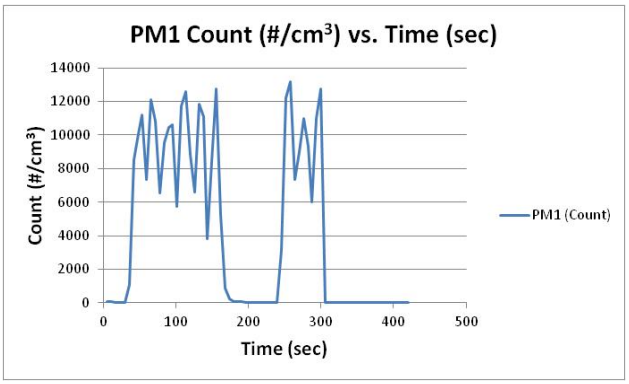

APPENDIX F

Third round test results: test 4

- Purpose: Photometric Correction Factor (PCF) Runs for Dust-Trak per manual
- Conditions: Used carbide cutter from Test 1, 6000 rpm, 635 mm/min feed, .762 radial depth of cut, 6.35mm axial depth of cut, climb, multi-directional laminate, bottom half and full laminate.
- **PTRAK 8525**

Test 004

Instrument		Data Properties	
Model	P-Trak	Start Date	05/04/2013
Meter S/N	8525-02130002	Start Time	11:57:49
		Stop Date	05/04/2013
		Stop Time	12:08:41
		Total Time	0:00:10:52
		Logging Interval	1 seconds

Statistics	
	Pt Conc
Avg	116856 pt/cc
Max	500000 pt/cc
Max Date	05/04/2013
Max Time	12:05:46
Min	21 pt/cc
Min Date	05/04/2013
Min Time	12:08:32
TWA (8 hr)	
TWA Start Date	
TWA Start Time	
TWA End Time	

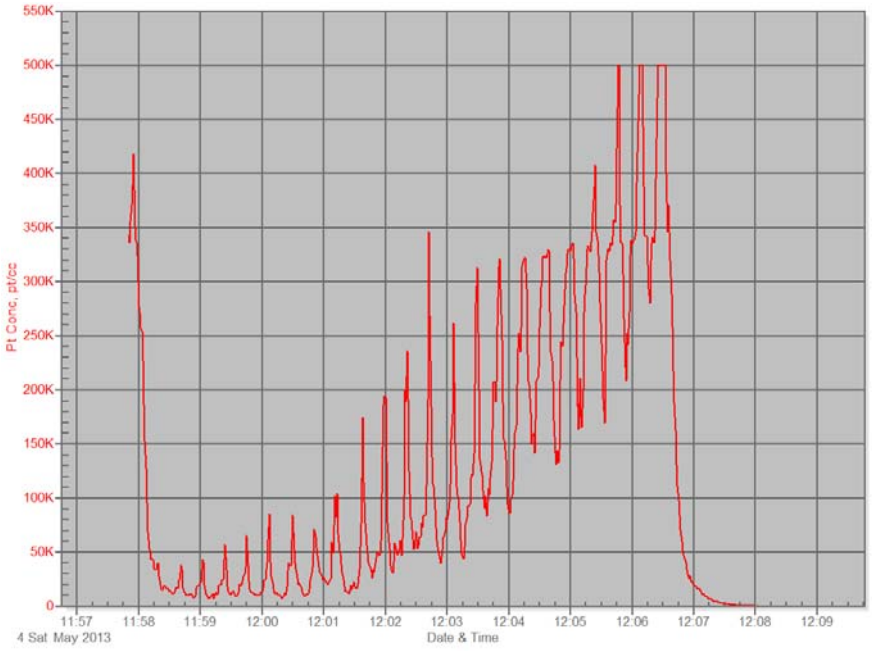

APPENDIX F

Third round test results: test 4

- Purpose: Photometric Correction Factor (PCF) Runs for Dust-Trak per manual
- Conditions: Used carbide cutter from Test 1, 6000 rpm, 635 mm/min feed, .762 radial depth of cut, 6.35mm axial depth of cut, climb, multi-directional laminate, bottom half and full laminate.
- DustTRAK values are cumulative
- **DustTRAK 8533**

ERROR: MAX TOTAL

Instrument		Data Properties	
Model	DustTrak DRX	Start Date	05/04/2013
Instrument S/N	8533101508	Start Time	11:44:30
		Stop Date	05/04/2013
		Stop Time	11:54:30
		Total Time	0:00:10:00
		Logging Interval	3 seconds

Statistics					
	PM1	PM2.5	RESP	PM10	TOTAL
Avg	16.400 mg/m^3	17.000 mg/m^3	20.000 mg/m^3	49.200 mg/m^3	57.300 mg/m^3
Max	65.100 mg/m^3	65.800 mg/m^3	71.200 mg/m^3	150.000 mg/m^3	150.000 mg/m^3
Max Date	05/04/2013	05/04/2013	05/04/2013	05/04/2013	05/04/2013
Max Time	11:47:33	11:47:33	11:47:33	11:47:12	11:46:48
Min	0.010 mg/m^3	0.011 mg/m^3	0.013 mg/m^3	0.034 mg/m^3	0.036 mg/m^3
Min Date	05/04/2013	05/04/2013	05/04/2013	05/04/2013	05/04/2013
Min Time	11:54:24	11:54:24	11:54:24	11:54:27	11:54:24
TWA (8 hr)	N/A	N/A	N/A	N/A	N/A
TWA Start Date	05/04/2013	05/04/2013	05/04/2013	05/04/2013	05/04/2013
TWA Start Time	11:44:30	11:44:30	11:44:30	11:44:30	11:44:30
TWA End Time	11:54:30	11:54:30	11:54:30	11:54:30	11:54:30

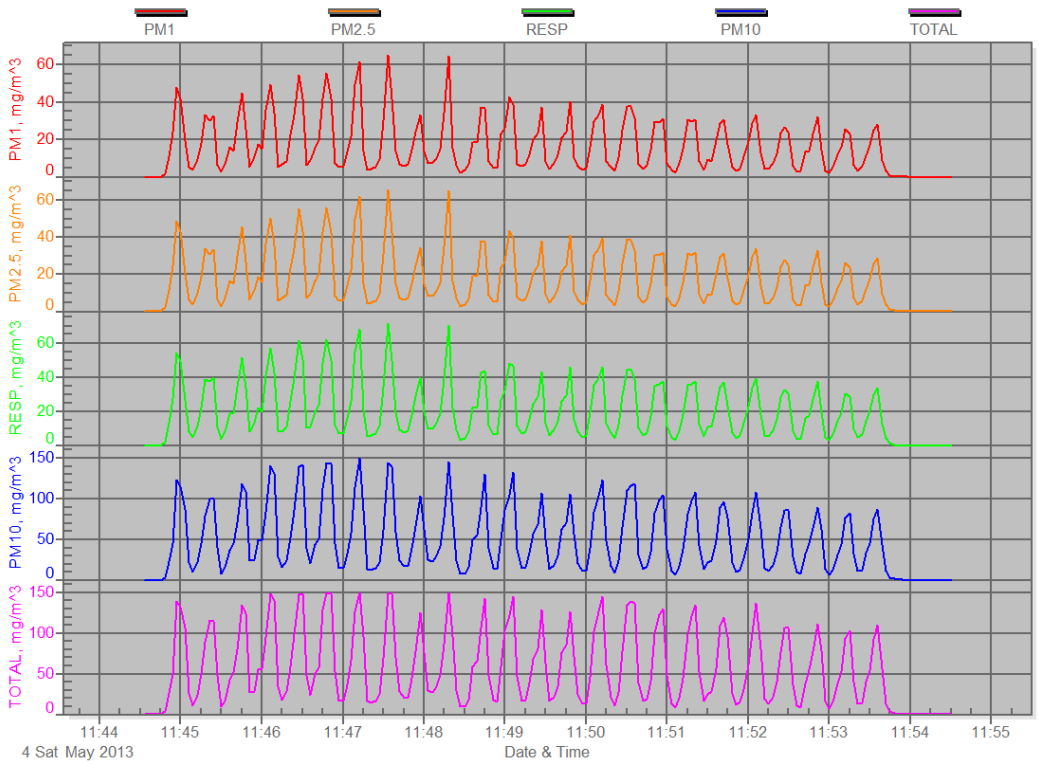

APPENDIX F

Third round test results: test 4

- Purpose: Photometric Correction Factor (PCF) Runs for Dust-Trak per manual
- Conditions: Used carbide cutter from Test 1, 6000 rpm, 635 mm/min feed, .762 radial depth of cut, 6.35mm axial depth of cut, climb, multi-directional laminate, bottom half and full laminate.
- **PDR DataRAM**

pDR-1000
Tag Number: 06
Number of logged points: 700
Start time and date: 09:32:24 04-May
Elapsed time: 00:11:40
Logging period (sec): 1
Calibration Factor (%): 100
Max Display Concentration: 11.951 mg/m³
Time at maximum: 09:35:32 May 04
Max STEL Concentration: 2.046 mg/m³
Time at max STEL: 09:42:54 May 04
Overall Avg Conc: 2.631 mg/m³

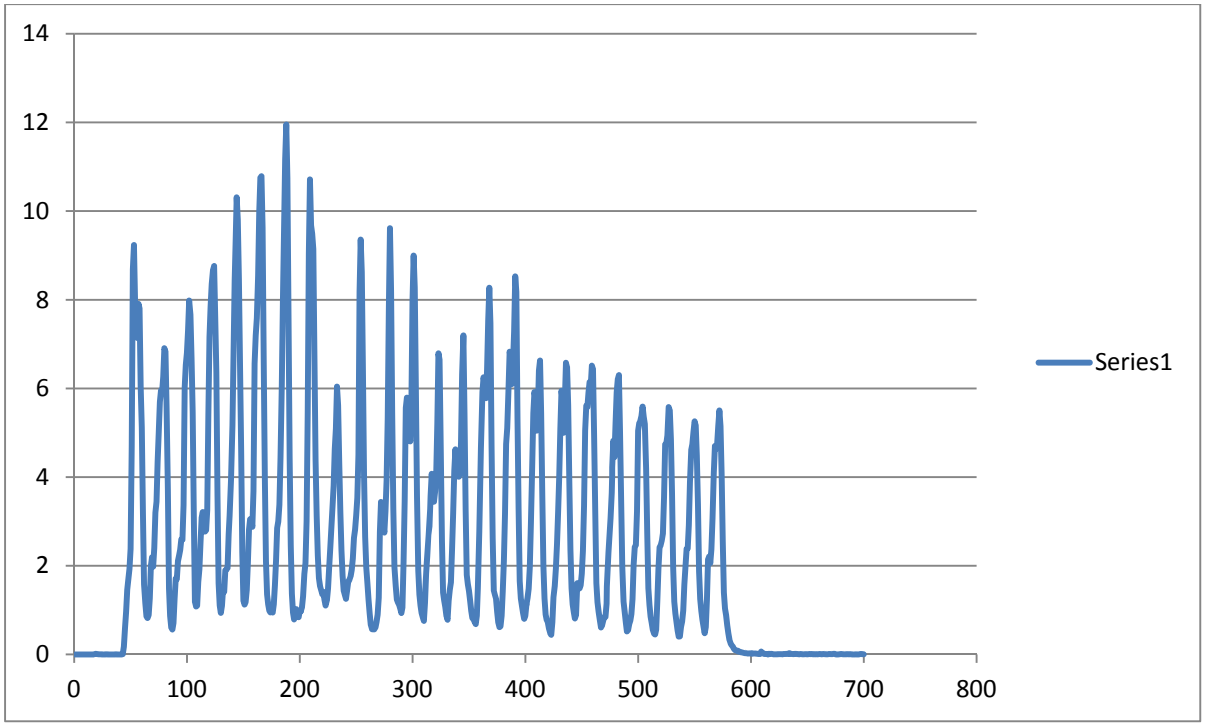

APPENDIX F

Third round test results: test 5

- Purpose: Check results of PCF calibration using SCF=.570 and PCF =2.068 on Dust Trak
- Conditions: Used carbide cutter from Test 4, 6000 rpm, 635 mm/min feed, .762 radial depth of cut, 12.7mm axial depth of cut, climb, multi-directional laminate, full laminate
- PTRAK has concentration limit of 500,000 cts/cm^3
- **PTRAK 8525**

Test 005

Instrument		Data Properties	
Model	P-Trak	Start Date	05/04/2013
Meter S/N	8525-02130002	Start Time	13:30:37
		Stop Date	05/04/2013
		Stop Time	13:37:29
		Total Time	0:00:06:52
		Logging Interval	1 seconds

Statistics	
	Pt Conc
Avg	279179 pt/cc
Max	500000 pt/cc
Max Date	05/04/2013
Max Time	13:31:58
Min	75 pt/cc
Min Date	05/04/2013
Min Time	13:37:29
TWA (8 hr)	
TWA Start Date	
TWA Start Time	
TWA End Time	

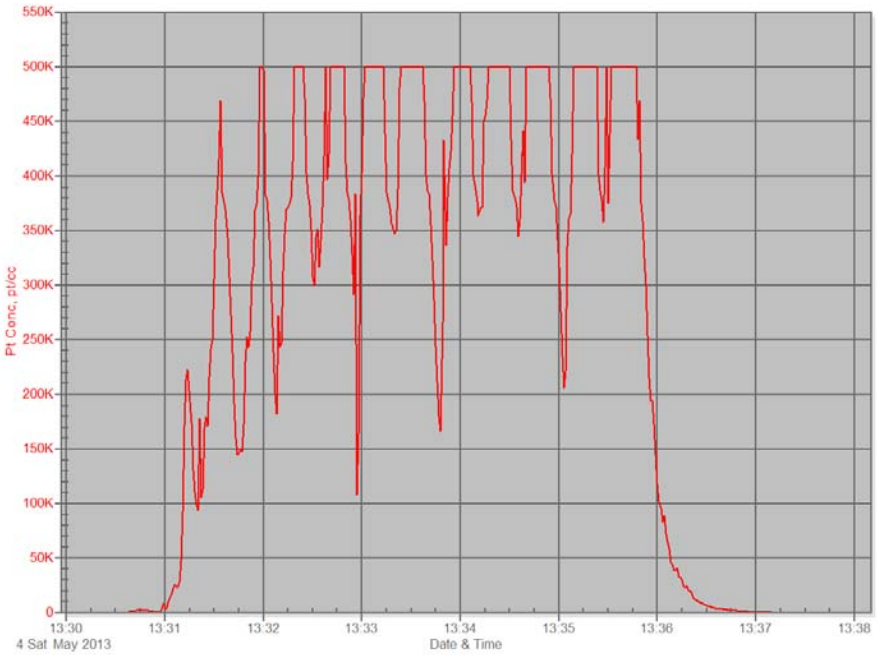

APPENDIX F

Third round test results: test 5

- Purpose: Check results of PCF calibration using SCF=.570 and PCF =2.068 on Dust Trak
- Conditions: Used carbide cutter from Test 4, 6000 rpm, 635 mm/min feed, .762 radial depth of cut, 12.7mm axial depth of cut, climb, multi-directional laminate, full laminate
- Average values
- **DustTRAK 8533**

Instrument		Data Properties	
Model	DustTrak DRX	Start Date	05/04/2013
Instrument S/N	8533101508	Start Time	13:17:44
		Stop Date	05/04/2013
		Stop Time	13:23:44
		Total Time	0:00:06:00
		Logging Interval	3 seconds

Statistics					
	PM1	PM2.5	RESP	PM10	TOTAL
Avg	14.700 mg/m^3	14.900 mg/m^3	15.600 mg/m^3	16.900 mg/m^3	16.900 mg/m^3
Max	53.300 mg/m^3	54.200 mg/m^3	56.500 mg/m^3	61.700 mg/m^3	61.700 mg/m^3
Max Date	05/04/2013	05/04/2013	05/04/2013	05/04/2013	05/04/2013
Max Time	13:21:08	13:21:08	13:21:08	13:21:08	13:21:08
Min	0.004 mg/m^3	0.004 mg/m^3	0.004 mg/m^3	0.004 mg/m^3	0.004 mg/m^3
Min Date	05/04/2013	05/04/2013	05/04/2013	05/04/2013	05/04/2013
Min Time	13:17:50	13:17:50	13:17:50	13:17:50	13:17:50
TWA (8 hr)	N/A	N/A	N/A	N/A	N/A
TWA Start Date	05/04/2013	05/04/2013	05/04/2013	05/04/2013	05/04/2013
TWA Start Time	13:17:44	13:17:44	13:17:44	13:17:44	13:17:44
TWA End Time	13:23:44	13:23:44	13:23:44	13:23:44	13:23:44

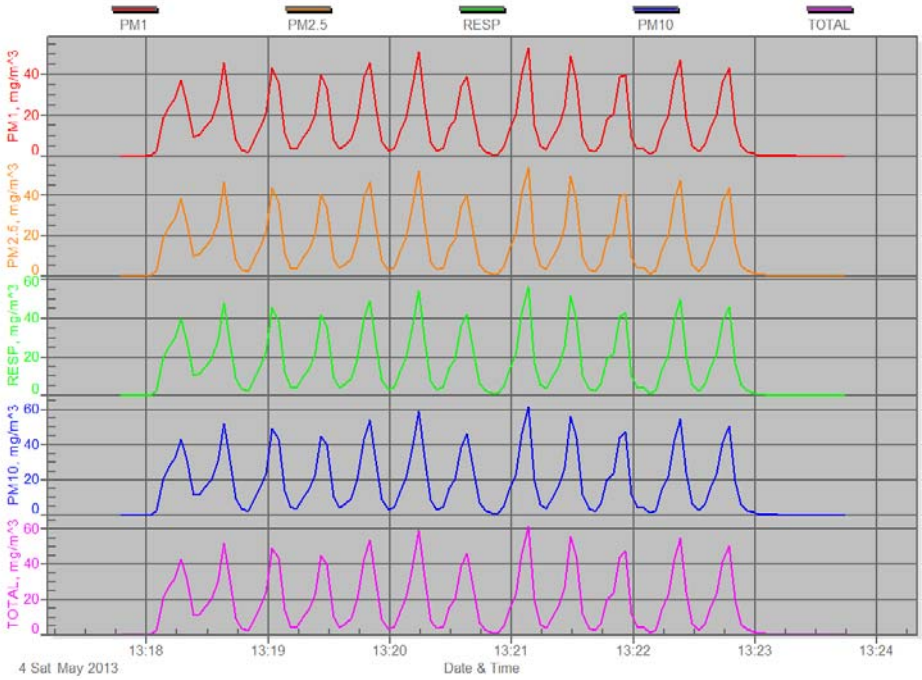

APPENDIX F

Third round test results: test 5

- Purpose: Check results of PCF calibration using SCF=.570 and PCF =2.068 on Dust Trak
- Conditions: Used carbide cutter from Test 4, 6000 rpm, 635 mm/min feed, .762 radial depth of cut, 12.7mm axial depth of cut, climb, multi-directional laminate, full laminate
- **PDR DataRAM**

pDR-1000
Tag Number: 07
Number of logged points: 396
Start time and date: 11:05:50 04-May
Elapsed time: 00:06:36
Logging period (sec): 1
Calibration Factor (%): 100
Max Display Concentration: 4.936 mg/m³
Time at maximum: 11:10:43 May 04
Max STEL Concentration: 0.510 mg/m³
Time at max STEL: 11:11:50 May 04
Overall Avg Conc: 1.160 mg/m³

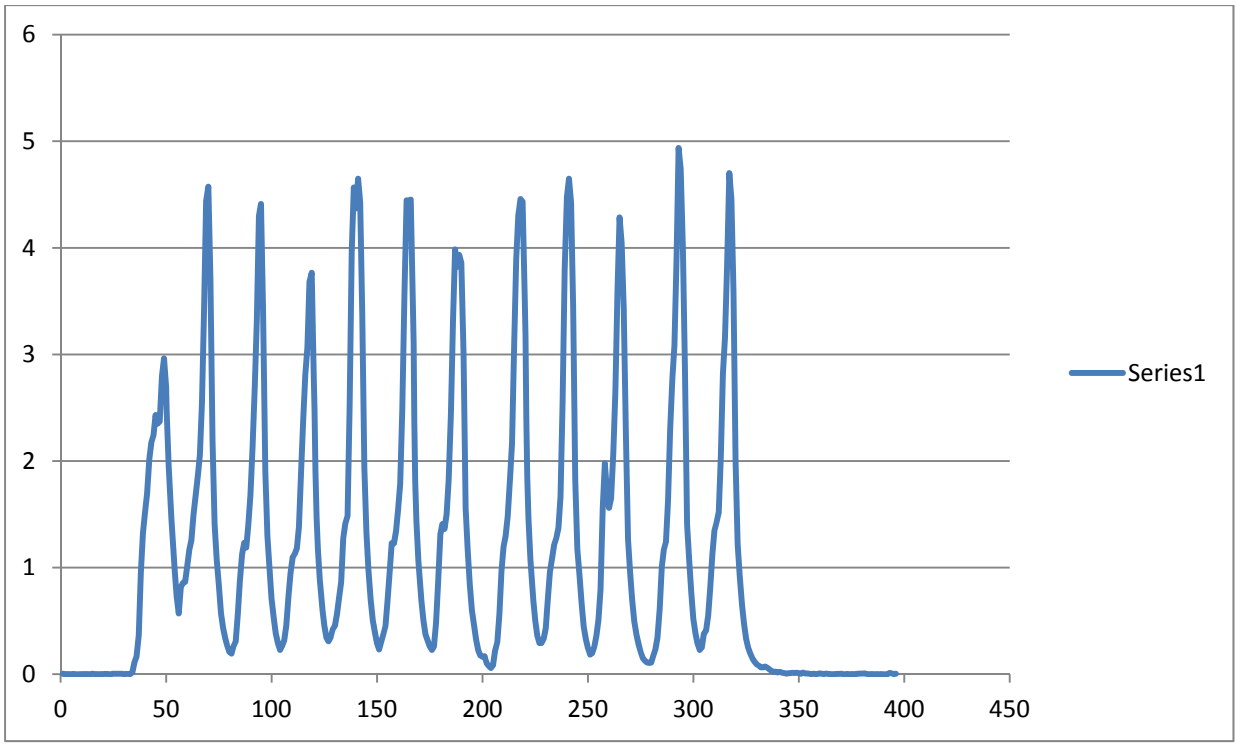

APPENDIX F

Third round test results: test 5

- Purpose: Check results of PCF calibration using SCF=.570 and PCF =2.068 on Dust Trak
- Conditions: Used carbide cutter from Test 4, 6000 rpm, 635 mm/min feed, .762 radial depth of cut, 12.7mm axial depth of cut, climb, multi-directional laminate, full laminate
- Average values
- **OPS 3330**

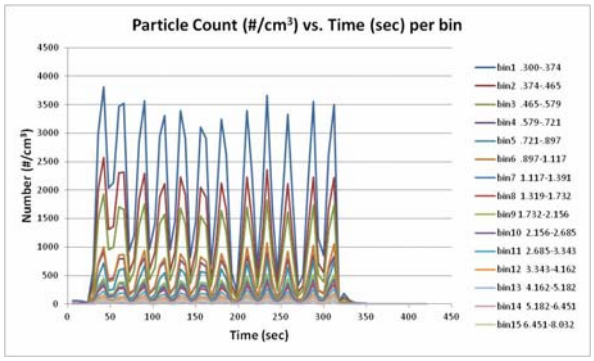

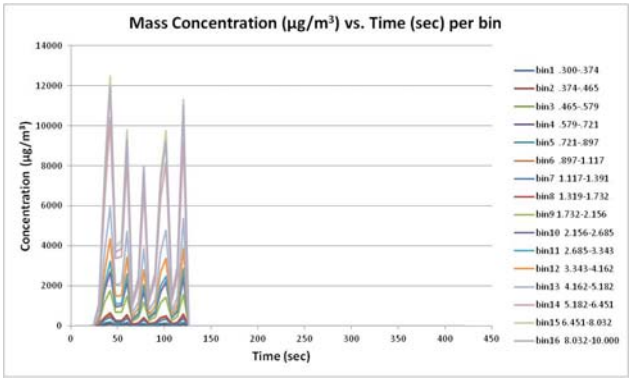

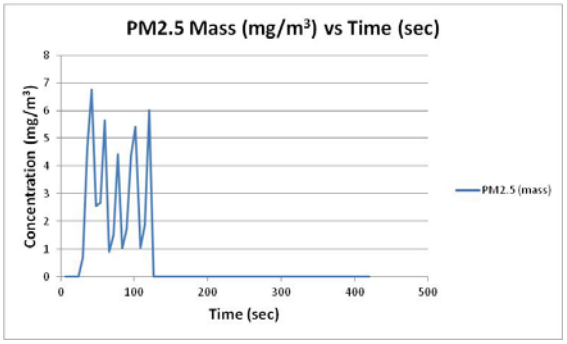

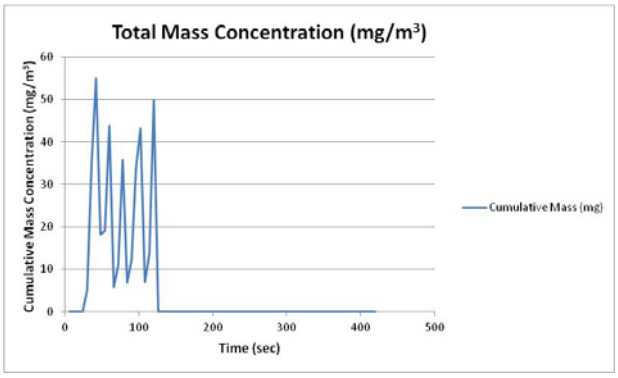

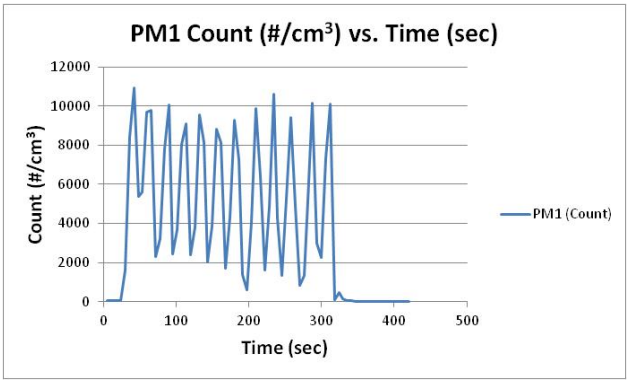

APPENDIX F

Third round test results: test 6

- Purpose: 2.5 Impactor Test on Dust-Trak (attempt to isolate 2.5 and below)
- Conditions: New 4-flute carbide cutter , 6000 rpm, 635 mm/min feed, .762 radial depth of cut, 6.35 mm axial depth of cut, climb, multi-directional laminate, top of laminate.
- **PTRAK 8525**

Test 006

Instrument		Data Properties	
Model	P-Trak	Start Date	05/05/2013
Meter S/N	8525-02130002	Start Time	11:41:23
		Stop Date	05/05/2013
		Stop Time	11:49:14
		Total Time	0:00:07:51
		Logging Interval	1 seconds

Statistics	
	Pt Conc
Avg	4839 pt/cc
Max	25600 pt/cc
Max Date	05/05/2013
Max Time	11:46:38
Min	0 pt/cc
Min Date	05/05/2013
Min Time	11:41:37
TWA (8 hr)	
TWA Start Date	
TWA Start Time	
TWA End Time	

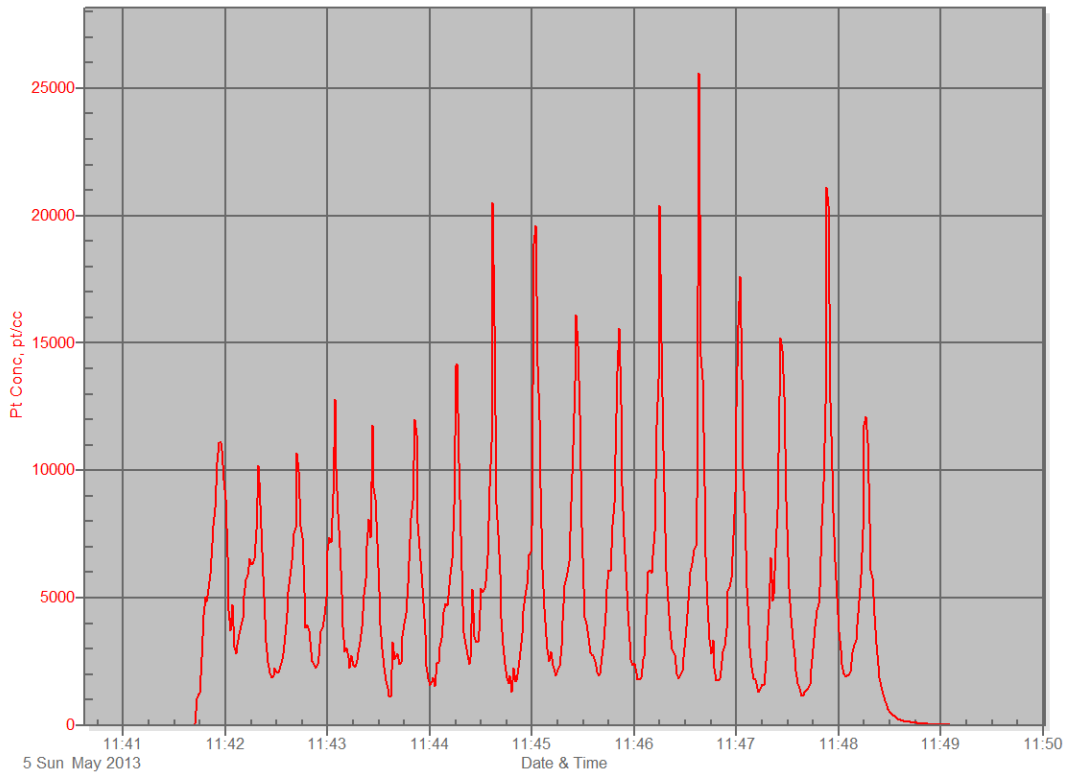

APPENDIX F

Third round test results: test 6

- Purpose: 2.5 Impactor Test on Dust-Trak (attempt to isolate 2.5 and below)
- Conditions: New 4-flute carbide cutter , 6000 rpm, 635 mm/min feed, .762 radial depth of cut, 6.35 mm axial depth of cut, climb, multi-directional laminate, top of laminate.
- **DustTRAK 8533**

Instrument		Data Properties	
Model	DustTrak DRX	Start Date	05/05/2013
Instrument S/N	8533101508	Start Time	11:28:27
		Stop Date	05/05/2013
		Stop Time	11:35:27
		Total Time	0:00:07:00
		Logging Interval	3 seconds

Statistics					
	PM1	PM2.5	RESP	PM10	TOTAL
Avg	10.300 mg/m^3	10.600 mg/m^3	11.100 mg/m^3	11.500 mg/m^3	11.500 mg/m^3
Max	34.400 mg/m^3	35.300 mg/m^3	36.800 mg/m^3	38.500 mg/m^3	38.500 mg/m^3
Max Date	05/05/2013	05/05/2013	05/05/2013	05/05/2013	05/05/2013
Max Time	11:33:09	11:33:09	11:33:09	11:33:09	11:33:09
Min	0.001 mg/m^3	0.001 mg/m^3	0.002 mg/m^3	0.003 mg/m^3	0.003 mg/m^3
Min Date	05/05/2013	05/05/2013	05/05/2013	05/05/2013	05/05/2013
Min Time	11:28:30	11:28:30	11:28:30	11:28:33	11:28:33
TWA (8 hr)	N/A	N/A	N/A	N/A	N/A
TWA Start Date	05/05/2013	05/05/2013	05/05/2013	05/05/2013	05/05/2013
TWA Start Time	11:28:27	11:28:27	11:28:27	11:28:27	11:28:27
TWA End Time	11:35:27	11:35:27	11:35:27	11:35:27	11:35:27

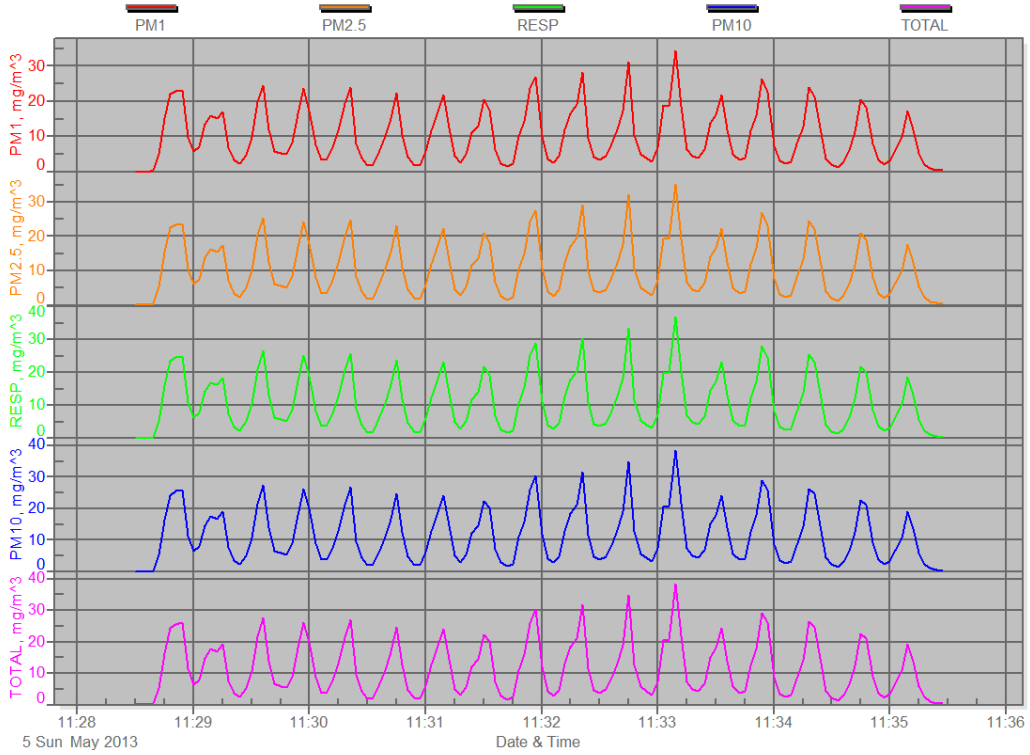

APPENDIX F

Third round test results: test 6

- Purpose: 2.5 Impactor Test on Dust-Trak (attempt to isolate 2.5 and below)
- Conditions: New 4-flute carbide cutter , 6000 rpm, 635 mm/min feed, .762 radial depth of cut, 6.35 mm axial depth of cut, climb, multi-directional laminate, top of laminate.
- **DustTRAK 8533**

pDR-1000
Tag Number: 08
Number of logged points: 483
Start time and date: 09:16:34 05-May
Elapsed time: 00:08:03
Logging period (sec): 1
Calibration Factor (%): 100
Max Display Concentration: 5.931 mg/m³
Time at maximum: 09:21:06 May 05
Max STEL Concentration: 0.790 mg/m³
Time at max STEL: 09:24:05 May 05
Overall Avg Conc: 1.472 mg/m³

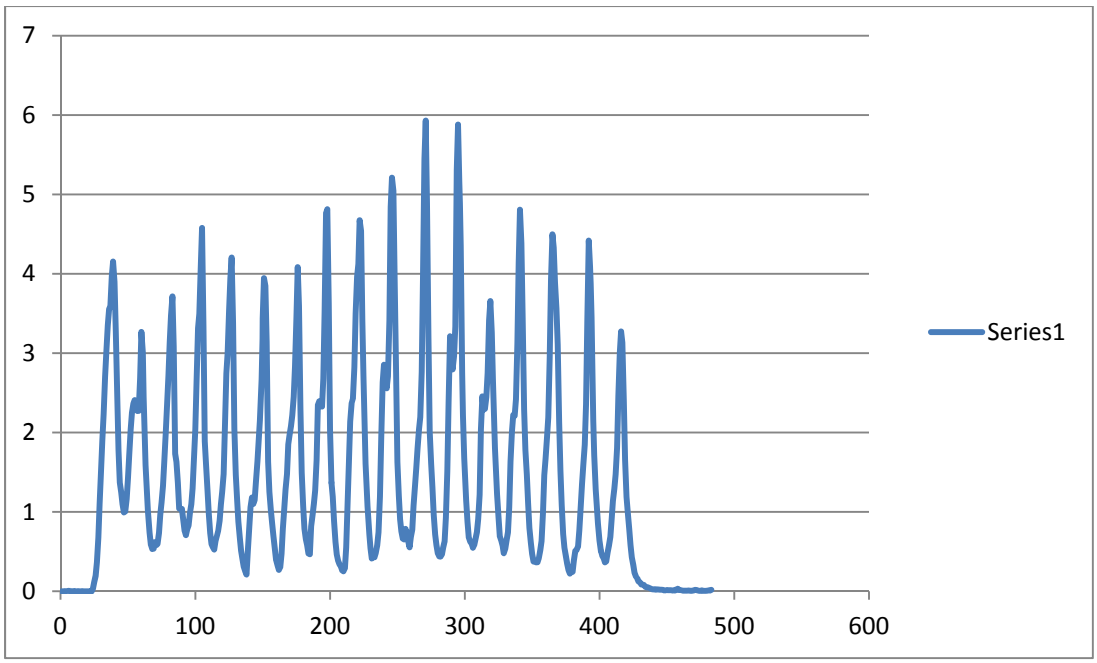

APPENDIX F

Third round test results: test 6

- Purpose: 2.5 Impactor Test on Dust-Trak (attempt to isolate 2.5 and below)
- Conditions: New 4-flute carbide cutter , 6000 rpm, 635 mm/min feed, .762 radial depth of cut, 6.35 mm axial depth of cut, climb, multi-directional laminate, top of laminate.
- **OPS 3330**

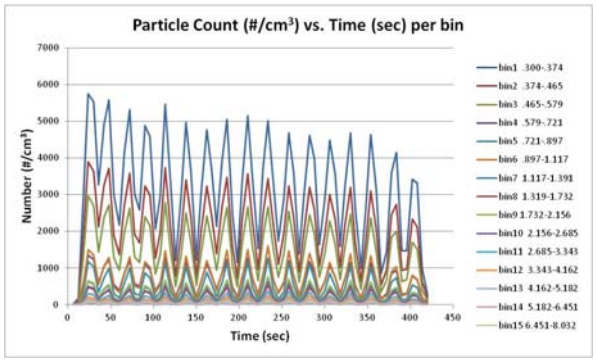

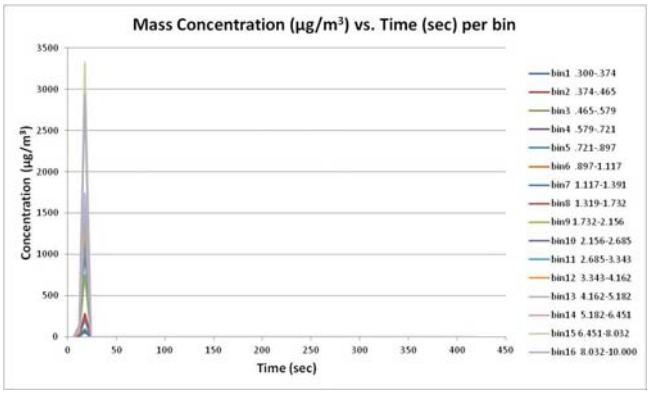

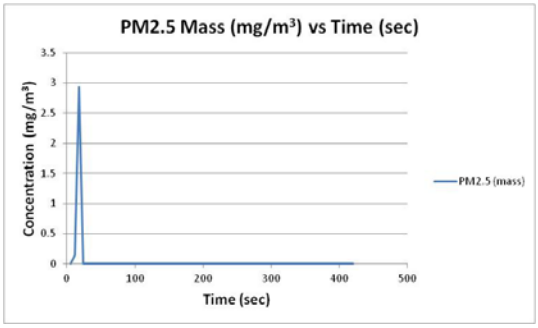

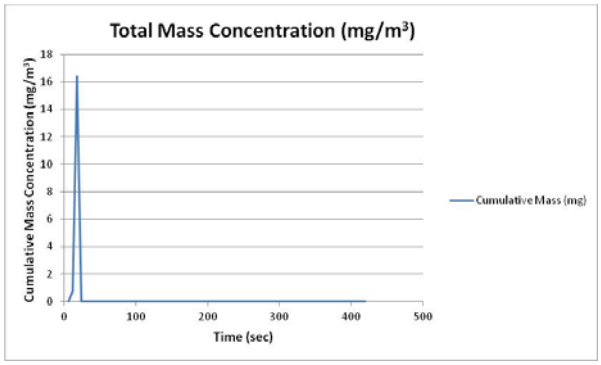

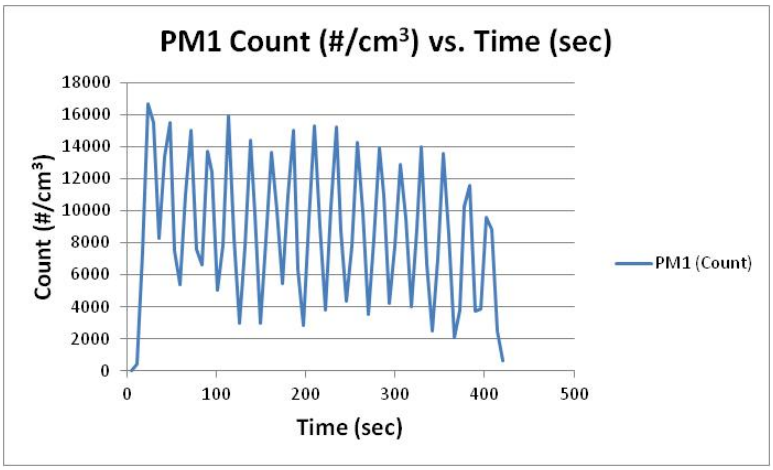

APPENDIX F

Third round test results: test 7

- Purpose: 2.5 Impactor Test on Dust-Trak (attempt to isolate 2.5 and below)
- Conditions: Same cutter as Test 6 , 6000 rpm, 635 mm/min feed, .762 radial depth of cut, 6.35 mm axial depth of cut, climb, multi-directional laminate, bottom of laminate.
- **PTRAK 8525**

Instrument		Data Properties	
Model	P-Trak	Start Date	05/05/2013
Meter S/N	8525-02130002	Start Time	12:06:40
		Stop Date	05/05/2013
		Stop Time	12:14:31
		Total Time	0:00:07:51
		Logging Interval	1 seconds

Statistics	
	Pt Conc
Avg	35187 pt/cc
Max	313000 pt/cc
Max Date	05/05/2013
Max Time	12:13:01
Min	1 pt/cc
Min Date	05/05/2013
Min Time	12:07:03
TWA (8 hr)	
TWA Start Date	
TWA Start Time	
TWA End Time	

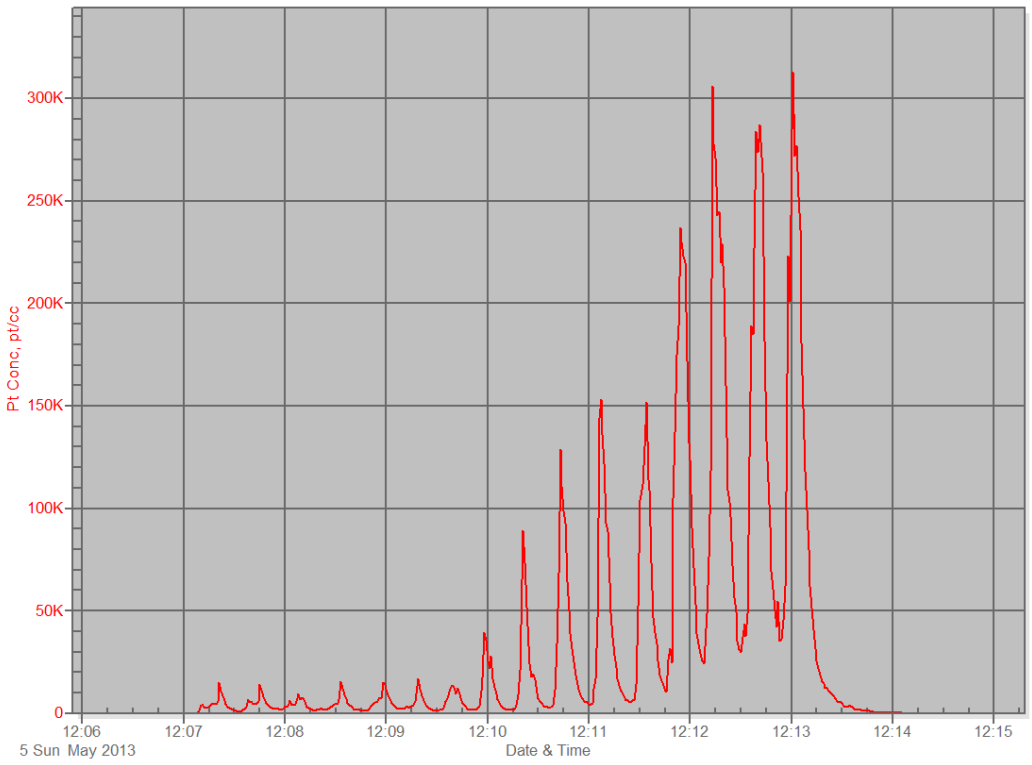

APPENDIX F

Third round test results: test 7

- Purpose: 2.5 Impactor Test on Dust-Trak (attempt to isolate 2.5 and below)
- Conditions: Same cutter as Test 6 , 6000 rpm, 635 mm/min feed, .762 radial depth of cut, 6.35 mm axial depth of cut, climb, multi-directional laminate, bottom of laminate.
- **DustTRAK 8533**

Test 007

Instrument		Data Properties	
Model	DustTrak DRX	Start Date	05/05/2013
Instrument S/N	8533101508	Start Time	11:53:47
		Stop Date	05/05/2013
		Stop Time	11:59:47
		Total Time	0:00:06:00
		Logging Interval	3 seconds

Statistics					
	PM1	PM2.5	RESP	PM10	TOTAL
Avg	9.710 mg/m^3	9.990 mg/m^3	10.400 mg/m^3	10.900 mg/m^3	10.900 mg/m^3
Max	31.500 mg/m^3	32.300 mg/m^3	33.800 mg/m^3	35.800 mg/m^3	35.800 mg/m^3
Max Date	05/05/2013	05/05/2013	05/05/2013	05/05/2013	05/05/2013
Max Time	11:57:38	11:57:38	11:57:38	11:57:38	11:57:38
Min	0.047 mg/m^3	0.049 mg/m^3	0.051 mg/m^3	0.053 mg/m^3	0.053 mg/m^3
Min Date	05/05/2013	05/05/2013	05/05/2013	05/05/2013	05/05/2013
Min Time	11:53:59	11:53:59	11:53:59	11:53:59	11:53:59
TWA (8 hr)	N/A	N/A	N/A	N/A	N/A
TWA Start Date	05/05/2013	05/05/2013	05/05/2013	05/05/2013	05/05/2013
TWA Start Time	11:53:47	11:53:47	11:53:47	11:53:47	11:53:47
TWA End Time	11:59:47	11:59:47	11:59:47	11:59:47	11:59:47

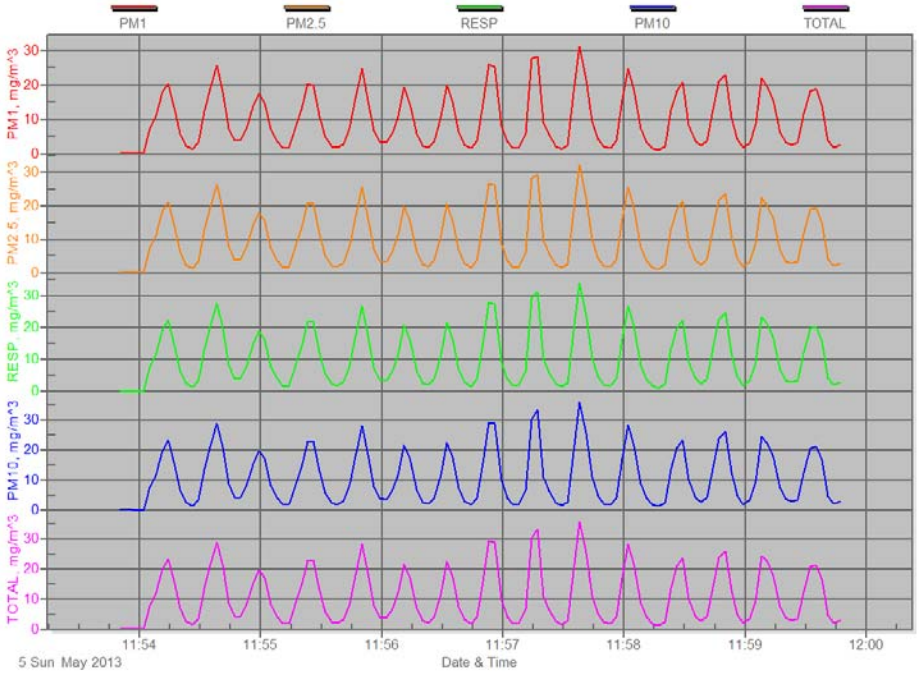

APPENDIX F

Third round test results: test 7

- Purpose: 2.5 Impactor Test on Dust-Trak (attempt to isolate 2.5 and below)
- Conditions: Same cutter as Test 6 , 6000 rpm, 635 mm/min feed, .762 radial depth of cut, 6.35 mm axial depth of cut, climb, multi-directional laminate, bottom of laminate.
- **PDR DataRAM**

pDR-1000
Tag Number: 10
Number of logged points: 483
Start time and date: 09:41:47 05-May
Elapsed time: 00:08:03
Logging period (sec): 1
Calibration Factor (%): 100
Max Display Concentration: 4.671 mg/m³
Time at maximum: 09:45:14 May 05
Max STEL Concentration: 0.476 mg/m³
Time at max STEL: 09:49:48 May 05
Overall Avg Conc: 0.886 mg/m³

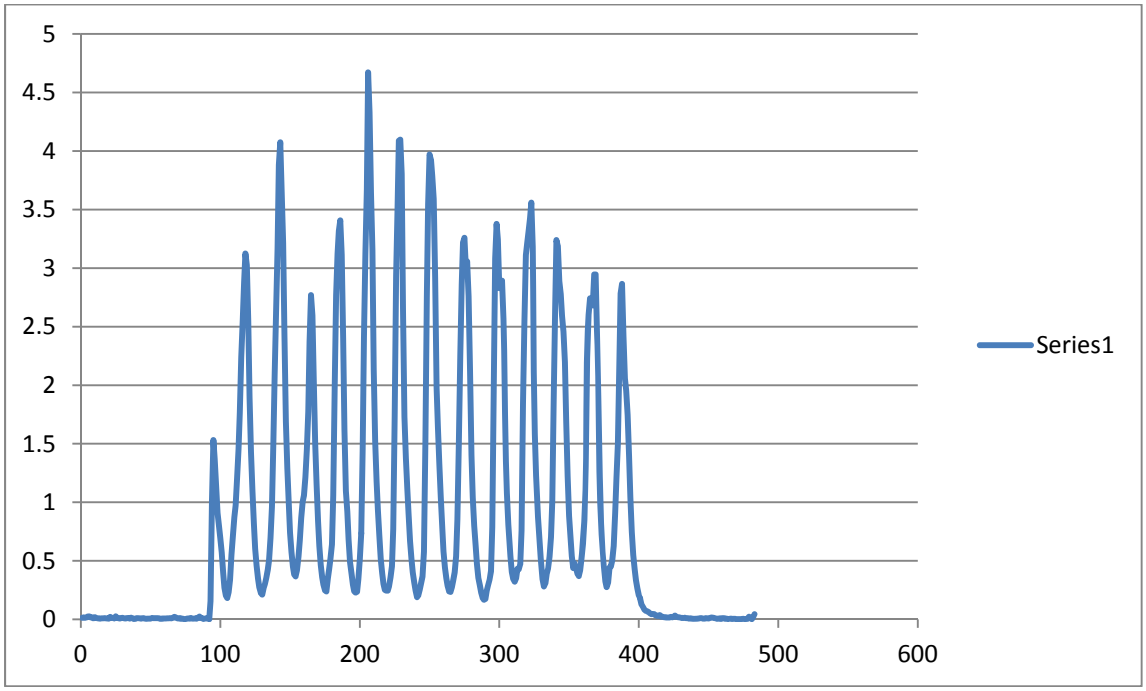

APPENDIX F

Third round test results: test 7

- Purpose: 2.5 Impactor Test on Dust-Trak (attempt to isolate 2.5 and below)
- Conditions: Same cutter as Test 6 , 6000 rpm, 635 mm/min feed, .762 radial depth of cut, 6.35 mm axial depth of cut, climb, multi-directional laminate, bottom of laminate.
- **OPS 3330**

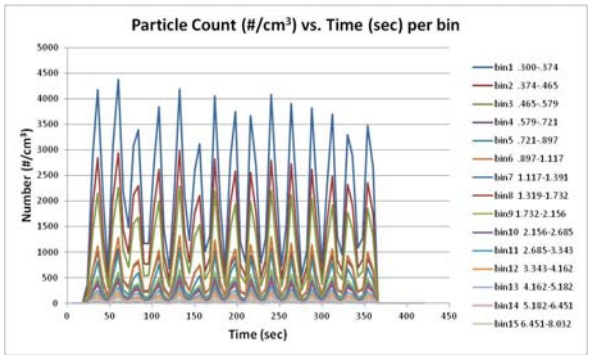

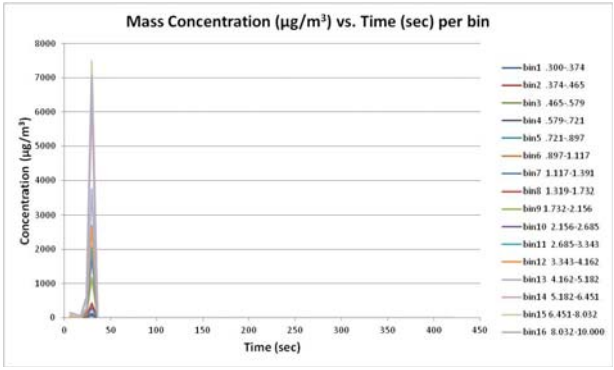

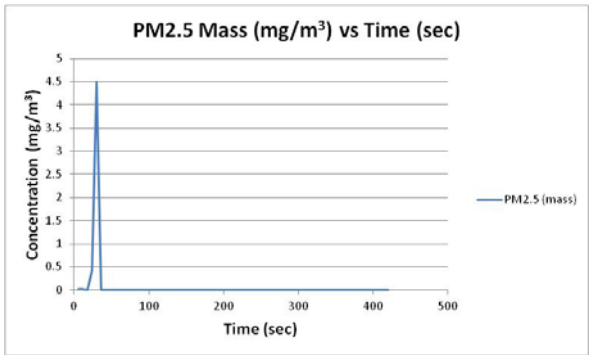

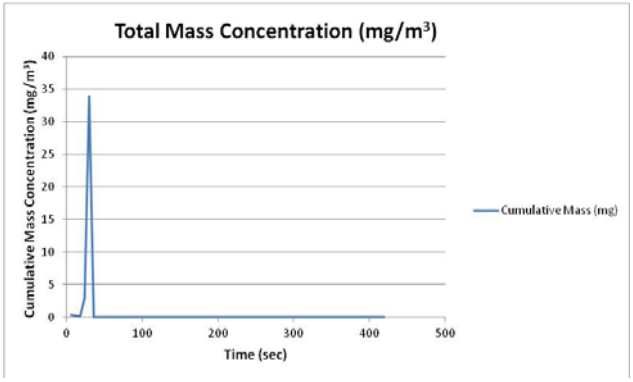

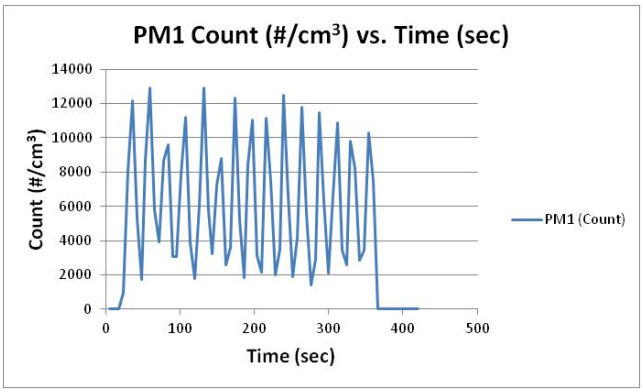

APPENDIX F

Third round test results: test 8

- Purpose: Test new type of cutter
- Conditions: 6-Flute PCD Cutter previously used in impactor D1 Test, 6000 rpm, 635 mm/min feed, .762 radial depth of cut, 6.35 mm axial depth of cut, climb, multi-directional laminate, top of laminate.
- **PTRAK 8525**

Instrument		Data Properties	
Model	P-Trak	Start Date	05/05/2013
Meter S/N	8525-02130002	Start Time	13:42:28
		Stop Date	05/05/2013
		Stop Time	13:49:19
		Total Time	0:00:06:51
		Logging Interval	1 seconds

Statistics	
	Pt Conc
Avg	9670 pt/cc
Max	106000 pt/cc
Max Date	05/05/2013
Max Time	13:43:00
Min	1 pt/cc
Min Date	05/05/2013
Min Time	13:49:19
TWA (8 hr)	
TWA Start Date	
TWA Start Time	
TWA End Time	

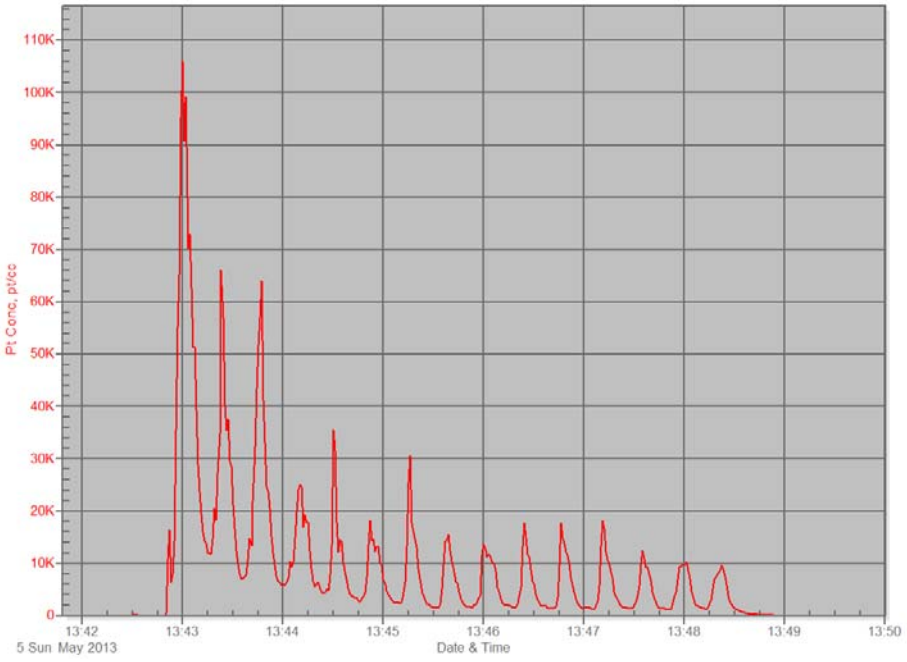

APPENDIX F

Third round test results: test 8

- Purpose: Test new type of cutter
- Conditions: 6-Flute PCD Cutter previously used in impactor D1 Test, 6000 rpm, 635 mm/min feed, .762 radial depth of cut, 6.35 mm axial depth of cut, climb, multi-directional laminate, top of laminate.
- **DustTRAK 8533**

Test 008

Instrument		Data Properties	
Model	DustTrak DRX	Start Date	05/05/2013
Instrument S/N	8533101508	Start Time	13:29:33
		Stop Date	05/05/2013
		Stop Time	13:35:33
		Total Time	0:00:06:00
		Logging Interval	3 seconds

Statistics					
	PM1	PM2.5	RESP	PM10	TOTAL
Avg	11.900 mg/m^3	12.200 mg/m^3	12.700 mg/m^3	13.300 mg/m^3	13.300 mg/m^3
Max	82.100 mg/m^3	82.800 mg/m^3	84.400 mg/m^3	86.800 mg/m^3	86.800 mg/m^3
Max Date	05/05/2013	05/05/2013	05/05/2013	05/05/2013	05/05/2013
Max Time	13:32:09	13:32:09	13:32:09	13:32:09	13:32:09
Min	0.005 mg/m^3	0.005 mg/m^3	0.006 mg/m^3	0.007 mg/m^3	0.007 mg/m^3
Min Date	05/05/2013	05/05/2013	05/05/2013	05/05/2013	05/05/2013
Min Time	13:29:36	13:29:36	13:29:36	13:29:36	13:29:36
TWA (8 hr)	N/A	N/A	N/A	N/A	N/A
TWA Start Date	05/05/2013	05/05/2013	05/05/2013	05/05/2013	05/05/2013
TWA Start Time	13:29:33	13:29:33	13:29:33	13:29:33	13:29:33
TWA End Time	13:35:33	13:35:33	13:35:33	13:35:33	13:35:33

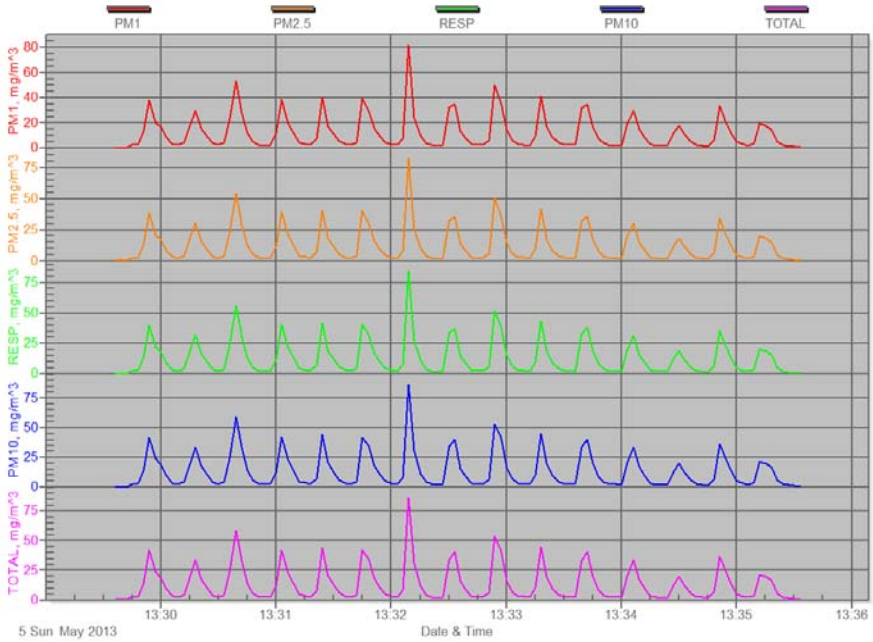

APPENDIX F

Third round test results: test 8

- Purpose: Test new type of cutter
- Conditions: 6-Flute PCD Cutter previously used in impactor D1 Test, 6000 rpm, 635 mm/min feed, .762 radial depth of cut, 6.35 mm axial depth of cut, climb, multi-directional laminate, top of laminate.
- **DustTRAK 8533**

pDR-1000
Tag Number: 12
Number of logged points: 403
Start time and date: 11:17:39 05-May
Elapsed time: 00:06:43
Logging period (sec): 1
Calibration Factor (%): 100
Max Display Concentration: 7.950 mg/m³
Time at maximum: 11:20:30 May 05
Max STEL Concentration: 0.555 mg/m³
Time at max STEL: 11:24:09 May 05
Overall Avg Conc: 1.239 mg/m³

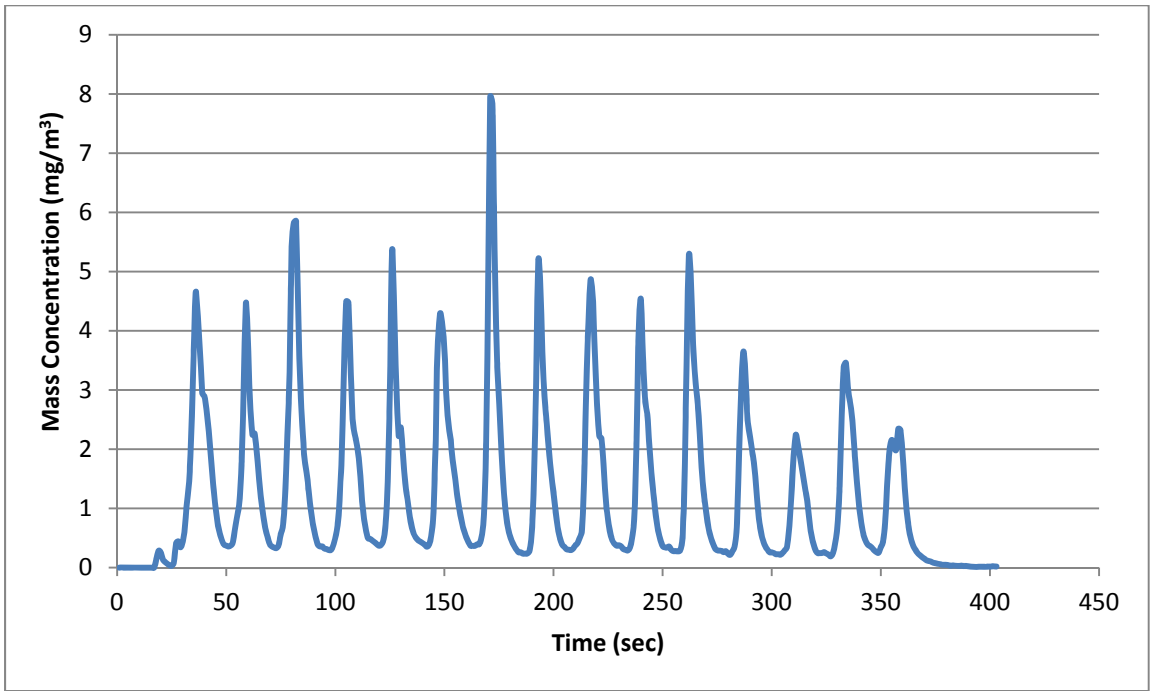

APPENDIX F

Third round test results: test 8

- Purpose: Test new type of cutter
- Conditions: 6-Flute PCD Cutter previously used in impactor D1 Test, 6000 rpm, 635 mm/min feed, .762 radial depth of cut, 6.35 mm axial depth of cut, climb, multi-directional laminate, top of laminate.
- **OPS 3330**
-

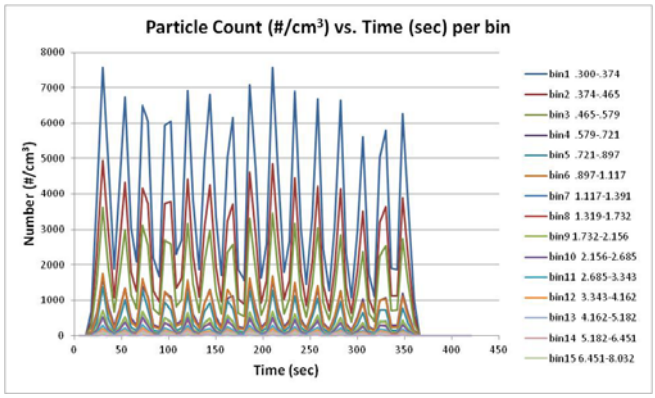

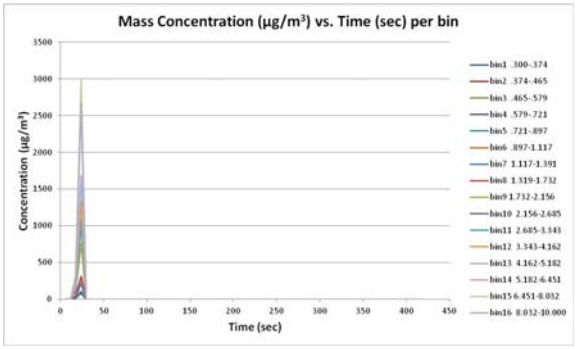

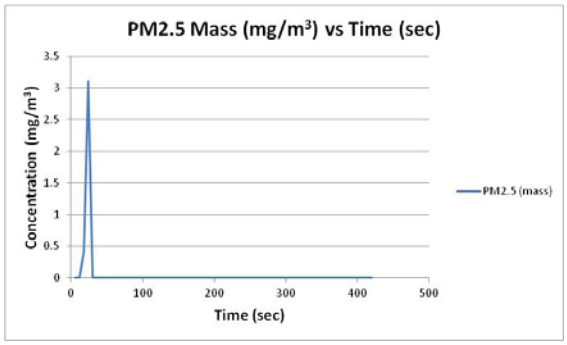

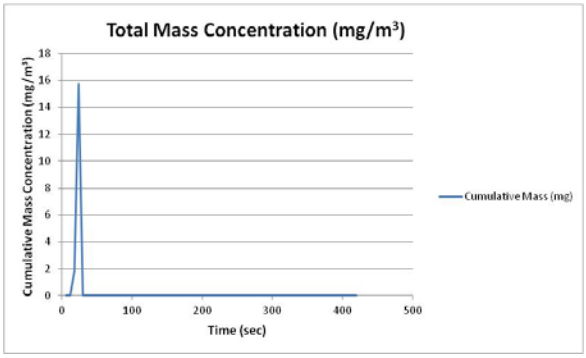

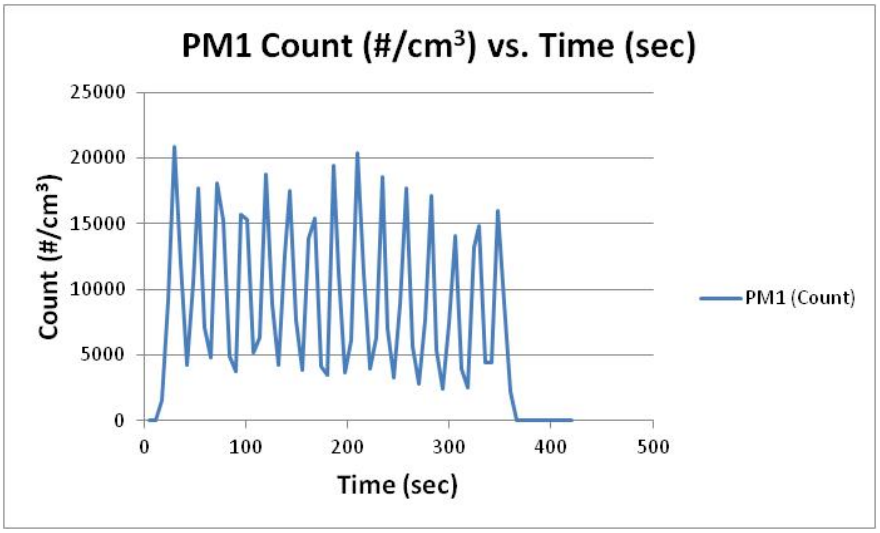

APPENDIX F

Third round test results: test 9

- Purpose: Test new type of cutter, with some additional wear
- Conditions: 6-Flute PCD Cutter used in Test 8 (from impactor D1 Test), 6000 rpm, 635 mm/min feed, .762 radial depth of cut, 6.35 mm axial depth of cut, climb, multi-directional laminate, top of laminate.
- **PTRAK 8525**

Instrument		Data Properties	
Model	P-Trak	Start Date	05/05/2013
Meter S/N	8525-02130002	Start Time	14:02:31
		Stop Date	05/05/2013
		Stop Time	14:10:08
		Total Time	0:00:07:37
		Logging Interval	1 seconds

Statistics	
	Pt Conc
Avg	7885 pt/cc
Max	30000 pt/cc
Max Date	05/05/2013
Max Time	14:04:38
Min	0 pt/cc
Min Date	05/05/2013
Min Time	14:10:06
TWA (8 hr)	
TWA Start Date	
TWA Start Time	
TWA End Time	

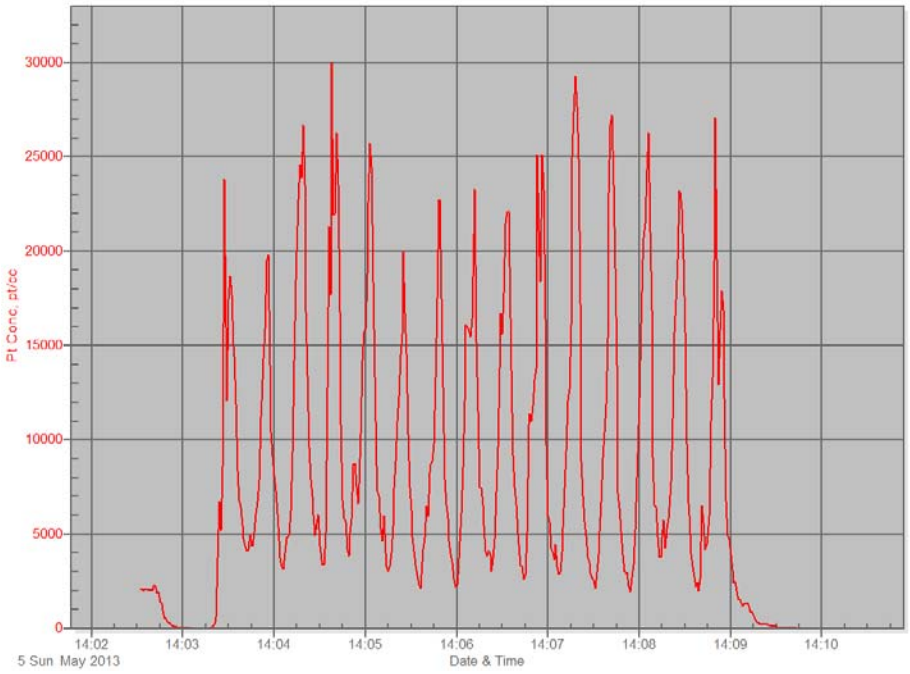

APPENDIX F

Third round test results: test 9

- Purpose: Test new type of cutter, with some additional wear
- Conditions: 6-Flute PCD Cutter used in Test 8 (from impactor D1 Test), 6000 rpm, 635 mm/min feed, .762 radial depth of cut, 6.35 mm axial depth of cut, climb, multi-directional laminate, top of laminate.
- **DustTRAK 8533**

Test 009

Instrument		Data Properties	
Model	DustTrak DRX	Start Date	05/05/2013
Instrument S/N	8533101508	Start Time	13:49:59
		Stop Date	05/05/2013
		Stop Time	13:55:59
		Total Time	0:00:06:00
		Logging Interval	3 seconds

Statistics					
	PM1	PM2.5	RESP	PM10	TOTAL
Avg	22.600 mg/m^3	23.100 mg/m^3	24.100 mg/m^3	25.500 mg/m^3	25.500 mg/m^3
Max	71.500 mg/m^3	72.600 mg/m^3	75.300 mg/m^3	79.500 mg/m^3	79.500 mg/m^3
Max Date	05/05/2013	05/05/2013	05/05/2013	05/05/2013	05/05/2013
Max Time	13:54:11	13:54:11	13:54:11	13:54:11	13:54:11
Min	0.032 mg/m^3	0.033 mg/m^3	0.035 mg/m^3	0.039 mg/m^3	0.039 mg/m^3
Min Date	05/05/2013	05/05/2013	05/05/2013	05/05/2013	05/05/2013
Min Time	13:50:08	13:50:08	13:50:08	13:50:08	13:50:08
TWA (8 hr)	N/A	N/A	N/A	N/A	N/A
TWA Start Date	05/05/2013	05/05/2013	05/05/2013	05/05/2013	05/05/2013
TWA Start Time	13:49:59	13:49:59	13:49:59	13:49:59	13:49:59
TWA End Time	13:55:59	13:55:59	13:55:59	13:55:59	13:55:59

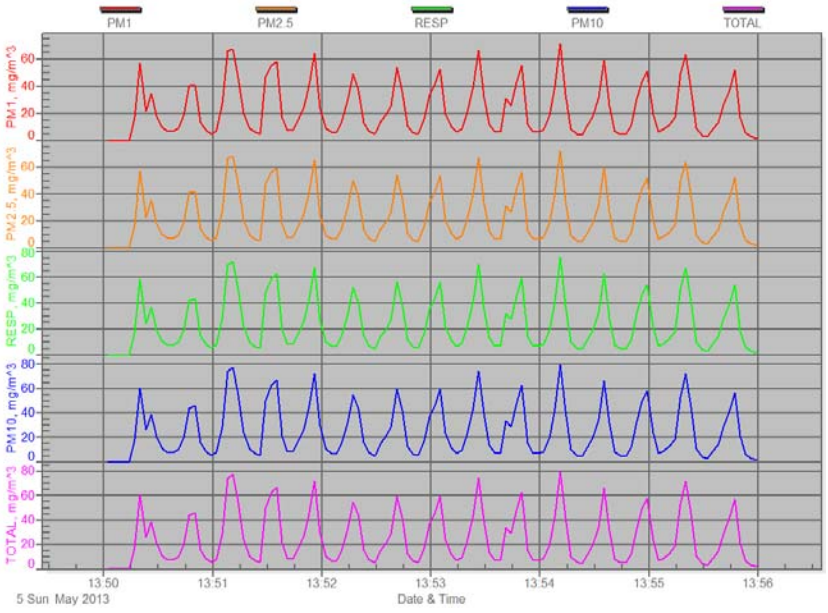

APPENDIX F

Third round test results: test 9

- Purpose: Test new type of cutter, with some additional wear
- Conditions: 6-Flute PCD Cutter used in Test 8 (from impactor D1 Test), 6000 rpm, 635 mm/min feed, .762 radial depth of cut, 6.35 mm axial depth of cut, climb, multi-directional laminate, top of laminate.
- **PDR DataRAM**

pDR-1000
Tag Number: 13
Number of logged points: 462
Start time and date: 11:37:35 05-May
Elapsed time: 00:07:42
Logging period (sec): 1
Calibration Factor (%): 100
Max Display Concentration: 9.099 mg/m³
Time at maximum: 11:42:33 May 05
Max STEL Concentration: 1.108 mg/m³
Time at max STEL: 11:45:05 May 05
Overall Avg Conc: 2.159 mg/m³

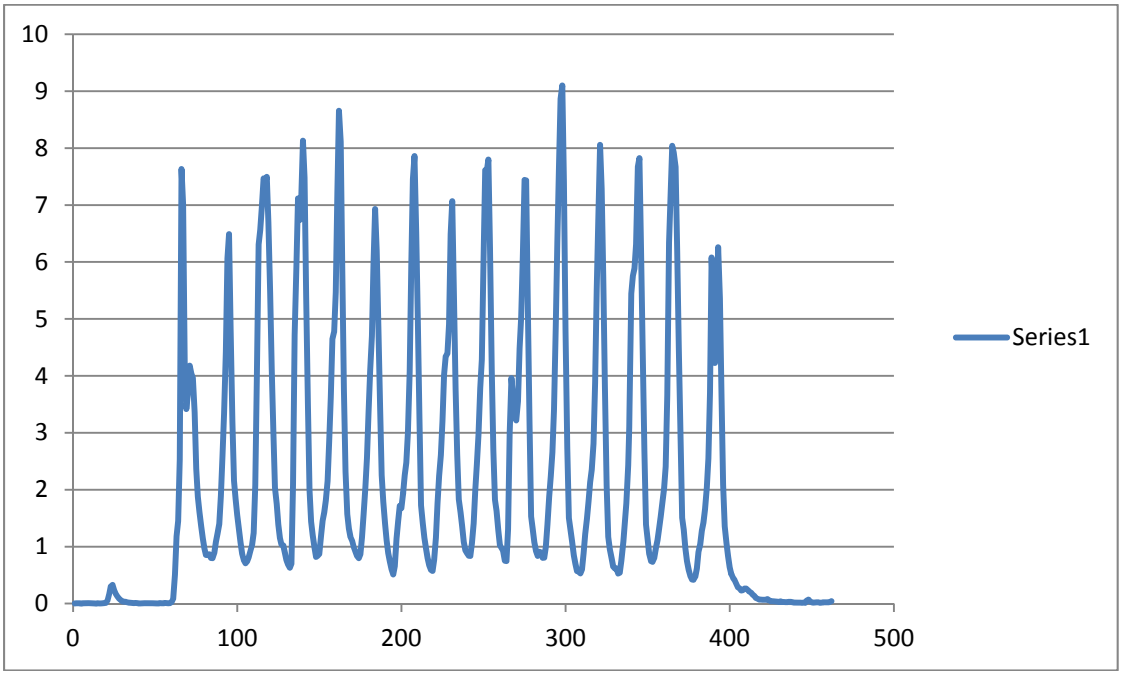

APPENDIX F

Third round test results: test 9

- Purpose: Test new type of cutter, with some additional wear
- Conditions: 6-Flute PCD Cutter used in Test 8 (from impactor D1 Test), 6000 rpm, 635 mm/min feed, .762 radial depth of cut, 6.35 mm axial depth of cut, climb, multi-directional laminate, top of laminate.
- **OPS 3330**

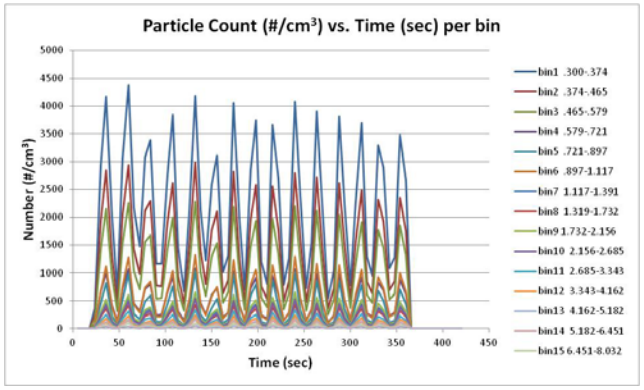

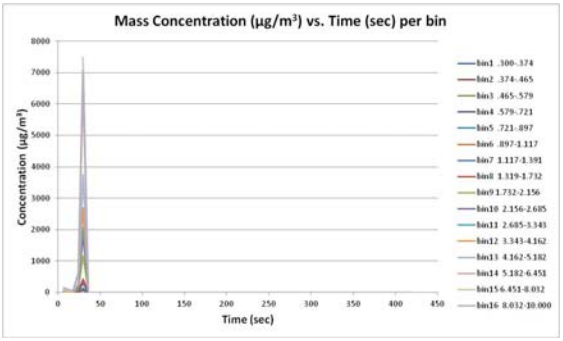

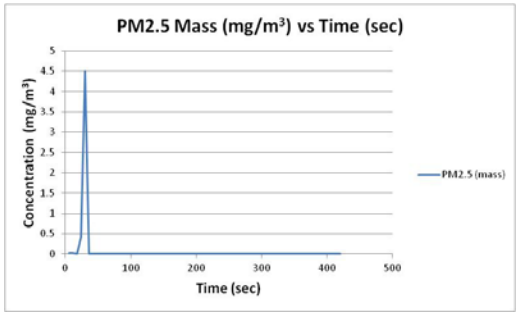

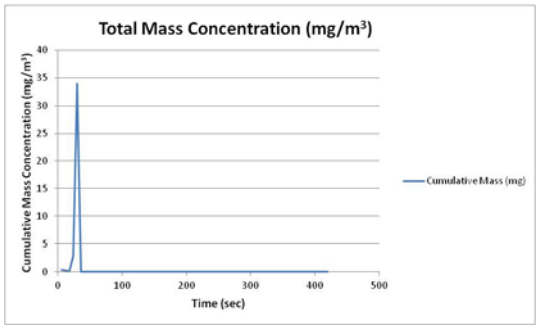

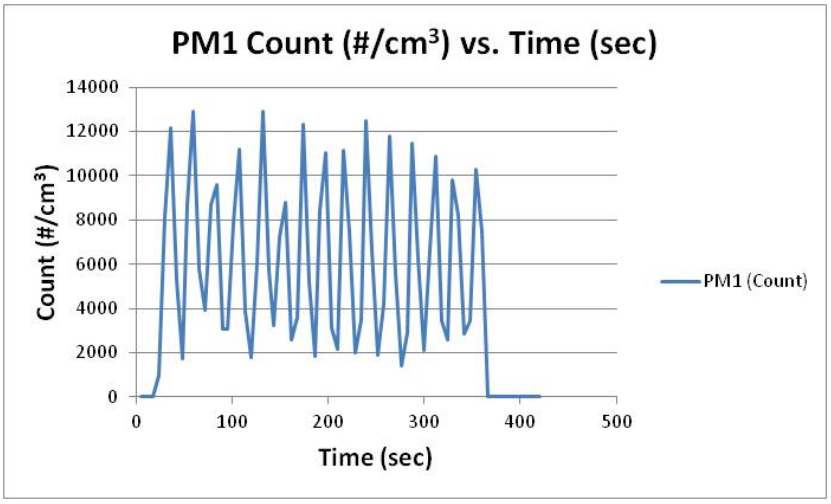

APPENDIX F

Third round test results: DustTRAK vs. PDR DataRAM Comparison

The figure below contrasts the results of two particle mass concentration measurement instruments. The dust profiles are very similar, but the magnitudes differ by a factor of 10.

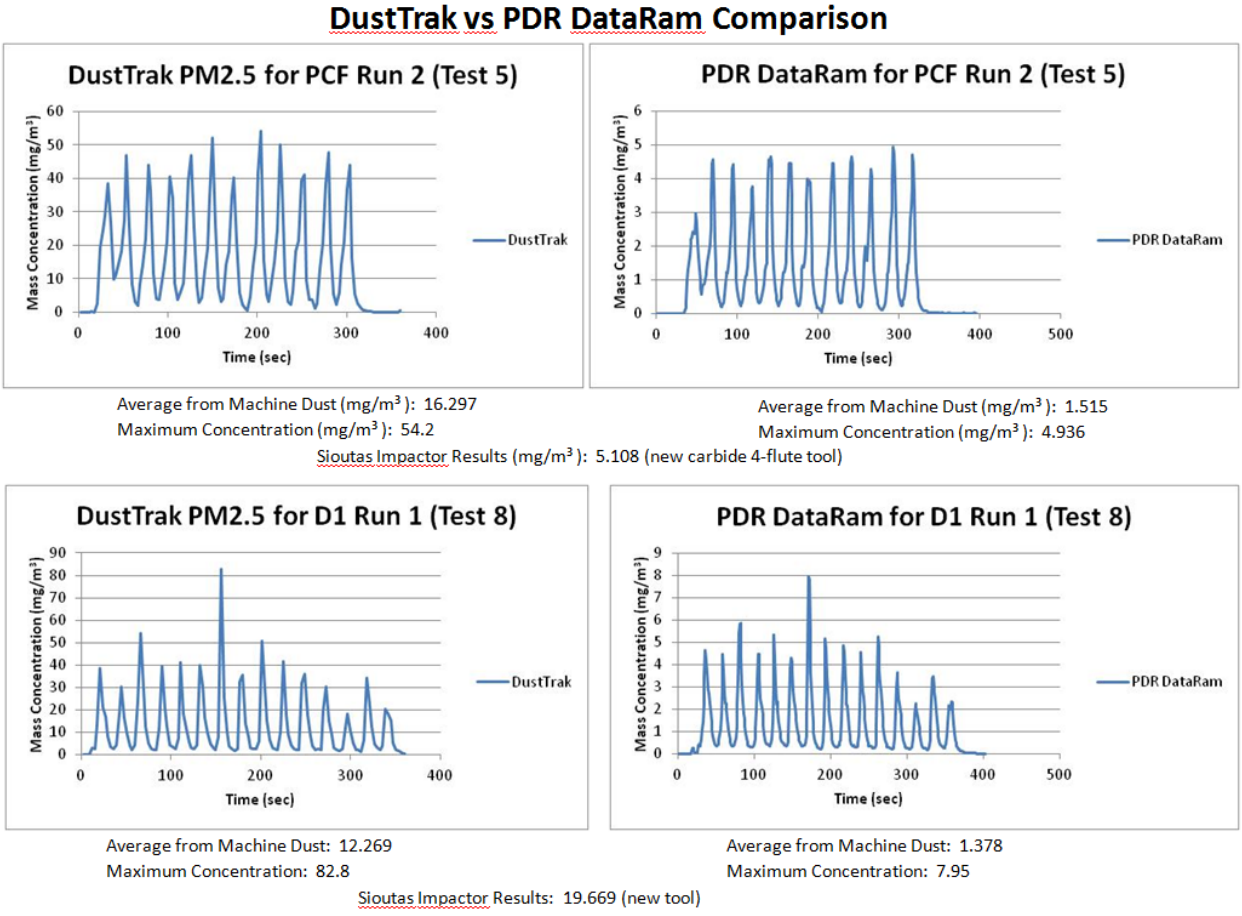

APPENDIX F

Third round test results: PTRAK vs. OPS 3330 Comparison

The figure below contrasts the results of two particle count concentration measurement instruments. The profiles are very similar, however, there are some differences in magnitude. The PTRAK hit the maximum concentration limits in the lower left plot. This could be attributed to improper cleaning before the test or overloading.

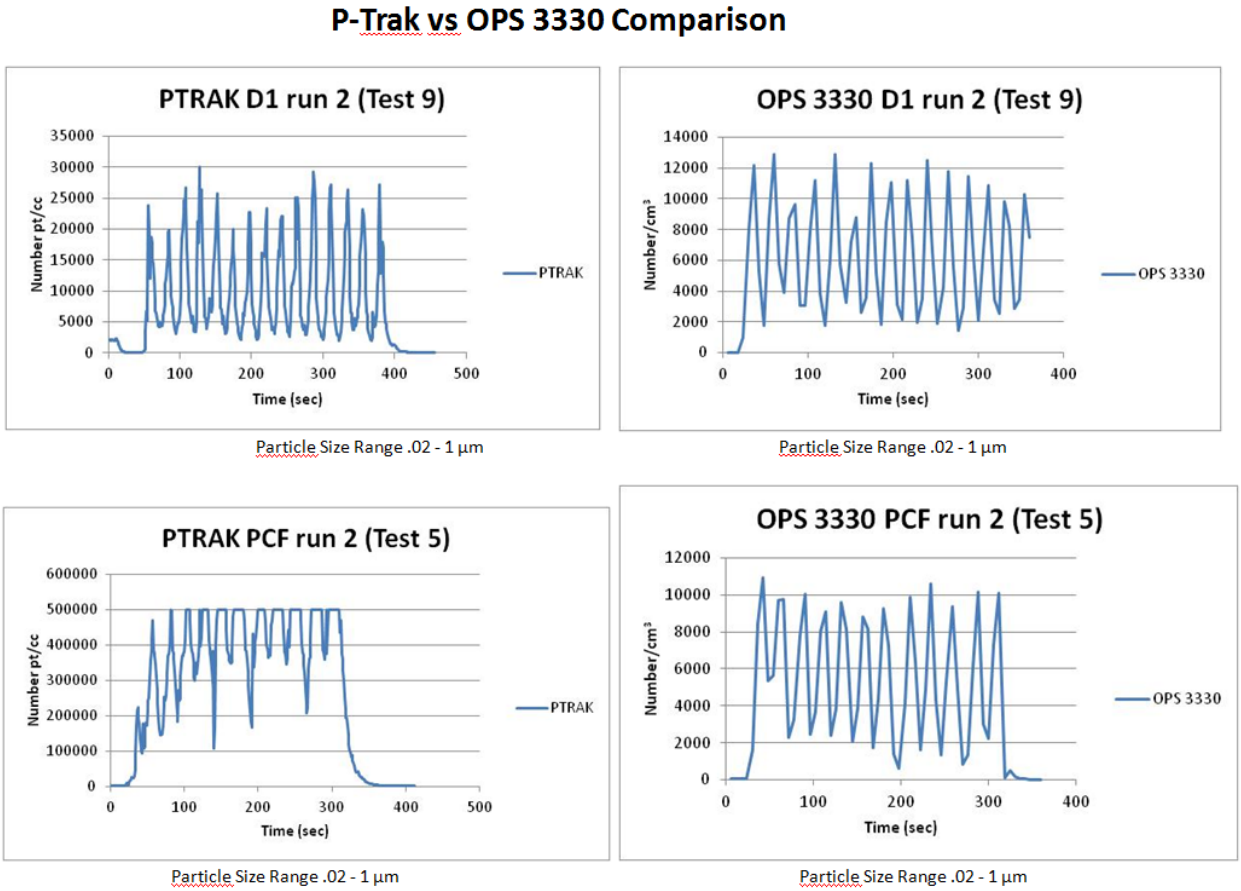

APPENDIX F

Third round test results: Gravimetric Comparison

The figure below contrasts compares gravimetric results between tests 4-7 to similar results of 3 cascade impactors. The DustTRAK appears to have higher concentration measurements by a factor of 3-4 compared to the impactors.

Gravimetric Comparison

Sample	Grav 1	Grav 2	Grav 3	Grav 4	D4 Impactor	E1 Impactor	A1 Impactor
Test	4	5	6	7			
Test Date	5/4/2013	5/4/2013	5/5/2013	5/5/2013	4/6/2013	4/16/2013	4/14/2012
Test Summary	Carbide cutter (used), multi, climb, top half	Carbide cutter (used), multi, climb, bottom half	Carbide cutter (new), TSI 2.5 oil impactor on tube inlet, multi, top half	Carbide cutter (used), TSI 2.5 oil impactor on tube inlet, multi, bottom half	D4 Impactor, multi, carbide, top half	multi, carbide, bottom half	multi, carbide, new cutter
Unexposed Filter Mass (mg)	91.7943	88.6725	90.3273	96.7808			
Exposed Filter Mass (mg)	94.1643	89.2430	90.6763	96.9928			
Sample Mass (mg)	2.3700	0.5705	0.3490	0.2120			
Flow Rate (assumed) (L/min)	2	2	2	2			
Total Sample Time (min)	10	6	7	6			
Cutting Time (min)	9:03	4:45	6:45	6			
Cutting Time (min-decimal)	9.05	4.75	6.75	6.00			
Concentration (Total) (mg/m^3)	118.5000	47.5417	24.9286	17.6667			
Concentration (Cutting) (mg/m^3)	130.9392	60.0526	25.8519	17.6667			
DustTrak Total Concentration (mg/m^3)	57.3000	16.9000	11.5000	10.9000			
SCF (per TSI) using Total	2.0681	2.8131	N/A	N/A			
Comment	Exceed max conc.	using PCF=2.0681 and SCF=.570	using PCF=2.0681, SCF=.570 and PM2.5 impactor	using PCF=2.0681, SCF=.570 and PM2.5 impactor	Impactor conc. Below	Impactor conc. Below	Impactor conc. Below
DustTrak PM2.5 Concentration (mg/m3)	17.0000	14.9000	10.6000	9.9900	4.5110	4.1400	5.1080

$$Concentration, \frac{mg}{m^3} = \frac{\left\{\begin{matrix}Filter\ Post\ Weight\ (mg) - \\ Filter\ Pre\ Weight\ (mg)\end{matrix}\right\}}{\frac{2}{3} \times \frac{\left\{\begin{matrix}DustTrak™\ Monitor \\ Flow\ Rate\ (L/min)\end{matrix}\right\}}{1000}} \times Total\ Sample\ Time\ (min)$$

7. Record the DustTrak monitor average concentration by viewing the sample average in the Data screen. (Data Screen is reviewed later in this chapter.)
8. Determine the mass concentration in mg/m^3 from your reference instrument. For gravimetric sampling this means weighing the gravimetric sample.

Note

If you used the internal gravimetric filter in the DustTrak Model 8533, the flow rate used to compute the concentration should be 2 L/min, not 3 L/min since only 2 L/min of aerosol flow reaches the filter.

9. Compute the new calibration constant, NewCal, using the following formula:

$$NewCal = \left(\frac{Reference\ \ Concentration}{DustTrak\ Concentration}\right) \cdot CurrentCal$$

APPENDIX E

DustTRAK gravimetric calibration

The data in Appendix E summarizes the DustTTRAK calibration calculations from the DustTRAK manual.

$$Concentration, \frac{mg}{m^3} = \frac{\left\{\begin{matrix} (Filter\ Post\ Weight\ (mg) - \\ Filter\ Pre\ Weight\ (mg) \end{matrix}\right\}}{\frac{2}{3} \times \frac{\left\{\begin{matrix} DustTrak™\ Monitor \\ Flow\ Rate\ (L/min) \end{matrix}\right\}}{1000}} \times Total\ Sample\ Time\ (min)$$

7. Record the DustTrak monitor average concentration by viewing the sample average in the Data screen. (Data Screen is reviewed later in this chapter.)
8. Determine the mass concentration in mg/m^3 from your reference instrument. For gravimetric sampling this means weighing the gravimetric sample.

Note
If you used the internal gravimetric filter in the DustTrak Model 8533, the flow rate used to compute the concentration should be 2 L/min, not 3 L/min since only 2 L/min of aerosol flow reaches the filter.

9. Compute the new calibration constant, NewCal, using the following formula:

$$NewCal = \left(\frac{Reference\ \ Concentration}{DustTrak\ Concentration}\right) \cdot CurrentCal$$

Step 1: PCF Calibration

- Install a $PM_{2.5}$ impactor at the inlet of the external gravimetric filter.
- Co-locate and run the gravimetric sample and DustTrak DRX monitor simultaneously to collect enough mass on the gravimetric filter.
- Calculate the $PM_{2.5}$ mass concentration ($PM_{2.5\_Grav}$) from the gravimetric filter based on the net mass collected on the filter, sampling time, flow rate, and total liters of air sampled.
- Read the DustTrak DRX monitor average $PM_{2.5}$ mass concentration ($PM_{2.5\_DRX}$) from the screen or through TrakPro Data Analysis Software.
- Calculate the new PCF

$$PCF_{New} = \frac{PM_{2.5\_Grav}}{PM_{2.5\_DRX}} \times PCF_{Old}$$

- Update the new PCF in user calibration settings.

APPENDIX G

Fourth round test results: test 1

- Purpose: Initial test of GRIMM portable aerosol spectrometer.
- Conditions: New 4-Flute Carbide Cutter used, 6000 rpm, 635 mm/min feed, .762 radial depth of cut, 6.35 mm axial depth of cut, climb, multi-directional laminate, top of laminate.
- Test both PTRAK and GRIMM units
- Standard fixed stationary side vacuum exhaust

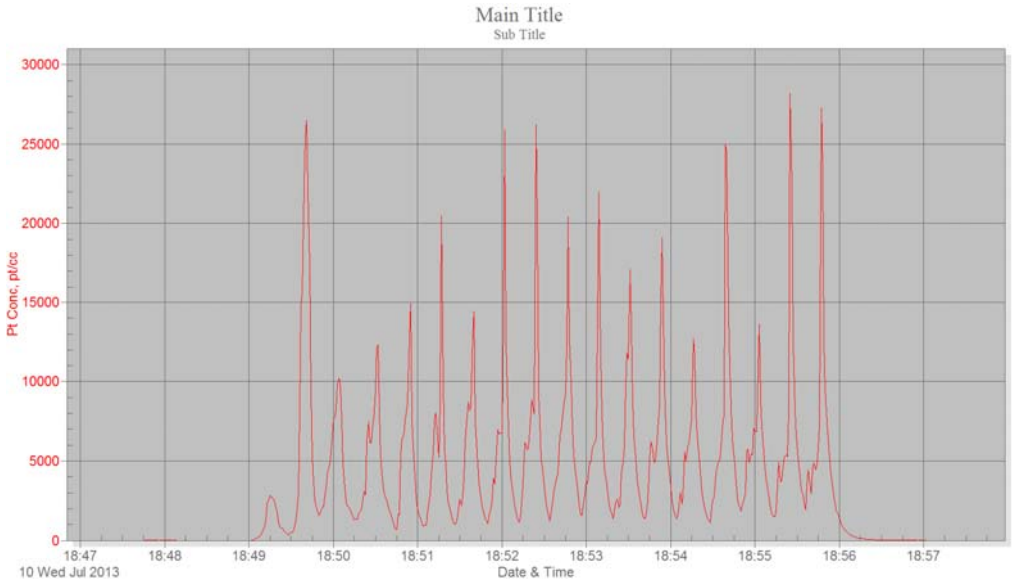

PTRAK results

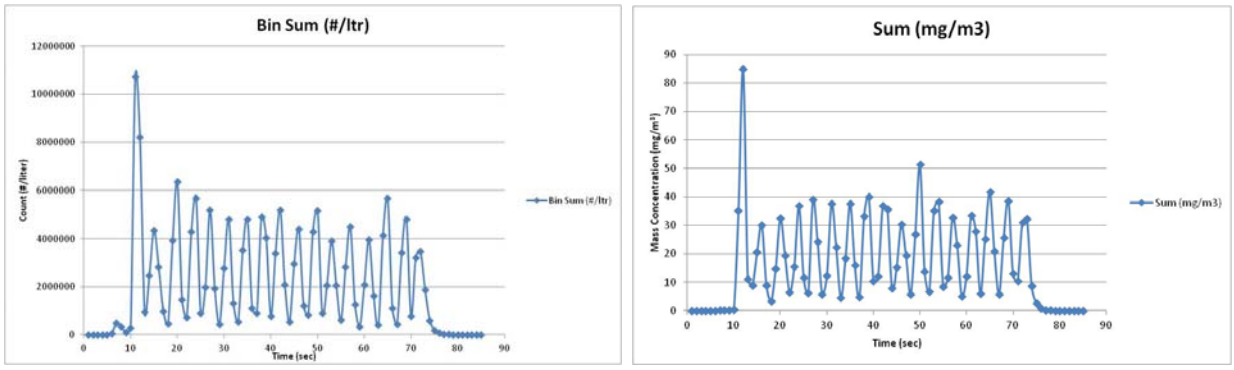

GRIMM results

Side dust vacuum configuration.

APPENDIX G

Fourth round test results: test 2

- Purpose: Initial test of GRIMM portable aerosol spectrometer.
- Conditions: New 4-Flute Carbide Cutter used, 6000 rpm, 635 mm/min feed, .762 radial depth of cut, 6.35 mm axial depth of cut, climb, multi-directional laminate, bottom of laminate.
- Test both PTRAK and GRIMM units
- Standard fixed stationary side vacuum exhaust

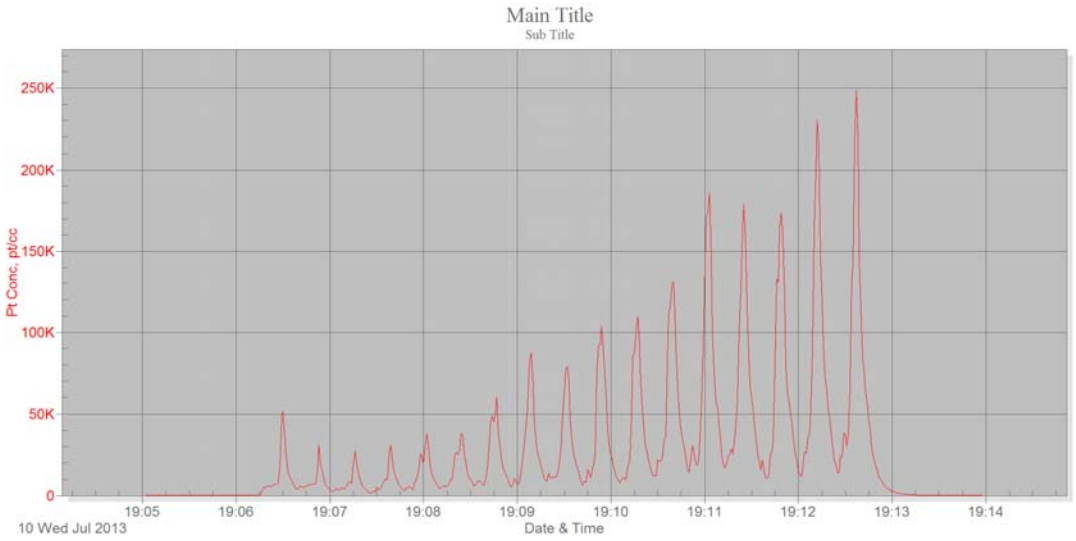

PTRAK results

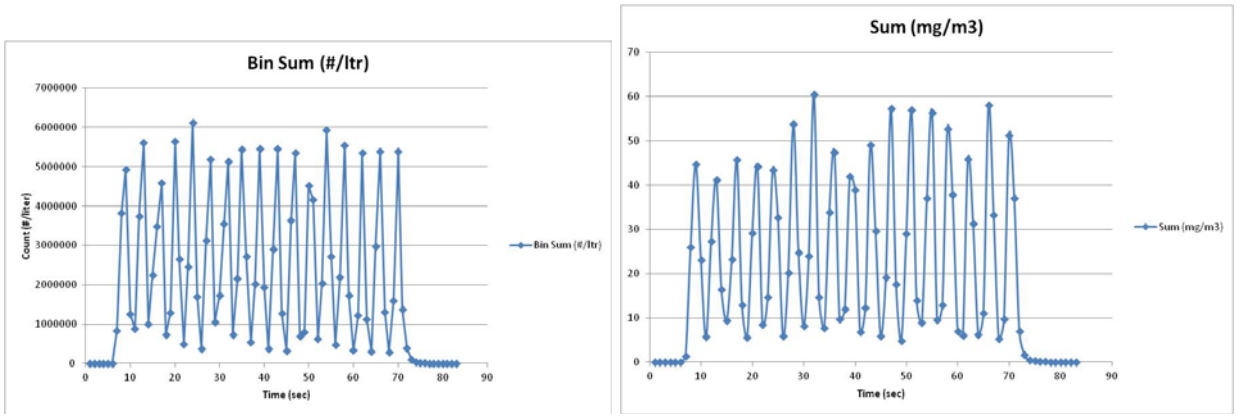

GRIMM results

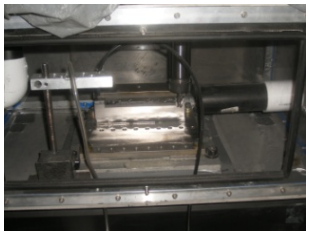

Side dust vacuum configuration.

APPENDIX G

Fourth round test results: test 3

- Purpose: Initial test of GRIMM portable aerosol spectrometer.
- Conditions: Same Carbide Cutter in this series, 6000 rpm, 635 mm/min feed, .762 radial depth of cut, 12.7 mm axial depth of cut, climb, multi-directional laminate, bottom of laminate.
- Test both PTRAK and GRIMM units and effect of moving Loc-line vacuum
- Loc-line moving vacuum on, side vacuum off

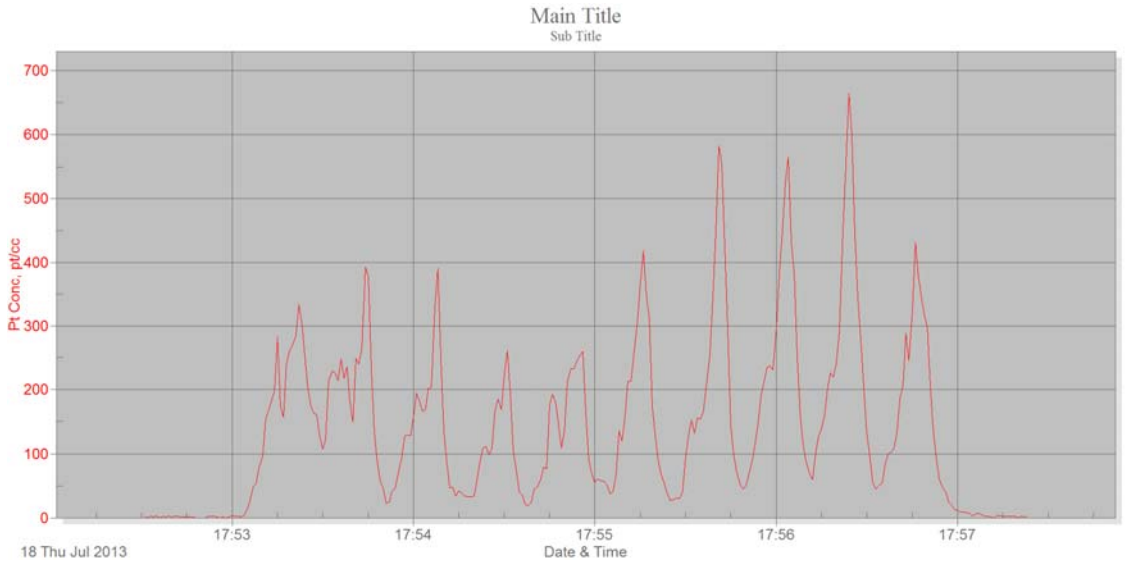

PTRAK results

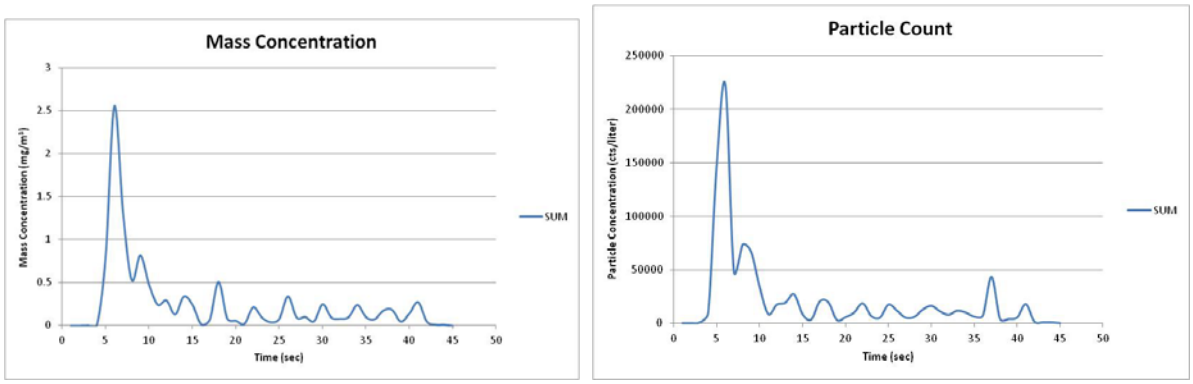

GRIMM results

Loc-line moving vacuum on, side vacuum off.

APPENDIX G

Fourth round test results: test 4

- Purpose: Initial test of GRIMM portable aerosol spectrometer.
- Conditions: Same Carbide Cutter in this series, 6000 rpm, 635 mm/min feed, .762 radial depth of cut, 12.7 mm axial depth of cut, climb, multi-directional laminate, bottom of laminate.
- Test both PTRAK and GRIMM units and effect of moving and fixed vacuums
- Loc-line moving vacuum on, side vacuum on

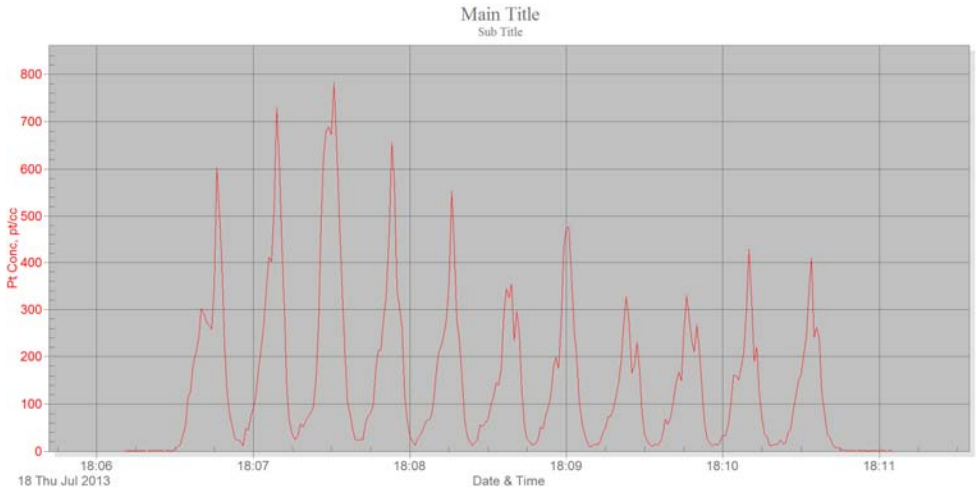

PTRAK results

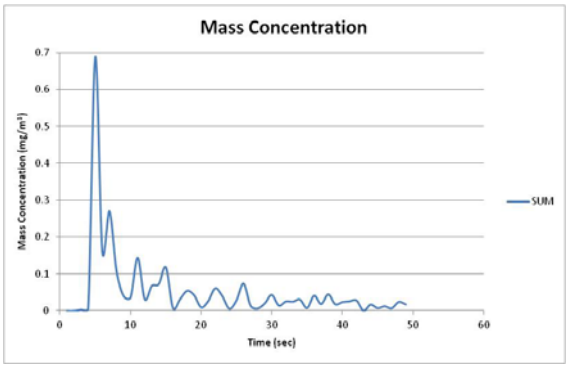

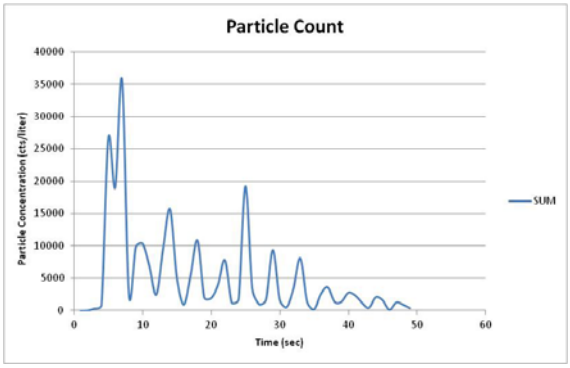

GRIMM results

Loc-line and side vacuum systems running

APPENDIX G

Fourth round test results: test 5

- Purpose: Initial test of GRIMM portable aerosol spectrometer.
- Conditions: Same Carbide Cutter in this series, 6000 rpm, 635 mm/min feed, .762 radial depth of cut, 12.7 mm axial depth of cut, climb, multi-directional laminate, bottom of laminate.
- Test both PTRAK and GRIMM units and effect of moving and fixed vacuums
- 2 links removed from Loc-line moving vacuum on, side vacuum off

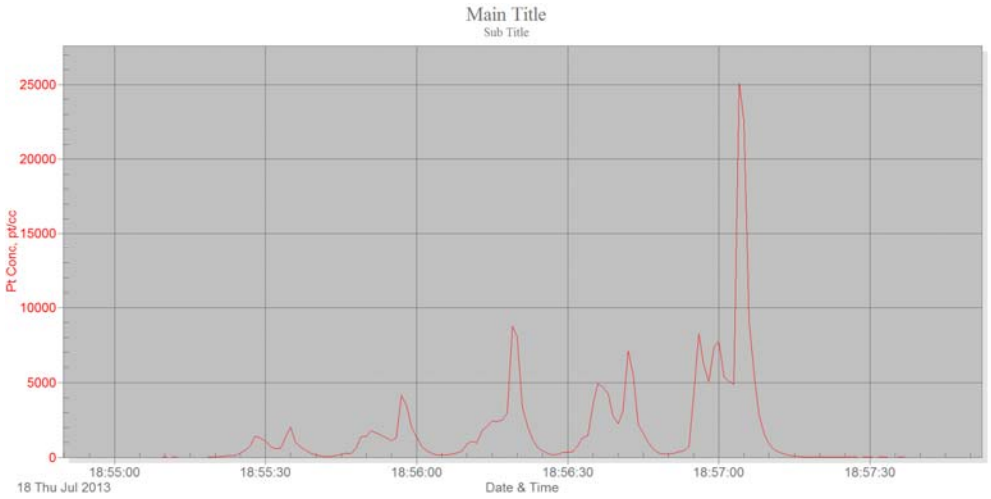

PTRAK results

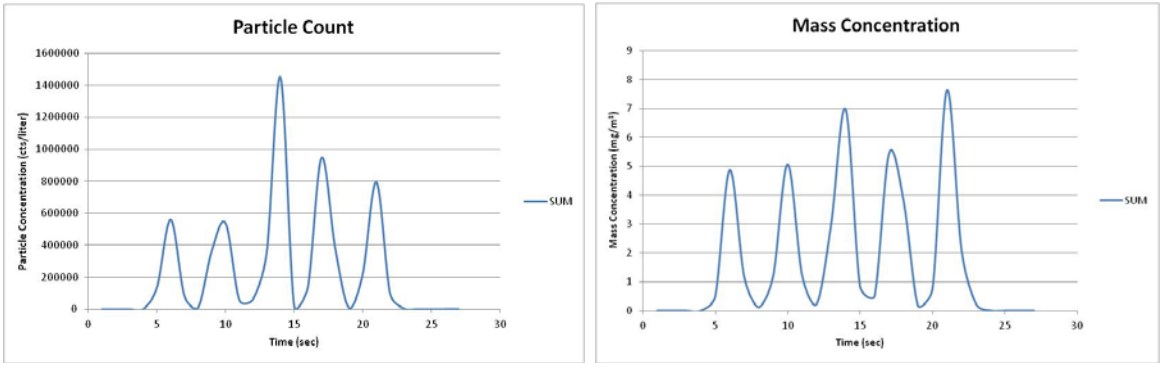

GRIMM results

2 links removed from Loc-line and side vacuum closed

APPENDIX H

Additional Isokinetic System Sketches

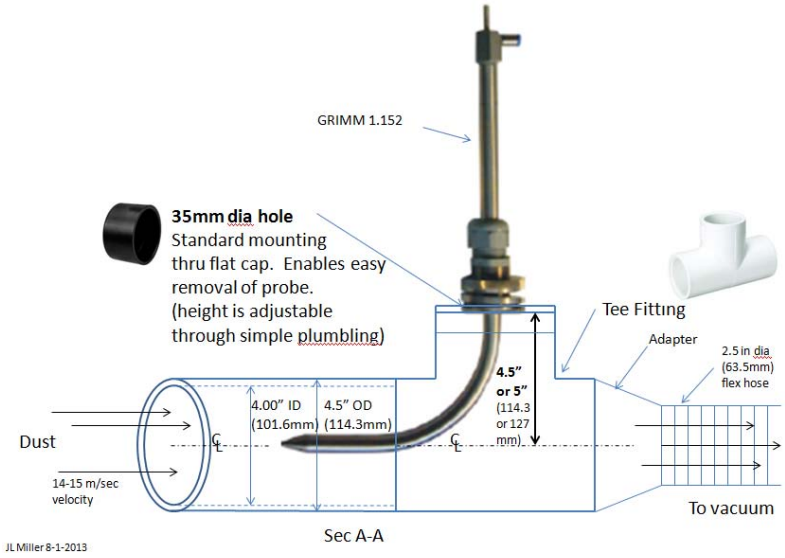

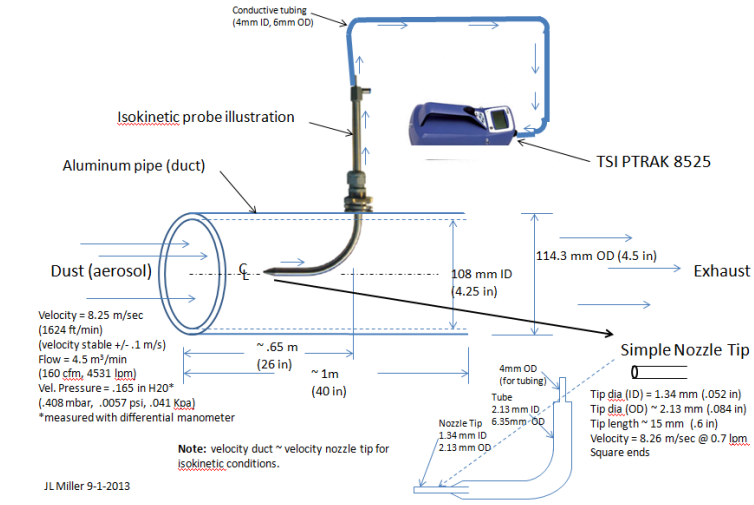

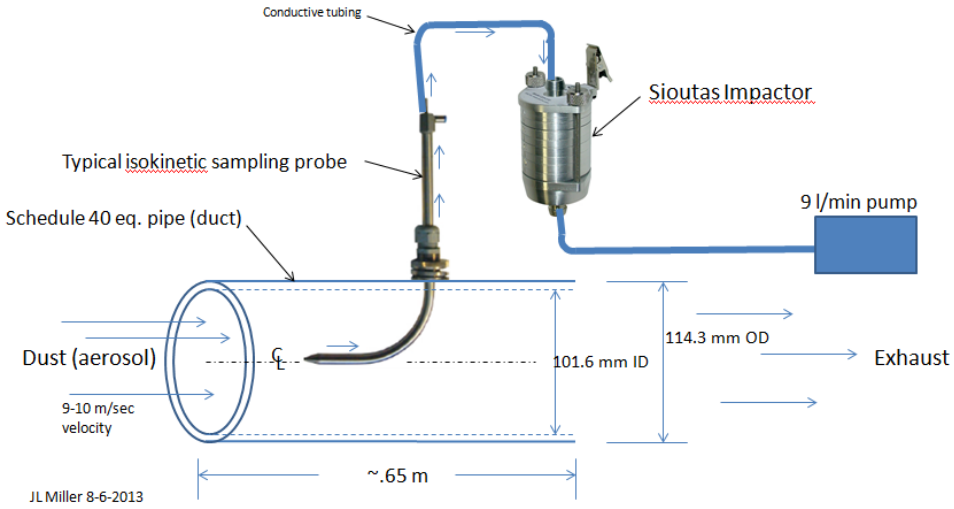

APPENDIX I
Flow Testing

Basic shop vacuum flow testing (Sears Craftsman 6.5 HP Shop Vac)

ID	Test Conditions	Test Objectives	Instruments	Results
7/27-1a	Old shop vacuum with 2.08" ID inlet, single hose, reducer and exhaust muffler	Flow velocity measurement	Kestrel Pocket Wind meter, K2000	28-47 m/sec
7/27-1b	New shop vacuum with 2.08" ID inlet, single hose, reducer and exhaust muffler	Flow velocity measurement	Kestrel Pocket Wind meter, K2000	53-61 m/sec
7/27/-2a	Old shop vacuum with 3" ABS open pipe (3.06" ID), single hose, reducer and exhaust muffler	Flow velocity measurement	Kestrel Pocket Wind meter, K2000	14.4 m/sec
7/27-2b	New shop vacuum with 3" ABS open pipe (3.06" ID), single hose, reducer and exhaust muffler	Flow velocity measurement	Kestrel Pocket Wind meter, K2000	15.2 m/sec
7/27/-3a	Old shop vacuum with 2.08" ID hose to 3" ABS pipe to 2.08" ID hose using reducers and exhaust muffler	Flow velocity measurement	Kestrel Pocket Wind meter, K2000	45 m/sec
7/27-3b	New shop vacuum with 2.08" ID hose to 3" ABS pipe to 2.08" ID hose using reducers and exhaust muffler	Flow velocity measurement	Kestrel Pocket Wind meter, K2000	45-52 m/sec off scale
7/27/-4a	Old shop vacuum with 2.08" ID hose to Loc-Line modular hose and exhaust muffler	Flow velocity measurement	Kestrel Pocket Wind meter, K2000	18.5 m/sec
7/27-4b	New shop vacuum with 2.08" ID hose to Loc-Line modular hose and exhaust muffler	Flow velocity measurement	Kestrel Pocket Wind meter, K2000	18.5 m/sec
7/27/-5a	Old shop vacuum with 2.08" ID hose to Loc-Line modular hose and exhaust through HEPA filter using 2.08" ID hose	Flow velocity measurement	Kestrel Pocket Wind meter, K2000	16.0 m/sec
7/27-5b	New shop vacuum with 2.08" ID hose to Loc-Line modular hose and exhaust through HEPA filter using 2.08" ID hose	Flow velocity measurement	Kestrel Pocket Wind meter, K2000	16.5 m/sec
7/27/-6a	Old shop vacuum with 2.08" ID hose to 3" ABS pipe to 2.08" ID hose using reducers and exhaust and exhaust through HEPA filter using 2.08" ID hose	Flow velocity measurement	Kestrel Pocket Wind meter, K2000	16.5 m/sec
7/27-6b	New shop vacuum with 2.08" ID hose to 3" ABS pipe to 2.08" ID hose using reducers and exhaust and exhaust through HEPA filter using 2.08" ID hose	Flow velocity measurement	Kestrel Pocket Wind meter, K2000	8.6 – 8.7 m/sec (broken vane, later replaced with Amprobe)

APPENDIX I

Flow Testing

HEPA filter pressure drop testing
Sears Craftsman 6.5 HP shop vacuum
HEPA Filter: SBM BioMax Model H10A3X1

ID	Test Conditions	Test Objectives	Instruments	Results
8/31-1	New shop vacuum, 2.08" ID hose from shop vacuum exhaust to 3"ABS pipe using reducer with muffler on shop vacuum inlet	Flow velocity measurement, baseline	Amprobe TMA-40A Wind Vane Anemometer	23.0 m/sec
8/31-2	New shop vacuum, 2.08" ID hose from shop vacuum exhaust to HEPA filter inlet, HEPA outlet to 3"ABS pipe using reducer with muffler on shop vacuum inlet	Flow velocity measurement, impact of HEPA filter	Amprobe TMA-40A Wind Vane Anemometer	21.6 m/sec
8/31-3	New shop vacuum, 2.50" ID , 6" long, hose from shop vacuum exhaust to HEPA filter inlet, HEPA outlet to 3"ABS pipe using reducer with muffler on shop vacuum inlet	Flow velocity measurement using shorter larger diameter hose. Does this increase velocity?	Amprobe TMA-40A Wind Vane Anemometer	25.0 m/sec
8/31-4	New shop vacuum, 2.50" ID , 6" long, hose from shop vacuum exhaust to 3"ABS pipe using reducer with muffler on shop vacuum inlet	Flow velocity measurement. Impact of shorter length, larger diameter hose without HEPA.	Amprobe TMA-40A Wind Vane Anemometer	30.0 m/sec
8/31/-5	New shop vacuum, 2.50" ID , 24.5 ft long, hose from shop vacuum exhaust to 3"ABS pipe using reducer with muffler on shop vacuum inlet	Flow velocity measurement. Impact of longer length, larger diameter hose without HEPA.	Amprobe TMA-40A Wind Vane Anemometer	24.8 m/sec
8/31/-6	New shop vacuum, 2.50" ID , 24.5 ft long, hose from shop vacuum inlet to 3"ABS pipe using reducer with muffler on shop vacuum exhaust	Flow velocity measurement. Impact of longer length, larger diameter hose without HEPA. Effect of suction vs. exhaust of flow velocity.	Amprobe TMA-40A Wind Vane Anemometer	22.8 m/sec

APPENDIX I

Flow Testing

Duct flow testing using wind vane anemometers and pitot tubes.

ID	Test Conditions	Test Objectives	Instruments	Results
9/16-1	New shop vacuum, 2.50" ID conductive hose, 3ft long, from shop vacuum inlet to 60" long pipe (39" + Tee + 23"), 4.25" ID, using reducer, shop vacuum exhaust open. Velocity measured at open pipe.	Flow velocity measurement. Evaluating duct flow velocity.	Amprobe TMA-40A Wind Vane Anemometer	13.0 m/sec
9/16-2	New shop vacuum, 2.50" ID conductive hose, 3ft long, from shop vacuum inlet to39" long pipe, 4.25" ID, using reducer, shop vacuum exhaust open. Velocity measured at open pipe.	Flow velocity measurement. Impact of shorter pipe and no tee.	Amprobe TMA-40A Wind Vane Anemometer	12.4 m/sec
9/16-3	New shop vacuum, 2.50" ID conductive hose, 3ft long, from shop vacuum inlet to 60" long pipe, 4.25" ID, using reducer, shop vacuum exhaust open. Velocity measured at open pipe and pitot tube.	Flow velocity measurement. Comparing wind vane to Dywer Series 160 pitot tube.	Amprobe TMA-40A Wind Vane Anemometer, Dwyer Series 160 pitot tube.	12.7 m/sec (wind vane), Pitot tube 16 in H20, ~ 8.15 m/sec
9/17-1	New shop vacuum, 2.50" ID conductive hose, 3ft long, from shop vacuum inlet to 60" long pipe, 4.25" ID, using reducer, shop vacuum exhaust open. Velocity measured at open pipe and pitot tube.	Flow velocity measurement. Comparing wind vane to Dwyer DS-300 pitot tube.	Amprobe TMA-40A Wind Vane Anemometer, Dwyer Series DS-300 pitot tube	13.0 m/sec (wind vane)
9/17-2	New shop vacuum, 2.50" ID conductive hose, 3ft long, from shop vacuum inlet to 60" long pipe (39" + Tee + 23"), 4.25" ID, using reducer, shop vacuum exhaust open. Velocity measured at open pipe and pitot tube.	Flow velocity measurement. Comparing wind vane to 2 types of pitot tubes (DS-300 and Series 160).	Amprobe TMA-40A Wind Vane Anemometer, Dwyer Series 160 pitot tube, Dwyer Series DS-300 pitot tube	13.2 m/sec (wind vane), DS-300 (32-35 in H20~7.59 m/sec), Series 160 (.19 in H20~8.88 m/sec) DS-300 fluctuated, Series 160 was steady.

APPENDIX J

Diluter filter life calculations

The spreadsheet estimates filter life under planned operating conditions using the manufacturers filter capacity assumptions. Since replacement filters are relatively expensive, the objective was to estimate how long they would last prior to requiring replacement. The results show that the filters should last nearly 500 hours under extreme conditions with particle diameter at 6 µm, particle count at 13E9/m^3, and GRIMM flow rate of 1.2 lpm.

Input	**Filter Capability**	**Particle Counter**	
Particle Size (µm)	0.4	6	
Particle Density (g/cm3)	1	1.81	
Number of Particles/m3	2.00E+12	13,000,000,000	
Flow Rate (liter/min)	28.32	1.2	
Time (min)	30000	30000	
Calculations			
Number of Particles/liter3	2.00E+09	13000000	
Number of Particles/cm3	2.00E+06	13000	
Particle Density (mg/m^3)	1000000000	1810000000	
Single Particle Volume (µm)^3	0.033510322	113.0973355	
Single Particle Volume (m^3)	3.35103E-20	1.13097E-16	
Single Particle Mass (mg)	3.35103E-11	2.04706E-07	
Quantity Mass Particles (mg)/m3	67.02064328	2661.180305	
Quantity Mass Particles (µg)/m3	67020.64328	2661180.305	
Quantity Volume Particles (µm^3/m3)	6.70E+10	1.47E+12	
Quanity Volume Particles (cc/m3)	6.70E-02	1.47E+00	
Flow Rate m3/min	0.02832	0.0012	
Total Air Flow Volume (m3)	849.6	36	
Total collected mass per flow time (mg)	56940.73853	95802.49098	
Total collected mass per flow time (g)	56.941	95.802	
Total collected volume per flow time (cc)	56.941	52.930	
Filter specification: Long term operation over 500h at minimum guaranteed (aerosol flow 1cfm with 2 x 10^6 particle/ccm^3 (<1µm)			
Density T800 fiber (g/cm3) = 1.81			
% reference of particle counter to filter capability by mass:		168.25%	1.682
% reference of particle counter to filter capability by volume:		92.96%	0.930

APPENDIX K

Multi-Instrument Isokinetic Experiments:

Test #1

- Purpose: Validate vacuum-only performance.

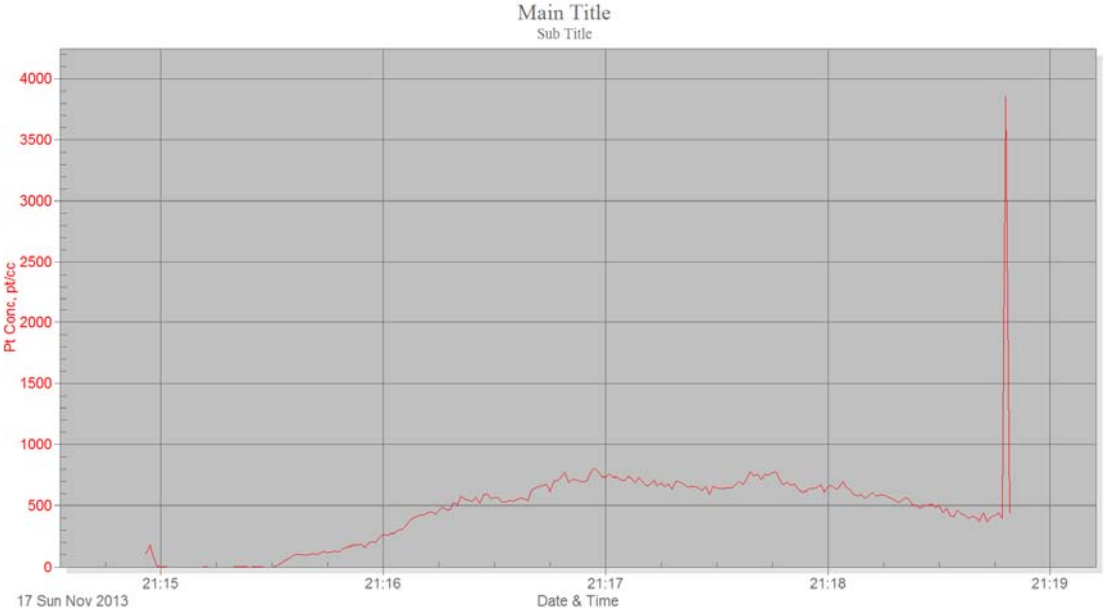

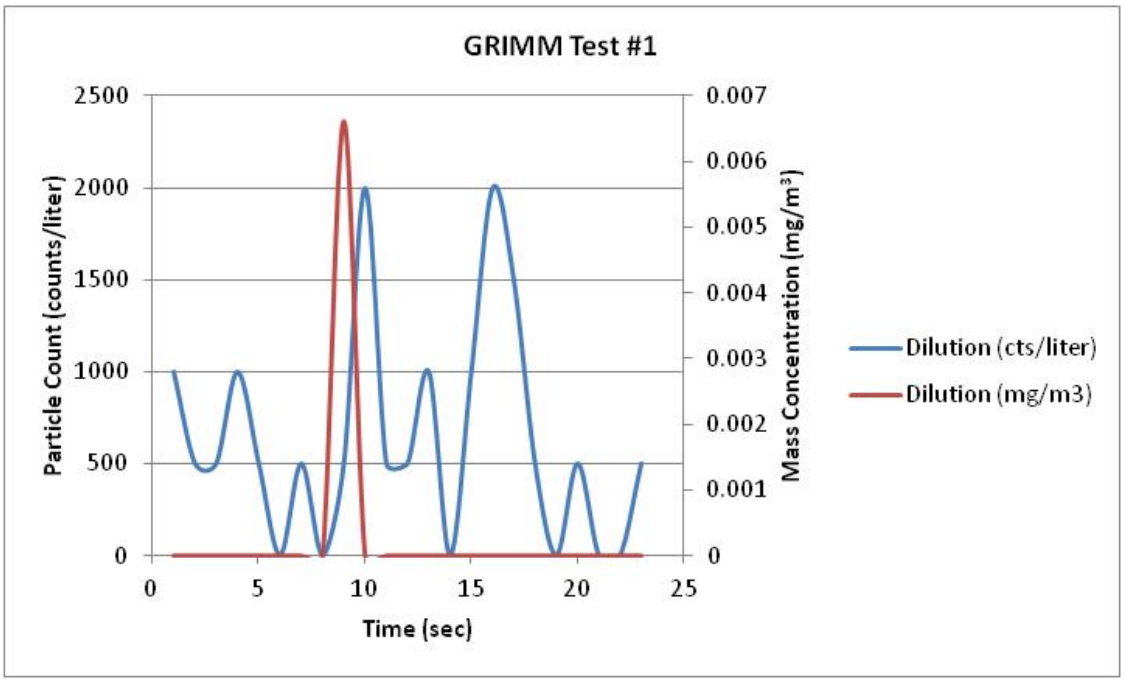

APPENDIX K

Multi-Instrument Isokinetic Experiments:

Test #2

- Purpose: Evaluate new 4-flute carbide cutter, top of laminate and new anti-static vacuum hose.

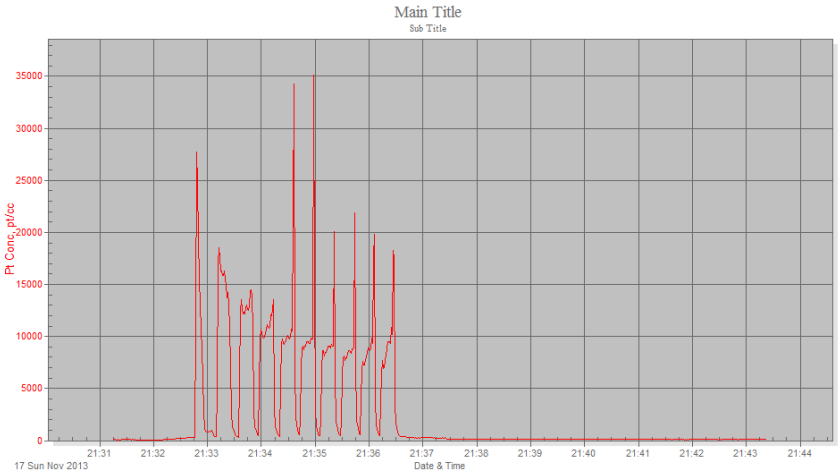

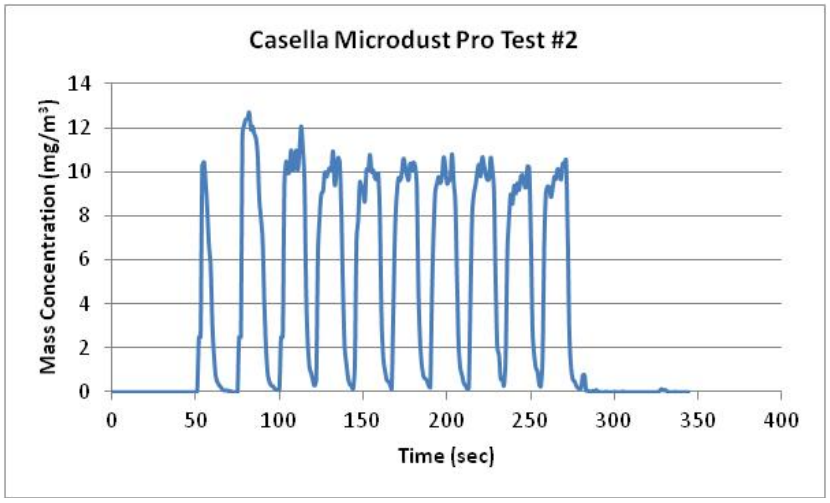

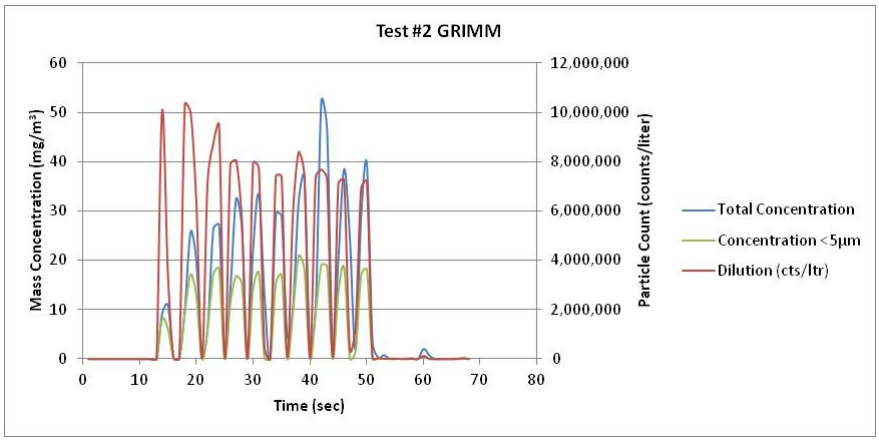

APPENDIX K

Multi-Instrument Isokinetic Experiments:

Test #3

- Purpose: Same 4-flute carbide cutter, bottom of laminate.

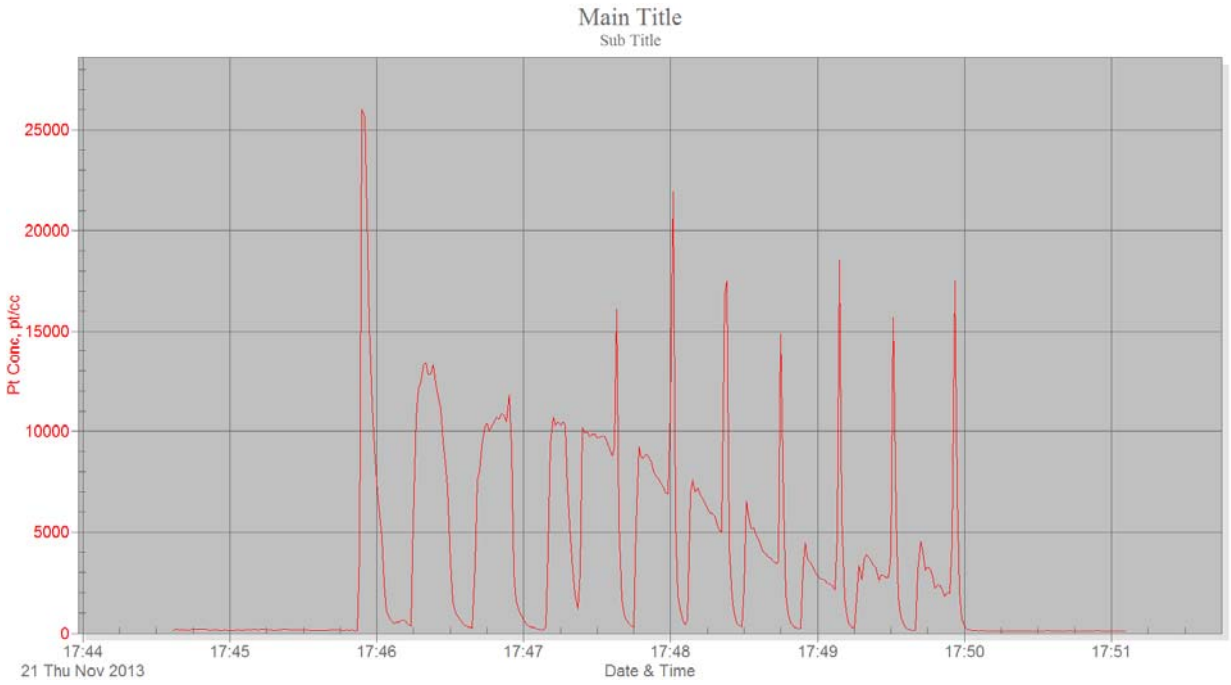

APPENDIX K

Multi-Instrument Isokinetic Experiments:

Test #4

- Purpose: Same 4-flute carbide top of laminate.

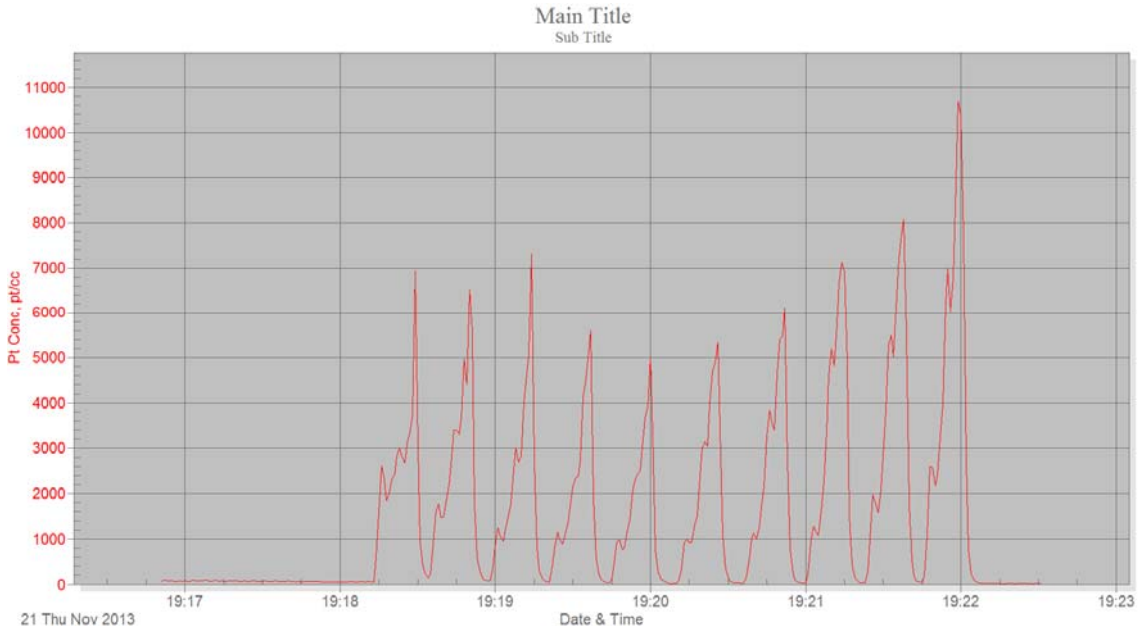

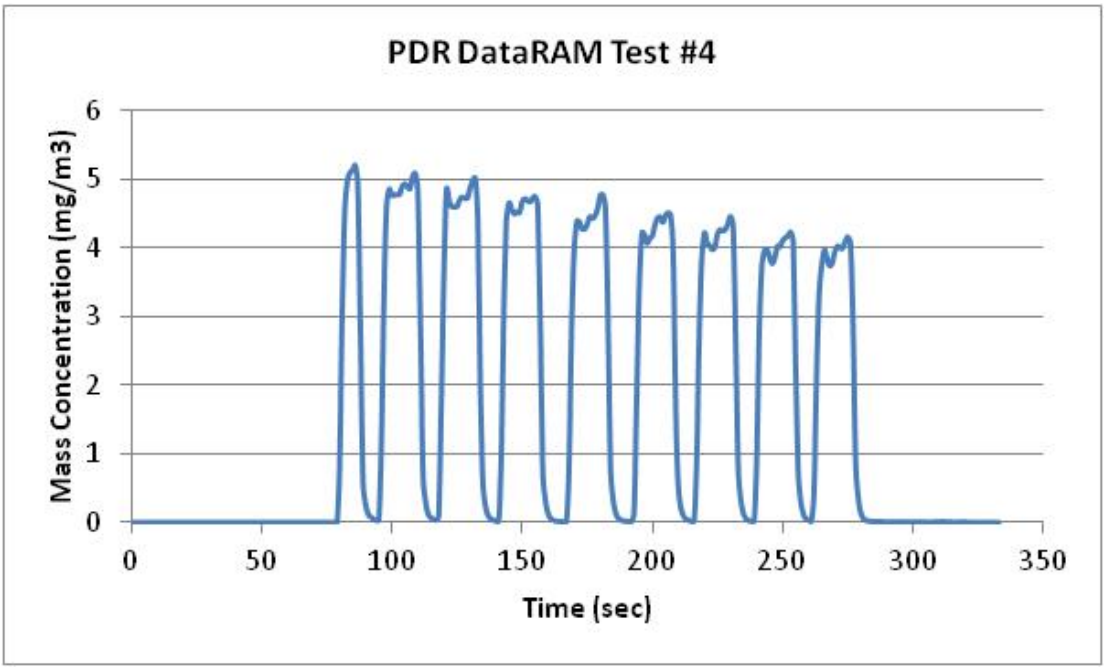

APPENDIX K

Multi-Instrument Isokinetic Experiments:

Test #5

- Purpose: Same 4-flute carbide cutter, bottom laminate.

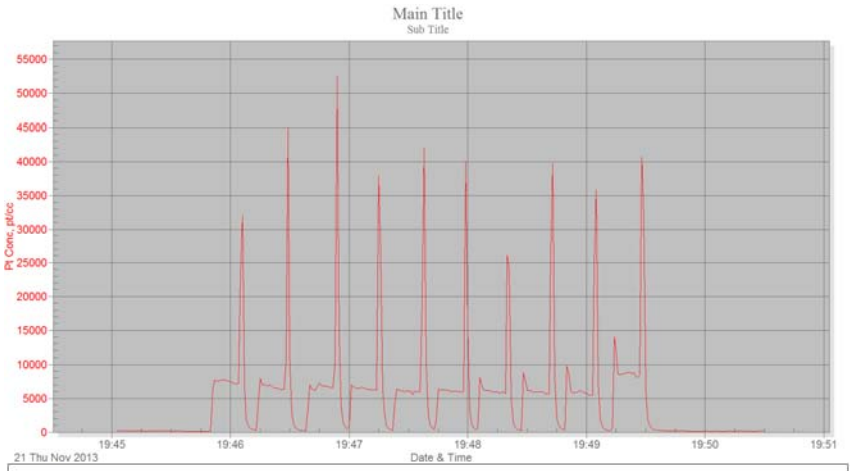

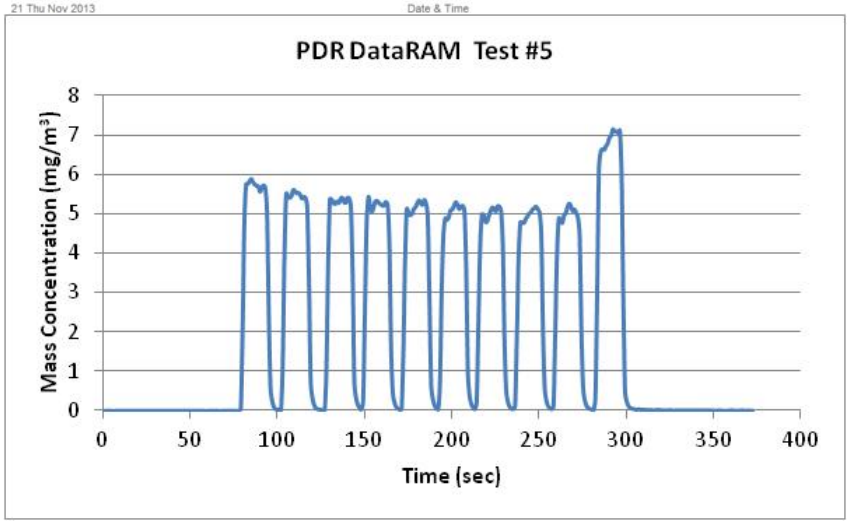

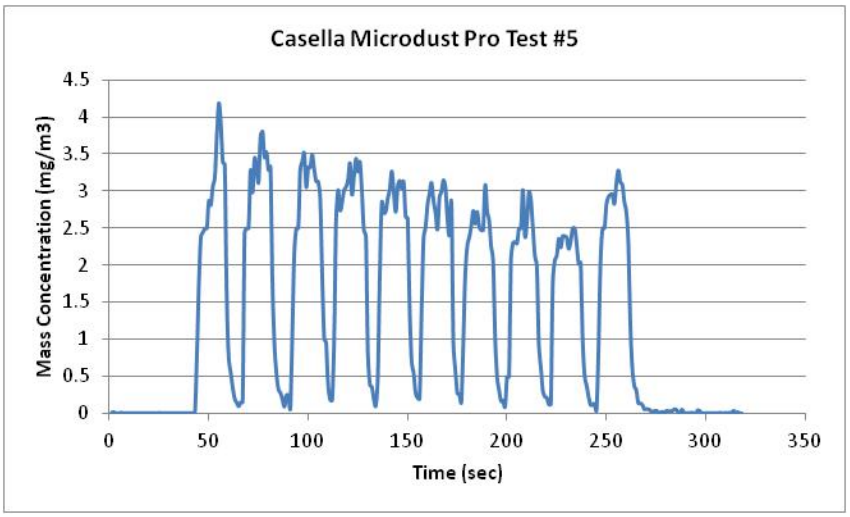

APPENDIX K

Multi-Instrument Isokinetic Experiments:

Test #6

- Purpose. Same 4-flute carbide cutter, full laminate (12.7 mm).

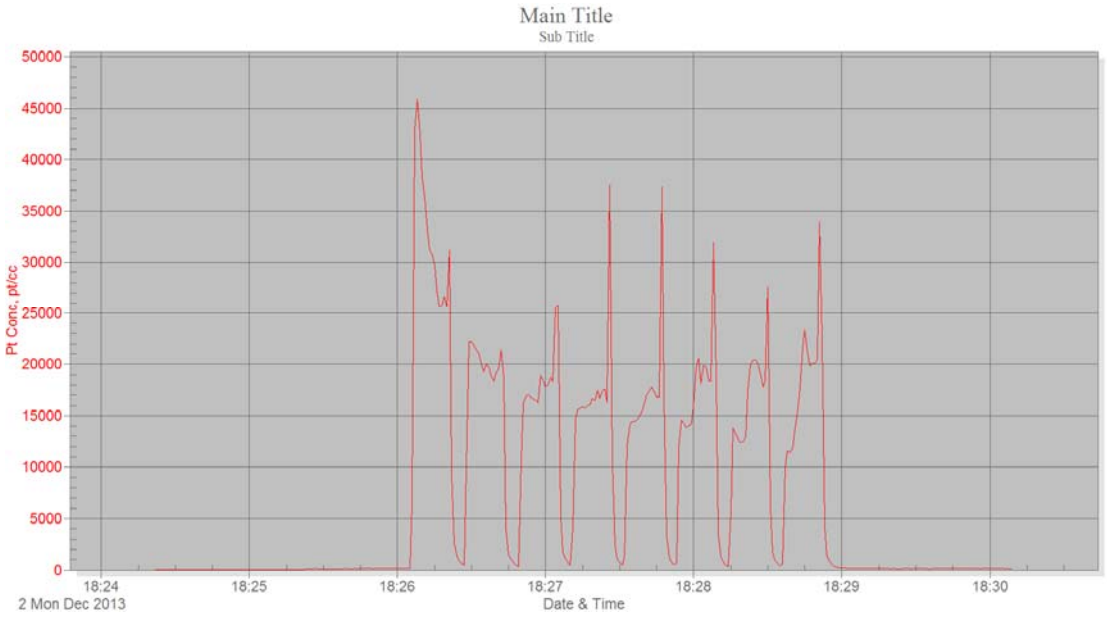

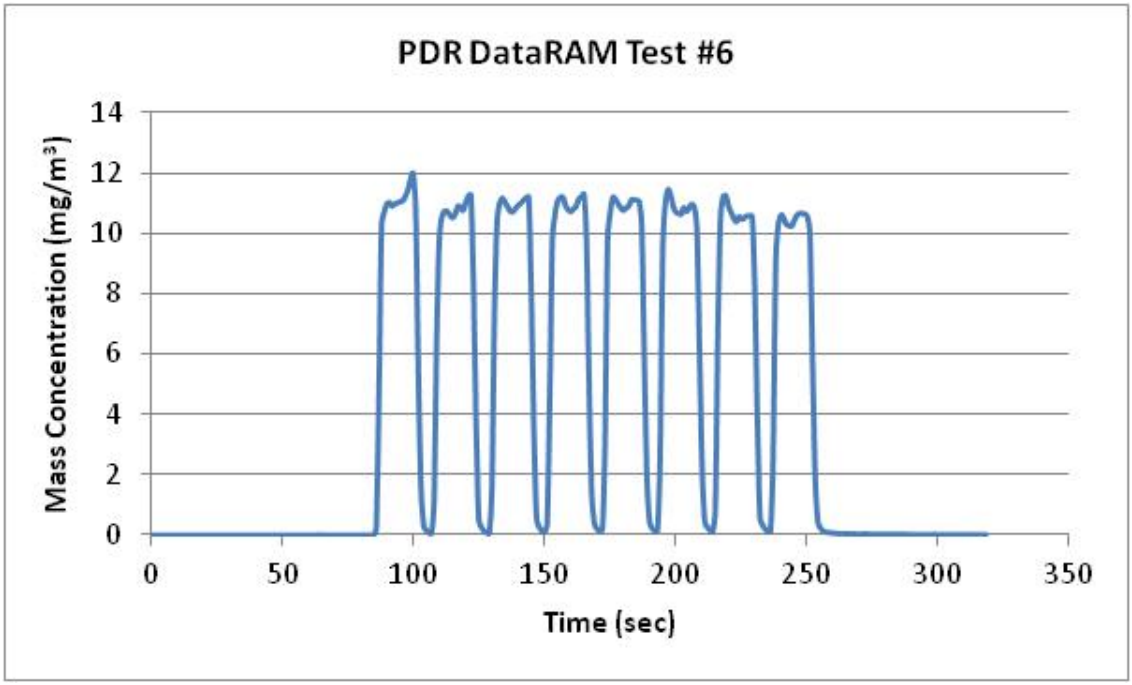

APPENDIX K

Multi-Instrument Isokinetic Experiments:

Test #7

- Purpose: Same 4-flute carbide cutter, full laminate (12.7mm).

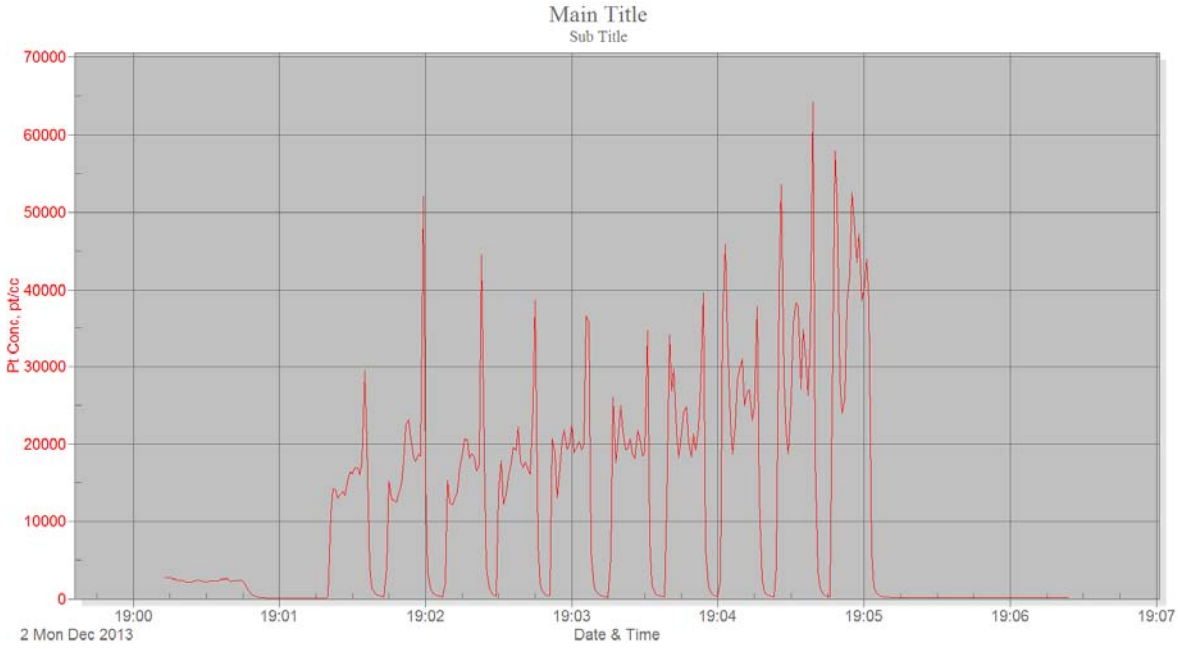

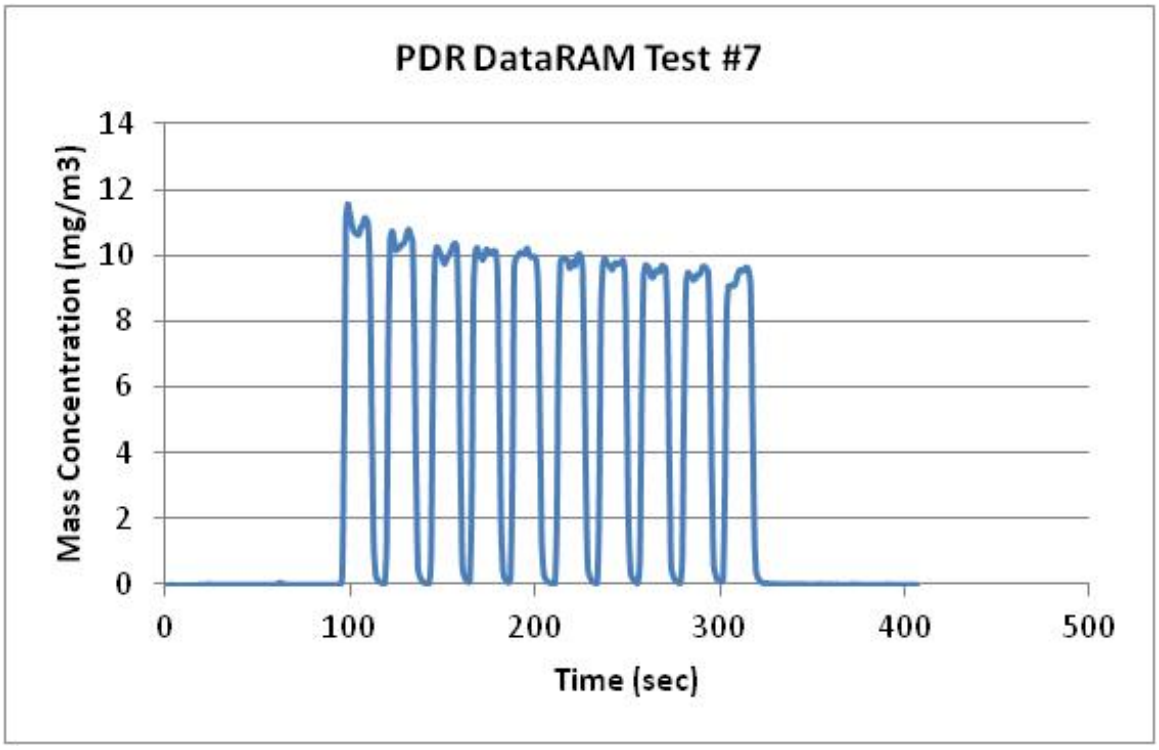

APPENDIX K

Multi-Instrument Isokinetic Experiments:

Test #8

- Purpose: Evaluate new baseline trimming configuration consisting of climb and conventional pass in a cycle using top half of laminate.

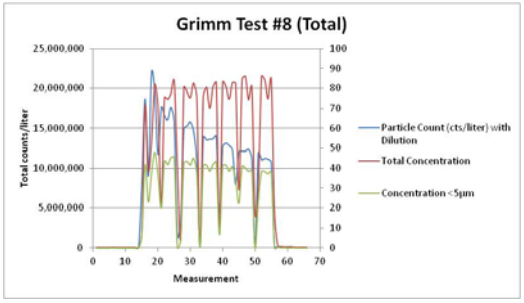

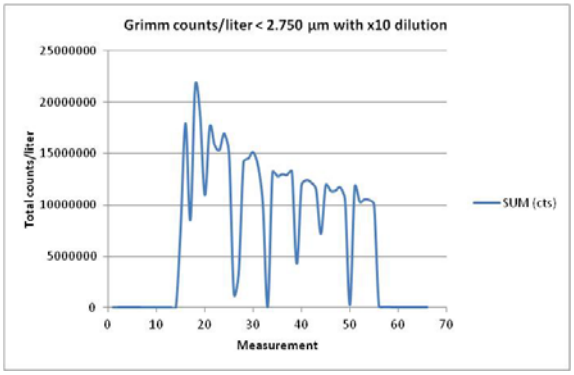

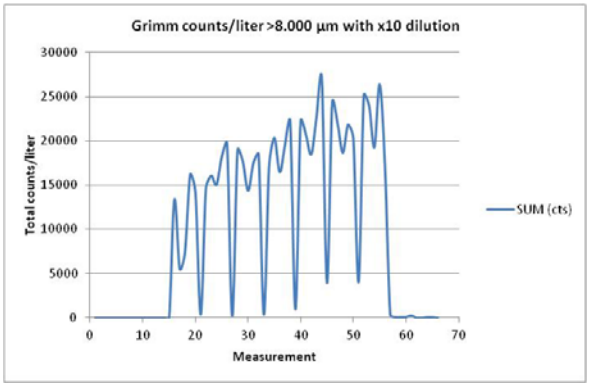

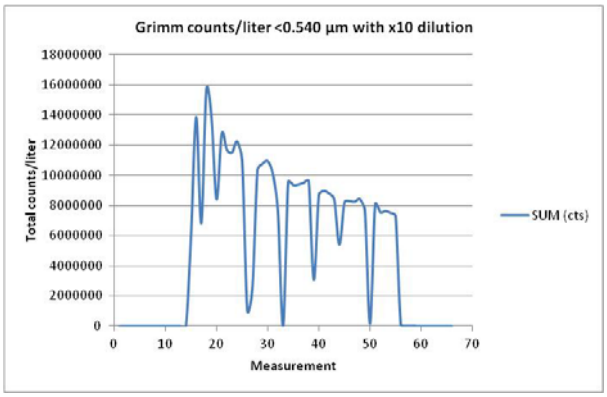

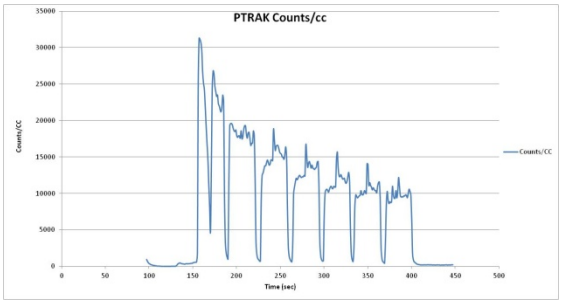

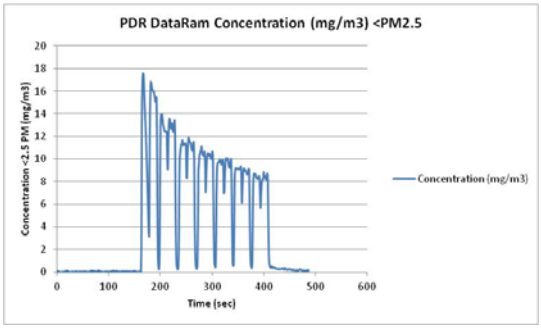

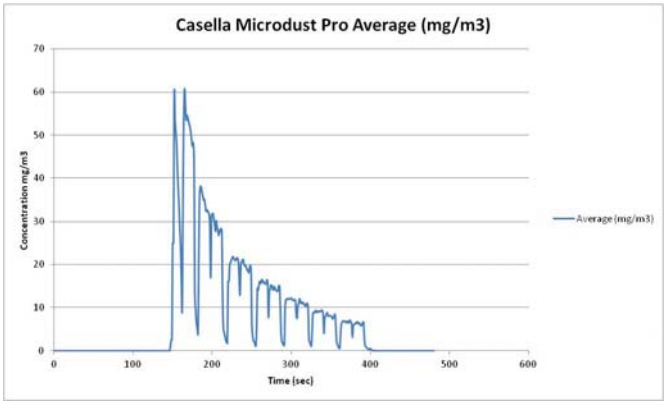

APPENDIX K

Multi-Instrument Isokinetic Experiments:

Test #9

- Purpose: Evaluate removal of 2.5 µm cyclone from PDR DataRAM. Continue using new climb and conventional pass cutting configuration. First 7 passes were bottom half of laminate, last 3 passes were full thickness laminate. Problem after first pass where exhaust duct moved and was re-positioned. Delay is clearly evident in the graphs. Note much higher PDR DataRAM measurements without cyclone as expected.

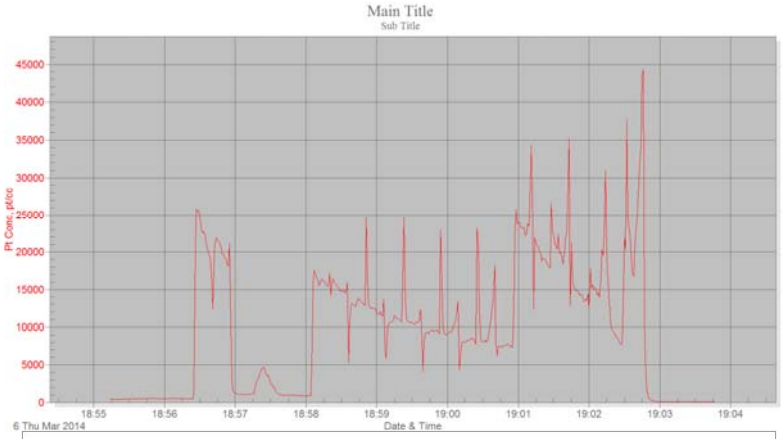

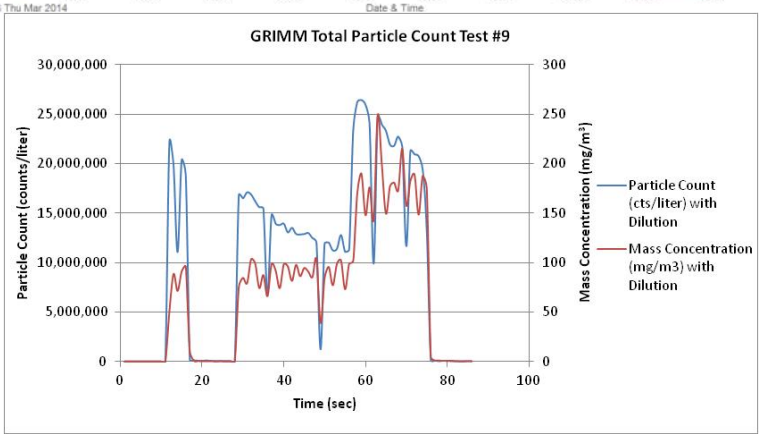

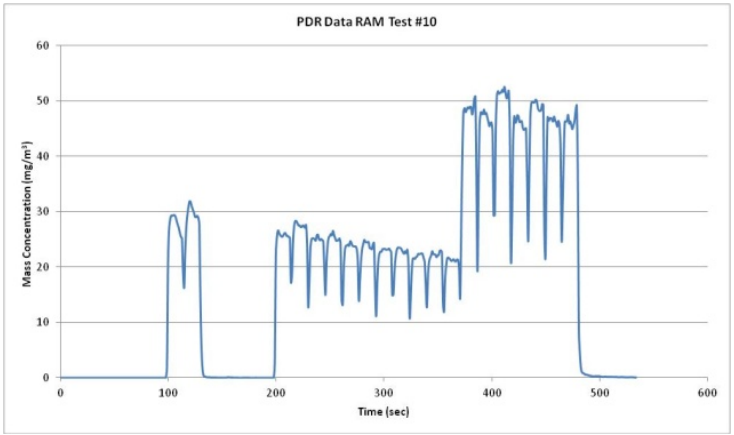

APPENDIX K

Multi-Instrument Isokinetic Experiments:

Test #10

- Purpose: Investigate swap of Casella and PDR DataRAM nozzles to see if results are impacted between Casella Microdust Pro and PDR DataRAM.

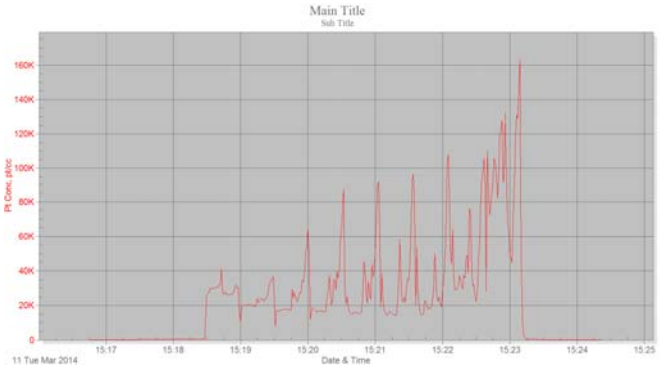

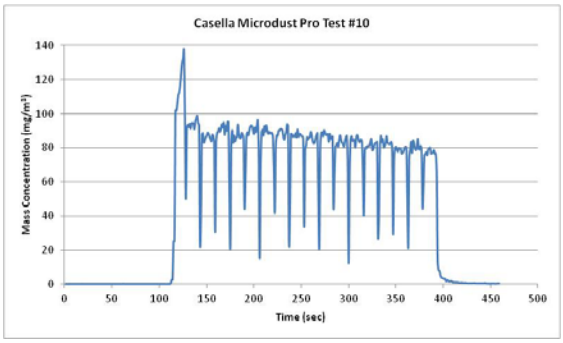

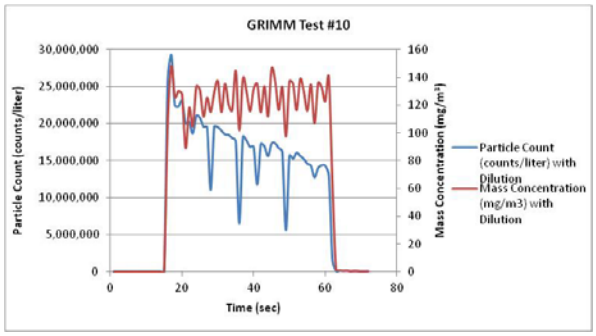

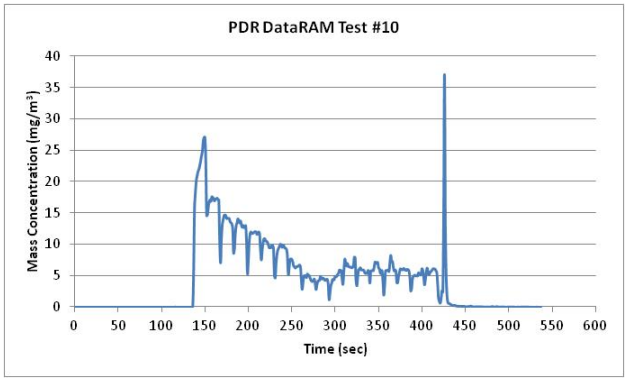

APPENDIX K

Multi-Instrument Isokinetic Experiments:

Test #11

- Purpose: Evaluate swapping of PDR DataRAM and Casella Microdust Pro nozzles. Used new 4-flute carbide cutter and top half of laminate. No cyclone on PDR DataRAM.

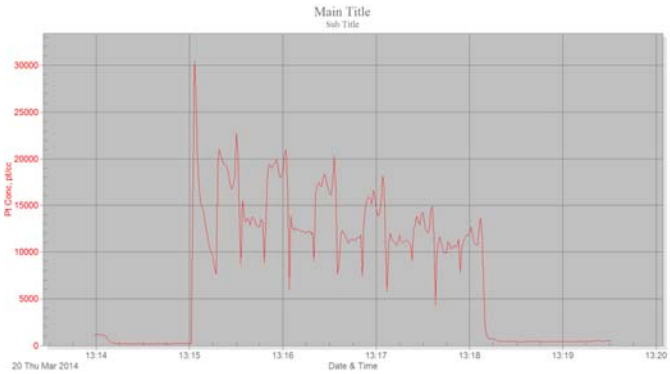

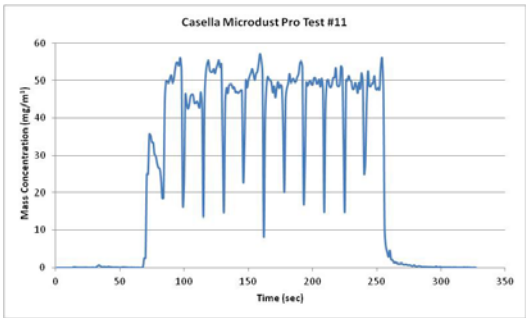

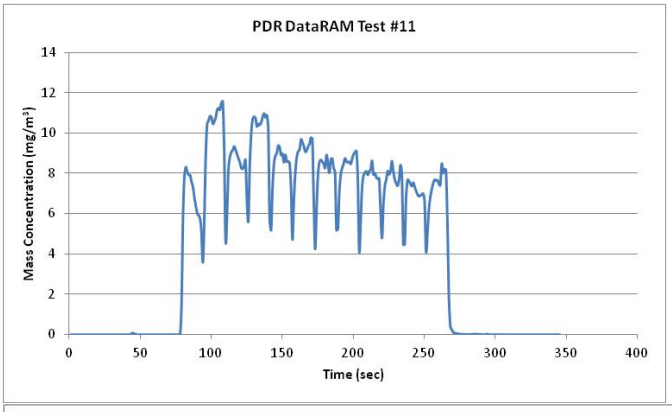

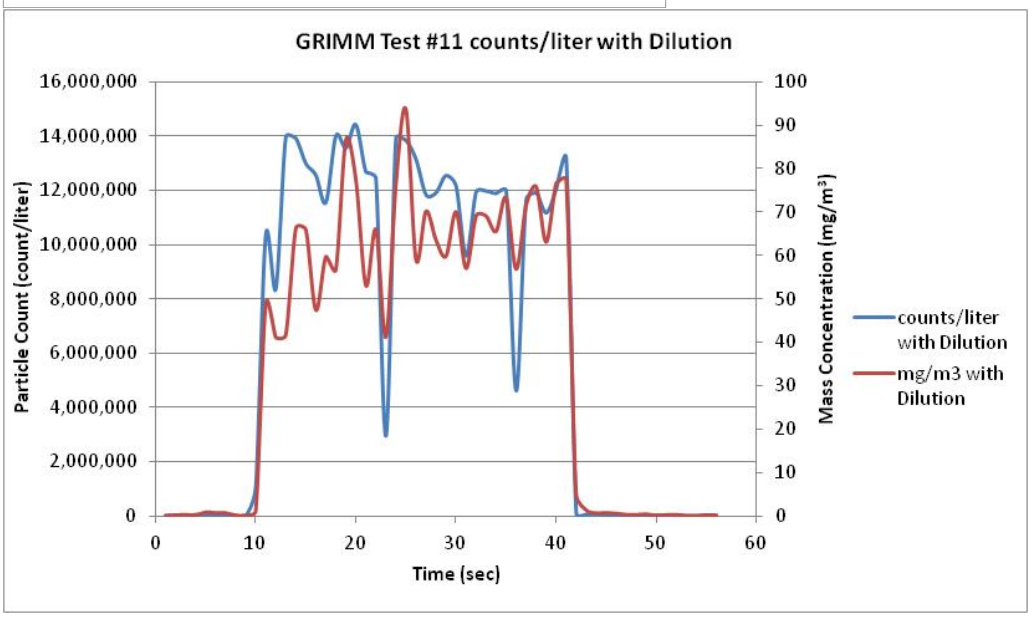

APPENDIX K

Multi-Instrument Isokinetic Experiments:

Test #12

- Purpose: Investigate switch of Casella and PDR DataRAM hoses.

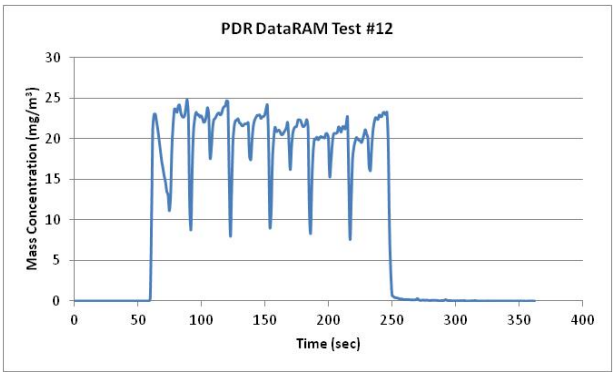

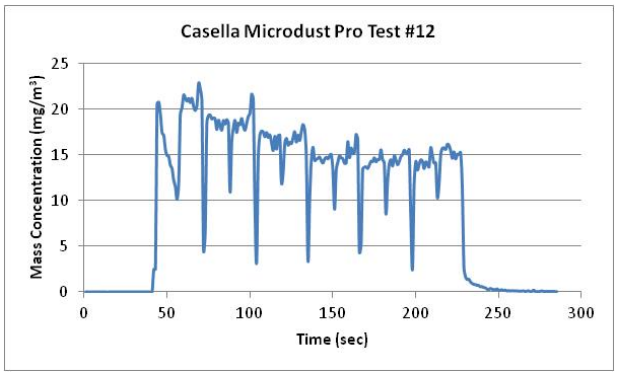

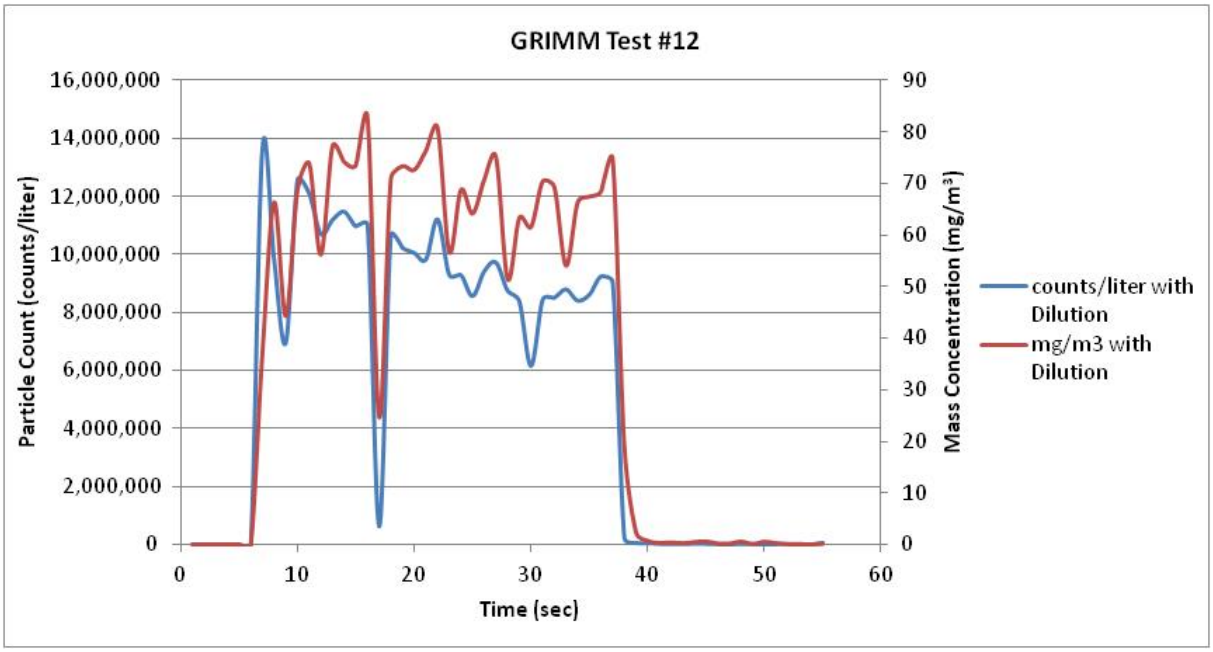

APPENDIX K

Multi-Instrument Isokinetic Experiments:

Test #13

- Purpose: Investigate PDR DataRAM and Casella Microdust Pro at same level in duct. Sharper nozzle was used on Casella MicroDust Pro with wider cut nozzle used with PDR DataRAM.

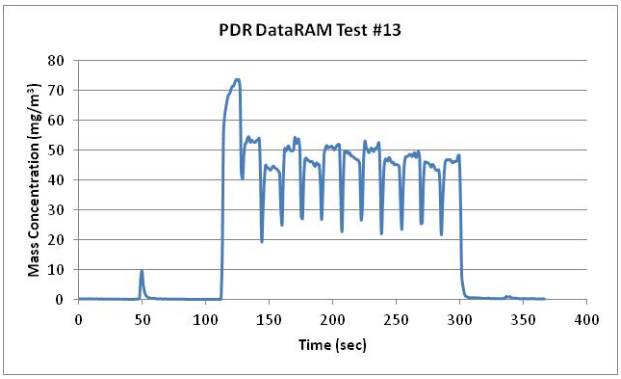

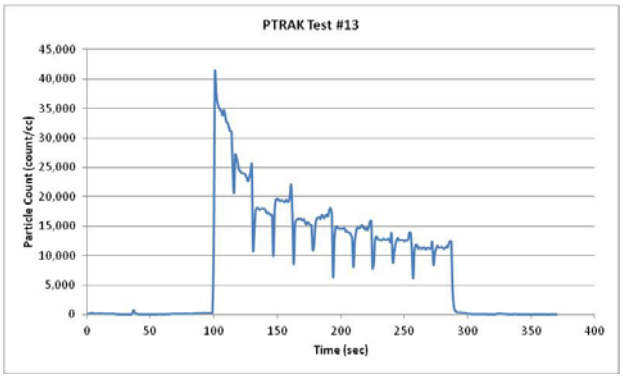

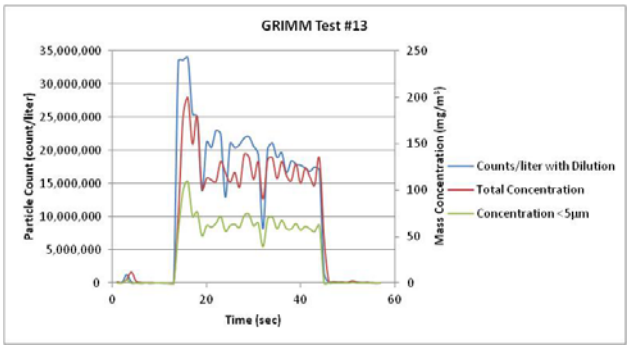

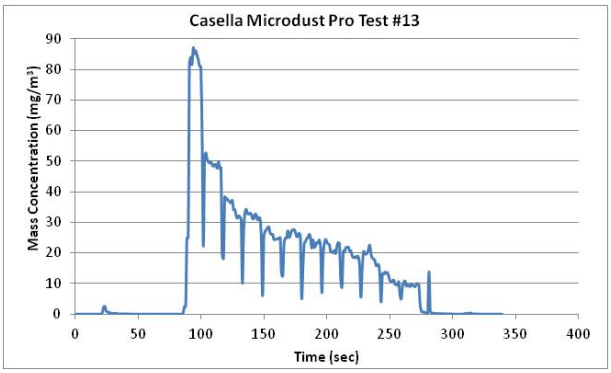

APPENDIX K

Multi-Instrument Isokinetic Experiments:

Test #14

- Purpose: Investigate effects of moving Casella nozzle just above GRIMM nozzle. New 4-flute carbide cutter.

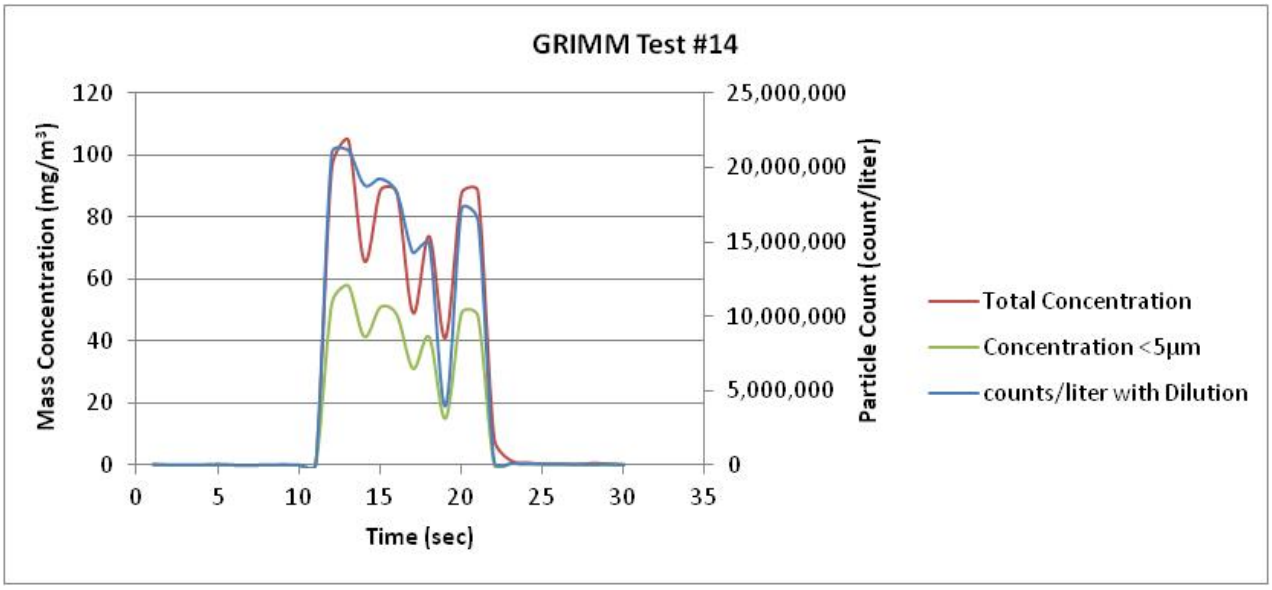

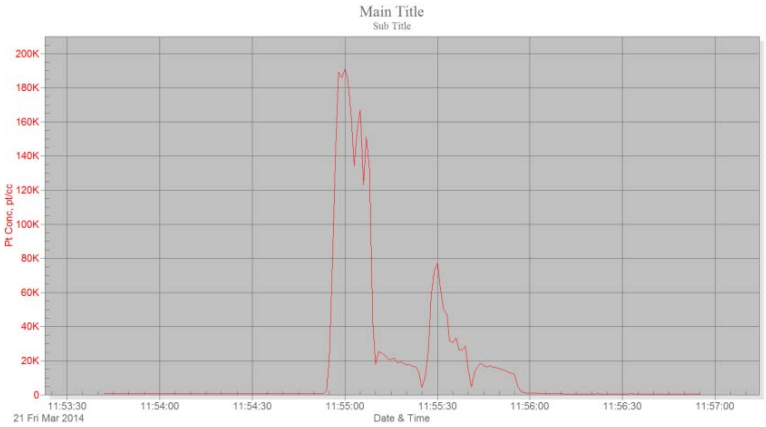

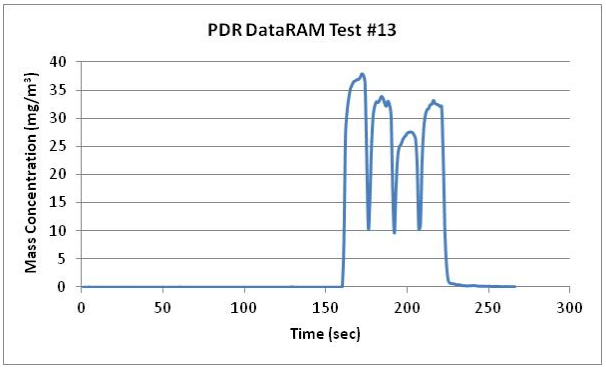

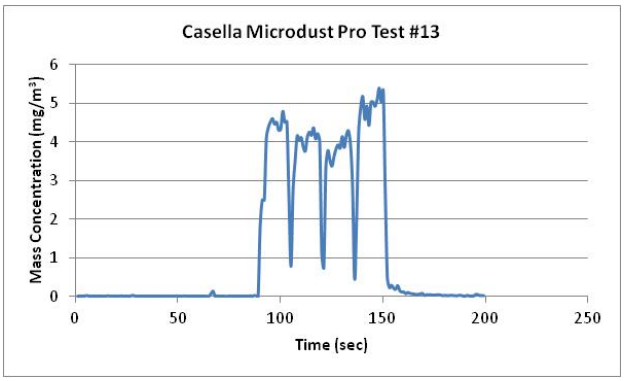

APPENDIX K

Multi-Instrument Isokinetic Experiments:

Test #15

- Purpose: Investigate effect of new filter in Casella Microdust Pro and cleaned shop vac HEPA filter. Same cutting tool as Test #14.

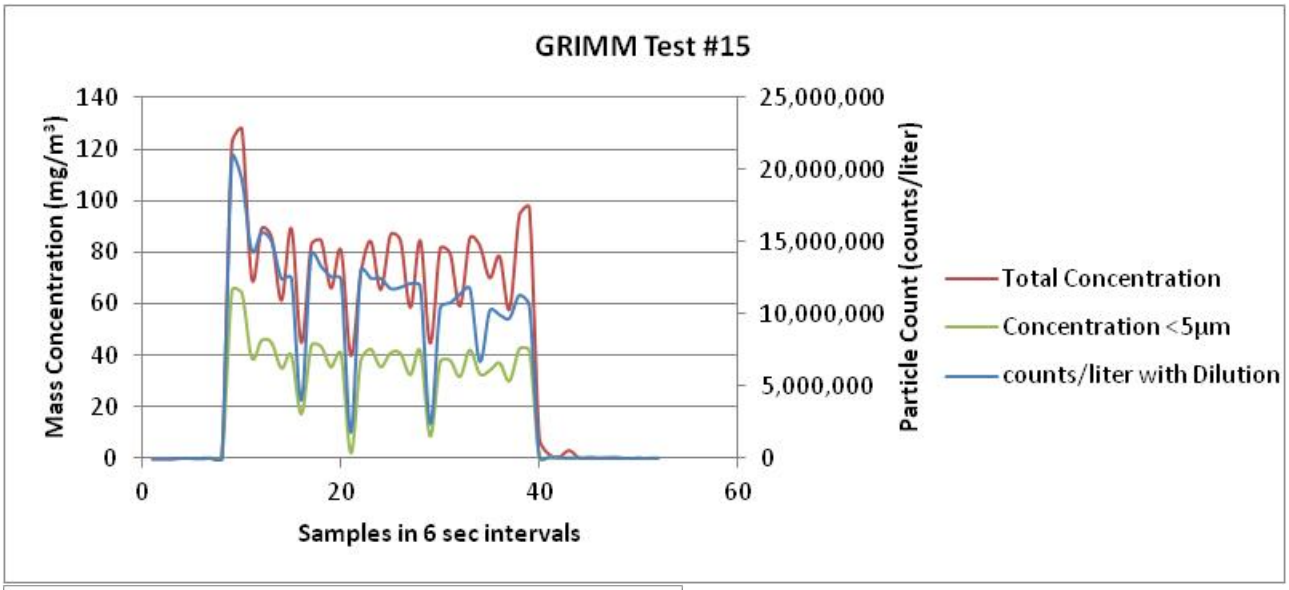

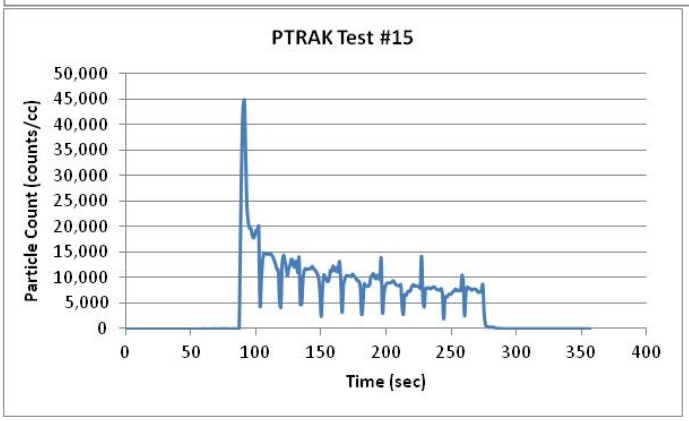

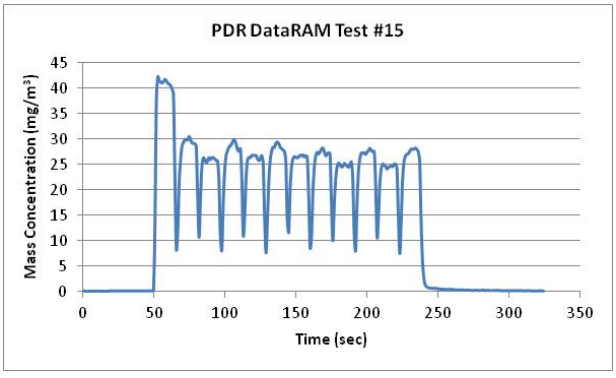

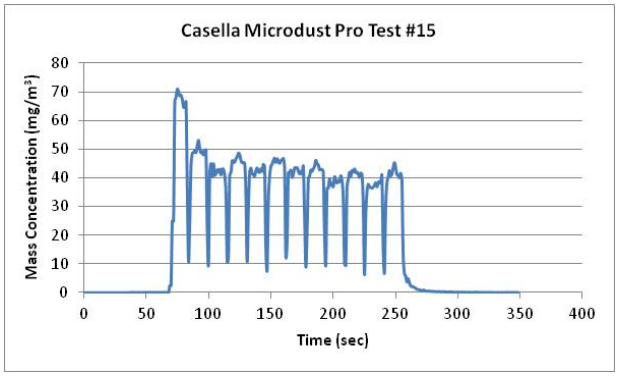

APPENDIX L

Composite circular slot test dust results:

- Purpose: Evaluate results from 2 real-time particle measurement instruments when milling circular slots.

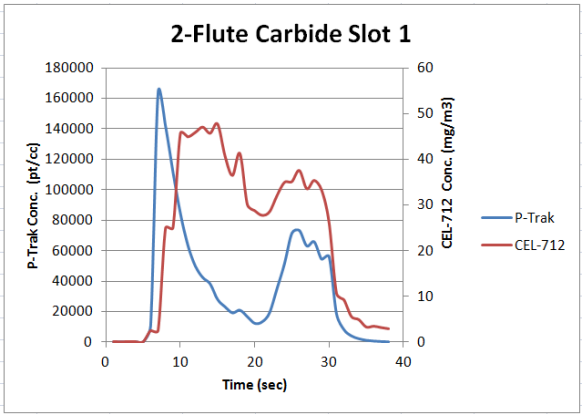

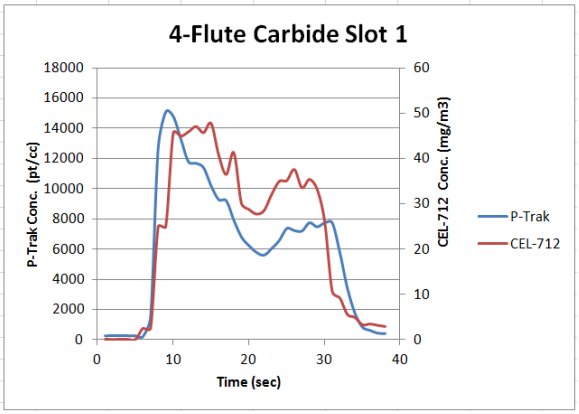

Slot 1 for 2 flute and 4 flute carbide cutter.

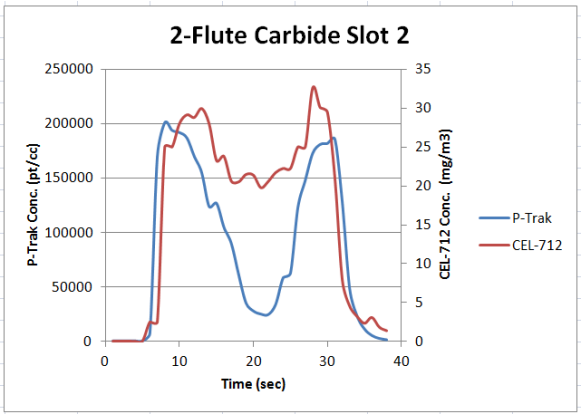

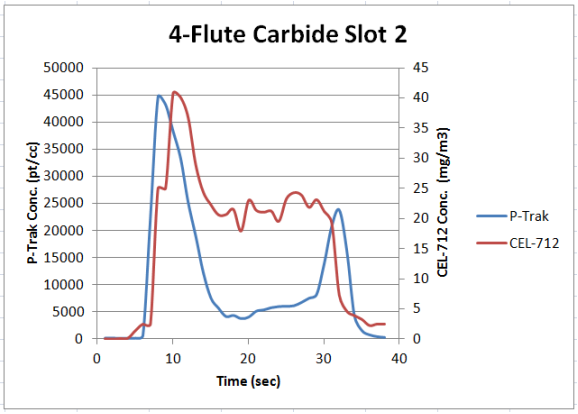

Slot 2 for 2 flute and 4 flute carbide cutter.

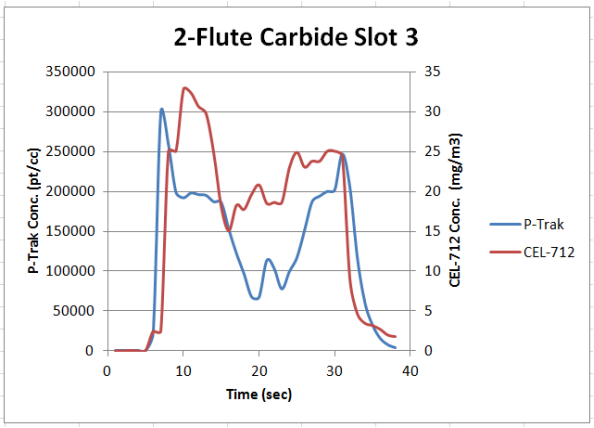

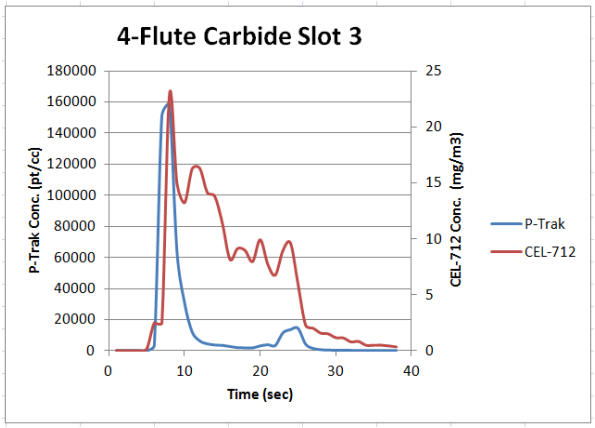

Slot 3 for 2 flute and 4 flute carbide cutter.

APPENDIX L

Composite circular slot test dust results (cont).

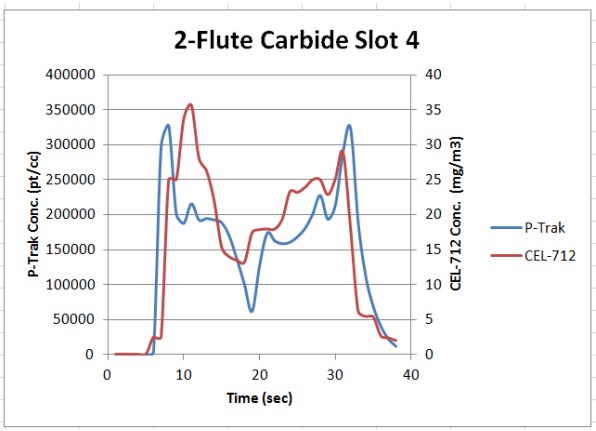

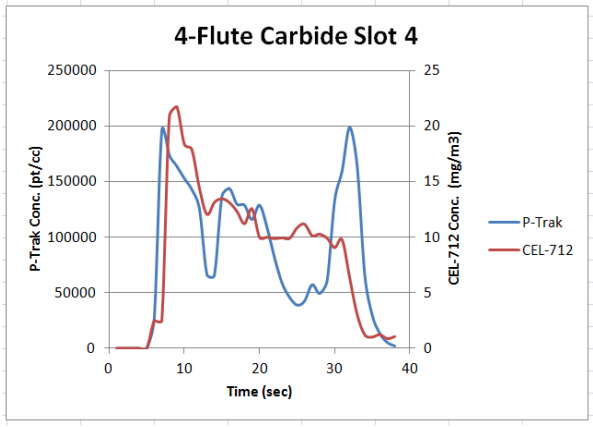

Slot 4 for 2 flute and 4 flute carbide cutter.

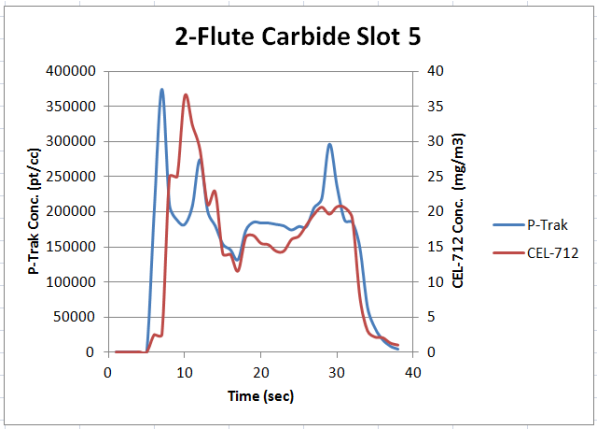

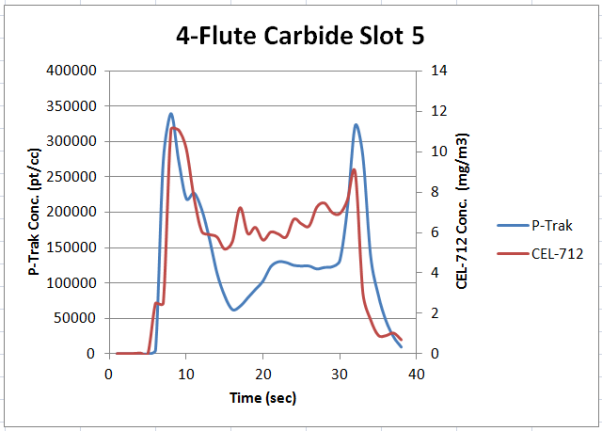

Slot 4 for 2 flute and 4 flute carbide cutter.

APPENDIX M

Cutting edge alignment test for aluminum and composite

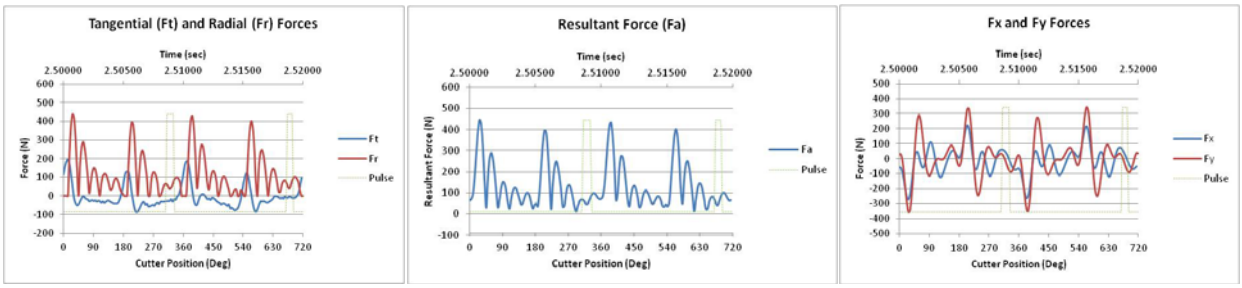

Climb Cut Aluminum

Conventional Cut Aluminum

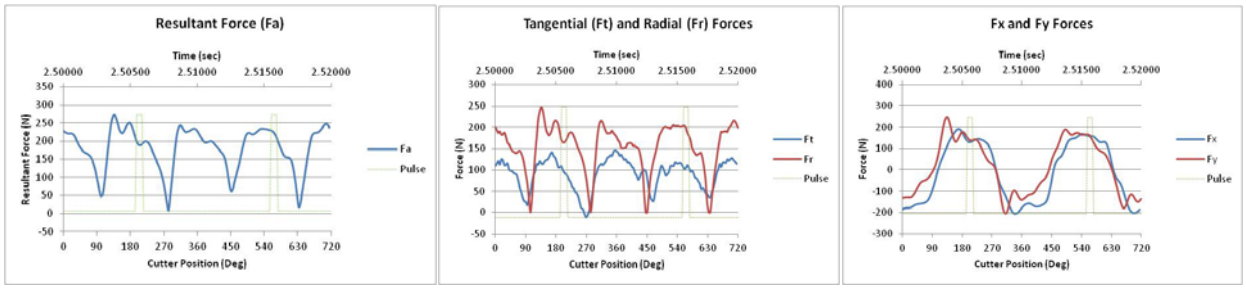

Slot Cut Aluminum

APPENDIX M

Cutting edge alignment test for aluminum and composite (cont.)

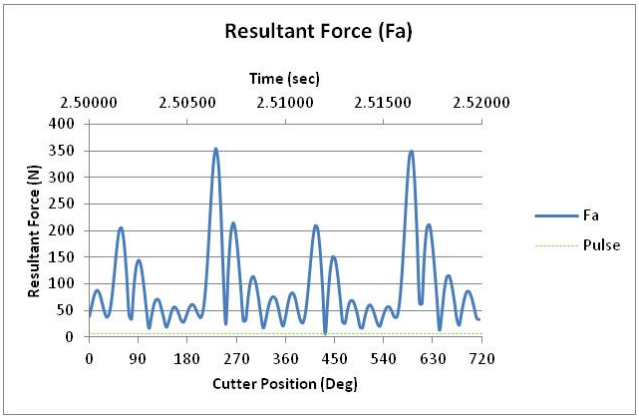

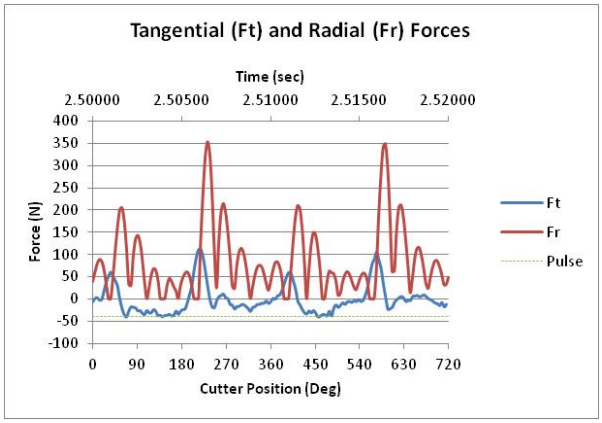

Climb Cut Composite

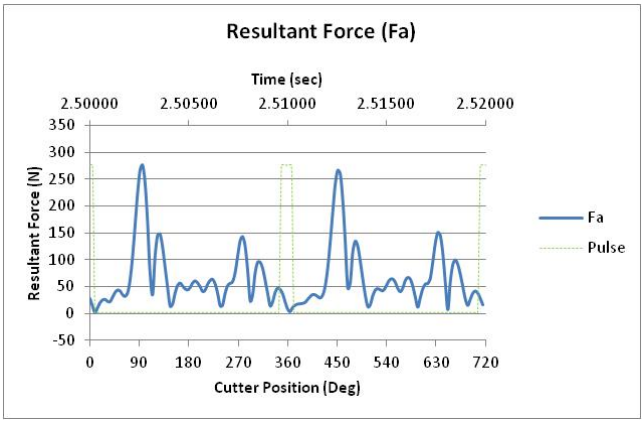

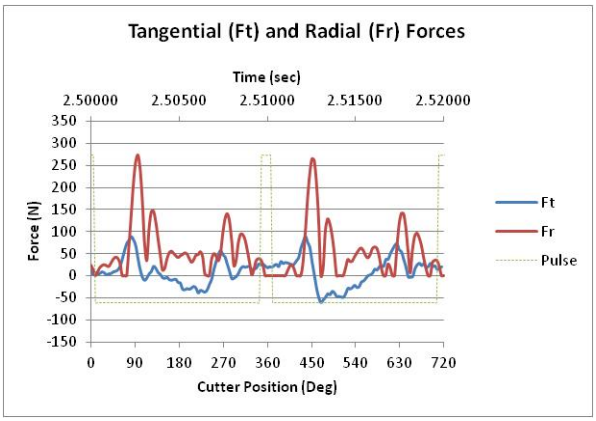

Conventional Cut Composite

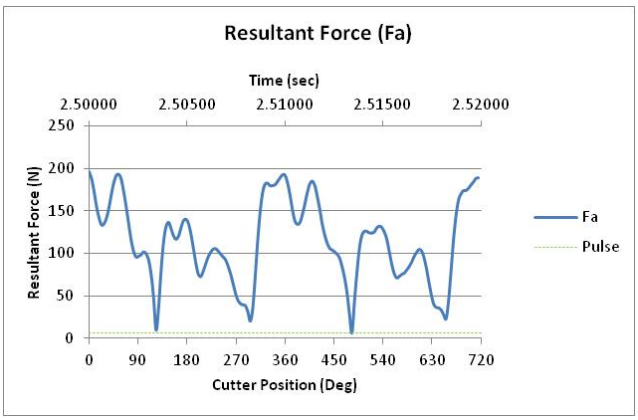

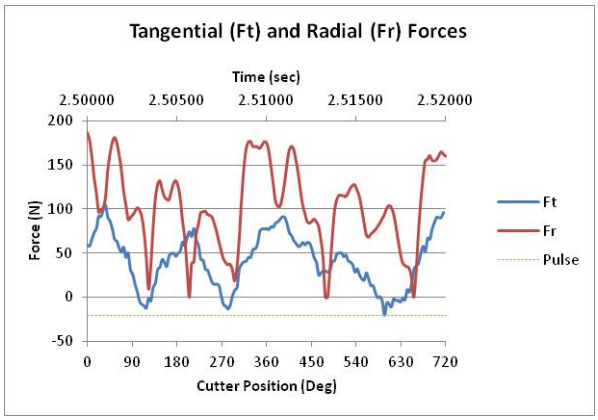

Slot Cut Composite

APPENDIX N

Dynamometer cutting edge alignment cases

Material: 6061-T6511 Aluminum, 76.2mm thick, Kurt Vise, clamp direct to HAAS Mill Bed
Cutting Process: Peripheral **Climb** Milling (side milling)
Cutter: 12.7mm diameter, 2-flute, 30deg helix, solid carbide, End Mill
RPM: 6000
Feedrate: .635 m/min
Axial Depth of Cut: 6.35mm
Radial Depth of Cut: .254mm

Cutter aligned to Kistler 9123C Fy

Run 1

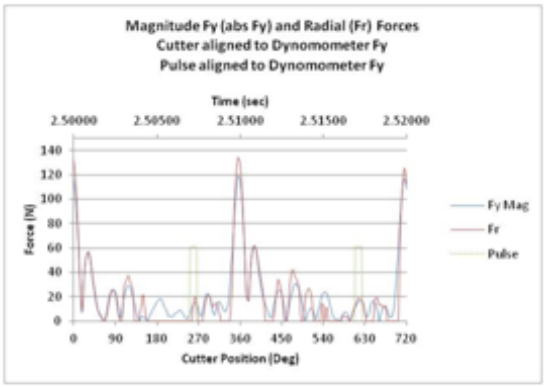

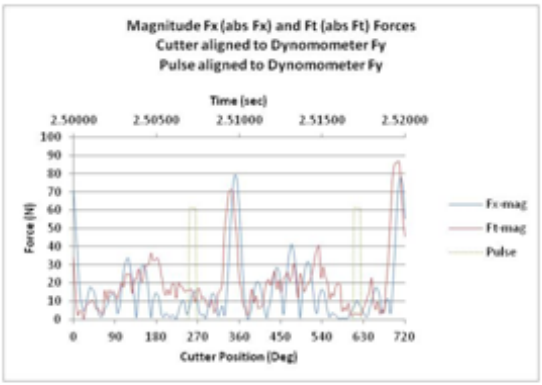

Run 2

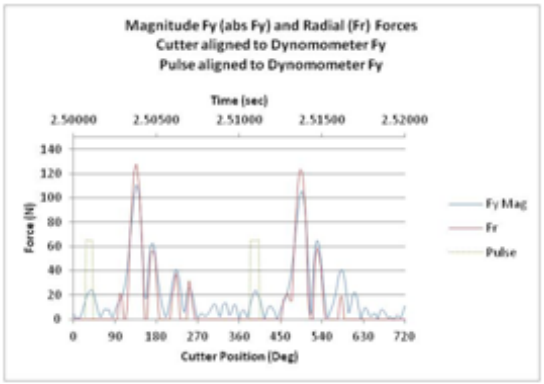

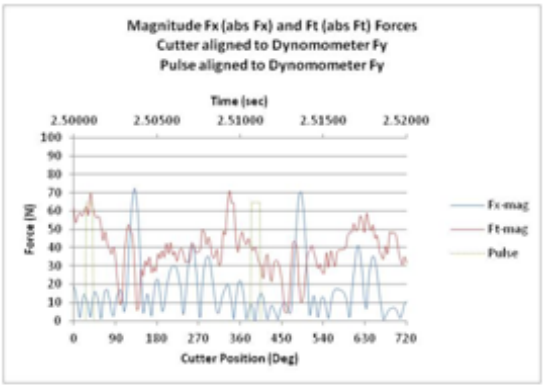

Run 3

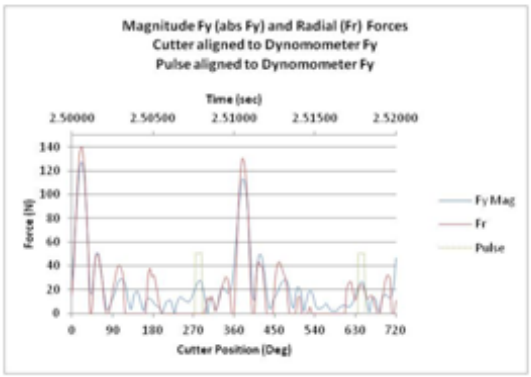

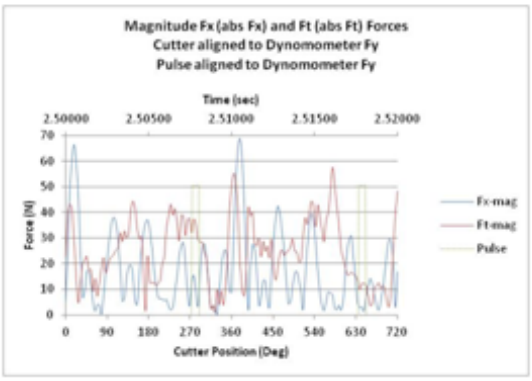

APPENDIX N

Dynamometer cutting edge alignment cases (cont.)

Material: 6061-T6511 Aluminum, 76.2mm thick, Kurt Vise, clamp direct to HAAS Mill Bed
Cutting Process: Peripheral **Climb** Milling (side milling)
Cutter: 12.7mm diameter, 2-flute, 30deg helix, solid carbide, End Mill
RPM: 6000
Feedrate: .635 m/min
Axial Depth of Cut: 6.35mm
Radial Depth of Cut: .254mm

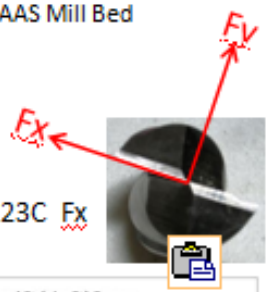

Cutter aligned to Kistler 9123C Fx

Run 1

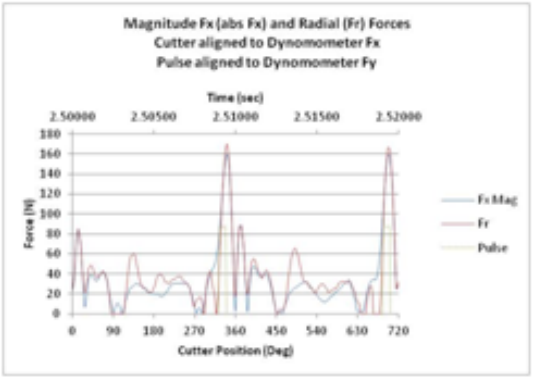

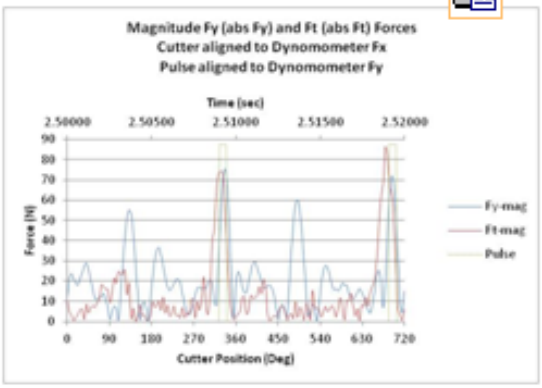

Run 2

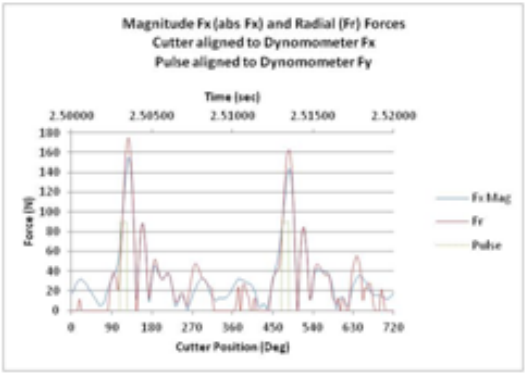

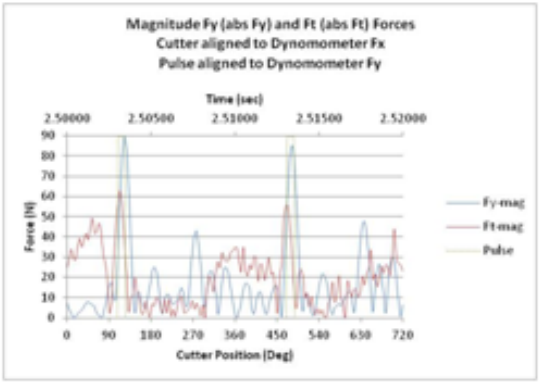

Run 3

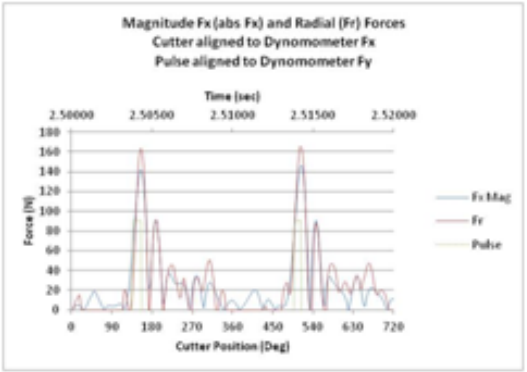

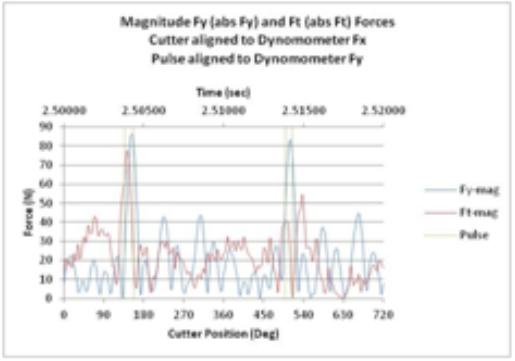

APPENDIX N

Dynamometer cutting edge alignment cases (cont.)

Material: 6061-T6511 Aluminum, 76.2mm thick, Kurt Vise, clamp direct to HAAS Mill Bed
Cutting Process: Peripheral **Conventional** Milling (side milling)
Cutter: 12.7mm diameter, 2-flute, 30deg helix, solid carbide, End Mill
RPM: 6000
Feedrate: .635 m/min
Axial Depth of Cut: 6.35mm
Radial Depth of Cut: .254mm

Cutter aligned to Kistler 9123C Fy

Run 1

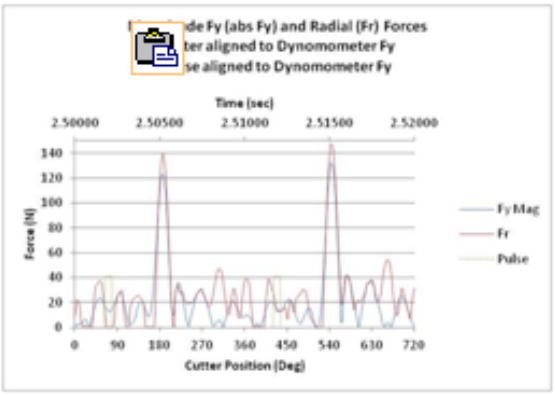

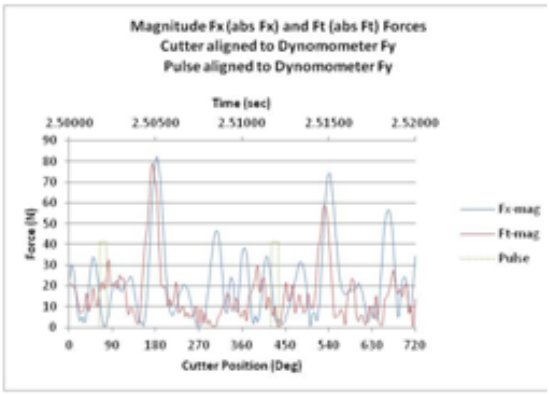

Run 2

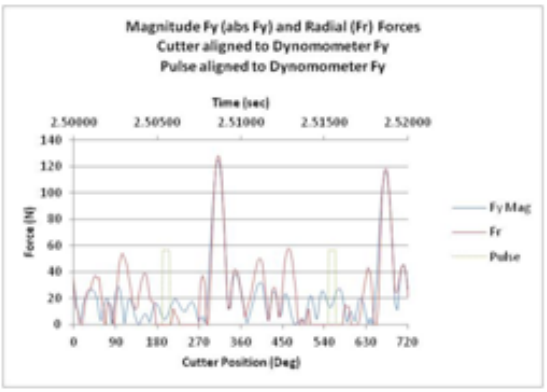

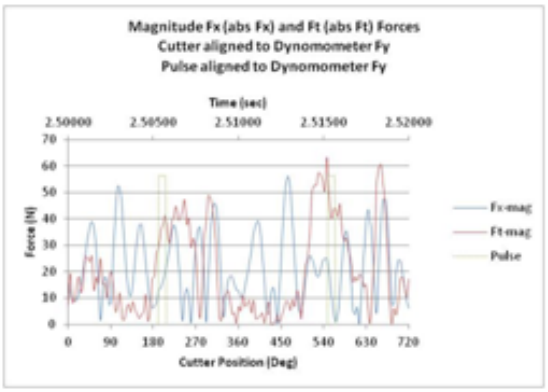

Run 3

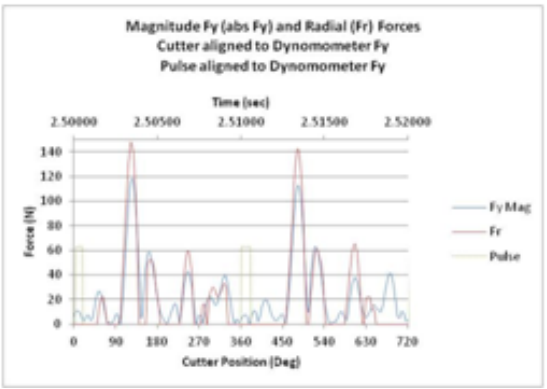

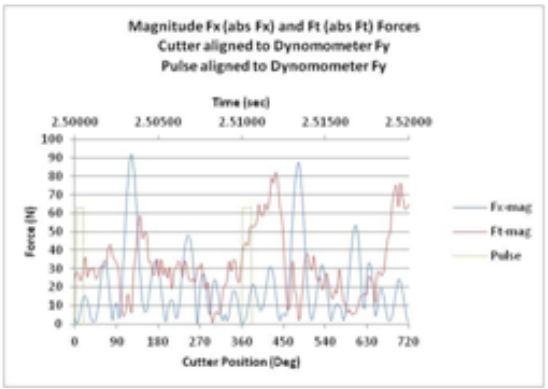

APPENDIX N

Dynamometer cutting edge alignment cases (cont.)

Material: 6061-T6511 Aluminum, 76.2mm thick, Kurt Vise, clamp direct to HAAS Mill Bed
Cutting Process: Slot Milling (full immersion)
Cutter: 12.7mm diameter, 2-flute, 30deg helix, solid carbide, End Mill
RPM: 6000
Feedrate: .635 m/min
Axial Depth of Cut: 6.35mm
Radial Depth of Cut: 2.54mm (in same slot, 1st pass 2.54, 2nd 5.08, 3rd 7.62mm deep)

Cutter aligned to Kistler 9123C Fy

Run 1

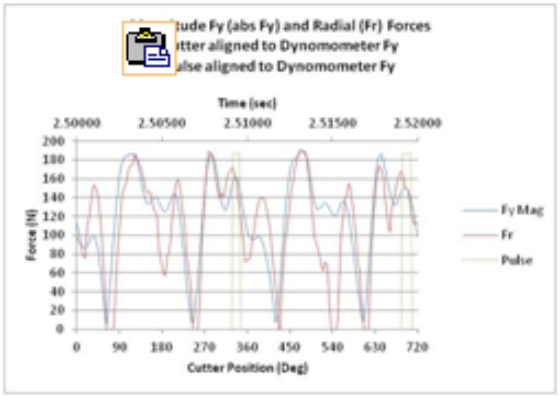

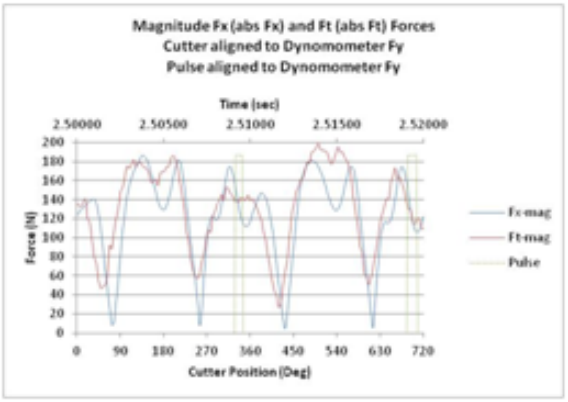

Run 2

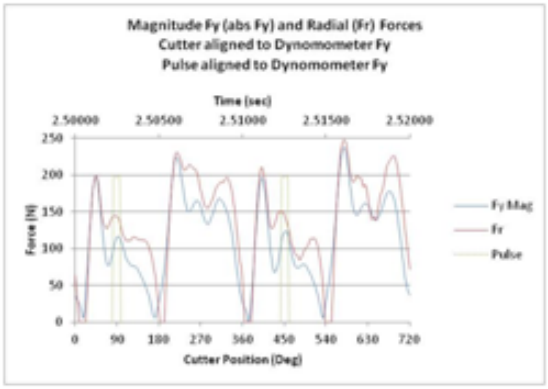

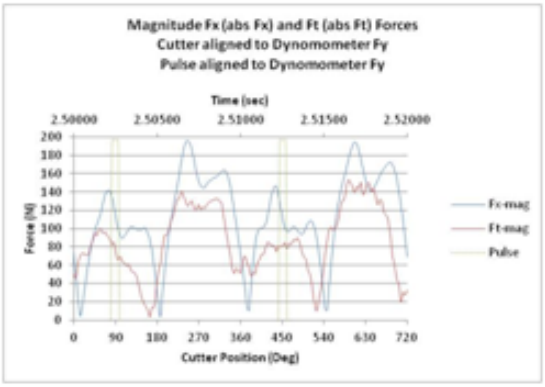

Run 3

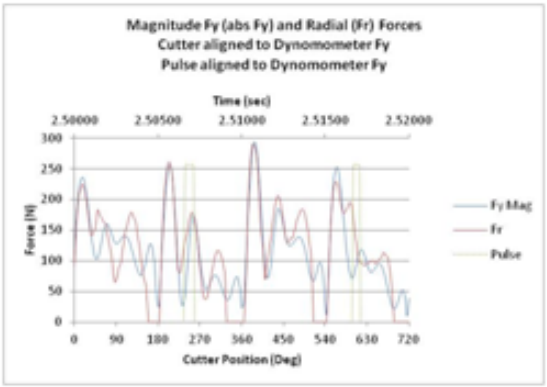

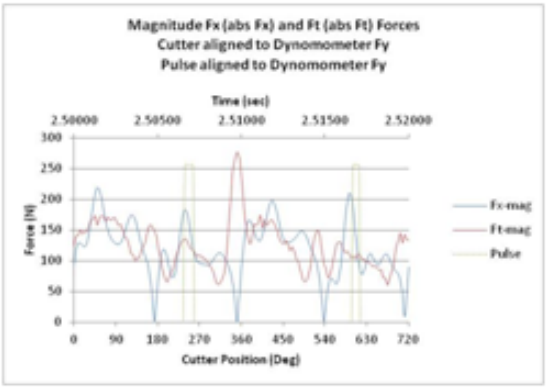

APPENDIX N

Dynamometer cutting edge alignment cases (cont.)

Material: 6061-T651 (.5 in thick)
Cutting Tool: ½" 2-Flute HSS 30 deg end mill
Machining: Peripheral Climb Milling
RPM: 3000
Axial Depth of Cut: .25 in
Radial Depth of Cut: .030 in.
Linear Feedrate: 25 ipm
Cutter aligned to Dynamometer X-Axis

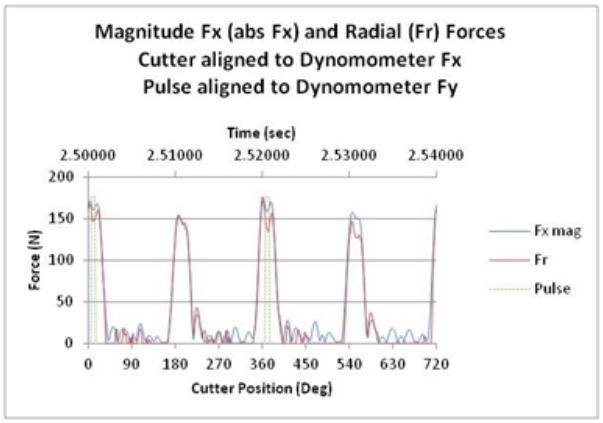

Material: 6061-T651 (.5 in thick)
Cutting Tool: ½" 2-Flute HSS 30 deg end mill
Machining: Peripheral Climb Milling
RPM: 3000
Axial Depth of Cut: .25 in
Radial Depth of Cut: .030 in.
Linear Feedrate: 25 ipm
Cutter aligned to Dynamometer Y-Axis

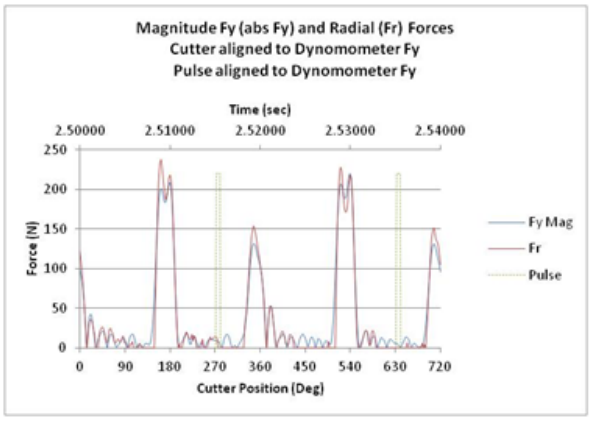

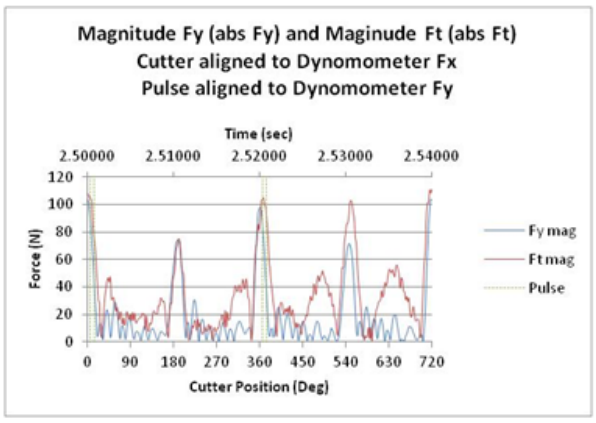

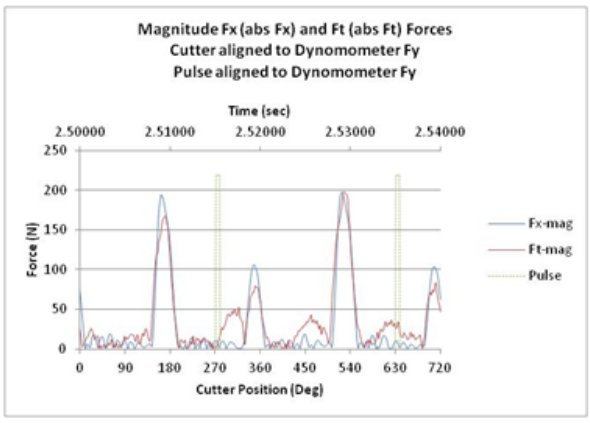

APPENDIX N

Dynamometer cutting edge alignment cases (cont.)

Material: 6061-T651 (.5 in thick)
Cutting Tool: ½" 2-Flute HSS 30 deg end mill
Machining: **Peripheral Conventional Milling**
RPM: 3000
Axial Depth of Cut: .25 in
Radial Depth of Cut: .030 in.
Linear Feedrate: 25 ipm
Cutter aligned to Dynamometer X-Axis

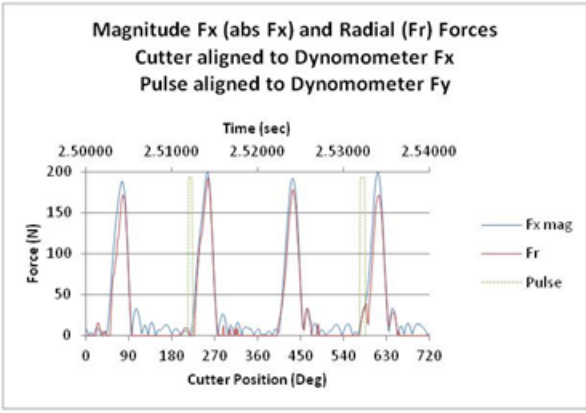

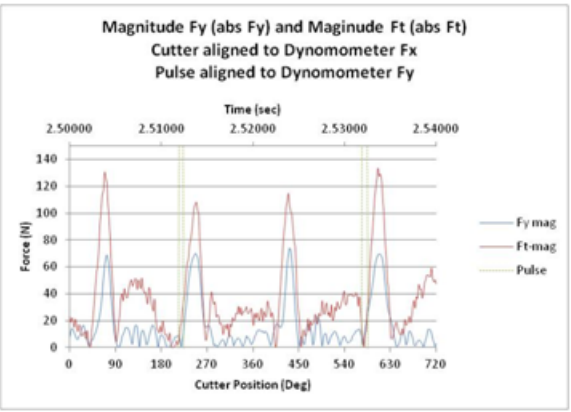

Material: 6061-T651 (.5 in thick)
Cutting Tool: ½" 2-Flute HSS 30 deg end mill
Machining: **Peripheral Conventional Milling**
RPM: 3000
Axial Depth of Cut: .25 in
Radial Depth of Cut: .030 in.
Linear Feedrate: 25 ipm
Cutter aligned to Dynamometer Y-Axis

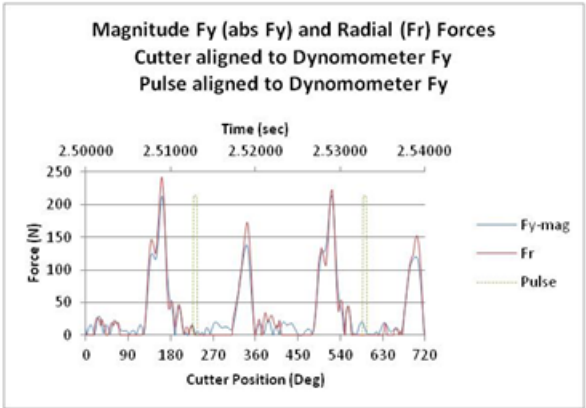

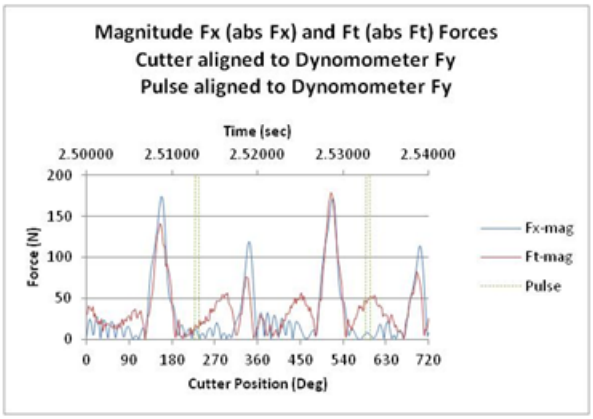

APPENDIX N

Dynamometer cutting edge alignment cases (cont.)

Material: 6061-T651 (.5 in thick)
Cutting Tool: ½" 2-Flute HSS 30 deg end mill
Machining: Slot Milling
RPM: 3000
Axial Depth of Cut: .1 in deep slot
Radial Depth of Cut: Full Immersion
Linear Feedrate: 25 ipm
Cutter aligned to Dynomometer Y-Axis

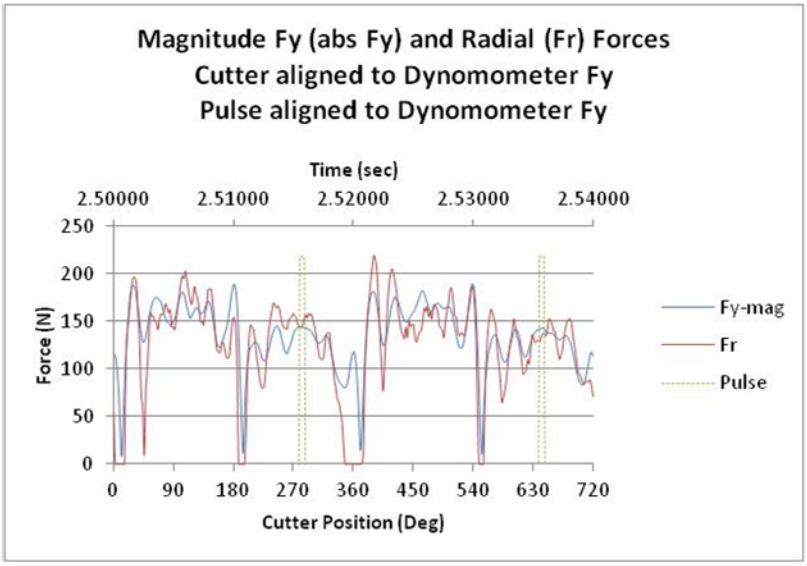

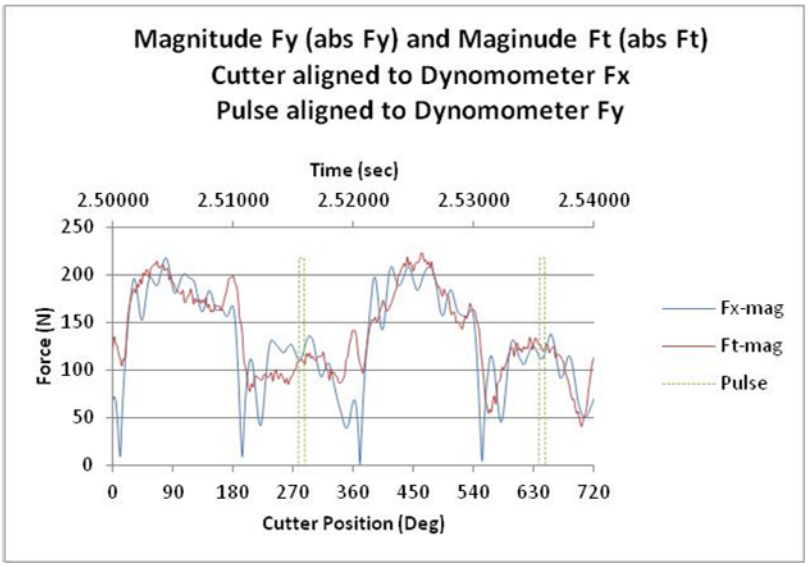

APPENDIX O

Signal drift compensation spreadsheet

The spreadsheet determines the signal drift compensation for Fx, Fy, Mz.

Input	**Units**	**Value**
Linear Feed Rate	ipm	**17.5**
Slot Circle Dia	in	**4.5**
Cutter Dia	in	**0.472441**
Cutter Offset from Edge of Part	in	**0.5**
Cutter Travel to Circle Start (linear)	in	**1**
RPM	rpm	**5600**
Number of Teeth on Cutter	#	**4**
Edge of Part Start Time from DynoWare	sec	**3.972653**
Drift comp cutter exit delay factor	sec	**1.5**
Mz Sensitivity	mV/MU	**1**
Output		
Edge of Part Start Row Number	Row Num	31008
Edge of Part Start Time	sec	3.972692
Time to Circle Cut Start	sec	0.90438686
Est. Circle Cut Start Time (0 deg)	sec	4.87707886
Slot Circle Start Row Number	Row Num	38063
Circle Travel Length	in	7.06858347
Circle Slot Cutting DurationTime	sec	24.2351433
Time at Completion of Circle Slot (180 deg)	sec	29.1122222
Slot Circle End Row Number	Row Num	227097
Time to Exit Workpiece (1/2 cutter dia)	sec	29.5644156
Row Interval per Degree of Semi-Circle	# row/deg	1044.38674
Feed per tooth	mm/tooth	0.01984
Time per each degree of slot	sec	0.13463969
Number of rotations per each deg of slot	# rot/deg	12.57
Number of rows for each cutter rotation	# row/rot	83.1096561
Rounded sample rows per deg of slot	# row/deg	998
feed per revolution (feed/rev)	mm/rev	0.07938
ply thickness (mm) - fixed	mm	0.1905
feed/rev percent of ply thickness	% ply	41.67
Dyno Sampling Start Time (fixed)	sec	0
Dyno Sampling Start Row Number (fixed)	Row Num	21
Edge of Part Start Time (entered)	sec	3.972653
Edge of Part Start Row Number (found)	Row Num	31007
Left Side Signal Drift Comp Value **Fx**	N	-3.3768135
Left Side Signal Drift Comp Value **Fy**	N	-15.634425
Left Side Signal Drift Comp Value **Mz**	Nm	-0.1911993
Left Side Signal Drift Comp Value **Ft** (calc)	N	-31.866553
Time at Full Cutter Exit	sec	31.516609
Row Number at Full Cutter Exit	Row Num	245851
Last Dyno Sample time	sec	34.997436
Row Number at Last Dyno Sample	Row Num	273001
Right Side Signal Drift Comp Value **Fx**	N	-3.5453266
Right Side Signal Drift Comp Value **Fy**	N	-16.095442
Right Side Signal Drift Comp Value **Mz**	Nm	-0.1692249
Right Side Signal Drift Comp Value **Ft** (calc)	N	-28.204152
Difference Left-Right Drift Comp **Fx**	N	0.16851307
Difference Left-Right Drift Comp **Fy**	N	0.46101753
Difference Left-Right Drift Comp **Mz**	Nm	-0.0219744
Difference Left-Right Drift Comp **Ft** (calc)	N	-3.6624008

APPENDIX P

Zoom magnification example

The graphics below illustrate the effects of zoom magnification of Mz.

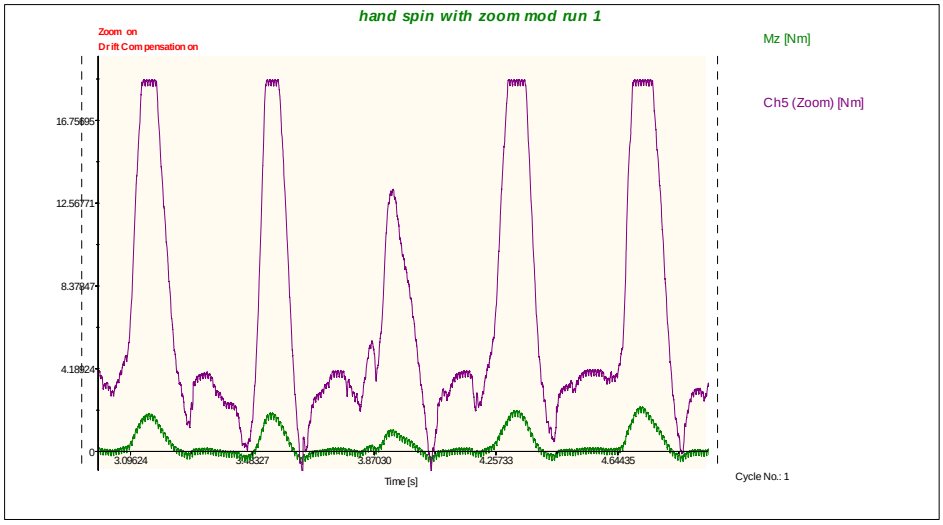

Signal drift compensation for Mz. Ch5 is 10x greater than Mz.

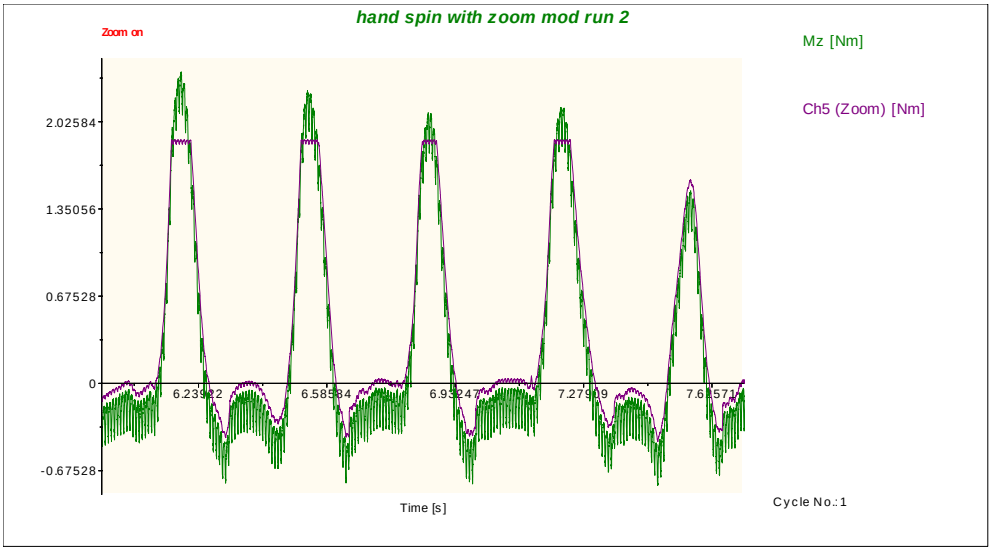

Signal drift compensation for Mz. Ch5 is approximately equal to Mz, but caps at 2 Nm as a result of the 20 Nm range for fine mode.

APPENDIX Q

Semi-circle milling calculator

The spreadsheet below is used to determine parameters for performing semi-circular slot tests. It enables the user to change input parameters to arrive at an optimal set of conditions for performing the experiments.

			Enter Purple Imperial Units						Derived Metric Units				
Input	**Symbol**	**Units**	**Inner Slot #1**	**Slot #2**	**Slot #3**	**Slot #4**	**Slot #5**	**Units**	**Inner Slot #1**	**Slot #2**	**Slot #3**	**Slot #4**	**Slot #5**
cutter diameter	D	in	0.472441	0.472441	0.472441	0.472441	0.472441	mm	12.000	12.000001	12.000001	12.000001	12.000001
# of teeth	z	# of teeth	4	4	4	4	4	# of teeth	4	4	4	4	4
spacing between slots	sp	in	0.152559	0.152559	0.152559	0.152559	0.152559	mm	3.8749986	3.8749986	3.8749986	3.8749986	3.8749986
lead in slot length	ld	in	0.5	0.5	0.5	0.5	0.5	ld	12.7	12.7	12.7	12.7	12.7
inner slot #1 radius (centerline)	R1	in (radius)	1	1.625	2.25	2.875	3.5	mm	25.4	41.275	57.15	73.025	88.9
Dyno sample rate	Hz	meas/sec	7800	7800	7800	7800	7800	meas/sec	7800	7800	7800	7800	7800
axial depth of cut	da	in	0.1	0.1	0.1	0.1	0.1	in	2.54	2.54	2.54	2.54	2.54
linear feed rate	Vf	in/min	9	13.25	17.5	21.75	26	mm/min	228.6	336.55	444.5	552.45	660.4
spindle speed	n	rot/min (rpm)	4800	5300	5600	5800	5943	rot/min	4800	5300	5600	5800	5943
solve for rpm (reference - not input)			4800	5300	5600	5800	5943						
Output						ew							
feed/tooth	**f**	**in/tooth**	**0.00047**	**0.00063**	**0.00078**	**0.00094**	**0.00109**	**mm/tooth**	**0.01191**	**0.01588**	**0.01984**	**0.02381**	**0.02778**
feed/revolution (ref. ply thickness =.0075 in. or .1905 mm)	ipr	in/rev	0.00188	0.00250	0.00313	0.00375	0.00437	mm/rev	0.04763	0.06350	0.07938	0.09525	0.11112
Semi-Circle Slot Diameter	dia	in	2	3.25	4.5	5.75	7		50.8	82.55	114.3	146.05	177.8
cutting speed	Vc	ft/min	593.7	655.5	692.6	717.4	735.1	m/min	181.0	199.8	211.1	218.7	224.0
half circle slot length		in	3.142	5.105	7.069	9.032	10.996	mm	79.796	129.669	179.542	229.415	279.288
half circle slot cutting time		**sec**	**20.94**	**23.12**	**24.24**	**24.92**	**25.37**	**sec**	**20.94**	**23.12**	**24.24**	**24.92**	**25.37**
half circle slot cutter rotations (#)		qty	1675.52	2042.04	2261.95	2408.55	2513.33	qty	1675.52	2042.04	2261.95	2408.55	2513.33
half circle slot cutter rotatations per degree of slot		**rot/degree**	**9.31**	**11.34**	**12.57**	**13.38**	**13.96**	**rot/degree**	**9.31**	**11.34**	**12.57**	**13.38**	**13.96**
half circle dyno measurement per degree of slot		meas/degree	907.6	1001.8	1050.2	1079.7	1099.6	meas/degree	907.57	1001.75	1050.19	1079.70	1099.56
half circle total dyno measurements		meas (qty)	163362.8	180315.6	189034.1	194345.4	197920.3	meas (qty)	163362.82	180315.56	189034.12	194345.42	197920.34
half circle total dyno measurements (check)		meas (qty)	163362.8	180315.6	189034.1	194345.4	197920.3	meas (qty)	163362.82	180315.56	189034.12	194345.42	197920.34
dyno measurements per cutter rotation		**meas/rot**	**97.5**	**88.3**	**83.6**	**80.7**	**78.7**	**meas/rot**	**97.50**	**88.30**	**83.57**	**80.69**	**78.75**
dyno measurements per cutter rotation (check)		meas/rot	97.5	88.3	83.6	80.7	78.7	meas/rot	97.50	88.30	83.57	80.69	78.75
cutter degrees per each dyno measurement		deg/meas	3.69	4.08	4.31	4.46	4.57						
lead in/out (each) slot length		in	0.5	0.5	0.5	0.5	0.5	mm	12.7	12.7	12.7	12.7	12.7
lead in/out (each) slot cutting time		sec	3.333333333	2.2641509	1.714286	1.37931	1.153846	sec	3.33333333	2.2641509	1.7142857	1.3793103	1.1538462
lead in/out (each) slot cutter rotations (#)		qty	266.7	200.0	160.0	133.3	114.3	qty	266.7	200.0	160.0	133.3	114.3
lead in/out (each) dyno measurements		meas (qty)	26000	17660.377	13371.43	10758.62	9000	meas (qty)	26000	17660.377	13371.429	10758.621	9000
Total length of cut (half circle + lead in/out)	L	in	4.142	6.105	8.069	10.032	11.996	mm	105.196	155.069	204.942	254.815	304.688
Total cutting time (half circle + lead in/out)	**t**	**sec**	**27.6**	**27.6**	**27.7**	**27.7**	**27.7**	**sec**	**27.6**	**27.6**	**27.7**	**27.7**	**27.7**
Total cutter rotations (half circle + lead in/out)		rot/deg	2208.8	6.783	7.172	7.431	7.616	rot/deg	2208.849	6.783	7.172	7.431	7.616
Total dyno measurements (half circle + lead in/out)		meas/slot	215362.8	215636	215777	215863	215920	meas/slot	215363	215636	215777	215863	215920
material removal rate	MRR	in3/min	0.4251969	0.6259843	0.826772	1.027559	1.228347	cm3/min	6.97	10.26	13.55	16.84	20.13
Total material removed per slot (half circle + lead in/out)		in3	0.196	0.29	0.38	0.47	0.57	cm3	3.21	4.73	6.25	7.77	9.29
maximum edge length (square part) in **X**-Axis		in	2.778	4.028	5.278	6.528	7.778	mm	70.5499986	102.3	134.05	165.8	197.55
maximum edge length (square part) in **Y**-Axis		in	1.8887795	2.5137795	3.13878	3.76378	4.38878	mm	47.9749993	63.849999	79.724999	95.599999	111.475
Cumulative Slot Length (cutter usage)		in	4.142	10.247	18.315	28.347	40.343	mm	105.20	260.27	465.21	720.02	1024.71

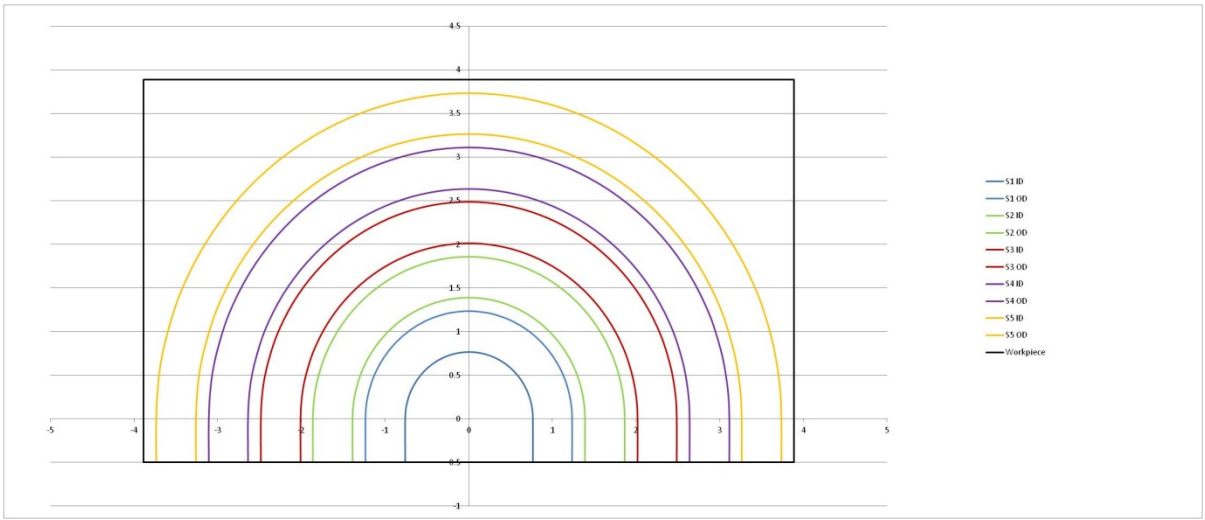

APPENDIX R

Cutter offset and timing

The graphic below illustrates the model for timing cutter offset prior to entering engaging the work piece.

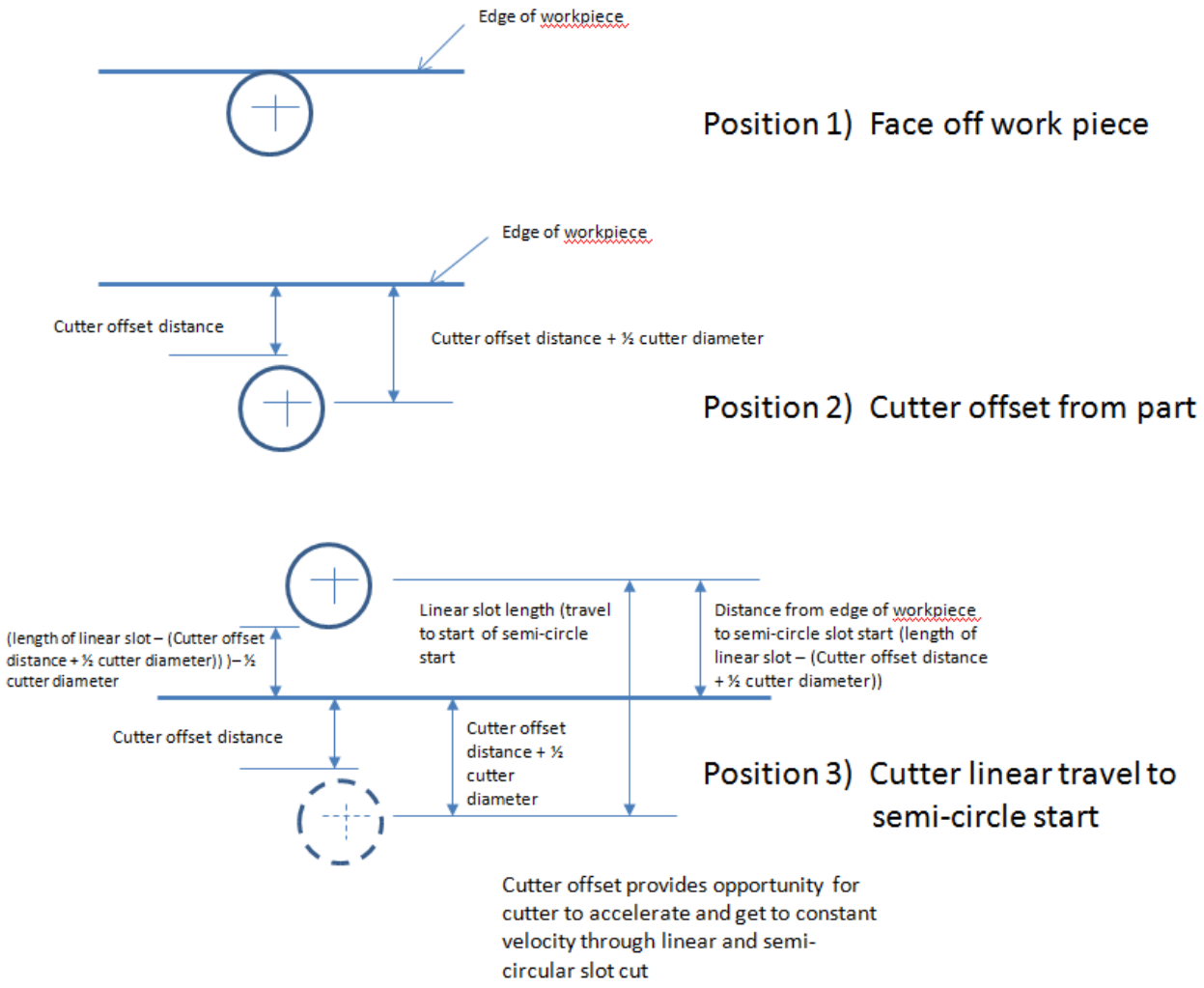

APPENDIX S

2-flute aluminum semi-circular slot

2-flute semi-circular slot detailed set up parameters and calculations for aluminum slot.

		Derived Metric Units				
Input	**Units**	**Inner Slot #1**	**Slot #2**	**Slot #3**	**Slot #4**	**Slot #5**
cutter diameter	mm	12.7	12.7	12.7	12.7	12.7
# of teeth	# of teeth	2	2	2	2	2
spacing between slots	mm	3.175	3.175	3.175	3.175	3.175
lead in slot length	ld	12.7	12.7	12.7	12.7	12.7
inner slot #1 radius (centerline)	mm	25.4	41.275	57.15	73.025	88.9
Dyno sample rate	meas/sec	7800	7800	7800	7800	7800
axial depth of cut	in	2.54	2.54	2.54	2.54	2.54
linear feed rate	mm/min	254	381	508	635	762
spindle speed	rot/min	3500	3500	3500	3500	3500
solve for rpm (reference - not input)						
Output						
feed/tooth	**mm/tooth**	**0.03629**	**0.05443**	**0.07257**	**0.09071**	**0.10886**
feed/revolution (ref. ply thickness =.0075 in. or .1905 mm)	mm/rev	0.07257	0.10886	0.14514	0.18143	0.21771
Semi-Circle Slot Diameter		50.8	82.55	114.3	146.05	177.8
cutting speed	m/min	139.6	139.6	139.6	139.6	139.6
half circle slot length	mm	79.796	129.669	179.542	229.415	279.288
half circle slot cutting time	**sec**	**18.85**	**20.42**	**21.21**	**21.68**	**21.99**
half circle slot cutter rotations (#)	qty	1099.56	1191.19	1237.00	1264.49	1282.82
half circle slot cutter rotatations per degree of slot	**rot/degree**	**6.11**	**6.62**	**6.87**	**7.02**	**7.13**
half circle dyno measurement per degree of slot	meas/degree	816.81	884.88	918.92	939.34	952.95
half circle total dyno measurements	meas (qty)	147026.54	159278.75	165404.85	169080.52	171530.96
half circle total dyno measurements (check)	meas (qty)	147026.54	159278.75	165404.85	169080.52	171530.96
dyno measurements per cutter rotation	**meas/rot**	**133.71**	**133.71**	**133.71**	**133.71**	**133.71**
dyno measurements per cutter rotation (check)	meas/rot	133.71	133.71	133.71	133.71	133.71
cutter degrees per each dyno measurement						
lead in/out (each) slot length	mm	12.7	12.7	12.7	12.7	12.7
lead in/out (each) slot cutting time	sec	3	2	1.5	1.2	1
lead in/out (each) slot cutter rotations (#)	qty	175.0	116.7	87.5	70.0	58.3
lead in/out (each) dyno measurements	meas (qty)	23400	15600	11700	9360	7800
Total length of cut (half circle + lead in/out)	mm	105.196	155.069	204.942	254.815	304.688
Total cutting time (half circle + lead in/out)	**sec**	**24.8**	**24.4**	**24.2**	**24.1**	**24.0**
Total cutter rotations (half circle + lead in/out)	rot/deg	1449.557	3.957	3.922	3.901	3.887
Total dyno measurements (half circle + lead in/out)	meas/slot	193827	190479	188805	187801	187131
material removal rate	cm3/min	8.19	12.29	16.39	20.48	24.58
Total material removed per slot (half circle + lead in/out)	cm3	3.39	5.00	6.61	8.22	9.83
maximum edge length (square part) in **X**-Axis	mm	69.85	101.6	133.35	165.1	196.85
maximum edge length (square part) in **Y**-Axis	mm	47.625	63.5	79.375	95.25	111.125
Cumulative Slot Length (cutter usage)	mm	105.20	260.27	465.21	720.02	1024.71

APPENDIX S

2-flute aluminum semi-circular slot (cont.)

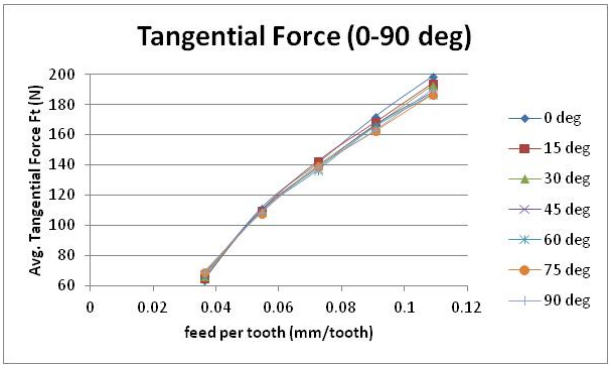

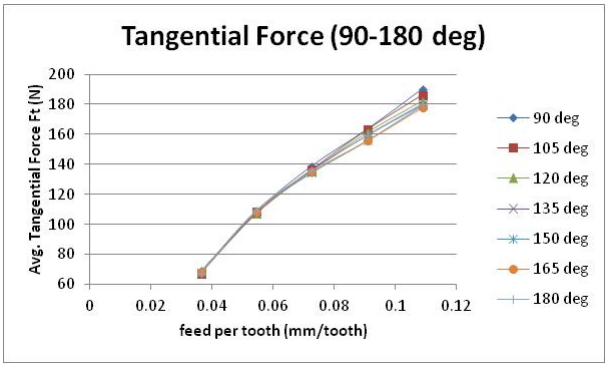

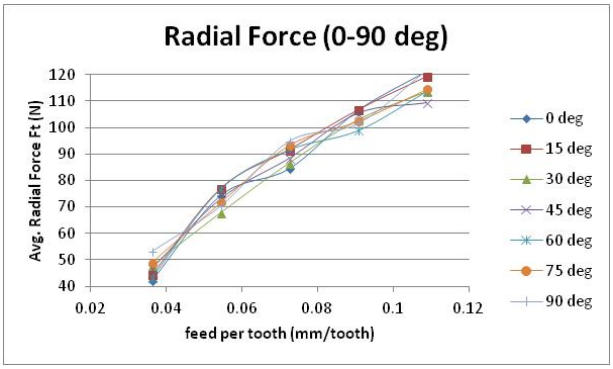

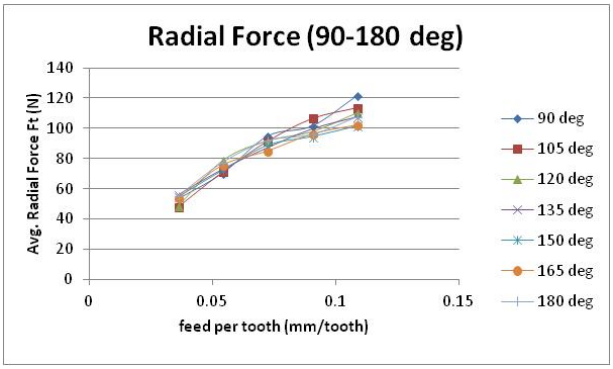

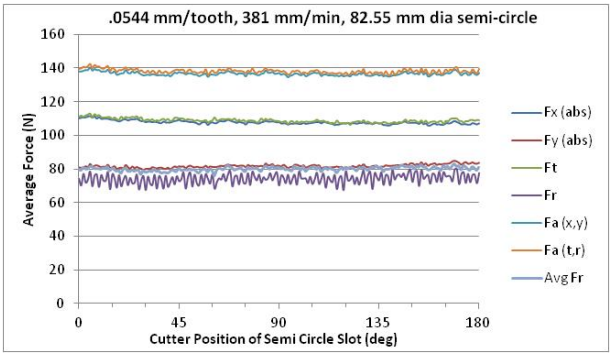

Slot 2

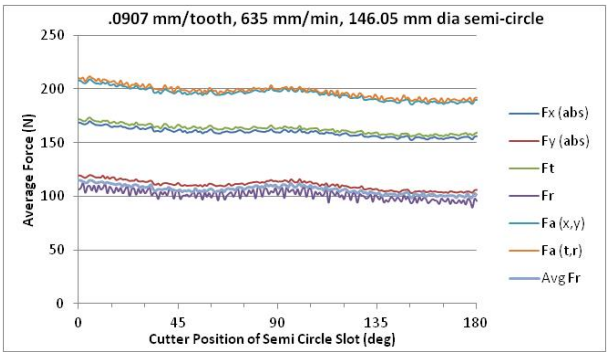

Slot 4

APPENDIX T

4-flute composite semi-circular slot

4-flute semi-circular slot detailed set up parameters and calculations for composite slot.

		Derived Metric Units				
Input	**Units**	**Inner Slot #1**	**Slot #2**	**Slot #3**	**Slot #4**	**Slot #5**
cutter diameter	mm	12.7	12.7	12.7	12.7	12.7
# of teeth	# of teeth	4	4	4	4	4
spacing between slots	mm	3.175	3.175	3.175	3.175	3.175
lead in slot length	ld	12.7	12.7	12.7	12.7	12.7
inner slot #1 radius (centerline)	mm	25.4	41.275	57.15	73.025	88.9
Dyno sample rate	meas/sec	7800	7800	7800	7800	7800
axial depth of cut	in	2.54	2.54	2.54	2.54	2.54
linear feed rate	mm/min	228.6	336.55	444.5	552.45	660.4
spindle speed	rot/min	4800	5300	5600	5800	5943
solve for rpm (reference - not input)						
Output						
feed/tooth	**mm/tooth**	**0.01191**	**0.01588**	**0.01984**	**0.02381**	**0.02778**
feed/revolution (ref. ply thickness =.0075 in. or .1905 mm)	mm/rev	0.04763	0.06350	0.07938	0.09525	0.11112
Semi-Circle Slot Diameter		50.8	82.55	114.3	146.05	177.8
cutting speed	m/min	191.5	211.5	223.4	231.4	237.1
half circle slot length	mm	79.796	129.669	179.542	229.415	279.288
half circle slot cutting time	**sec**	**20.94**	**23.12**	**24.24**	**24.92**	**25.37**
half circle slot cutter rotations (#)	qty	1675.52	2042.04	2261.95	2408.55	2513.33
half circle slot cutter rotatations per degree of slot	**rot/degree**	**9.31**	**11.34**	**12.57**	**13.38**	**13.96**
half circle dyno measurement per degree of slot	meas/degree	907.57	1001.75	1050.19	1079.70	1099.56
half circle total dyno measurements	meas (qty)	163362.82	180315.56	189034.12	194345.42	197920.34
half circle total dyno measurements (check)	meas (qty)	163362.82	180315.56	189034.12	194345.42	197920.34
dyno measurements per cutter rotation	**meas/rot**	**97.50**	**88.30**	**83.57**	**80.69**	**78.75**
dyno measurements per cutter rotation (check)	meas/rot	97.50	88.30	83.57	80.69	78.75
cutter degrees per each dyno measurement						
lead in/out (each) slot length	mm	12.7	12.7	12.7	12.7	12.7
lead in/out (each) slot cutting time	sec	3.333333333	2.26415094	1.71428571	1.3793103	1.153846154
lead in/out (each) slot cutter rotations (#)	qty	266.7	200.0	160.0	133.3	114.3
lead in/out (each) dyno measurements	meas (qty)	26000	17660.3774	13371.4286	10758.621	9000
Total length of cut (half circle + lead in/out)	mm	105.196	155.069	204.942	254.815	304.688
Total cutting time (half circle + lead in/out)	**sec**	**27.6**	**27.6**	**27.7**	**27.7**	**27.7**
Total cutter rotations (half circle + lead in/out)	rot/deg	2208.849	6.783	7.172	7.431	7.616
Total dyno measurements (half circle + lead in/out)	meas/slot	215363	215636	215777	215863	215920
material removal rate	cm3/min	7.37	10.86	14.34	17.82	21.30
Total material removed per slot (half circle + lead in/out)	cm3	3.39	5.00	6.61	8.22	9.83
maximum edge length (square part) in **X**-Axis	mm	69.85	101.6	133.35	165.1	196.85
maximum edge length (square part) in **Y**-Axis	mm	47.625	63.5	79.375	95.25	111.125
Cumulative Slot Length (cutter usage)	mm	105.20	260.27	465.21	720.02	1024.71

APPENDIX T

4-flute composite semi-circular slot

Slot 3 of 5 was unusable.

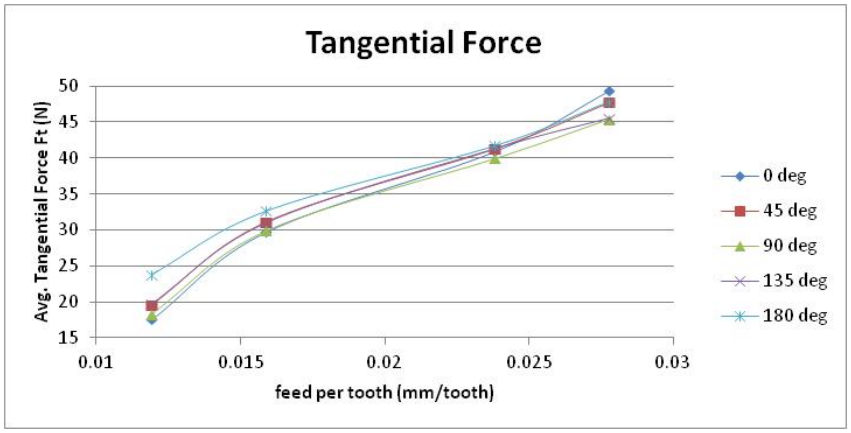

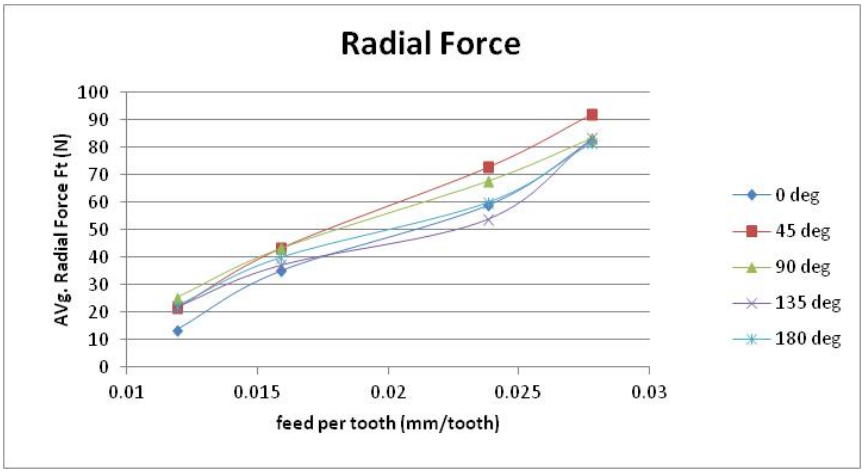

APPENDIX T

4-flute composite semi-circular slot

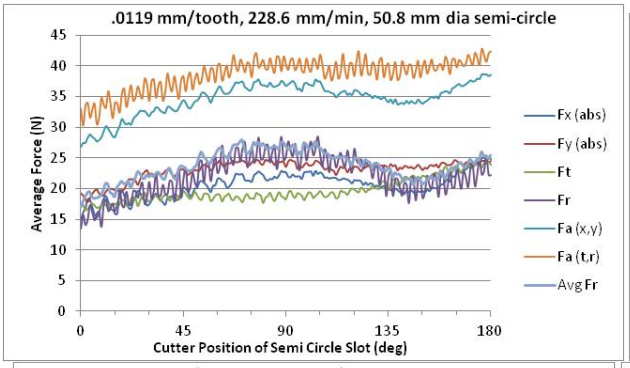

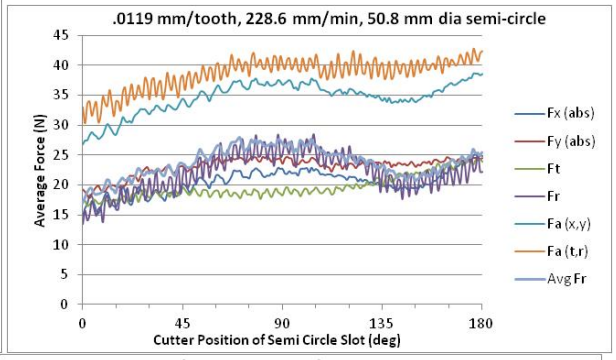

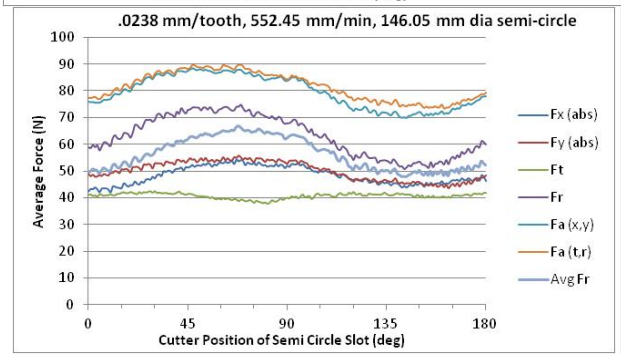

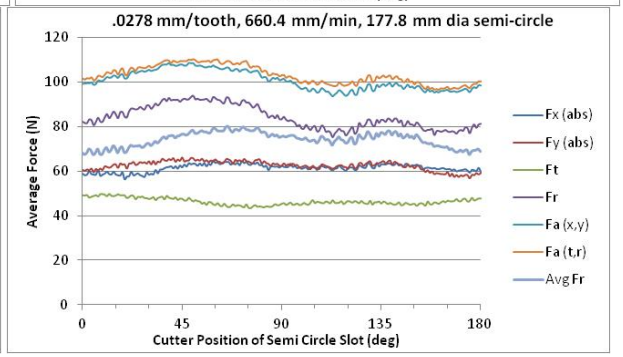

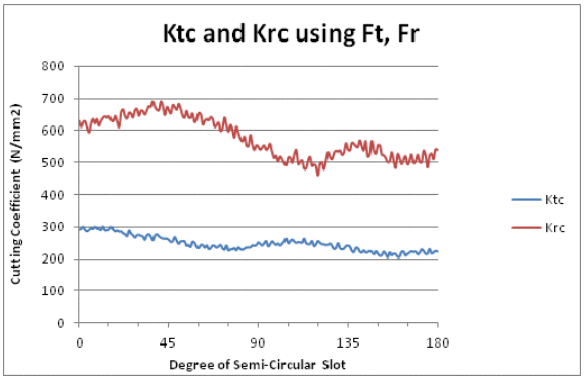

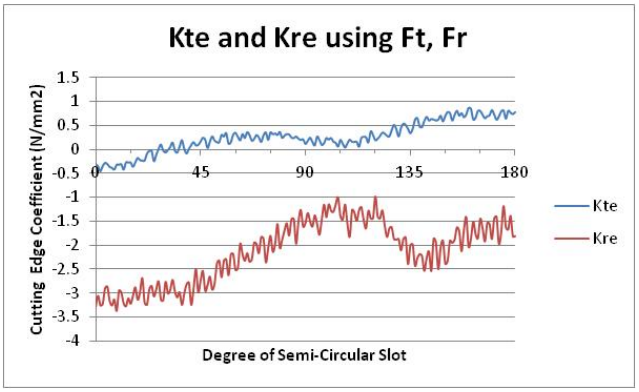

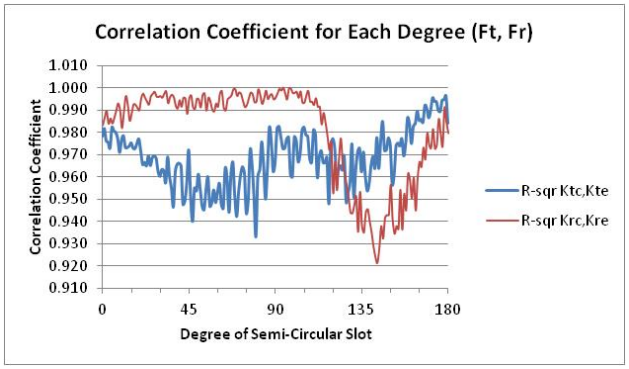

APPENDIX U

2-flute composite semi-circular slot

2-flute semi-circular slot detailed set up parameters and calculations for composite slot.

		Derived Metric Units				
Input	**Units**	**Inner Slot #1**	**Slot #2**	**Slot #3**	**Slot #4**	**Slot #5**
cutter diameter	mm	12.7	12.7	12.7	12.7	12.7
# of teeth	# of teeth	2	2	2	2	2
spacing between slots	mm	3.175	3.175	3.175	3.175	3.175
lead in slot length	ld	12.7	12.7	12.7	12.7	12.7
inner slot #1 radius (centerline)	mm	25.4	41.275	57.15	73.025	88.9
Dyno sample rate	meas/sec	7800	7800	7800	7800	7800
axial depth of cut	in	2.54	2.54	2.54	2.54	2.54
linear feed rate	mm/min	228.6	336.55	444.5	552.45	660.4
spindle speed	rot/min	4800	5300	5600	5800	5943
solve for rpm (reference - not input)						
Output						
feed/tooth	**mm/tooth**	**0.02381**	**0.03175**	**0.03969**	**0.04763**	**0.05556**
feed/revolution (ref. ply thickness =.0075 in. or .1905 mm)	mm/rev	0.04763	0.06350	0.07938	0.09525	0.11112
Semi-Circle Slot Diameter		50.8	82.55	114.3	146.05	177.8
cutting speed	m/min	191.5	211.5	223.4	231.4	237.1
half circle slot length	mm	79.796	129.669	179.542	229.415	279.288
half circle slot cutting time	**sec**	**20.94**	**23.12**	**24.24**	**24.92**	**25.37**
half circle slot cutter rotations (#)	qty	1675.52	2042.04	2261.95	2408.55	2513.33
half circle slot cutter rotatations per degree of slot	**rot/degree**	**9.31**	**11.34**	**12.57**	**13.38**	**13.96**
half circle dyno measurement per degree of slot	meas/degree	907.57	1001.75	1050.19	1079.70	1099.56
half circle total dyno measurements	meas (qty)	163362.82	180315.56	189034.12	194345.42	197920.34
half circle total dyno measurements (check)	meas (qty)	163362.82	180315.56	189034.12	194345.42	197920.34
dyno measurements per cutter rotation	**meas/rot**	**97.50**	**88.30**	**83.57**	**80.69**	**78.75**
dyno measurements per cutter rotation (check)	meas/rot	97.50	88.30	83.57	80.69	78.75
cutter degrees per each dyno measurement						
lead in/out (each) slot length	mm	12.7	12.7	12.7	12.7	12.7
lead in/out (each) slot cutting time	sec	3.33333333	2.264150943	1.714285714	1.379310345	1.153846154
lead in/out (each) slot cutter rotations (#)	qty	266.7	200.0	160.0	133.3	114.3
lead in/out (each) dyno measurements	meas (qty)	26000	17660.37736	13371.42857	10758.62069	9000
Total length of cut (half circle + lead in/out)	mm	105.196	155.069	204.942	254.815	304.688
Total cutting time (half circle + lead in/out)	**sec**	**27.6**	**27.6**	**27.7**	**27.7**	**27.7**
Total cutter rotations (half circle + lead in/out)	rot/deg	2208.849	6.783	7.172	7.431	7.616
Total dyno measurements (half circle + lead in/out)	meas/slot	215363	215636	215777	215863	215920
material removal rate	cm3/min	7.37	10.86	14.34	17.82	21.30
Total material removed per slot (half circle + lead in/out)	cm3	3.39	5.00	6.61	8.22	9.83
maximum edge length (square part) in **X**-Axis	mm	69.85	101.6	133.35	165.1	196.85
maximum edge length (square part) in **Y**-Axis	mm	47.625	63.5	79.375	95.25	111.125
Cumulative Slot Length (cutter usage)	mm	105.20	260.27	465.21	720.02	1024.71

APPENDIX U

2-flute composite semi-circular slot

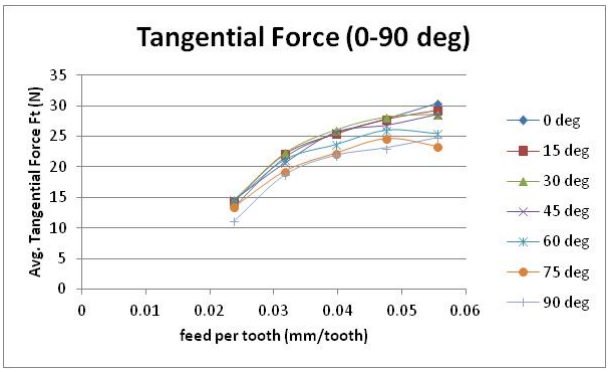

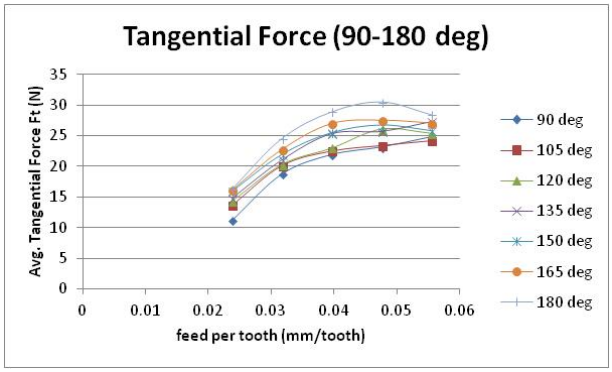

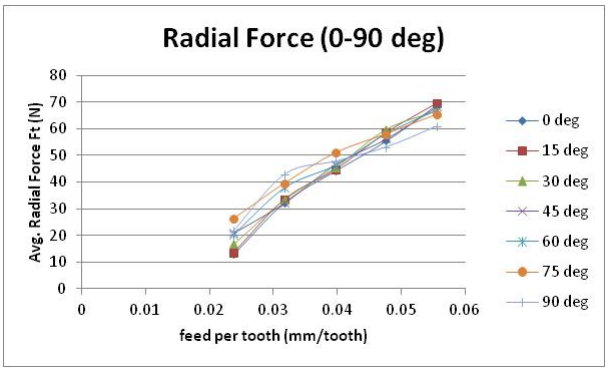

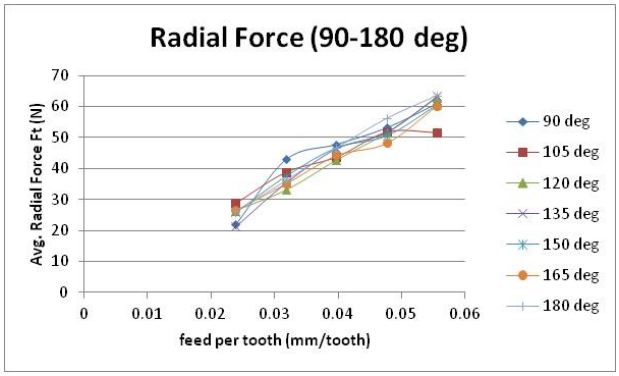

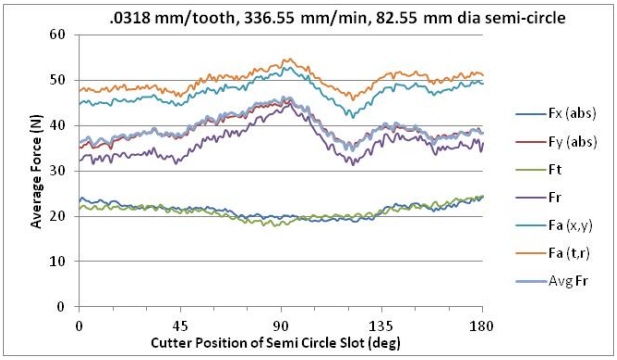

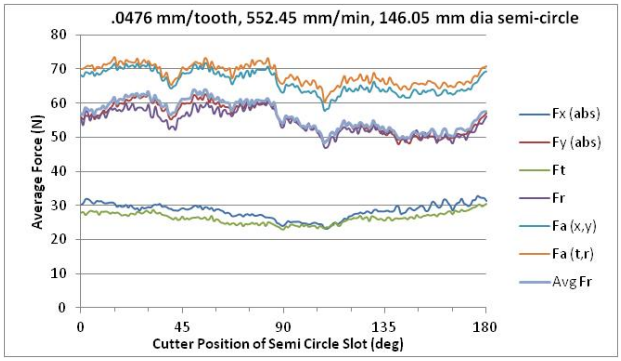

Slot 2 Slot 4

APPENDIX V

GRIMM particle model

The particle model developed for the GRIMM is summarized. A sample of each work sheet is included.

<Header>													
User name: Jeff Miller													
Location: MSTL													
Model: 1.109													
Serial No.:													
Software revision: Version 2.5.4													
Unit: counts/liter (differential)													
C-factor: 1.00													
Comment: First diluter test using multi lam and isokinetic probe with nozzle													
date & time	0.265 µm	0.290 µm	0.325 µm	0.375 µm	0.425 µm	0.475 µm	0.540 µm	0.615 µm	0.675 µm	0.750 µm	0.900 µm	1.150 µm	1.450 µm
9/22/2013 7:24:38 PM	0	0	0	100	0	0	50	0	0	0	0	0	0
9/22/2013 7:24:44 PM	0	0	0	50	0	50	0	50	0	0	0	0	0
9/22/2013 7:24:50 PM	0	0	0	100	0	0	0	0	100	50	0	0	0
9/22/2013 7:24:56 PM	0	0	0	0	0	0	0	0	0	0	0	0	0
9/22/2013 7:25:02 PM	0	200	200	50	50	50	50	0	50	0	0	50	0
9/22/2013 7:25:08 PM	141760	220310	381710	385630	203980	96180	129690	72250	55450	67350	42950	34500	18550
9/22/2013 7:25:14 PM	28120	40420	62220	63200	37600	16950	23600	13250	9550	11350	9000	6050	3100

Load worksheet. Particle count values are copy and pasted from GRIMM Excel output using LabVIEW 1178 software, truncated for presentation.

User Defined Density	**1.67**	**g/cm3**	1.67E-06	µg/µm3		**Correction**	**0.000001**	**µg**		**Dilution**	**10**	**factor**
Low Bin	**User Defined**	0.25	0.28	0.3	0.35	0.4	0.45	0.5	0.58	0.65	0.7	0.8
High Bin	**Backup**	0.28	0.3	0.35	0.4	0.45	0.5	0.58	0.65	0.7	0.8	1
Bin Midpoint	**Filter**	0.265	0.29	0.325	0.375	0.425	0.475	0.54	0.615	0.675	0.75	0.9
date & time (µg/m3)	**Mass (µg/m3)**	0.265 µm	0.290 µm	0.325 µm	0.375 µm	0.425 µm	0.475 µm	0.540 µm	0.615 µm	0.675 µm	0.750 µm	0.900 µm
9/22/2013 7:24:38 PM	**1**	0.000001	0.000001	0.000001	0.046111	0.000001	0.000001	0.068844	0.000001	0.000001	0.000001	0.000001
9/22/2013 7:24:44 PM	**1**	0.000001	0.000001	0.000001	0.023056	0.000001	0.04685608	0.000001	0.101698	0.000001	0.000001	0.000001
9/22/2013 7:24:50 PM	**1**	0.000001	0.000001	0.000001	0.046111	0.000001	0.000001	0.000001	0.000001	0.268922	0.1844458	0.000001
9/22/2013 7:24:56 PM	**1**	0.000001	0.000001	0.000001	0.000001	0.000001	0.000001	0.000001	0.000001	0.000001	0.000001	0.000001
9/22/2013 7:25:02 PM	**1**	0.000001	0.042652	0.06003371	0.023056	0.033562	0.04685608	0.068844	0.000001	0.134461	0.000001	0.000001
9/22/2013 7:25:08 PM	**1**	23.06781	46.98328	114.577334	177.8196	136.9208	90.1323501	178.5677	146.9529	149.1173	248.44856	273.78257
9/22/2013 7:25:14 PM	**1**	4.575811	8.619963	18.6764867	29.14244	25.23886	15.8842102	32.49439	26.94985	25.68206	41.869208	57.370037

Mass calculation work sheet. User enters density (can be done for each individual bin), correction factor, dilution factor, and option for backup filter mass, truncated.

blank												
Low Bin	0.25	0.28	0.3	0.35	0.4	0.45	0.5	0.58	0.65	0.7	0.8	1
High Bin	0.28	0.3	0.35	0.4	0.45	0.5	0.58	0.65	0.7	0.8	1	1.3
blank												
date & time (µg/m3)	0.265 µm	0.290 µm	0.325 µm	0.375 µm	0.425 µm	0.475 µm	0.540 µm	0.615 µm	0.675 µm	0.750 µm	0.900 µm	1.150 µm
9/22/2013 7:24:38 PM	89.68743	89.68751	89.6876	89.68769	93.82331	93.8234	93.82349	99.99794	99.99803	99.99812	99.99821	99.9983
9/22/2013 7:24:44 PM	85.35071	85.3508	85.35089	85.35097	87.31879	87.31888	91.31808	91.31816	99.99812	99.99821	99.99829	99.99838
9/22/2013 7:24:50 PM	66.68861	66.68868	66.68875	66.68881	69.76392	69.76399	69.76406	69.76412	69.76419	87.69823	99.99867	99.99873
9/22/2013 7:24:56 PM	99.997	99.9971	99.9972	99.9973	99.9974	99.9975	99.9976	99.9977	99.9978	99.9979	99.998	99.9981
9/22/2013 7:25:02 PM	4.733281	4.733286	4.93517	5.219326	5.328456	5.487316	5.709099	6.034957	6.034962	6.671403	6.671408	6.671413
9/22/2013 7:25:08 PM	0.006647	0.159974	0.472264	1.233839	2.415774	3.325862	3.924955	5.111863	6.088632	7.079788	8.731181	10.55096
9/22/2013 7:25:14 PM	0.004649	0.02592	0.065992	0.152813	0.288287	0.405614	0.479455	0.630511	0.755792	0.87518	1.069817	1.336512

Cumulative mass work sheet. Cumulative mass for each bin size is calculated, truncated.

APPENDIX V

GRIMM particle model (cont.)

blank											
Low Bin	0.25	0.28	0.3	0.35	0.4	0.45	0.5	0.58	0.65	0.7	0.8
High Bin	0.28	0.3	0.35	0.4	0.45	0.5	0.58	0.65	0.7	0.8	1
blank											
date & time ln(Cut Dia)	0.265 µm	0.290 µm	0.325 µm	0.375 µm	0.425 µm	0.475 µm	0.540 µm	0.615 µm	0.675 µm	0.750 µm	0.900 µm
9/22/2013 7:24:38 PM	-1.38629	-1.27297	-1.20397	-1.04982	-0.91629	-0.79851	-0.69315	-0.54473	-0.43078	-0.35667	-0.22314
9/22/2013 7:24:44 PM	-1.38629	-1.27297	-1.20397	-1.04982	-0.91629	-0.79851	-0.69315	-0.54473	-0.43078	-0.35667	-0.22314
9/22/2013 7:24:50 PM	-1.38629	-1.27297	-1.20397	-1.04982	-0.91629	-0.79851	-0.69315	-0.54473	-0.43078	-0.35667	-0.22314
9/22/2013 7:24:56 PM	-1.38629	-1.27297	-1.20397	-1.04982	-0.91629	-0.79851	-0.69315	-0.54473	-0.43078	-0.35667	-0.22314
9/22/2013 7:25:02 PM	-1.38629	-1.27297	-1.20397	-1.04982	-0.91629	-0.79851	-0.69315	-0.54473	-0.43078	-0.35667	-0.22314
9/22/2013 7:25:08 PM	-1.38629	-1.27297	-1.20397	-1.04982	-0.91629	-0.79851	-0.69315	-0.54473	-0.43078	-0.35667	-0.22314
9/22/2013 7:25:14 PM	-1.38629	-1.27297	-1.20397	-1.04982	-0.91629	-0.79851	-0.69315	-0.54473	-0.43078	-0.35667	-0.22314

Log cut point diameter worksheet. Simply calculates the natural logarithm of the low bin diameter for each size range to be used in the log-probablity plot, truncated.

blank											
Low Bin	0.25	0.28	0.3	0.35	0.4	0.45	0.5	0.58	0.65	0.7	0.8
High Bin	0.28	0.3	0.35	0.4	0.45	0.5	0.58	0.65	0.7	0.8	1
blank											
date & time (probits)	0.265 µm	0.290 µm	0.325 µm	0.375 µm	0.425 µm	0.475 µm	0.540 µm	0.615 µm	0.675 µm	0.750 µm	0.900 µm
9/22/2013 7:24:38 PM	1.26394	1.263945	1.26395	1.263955	1.540109	1.540117	1.540124	4.10033	4.110604	4.121333	4.132557
9/22/2013 7:24:44 PM	1.051594	1.051598	1.051602	1.051606	1.141591	1.141595	1.360605	1.360611	4.122033	4.132734	4.143931
9/22/2013 7:24:50 PM	0.431331	0.431333	0.431335	0.431336	0.517623	0.517625	0.517627	0.517628	0.51763	1.160033	4.200136
9/22/2013 7:24:56 PM	4.012818	4.02081	4.029068	4.037611	4.046458	4.055634	4.065165	4.07508	4.085412	4.0962	4.107487
9/22/2013 7:25:02 PM	-1.67128	-1.67128	-1.65117	-1.62395	-1.61381	-1.59933	-1.57967	-1.55185	-1.55185	-1.50072	-1.50072
9/22/2013 7:25:08 PM	-3.82095	-2.94789	-2.5955	-2.24643	-1.97458	-1.83492	-1.75946	-1.6341	-1.54738	-1.46987	-1.3575
9/22/2013 7:25:14 PM	-3.90823	-3.47106	-3.21163	-2.96202	-2.76081	-2.64736	-2.5903	-2.49459	-2.42959	-2.37595	-2.30092

Probit calculation worksheet. Calculates the Excel NORMSINV function for the cumulative mass for each time and bin to be used in the log-probability plot, truncated for presentation. NORMSINV(p) returns the value z such that, with probability p, a standard normal random variable takes on a value that is less than or equal to z.

APPENDIX V

GRIMM particle model (cont.)

blank									
blank									
blank									
blank				<1 (µm)	<2.5 (µm)	<4 (µm)	<10 (µm)	Total. Conc.	Total Counts
date & time	MMD (D_{50})(µm)	σ_g	R^2	(mg/m^3)	(mg/m^3)	(mg/m^3)	(mg/m^3)	(mg/m3)	(#/liter)
9/22/2013 7:24:38 PM	0.080	2.526	0.593	0.001	0.001	0.001	0.001	0.001	1500
9/22/2013 7:24:44 PM	0.122	2.326	0.632	0.001	0.001	0.001	0.001	0.001	1500
9/22/2013 7:24:50 PM	0.266	1.999	0.710	0.001	0.001	0.001	0.001	0.001	2500
9/22/2013 7:24:56 PM	0.000	2045.219	0.880	0.001	0.001	0.001	0.001	0.001	0
9/22/2013 7:25:02 PM	1.174	1.528	0.830	0.001	0.012	0.021	0.021	0.021	8500
9/22/2013 7:25:08 PM	1.357	1.524	0.942	1.587	9.179	14.845	15.045	15.045	19606100
9/22/2013 7:25:14 PM	2.606	1.497	0.798	0.288	0.655	0.655	20.164	21.511	3416600

Results worksheet. In this worksheet the particle median diameter, D_{50}, geometric standard deviation, σ_g, correlation coefficient, R^2, and any desired combination of particle mass distributions are calculated (<1µm, < 2.5 µm, < 10 µm, etc.), truncated for presentation.

D_{50}: EXP(INTERCEPT(Log Cut Point, Probit)), where:

EXP is the natural logarithm, e, raised to the power of the number,

INTERCEPT returns the y-intercept of the linear regression line of the arguments, Log Cut Point, and Probit from the prior worksheets for all 31 bin sizes.

σ_g: EXP(SLOPE(Log Cut Point, Probit)), where:

SLOPE returns the slope of the linear regression line of the arguments, Log Cut Point, and Probit from the prior worksheets for all 31 bin sizes.

R^2: CORREL(Log Cut Point, Probit)^2, where:

CORREL returns the correlation coefficient for the argunments Log Cut Point and Probit from the prior worksheets for all 31 bin sizes.

Particle count and mass distributions are simply summations from the mass spreadsheets to the cut points of interest and are plotted against time to show the mass concentration over time of the cut and shown on the following page.

APPENDIX V

GRIMM particle model (cont.)

	MMD (µm)	σ_g	R^2	<1 (µm) (mg/m^3)	<2.5 (µm) (mg/m^3)	<4 (µm) (mg/m^3)	<10 (µm) (mg/m^3)	<32 (µm) (mg/m^3)
Minimum	0.00	1.43	0.59	0.00	0.00	0.00	0.00	0.00
Maximum	10.53	2045.22	0.97	1.90	9.50	22.92	56.76	61.99
Range	10.53	2043.79	0.38	1.90	9.50	22.92	56.76	61.99
Mean	2.53	32.14	0.84	0.76	3.52	9.77	24.05	25.46
Median	2.29	1.53	0.85	0.51	1.40	7.53	20.01	20.01
Standard Deviation	1.45	249.66	0.07	0.73	3.54	9.68	21.64	22.80

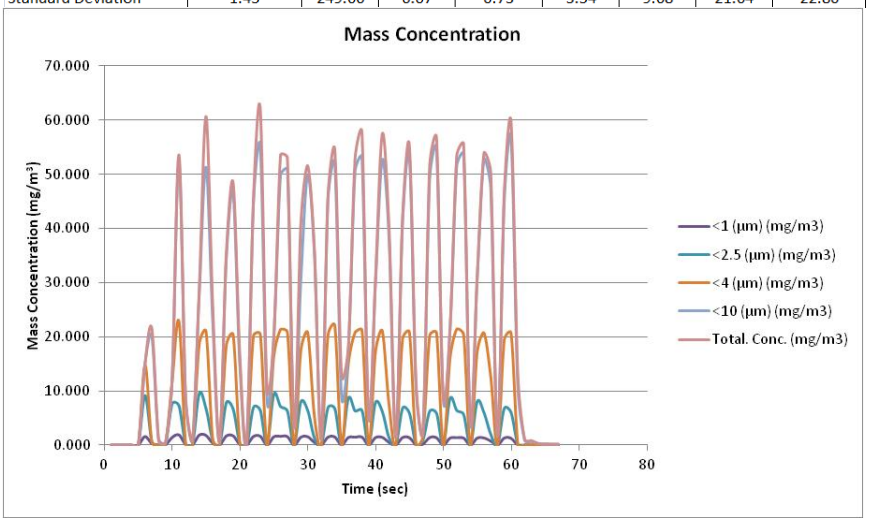

	MMD (µm)	σ_g	R^2	<1 (µm) (cts/liter)	<2.5 (µm) (cts/liter)	<4 (µm) (cts/liter)	<10 (µm) (cts/liter)	<32 (µm) (cts/liter)
Minimum	0.00	1.43	0.59	0	0	0	0	0
Maximum	10.53	2045.22	0.97	20790900	21795700	22289600	22364700	22364800
Range	10.53	2043.79	0.38	20790900	21795700	22289600	22364700	22364800
Mean	2.53	32.14	0.84	8228849	8731754	8913952	8954025	8954140
Median	2.29	1.53	0.85	5593100	5767600	6074000	6155300	6155500
Standard Deviation	1.45	249.66	0.07	7898512	8392256	8551658	8573823	8573896

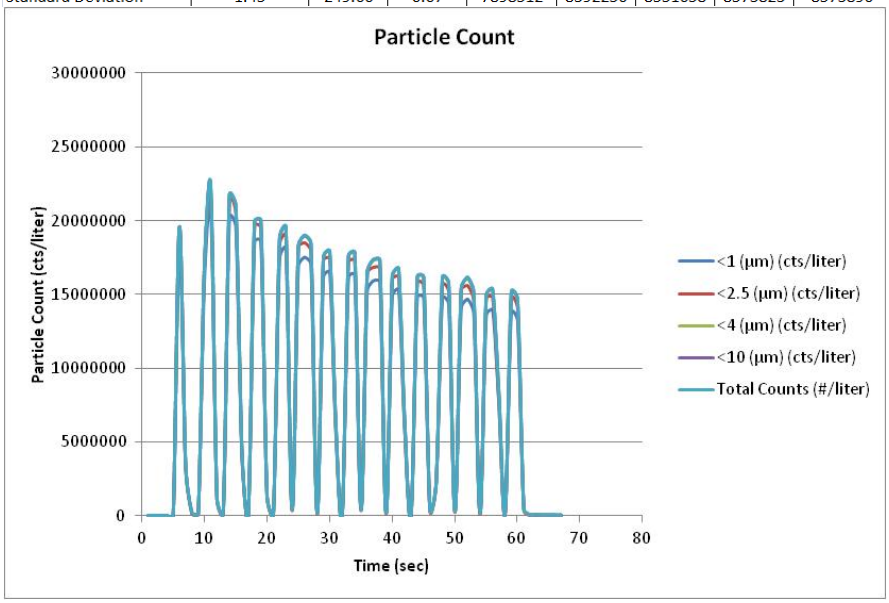

APPENDIX V

GRIMM particle model (cont.)

Select Row (Sample) to Plot	28										
Date/Time of Sample Selected is:	9/22/2013 7:26:50 PM										
A	B	C	D	E	F	G	H	I	J	K	L
Data Needed for Log Probability Plot	0.265 µm	0.290 µm	0.325 µm	0.375 µm	0.425 µm	0.475 µm	0.540 µm	0.615 µm	0.675 µm	0.750 µm	0.900 µm
9/22/2013 7:26:50 PM Cum Data	0.001613	0.0386571	0.11171193	0.284125545	0.5581634	0.777875134	0.924018521	1.227559	1.484285598	1.736964	2.173723163
9/22/2013 7:26:50 PM Probits	-4.15689	-3.362235	-3.05718832	-2.76556024	-2.5375461	-2.419134124	-2.355850161	-2.24839	-2.1742587	-2.11138	-2.01912275
9/22/2013 7:26:50 PM Log Cut Dia	-1.386294	-1.272966	-1.2039728	-1.04982212	-0.9162907	-0.798507696	-0.693147181	-0.54473	-0.43078292	-0.35667	-0.22314355
Lower Bin Cut Point	0.25	0.28	0.3	0.35	0.4	0.45	0.5	0.58	0.65	0.7	0.8
Calculate Intercept	1.5488211										
Calculate Slope	0.8318525										
Calculate Regresion Value	0.148214	0.2870604	0.369979161	0.47155617	0.5700433	0.629051823	0.663054085	0.725054	0.771173875	0.812581	0.877400971

Plotting worksheet. In this worksheet the user can select any sample to plot. The GRIMM samples every 6 seconds, so an individual log-probability plot is created for every sample of interest. The extracted values from the prior worksheets are truncated for presentation.

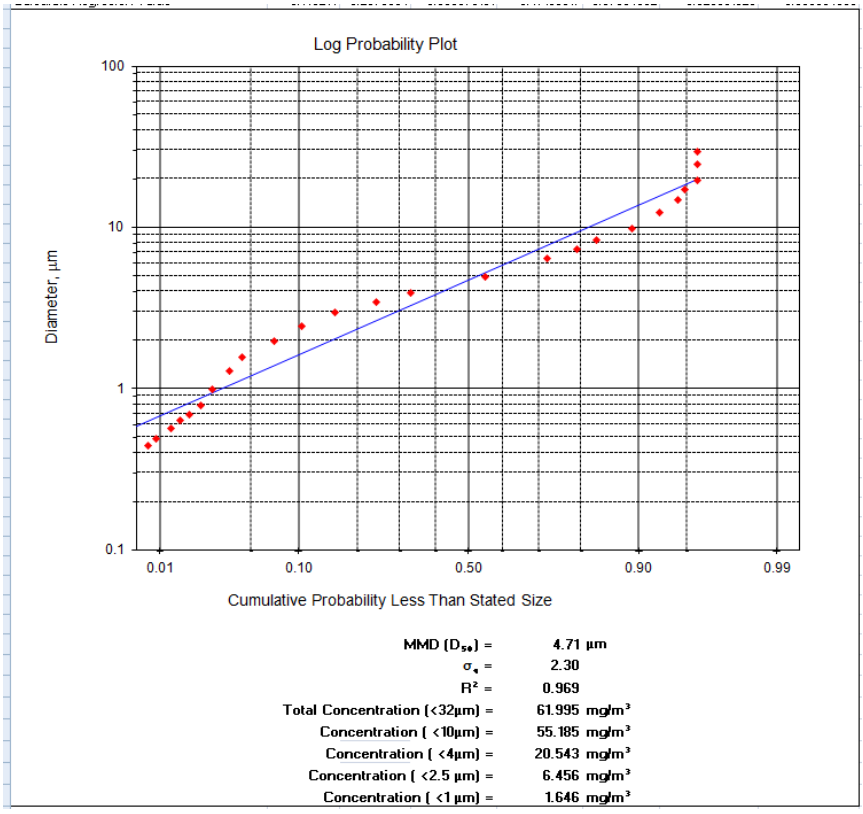

Additional plots automatically generated for the same sample include:

- Particle Count and Normalized Particle Count distribution
- Particle Mass and Normalized Particle Mass distribution
- Surface Area and Normalized Surface Area distribution

APPENDIX V

GRIMM particle model (cont.)

Data Needed for Count Plots (Multiplied by Dilution Factor)											
date & time	0.265 µm	0.290 µm	0.325 µm	0.375 µm	0.425 µm	0.475 µm	0.540 µm	0.615 µm	0.675 µm	0.750 µm	0.900 µm
Low Bin	0.25	0.28	0.3	0.35	0.4	0.45	0.5	0.58	0.65	0.7	0.8
High Bin	0.28	0.3	0.35	0.4	0.45	0.5	0.58	0.65	0.7	0.8	1
9/22/2013 7:26:50 PM	1411300	2123700	3560900	3684300	2029200	966800	1366700	782500	582500	734000	468000
Normalized Count/Liter dN/dlogDp	28674455	70876887	53190003.88	63531234.8	39669598	21128781.06	21202957.41	15812757	18098671.14	12656930	4829222.342

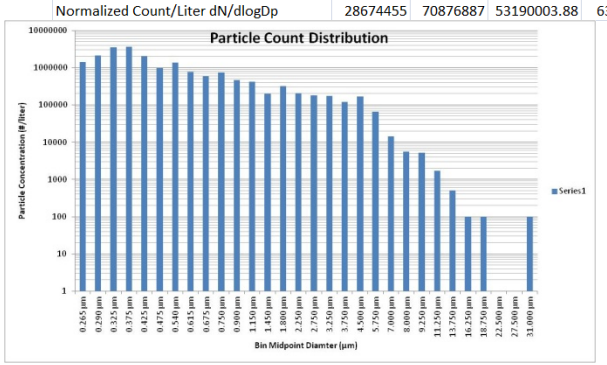

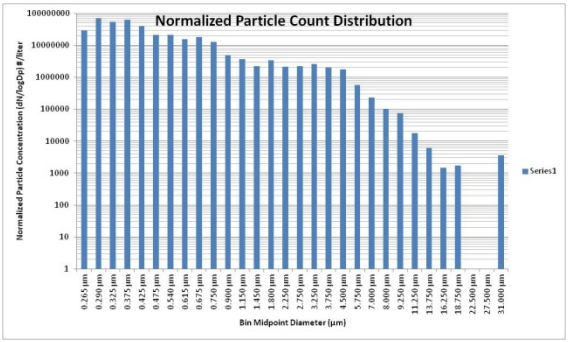

Data Needed for Mass Plots (Multiplied by Dilution Factor)											
date & time (µg/m3)	Filter (µm)	0.265 µm	0.290 µm	0.325 µm	0.375 µm	0.425 µm	0.475 µm	0.540 µm	0.615 µm	0.675 µm	0.750 µm	0.900 µm
Low Bin	0.02	0.25	0.28	0.3	0.35	0.4	0.45	0.5	0.58	0.65	0.7	0.8
High Bin	0.25	0.28	0.3	0.35	0.4	0.45	0.5	0.58	0.65	0.7	0.8	1
9/22/2013 7:26:50 PM	1	22.965296	45.28999307	106.8870163	169.88846	136.2092925	90.6009109	188.1783	159.1566491	156.6471	270.7665077	298.3241933
Normalized Mass dM/dlogDp (µg/m3)	0.9116518	466.6034	1511.519388	1596.596594	2929.5182	2662.806955	1980.023594	2919.395	3216.236868	4867.132	4669.036337	3078.362947

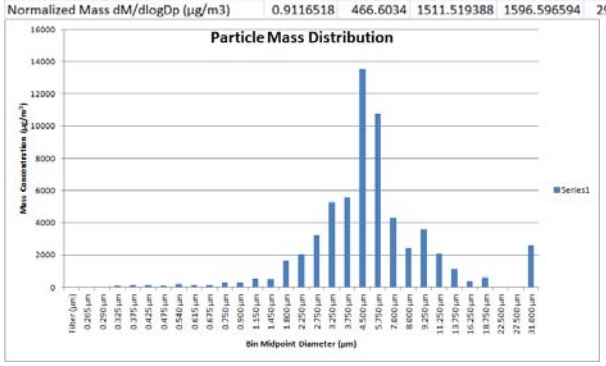

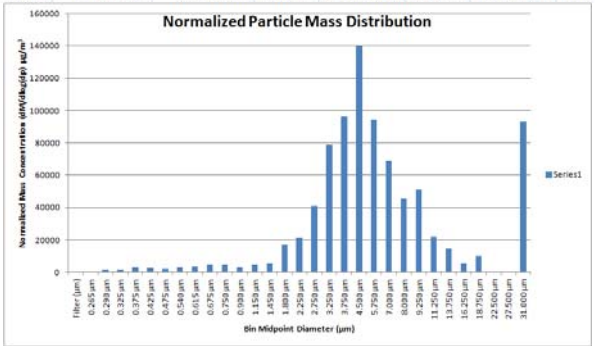

Data Needed for Surface Area Plots (Multiplied by Dilution Factor)											
date & time	0.265 µm	0.290 µm	0.325 µm	0.375 µm	0.425 µm	0.475 µm	0.540 µm	0.615 µm	0.675 µm	0.750 µm	0.900 µm
Low Bin	0.25	0.28	0.3	0.35	0.4	0.45	0.5	0.58	0.65	0.7	0.8
High Bin	0.28	0.3	0.35	0.4	0.45	0.5	0.58	0.65	0.7	0.8	1
Bin Midpoint Calculated	0.265	0.29	0.325	0.375	0.425	0.475	0.54	0.615	0.675	0.75	0.9
Sphere Diameter (mm)	0.000265	0.00029	0.000325	0.000375	0.000425	0.000475	0.00054	0.000615	0.000675	0.00075	0.0009
9/22/2013 7:26:50 PM Counts #/liter	1411300	2123700	3560900	3684300	2029200	966800	1366700	782500	582500	734000	468000
Sphere Surface Area (mm2/liter)	0.3113587	0.5610984	1.181616025	1.62767388	1.1514699	0.685288957	1.252018041	0.929789	0.833783599	1.297085	1.190914943
Norm. Surf. Area dS/dlogDp (mm2/liter)	6.3261109	18.726236	17.6500775	28.06723976	22.51052	14.97654152	19.4237837	18.78917	25.90622345	22.36664	12.28887404

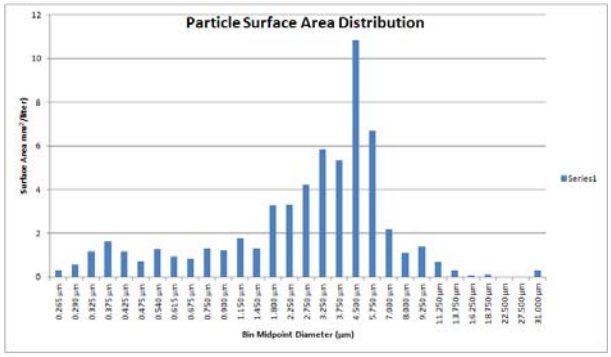

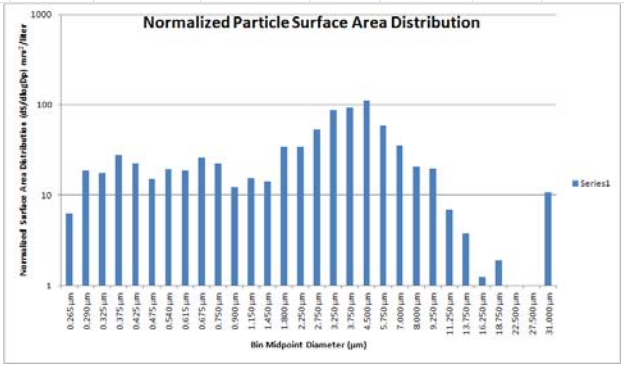

APPENDIX V

GRIMM particle model (cont.)

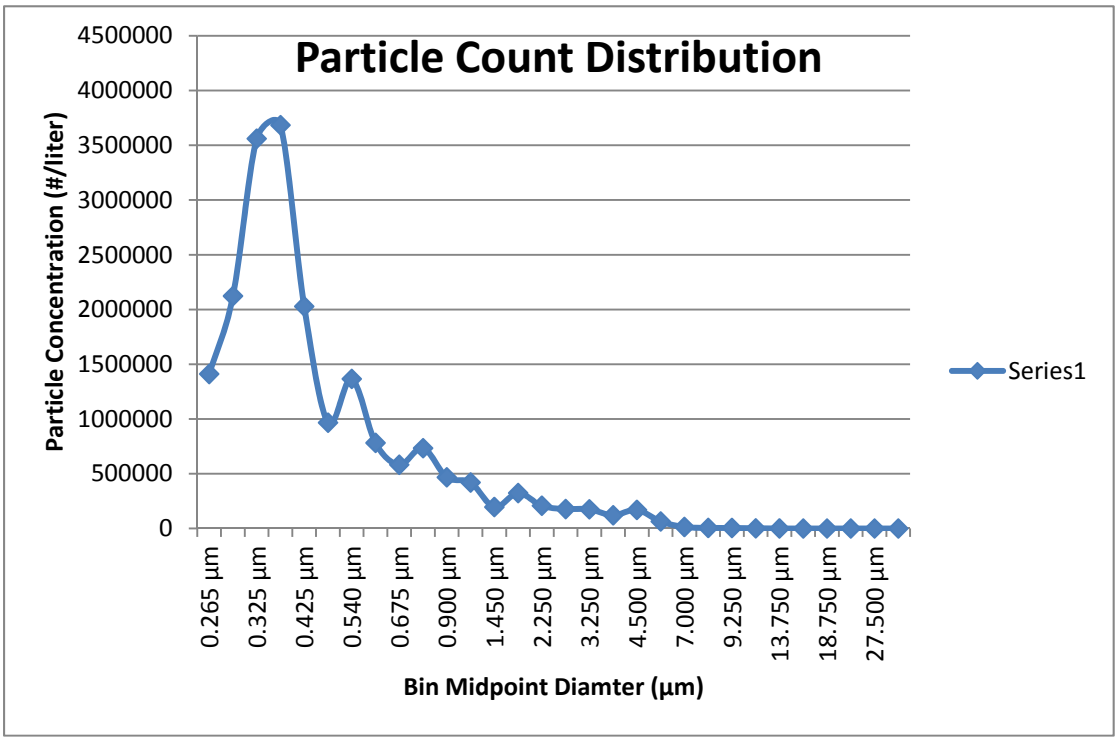

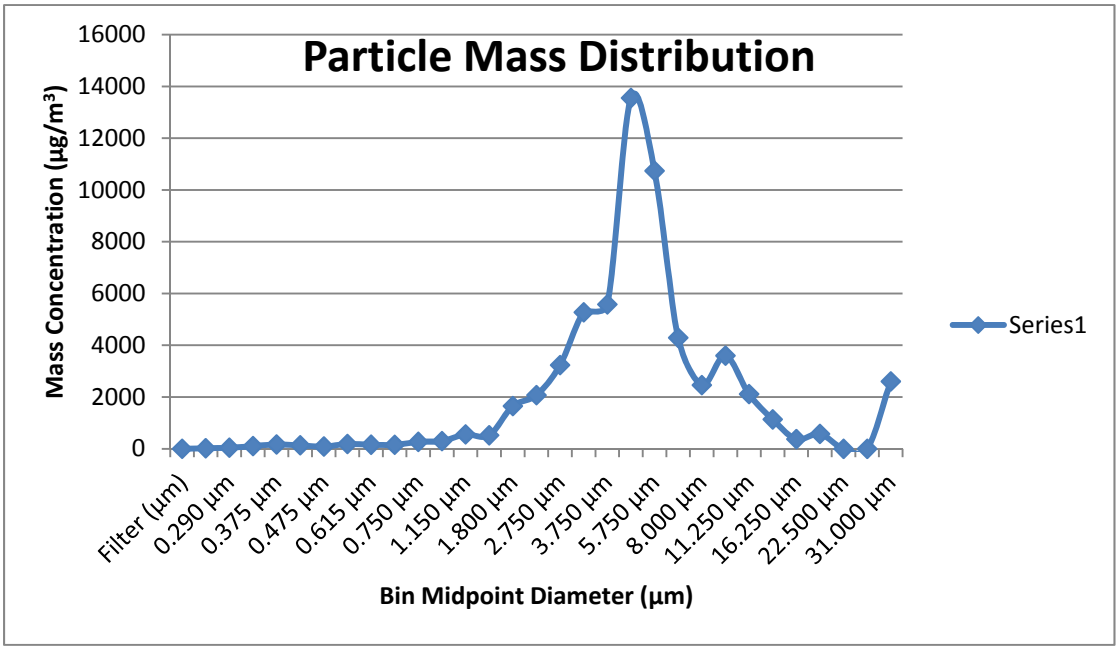

APPENDIX V

GRIMM particle model (cont.)

Aerodynamic toolkit. In this spreadsheet and accompanying MatLAB program, the user can convert from optical diameter to aerodynamic diameter. The purpose is to modify the GRIMM ranges for aerodynamic diameter in the previous tool. In this manner, the concentrations can be compared to gravimetric results from a cascade impactor. The user enters the constants including mean free diameter, λ,standard density, ρ_a, particle density, ρ_e, dyamic shape factor, χ, and MP which is a multiplier for sizing between the bin low and high ranges where 0.5 is the midpoint. Individual densities can also be entered. The spreadsheet below is truncated for clarity.

Constants													
λ	0.066	µm	Mean free path (fixed, used in Matlab)										
ρ_a	1	g/cm3	Denisty equivalent aerodynamic particle (fixed, used in Matlab)										
ρ_e	1.67	g/cm3	Density equivalent volume particle (can be modified for input into Matlab below for unique bin density)										
χ	1.5		Shape factor (can be modified for input into Matlab for unique bin shape factor)										
MP	0.5		Midpoint diameter (MP * (low bin + high bin)) (can be modified for calculations below, this is not used in Matlab)										
ORIGINAL BIN STRUCTURE (EQUIVALENT VOLUME DIAMETER) - INPUT Paste cells C9:N12 into Matlab variable "equiv" cells C9:N12													
ρ_e		1.67	1.67	1.67	1.67	1.67	1.67	1.67	1.67	1.67	1.67	1.67	1.67
χ		1.5	1.5	1.5	1.5	1.5	1.5	1.5	1.5	1.5	1.5	1.5	1.5
de (Low Bin)	**blank**	0.25	0.28	0.3	0.35	0.4	0.45	0.5	0.58	0.65	0.7	0.8	1
de (High Bin)	**blank**	0.28	0.3	0.35	0.4	0.45	0.5	0.58	0.65	0.7	0.8	1	1.3
MP		0.5	0.5	0.5	0.5	0.5	0.5	0.5	0.5	0.5	0.5	0.5	0.5
ORIGINAL BIN STRUCTURE (EQUIVALENT VOLUME DIAMETER) - reference													
de (Low Bin)	**User Defined**	0.25	0.28	0.3	0.35	0.4	0.45	0.5	0.58	0.65	0.7	0.8	1
de (High Bin)	**Backup**	0.28	0.3	0.35	0.4	0.45	0.5	0.58	0.65	0.7	0.8	1	1.3
de (Bin Midpoint)	**Filter**	0.265	0.29	0.325	0.375	0.425	0.475	0.54	0.615	0.675	0.75	0.9	1.15
date & time (µg/m3)	**Mass (µg/m3)**	0.265 µm	0.290 µm	0.325 µm	0.375 µm	0.425 µm	0.475 µm	0.540 µm	0.615 µm	0.675 µm	0.750 µm	0.900 µm	1.150 µm
REVISED BIN STRUCTURE (AERODYNAMIC DIAMETER) pasted from Matlab. Paste cells from Matlab variable "aero" into cells C24:N29													
ρ_e		1.67	1.67	1.67	1.67	1.67	1.67	1.67	1.67	1.67	1.67	1.67	1.67
χ		1.5	1.5	1.5	1.5	1.5	1.5	1.5	1.5	1.5	1.5	1.5	1.5
Ce (Low Bin)		1.66528	1.594	1.5544	1.4752	1.4158	1.3696	1.33264	1.286759	1.255877	1.2376	1.2079	1.16632
Ca (Low Bin)		1.622325	1.556249	1.519491	1.445864	1.390537	1.347438	1.312913	1.269995	1.24107	1.223935	1.196067	1.156996
Ce (High Bin)		1.594	1.5544	1.4752	1.4158	1.3696	1.33264	1.286759	1.255877	1.2376	1.2079	1.16632	0
Ca (High Bin)		1.556249	1.519491	1.445864	1.390537	1.347438	1.312913	1.269995	1.24107	1.223935	1.196067	1.156996	0
da (Low Bin)	**User Defined**	0.267	0.299	0.320	0.373	0.426	0.479	0.532	0.616	0.690	0.743	0.848	1.059
da (High Bin)	**Backup**	0.299	0.320	0.373	0.426	0.479	0.532	0.616	0.690	0.743	0.848	1.059	1.372
da (Bin Midpoint)	**Filter**	0.283	0.310	0.347	0.399	0.452	0.505	0.574	0.653	0.716	0.795	0.954	1.216
date & time (µg/m3)	**Mass (µg/m3)**	0.283 µm	0.309 µm	0.346 µm	0.399 µm	0.452 µm	0.505 µm	0.573 µm	0.652 µm	0.716 µm	0.795 µm	0.953 µm	1.215 µm

The portions in blue are exported into a Matlab program which solves for the yellow portion which includes the Cunningham Slip Correction Factors and revised aerodynamic bin values. This is only done for the bin sizes below 1 µm. The MatLAB program follows.

APPENDIX V

GRIMM particle model (cont.)

MatLAB code for Cunningham Slip Correction Solver

```
% IMPORTANT - READ THIS
% Ensure "equiv" matrix is in Matlab workspace as it provides
the necessary
% input data.  "equiv" matrix comes from Excel.

% variable definitions
% de = equivalent volume diameter (micrometer)
% da = aerodynamic diameter (micrometer)
% Ca = Cunningham slip correction factor for aerodynamic
diameter
% Ce = Cunningham slip correction factor for equivalent volume
diameter
% X = Shape factor
% pe = Equivalent volume density particle (g/cm3)
% pa = Equivalent aerodynamic density (g/cm3)
% la = Mean free path (micrometer)

% initialize constants
pa = 1;  % standard density (g/cm3)
L = .066; % mean free diameter (micrometers)

% Calculate Low Bin Values
for z=1:12

    pe = equiv(1,z); % Equivalent volume density particle from
equiv matrix
    X = equiv(2,z); % Shape Factor from equiv matrix
    de = equiv(3,z); % Low bin equivalent diameter from equiv
matrix


    syms Ca; %set up ca for Matlab solve function

    Ce = double(1 +((2.52*L)/de)); % calculate Ce low bin
    Ca = double(solve((de*sqrt((Ce*pe)/(Ca*pa*X))*(Ca-
1))/(2.52*L) == 1, Ca));  % calculate Ca low bin
    da = double((2.52*L)/(Ca-1)); % calculate da low bin

    aero(1,z) = Ce;
    aero(2,z) = Ca;
    aero(5,z) = da;
```

APPENDIX V

GRIMM particle model (cont.)

MatLAB code for Cunningham Slip Correction Solver (cont.)

```
end

%Calculate High Bin Values
for z=1:11

    aero(3,z) = aero(1,(z+1)); %calculate Ce high bin using Ce
from low bin
    aero(4,z) = aero(2,(z+1)); %calculate Ca high bin using Ca
from low bin
    aero(6,z) = aero(5,(z+1)); %calculate da high bin using da
from low bin

end

% assign correct equivalent high bin dia for last high bin
% see Hinds pg. 55; does not use slip correction since > 1
micrometer
aero(6,12) = equiv(4,12)*sqrt(equiv(1,12)/(pa*equiv(2,12)));

% Paste aero matrix into Excel
```

APPENDIX W

MATLAB Milling Model

```
% Semi-Circle Milling Force Model
% Revision 2 11/4/2014
% JL Miller
% changes include modifying program for semi-circular slot
configuration
% changes include reversing order of Ktc,Kte,Krc,Kre for cut and
paste
% changes include adding absolute value to instantaneous chip
thickness
% variables needed to run (from external Excel sources)
        % circinput (setup variables, single row array)
        % plytable (laminate plytable, single row array)
        % cutcoef (column matrix (0 to 180 deg)
(deg,Ktc,Kte,Krc,Kre)
% to run as homogeneous case
    % set "plythick" (plythickness) equal to "a" (axial depth of
cut)
    % set "totplies" (total plies) equal to 1
    % set plytable = 0 in row 1 (bottom of laminate from left to
right!!)
    % use one set of cutting coefficient in row 1
(0,Ktc,Kte,Krc,Kre)

% load input variables from circinput spreadsheet

a = circinput(1); % axial depth of cut in mm
c = circinput(2); % feed rate in mm/tooth
n = circinput(3); % spindle speed in rpm
cutentang = circinput(4); % cutter entry angle in radians
cutexitang = circinput(5); % cutter exit angle in radians
D = circinput(6); % cutter diameter in mm
N = circinput(7); % number of flutes in cutter
helix = circinput(8); % cutter helix angle in radians
angint = circinput(9); % angular integration interval in radians
totplies = circinput(10); % number of total plies in laminate
plythick = circinput(11); % ply thickness
steperply = circinput(12); % number of vertical integration
steps per ply

% Setup calculations
cutpitch = (2*pi)/N; % cutter pitch angle
K = round(((2*pi)/angint)+angint); % number of angular
integration steps (radians) round up
```

```
%  L = a/heightint; % number of axial integration steps
count = 0; %temporary counter for debugging
numfullply = ceil(a/plythick);  % number of full plies for axial
depth of cut, round up
partialply = rem(a,plythick); % partial ply thickness by axial
depth of cut, if not integer number of plies
bottomply = totplies - numfullply + 1;  % bottom ply at tip of
cutting tool
% heightint

for i = 1:K, % angular integration loop (radians)
    imang(i) = cutentang + ((i*angint)-angint); % immersion
angle of flute bottom, from 0
    checkimang=imang(1);  % just a check of the first value of
imang(1)
    Fx(i)=0;  % initialize force integration registers
    Fy(i)=0;  % initialize force integration registers
    Ft(i)=0;  % initialize force integration registers
    Fr(i)=0;  % initialize force integration registers
    % trackchipthick(i) = 0;  % initialize
    for k = 1:N,  % calculate force contributions of all teeth
        imang1 = imang(i) + ((k-1)*cutpitch); % immersion angle
for tooth k

         trackimang1(i)=imang1;  % track imersion angle 1

        imang1 = imang1-(floor(imang1/(2*pi))*(2*pi));  %
correct multiple rotation angles
        imang2 = imang1; % memorize present immersion
plycount = 0; % initialize ply counter

        for j = bottomply:totplies,  % integrate along axial
depth of cut by ply from bottom to top
            plycount = plycount + 1;  % keep track of number
plies moving up cutter
            for s = 1:steperply, % number of steps per ply
                if (j == bottomply) & (partialply >0)  % if on
bottom ply at tip of cutter and partial ply
                    axpos = partialply;  % equals partial ply
thickness only for bottom ply
                    heightint = partialply;  % height
integration for bottom ply only
                    plycount = 0;  % for case where there is
partial ply on the bottom ply
                else
                    axpos = (s*plycount*(plythick/steperply)) +
partialply;
```

```
                    heightint = plythick/steperply;  % height
integration for plies other than bottom
                end

            imang2 = imang1 - ((2*tan(helix)/D)*axpos); % update
immersion angle due to to helix

             trackimang2(i)=imang2;  % track immersion angle 2

            imang2 = imang2-(floor(imang2/(2*pi))*(2*pi));  %
correct multiple rotation angles

            % below for up and down milling
            % up milling entry angle 0, exit angle < 1.57 (1.57
half immersion)
            % down milling entry angle > 4.71, exit angle 6.28
(4.17 half immersion)
            % face milling ex. entry 75 and exit 105 deg
            % slot milling entry angle = 3.14 and exit angle =
6.28 (full)
            if (imang2 >= cutentang) & (imang2 <= cutexitang)  %
if cutting edge is cutting then:

            % find cutting coefficients using ply table lookup,
+1 becuase
            % matlab can't index with 0 row number, 0 deg is row
1,
            % 1 deg is row 2, 2 deg is row 3, etc.
                Ktc = cutcoef(plytable(j)+1,2);
                Kte = cutcoef(plytable(j)+1,3);
                Krc = cutcoef(plytable(j)+1,4);
                Kre = cutcoef(plytable(j)+1,5);

                chipthick = abs(c*sin(imang2)); % chip thickness
at this point, note abs value

                difFt = heightint*((Ktc*chipthick)+ Kte); %
differential tangential force
                difFr = heightint*((Krc*chipthick)+ Kre); %
differential radial force
                difFx = (-difFt*cos(imang2))-
(difFr*sin(imang2));  % differential feed force
                difFy = (difFt*sin(imang2))-(difFr*cos(imang2));
% differential normal force
                Fx(i) = Fx(i) + difFx; % sum Fx feed cutting
force
```

```
                Fy(i) = Fy(i) + difFy; % sum Fy normal cutting
force
                Ft(i) = Ft(i) + difFt; % sum Ft tangential
cutting cutting force
                Fr(i) = Fr(i) + difFr; % sum Fr radial cutting
cutting force
            end % end if section
            end % next s step in ply
        end % next j ply
    end % next k
    Rxy(i) = sqrt((Fx(i)^2)+(Fy(i)^2));  % resultant cutting
force Fx,Fy
    Rtr(i) = sqrt((Ft(i)^2)+(Fr(i)^2));  % resultant cutting
force Ft,Fr
    Tc(i) = D/2*Ft(i)/1000; % cutting torque in Nm

    %  Plotting Structure:  Create FPlot matrix of deg, by each
variable
    FPlot(i,1) = i*(360/K);  % convert i to degrees, assume 1
rotation
    FPlot(i,2) = Fx(i); % for plotting Fx
    FPlot(i,3) = Fy(i); % for plotting Fy
    FPlot(i,4) = Ft(i); % for plotting Ft
    FPlot(i,5) = Fr(i); % for plotting Fr
    FPlot(i,6) = Rxy(i); % for plotting Resultant force based on
Fx,Fy (Fa)
    FPlot(i,7) = Rtr(i); % for plotting Resultant force based on
Ft,Fr (Fa)
    FPlot(i,8) = Tc(i); % for cutting torque (moment)
    % FPlot(i,9) = trackchipthick(i);  % just to hold a value
for chip thick
end % next i
% plotting
plot(FPlot(:,1), FPlot(:,6)); hold on;
figure
subplot(4,1,1);
plot(FPlot(:,1), FPlot(:,2), FPlot(:,1), FPlot(:,3));  % Fx, Fy
subplot(4,1,2);
plot(FPlot(:,1), FPlot(:,4), FPlot(:,1), FPlot(:,5));  % Fr, Ft
subplot(4,1,3);
plot(FPlot(:,1), FPlot(:,6), FPlot(:,1), FPlot(:,7));  % Rxy,
Rtr
subplot(4,1,4);
plot(FPlot(:,1), FPlot(:,8));  % Tc
```

APPENDIX X

Acoustic Emission Read File for creating Excel Output and Quick Plot

```
% Script for reading AE text file and creating excel output file
% AE text file created from AEWinPost
% First, manually import AE text file into Matlab
% Program works with array called "data", import default
% Pretrigger is first requested
% Program writes excel file for post processing

format longg;  %long format for number display

display('Input File Verification');  %Verifying file input
information
display(strcat(textdata{8,1},textdata{9,1},' from AE file'));
%Relative time recorded
display(strcat(textdata{12,1},textdata{13,1}, ' from AE file'));
%Number of samples
pretrigger=str2num(strrep(textdata{37,1},'Pre-trigger (Samples):
-',''));  %pretrigger extraction from file
display(strcat(textdata{37,1},' from AE file'));
display(strcat('Pre-Trigger used in calculation:
',num2str(pretrigger))); %Displays extracted pre-trigger

display(strcat('AE file line 0 #, time, voltage: ',
num2str(data(1,1:3))));  %Display AE file #0 for reference
against relative time

% display(pretrigger);  %Displays extracted pre-trigger
display(strcat('External trigger time zero becomes #, time,
voltage: ', num2str(data((pretrigger+1),1:3))));  %Verify
external trigger zero
%display%(data((pretrigger+1),1:3));  %Verify relative time
recorded, added 1 because of 0 row conversion

%pretrigger=input('enter pretrigger in microseconds ');
starttime=input('Enter start point in seconds for excel output
file:: ' );  %sample start point
duration=input('Enter duration of excel output file in seconds::
');  %sample duration
filename=input('Enter file name and tab name for excel output
file:: ','s');  %excel output file name

datarows=length(data); % number of rows in raw AE text data file
```

```
Posttrigger=data((pretrigger+1):datarows,1:3);  %only post
trigger data

numberrows=length(Posttrigger);  % number of rows of text data
file at postrigger

Deltatime=Posttrigger(1,2); % amount to subract to make
posttrigger t=0

Triggertime=Posttrigger;  % post trigger data

Triggertime(1:numberrows,2)=Posttrigger(1:numberrows,2)-
Deltatime;
% Triggertime row 1, time is now zero, and all subsequent rows
adjusted

numsamples = duration*1000000;  % number of samples based on
input duration

Sample=Triggertime(((starttime*1000000)+1):((starttime*1000000)+
numsamples),1:3);
% Note 1 microsoft correction with start time since AE text
starts at row 0
%Creating Sample array

%Sample=Triggertime((starttime*1000000):((starttime*1000000)+num
samples),1:3);
%version without correction

xlswrite(filename,Sample,filename,'A1');   %Writing Sample Array
to excel output file

% Plotting routines generated below to verify excel output

%CREATEFIGURE(X1,Y1)
%  X1:  vector of x data
%  Y1:  vector of y data

%  Auto-generated by MATLAB on 11-Jun-2012 14:10:16

% Create figure
figure1 = figure;

% Create axes
axes1 = axes('Parent',figure1);
box(axes1,'on');
hold(axes1,'all');
```

```
% Create plot
% plot(X1,Y1);

plot(Sample(:,2),Sample(:,3));  % generate graphical data
preview

% Create xlabel
xlabel('Time');

% Create ylabel
ylabel('Voltage');

% Create title
% title('AE Waveform');
title(strcat(filename,' Waveform'));
```

APPENDIX Y

NC Programs

```
%
O12346 (CLIMB THEN CONVENTIONAL - 10 passes)
T1 H01 G43
G91          (incremental)
M03 S6000      (spindle on cw)

G01 F25. Y0.03 (feed 25 .03 in Y-pass1)
G01 F25. X-6.5 (climb cut in X)
G01 F25. Y0.03 (feed into part .03)
G01 F25. X6.5  (Conventional cut in X)

G01 F25. Y0.03 (feed 25 .03 in Y-pass2)
G01 F25. X-6.5 (climb cut in X)
G01 F25. Y0.03 (feed into part .03)
G01 F25. X6.5  (Conventional cut in X)

G01 F25. Y0.03 (feed 25 .03 in Y-pass3)
G01 F25. X-6.5 (climb cut in X)
G01 F25. Y0.03 (feed into part .03)
G01 F25. X6.5  (Conventional cut in X)

G01 F25. Y0.03 (feed 25 .03 in Y-pass4)
G01 F25. X-6.5 (climb cut in X)
G01 F25. Y0.03 (feed into part .03)
G01 F25. X6.5  (Conventional cut in X)

G01 F25. Y0.03 (feed 25 .03 in Y-pass5)
G01 F25. X-6.5 (climb cut in X)
G01 F25. Y0.03 (feed into part .03)
G01 F25. X6.5  (Conventional cut in X)

G01 F25. Y0.03 (feed 25 .03 in Y-pass6)
G01 F25. X-6.5 (climb cut in X)
G01 F25. Y0.03 (feed into part .03)
G01 F25. X6.5  (Conventional cut in X)

G01 F25. Y0.03 (feed 25 .03 in Y-pass 7)
G01 F25. X-6.5 (climb cut in X)
G01 F25. Y0.03 (feed into part .03)
G01 F25. X6.5  (Conventional cut in X)

G01 F25. Y0.03 (feed 25 .03 in Y-pass8)
G01 F25. X-6.5 (climb cut in X)
G01 F25. Y0.03 (feed into part .03)
```

```
G01 F25. X6.5  (Conventional cut in X)

G01 F25. Y0.03 (feed 25 .03 in Y-pass9)
G01 F25. X-6.5 (climb cut in X)
G01 F25. Y0.03 (feed into part .03)
G01 F25. X6.5  (Conventional cut in X)

G01 F25. Y0.03 (feed 25 .03 in Y-pass10)
G01 F25. X-6.5 (climb cut in X)
G01 F25. Y0.03 (feed into part .03)
G01 F25. X6.5  (Conventional cut in X)

M30          (end of program)
%

%
O12350 (Climb Cut Only)
T1 H01 G43
G91
M03 S6000
G01 F25. Y0.03
G01 F25. X-6.5
M05
G00 Z3.
G00 X6.5
G00 Z-3.
M30
%

%
O12346 (CLIMB THEN CONVENTIONAL)
T1 H01 G43
G91          (incremental)
M03 S6000     (spindle on cw)
G01 F25. Y0.03 (feed 25 .03 in Y)
G01 F25. X-6.5 (climb cut in X)
G01 F25. Y0.03 (feed into part .03)
G01 F25. X6.5  (Conventional cut in X)
M30          (end of program)
%

%
O12355               (Half slot Milling ALL CUTS)
T1 H01 G43
G91
```

```
M03 S4800
G01 F25. X-1.
G01 F9. Y1.
G02 X2. Y0. I1. J0. F9.
G01 F9. Y-1.
G01 F25. X-1.

M03 S5300
G01 F25. X-1.625
G01 F13.25 Y1.
G02 X3.25 Y0. I1.625 J0. F13.25
G01 F13.25 Y-1.
G01 F25. X-1.625

M03 S5600
G01 F25. X-2.25
G01 F17.5. Y1.
G02 X4.5 Y0. I2.25 J0 F17.5
G01 F17.5 Y-1.
G01 F25. X-2.25

M03 S5800
G01 F25. X-2.875
G01 F21.75 Y1.
G02 X5.75 Y0. I2.875 J0 F21.75
G01 F21.75 Y-1.
G01 F25. X-2.875

M03 S5943
G01 F25. X-3.5
G01 F26. Y1.
G02 X7. Y0. I3.5 J0. F26.
G01 F26. Y-1.
G01 F25. X-3.5
M30
%
```

APPENDIX Z

MATLAB Program for reading and plotting DynoWare data

```
% Script for reading Dynoware text file
% Dynamometer text file created from Dynoware
% First, manually IMPORT Dynoware file into Matlab
% Program works with array called "dyno" -- convert "data" to
"dyno"
format longg;  %long format for number display
rpm = input('Enter rpm of cutting test:: ' );  %rpm of cutting
test
starttime = input('Enter start point in seconds for excel output
file:: ' );  %sample start point
cutterrot = input('Enter number of cutter rotations to be
displayed ' );  %number of cutter rotations
%input verification
%optional -- display sample rate from header at later date
display('Input File Verification');  %Verifying file input
information
display('Sample rate of 7862');

%duration calculation -- can be used for AE read in
duration = cutterrot * 1/(rpm/60); %requested duration for plot
in sec.
display(strcat('duration of plot in seconds:
',num2str(duration)));  %display plot time

startpt = round(1 + (starttime*7862));  %array index of dyno for
start of plot sample
endpt = round(startpt + (duration*7862));  %array index of dyno
for end of plot sample

numsamples = endpt - startpt + 1; %number of samples in plot
 display(strcat('Number of samples in plot:
',num2str(numsamples)));  %display number of sample
t = dyno(startpt:endpt,1);
Fx = dyno(startpt:endpt,2);
Fy = dyno(startpt:endpt,3);
Fz = dyno(startpt:endpt,4);
Mz = dyno(startpt:endpt,5);
Ft = dyno(startpt:endpt,8);
Fr = dyno(startpt:endpt,9);
Pulse = dyno(startpt:endpt,7);
Fa = sqrt((Fx.^2)+(Fy.^2));
deg = (0:(numsamples-1)) * ((cutterrot*360)/(numsamples-1));
%vector of degrees for each sample
doubleaxisplottest1(t,Fx,t,Fy)
plotpulse(t,Fa,deg,Pulse)
```